# SCHOLARLY PUBLICATIONS

*A CURRENT AWARENESS BULLETIN*
*OF RESEARCH OUTPUT*

## @DTU

(37th Edition)

***JANUARY 2016***

## BY: CENTRAL LIBRARY


DELHI TECHNOLOGICAL UNIVERSITY
(FORMERLY *DELHI COLLEGE OF ENGINEERING)*
GOVT. OF N.C.T. OF DELHI
SHAHBAD DAULATPUR, MAIN BAWANA ROAD
DELHI 110042

# PREFACE

This is the **Thirty Seventh** Issue of Current Awareness Bulletin started by Delhi Technological University, Central Library. The aim of the bulletin is to compile, preserve and disseminate information published by the faculty, students and alumni for mutual benefits. The bulletin also aims to propagate the intellectual contribution of Delhi Technological University (DTU) as a whole to the academia.

The bulletin contains information resources available in the internet in the form of articles, reports, presentations published in international journals, websites, etc. by the faculty and students of DTU. The publications of faculty and student which are not covered in this bulletin may be because of the reason that the full text either was not accessible or could not be searched by the search engine used by the library for this purpose.

The learned faculty and students are requested to provide their uncovered publications to the library either through email or in CD, etc to make the bulletin more comprehensive.

This issue contains the information published during **January 2016**. The arrangement of the contents is alphabetical. The full text of the article which is either subscribed by the university or available in the web is provided in this bulletin.

**Central Library**

# CONTENTS


1. A novel power-flow model of multi-terminal VSC-HVDC systems, ***3.Shagufta Khan*** & ***3.Suman Bhowmick***, Electrical Engineering, DTU

2. A proposed unified framework for the recognition of human activity by exploiting the characteristics of action dynamics, ***3.Dinesh K Vishwakarma***, ***3.Rajiv Kapoor*** & ***3.Ashish Dhiman***, Electronics and Communication Engineering, DTU

3. Comparative Performance of Wiener Filter and Adaptive Least Mean Square Based Control for Power Quality Improvement, ***8.Manoj Badoni***, ***3.Alka Singh***, Senior Member, IEEE, and Bhim Singh, Electrical Engineering, DTU

4. Complementary Performance enhancement of PV energy system Through thermoelectric generation, ***3.Vishal Verma***, Aarti kane & Bhim Singh, DTU

5. COMPUTATION OF OPTIMUM PARAMETERS OF A HALF EFFECT WATER-LITHIUM BROMIDE VAPOUR ABSORPTION REFRIGERATION SYSTEM, ***3.Akhilesh Arora***, Manoj Dixit & S.C. Kaushik, Mechanical Engineering, DTU

6. Dynamic Cumulative Residual and Past Inaccuracy Measures, Vikas Kumar & ***3.H. C. Taneja***, Applied Mathematics, DTU

7. Dynamic Positive-Feedback Source-Coupled Logic (D-PFSCL), ***3.Kirti Gupta***, ***3.Neeta Pandey*** & Maneesha Gupta, E C Engineering, DTU

8. Economic Analysis of the Nisargruna Based Bio-Methanation Plant, 3.Aftab Anjum, ***3.Mohit Gupta*** & ***3.Aadish Jain***, Mechanical Engineering, DTU

9. Effect of ion beam irradiation on dielectric properties of BaTiO3 thin film using surface plasmon resonance, ***3.Savita Sharma***, Ayushi Paliwal, Monika Tomar, Fouran Singh, ***3. Nitin K. Puri*** & Vinay Gupta, Applied Physics, DTU

**10.** Estimation of Electrical Energy Generation from Waste to Energy using Incineration Technology, ***3.Shubham Gupta*** & ***3.R. S. Mishra***, Mechanical Engineering, DTU

**11.** Finite Element Analysis of Silicon Gate All Around Nanowire Transistor with Different High-k dielectrics, Neel Chatterjee, Kshitij Chopra, ***3.Kshitij Bhatia***, Sujata Pandey, Applied Physics, DTU

**12.** Grid Integration of Fuel Cell with MPPT under Variable Air Flow Rate, Gitanjali Pandove & ***3. Mukhtiar Singh***, Electrical Engineering, DTU

**13.** Identification, selection and evaluation of COTS selection criteria using Fuzzy Set Theory, Rakesh Garg, R. K. Sharma & ***3.Kapil Sharma***, Computer Science and Engineering, DTU

**14.** In Silico Designing and Analysis of Inhibitors against Target Protein Identified through Host-Pathogen Protein Interactions in Malaria, ***3.Monika Samant***, Nidhi Chadha, Anjani K. Tiwari & ***3 Yasha Hasija***, Biotechnology, DTU

**15.** Microwave device jig characterization for ferromagnetic resonance induced spin Hall effect measurement in bilayer thin films, Saood Ahmad, Jyoti Shah, Anurag K Katiyar, ***3.Rishu Chaujar***, ***3.Nitin K Puri***, P S Negi & R K Kotnala, Applied Physics, DTU

**16.** Mixing of Various Renewable Energy Technologies towards Development of Village Energy Need, ***3.Shubham Gupta*** & ***3.R. S. Mishra***, Mechanical Engineering, DTU

**17.** Irreversibility Optimization Using Energy-Exergy Analysis of Three Stage Vapour Compression Refrigeration Systems with Flash-Intercooler Using Ecofriendly Refrigerants (R410a, R290, R600, R600a, R1234yf, R125, R717 And R134A) for Reducing Global Warming and Ozone Depletion, ***3.R.S. Mishra***, ***3.Kapil Chopra*** & ***3.V. Sahni***, Mechanical Engineering, DTU

**18.** Performance analysis of Solar Distillation and Domestic Heating Water System, ***3.Rajesh Kumar***, ***3.Santosh Kumar*** & ***3.Jigmet Lodoea***, Mechanical Engineering, DTU

**19.** Power gain assessment of ITO based Transparent Gate Recessed Channel (TGRC) MOSFET for RF/Wireless Applications, ***6.Ajay Kumar***, ***6.Neha Gupta*** & ***3.Rishu Chaujar,*** Microelectronics Research Lab, Engineering Physics, DTU

**20.** Prediction of Heat Affected Zone and Effect of Heat Input in GTA Welded Al Alloy 6061 Pawan Kumar, Kishor P Kolhe, Sham H Mankar & ***3.Sanjay Kumar***, DTU

**21.** Production of Biodiesel from a mixture of Karanja and Linseed oils: Optimization of process parameters, Sanjay Mohite, Sudhir Kumar, ***3.Sagar Maji*** & ***3.Amit Pal***, Mechanical Engineering, DTU

**22.** Ranking and selection of commercial off-the-shelf using fuzzy distance based approach, **3.Rakesh Garg**, R. K. Sharma & ***3.Kapil Sharma***, Computer Science and Engineering, DTU

**23.** Recent advances on multicue object tracking: a survey, Gurjit Singh Walia & ***3.Rajiv Kapoor***, Electronics and Communication, DTU

**24.** Role of Plasma and Doping Elements on the Growth and Field Emission Properties of Metallic Carbon Nanotube (CNT) Tip Placed over Cylindrical Surface Research Article, ***3.Suresh C. Sharma***, ***6.Aarti Tewari*** & ***6.Ravi Gupta***, Applied Physics, DTU

**25.** Role of Plasma Parameters on the Growth and Field Emission Properties of 2D Graphene Sheet Research Article, ***6.Neha Gupta***, ***6.Aarti Tewari*** & ***3.Suresh C. Sharma***, Applied Physics, DTU

**26.** Studies of Banana SAP used as mordant for natural dye, Shyam Barhanpurkar, Prabhakar Bhat, ***3.Alok Kumar*** & Roli Purwar, Polymer Science, DTU

**27.** TCAD RF performance investigationof Transparent GateRecessed Channel MOSFET, ***6.AjayKumar***, ***6.NehaGupta*** & ***3.RishuChaujar***, Engineering Physics, DTU

**28.** Terahertz Radiation Emission from A Surface Wave Pumped Free Electron Laser Research Article, ***6..Jyotsna Panwar***, ***3.Suresh C. Sharma*** & ***3.Rinku Sharma***, Applied Physics, DTU

**29.** Thermodynamic Performance Comparison Using HFO-1234yf and HFO-1234ze in the High Temperature Cascade Refrigeration Systems and Ecofriendly Refrigerants in Low Temperature Applications***, 3.R. S. Mishra***, Mechanical Engineering, DTU

**30.** Unified framework for human activity recognition: An approach using spatial edge distribution and -transform, ***3.D. K. Vishwakarma***, ***3.Rajiv Kapoor*** & ***3.Ashish Dhiman***, Electronics and Communication Engineering, DTU

**31.** Vapour Compression Refrigeration Technology for Sustainable Development, ***3.R.S. Mishra***, Mechanical Engineering, DTU

| | |
|---|---|
| ***1. Vice Chancellor*** | ***1.1. Ex Vice Chancellor*** |
| ***2. Pro Vice Chancellor*** | ***2.1. Ex Pro Vice Chancellor*** |
| ***3. Faculty*** | ***3.1. Ex Faculty*** |
| ***4. Teaching-cum-Research Fellow*** | |
| ***5. Alumni*** | |
| ***6. Research Scholar*** | ***6.1. Ex Research Scholar*** |
| ***7. PG Scholar*** | ***7.1. Ex PG Scholar*** |
| ***8. Undergraduate Student*** | ***8.1. Ex Undergraduate Student*** |

Electric Power Systems Research 133 (2016) 219–227

Contents lists available at ScienceDirect

Electric Power Systems Research

journal homepage: www.elsevier.com/locate/epsr

# A novel power-flow model of multi-terminal VSC-HVDC systems

Shagufta Khan*, Suman Bhowmick

*Department of Electrical Engineering, Delhi Technological University, Delhi 110042, India*

ARTICLE INFO

*Article history:*
Received 27 August 2015
Received in revised form
17 November 2015
Accepted 23 December 2015

*Keywords:*
VSC
M-VSC-HVDC
PTP
Control modes

ABSTRACT

This paper proposes a generalized framework for power-flow modeling of voltage-sourced converter (VSC) based multi-terminal high voltage DC (M-VSC-HVDC) network(s). The modeling strategy pertains to the point-to-point (PTP) HVDC network configuration, which is more generic and widely used than its back-to-back (BTB) counterpart. Unlike existing models, the modulation indices of the pulse width modulation (PWM) converters also appear as unknowns in the proposed model. In addition, both the HVDC network topology and the number of converters can be arbitrarily chosen in the generalized model. For the master converter, either the DC side voltage or the modulation index can be chosen as an unknown, which renders the model more versatile. Numerous case studies carried out by applying different control modes to varying topologies of M-VSC-HVDC networks incorporated in the IEEE-300 bus test system validate the model.

© 2015 Elsevier B.V. All rights reserved.

## 1. Introduction

Since the last few decades, the construction of both generation facilities and in particular, new transmission lines have been delayed due to energy cost, environmental concerns, rights-of-way (RoW) restrictions and other legislative and cost problems. In this respect, HVDC transmission has proved to be a cost-effective option. For a given power level, a DC link requires a smaller RoW, simpler and cheaper transmission towers, reduced conductor and insulator costs along with reduced losses [1,2]. A HVDC link can also be used to improve system reliability by interconnecting two asynchronous AC systems. In addition, stability considerations limit the length of AC transmission links. No such limitation exists for HVDC transmission. All these led to the development of HVDC transmission systems.

The first commercial application of HVDC transmission took place between the Swedish mainland and the island of Gotland in 1954, using mercury-arc valves. Subsequently, the first 320 MW, thyristor based HVDC system was commissioned in 1972 between Canadian provinces of New-Brunswick and Quebec [2]. Over the years, developments in conversion equipment reduced their size and cost which resulted in more widespread use of HVDC transmission. This so-called line-commutated converter (LCC) based HVDC technology now constitutes the bulk of the installed DC transmission capacity over the world.

The advancement of power-electronics led to the development of insulated gate bipolar transistor (IGBT), which paved the way for VSC based HVDC technology. VSC-HVDC offered significant advantages over the LCC-HVDC like low cost and size of converter stations and reliable operation with weak AC systems. VSC-HVDC based on PWM scheme has the advantage of independent active and reactive power control, along with reduction in filter size [1–7]. Compact, modular design of the VSC facilitates rapid installation, commissioning and relocation. In recent years, the harnessing of renewable sources of energy is becoming an attractive and necessary option, in light of dwindling fossil fuel resources. The use of lighter and stronger cross linked poly-ethylene (XLPE) DC cables allows VSC based HVDC systems particularly attractive for offshore transmission. This has made possible the integration of offshore wind farms with AC grids and augments power transmission capacity.

Unlike a two-terminal HVDC interconnection, a M-VSC-HVDC system is more versatile and better capable of utilizing the economic and technical advantages of the VSC HVDC technology. It is also better suited if futuristic integration of renewable energy sources are planned [8–10].

In a M-VSC-HVDC system, the converters stations can be located closely, in the same sub-station or remotely, at different locations. The corresponding configurations are known as BTB or PTP, respectively. Most of the M-VSC-HVDC systems installed worldwide are in the PTP configuration, their DC sides being interconnected through DC links or cables.

In a M-VSC-HVDC system, one of the converters acts as a master or secondary converter [11] while the rest act as slave or primary converters. The master converter controls the voltage magnitude of its AC terminal bus while the slave converters control the active and

* Corresponding author. Tel.: +91 01222323889.
*E-mail addresses:* khan.shagufta7@gmail.com (S. Khan), suman.bhowmick@dce.ac.in (S. Bhowmick).

http://dx.doi.org/10.1016/j.epsr.2015.12.031
0378-7796/© 2015 Elsevier B.V. All rights reserved.

**List of symbols**

| | |
|---|---|
| $V_{DCg}, I_{DCg}, P_{DCg}$ | DC voltage, current and power of the $g$th converter, respectively |
| $m_g$ | modulation index of the $g$th converter |
| $Y_{ij}$ | magnitude of the element in the $i$th row and $j$th column of the bus admittance matrix |
| $\phi_{ij}$ | phase angle of the element in the $i$th row and $j$th column of the bus admittance matrix |
| $R_{DCij}$ | resistance of the DC link between DC buses '$i$' and '$j$' |
| $\mathbf{Y_{DC}}$ | admittance matrix of the DC grid |
| $Y_{DCij}$ | element in the $i$th row and $j$th column of the admittance matrix of the DC network |
| $\mathbf{Z_{sh}}$ | leakage impedance of the converter coupling transformer |
| $R_{sh}, X_{sh}$ | resistance and leakage reactance of the coupling transformer, respectively |
| $V_i, \theta_i$ | bus voltage magnitude (rms) and phase angle at AC bus '$i$', respectively |
| $V_{shg}, \theta_{shg}$ | magnitude (rms) and phase angle of the output voltage of the $g$th converter, respectively |
| $P_{shg}, Q_{shg}$ | active and reactive powers at the terminal end of the line connected to the $g$th converter, respectively |

reactive powers at the terminal end of the lines connecting them to their terminal buses. Some excellent research works on control of VSC-HVDC systems are reported in [12–16].

Now, for planning, operation and control of AC power systems incorporating M-VSC-HVDC networks, suitable power-flow models of such hybrid systems is an essential requirement. [11,17–26] present some comprehensive power-flow and optimal power flow (OPF) models of VSC-HVDC systems. However, it is observed that most of the existing models do not take into account the modulation index of a converter. The modulation index '$m$' is an important parameter for VSC operation. It has been reported that although an increase in the amount of reactive power delivered by the VSC at the PCC bus requires a high value of '$m$', overmodulation ($m > 1$) results in low-order harmonics in the AC voltage spectrum [27]. For these reasons, usually, '$m$' should not exceed unity. In a similar manner, a low '$m$' limits the maximum fundamental AC side voltage of the VSC. Practical ranges of the modulation index '$m$' have been reported in [28].

Thus, operational considerations limit the minimum and maximum value of the modulation index. A power-flow model should yield the value of '$m$' and '$V_{DC}$' directly, for a given operating condition, so that it can be checked whether '$m$' lies within its specified limits (with sufficient margin for a dynamic response), along with '$V_{DC}$'. In the proposed model, the converter modulation indices appear as unknowns along with the converter DC side voltages and the phase angles of the converter AC side voltages. However, inclusion of the modulation index as an unknown does not exclude them from being effective control variables for the VSC operation. In this respect, it may be noted that control variables like tap settings of transformers and phase shifters along with converter control angles (firing angles of rectifiers or extinction angles of inverters) in LCC-HVDC have long been included as unknowns in Newton–Raphson Power-flow algorithms [29–31].

Furthermore, both the HVDC network topology and the number of converters can be arbitrarily chosen in the generalized model. This model also offers the flexibility of choosing either the DC side voltage or the modulation index of the master converter as an unknown. This renders the model more versatile. Due to the adoption of the AC–DC unified method, the quadratic convergence of the Newton–Raphson algorithm is retained in the proposed model.

Numerous case studies are carried out by applying different control modes to varying topologies of M-VSC-HVDC networks incorporated in the IEEE-300 bus test system [32]. The convergence features validate the proposed model.

The remainder of this paper is structured as follows: In Section 2, the mathematical modeling for the PTP M-VSC-HVDC is presented. Section 3 details the Newton power flow equations for the PTP M-VSC-HVDC system. The case studies and results are presented in Section 4. The conclusions are presented in Section 5.

## 2. Mathematical modeling of the PTP-M-VSC HVDC system

For the power flow modeling of a M-VSC-HVDC system, the following assumptions have been adopted [5,11].

- The supply voltages are sinusoidal and balanced (contain only fundamental frequency and positive sequence components).
- The harmonics generated by the converters are neglected.
- The switches are assumed to be ideal.

In the rest of the paper, bold quantities represent complex variables and matrices while regular variables denote scalar variables. All the transmission lines are represented by their equivalent-pi models.

Fig. 1 shows a '$n$' bus AC power system network incorporating a M-VSC-HVDC system, which is interconnected in the PTP configuration. The M-VSC-HVDC comprises '$p$' converters which are connected to '$p$' AC buses through their respective coupling transformers. Without loss of generality, it is assumed that the '$p$' VSC converters are connected to AC buses '$i$', '$(i+1)$', and so on, up to bus '$(i+p-1)$'. The equivalent circuit of Fig. 1 is shown in Fig. 2.

In Fig. 2, the VSCs are represented by '$p$' fundamental frequency, positive sequence voltage sources. The $g$th $(1 \le g \le p)$ voltage source $\mathbf{V_{shg}}$ (not shown) is connected to AC bus '$(i+g-1)$' through the leakage impedance $\mathbf{Z_{shg}} = R_{shg} + jX_{shg}$ of the $g$th coupling transformer.

Now, let $\mathbf{y_{shg}} = 1/\mathbf{Z_{shg}}$. Then, from Fig. 2, the current through the $g$th $(1 \le g \le p)$ coupling transformer can be written as

$$\mathbf{I_{shg}} = \mathbf{y_{shg}} \left( \mathbf{V_{shg}} - \mathbf{V_{i+g-1}} \right) \tag{1}$$

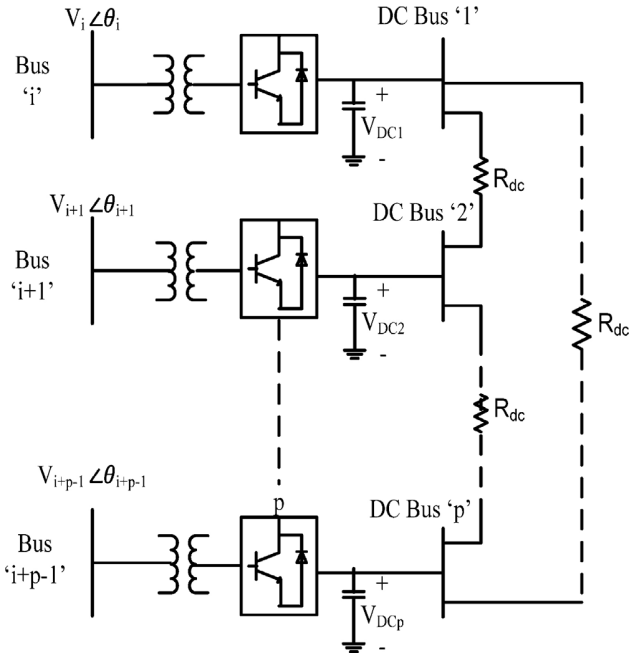


**Fig. 1.** Schematic diagram of a '$p$' terminal PTP M-VSC-HVDC system.

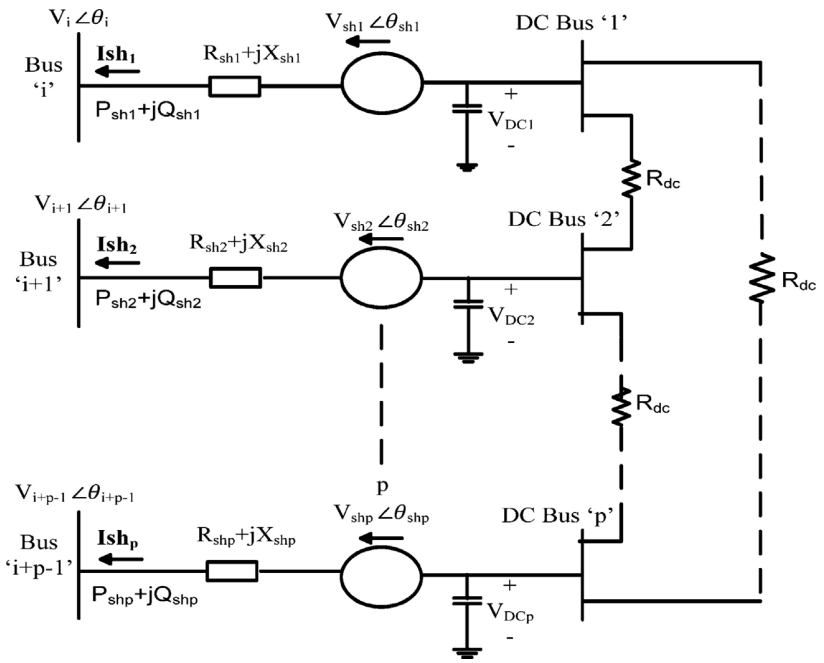


**Fig. 2.** Equivalent circuit of the '*p*' terminal PTP M-VSC-HVDC system.

where $\mathbf{V_{shg}}$ is the voltage phasor representing the output of the *g*th VSC and is given by $\mathbf{V_{shg}} = V_{shg}\angle\theta_{shg} = m_g c V_{DCg}\angle\theta_{shg}$, where '$m_g$' is the modulation index of the *g*th $(1 \le g \le p)$ converter and '*c*' is a constant which depends on the type of converter [18]. The *g*th converter is connected to the AC terminal bus '$(i+g-1)$' whose voltage is represented by the phasor $\mathbf{V_{i+g-1}} = V_{i+g-1}\angle\theta_{i+g-1}$.

Hence from Fig. 2, the net current injection at the AC bus '$(i+g-1)$' connected to the *g*th $(1 \le g \le p)$ converter can be written as

$$\mathbf{I_{i+g-1}} = \left[\mathbf{Y^{old}_{(i+g-1)(i+g-1)}} + \mathbf{y_{shg}}\right]\mathbf{V_{i+g-1}} + \sum_{\mathbf{k=1,\ k\neq i+g-1}}^{\mathbf{n}} \mathbf{Y_{(i+g-1)k}V_k} - \mathbf{y_{shg}V_{shg}} \quad (2)$$

where $\mathbf{Y^{old}_{(i+g-1)(i+g-1)}} = \mathbf{y_{(i+g-1)0}} + \sum_{\mathbf{k=1,\ k\neq i+g-1}}^{\mathbf{n}} \mathbf{y_{(i+g-1)k}}$ is the self admittance of bus '$(i+g-1)$' for the original '*n*' bus AC system without any converter and '$\mathbf{y_{(i+g-1)0}}$' accounts for the shunt capacitances of all the transmission lines connected to bus '$(i+g-1)$'.

Substituting Eqs. (1) in (2) and manipulating, we get

$$\mathbf{I_{i+g-1}} = \sum_{\mathbf{k=1}}^{\mathbf{n}} \mathbf{Y_{(i+g-1)k}V_k} - \mathbf{y_{shg}V_{shg}} \quad (3)$$

where $\mathbf{Y_{(i+g-1)(i+g-1)}} = \mathbf{Y^{old}_{(i+g-1)(i+g-1)}} + \mathbf{y_{shg}}$ is the new value of self admittance for the bus '$(i+g-1)$' with the *g*th VSC connected.

Thus, with the *g*th $(1 \le g \le p)$ VSC connected, the net injected active power at the corresponding AC terminal bus can be written as

$$P_{i+g-1} = Re\left\{\mathbf{V_{i+g-1}I^*_{i+g-1}}\right\} = \sum_{k=1}^{n} V_{i+g-1}V_k Y_{(i+g-1)k}\cos\left[\theta_{i+g-1} - \theta_k - \phi_{(i+g-1)E}\right] - m_g c V_{DCg} V_{i+g-1} y_{shg}\cos\left(\theta_{i+g-1} - \theta_{shg} - \phi_{shg}\right) \quad (4)$$

since $V_{shg} = m_g c V_{DCg}$, as already discussed.

In a similar manner, the net injected reactive power at bus '*n*' can be written as

$$Q_{i+g-1} = \sum_{k=1}^{n} V_{i+g-1}V_k Y_{(i+g-1)k}\sin\left[\theta_{i+g-1} - \theta_k - \phi_{(i+E-1)k}\right] - m_g c V_{DCg} V_{i+g-1} y_{shg}\sin(\theta_{i+g-1} - \theta_{shg} - \phi_{shg}) \quad (5)$$

Also from Fig. 2, the active and reactive power flows at the terminal end of the line connecting the *g*th VSC to AC bus '$(i+g-1)$' can be written as

$$P_{shg} = Re\left[\mathbf{V_{i+g-1}I^*_{shg}}\right] = m_g c V_{DCg} V_{i+g-1} y_{shg}\cos\left(\theta_{i+g-1} - \theta_{shg} - \phi_{shg}\right) - V^2_{i+g-1} y_{shg}\cos\phi_{shg} \quad (6)$$

$$Q_{shg} = m_g c V_{DCg} V_{i+g-1} y_{shg}\sin\left(\theta_{i+g-1} - \theta_{shg} - \phi_{shg}\right) + V^2_{i+g-1} y_{shg}\sin\phi_{shg} \quad (7)$$

now from Fig. 2, in the '*p*' terminal DC system, the net current injection at the *h*th $(1 \le h \le p)$ DC bus i.e. at the DC terminal of the *h*th VSC, is given as

$$I_{DCh} = \sum_{j=1}^{p} Y_{DChj} V_{DCj} \quad (8)$$

where $Y_{DChj} = -1/R_{DChj}$, '$R_{DChj}$' being the DC link resistance between DC buses '*h*' and '*j*'.now from Fig. 2, the active power delivered by the the *g*th $(1 \le g \le p)$ converter at its AC terminal can be written as $P_{ACg} = Re\left(\mathbf{V_{shg}I^*_{shg}}\right)$. In a similar manner, the net power injection at the *g*th DC terminal is given by $P_{DCg} = V_{DCg}I_{DCg} = \sum_{j=1}^{p} V_{DCg}V_{DCj}Y_{DCgj}$.

Again from Fig. 2, if the converter is lossless, $P_{ACg} = -P_{DCg}$ i.e.

$$Re\left(\mathbf{V_{shg}I^{*}_{shg}}\right) = -\sum_{j=1}^{p} V_{DCg}V_{DCj}Y_{DCgj} \tag{9}$$

On substitution of Eq. (1) and manipulating, we get,

$$\left(m_g c V_{DCg}\right)^2 y_{shg}\cos\phi_{shg} - m_g c V_{DCg}V_{i+g-1}y_{shg} \times \cos\left(\theta_{shg} - \theta_{i+g-1} - \phi_{shg}\right) + \sum_{j=1}^{p} V_{DCg}V_{DCj}Y_{DCgj} = 0 \tag{10}$$

or, $f_g = 0$

where $1 \le g \le p$.

Thus, '$p$' independent equations are obtained.

It can be observed that unlike in [11,17,19,20,24,25], where the VSC is modeled as an injected voltage, the proposed model incorporates the VSC modulation index '$m$' as an unknown. [21] has considered '$m$' for all the VSCs as specified quantities, which is possible only as a special case for the master converter. In addition, while the analyses of [17,18,22] are limited to two terminal VSC-HVDC systems, the proposed model pertains to a M-VSC-HVDC configuration, similar to [11]. The proposed model also includes the converter transformer losses into account, unlike [20]. However, the proposed model has considered the control specifications at the AC terminal buses similar to [11], unlike at the converter buses in [21].

Again from Fig. 2, for the VSC-HVDC system with '$p$' converters, there will be one master converter and '$(p-1)$' slave converters. The master converter is used to control the voltage magnitude of its AC terminal bus while the slave converters operate in the PQ or PV control modes. The slave converters control the active and reactive power flows $P_{sh}$ and $Q_{sh}$ {as given by Eqs. (6) and (7), respectively} at the terminal end of the lines connecting the converters to their respective AC terminal buses. Again, without loss of generality, if the $q$th $(1 \le q \le p)$ converter is chosen to be the master converter, the additional equations obtained for the slave converters can be expressed as

$$P^{sp}_{shg} - P^{cal}_{shg} = 0 \tag{11}$$

$$Q^{sp}_{shg} - Q^{cal}_{shg} = 0 \tag{12}$$

$$\forall g, \quad 1 \le g \le p, \quad g \ne q$$

In the above equations, $P^{sp}_{shg}$ and $Q^{sp}_{shg}$ are the specified active and the reactive powers respectively, in the line connecting the $g$th converter $\{1 \le g \le p, \quad g \ne q\}$ to its AC terminal bus '$(i+g-1)$' while $P^{cal}_{shg}$ and $Q^{cal}_{shg}$ are their calculated values which can be obtained using Eqs. (6) and (7).

Thus, we get '$(2p-2)$' independent equations.

Now, the master converter '$q$' controls the voltage magnitude at its AC terminal bus. For the AC terminal bus corresponding to the $g$th converter, if $V^{sp}_{i+g-1}$ is the bus voltage control reference and $V^{cal}_{i+g-1}$ is the calculated value of the voltage magnitude at bus '$(i+g-1)$', this can be expressed as

$$V^{sp}_{i+g-1} - V^{cal}_{i+g-1} = 0 \tag{13}$$

$\forall g$, $1 \le g \le p$, $g = q$, {as the $q$th $(1 \le q \le p)$ converter is chosen to be the master converter}.

It may be noted that a slave converter may be used to control the AC bus voltage magnitude rather than the line reactive power, in which case Eq. (12) becomes

$$V^{sp}_{i+g-1} - V^{cal}_{i+g-1} = 0 \tag{14}$$

$$\forall g, \quad 1 \le g \le p, \quad g \ne q.$$

Now, similar to AC power flow, a slack bus is chosen for the DC power flow and its voltage is pre specified. It serves the dual role of providing the DC voltage control and balancing the active power exchange among the converters. From Fig. 2, in the '$p$' terminal DC system, the first terminal is chosen as the DC slack bus, by convention. This is represented as

$$V^{sp}_{DC1} - V^{cal}_{DC1} = 0 \tag{15}$$

Instead of specifying $V_{DC1}$, the modulation index '$m_1$' of the first converter can also be specified as

$$m^{sp}_{1} - m^{cal}_{1} = 0 \tag{16}$$

At this stage, it is worthwhile to take stock of the unknown and the specified quantities. Corresponding to each converter, three new variables enter into the picture. These include the converter modulation index '$m$', the converter DC side voltage '$V_{DC}$' and the phase angle '$\theta_{sh}$' of the converter AC output voltage (phasor). Also, as discussed earlier, the DC side voltage '$V_{DC1}$' of the first converter is chosen as a slack bus. Thus, due to incorporation of the VSC-HVDC comprising '$p$' converters, '$(3p-1)$' additional variables need to be solved.

Against this, we have '$p$' independent equations corresponding to the function '$f$' {Eq. (10)} along with '$(2p-2)$' independent equations for the line active and reactive powers {Eqs. (11) and (12)} corresponding to the '$(p-1)$' slave converters. This gives as $(3p-2)$ independent equations. Now as the master converter '$q$' controls the voltage of its AC terminal bus, the net reactive power injection

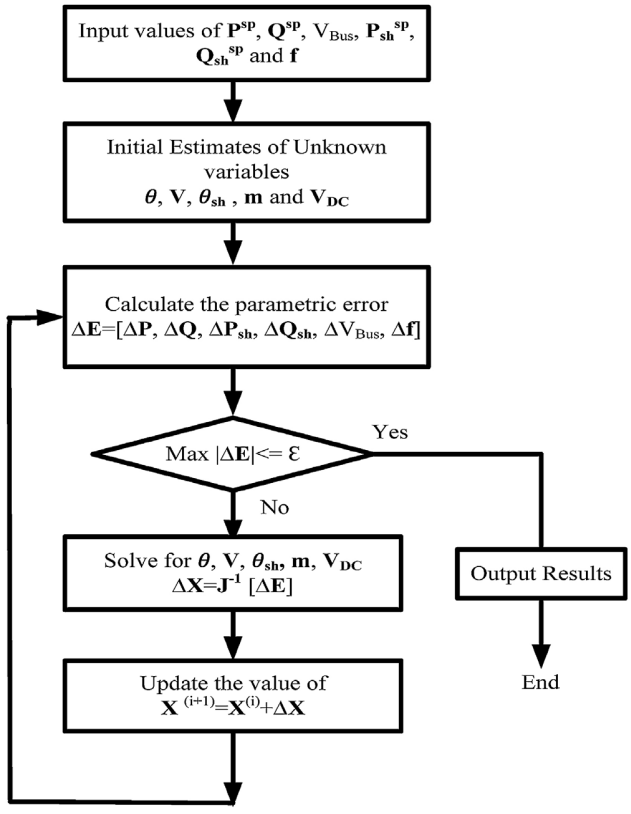


**Fig. 3.** Flow Chart of the NR AC–DC power-flow algorithm.

at that bus is available as a specified quantity. This can be expressed as

$$Q_{i+g-1}^{sp} - Q_{i+g-1}^{cal} = 0 \quad (17)$$

$\forall g,\ 1 \le g \le p,\ g = q$. This completes the formulation.

## 3. Newton power flow equations of the PTP M-VSC-HVDC system

In Fig. 1, without any loss of generality, if it is assumed that there are '$r$' generators connected at the first '$r$' buses of the '$n$' bus AC system with bus 1 being the slack bus, then the Newton power-flow equation for the AC power system network incorporated with the '$p$' terminal HVDC system can be written as

Solve: $\boldsymbol{\theta}, \mathbf{V}, \mathbf{X}$

Specified: $\mathbf{P}, \mathbf{Q}, \mathbf{R}$

Where,

$$\theta = \left[\theta_2, \ldots, \theta_n\right]^T, \quad \mathbf{V} = [V_{r+1}, \ldots, V_n]^T, \boldsymbol{\theta}_{\mathbf{sh}} = \left[\theta_{\mathrm{sh}1}, \ldots, \theta_{\mathrm{p}}\right]^T,$$

$$\mathbf{m} = \left[m_1, \ldots, m_p\right]^T$$

$$\mathbf{V_{DC}} = \left[V_{\mathrm{DC}2}, \ldots, V_{\mathrm{DC}p}\right]^T \quad \text{and} \quad \mathbf{X} = \left[\boldsymbol{\theta}_{\mathbf{sh}}^{\mathbf{T}}, \mathbf{m}^{\mathbf{T}}, \mathbf{V}_{\mathbf{DC}}^{\mathbf{T}}\right]^T$$

$$\mathbf{P} = [P_2, \ldots, P_n]^T, \quad \mathbf{Q} = [Q_{r+1}, \ldots, Q_n]^T, \quad \mathbf{P_{sh}} = [P_{\mathrm{sh}2}, \ldots P_{\mathrm{sh}p}],$$

$$\mathbf{Q_{sh}} = \left[Q_{\mathrm{sh}2}, \ldots, Q_{\mathrm{sh}p}\right],$$

$$\boldsymbol{f} = \left[f_1, \ldots, f_p\right] \quad \text{and} \quad \boldsymbol{R} = \left[\mathbf{P_{sh}}, \mathbf{Q_{sh}}, V_{i+q-1}, \boldsymbol{f}\right]^T$$

Thus the basic load flow equation for the Newton power flow analysis is given below

$$\begin{bmatrix} \mathbf{J_{old}} & \begin{matrix} \frac{\partial \mathbf{P}}{\partial \boldsymbol{\theta}_{\mathbf{sh}}} & \frac{\partial \mathbf{P}}{\partial \mathbf{m}} & \frac{\partial \mathbf{P}}{\partial \mathbf{V_{DC}}} \\ \frac{\partial \mathbf{Q}}{\partial \boldsymbol{\theta}_{\mathbf{sh}}} & \frac{\partial \mathbf{Q}}{\partial \mathbf{m}} & \frac{\partial \mathbf{Q}}{\partial \mathbf{V_{DC}}} \end{matrix} \\ \begin{matrix} \frac{\partial \mathbf{R}}{\partial \boldsymbol{\theta}} & \frac{\partial \mathbf{R}}{\partial \mathbf{V}} \end{matrix} & \begin{matrix} \frac{\partial \mathbf{R}}{\partial \boldsymbol{\theta}_{\mathbf{sh}}} & \frac{\partial \mathbf{R}}{\partial \mathbf{m}} & \frac{\partial \mathbf{R}}{\partial \mathbf{V_{DC}}} \end{matrix} \end{bmatrix} \begin{bmatrix} \Delta\boldsymbol{\theta} \\ \Delta\mathbf{V} \\ \Delta\boldsymbol{\theta}_{\mathbf{sh}} \\ \Delta\mathbf{m} \\ \Delta\mathbf{V_{DC}} \end{bmatrix} = \begin{bmatrix} \Delta\mathbf{P} \\ \Delta\mathbf{Q} \\ \Delta\mathbf{R} \end{bmatrix} \quad (18)$$

In Eq. (18), $\mathbf{J_{old}}$ is the conventional load flow (without incorporating HVDC link) Jacobian sub-block given as follows

$$\mathbf{J_{old}} = \begin{bmatrix} \frac{\partial \mathbf{P}}{\partial \boldsymbol{\theta}} & \frac{\partial \mathbf{P}}{\partial \mathbf{V}} \\ \frac{\partial \mathbf{Q}}{\partial \boldsymbol{\theta}} & \frac{\partial \mathbf{Q}}{\partial \mathbf{V}} \end{bmatrix}$$

In Eq. (18), '$\Delta\mathbf{P}$', '$\Delta\mathbf{Q}$' and '$\Delta\mathbf{R}$' represent the mismatch vectors. In addition, $\Delta\boldsymbol{\theta}$, $\Delta\mathbf{V}$, $\Delta\boldsymbol{\theta}_{\mathbf{sh}}$, $\Delta\mathbf{m}$ and $\Delta\mathbf{V_{DC}}$ represent correction vectors. It may be noted that '$\Delta m_1$' may replace '$\Delta V'_{\mathrm{DC}_1}$' in '$\Delta\mathbf{R}$', in which case the elements of $\mathbf{J}$ would be modified accordingly.

Fig. 3 depicts the flow chart of the NR power flow method for the PTP M-VSC-HVDC system.

## 4. Case studies and results

Numerous case studies were carried out to validate the proposed model. In each of these case studies, a M-VSC-HVDC network was incorporated in the IEEE 300-bus test system. The resistances and the leakage reactances of all the converter transformers were taken as 0.001 p.u. and 0.1 p.u., respectively, for all the case studies. The resistance of each DC link was taken as 0.01 p.u. for all the case studies. In addition, the value of '$c$' for the VSC based converters was uniformly chosen to be $1/2\sqrt{2}$ [18]. A convergence tolerance of $10^{-10}$ p.u. was uniformly adopted for all the case studies.

In each of the case studies, 'NI' and 'CT' denote the number of iterations and the computational time in seconds {on a Intel® Core(TM) 2 Duo CPU T6400, 2 GHz, 2 GB RAM processor} for the algorithm to converge.

Case study I: In this case study, three separate studies are conducted with a three terminal VSC-HVDC network incorporated in the IEEE-300 bus test system. The three different studies are conducted to demonstrate the versatility of the proposed model. In all the three studies, the VSC-HVDC network is connected between AC buses 266, 270 and 271.

In the first study, the converter connected to AC bus no. '266' acts as the master converter while those connected to AC buses '270' and '271' act as slave converters. Both the slave converters operate in the PQ control mode. The master converter maintains the voltage magnitude of AC bus no. 266 at a value of 1.02 p.u. The active powers at the terminal end of the lines connecting the converters to AC

**Table 1**
First case study of IEEE-300 bus system with a three terminal VSC-HVDC network.

| HVDC link: connection details | | HVDC link: specified quantities | | Power flow solution | | |
|---|---|---|---|---|---|---|
| | | | | Base case power flow converged in six iterations (NI = 6) with CT = 0.56 s; $\boldsymbol{V_i} = 1.011\angle -11.24$; $\boldsymbol{V_j} = 1.011\angle -11.32$; $\boldsymbol{V_k} = 0.998\angle -17.67$; | | |
| | | | | AC terminal buses | HVDC variables | |
| Master converter | Slave converters | Master converter | Slave converters | Master converter | Slave converters | |
| I | $j, k$ | $V_{\mathrm{DC}i} = 3$; $V_i = 1.02$; | $P_{shj} = 0.2$; $Q_{shj} = 0.05$; $P_{shk} = 0.3$; $Q_{shk} = 0.05$; | $\boldsymbol{V_j} = 1.02\angle -11.29$; $\boldsymbol{V_k} = 1.0463\angle -10.1$; $\theta_i = -11.25$; | $\boldsymbol{V_{shi}} = 1.056\angle -13.94$; $m_i = 0.996$; NI = 6; CT = 1.11 s | $V_{\mathrm{DC}j} = 2.9992$; $V_{\mathrm{DC}k} = 2.9991$; $m_j = 0.9669$; $m_k = 0.9919$; $\boldsymbol{V_{shj}} = 1.0253\angle -10.19$; $\boldsymbol{V_{shk}} = 1.0517\angle -8.54$; |
| I | $j, k$ | $V_{\mathrm{DC}i} = 3$; $V_i = 1.02$; | $P_{shj} = 0.2$; $V_j = 1.02$; $P_{shk} = 0.3$; $V_k = 1$; | $\theta_i = -11.2565$; $\theta_j = -11.2889$; $\theta_k = -9.9264$; | $\boldsymbol{V_{shi}} = 1.067\angle -13.91$; $m_i = 1.0060$; NI = 6; CT = 1.05 s | $V_{\mathrm{DC}j} = 2.9992$; $V_{\mathrm{DC}k} = 2.9991$; $m_j = 0.9667$; $m_k = 0.9396$; $\boldsymbol{V_{shj}} = 1.0250\angle -10.1954$; $\boldsymbol{V_{shk}} = 0.9963\angle -8.1982$; |
| I | $j, k$ | $m_i = 1$; $V_i = 1.02$; | $P_{shj} = 0.3$; $Q_{shj} = 0.05$; $P_{shk} = 0.2$; $Q_{shk} = 0.05$; | $\boldsymbol{V_j} = 1.0201\angle -11.26$; $\boldsymbol{V_k} = 1.0436\angle -12.53$; $\theta_i = -11.2530$; | $\boldsymbol{V_{shi}} = 1.056\angle -13.93$; $V_{\mathrm{DC}i} = 2.9885$; NI = 6; CT = 1.08 s | $V_{\mathrm{DC}j} = 2.9876$; $V_{\mathrm{DC}k} = 2.9877$; $m_j = 0.9711$; $m_k = 0.9929$; $\boldsymbol{V_{shj}} = 1.0257\angle -9.6261$; $\boldsymbol{V_{shk}} = 1.0488\angle -11.4856$; |

*Note:* For the above case study, $i = 266$, $j = 270$, $k = 271$; Values of voltage magnitudes and phase angles are in p.u. and degrees, respectively.

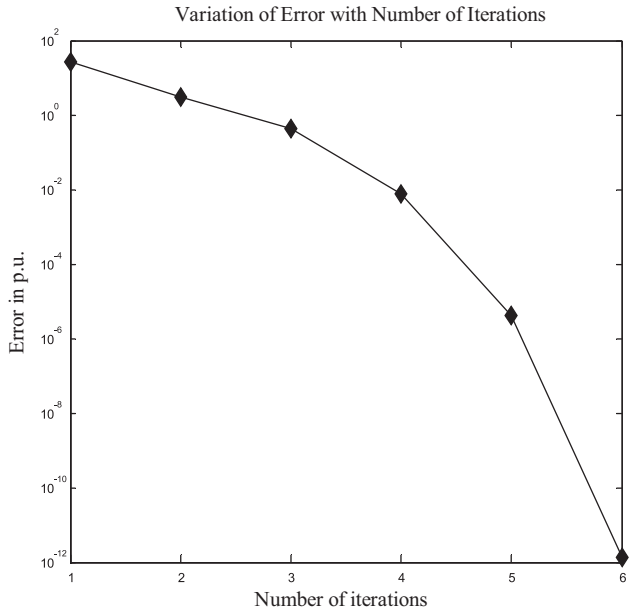


**Fig. 4.** Convergence characteristics for the base case power flow in IEEE-300 bus system.

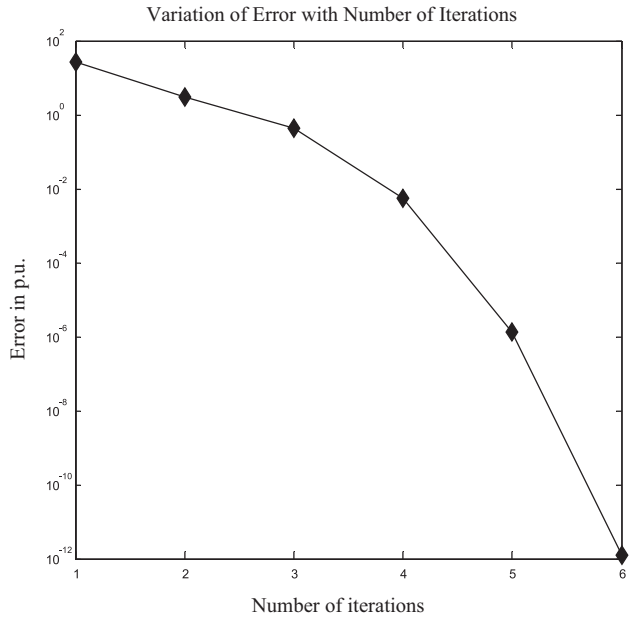


**Fig. 5.** Convergence characteristics for the first sub-case study of Table 1.

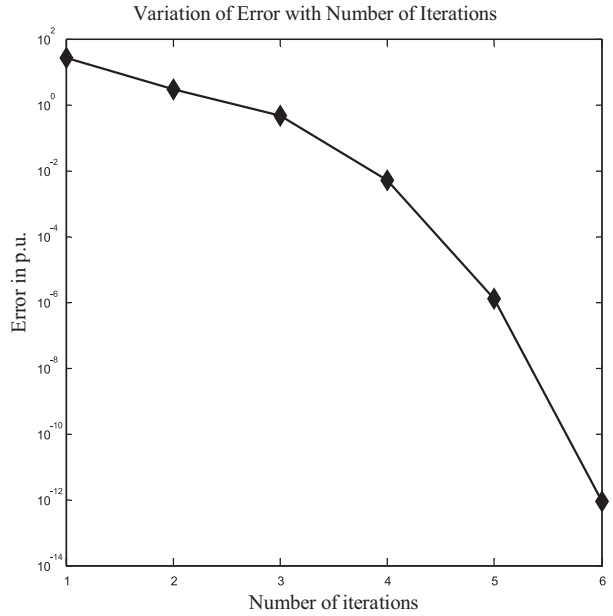


**Fig. 6.** Convergence characteristics for the second sub-case study of Table 1.

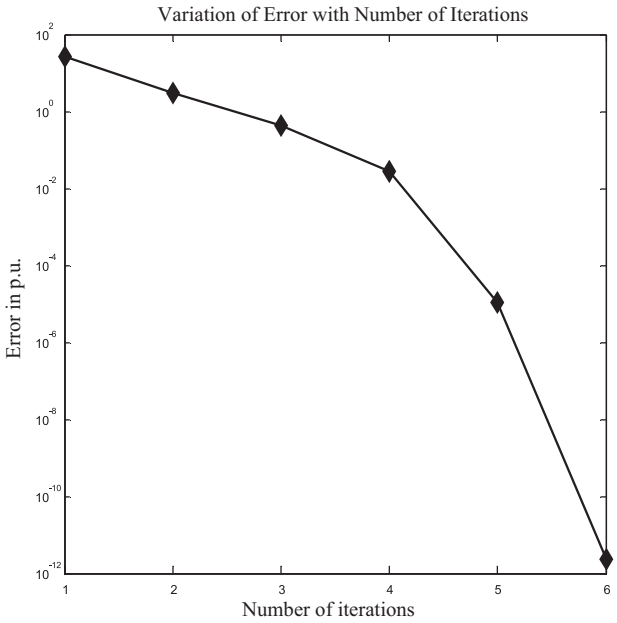


**Fig. 7.** Convergence characteristics for the third sub-case study of Table 1.

buses '270' and '271' are specified as 0.2 and 0.3 p.u., respectively. The line reactive powers for both the slave converters are specified as 0.05 p.u. These specified values are shown in the first row and columns 3–4 of Table 1. The power flow solution is shown in the first row and columns 5–7 of Table 1.

The subsequent study is conducted on the same AC–DC system but with both the slave converters (connected to AC buses '270' and '271') operated in the PV control mode. Their terminal end line active powers are specified as 0.2 and 0.3 p.u., respectively. The voltages of the AC buses '270' and '271' connected to the slave converters are specified as 1.02 and 1.0 p.u., respectively. The specified quantities for this study are shown in the second row and columns 3–4 of Table 1. The power flow results are shown in the second row and columns 5–7 of Table 1.

The third study is also conducted on the same AC–DC system as the first two studies. However, in this study, the modulation index of converter '1' is specified instead of its DC side voltage '$V_{DC1}$'. Thus unlike existing models, the flexibility of selection of either the modulation index or the DC side voltage for the converter exists. The specified quantities for this study are given in the third row and columns 3–4 of Table 1. The power flow results are shown in the third row and columns 5–7 of Table 1.

From Table 1, it can be observed that for all the three case studies, 'NI' is identical to that in the base case. However, due to increase in the number of unknowns involved, 'CT' increases than that in the base case. It however, does not vary much with the control modes.

The convergence characteristic plots (variation of mismatch error in p.u. with number of iterations) for the power flows of

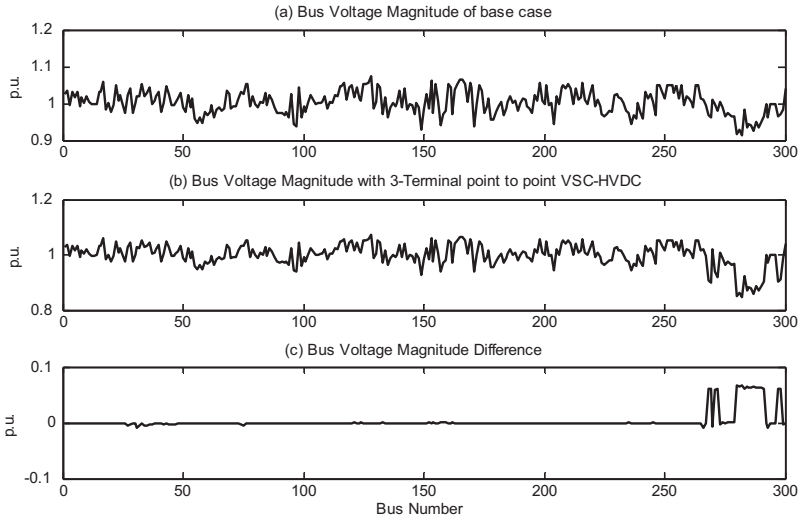


**Fig. 8.** Bus voltage profile for the first study (first row of Table 1).

**Table 2**
Second case study of IEEE-300 bus system with four-terminal VSC-HVDC network.

| HVDC link: connection details | | HVDC link: specified quantities | | Power flow solution | | |
|---|---|---|---|---|---|---|
| | | | | Base case power flow converged in six iterations (NI = 6) with CT = 0.56 s; $\boldsymbol{V_i} = 1.011\angle -11.24$ ; $\boldsymbol{V_j} = 1.011\angle -11.32$ ; $\boldsymbol{V_k} = 0.998\angle -17.67$ ; $\boldsymbol{V_l} = 0.981\angle -19.46$ ; | | |
| | | | | | HVDC variables | |
| Master converter | Slave converters | Master converter | Slave converters | AC terminal buses | Master converter | Slave converters |
| I | *j, k, l* | $V_{DCi} = 3$ ; $V_i = 1.02$ ; | $P_{shj} = 0.3$ ; $Q_{shj} = 0.1$ ; $P_{shk} = 0.2$ ; $Q_{shk} = 0.05$ ; $P_{shl} = 0.4$ ; $Q_{shl} = 0.05$ ; | $\boldsymbol{V_j} = 1.0202\angle -11.2814$ ; $\boldsymbol{V_k} = 1.0646\angle -3.0251$ ; $\boldsymbol{V_l} = 1.0731\angle -0.9414$ ; $\theta_i = -11.2660$ ; | $\boldsymbol{V_{shi}} = 1.0541\angle -16.09$ ; $m_i = 0.9938$ ; NI = 6; CT = 1.13 s | $V_{DCj} = 2.9990$ ; $V_{DCk} = 2.9991$ ; $V_{DCl} = 2.9989$ ; $m_j = 0.9721$ ; $m_k = 1.0088$ ; $m_l = 1.0175$ ; $\boldsymbol{V_{shj}} = 1.0308\angle -9.6522$ ; $\boldsymbol{V_{shk}} = 1.0697\angle -2.0213$ ; $\boldsymbol{V_{shl}} = 1.0788\angle 1.0362$ ; |

*Note:* For the above study, $i = 266$, $j = 270$, $k = 271$ and $l = 272$; Values of voltage magnitudes and phase angles are in p.u. and degrees, respectively.

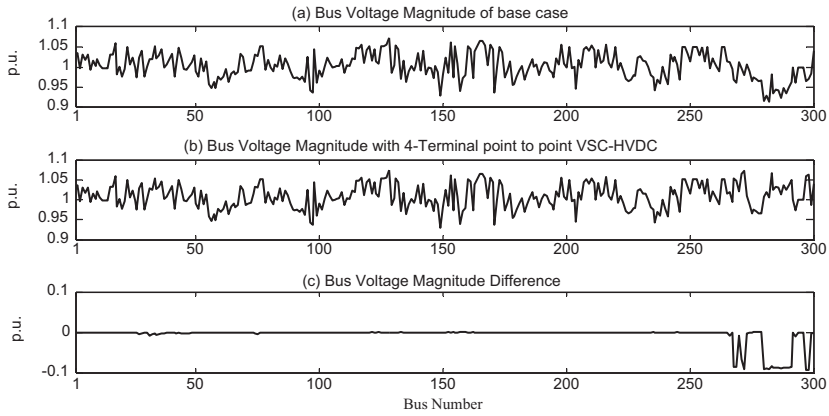


**Fig. 9.** Bus voltage profile for the study of Table 2.

the base case (without any VSC-HVDC network incorporated) and the three studies of Table 1 are shown in Figs. 4–7, respectively. From Figs. 5–7, it can be observed that the proposed model possesses quadratic convergence characteristics, similar to the base case power-flow. This is similar to [11,17,22,26], which employ unified method. However, in both [24,25], the quadratic convergence characteristics of the Newton–Raphson method is sacrificed due to adoption of the sequential power flow method. Also, the proposed model employs DC slack bus control (master–slave control) as in [11,17,21,24,26,27]. In this respect, [23,25] address VSC-HVDC droop control. However, the analysis of [23] does not include nonlinear power flow.

The bus voltage profile for the first study (first row of Table 1) is shown in Fig. 8. From Fig. 8, it is observed that the bus voltage

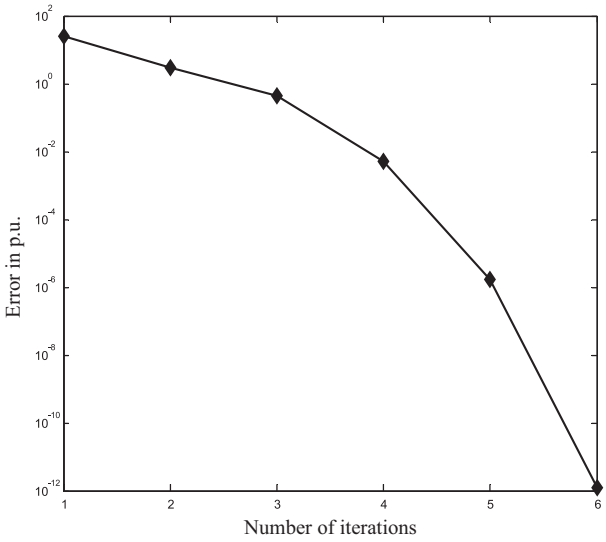


**Fig. 10.** Convergence characteristics for the study of Table 2.

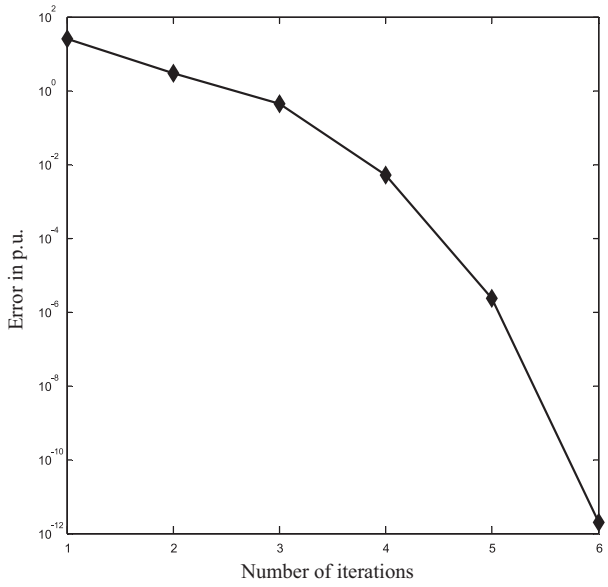


**Fig. 11.** Convergence characteristics for the study of Table 3.

profile hardly changes except for the AC terminal buses at which the VSCs are installed. Due to a lack of space, the voltage profiles for the second and third studies of Table 1 are not shown in this paper.

Case study II: In this case study, a four terminal VSC-HVDC network is incorporated in the test system between buses 266, 270, 271 and 272. The converter connected to AC bus no. 266 acts as the master converter while the converters connected to AC buses 270, 271 and 272 act as slave converters. The master converter maintains the voltage magnitude of AC bus no. 266 at 1.02 p.u. All the slave converters operate in the PQ control mode. The specified quantities are shown in columns 3–4 of Table 2. The power flow solution is shown in columns 5–7 of Table 2. The bus voltage profile for the above study is shown in Fig. 9. From Fig. 9, it can be observed that the bus voltage profile does not change much except at the AC terminal buses to which the converters are connected. The proposed model is validated by the quadratic convergence characteristic of this case study as shown in Fig. 10.

Case study III: This case study reiterates the versatility of the model. In this case study, a five terminal VSC-HVDC network is incorporated in the test system between buses 266, 270, 271, 272 and 273. The converter connected to bus no. 266 acts as the master converter while the converters connected to buses 270, 271, 272 and 273 act as slave converters. The master converter maintains the voltage magnitude of AC bus no. 266 at 1.02 p.u. The slave converters connected to buses 272 and 273 operate in the PV control mode while those connected to buses 270 and 271 operate in the PQ control mode. The specified quantities are shown in columns 3–4 of Table 3. The power flow solution is shown in columns 5–7 of Table 3. The convergence characteristic for this case study is shown in Fig. 11. From Fig. 11, it can again be observed that the proposed model is able to retain the quadratic convergence characteristics of the Newton–Raphson algorithm. The bus voltage profile for this case study could not be accommodated in this paper due to limitations of space.

From Tables 1–3, it can be observed that 'CT' increases slightly with increase in the number of DC terminals, due to the increase in the number of unknowns. However, 'NI' remains identical to that in the base case. It is also observed to be independent of the DC network size and topology. This demonstrates the robustness of the proposed algorithm.

Although the model was not applied on larger-size networks for real-scale system validation, the convergence features of the model were tested on the standard IEEE 300-bus test system. Since the proposed model exhibits quadratic convergence characteristics in the IEEE 300-bus test system, it is expected that these convergence characteristics would be retained in a larger-size network too.

**Table 3**
Study of IEEE-300 bus system with five terminal PTP VSC-HVDC system.

| HVDC link | | HVDC link specification | | Power flow solution | | |
|---|---|---|---|---|---|---|
| | | | | Base case power flow converged in six iterations (NI = 6) with CT = 0.56 s; $\boldsymbol{V_i} = 1.011\angle -11.24$; $\boldsymbol{V_j} = 1.011\angle -11.32$; $\boldsymbol{V_k} = 0.998\angle -17.67$; $\boldsymbol{V_l} = 0.981\angle -19.46$; $\boldsymbol{V_m} = 1.006\angle -17.47$; | | |
| | | | | | HVDC variables | |
| Master converter | Slave converters | Master converter | Slave converters | AC terminal buses | Master converter | Slave converters |
| I | *j, k, l, m* | $V_{DCi} = 3$; $V_i = 1.02$; | $P_{shj} = 0.3$; $V_l = 0.99$; $P_{shk} = 0.4$; $V_m = 1.01$; $P_{shl} = 0.3$; $P_{shm} = 0.4$; $Q_{shj} = 0.1$; $Q_{shk} = 0.05$; | $\theta_i = -11.2842$; $\theta_j = -11.2997$; $\theta_k = 0.1653$;; $\theta_l = 1.7717$; $\theta_m = -2.6040$; $V_j = 1.0202$; $V_k = 1.0059$; | $\boldsymbol{V_{shi}} = 1.0775\angle -18.6465$; $m_i = 1.0158$; NI = 6; CT = 1.15 s | $V_{DCj} = 2.9989$; $V_{DCk} = 2.9988$; $V_{DCl} = 2.9989$; $V_{DCm} = 2.9988$; $m_j = 0.9722$; $m_k = 0.9545$; $m_l = 0.9285$; $m_m = 0.9527$; $\boldsymbol{V_{shj}} = 1.0308\angle -9.6704$; $\boldsymbol{V_{shk}} = 1.0120\angle 2.4145$; $\boldsymbol{V_{shl}} = 0.9845\angle 3.5391$; $\boldsymbol{V_{sh\,m}} = 1.0101\angle -0.3564$; |

*Note:* For the above study, $i = 266$, $j = 270$, $k = 271$, $l = 272$ and $m = 273$; Values of voltage magnitudes and phase angles are in p.u. and degrees, respectively.

**Table 4**
A comparison of convergence features with existing models.

| Reference no. | Tolerance (p.u.) | No. of buses in the system | | NI | CT (in seconds) |
|---|---|---|---|---|---|
| | | AC | DC | | |
| [25] | $10^{-8}$ | 29 | 5 | Min: 3; Max: 15 (depending on wind power generation) | Min: 0.37 (for weak wind) Max: 1.99 (for strong wind) |
| [26] | $10^{-6}$ | 9 | 4 | 6 | 0.2 |
| | | 32 | 4 | 7 | 0.45 |
| Proposed model | $10^{-10}$ | 300 | NIL (base case) | 6 | 0.56 |
| | | | 3 | 6 | Min: 1.05 (PV); Max: 1.11 (PQ) |
| | | | 4 | 6 | 1.13 |
| | | | 5 | 6 | 1.15 |

A comparison of the convergence features of the proposed model vis-à-vis existing models in the literature is shown in Table 4.

## 5. Conclusions

In this paper, a unified Newton–Raphson Power Flow model of a AC–DC hybrid system has been presented. Unlike existing models, the modulation indices of the VSC converters can be expressed as unknowns in this model. The proposed methodology is implemented by incorporating different topologies of multi-terminal DC networks in the IEEE 300-bus test system. To demonstrate the versatility of the proposed model, multiple control modes for the VSC-HVDC are implemented. The power flow solutions and the excellent convergence characteristics validate the feasibility of the proposed work.

## References


[1] J. Arrillaga, Y.H. Liu, N.R. Watson, Flexible Power Transmission: The HVDC Options, John Wiley & Sons Ltd, Chichester, West Sussex, UK, 2007.
[2] V.K. Sood, HVDC and FACTS Controllers—Applications of Static Converters in Power Systems, Kluwer, Boston, USA, 2004.
[3] E. Acha, V.G. Agelidis, O. Anaya Lara, T.J.E. Miller, Power Electronic Control in Electrical Systems, Newnes, Butterworth, Oxford, 2002.
[4] E. Acha, C.R. Fuerte-Esquivel, H.A. Perez, C.A. Camacho, FACTS Modelling and Simulation in Power Networks, John Wiley, Chichester, West Sussex, UK, 2004.
[5] K.R. Padiyar, HVDC Power Transmission Systems, second ed., New Age International Publishers, New Delhi, India, 2012.
[6] X.P. Zhang, C. Rehtanz, B. Pal, Flexible AC Transmission Systems: Modelling and Control, Springer, Berlin, Germany, 2006.
[7] Gunnar Asplund, Application of HVDC light to power system enhancement, in: Proc. IEEE PES Winter Meeting, January, 2000.
[8] J. Blau, Europe plans a North Sea grid, IEEE Spectr. 47 (3) (2010) 12–13, March.
[9] Temesgen M. Haileselassie, Kjetil Uhlen, Power system security in a meshed North Sea HVDC grid, IEEE Proc. 101 (4) (2013) 978–990, Invited Paper.
[10] N. Flourentzou, V.G. Agelidis, G.D. Demetriades, VSC-based HVDC power transmission systems: an overview, IEEE Trans. Power Electron. 24 (3) (2009) 592–602.
[11] X.P. Zhang, Multiterminal voltage-sourced converter-based HVDC models for power flow analysis, IEEE Trans. Power Syst. 19 (Nov (4)) (2004) 1877–1884.
[12] W. Lu, B.T. Ooi, Premium quality power park based on multi-terminal HVDC, IEEE Trans. Power Delivery 20 (April (2)) (2005) 978–983.
[13] L. Xu, B.W. Williams, L. Yao, Multi-terminal DC transmission systems for connecting large offshore wind farms, in: IEEE Proc. PES General Meeting-Conversion and Delivery of Electrical Energy, 21st Century, July, 2008, pp. 1–7.
[14] R. da Silva, R. Teodorescu, P. Rodriguez, Power delivery in MTDC transmission system for offshore wind power applications, in: IEEE Proc. PES ISGT Europe, Oct, 2010, pp. 1–8.
[15] A. Moawwad, M.S. El Moursi, W. Xiao, J.L. Kirtley Jr., Novel configuration and transient management control strategy for VSC-HVDC, IEEE Trans. Power Syst. 29 (Sep (5)) (2014) 2478–2488.
[16] W. Chen, X. Zhu, L. Yao, X. Ruan, Z. Wang, Y. Cao, An interline DC power-flow controller (IDCPFC) for multiterminal HVDC system, IEEE Trans. Power Delivery 30 (Aug (4)) (2015) 2027–2036.
[17] C. Angeles-Camacho, O.L. Tortelli, E. Acha, C.R. Fuerte-Esquivel, Inclusion of a high voltage DC voltage source converter model in a Newton–Raphson power flow algorithm, Proc. Inst. Electr. Eng. Gen. Transm. Distrib. 150 (Nov (6)) (2003) 691–696.
[18] A. Martinez, C. Esquivel, H. Perez, E. Acha, Modeling of VSC-Based HVDC systems for a Newton–Raphson OPF algorithm, IEEE Trans. Power Syst. 22 (Nov (4)) (2007) 1794–1799.
[19] J. Cao, W. Du, H.F. Wang, An improved corrective security constrained OPF for meshed AC/DC grids with multi-terminal VSC-HVDC, IEEE Trans. Power Syst. 31 (1) (2015) 1–11, Early Access Articles.
[20] Q. Chen, G.-Q. Tang, W. Xun, AC–DC power flow algorithm for multi-terminal VSC-HVDC systems, Electr. Power Automot. Equip. 25 (6) (2005) 1–6.
[21] L. Gengyin, Z. Ming, H. Jie, L. Guangkai, L. Haifeng, Power flow calculation of power systems incorporating VSC-HVDC, in: Proc. Int. Conf. Power System Technology (PowerCon), vol. 2, Nov, 2004, pp. 1562–1566.
[22] E. Acha, Behzad Kazemtabrizi, Luis M. Castro, A new VSC HVDC model for power flows using the Newton–Raphson method, IEEE Trans. Power Syst. 28 (August (3)) (2013) 2602–2612.
[23] T.M. Haileselassie, K. Uhlen, Impact of DC line voltage drops on power flow of MTDC using droop control, IEEE Trans. Power Syst. 27 (3) (2012) 1441–1449.
[24] J. Beerten, S. Cole, R. Belmans, Generalized steady-state VSC MTDC model for sequential AC/DC power flow algorithms, IEEE Trans. Power Syst. 27 (May (2)) (2012) 821–829.
[25] W. Wang, Mike Barnes, Power flow algorithms for multi-terminal VSC-HVDC with droop control, IEEE Trans. Power Syst. 29 (July (4)) (2014) 1721–1730.
[26] M. Baradar, M. Ghandhari, A multi-option unified power flow approach for hybrid AC/DC grids incorporating multi-terminal VSC-HVDC, IEEE Trans. Power Syst. 28 (Aug (3)) (2013) 2376–2383.
[27] A. Yazdani, R. Iravani, Voltage-Sourced Converters in Power Systems: Modeling, Control and Applications, Wiley-IEEE Press, New Jersey, USA, 2010, pp. 171.
[28] G. Daelemans, VSC HVDC in Meshed Networks, Katholieke Universiteit Leuven, Belgium, 2008, pp. 11, Master's Thesis.
[29] Norris M. Peterson, Scott E. Meyer, Automatic adjustment of transformer and phase-shifter taps in the Newton power flow, IEEE Trans. Power Apparatus Syst. PAS-90 (1) (1971) 103–108.
[30] D.A. Braunagel, L.A. Kraft, J.L. Whysong, Inclusion of DC converter and transmission equations directly in a Newton power flow, IEEE Trans. Power Apparatus Syst. PAS-95 (1) (1976) 76–88.
[31] J. Arrillaga, B.J. Harker and K.S. Turner, "Clarifying an ambiguity in recent AC–DC load-flow formulations", Proceedings of the IEE, 127, Part-C(5), pp. 324–325.
[32] ⟨http://www.ee.washington.edu/research/pstca⟩.

This article has been accepted for publication in a future issue of this journal, but has not been fully edited. Content may change prior to final publication. Citation information: DOI 10.1109/TIE.2016.2515558, IEEE Transactions on Industrial Electronics



# Comparative Performance of Wiener Filter and Adaptive Least Mean Square Based Control for Power Quality Improvement

Manoj Badoni, Alka Singh, *Senior Member, IEEE,* and Bhim Singh, *Fellow, IEEE*

***Abstract*—This paper presents a three phase shunt active power filter (SAPF) for mitigating power quality problems at the distribution level. Power quality problems such as harmonics, reactive power and unbalancing in the loads are mitigated for both unity power factor and voltage regulation modes. A three phase voltage source converter (VSC) is used as a SAPF for performing all these functions. The linear optimum discrete time filtering technique namely Wiener filtering based control algorithm is developed for the extraction of reference supply currents from distorted load currents. The performance of Wiener filter is compared with least mean square (LMS) adaptive filter based control algorithm. Experimental validation of proposed control algorithm has been performed on a prototype developed in the laboratory. The filtering action of SAPF is able to achieve the total harmonic distortion (THD) of supply current within the limit specified by an IEEE-519 standard.**

***Index Terms*—LMS, Power quality, SAPF, unity power factor, voltage regulation, Wiener filter.**

## I. Introduction

An increase in the power electronics based loads causes injection of harmonics at the distribution level, which is responsible for distorting supply voltages and currents. These types of loads are nonlinear in nature and can be classified as harmonics current sources and harmonics voltage sources. Some examples of harmonic producing loads are ac-dc converters, switch mode power supplies, electric arc furnaces, inverters and computers. Unbalancing in loads and unregulated supply voltages are some other causes of poor power quality [1]-[2]. Guidelines for harmonics limit and other power quality related problems are stipulated in IEEE and IEC international standards [3]-[4]. An improvement in the quality of power can be attained with passive, active and hybrid filters [5]. Achievements in the field of digital signal processing and digital filtering techniques have led to the design of active power filter (APF) for power quality improvement. The APF is a shunt compensating device and named as shunt active power filter (SAPF) which is used for mitigating current related power quality problems such as harmonics reduction, compensation of reactive power and balancing the loads. It can be controlled to work in power factor correction mode or voltage regulation mode.

The effectiveness of SAPF depends upon the control technique used for estimation of reference currents and generation of switching pulses. Many conventional time domain control algorithms are reported in the literature for extraction of reference currents, and two commonly used algorithms for reference currents generation are instantaneous reactive power theory (IRPT) [6] which utilizes three phase to two phase transformation and synchronous reference frame theory (SRFT) [7] based on conversion from stationary frame to rotating frame. Other algorithms reported in the literature include symmetrical component theory [8], feedback-feedforward PI-type iterative learning [9], model based controller [10] for single phase cascaded H-bridge multilevel converter, one cycle control for active harmonic filter [11], composite observer based [12] algorithm, which is based on continuous composite observer function of non-sinusoidal load current, linear feedback control [13], noniterative optimized algorithm [14], back propagation control algorithm [15] which includes the feed forward of the input signal training and frequency-adaptive fractional-order repetitive control [16].

Some control algorithms are based on intelligent techniques such as artificial neural network (ANN) and adaptive neuro fuzzy inference system [17]. These control algorithms possess fast convergence and have improved performance under dynamics, but they require offline training of system parameters. Recent literature has reported several adaptive filtering techniques [18]-[19], for extracting sinusoidal waveform from the distorted load current such as adaptive robust predictive current control [20] for grid connected three phase inverters, adaptive neural filtering [21] for single phase shunt active power filter, modified reduced order digital adaptive notch filter [22] employed to extract the harmonics of current or voltage and used for microgrid power quality enhancement. Some control algorithms are not suitable under

Manuscript received March 25, 2015; revised July 15, 2015 and October 25, 2015; accepted December 2, 2015.

Copyright (c) 2015 IEEE. Personal use of this material is permitted. However, permission to use this material for any other purposes must be obtained from the IEEE by sending a request to pubs-permissions@ieee.org.

Manoj Badoni and Alka Singh are with the Department of Electrical Engineering, Delhi Technological University, Delhi, India (e-mail: manojbadoni23@gmail.com, alkasingh.dr@gmail.com).

Bhim Singh is with the Department of Electrical Engineering, Indian Institute of Technology, Delhi, India (e-mail: bhimsingh7nc@gmail.com).

0278-0046 (c) 2015 IEEE. Personal use is permitted, but republication/redistribution requires IEEE permission. See http://www.ieee.org/publications_standards/publications/rights/index.html for more information.

This article has been accepted for publication in a future issue of this journal, but has not been fully edited. Content may change prior to final publication. Citation information: DOI 10.1109/TIE.2016.2515558, IEEE Transactions on Industrial Electronics



distorted supply voltages condition, whereas the design of some other control algorithms is complex.

The shift invariant control technique is based on Wiener-Hopf equation [23], which is also known as Wiener filter. The steepest-descent algorithm is used to solve the Wiener-Hopf equation. The Wiener filter based control algorithm is well behaved in terms of its convergence properties. In many respects, the design of adaptive (self-varying) control technique is much more difficult than the design of a shift invariant control approach because for each sample time it is necessary to find the set of optimum filter coefficients.

This paper proposes a control algorithm for shunt active power filter using linear optimum discrete time filter such as Wiener filter [24]-[25]. The algorithm is realized to minimize an appropriate function of error known as mean square error (MSE) and extract the weight corresponding to fundamental active and reactive components of load currents. This filtering approach provides fast and accurate estimation of sinusoidal reference currents from distorted load currents by minimizing the error between sensed and estimated currents. It is not computationally demanding and can be implemented real time. The performance of optimum Wiener filtering based control algorithm is compared with an adaptive least mean square (LMS) filtering based control algorithm which is one of the most widely used and preferred control algorithm due to its simplicity and robustness. Both the techniques are iterative in nature, weight based and designed to converge to a solution with minimum error. The LMS technique along with its variants has been used in several power system studies including shunt compensation. Several advantages offered by LMS algorithm viz. simplicity and computationally efficiency make it a perfect choice for comparing it with proposed algorithm. Hence, both the adaptive control techniques are compared in terms of weight convergence, steady state error, computational complexity for different power quality aspects. A detailed investigation into the performance comparison of the two algorithms is another highlight of this paper. Real time performances of both these algorithms are tested on a prototype developed in the laboratory. Extensive simulation results and test results are conducted for a wide variation in system loading. All the results are thoroughly investigated for rate of convergence, tracking speed and error.

## II. System Configuration

Fig. 1 shows the block diagram of a three-phase SAPF which is connected in shunt with three-phase ac mains with grid impedance, represented using series $L_s$-$R_s$ branch, feeding three-phase load. The SAPF is designed using three-phase, three-leg voltage source converter (VSC) and uses six insulated gate bipolar transistors (IGBTs) with anti-parallel diodes and high value capacitor at dc side. The SAPF is connected at the point of common coupling (PCC) with interfacing inductors ($L_f$). Series connected capacitive ($C_f$) and resistive ($R_f$) elements at PCC form ripple filters which are needed to filter out high frequency switching noise generated from IGBTs. A three-phase nonlinear load in the form of uncontrolled bridge rectifier is connected at PCC. A prototype of this system is implemented in the laboratory and the proposed control algorithm is verified under steady state and dynamic conditions. The parameters for simulation and experimental setup are presented in Appendices-A and B.

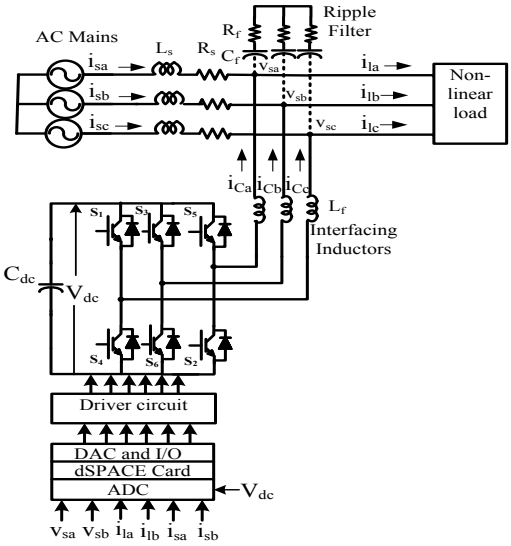


Fig. 1 Schematic diagram of SAPF

## III. Control Algorithm

This section is divided into three parts. The first part explains the adaptive least mean square (LMS) method for extracting the fundamental active and reactive weighted values of the load currents. The second part explains the proposed Wiener based control algorithm as shown in Fig. 2. The filter cost function is defined and a method for weight updation for extracting the fundamental weights is proposed. The third part deals with the generation of switching pulses for a three-phase VSC which is made to work as a SAPF.

### *A. Estimation of Weights Corresponding to Active and Reactive Power Components of Load by Adaptive Least Mean Square (LMS) Method*

The load current ($i_{est}$) can be estimated from the weight vector $W^T$ and input vector $X(n)$ as,

$$i_{est}(n) = w^T X(n) \quad (1)$$

where weight vector is given as,

$w^T = [w_{a1}\, w_{b1} w_{a5} w_{b5} \dots]$ and input vector is $X(n) = [\sin \omega n \cos \omega n \ \sin 5\omega n \cos 5\omega n \dots]^T$.

Let $i_l(n)$ be the actual load current, then the error $e(n)$ between the actual and estimated load current is given as,

$$e(n) = i_l(n) - w^T X(n) \quad (2)$$

The minimum MSE $E[e^2(n)]$ here is achieved using an adaptive least mean square (LMS) based method [26]. In this method, the weights are iteratively determined to achieve minimum error, by using the updation rule given as,

$$w(n+1) = w(n) + 2\beta e(n) X(n) \quad (3)$$

where $w(n+1)$ and $w(n)$ are the updated and the previous weight and $\beta$ is the step size. An optimum value of $\beta$ needs to be selected to achieve optimum weights at a high convergence rate without losing stability. The weighted values

0278-0046 (c) 2015 IEEE. Personal use is permitted, but republication/redistribution requires IEEE permission. See http://www.ieee.org/publications_standards/publications/rights/index.html for more information.

This article has been accepted for publication in a future issue of this journal, but has not been fully edited. Content may change prior to final publication. Citation information: DOI 10.1109/TIE.2016.2515558, IEEE Transactions on Industrial Electronics



corresponding to fundamental active and reactive power components of load currents are estimated using weight update rule given by (3).

*B. Estimation of Weights Corresponding to Active and Reactive Power Components of Load Currents by Wiener Filter Based Control Algorithm*

This is a linear optimization discrete time filtering technique which requires a priori information about the statistics of the data to be processed. These filters are optimum because an appropriate function of error, known as MSE is minimized. The objective here is the same as in LMS algorithm, to extract fundamental active and reactive components of load current ($i_{lfp} + i_{lfq} = i_{lf}$) from the non-sinusoidal load current ($i_l$). The MSE function, $J$(n) to be minimized is defined as,

$$J(n) = E\left[\left(i_l(n) - \hat{\imath}_{lf}(n)\right)^2\right] = E[e^2(n)] \quad (4)$$

where $i_l(n)$ actual load current and $\hat{\imath}_{lf}(n)$ is estimated fundamental load current at the $n^{th}$ sampling instant.

The estimated quantity can be given as,

$$\hat{\imath}_{lf}(n) = \sum_{m=0}^{M-1} w_m x(n-m) = w^T X(n) \quad (5)$$

where $w = [w_1, w_2, \ldots w_{M-1}]^T$ represents M×1 vector of the filter coefficients, $X(n) = [x(n), x(n-1) \ldots x(n-M+1)]^T$ is M×1 vector of input parameters and M is the order of filter.

From above equations, MSE for estimation of fundamental load current is given as,

$$J(n) = E\{[i_l(n) - w^T X(n)]^2\}$$
$$= E\{[i_l(n) - w^T X(n)][i_l(n) - w^T X(n)]^T\}$$
$$= E\{{i_l}^2(n)\} - 2w^T E\{i_l(n)X(n)\} + w^T E\{X(n)X^T(n)\}w \quad (6)$$

It can be rewritten as,

$$J(n) = \sigma_d^2 - 2w^T P_{dx} + w^T R_x w \quad (7)$$

where $\sigma_d^2$ is variance of load current, $i_l(n)$, $P_{dx} = [p_{dx}(0), p_{dx}(1), \ldots, p_{dx}(M-1)]^T$ represents the cross-correlation vector between the desired quantity and input vector and $R_x$ is correlation matrix of input data, which is a symmetric matrix.

The steepest-descent algorithm is used here to find the minimum value for MSE ($J_{min}$) and update the weights until they achieve their optimum value. The procedure for weight updation requires initial values for $w(0)$and the value of gradient vector $-\nabla J(w(0))$ is computed and added to $w(0)$ to obtain $w(1)$. If $w(n)$ is the filter coefficient vector at sampling time $n$ then its updation is given as,

$$w(n+1) = w(n) - \mu \nabla J(w(n)) \quad (8)$$

where, $w(n+1)$ is updated value of the filter-coefficient vector.

The gradient vector is given as,

$$\nabla J\big(w(n)\big) = -2P_{dx} + 2R_x w(n) \quad (9)$$

From (8) and (9) coefficient updation can be calculated as,

$$w(n+1) = w(n) + 2\mu[P_{dx} - R_x w(n)]$$
$$= [I - \mu' R_x]w(n) + \mu' P_{dx} \quad (10)$$

where step size $\mu' = 2\mu$ and $I$ is the identity matrix. The value of step size parameter $\mu'$ must be less than 0.5 for convergence. The auto correlation matrix and the cross-correlation vector, applied in steepest-descent algorithm, are required to estimate first. The optimum coefficients corresponding to fundamental active power components ($w_{pa}$, $w_{pb}$ and $w_{pc}$) and reactive power components ($w_{qa}$, $w_{qb}$ and $w_{qc}$) of load currents are achieved using the updation rule given by (10). Minimum value of MSE is achieved when the filter coefficient vector of the filter approaches the optimum value. The algorithm uses exact measurement of the gradient vector at each iteration of the algorithm and has the capability to achieve minimum MSE [27]-[28].

The LMS method, in which weight updation is given by $w(n+1) = w(n) + 2\beta e(n)X(n)$ where $\beta$ is step size, relies on a noisy instantaneous estimate for the gradient vector, with the result that the filter coefficients estimated fluctuate around the optimum value for large iterations. The method is highly dependent on the step size $\beta$ which needs careful selection for proper convergence of the algorithm.

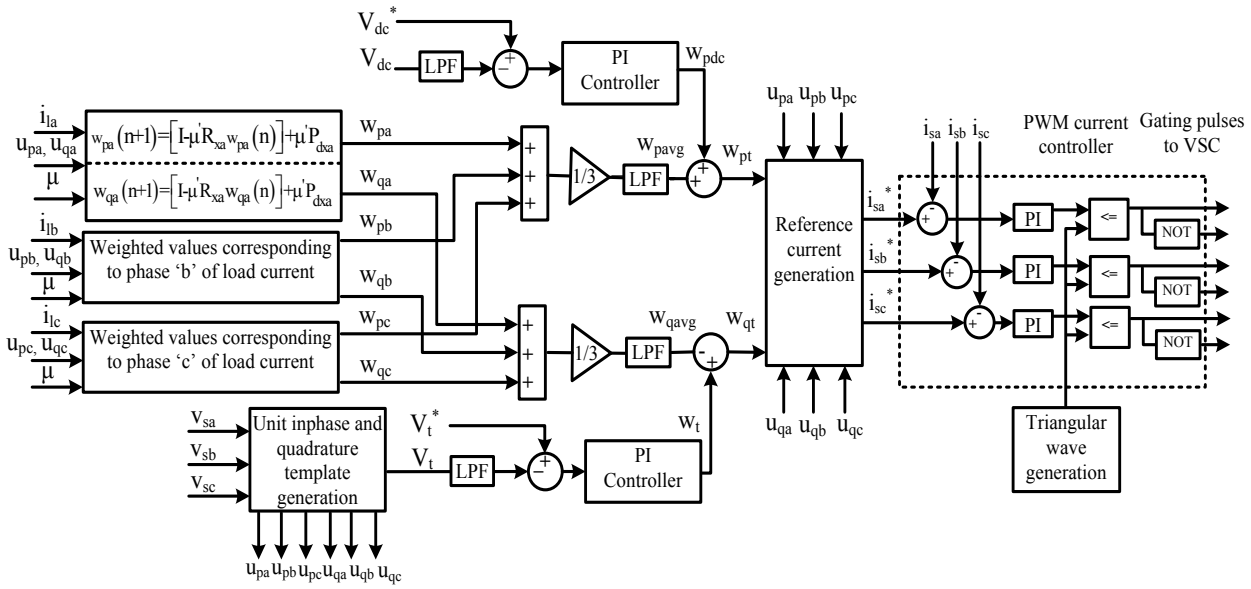


Fig. 2 Control algorithm based on Wiener filtering scheme

0278-0046 (c) 2015 IEEE. Personal use is permitted, but republication/redistribution requires IEEE permission. See http://www.ieee.org/publications_standards/publications/rights/index.html for more information.

This article has been accepted for publication in a future issue of this journal, but has not been fully edited. Content may change prior to final publication. Citation information: DOI 10.1109/TIE.2016.2515558, IEEE Transactions on Industrial Electronics



### C. Generation of Switching Pulses for Three Phase VSC

Fig. 2 shows the block diagram of Weiner based control algorithm where phase voltages ($v_{sa}$, $v_{sb}$ and $v_{sc}$) at PCC are sensed and their amplitude is estimated as,

$$V_t = \sqrt{2(v_{sa}^2 + v_{sb}^2 + v_{sc}^2)/3} \quad (11)$$

The unit inphase components are computed using PCC voltages as,

$$u_{pa} = v_{sa}/V_t; u_{pb} = v_{sb}/V_t \text{ and } u_{pc} = v_{sc}/V_t \quad (12)$$

The voltage at dc bus ($V_{dc}$) is sensed and subtracted from the reference dc bus voltage ($V_{dc}^*$) for generation of error signal ($v_{de}$). The error signal is passed through proportional integral (PI) controller which output ($w_{pdc}$) maintains dc bus voltage at reference value and meets VSC losses. The PI controller output at $n^{th}$ sampling instant is given as,

$$w_{pdc}(n) = w_{pdc}(n-1) + k_{pd}\big(v_{de}(n) - v_{de}(n-1)\big) + k_{id}\big(v_{de}(n)\big) \quad (13)$$

where $k_{pd}$ and $k_{id}$ are the gains of PI controller.

The average magnitude of weights corresponding to the active power components ($w_{pa}$, $w_{pb}$ and $w_{pc}$) can be given as,

$$w_{pavg} = (w_{pa} + w_{pb} + w_{pc})/3 \quad (14)$$

Total weight ($w_{pt}$) of active power component of load is obtained by adding the average weight ($w_{pavg}$) and output of PI controller ($w_{pdc}$),

$$w_{pt} = w_{pavg} + w_{pdc} \quad (15)$$

Reference currents corresponding to fundamental active power component can be computed by using unit inphase templates and (15) as,

$$i_{pa}^* = w_{pt}u_{pa},\ i_{pb}^* = w_{pt}u_{pb} \text{ and } i_{pc}^* = w_{pt}u_{pc} \quad (16)$$

The unit quadrature vectors of PCC voltages are calculated as,

$$u_{qa} = -u_{pb}/\sqrt{3} + u_{pc}/\sqrt{3} \quad (17)$$

$$u_{qb} = \sqrt{3}\,u_{pa}/2 + (u_{pb} - u_{pc})/2\sqrt{3} \quad (18)$$

$$u_{qc} = -\sqrt{3}\,u_{pa}/2 + (u_{pb} - u_{pc})/2\sqrt{3} \quad (19)$$

For voltage regulation, the error ($v_{te}$) between amplitude of PCC voltage ($V_t$) and its reference quantity ($V_t^*$) is calculated and passed through PI controller. The output ($w_t$) of PI controller is computed at $n^{th}$ sampling instant as,

$$w_t(n) = w_t(n-1) + k_{pq}\big(v_{te}(n) - v_{te}(n-1)\big) + k_{iq}\big(v_{te}(n)\big) \quad (20)$$

where $k_{pq}$ and $k_{iq}$ are gains for ac bus PI controller.

The average weight of load reactive power component is calculated from the amplitude of load reactive weight components ($w_{qa}$, $w_{qb}$ and $w_{qc}$) such as,

$$w_{qavg} = (w_{qa} + w_{qb} + w_{qc})/3 \quad (21)$$

The amplitude of reactive power component of reference current is calculated by subtracting the output of PI controller ($w_t$), which is the leading reactive power component used to compensate for voltage drop due to source impedance and loading of the system and average reactive weight ($w_{qavg}$) as,

$$w_{qt} = w_t - w_{qavg} \quad (22)$$

The reference currents corresponding to fundamental reactive power component is calculated using unit quadrature templates and (22) as,

$$i_{qa}^* = w_{qt}u_{qa},\ i_{qb}^* = w_{qt}u_{qb} \text{ and } i_{qc}^* = w_{qt}u_{qc} \quad (23)$$

The fundamental active ($i_{pa}^*, i_{pb}^*$ and $i_{pc}^*$) and reactive ($i_{qa}^*, i_{qb}^*$ and $i_{qc}^*$) power components of supply currents obtained using (16) and (23) are added and total reference supply currents ($i_{sa}^*, i_{sb}^*$ and $i_{sc}^*$) are estimated. The estimated reference supply currents are compared with the sensed supply currents ($i_{sa}, i_{sb}$ and $i_{sc}$) and current errors are generated. These current errors passed through PI controllers, which are used to amplify current errors. Output signals from PI controllers are compared with triangular waveform of 10 kHz frequency and switching pulses are generated for three phase VSC.

## IV. Results And Discussion

A Matlab/Simulink model of proposed system is developed using Sim Power System (SPS) tool box. The performance of the Wiener filter based control algorithm is verified for power factor correction (PFC) and voltage regulation under steady state and unbalanced load conditions. The performance of optimum Wiener filter based control algorithm is compared with adaptive LMS filter based control algorithm. The performance of the system is observed under balanced/unbalanced loads.

### A. Performance of SAPF in PFC Mode with Wiener Filter Based Control Algorithm

The steady-state and dynamic performances of SAPF in PFC mode under nonlinear loads are shown in Fig. 3. These waveforms shown are PCC voltages ($v_{pcc}$), supply currents ($i_s$), load currents ($i_{la}$, $i_{lb}$ and $i_{lc}$), SAPF currents ($i_{Ca}$, $i_{Cb}$ and $i_{Cc}$) and self-sustained dc bus voltage ($V_{dc}$).It can be observed from Fig. 3 that the system is under steady state condition till t=0.3s, and the dc bus voltage ($V_{dc}$) is maintained at its reference voltage of 200V. The supply currents are balanced and sinusoidal and unity power factor is maintained at the

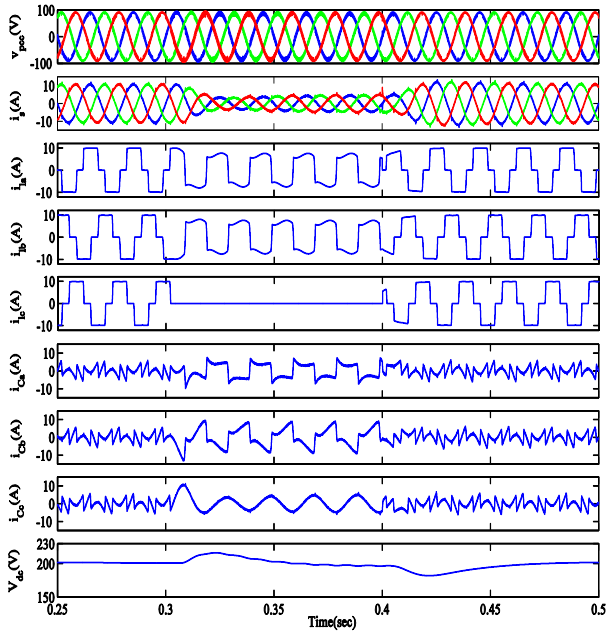


Fig. 3 Steady state and dynamic performances of SAPF in PFC mode under nonlinear load

0278-0046 (c) 2015 IEEE. Personal use is permitted, but republication/redistribution requires IEEE permission. See http://www.ieee.org/publications_standards/publications/rights/index.html for more information.

This article has been accepted for publication in a future issue of this journal, but has not been fully edited. Content may change prior to final publication. Citation information: DOI 10.1109/TIE.2016.2515558, IEEE Transactions on Industrial Electronics



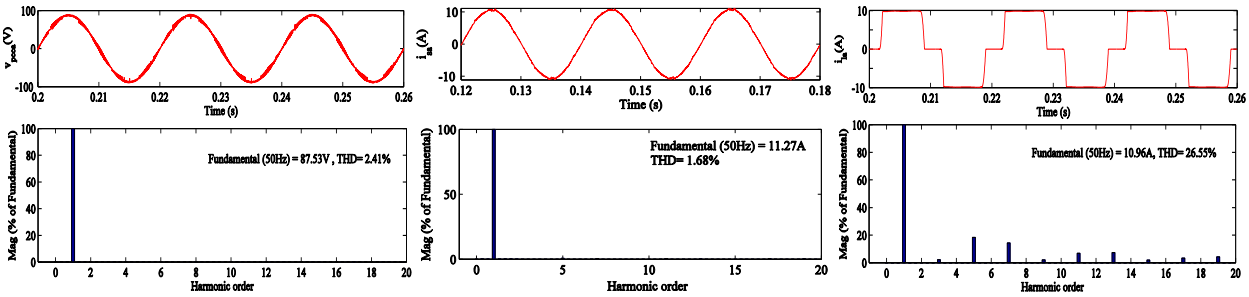


(a) (b) (c)

Fig. 4 Harmonic spectra of (a) PCC voltage, $v_{pcca}$ (b) supply current, $i_{sa}$ (c) load current, $i_{la}$ in PFC mode

supply side. The dynamic performance of SAPF is observed for a duration t=0.3s upto t=0.4s when phase 'c' of the load is switched off. During this disturbance, the dc bus voltage is regulated to its reference value of 200V within a couple of cycles by the action of the PI controller. The supply currents are observed to be again balanced and sinusoidal although reduced in magnitude. After t=0.4s, phase 'c' load is restored back and the system comes back to steady state condition within a couple of cycles.

Fig. 4 shows the waveforms and harmonic spectra of phase 'a' of PCC voltage ($v_{pcca}$), supply current ($i_{sa}$) after compensation and load current ($i_{la}$). The THDs of phase 'a' of PCC voltage, supply current and load current are observed to be 2.41%, 1.68% and 26.55% respectively. It is observed from these results that harmonic distortions of PCC voltage and supply current are within 5% limit specified by IEEE-519 standard [3].

### *B. Performance of SAPF in Voltage Regulation Mode with Wiener Filter Based Control Algorithm*

The steady state and dynamic performances of SAPF in voltage regulation mode under nonlinear load are shown in Fig. 5. Waveforms in this figure show PCC voltages ($v_{pcc}$), supply currents ($i_s$), load currents ($i_{la}$, $i_{lb}$ and $i_{lc}$), SAPF currents ($i_{Ca}$, $i_{Cb}$ and $i_{Cc}$), self-supported dc bus voltage ($V_{dc}$) and regulated magnitude of PCC voltage ($V_t$). It is observed from Fig. 5 that the system is under steady state condition (from t=0.25s to t=0.3s) and the dc bus voltage and magnitude of PCC voltage are maintained at their reference values of 200V and 89.8V respectively. An unbalancing in loads is created when phase 'c' of load is switched off from t=0.3s to t=0.4s. It is observed that even during unbalanced load condition, the supply currents are balanced and sinusoidal with reduced magnitude due to action of SAPF. The dc bus voltage and PCC voltage magnitude are regulated to their reference values under different loading conditions. The action of second PI controller regulates the magnitude of PCC voltage.

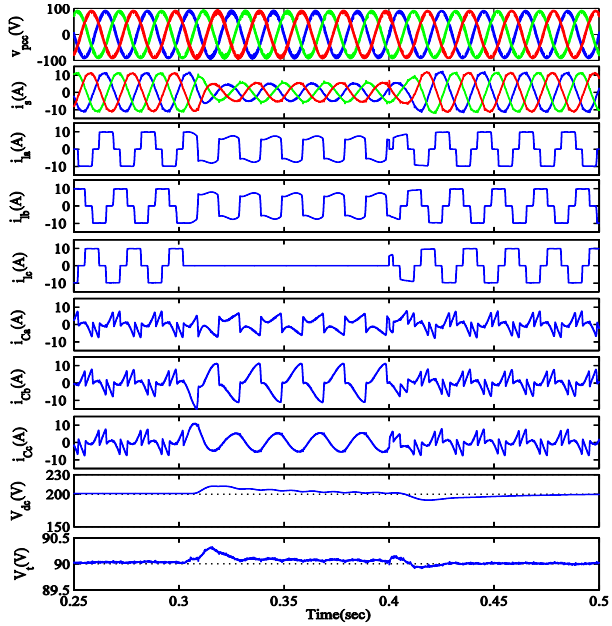


Fig. 5 Steady state and dynamic performances of SAPF in voltage regulation under nonlinear load

Fig. 6 depicts the waveforms and harmonic spectra of phase 'a' of PCC voltage ($v_{pcca}$), supply current ($i_{sa}$) after compensation and load current ($i_{la}$). The values of THDs of the phase 'a' of PCC voltage, supply current and load current are observed to be 3.14%, 2.55% and 26.72% respectively. It can be observed that SAPF controlled using Weiner filter based control algorithm can be used to mitigate a number of power quality problems and controlled to work in power factor correction as well as voltage regulation modes.

### *C. Comparative Performance of Optimum Wiener and Adaptive LMS Filter Based Algorithms for SAPF*

Fig. 7(a) shows the convergence of weights corresponding to active power component of phase 'a' of load current with both Wiener and LMS based control algorithms. It is observed from these results that phase 'a' weight converges within two cycles and achieves a value with small amplitude of oscillations around mean value using Wiener based control algorithm. However weight convergence achieved with LMS based control algorithm is slow and the weight oscillates around mean value with large amplitude. Fig. 7(b) shows the weights extracted using LMS and Wiener filter based control algorithm under unbalanced load condition. An improved convergence is achieved with Wiener based control algorithm under load change/ unbalanced load condition as compared to the LMS based control algorithm.

Fig. 8 shows the harmonic spectrum of phase 'a' of supply current in PFC mode with LMS based control algorithm. This results show the THD of 3% with LMS based algorithm,

0278-0046 (c) 2015 IEEE. Personal use is permitted, but republication/redistribution requires IEEE permission. See http://www.ieee.org/publications_standards/publications/rights/index.html for more information.

This article has been accepted for publication in a future issue of this journal, but has not been fully edited. Content may change prior to final publication. Citation information: DOI 10.1109/TIE.2016.2515558, IEEE Transactions on Industrial Electronics



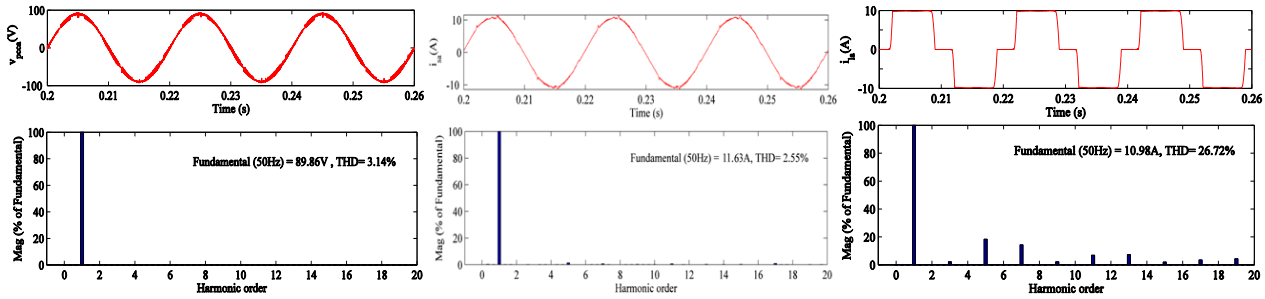


(a) (b) (c)

Fig. 6 Harmonic spectra of (a) PCC voltage, $v_{pcca}$ (b) supply current, $i_{sa}$ (c) load current, $i_{la}$ in voltage regulation mode

whereas THD of 1.68% is achieved using Wiener based control algorithm. The comparative performance of the system with both control algorithms is summarized in Table-I.

## V. Experimental Results

Fig. 9 shows a prototype of SAPF developed in the laboratory. It consists of a three-phase, three-leg VSC, interfacing inductors, three-phase bridge diode rectifier as a nonlinear load and DSP (dSPACE-1104) as a controller. Voltage and current sensing is performed with Hall Effect voltage sensors (LEM LV-25) and current sensors (LEM LA-25) respectively. The sensing circuits are designed and sensed voltages and currents are entered DSP (Digital Signal Processor) through ADC (Analog to Digital Converter) channels. Test results for steady state and dynamic load conditions are recorded using power quality analyzer (Fluke 43B) and DSO (Agilent DSO-X 2014A).

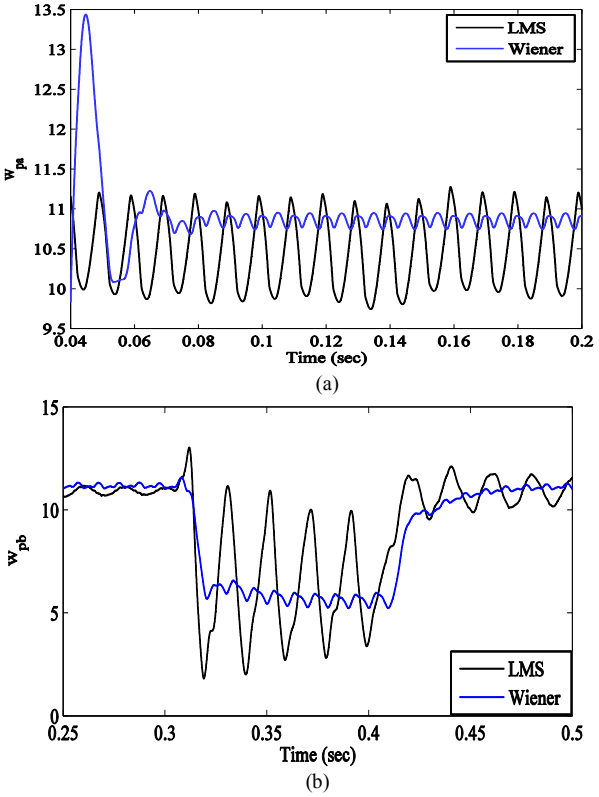


(a)

(b)

Fig. 7 Convergence of active power weights of load current in (a) steady state condition (b) unbalance load condition

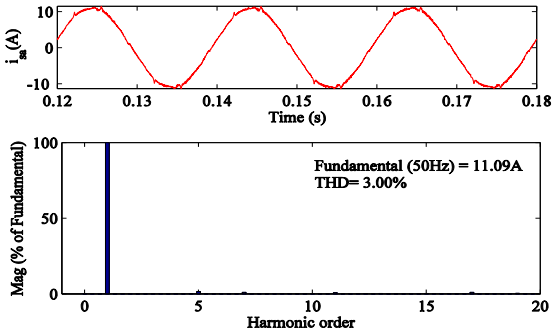


Fig. 8 Harmonic spectra of supply current in PFC using LMS based control algorithm

### A. Response of SAPF with Wiener Filter Based Control Algorithm Under Nonlinear Load

The intermediate signals of proposed control algorithm are shown in Figs. 10(a)-(e). Fig. 10(a) shows cross-correlation vector ($P_{dxa}$) and correlation matrix ($R_{xa}$) of input data corresponding to phase 'a' of load current along with phase 'a' of PCC voltage ($v_{sa}$) and phase 'a' of load current. Fig. 10(b) shows the reference dc bus voltage ($V_{dc}^{*}$), sensed dc bus voltage ($V_{dc}$), filtered dc bus voltage ($V_{dcf}$) and output of PI controller ($w_{pdc}$).Fig. 10(c) shows the waveforms of active power weights ($w_{pa}$, $w_{pb}$ and $w_{pc}$) along with their average value ($w_{pavg}$). Waveform of dc bus voltage ($V_{dc}$), output of dc bus PI controller ($w_{pdc}$), average active power weights ($w_{pavg}$) and reference active power weight ($w_{pt}$) are shown in Fig.

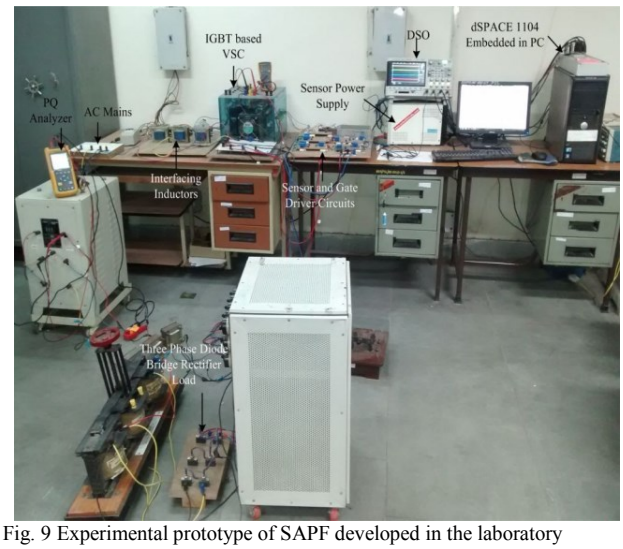


Fig. 9 Experimental prototype of SAPF developed in the laboratory

0278-0046 (c) 2015 IEEE. Personal use is permitted, but republication/redistribution requires IEEE permission. See http://www.ieee.org/publications_standards/publications/rights/index.html for more information.

This article has been accepted for publication in a future issue of this journal, but has not been fully edited. Content may change prior to final publication. Citation information: DOI 10.1109/TIE.2016.2515558, IEEE Transactions on Industrial Electronics



10(d). Fig. 10(e) shows the waveforms of reference supply currents ($i_{sa}^*$, $i_{sb}^*$ and $i_{sc}^*$) along with phase 'a' of sensed supply current ($i_{sa}$). All these signals are shown under steady state as well as unbalanced load conditions. The sensed supply currents track the reference supply currents perfectly which indicates satisfactory performance of the Weiner filter based control algorithm.

### *B. Comparative Performance of SAPF With Wiener Filter and LMS Based Control Algorithms*

Fig. 11 shows the steady state performance of the system with SAPF controlled using Wiener filter based algorithm. It shows the waveforms of supply current ($i_{sa}$), load current ($i_{la}$) and SAPF current ($i_{Ca}$) along with PCC voltage ($v_{sa}$) in Figs. 11(a), (c) and (e). Harmonic spectra corresponding to phase 'a' of supply current ($i_{sa}$), load current ($i_{la}$) and PCC voltage are observed in Figs. 11(b), (d) and (f). The value of THD in supply current, load current and PCC voltage are observed to be 2.3%, 22.4% and 3.1% respectively. The THD in supply current is reduced to 2.3% and the supply current becomes sinusoidal after compensation by SAPF.

Fig. 12 shows the steady state performance of the system with SAPF controlled using LMS algorithm. Figs. 12 (a), (c) and (e) show the waveforms for phase 'a' of supply current ($i_{sa}$), load current ($i_{la}$) and SAPF current ($i_{Ca}$) along with PCC voltage ($v_{sa}$). Figs. 12(b), (d) and (f) show the harmonic

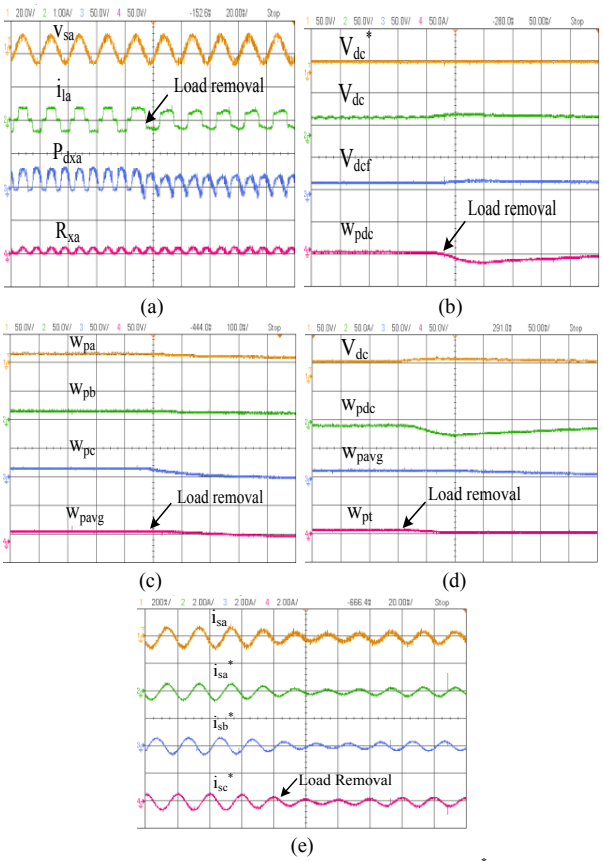


Fig. 10 Intermediate signals (a) $v_{sa}$, $i_{la}$, $P_{dxa}$ and $R_{xa}$ (b) $V_{dc}^*$, $V_{dc}$, $V_{dcf}$ and $w_{pdc}$ (c) $w_{pa}$, $w_{pb}$, $w_{pc}$ and $w_{pavg}$ (d) $V_{dc}$, $w_{pdc}$, $w_{pavg}$ and $w_{pt}$ (e) reference supply currents along with $i_{sa}$

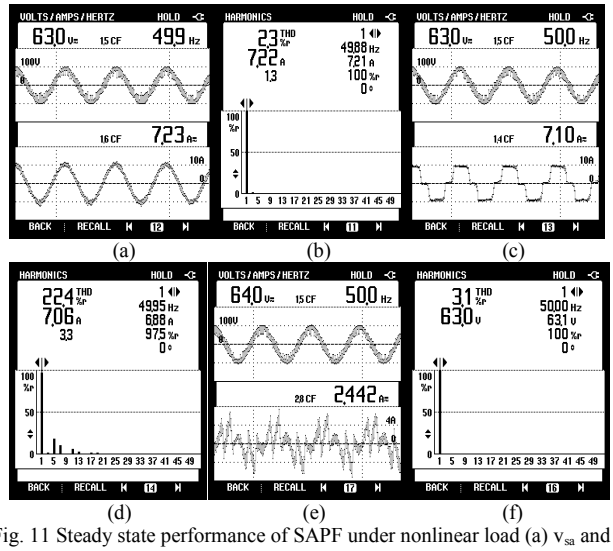


Fig. 11 Steady state performance of SAPF under nonlinear load (a) $v_{sa}$ and $i_{sa}$ (b) harmonic spectrum of $i_{sa}$ (c) $v_{sa}$ and $i_{la}$ (d) harmonic spectrum of $i_{la}$ (e) $v_{sa}$ and $i_{Ca}$ (f) harmonic spectrum $v_{sa}$ with Wiener filter based control algorithm

spectra of supply current ($i_{sa}$), load current ($i_{la}$) and PCC voltage ($v_{sa}$). These results show THD of 4.1%, 21.9% and 3.2% in $i_{sa}$, $i_{la}$ and $v_{sa}$ respectively. It is observed from these results that THD of supply current is within the limit of 5% as specified by IEEE 519 standard with both the control algorithms. However, the THD of supply current obtained with LMS based control algorithm is higher than achieved with Wiener filter based control algorithm, which is also presented in Table-I.

Some of the factors influencing the choice of algorithm for control of VSC are tracking speed, rate of convergence, steady state error and computational time. Comparing the two algorithms on these parameters, the convergence of weights is better with Weiner filter based control algorithm. One major problem with the LMS algorithm is the tradeoff between the convergence rate and stability. A low value of learning rate (β) improves the convergence rate but stability cannot be ensured.

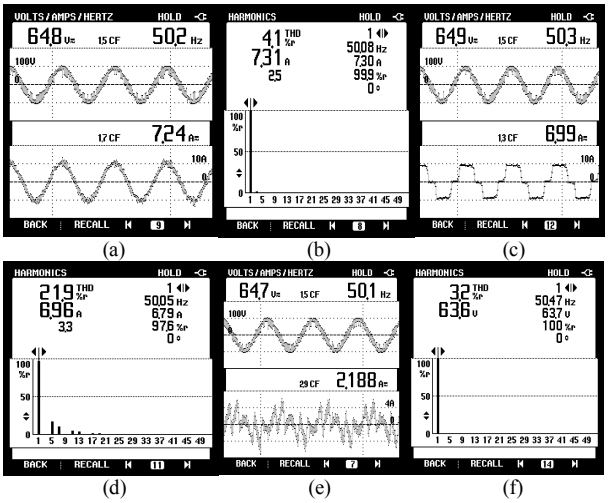


Fig. 12 Steady state performance of SAPF under nonlinear load (a) $v_{sa}$ and $i_{sa}$ (b) harmonic spectrum of $i_{sa}$ (c) $v_{sa}$ and $i_{la}$ (d) harmonic spectrum of $i_{la}$ (e) $v_{sa}$ and $i_{Ca}$ (f) harmonic spectrum $v_{sa}$ with LMS based control algorithm

0278-0046 (c) 2015 IEEE. Personal use is permitted, but republication/redistribution requires IEEE permission. See http://www.ieee.org/publications_standards/publications/rights/index.html for more information.

This article has been accepted for publication in a future issue of this journal, but has not been fully edited. Content may change prior to final publication. Citation information: DOI 10.1109/TIE.2016.2515558, IEEE Transactions on Industrial Electronics



This necessitates the use of time varying β and different variants of LMS algorithm are being reported although computational complexity increases.

### C. Dynamic Performance of SAPF With Wiener Filter Based Control Algorithm Under Nonlinear Load

Dynamic performance of SAPF is depicted in Fig. 13. Waveforms of the supply currents ($i_{sa}$, $i_{sb}$ and $i_{sc}$), load currents ($i_{la}$, $i_{lb}$ and $i_{lc}$), SAPF currents ($i_{Ca}$, $i_{Cb}$ and $i_{Cc}$) with phase 'a' of filtered PCC voltage ($v_{sa}$) are observed in Figs. 13(a)-(c). It can be observed from these figures that supply currents are balanced and sinusoidal even under unbalanced load conditions. Fig. 13(d) shows waveforms of dc bus voltage ($V_{dc}$), phase 'c' of supply current ($i_{sc}$), phase 'c' of load current ($i_{lc}$) and phase 'c' of SAPF current ($i_{Cc}$). It can be observed from this figure that the dc bus voltage achieves its reference voltage of 200V within a couple of cycles, when one phase of load is removed. These results show satisfactory performance of SAPF with Wiener filter based control algorithm under dynamic load changes.

## VI. Conclusion

Simulation and real time implementation of three phase SAPF have been performed for improving various power quality aspects at distribution level. The Wiener filter based control algorithm as well as LMS based control algorithm have been used to extract the fundamental components of the load currents. The updated weights have been utilized for reference current extraction. Online weight update has been implemented and weights have been observed to vary under dynamic load conditions. The performance of the proposed Wiener filter based control algorithm has been thoroughly investigated and compared with least mean square based control algorithm. The comparison of results has shown that Wiener filter based control algorithm achieves faster convergence of weights under a variety of steady state as well as dynamic load conditions. The Wiener filter based control algorithm is not complex and has been easily implemented on DSP. The performance of the proposed control algorithm has been found satisfactory in achieving harmonics reduction, compensation of reactive power and balancing the supply currents in both the modes viz. unity power factor and voltage regulation modes. Test results have shown better performance with Weiner filter based control algorithm in terms of lower THD in supply currents and faster convergence of weights under variety of loading conditions including one phase removal of load. The algorithm can be easily applied to control a number of distributed energy sources interfaced to the grid through voltage source converters.

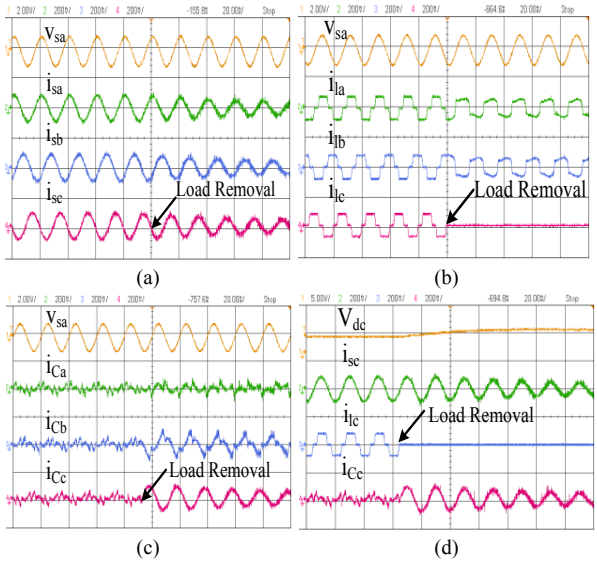


Fig. 13 Dynamic performance of SAPF under nonlinear load (a) $v_{sa}$, supply currents (b) $v_{sa}$, load currents (c) $v_{sa}$, SAPF currents (d) $V_{dc}$, $i_{sc}$, $i_{lc}$ and $i_{Cc}$

TABLE I
Performance of Wiener vs. LMS Control Algorithms

| Operation | Wiener based control algorithm | LMS based control algorithm |
|---|---|---|
| Type | Linear optimum filter | Adaptive filter |
| Convergence | Within two cycles | Oscillate around mean value |
| Stability | Better | Good |
| THD obtained in UPF mode (In Simulation) | Supply current $i_{sa}$=11.27A, THD 1.68% | Supply current $i_{sa}$=11.09A, THD 3.00% |
| | Load current $i_{la}$=10.96A, THD 26.55% | Load current $i_{la}$=10.96A, THD 26.55% |
| THD obtained in UPF mode (In Experiment) | Supply current $i_{sa}$=7.23A,THD 2.3% | Supply current $i_{sa}$=7.31A,THD 4.1% |
| | Load current $i_{la}$=7.10A, THD 22.4% | Load current $i_{la}$=6.96A,THD 21.9% |
| Sample time taken | 40μs | 50μs |

## Appendix-A

AC mains: 110V, 3ph, 50 Hz; $R_s$=0.05Ω, $L_s$=0.5mH; $C_f$=5μF; $L_f$=3.4mH; $C_{dc}$=1650μF; $V_{dc}$=200V; gains of dc bus PI controller $k_{pd}$=0.21, $k_{id}$=0.8; gains of ac bus PI controller $k_{pq}$=0.014, $k_{iq}$=0.001; nonlinear load diode rectifier with $R$=15Ω and $L$=100mH; step size for LMS $\beta$=0.56, step size for Wiener filter $\mu'$=0.23; cutoff frequency of dc bus low pass filter (LPF)=12Hz; cutoff frequency of ac bus LPF=10Hz.

## Appendix-B

AC mains: 110V, 3-ph and 50 Hz; $L_f$=3.4mH; $C_{dc}$=1650μF; $V_{dc}$=200V; nonlinear load diode rectifier with $R$=18Ω and $L$=100mH; gains of dc bus PI controller $k_{pd}$=0.25 and $k_{id}$=0.6; step size for LMS $\beta$=0.56, step size for Wiener filter $\mu'$=0.23; cutoff frequency of dc bus voltage LPF=12Hz.

## References

[1] B. Singh, A. Chandra, and K. Al-Haddad, *Power Quality: Problems and Mitigation Techniques*, John Wiley and Sons, U.K., 2015.
[2] G. Benysek and M. Pasko, *Power Theories for Improved Power Quality,* New York, NY, USA: Springer-Verlag, 2012.
[3] *IEEE Recommended Practices and requirement for Harmonic Control on electric power System,* IEEE Std. 519, 1992.
[4] *Limits for Harmonic Current Emissions*, Standard IEC-61000-3-2, 2000.
[5] F.Z. Peng, H. Akagi, and A. Nabae, "A new approach to harmonic compensation in power systems- Combined System of Shunt Passive

0278-0046 (c) 2015 IEEE. Personal use is permitted, but republication/redistribution requires IEEE permission. See http://www.ieee.org/publications_standards/publications/rights/index.html for more information.

This article has been accepted for publication in a future issue of this journal, but has not been fully edited. Content may change prior to final publication. Citation information: DOI 10.1109/TIE.2016.2515558, IEEE Transactions on Industrial Electronics



and Series Active Filters" *IEEE Trans. Power Syst.*, vol. 26, no. 6, pp. 983-990, Feb. 1990.

[6] H. Akagi, Y. Kanazawa, and A. Nabae, "Generalized theory of the instantaneous reactive power in three-phase circuits," in *Proc. IEEE and JIEE IPEC*, 1983, pp. 821–827.

[7] B. Singh and V. Verma, "Selective compensation of power-quality problems through active power filter by current decomposition," *IEEE Trans. Pow. Delivery*, vol. 23, no. 2, pp. 792-799, Apr. 2008.

[8] U. K. Rao, M. K. Mishra, and A. Ghosh, "Control strategies for load compensation using instantaneous symmetrical component theory under different supply voltages," *IEEE Trans. Pow. Delivery*, vol. 23, no. 4, pp. 2310-2317, Oct. 2008.

[9] An Luo, Xianyong Xu, Lu Fang, Houhui Fang, Jingbing Wu, and Chuanping Wu, "Feedback-feedforward PI-type iterative learning control strategy for hybrid active power filter with injection circuit," *IEEE Trans. Ind. Electron.,* vol. 57, no. 11, pp. 3767-3779, Nov. 2010.

[10] Andrés A. Valdez-Fernández, Pánfilo R. Martínez-Rodríguez, Gerardo Escobar, Cesar A. Limones-Pozos, and José M. Sosa, "A model-based controller for the cascade H-bridge multilevel converter used as a shunt active filter," *IEEE Trans. Ind. Electron.,* vol. 60, no. 11, pp. 5019-5028, Nov. 2013.

[11] E.S. Sreeraj, E.K.K. Prejith, K. Chatterjee, and S. Bandyopadhyay, "An active harmonic filter based on one-cycle control," *IEEE Trans. Ind. Electron.*, vol. 61, no. 8, pp.3799-3909, Aug. 2014.

[12] S. Arya and B. Singh, "Composite observer-based control algorithm for distribution static compensator in four-wire supply system," *IET Power Electron*., vol. 6, iss. 2, pp. 251–260, 2013.

[13] T. Al Chaer, J.P. Gaubert, L. Rambault, and M. Najjar, "Linear feedback control of a parallel active harmonic conditioner in power systems," *IEEE Trans. Power Electron.*, vol. 24, no. 3, pp. 641-653, Mar. 2009.

[14] P. Kanjiya, V. Khadkikar, and H. H. Zeineldin, "A noniterative optimized algorithm for shunt active power filter under distorted and unbalanced supply voltages," *IEEE Trans. Ind. Electron.,* vol. 60, no. 12, pp.5376-5390, Dec. 2013.

[15] B. Singh and S. Arya, "Back-propagation control algorithm for power quality improvement using DSTATCOM," *IEEE Trans. Ind. Electron.,* vol. 61, no. 3, pp.1204-1212, Mar. 2014.

[16] Z. Zou, K. Zhou, Z. Wang, and M. Cheng, "Frequency-adaptive fractional-order repetitive control of shunt active power filters," *IEEE Trans. Ind. Electron.*, vol. 62, no. 3, pp. 1659-1668, Mar. 2015.

[17] S. Arya and B. Singh, "Neural network based conductance estimation control algorithm for shunt compensation," *IEEE Trans. Ind. Informatics*, vol. 10, no. 1, pp. 569-577, Feb. 2014.

[18] R. R. Pereira, C. H. da Silva, L. E. B. da Silva, G. Lambert-Torres, and J.O.P. Pinto, "New strategies for application of adaptive filters in active power filters," *IEEE Trans. Ind. Applications*, vol. 47, no. 3, pp. 1136-1141, May-June 2011.

[19] B. Singh, S. Arya, A. Chandra, and K. Al-Haddad, "Implementation of adaptive filter in distribution static compensator," *IEEE Trans. Ind. Applications*, vol. 50, no. 5, pp. 3026-3036, Sep. 2014.

[20] J. M. Espi, J. Castello, R. Garcia-Gil, G. Garcera, and E. Figueres, "An adaptive robust predictive current control for three-phase grid connected inverters," *IEEE Trans. Ind. Electron.*, vol. 58, no. 8, pp. 3537–3546, Aug. 2011.

[21] M. Cirrincione, M. Pucci, G. Vitale, S. Scordato, and A. Miraoui, "Current harmonic compensation by a single-phase shunt active power filter controlled by adaptive neural filtering," *IEEE Trans. Ind. Electron.*, vol. 56, no. 8, pp. 3128–3143, Aug. 2009.

[22] S. Rafiei, A. Moallem, A. Bakhshai, and D. Yazdani, "Application of a digital ANF-based power processor for micro-grids power quality enhancement" in *Proc. Applied Power Electronics Conference and Exposition (APEC)*, Mar. 2014, pp. 3055-3059.

[23] Simon S. Haykin, *Adaptive Filter Theory*, Person Education India, 2008.

[24] B. Widrow and S. D. Stearns, *Adaptive Signal Processing*, Englewood Cliffs, NJ: Prentice-Hall, 1985.

[25] J. Chen, J. Benesty, Y. Huang, and S. Doclo, "New insights into the noise reduction wiener filter," *IEEE Trans. Audio, Speech and Language Processing*, vol. 14, no. 4, pp. 1218-1234, July 2006.

[26] B. Singh and J. Solanki, "A comparison of control algorithms for DSTATCOM,"*IEEE Trans. Ind. Electron.*, vol. 56, no. 7, pp. 2738-2745, Jul. 2009.

[27] Monson H. Hayes, *Statistical Digital Signal Processing and Modeling*, John Wiley and Sons, New York, 2008.

[28] R. Serizel, M. Moonen, B. Van Dijk, and J. Wouters, "Low-rank approximation based multichannel Wiener filter algorithms for noise reduction with application in cochlear implants," IEEE/ACM Trans. Audio, Speech, and Lang. Process., vol. 22, no. 4, pp. 785-799, Apr. 2014.

**Manoj Badoni** received the B. Tech. in Instrumentation Engineering form University Science and Instrumentation Centre, Srinagar Garhwal, Uttrakhand in 2006 and M.E. degree in Electronics Engineering from Punjab Engineering College, Chandigarh, India in 2008. He is currently working towards the Ph.D Degree in the Electrical Engineering Department of Delhi Technological University, Delhi, India. His areas of research interest include power electronics, power quality, and distributed generation.

**Alka Singh** (SM'15 received the B.E. in Electrical Engineering from Delhi College of Engineering, Delhi, India in 1996, M.Tech. in Power Systems from the Indian Institute of Technology, New Delhi, India in 2001 and Ph.D from Netaji Subash Institute of Technology (Delhi University), Delhi, India in 2006. She is currently working as an Associate Professor in the Department of Electrical Engineering, Delhi Technological University, Delhi. Her research interests include FACTS, power systems and power quality. She has over fifteen years of teaching and industrial experience. She is a IEEE Senior member and Life Member of the Indian Society for Technical Education.

**Bhim Singh** (SM'99–F'10) received the B.E. (Electrical) degree from the University of Roorkee, Roorkee, India, in 1977 and the M.Tech. (Power Apparatus & Systems) and Ph.D. degrees from the Indian Institute of Technology (IIT) Delhi, New Delhi, India, in 1979 and 1983, respectively. In 1983, he joined the Department of Electrical Engineering, University of Roorkee, as a Lecturer. He became a Reader there in 1988. In December 1990, he joined the Department of Electrical Engineering, IIT Delhi, as an Assistant Professor, where he became an Associate Professor in 1994 and a Professor in 1997. He has guided 59 Ph.D. dissertations and 156 M.E./M.Tech. theses. He has been granted one U.S. patent and filed 17 Indian patents. He has executed more than 75 sponsored and consultancy projects. Prof. Singh is a Fellow of the Indian National Academy of Engineering, the National Science Academy, the Indian Academy of Science, the Institute of Engineering and Technology, U.K., the Institution of Engineers (India), the World Academy of Sciences (FTWAS), the Indian National Science Academy, and the Institution of Electronics and Telecommunication Engineers. He has also received Shri Om Prakash Bhasin Award-2014 in the field of Engineering including Energy & Aerospace.

0278-0046 (c) 2015 IEEE. Personal use is permitted, but republication/redistribution requires IEEE permission. See http://www.ieee.org/publications_standards/publications/rights/index.html for more information.

Renewable and Sustainable Energy Reviews 58 (2016) 1017–1026

Contents lists available at ScienceDirect

Renewable and Sustainable Energy Reviews

journal homepage: www.elsevier.com/locate/rser

# Complementary performance enhancement of PV energy system through thermoelectric generation

Vishal Verma [a], Aarti Kane [b], Bhim Singh [c]

[a] Delhi Technological University, Delhi, India
[b] Bharati Vidyapeeth's College of Engineering, Delhi, India
[c] IIT, Delhi, India

ARTICLE INFO

*Article history:*
Received 17 April 2015
Received in revised form
5 September 2015
Accepted 18 December 2015

*Keywords:*
Photovoltaic
Thermoelectric module
Thermoelectric generation
Converter
Maximum power point tracking
Mathematical modeling

ABSTRACT

The solar insolation received on earth have different components in which power is embedded. Out of many, visible spectrum and thermal spectrum are separately used to harvest energy through solar thermal or solar photovoltaic systems respectively. Photovoltaic (PV) panels are reported to experience undesirably high temperature rise due to heat accumulation from solar radiation which is not actively converted into electricity. This undesirable heat decreases conversion efficiency of PV panels. Thermoelectric module (TEM) in coordination with PV panel is proposed to recover and convert this waste heat energy to useful electrical energy. This paper demonstrates the capability of proposed system for electrical power generation from waste heat developed in PV panel in addition to generation from PV systems. Dynamic model of photovoltaic thermoelectric hybrid (PTH) system is developed in SIMULINK/MATLAB environment based on electrical and thermal characteristics of the material. Simulation results for maximum energy harvesting for PTH system are presented under dynamic perturbations in solar radiations. Proposed control scheme ensures maximum energy harvesting without allowing system to operate at temperature out of prescribed limits for PV or TEM. It has been observed in the simulation that PTH system effectively handles the load and source transitions, which validates the scheme.

© 2015 Elsevier Ltd. All rights reserved.

**Contents**

1. Introduction . . . 1017
2. System configuration . . . 1018
3. Modeling of PV panel . . . 1019
   3.1. Dynamic modeling of PV cell . . . 1019
   3.2. Modeling of boost converter . . . 1020
4. Modeling of TEG system . . . 1021
5. Integration of PV and TEG for PTH system . . . 1021
6. Performance evaluantion . . . 1022
7. Conclusion . . . 1024
Appendix A. Supplementary material . . . 1025
References . . . 1025

## 1. Introduction

Energy requirement is increasing at an alarming rate and world is facing critical problems regarding energy deficiencies. Solution to this situation lies in shifting on dependencies of energy requirement from conventional energy sources to renewable energy sources. Solar energy, a clean and abundantly available renewable source of energy is seriously being researched as strong

*Abbreviations:* PV, Photovoltaic; TE, Thermoelectric; TEM, Thermoelectric module; TEC, Thermoelectric cooler; TEG, Thermoelectric generator; PTH, Photovoltaic Thermoelectric Hybrid; MPP, Maximum power point; MPPT, Maximum power point tracking

*E-mail addresses:* vishalverma@dce.ac.in (V. Verma), sanikakane@rediffmail.com (A. Kane), bsingh@ee.iitd.ac.in (B. Singh).

http://dx.doi.org/10.1016/j.rser.2015.12.212
1364-0321/© 2015 Elsevier Ltd. All rights reserved.

**Nomenclature**

| | |
|---|---|
| a | Short circuit current temperature coefficient (%/C) |
| $C_{mod}$ | Heat capacity of module (J/kg K) |
| $G$ | Solar irradiance (kW/m$^2$) |
| $I$ | TEG current (A) |
| $I_d$ | Diode current (A) |
| $I_L$ | Light generated current (A) |
| $I_0$ | Reverse saturation current of a diode (A) |
| $I_{pv}$ | PV cell current (A) |
| $I_{sc}$ | Short circuit current of the PV cell (A) |
| $k$ | Boltzmann's constant ($1.38 \times 10^{-23}$ J/K) |
| $K$ | Thermal conductance of TEG (W/K) |
| $K_1$ | Thermal conductance between thermoelectric generator and heat source (W/K) |
| $K_2$ | Thermal conductance between thermoelectric generator and heat sink (W/K) |
| n | Diode ideality factor (typically between 1 and 2) |
| q | Electric charge ($1.69 \times 10^{-19}$ C) |
| $q_{conv}$ | Convected heat (W) |
| $q_{cond}$ | Conducted heat (W) |
| $q_h$ | Heat transfer from the heat source to the TEG(W) |
| $q_c$ | Heat transfer from TEG to heat sink(W) |
| $q_{rad}$ | Radiated heat (W) |
| $q_e$ | Heat at hot side of TEG (W) |
| $R_s$ | Series resistance (Ω) |
| $R_{sh}$ | Parallel resistance (Ω) |
| $T$ | Absolute temperature (K) |
| $T_{amb}$ | PV module temperature (K) |
| $T_{ref}$ | Reference temperature (K) |
| $T_a$ | Temperature of heat absorbing junction of TEG (K) |
| $T_e$ | Temperature of heat emitting junction of TEG (K) |
| $T_h$ | TEG Hot side temperature (K) |
| $T_c$ | TEG cold side temperature (K) |
| $Tp(x)$ | Temperature at specified length of TEG (K) |
| $V_{pv}$ | PV Output voltage (V) |
| $V_{TEG}$ | TEG output voltage (V) |
| $w_s$ | wind speed (m/s) |
| $\alpha$ | Seebeck coefficient (V/K) |
| $\alpha(T)$ | Seebeck coefficient at specified temperature(V/K) |
| $\alpha(x)$ | Seebeck coefficient at specified length of TEG (V/K) |

contender for future energy solutions. Photovoltaic (PV) system is noiseless, free of moving parts having less maintenance and operational costs and can be produced near load centers, hence can be efficiently utilized and integrated in power systems.

Conversion efficiency of commercial PV modules has been reported very low in the range of 12–18% [1]. PV technology utilizes only visible spectrum of solar insolation, whereas the infrared (IR) spectrum is converted into heat which in turn increases the operating temperature of solar PV system and adversely affect its power generation. In summers temperature of the panel reaches 243–253 K while acting as virtual black body [2–3]. This unwanted heat cannot be recycled effectively by conventional methods. Since heat generated in PV system is low in temperature and low in density, thus conventional thermodynamic cycles cannot be used for the generation of electrical power. Thermoelectric (TE) generation technology appears to have advantages in this area of low grade waste heat recovery. Thermoelectric module can be used as a Thermoelectric Generator (TEG) to produce electric power when temperature gradient is available.

Thermoelectric technology is reported as waste heat recovery system in automobiles reusing the waste heat from internal combustion engine and using it for electrical work [4–5]. Author [6] developed the thermoelectric waste heat recovery system using 24 TEG modules. This system is connected to the exhaust pipe of automobiles and results show that 12.41 W electrical power is generated for the temperature difference of 30 K. Although conversion efficiency of TEG is very small, TEG find its application as waster heat recovery system; as the input thermal energy is available at no cost then low conversion efficiency is not a serious issue. In such cases thermoelectric converters have not only demonstrated potential scope but proved to most economical and viable option of power generation. Thermoelectric technology being environment friendly and categorized under green technology is strongly advocated for increased use in day-to-day life [7–11]. It has been reported in the literature that thermoelectric figure of merit for thermoelectric (TE) modules fabricated using quantum wall (QW) and quantum dot (QD) technology may be greater than the bulk value [12–13] which can increase the conversion efficiency of TE modules. Hi-Z technologies have developed the TE module with figure of merit four times more than currently available materials [14]. A case of PV, TE and thermal hybrid system reported to have enhancement in electrical power output with high efficiencies [15]. Research is reported in PV-TE hybrid system both for material and balance of systems [16–20] presenting the possibility of PV-TE integrated system.

The hybridization of PV-TE as integrated module is in the initial stage of research with no substantial and proven power electronic circuits so far reported for cogeneration with such different sources. This paper deals with a dynamic model devising converters for integrating PV and thermoelectric generators (TEG) for optimum performance. A MATLAB/SIMULINK based model of TEG and photovoltaic thermoelectric hybrid (PTH) in two dimensions (both in time and space), compatible with SimPowerSystem (SPS) is developed to explore the interface with power converter circuits to produce usable form of electricity. A maximum power point tracking (MPPT) system is also proposed which operates both PV system and TEG at respective maximum power point (MPP) and evacuates maximum energy developed by PTH. The MPPT controller corroborates each other such that operating point settles down to a temperature quickly to extract the maximum energy from the system. The presented simulation result demonstrates the effectiveness of the control scheme to produce power with increased efficiency. The rest of the section in this paper is organized as follows: in Section 2 architecture of PTH system is described; Section 3 explains the governing equations for PV operation and computational model developed for maximum power point tracking; Section 4 introduces modeling of TEG system considering temperature dependent parameters of TEG along with converter and current controller; Section V explains the integration of PV and TEG system using power converter interface; Section 6 presents computational results of PTH system and Section 7 concludes the paper.

## 2. System configuration

For purpose of power generation, TEG is attached to the rear side of PV panel. Temperature difference between panel and ambient provides opportunity for TEG to operate in generator mode. Heat is utilized in TEG which otherwise would have got rejected into the environment as a waste heat. A virtual heat pump thus created allows lowering the temperature of PV panel which in

turn enhances the efficiency of PV panel, since the efficiency is inversely proportional to PV panel temperature. Heat sink embodying TEG on both sides for facilitating heat transfer process is shown in Fig. 1. Thermoelectric module is composed of P-type and N-type thermo elements that are connected electrically in series and thermally in parallel between the ceramic plates.

It is envisaged that low generating cost of TEG due to low conversion efficiency will offset the capital cost. MPPT system is implemented to harvest maximum energy from both PV and TEG systems separately. MPPT system shifts the operating point of TEG towards its optimal point of operation. In this work uses perturb and observe (P&O) algorithm is used to track MPP for both PV panel and TEG for PTH. For TEG, MPPT algorithm is developed by power versus current characteristics of TEG. In case of PV, MPPT is implemented on the basis of power versus voltage characteristics.

Power management circuitry is designed to interface varying voltage of PV and varying current TEG source to a fixed voltage load with high efficiency. Fig. 2 shows the proposed system for energy harvesting. Based on MPPT controller designed for both PV and TEG branches, PTH can achieve maximum power harvesting.

Visible spectrum of light is converted into useful electrical energy whereas IR spectrum is converted into heat by PV which is utilized by TEG. A PTH system is designed for 80 W rating with MAX60 solar panel with maximum power output of 60 W at standard operating conditions. Specifications of MAX60 solar panel are provided in Table 1. A two stage conversion with a boost converter having small boost capacity is employed for MPPT operation of both PV and TEG sources and a battery is employed to regulate the DC bus voltage of PTH system. TEG array comparing of 24 TEM having net capacity of 30 W for an average temperature difference of 50 °C is employed for proposed PTH. The TEG presents a voltage source at DC bus of PTH whereas PV source presents a current source for coexistence of the two sources.

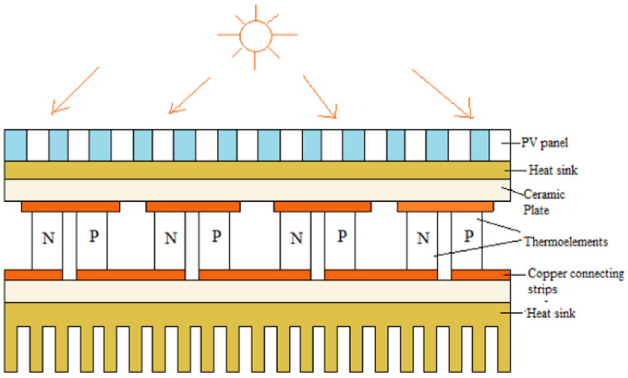


**Fig. 1.** PV–TEG hybrid system (PTH).

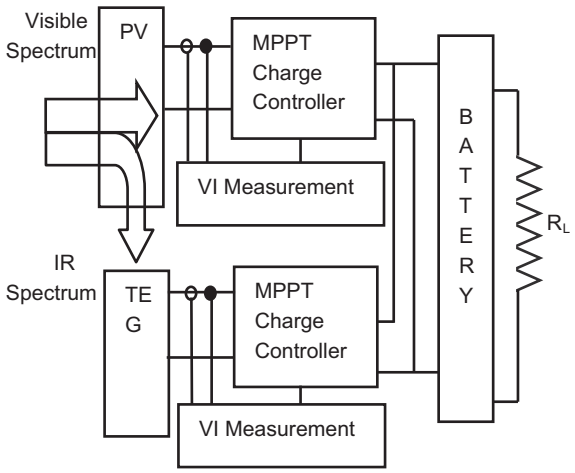


**Fig. 2.** Proposed system for waste heat recovery with converter.

**Table 1**

Solar array datasheet parameters.

| Parameter | Value |
|---|---|
| Open circuit voltage ($V_{oc}$) | 21.1 V |
| Short circuit current($I_{sc}$) | 3.8 A |
| Maximum power | 59.5 ≅ 6 0W |
| Voltage at MPP | 17.1 V |
| Current at MPP | 3.5 A |
| Number of cells in series | 36 |

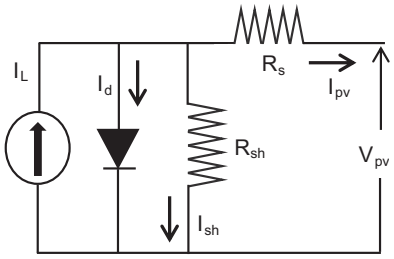


**Fig. 3.** Equivalent circuit of solar cell.

## 3. Modeling of PV panel

### 3.1. Dynamic modeling of PV cell

Solar cells with similar characteristics are connected and encapsulated to form the modules which, in turn are the basic building blocks of solar arrays. Solar cells are connected in series and parallel to obtain desired voltage and current respectively for the solar panel. In ideal solar cell, series and parallel resistances are not present but in practical case series and shunt resistance are included due to ohmic resistances and leakage current as shown in Fig. 3. Major contributors to the series resistance are the bulk resistance of semiconductor material, the metallic contacts, and interconnections. Series resistance has significant effect on the PV power output. The shunt resistance is due to p–n junction non-idealities and impurities near the junction.

Energy balance equations for solar cell are given below, solar cell behaves as a diode and if external supply is connected then diode current flow in external circuit which is given as [21–23],

$$I_d = I_0\left\{\exp\left[\frac{qv_d}{nkT}\right]-1\right\} \quad (1)$$

where $I_d$- Diode current
$I_0$- Reverse saturation current of a diode

$q$ -Electric charge ($1.69\times10^{-19}$ C)
$v_d$- Voltage across diode
$k$-Boltzmann's constant ($1.38\times10^{-23}$ J/K)
$T$ -Absolute temperature (K)
$T_{ref}$- Reference temperature (K)
$n$- Diode ideality factor (typically between 1 and 2)

When PV cell is exposed to solar radiation the output current from the PV cell ($I_{pv}$) can be found using the equation,

$$I_{pv} = I_L - I_d - I_{sh} \quad (2)$$

where $I_L$ is light generated current and is given as,

$$I_L = G[I_{sc}\{1+a(T-T_{ref})\}] \quad (3)$$

where

$G$- Solar irradiance (W/m$^2$)
$I_{sc}$-Short circuit current of the PV cell
$a$-Short circuit current temperature coefficient (%/C)
$I_{sc}$-Maximum current at zero voltage and it is directly proportional to solar irradiance

Characteristic equation of PV cell is given as

$$I_{pv} = I_L - I_0\left\{\exp\left[\frac{q(V_{pv}+IR_s)}{nkT}\right]-1\right\} - \frac{V_{pv}+IR_s}{R_{sh}} \quad (4)$$

$R_s$-Series resistance
$R_{sh}$- Parallel resistance
$V_{pv}$- PV output voltage

PV efficiency is insensitive to variation in $R_{sh}$ and it is considered as infinity and therefore current through parallel resistance $I_{sh}$ is very less and therefore neglected in the present model [24].

Since the thermal behavior of solar cell is necessarily to be incorporated, the determination of the temperature thus becomes mandatory. The temperature equation is modeled for PV panel by evaluating energy inputs and outputs through radiation, convection and conduction and generation of power [2,25–28]. Convection heat transfer from front surfaces of the module and heat conducted from PV panel to thermoelectric module are most significant while radiation heat transfer can be neglected for development of model of PV panel. Temperature determination of PV panel is given by applying energy balance equation as follows,

$$C_{mod}\frac{dT}{dt} = q_{conv} - q_{cond} - q_{rad} - p_{out} \quad (5)$$

$C_{mod}$ is heat capacity of module expressed in J/kg K and $q_{conv}$, $q_{cond}$, and $q_{rad}$ is convected heat, conducted heat and radiated heat expressed in W whereas $p_{out}$ is output power of PV panel expressed in W.

Temperature of PV panel varies with variation in solar irradiation, ambient temperature and wind speed [29] and can be computed as

$$T_{mod} = 0.943T_{amb} + 0.028G * 1000 - 1.521w_s + 4.3 \quad (6)$$

where $w_s$ is average wind speed is considered as 1 m/s, and $G$ solar irradiation in kW/m$^2$. Output power of the PV panel depends upon temperature of panel. This temperature is used as one of the input parameter in TEG modeling.

PV array is operating around an open circuit voltage before connecting to the load. When PV is connected to the load it does not operate at open circuit voltage and voltage drops to a new point and this voltage depends upon the impedance of the load. The output voltage also depends upon temperature and solar insolation. Fig. 4 shows a block diagram of MPPT system with converter. MPPT algorithm works on two loops, the first loop includes MPPT algorithm to compute the MPP and second loop contains proportional–integral (PI) controller to maintain the MPP voltage.

For MPPT, large numbers of algorithms with significant researches are available and successfully implemented [30–32]. A comparison between perturb and observe (P&O) and incremental conductance algorithm has been carried out by Dezso Sera el. [33] and they confirmed that both the algorithms are equivalent. Perturb and Observe (P&O) method is widely used and hence selected for present work due to simplicity and ease of operation. P&O method is based on perturbation of voltage. Control algorithm can be expressed in the following expression,

$$V_{ref}(i+1) = V_{ref}(i) \pm \Delta V \quad (7)$$

$V_{ref}$ is reference voltage and $\Delta V$ is the perturbation in reference voltage and its sign is determined by power slope. MPPT loop calculates the power by sampling voltage and current values. Power change is detected by comparing the present and previous power values. If there is an increase in power the subsequent perturbation of the reference voltage is kept in the same direction to reach MPP and the perturbation should be reversed if power is decreased. Thus MPPT algorithm provides reference voltage and PI controller is implemented to regulate the PV output voltage. PI controller also provides system stability. Fig. 4 shows developed mathematical model using Eq. (1)–(10).

### 3.2. Modeling of boost converter

The DC–DC boost converter is used to interface PV panel with the DC bus. The operation of DC–DC converter is based on switching of current or voltage through inductor. An implementation of boost converter ensures the MPPT tracking as the open circuit voltage of PV panel is below the desired converter output voltage [34,35]. High frequency converter is designed to reduce the size of inductor and capacitor as with increasing switching frequency, the minimum size of inductor and capacitor decreases. For simulation the inductor is selected with high value than calculated value to maintain continuous current. The capacitor is selected to limit output ripple, to withstand peak output voltage and to carry required rms current. The size of inductor and

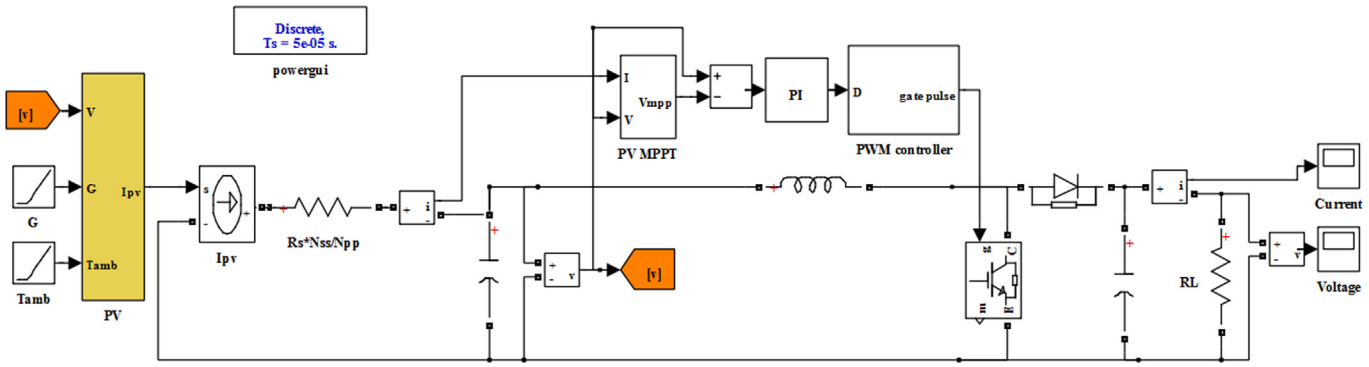


**Fig. 4.** Mathematical model developed in Matlab/Simulink for PV MPPT system.

capacitor are calculated using Eqs. (8) and (9) respectively.

$$L = 1.25\left[\frac{D(1-D)^2 R_L}{2f}\right] \tag{8}$$

$$C = \frac{D}{R_L\left[\frac{\Delta V_0}{V_0}\right]f} \tag{9}$$

where $D$ is duty ratio, $R_L$ is load resistance, $f$ switching frequency and $V_0$ is output voltage.

## 4. Modeling of TEG system

Dynamic model of TEM system is developed by considering temperature dependent parameters of TEM. Performance is simulated in time and space by incorporating parameter variation in each step of computation. There are two stages of functioning of the model: (i) in Time and (ii) in Space domain as shown in Fig. 5. These two stages are not only complementing each other but also happening simultaneouslys and therefore dynamically affect electrical parameters of TEM [36].

TEG can be modeled as a voltage source in series with its internal voltage [37–40]. The rate of heat transfer; $q_h$ from the heat source to the single-couple TEG and from the device to the heat sink; $q_c$ can be obtained by introducing Peltier effect $\alpha IT_h$ and $\alpha ITc$ at the two boundary points and Joulean heat terms,

$$q_h = q_p(0) + q_n(0) + \alpha IT_h = \alpha IT_h + K(T_h - T_c) - I^2\frac{R}{2} \tag{10}$$

$$q_c = q_p(L) + q_n(L) + \alpha IT_c = \alpha IT_c + K(T_h - T_c) - I^2\frac{R}{2} \tag{11}$$

where $R$ is internal resistance of TEG, $\alpha$ is Seebeck coefficient (V/K) and $T_h$ and $T_c$ are hot and cold side temperatures, $K$ is the thermal conductance (W/K), $q_p$ and $q_n$ are rate of heat transfer at p and n leg of TEG. If two externally irreversible heat transfer processes are considered, we can get:

$$q_h = K_1(T_e - T_h) \tag{12}$$

$$q_c = K_2(T_c - T_a) \tag{13}$$

where $K_1$ and $K_2$ are the interface thermal conductance between the generator and the heat source and sink in the hot and cold sides, respectively. By solving equations (12)–(13), hot side and cold side temperature can be computed. Open circuit voltage of the TEG, $V_{TEG}$ is proportional to the temperature gradient given as,

$$V_{TEG} = \propto (T_h - T_c) - IR \tag{14}$$

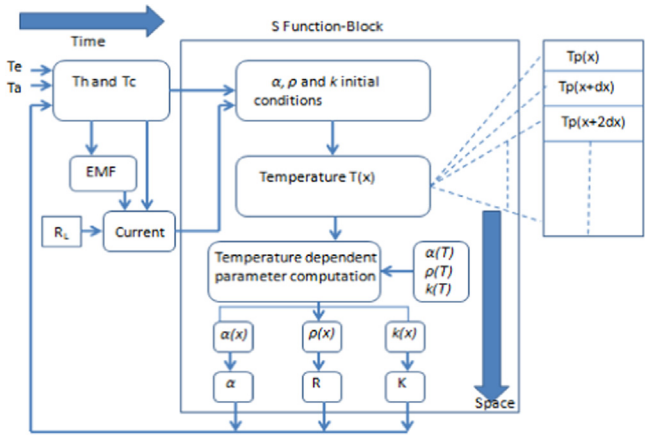


**Fig. 5.** Flow chart for model development in time and space domain.

The expression of current in the generator supplied by the built-in Seebeck voltage is given as,

$$I = \frac{\propto (T_h - T_c)}{R + R_L} \tag{15}$$

where $R_L$ is the load resistance

The output power of TEG is given as,

$$P = \propto (T_h - T_c)I - I^2R \tag{16}$$

The maximum generated power is estimated by computing first partial derivative of and setting it to zero and matching load resistance with the internal resistance of TEG which gives,

$$I_m = \frac{\propto (T_h - T_c)}{2R} \tag{17}$$

$$P_m = \propto_m [(T_{hm}) - (T_{cm})]I_m - (I_m)^2R \tag{18}$$

To extract maximum power from TEG, a novel voltage based MPPT method without using current sensor has been developed by Authors [41,42]. In this system minimal disconnection of the load is required. Voltage and current based MPPT controller along with DC–DC converter has been investigated in present work. MPPT controller dynamically controls the switching frequency of converter by sensing output voltage and current of TEG and operates TEG at maximum power. In case of TEG, P&O algorithm is based on perturbation of TEG current which can be expressed as,

$$I_{ref}(i+1) = I_{ref}(i) \pm \Delta I \tag{19}$$

Fig. 6 shows the schematic of proposed thermoelectric energy harvesting system.

In case of TEG, P&O algorithm is designed by considering PI characteristics of TEG [43,44]. Hysteresis current controller is developed to regulate current to MPP value. DC–DC boost converter is designed using Eqs. (8) and (9).

## 5. Integration of PV and TEG for PTH system

PV system is interpreted to act as current source where current varies with change in environmental conditions. In simulation also, PV is modeled as current source. In case of TE, output voltage changes according to temperature gradient across the junctions it is therefore TE can be modeled as voltage source where voltage is dependent on external conditions. For coupling, these two sources, power converter interface need to be developed for their incorporation as distinct sources. TEG acts at voltage source maintaining voltage at DC bus and power from PV system is evacuated as current for peaceful coexistence of both sources with minimal interference. MAX60 solar cell is used for simulation purpose and specifications are shown in Table 1.

Commercially available $Be_2Te_3$ semiconductor thermoelectric module is selected for simulation and results are computed using the material parameters given in Table 2 for p-type semiconductor (25%$Be_2$ $Te_3$ and 75% $Sb_2$ $Te_3$) and n-type semiconductor material (75%$Be_2$ $Te_3$ and 25% $Bi_2$ $Se_3$).

Mathematical model of developed PTH system is developed as shown in Fig. 7.

Temperature gradient for TEG is developed by connecting TEG to the rear of PV panel. PV panel temperature $T_{mod}$ is hot junction temperature of TEG and other side of TEG is at ambient temperature. TEG system operates as a voltage source and PV system operates as current source. Both sources are connected in parallel where TEG provides constant output voltage required to drive the load. In PTH system 24 TEM's are connected which gives total TEG output of approximately 30 W when temperature difference is 50 K.

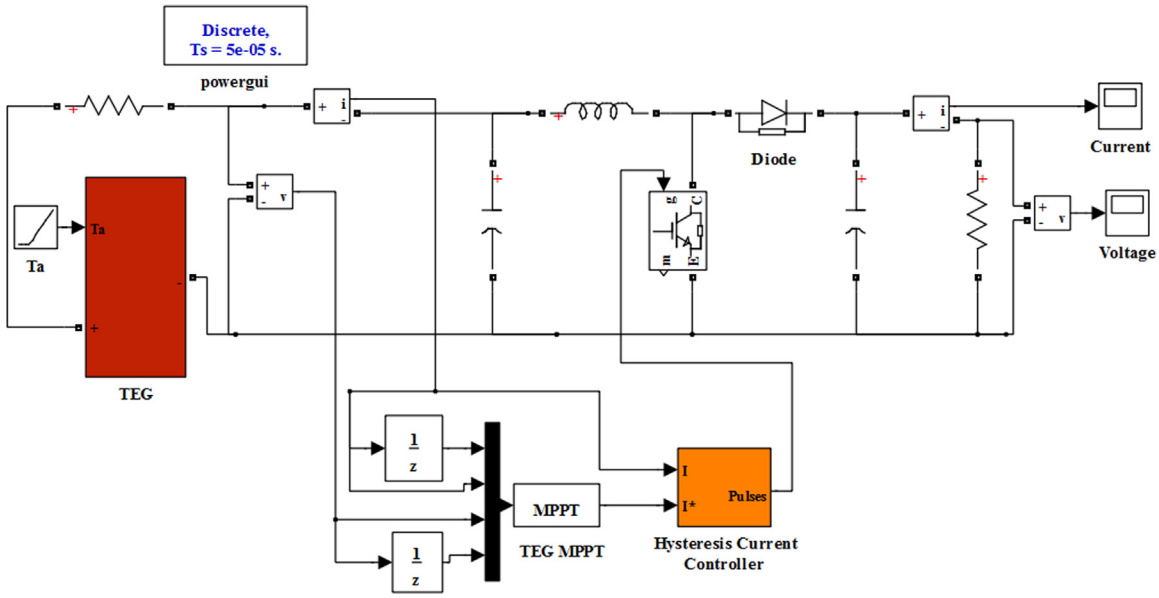


**Fig. 6.** Proposed MPPT circuit for TEG along with current controller and converter.

**Table 2**
Parameters of TEG used for simulation.

| Parameter | Value |
|---|---|
| Seebeck coefficient (V/K) | $\alpha_p = 230*10^{-6} \alpha_n = 195*10^{-6}$ |
| Thermal conductivity (W/cm K) | $K_p = 0.014$, $K_n = 0.012$ |
| Electrical resistivity (Ohm-cm) | $\rho_p = 1.75*10^{-3} \rho_n = 1.35*10^{-3}$ |
| Interface thermal conductance (W/cm$^2$ K) | $G_1 = 0.7$, $G_2 = 0.7$ |
| Length of cell (cm) | $L_p = 1$ cm, $L_n = 1$ cm |
| Area of the cell (cm$^2$) | $A_p = 1$ cm$^2$, $An = 1.14$ cm$^2$ |
| Area of the interface heat exchangers (cm$^2$) | $Ah = 0.104$ cm$^2$, $Al = 0.104$ cm$^2$ |

## 6. Performance evaluantion

The performance evaluation of the developed models in MATLAB/SIMULINK platform is done by utilizing power electronics components of SimPowerSystem (SPS) for realization of integrated PTH system. The extensive simulation study is made in three discrete parts to gauge the system first independently and then integrating into PTH system. The developed models are verified for their operational characteristics close to commercially available PV and TEG modules. The developed models are tested at different temperature conditions for power output with respect to electrical parameter, namely voltage and current. Along with the verification of the models, the MPPT algorithm is also individually verified through simulation for both PV and TEG modules.

Fig. 8 shows power versus voltage curve of PV module obtained by varying load resistance for various operating temperatures. Output power of PV panel decreases with increase in module temperature. The solar insolation of 1 kW/m$^2$ is assumed to be incident on PV module. For 328 K module temperature, 53 W output power is recorded. The MPP of each curve varies near linearly in the temperature range of 328–358 K. The peak power varies as 53 W at 328 K, 49.5 W at 338 K, 47 W at 348 K and 44.5 W at 358 K.

Fig. 9 shows the performance of MPPT controller for PV module in terms of output power and voltage. P&O algorithm is used for realization of MPPT tracking. While realiazing the algorithm, output voltage approaches to 15 V which confirms to the datasheet of the considered module. It may be obseved that MPPT converges within 0.015 s to steady state condition having an overshoot in both power and voltage staggered by 0.0015 s which preceding to 52.5 W at 0.008 sec and 16 V at 0.1 s respectively.

TEM exhibits a complementary trend where increasing temperature change is incorporated. Fig. 10 shows electrical characteristics of TEG at different hot junction temperatures. It may be observed that voltage curve is linearly rising as voltage is proportional to temperature gradient and seebeck coefficient where as power varies quadratically with temperature difference between hot and cold junctions of TEM. Maximum power obtained for a single TEM is 1.26 W at 0.68 V when temperature difference 50 K is maintained across the two junctions of TEG.

Measurement of electrical parameters of TEG has been recorded by varying external load from 0 Ω to 5 Ω as shown in Fig. 11. Maximum power is obtained at matching load condition of 1 Ω. In this simulation temperature difference of 50 K is maintained between two sides of TEG.

The correct measure of assessment of the model can be done through *P–I* characteristics of TEG analogs to *P–V* characteristics of PV module. Fig. 12 shows *P–I* characteristics of TEG at various temperature differences $\Delta T$ between hot and cold sides. It may be observed that with increase in $\Delta T$, output power of TEG increases. Maximum power can be easily tracked by varying current, as TEG acts as a weak voltage source. The peak power varies from 0.43 W with $\Delta T$ of 25 K, through 1.26 W at $\Delta T = 50$ K to 3.75 W with $\Delta T = 75$ K, which shows the quadratic variation, more effective with large temperature difference, complementing well with PV module. Fig. 13 shows performance of TEG–MPPT controller. The MPPT controller operates on current using hysteresis current controller for tracking the MPP point. It may be observed that MPPT converges within 0.05 s to steady state condition with literally no overshoot in power and current and quickly settles to 31.5 W at 1.1 A for an array of 24 TEG modules.

The module of PTH is integrated by using one PV panel and on its rear side twenty four modules of TEG. TEG modules are arranged in series to have approximately same voltage level. The rated capacity of PV panel is nearly 60 W and accumulated power of 24 units of TEG to be 30 W at $\Delta T$ of 50 K with ambient which is reached in summers for solar insolation of 1 kW/m$^2$. The performance of developed PTH system is analyzed for variations of input power in terms of solar insolation and load side conditions. Such isolated system is also hybridized with battery for reliable operation with load perturbations and changing source conditions. Fig. 14 shows dynamic performance of PTH system for load perturbations. The environmental conditions are kept constant, 1 kW/

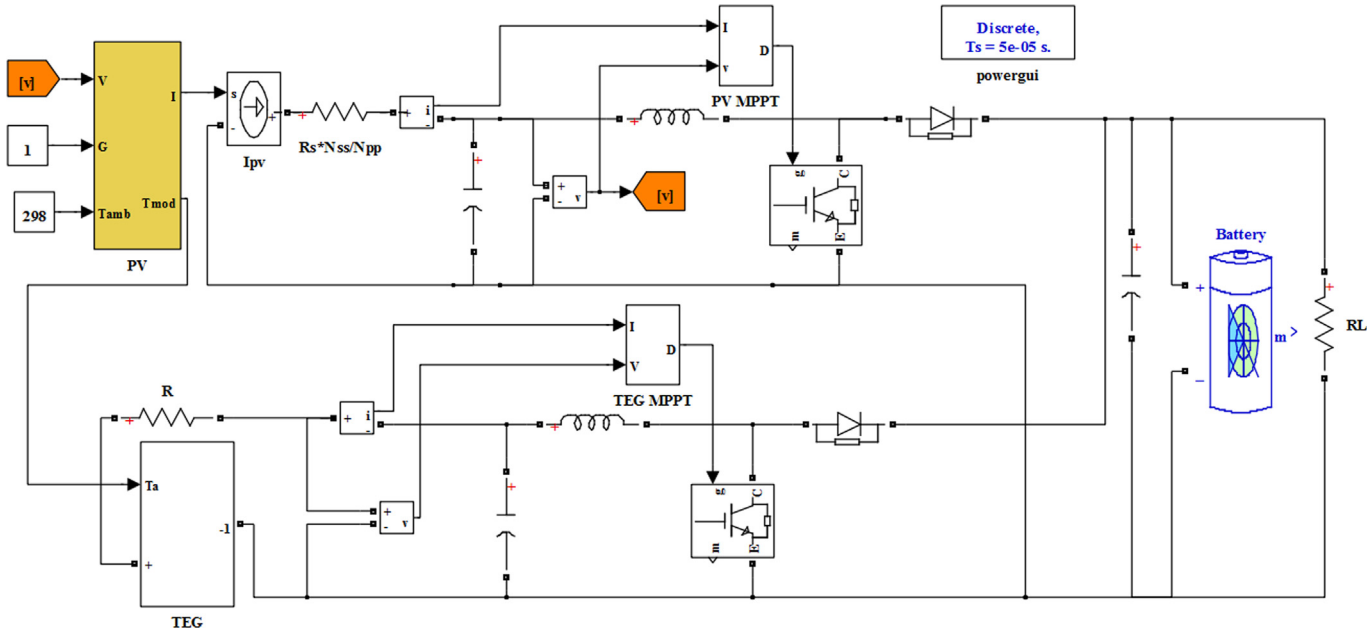


**Fig.7.** Mathematical model of PV–TEG hybrid system developed for energy harvesting.

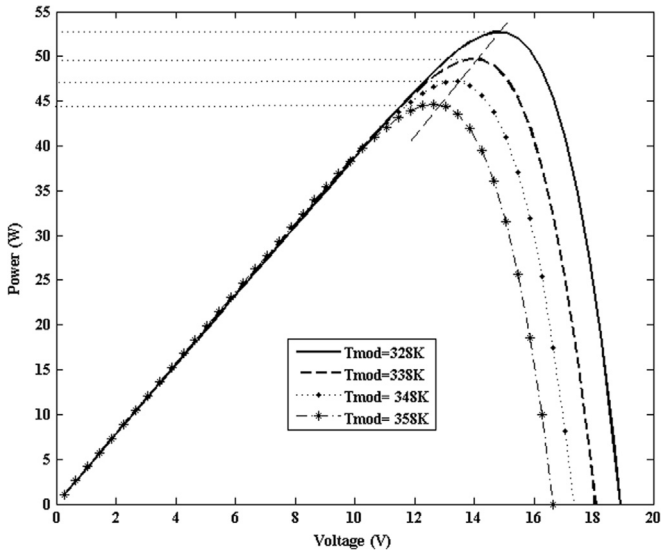


**Fig.8.** *P–V* characteristic of PV panel at various temperature with constant solar irradiation ($G=1$ kW/m$^2$).

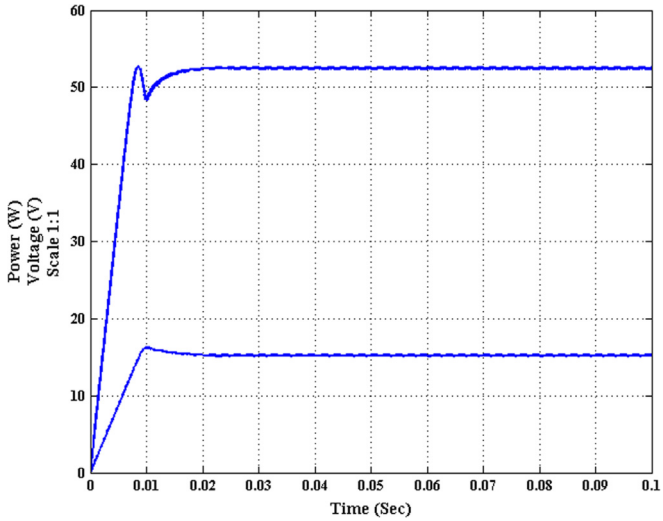


**Fig.9.** Performance for MPPT controller for PV module.

m$^2$ of solar insolation at ambient temperature of 298 K. It is repeated in the literature that junction temperature of solar panel reaches 348 K which offers a temperature gradient of 50 K for TEG modules. Battery is considered to be charged to 80% and it may be observed that before the load is switched from $t=0$ s to $t=0.1$ s the net generated current is absorbed in the battery. When at $t=0.1$ s, the load of 81 W is switched in the power is diverted to load and charging current for battery reduces to $-0.03$ A as shown in Fig. 14(f). The load at this time draws 2.82 A, thus a total output of power 83 W is shared between load and battery as 81 W and 2 W respectively as shown in Fig. 14(h), (i) and (j). At time $t=0.2$ s, the load is increased to 100 W, it may be seen that MPPT of PV and TEG modules evacuates the maximum generated power of 53 W and 30 W respectively and the deficit of power is acquired from battery amounting to 17 W, the same may be verified by battery current which changes its polarity and is amounting to 0.64 A and PV panel and TEG current which respectively are 1.76 A and 1.1 A as shown in Fig. 14(b) and (d). The load is again perturbed at $t=0.3$ s, from 100 W to 81 W, the normal rated level. At $t=0.4$ s, load is decreased to 53 W, equivalent to load current of 1.8 A, under such conditions power generated by PTH system is more than the requirement of load. This extra power of 30 W is absorbed into the battery and the same may be observed for rise in battery current from $-0.03$ A to $-1.06$ A. It is pertinent to observe that for all loading conditions MPPT continues to extract the maximum power for PTH system, whereas the deficit/excess power is supplied/ absorbed by the battery.

Fig. 15 shows performance of PTH system amidst variations in solar insolation. Solar insolation is varied from rated normal of 1 kW/m$^2$ to a low 0.8 kW/m$^2$ and then resumed back to 1 kW/m$^2$ for fixed loading conditions. As solar insolation is reduced PV power output reduces and same is reflected in reduction of current since the terminal voltage is held constant by battery as shown in Fig. 15(a), (c), (e) and (g). It is important to note that with the reduction in solar insolation, temperature of PV panel also reduces, which in turn reduces hot side temperature of TEG, and hence TEG power produced by modules also reduces. Starting transient persists from $t=0$ s to $t=0.1$ s, where solar insolation is 1 kW/m$^2$ and

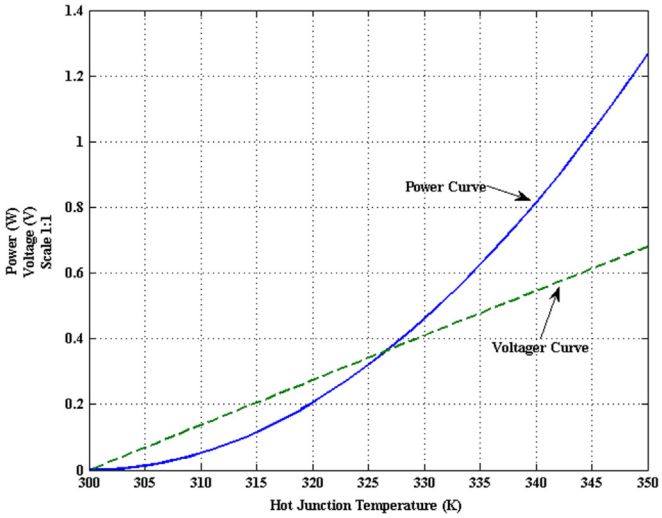


**Fig. 10.** Response in terms of output power and voltage of TEG with temperature change (hot junction temperature varied from 300 K to 350 K and cold junction kept at 300 K).

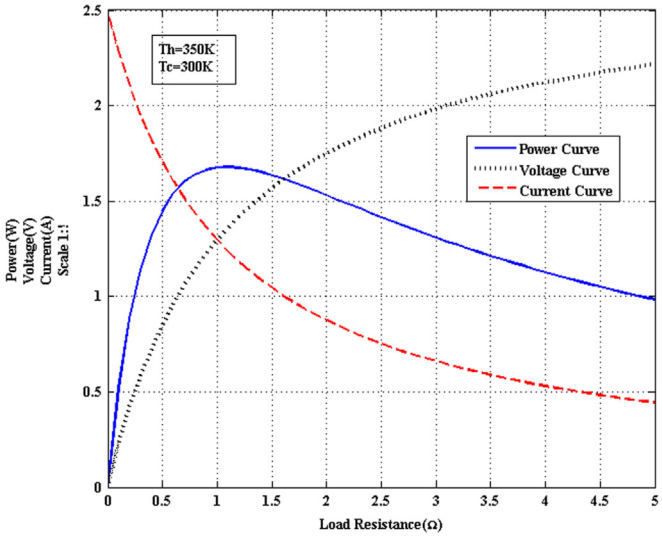


**Fig. 11.** Loading characteristics of TEG voltage, current and power.

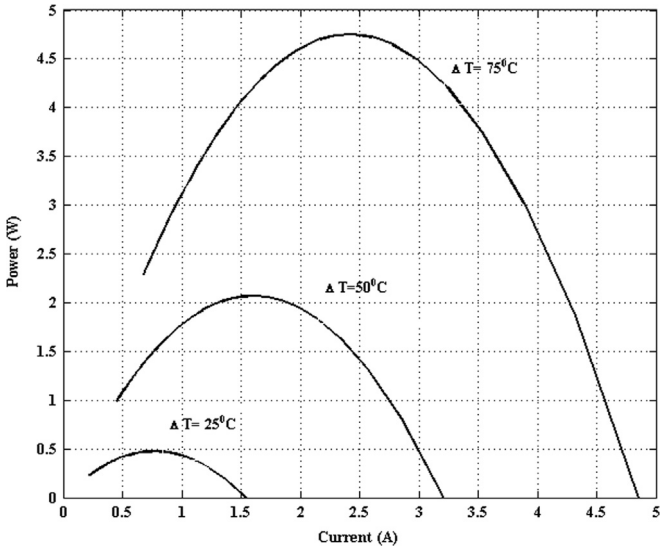


**Fig. 12.** *P–I* characteristics of singe TEG module.

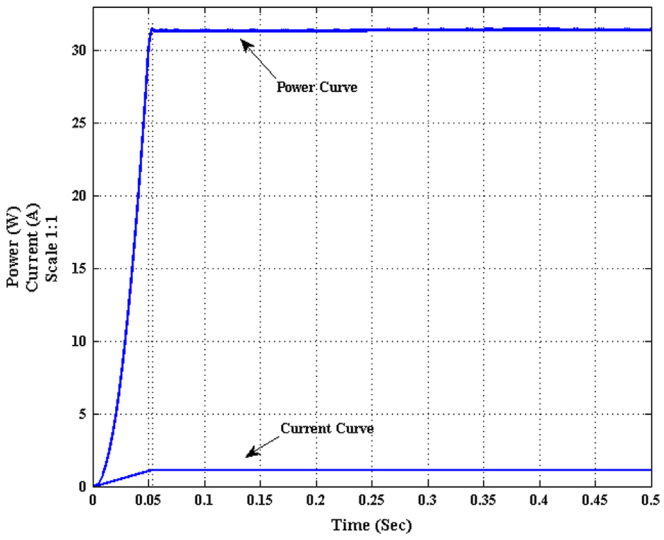


**Fig. 13.** Performance of MPPT circuit in case of TEG.

PV, TEG, battery and load currents are 1.76 A, 1.1 A,-0.03 A and 2.83 A respectively as shown in Fig. 15(b), (d), (f), (h) Power generated by PV, TEG is 53 W and 30 W as shown in Fig. 15(i), power supplied to the load is 83 W with 2 W battery storage shown in Fig. 15(j). After 0.1 s, solar insolation is reduced and PV and TEG current reduces to 1.50 A and 0.72 A respectively and as the load is fixed load current constant. PV and TEG powers are reduced to 43 W and 20 W respectively but the power demanded by the load is constant. Extra power of about 20 W is supplied by the battery. This model works well for both current and source transitions.

## 7. Conclusion

The models of TEM and PV including variation in temperature and temperature dependent parameters have been developed. Simulated results have conformed to the specifications of the considered commercial modules. The MPPT operation of individual developed model has been studied and compared with integrated PTH (PV+TEG) system to demonstrate close matching. The integrated system has been controlled under master-slave configuration with battery source operating as a Master for both PV and TEM. The voltage at point of common coupling is maintained by the battery. The performance of PTH system is evaluated for load perturbations and the variations in the solar insolation. The master slave control effectively handles the fluctuating power evacuated from both PV and TEG sources and complements the power from battery to cater the demand of perturbing load. Such hybrid system proposes a clean energy source by absorbing residual heat, unnecessarily accumulated on PV panel, thus enhancing conversion efficiency of PTH system largely when compared with the PV panel, presenting a huge power density per unit surface area suitable for roof top applications in metros. Hybrid system is applicable for all seasons and operates with approximately equal efficiency for both summer and winter seasons. The system can be deployed at any place with hot and cold climate conditions with matching efficiency. In the present work the considered system operates in standalone condition.

Future work is also planned to transform standalone PTH system to grid connected preposition for optimization of the efficiency. It is also proposed to develop appropriate power electronic switching circuit including auto changeover based on temperature and solar irradiation to cope with intermittent shedding condition

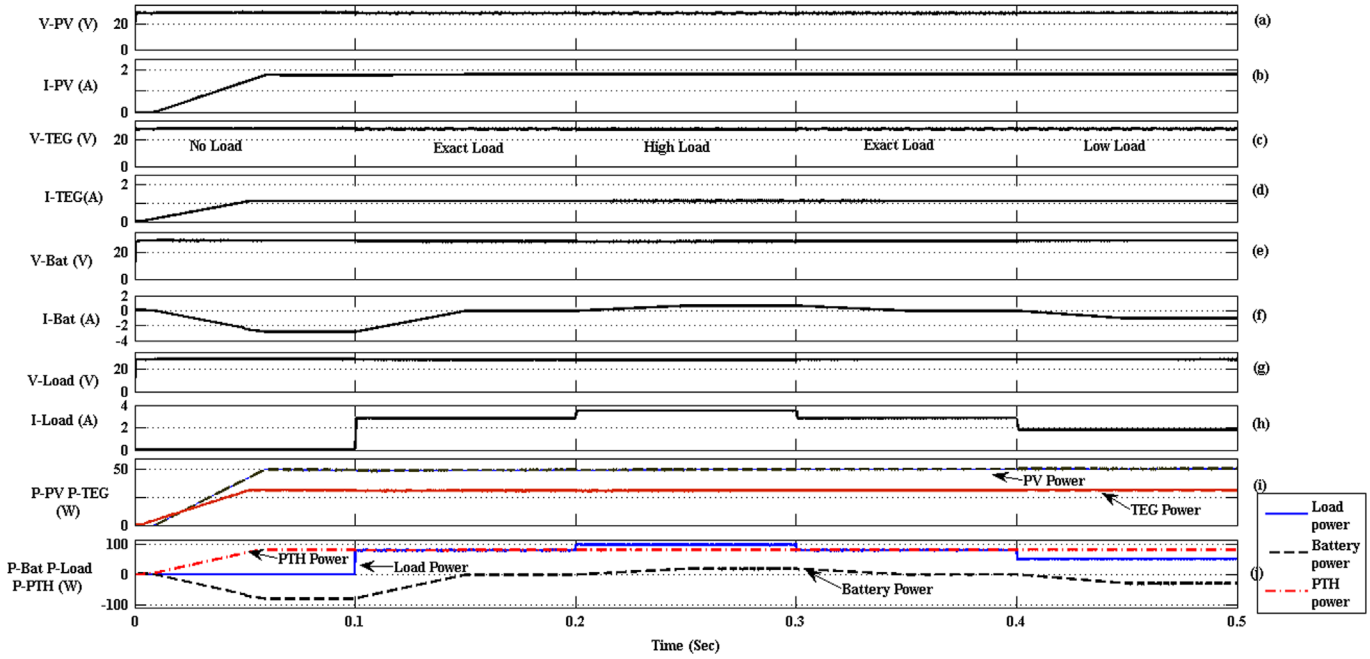


**Fig. 14.** Performance of PTH system for load transitions (load transition at every 0.1 s.) (a) PV voltage (b)PV current (c)TEG voltage (d) TEG current (e) battery voltage (f) battery current (g) load voltage (h) load current (i) PV power and TEG power (j) load power, battery power and PTH power.

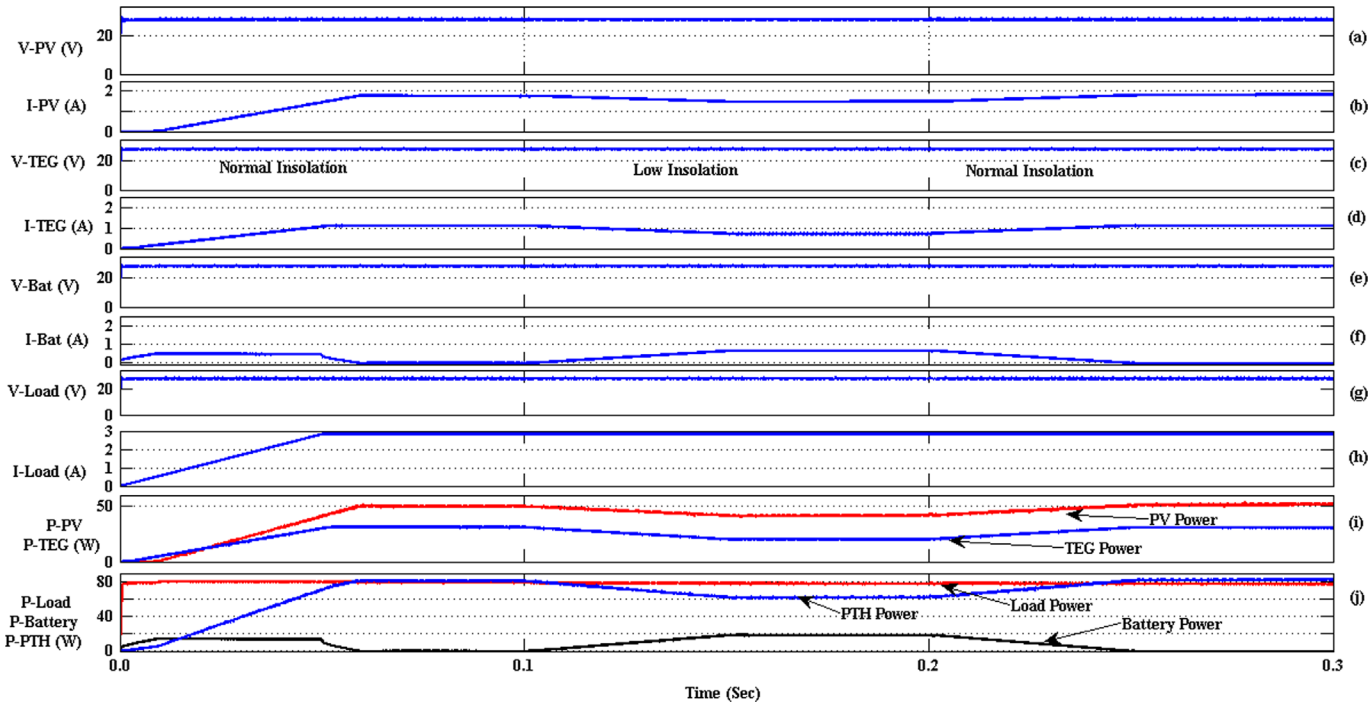


**Fig.15.** Performance of PTH system for source transitions (low insolation of 0.8 kW/m$^2$ and normal insolation of 1 kW/m$^2$ occurs at 0.1 and 0.2 s respectively) (a) and b) PV voltage and current, (c) and (d) TEG voltage and current (e) and (f) battery voltage and current, (g) and (h) load voltage and load current, (i) PV power and TEG power and (j) Load power, battery power and PTH power.

and its effects on generation. Proposed solution will be effectively a breakthrough solution for optimization of efficiency of solar generation.

## Appendix A. Supplementary material

Supplementary data associated with this article can be found in the online version at http://dx.doi.org/10.1016/j.rser.2015.12.212.

## References

[1] Tyagi VV, Nurul AA, Rahim, Rahim NA, JeyrajA./L. Selvaraj. Progress in solar PV technology: research and achievement. Renew Sustain Energy Rev 2013;20:443–61.

[2] Wang YN, Lin TT, Leong JC, Hsu YT, Yeh CP, Lee PH, Tsai CH. Numerical investigation of high-concentration photovoltaic module heat dissipation. Renew Energy 2013;50:20–6.

[3] Vorobiey Y, Gonzalez-Hernandez J, Bulat L. Thermal-photovoltaic solar hybrid system for efficient solar energy conversion. Sol Energy 2006;80:170–6.

[4] Saidur R, Rezaei M, Muzammil WK, Hassan MH, Paria S, Hasanuzzaman M. Technologies to recover exhaust heat from internal combustion engines. 2012;16:5649–59.
[5] Kumar Sumeet, Heister Stephen D, Xu Xianfan, Salvador James R, Meisner Gregory P. Thermoelectric generators for automotive waste heat recovery systems part I: numerical modeling and baseline model analysis. J Electron Mater 2013;42:665–74.
[6] Niu Xing, Yu Jianlin. Experimental study on low-temperature waste heat thermoelectric generator. J Power Sources 2009;188:621–6.
[7] Rowe DM. Thermoelectric waste heat recovery as a renewable energy source. Int J Innov Energy Syst Power 2006;1:13–23.
[8] Rowe DM, et al. CRC Handbook of Thermoelectric. CRC Press; 1995.
[9] Gould CA, Shammas NYA, Grainger S, Taylor I. Comprehensive review of thermoelectric technology, micro-electrical and power generation properties. Phil Trans R Soc. Lond 1955;A247:529–51.
[10] Zheng XF, Yan YY, Simpson K. A potential candidate for the sustainable and reliable domestic energy generation – thermoelectric Cogeneration System. Appl Therm Eng 2013;53:305–11.
[11] Muhtaroglu A, Yokochi A, Von Jouanne A. Integration of thermoelectrics and photovoltaics as auxiliary power source in mobile computing applications. J Power Sources 2008;177:239–46.
[12] Ghamaty S., Elsner N. Si/SiGe, Quantum well thermoelectric materials and devices for waste heat recovery from vehicles and industrial plants, in: Proceedings of the international symposium on nano-thermoelectrics, Osaka, Japan, 2007.
[13] Harman TC, Taylor PJ, Walsh MP, LaForge BE. Quantum dot super lattice thermoelectric materials and devices. Science 2002;29:2229–32.
[14] Karri MA, Thacher EF, Helenbrook BT. Exhaust energy conversion by thermoelectric generator: Two case studies. Energy Convers Manag 2011; l52:1596–611.
[15] Yang DJ, Yuan ZF, Lee PH, Yin HM. Simulation and experimental validation of heat transfer in a novel hybrid solar panel. Int J Heat Mass Transf 2012;55:1076–82.
[16] Kraemer D, Hu L, Muto A, Chen X, Chen G, Chiesa M. Photovoltaic-thermoelectric hybrid systems: a general optimization methodology. Appl Phys Lett 2008;92:243503/3.
[17] WGJHM Van Sark. Feasibility of photovoltaic – thermoelectric hybrid modules. Appl Energy 2011;88:2785–90.
[18] Bjork R, Nielsen KK. The performance of combined solar photovoltaic (PV) and thermoelectric generator (TEG) system. Sol Energy 2015;120:187–94.
[19] Hsu Cheng-Ting, Huang Gia-Yeh, Chu Hsu-Shen, Yao Ben Yu Da-Jeng. Experiments and simulations on low-temperature waste heat harvesting system by thermoelectric power generators. Appl Energy 2011;88:1291–7.
[20] Xiaolong Gou Heng Xiao, Yang Suwen. Modeling, experimental study and optimization on low-temperature waste heat thermoelectric generation system. Appl Energy 2010;87:3131–6.
[21] Soto WD, Klein SA, Beckman WA. Improvement and validation of a model for photovoltaic array performance. Sol Energy 2006;80:78–88.
[22] Duffie JA, Beckman WA. Solar Engineering of Thermal Processes. second ed.. New York: John Wiley & Sons Inc.; 1991.
[23] Chenni R, Makhlouf M, Kerbache T, Bouzid A. A detailed modeling method for photovoltaic cells. Energy 2007;32:1724–30.
[24] Bose BK, Szczeny PM, Steigerwald RL. Microcomputer control of a residential photovoltaic power conditioning system. IEEE Trans Ind Appl 1985;IA-21 (5):1182–91.
[25] Jones AD, Underwood CP. A thermal model for photovoltaic systems. Sol Energy 2001;70:349–59.
[26] Armstrong S, Hurley WG. A thermal model for photovoltaic panels under varying atmospheric conditions. Applied Thermal Engineering 2010;30:1488–95.
[27] Mattei M, Notton G, Cristofari C, Muselli M, Poggi P. Calculation of the polycrystalline PV module temperature using a simple method of energy balance. Renew Energy 2006;31:553–67.
[28] Huang BJ, Yang PE, Lin YP, Lin BY, Chen HJ, Lai RC, et al. Solar cell junction temperature measurement of PV module. Sol Energy 2011;85:388–92.
[29] Skoplaki E, Palyvos JA. On the temperature dependence of photovoltaic module electrical performance: a review of efficiency/power correlations. Sol Energy 2009;83:614–24.
[30] Rezk Hegazy, Eltamaly Ali M. A comprehensive comparison of different MPPT techniques for photovoltaic systems. Sol Energy 2015;112:1–11.
[31] Issam Houssamo Fabrice Locment, Sechilariu Manuela. Maximum power tracking for photovoltaic power system: development and experimental comparison of two algorithms. Renew Energy 2010;35:2381–7.
[32] Salas V, Olias E, Barrado A, Lazaro A. Review of maximum power point tracking algorithms for stand-alone photovoltaic systems. Sol Energy Mater Sol Cells 2006;90:1555–78.
[33] Sera Dezso, Mathe Laszlo, Kerekes Tamas, Spataru Sergiu Viorel, Teodorescu Remus. On the perturb-and-observe and incremental conductance MPPT methods for PV Systems. IEEE J Photovolt 2013;3:1070–8.
[34] Enrique JM, Duran E, Sidrach-de-Cardona M, Andujar JM. Theoretical assessment of the maximum power point tracking efficiency of photovoltaic facilities with different converter topologies. Sol Energy 2007;81:31–8.
[35] Walker Geoffrey R, Sernia Paul C. Cascaded DC–DC converter connection of photovoltaic modules. IEEE Trans Power Electron 2004;19:1030–9.
[36] Kane A., Verma V., Singh B. Temperature dependent analysis of thermoelectric module using Matlab/SIMULINK. Power and Energy (PECon), 2012 IEEE Inter. Conf. 2012:632-37.
[37] Wu Chih. Analysis of waste-heat thermoelectric power generator. Appl Therm Eng 1996;16:63–9.
[38] Lineykin Simon, Shmuel Ben-Yaakov. Modeling and analysis of thermoelectric modules. IEEE Trans Ind Appl 2007;43:505–12.
[39] Sandoz-Rosado Emil, Stevens Robert J. Experimental characterization of thermoelectric modules and comparison with theoretical models for power generation. J Electron Mater 2009;38:1239–44.
[40] Kim Shiho. Analysis and modeling of effective temperature differences and electrical parameters of thermoelectric generators. Appl Energy 2013;102:1458–63.
[41] Bond Matthew, Park Jae-Do. Current sensorless power estimation and MPPT implementation for TEG. IEEE Trans Ind Electron 2014;63(9):5539–48.
[42] Andrea Montecucco Andrew R. Knox. Maximum power point tracking converter based on the open-circuit voltage method for thermoelectric generators. IEEE Trans Power Electron 2015;30:828–39.
[43] Phillip N, Magnaga O, Burnah KJ. Investigation of maximum power point tracking for thermoelectric generators. J Electron Mater 2013;42:1900–6.
[44] Rodriguez A, Vian JG, Astrain D, Martinez. Study of thermoelectric systems applied to electric power generation. Energy Convers Manag 2009;50:1236–43.

Research Article – JTEN – 2015 – 36

**Journal of Thermal Engineering**
**Yildiz Technical University Press, Istanbul, Turkey**
**Vol. 2, No. 2, pp. 683-692, April, 2016.**

*http://eds.yildiz.edu.tr/journal-of-thermal-engineering/Articles*
*Manuscript Received April 21, 2015; Accepted June 03, 2015*

*This paper was recommended for publication in revised form by Regional Editor Balaram Kundu*

# COMPUTATION OF OPTIMUM PARAMETERS OF A HALF EFFECT WATER-LITHIUM BROMIDE VAPOUR ABSORPTION REFRIGERATION SYSTEM

**Akhilesh Arora**
Department of Mechanical Engineering, Delhi Technological University
Delhi, Delhi, India

***Manoj Dixit**
Centre for Energy Studies,
Indian Institute of Technology Delhi
New Delhi, Delhi, India

**S.C. Kaushik**
Centre for Energy Studies,
Indian Institute of Technology Delhi
New Delhi, Delhi, India

*Keywords:* Half effect, exergy analysis, Vapour Absorption Refrigeration, Water-lithium bromide
* *Corresponding author:* Phone: 91-9540660289
*E-mail address:* mandix@ces.iitd.ac.in

## ABSTRACT

In this research paper, energy and exergy analyses of water lithium bromide half effect vapour absorption refrigeration system has been carried out. Based on energy and exergy analysis the optimum intermediate pressure is computed corresponding to maximum values of coefficient of performance and exergetic efficiency under various operating conditions. It is found that the optimum intermediate pressure corresponding to maximum values of coefficient of performance and exergetic efficiency is same. The effects of low and high pressure generator temperatures, evaporator temperature, effectiveness of solution heat exchangers and difference between low and high pressure generator temperatures have been considered in computing optimum intermediate pressure. The maximum COP varies between 0.415 - 0.438 and maximum exergetic efficiency varies between 6.96-13.74%.

## INTRODUCTION

Refrigeration and air-conditioning systems have a major impact on energy demand with nearly 30% of the total energy consumption in the world (Buzelin et al., 2005). The fast depletion of fossil fuels has led the scientists to search for refrigeration systems that consume less high grade energy for their operation. The vapour absorption refrigeration (VAR) systems are a good option in this context. Arivazhagan, Saravanan and Renganarayanan (2006) expressed that low temperature heat sources such as waste heat, low pressure steam, solar heat, geothermal energy, etc. can be used as input in the absorption machines. A half effect absorption cooling cycle promises the utilization of low temperature heat source such as geothermal energy or waste heat available at 60ºC to 80ºC (Herold, Radermacher and Klein, 1996). Many researches have reported theoretical and experimental works on single and double effect absorption systems in the recent years. However the literature on half effect VAR systems is scant. Ma and Deng (1996) carried out theoretical analysis of low-temperature hot source driven two-stage half effect water lithium bromide absorption refrigeration system. The effects of varying hot water and chilled water temperatures on COP of the system have been examined. Their results revealed that the COP of half effect cycle is lower than that of single effect VAR system using water lithium bromide. Sumathy, Huang and Li (2002) developed a model of two-stage lithium bromide solar absorption chiller and reported that two stage chiller could be driven by low temperature hot water ranging from 60 to 75°C. Arivazhagan et al. (2005) carried out simulation studies of a half effect vapour absorption cycle using R134a-DMAC refrigerant-absorbent pair with low temperature heat sources for cold storage applications. The intermediate pressure of the cycle was optimized for maximum COP. It was reported that the effect of the temperature of the low absorber on the performance is more pronounced than that of the high absorber. The COP for the baseline system was found to vary from 0.35 for low evaporating and high condensing temperatures to 0.46 for high evaporating and low condensing temperatures. The second law efficiency was reported to be varying between 28-

44% for the sink temperature less than 30°C. Arivazhagan, Saravanan and Renganarayanan (2006) carried out experimental investigations of a half effect vapour absorption cycle using R134a-DMAC refrigerant-absorbent pair. The performance of the system in terms of degassing range, coefficient of performance and second law efficiency was examined. The system was able to operate at as low as -7°C evaporator temperature with generator temperatures varying from 55 to 75°C. The degassing range kept in high absorber was 40% more than in low absorber when the high absorber is operated at optimum intermediate pressure.

Domínguez-Inzunza et al. (2014) studied the performance of single-effect, half-effect and double-effect in series, double-effect inverse and triple-effect absorption cooling systems operating with ammonia-lithium nitrate. The COP obtained was 0.3 for half effect systems at the lowest evaporator and generator temperatures Crepinsek, Goricanec and Krope (2009) examined the performance on the basis of coefficient of performance and circulation ratio of single effect and half effect absorption refrigeration cycles for refrigeration temperatures below 0°C. The focus, in this paper, was to compare performances of the ammonia-water and possible alternative refrigerant absorbent pairs viz. ammonia-lithium nitrate, ammonia sodium thiocyanate, monomethylamine-water, R22-DMEU, R32-DMEU, R124-DMEU, R152a-DMEU, R125-DMEU, R134a-DMEU, trifluoroethanol (TFE)-tetraethylenglycol dimethyl ether (TEGDME), methanol-TEGDME and R134a-DMAC.

Gebreslassie, Medrano and Boer (2010) carried out exergy analysis for single, double, triple and half effect Water–Lithium bromide absorption cycles and calculated unavoidable exergy destruction. Their study did not include the computation of optimal values of intermediate pressure in half effect cycle. Gomri (2010) used solar energy as a heat source for computing the performance of a 10 kW capacity two stage half-effect absorption cooling system. The performance was computed based on the energy and exergy analysis principles.

Thus it is obvious from the literature review that the studies carried out on half effect VAR system are either theoretical (based on energy analysis) using water lithium bromide as refrigerant absorbent pair or experimental wherein the R134a-DMAC and many other absorbent refrigerant pairs are used.

In the works mentioned above, none of the researchers explained logically about the variation of various parameters. The criteria of the researchers for the analysis was to compute either the COP or the exergetic efficiency of the half effect LiBr- $H_2O$ vapour absorption refrigeration system. None of the researcher examined the optimum performance parameters for the operation of the system for water lithium bromide system. The optimum parameters include the intermediate system pressure (i.e. LP generator pressure or HP absorber pressure), maximum COP, maximum exergetic efficiency, optimum solution circulation ratio in LP and HP circuits and effect of heat exchanger effectiveness on the maximum COP and maximum exergetic efficiency.

Considering the above facts, the objective of the present work is chosen to be the energy and exergy analysis of the water lithium bromide half effect VAR system. The energy and exergy analyses are carried out to compute the optimum intermediate pressure corresponding to maximum COP and maximum exergetic efficiency. The effects of LP and HP generators temperatures, absorber temperature, evaporator temperature and effectiveness of solution heat exchangers are studied on optimum solution circulation ratio, maximum COP and maximum exergetic efficiency of the system.

## DESCRIPTION OF HALF EFFECT VAR SYSTEM

The half effect water lithium bromide absorption refrigeration system shown schematically in Fig. 1 comprises of an evaporator, LP & HP absorbers, LP & HP generators, LP and HP solution heat exchangers, condenser, solution pumps and solution and refrigerant throttle valves. The condenser and HP generator operate at same pressure which is the highest system pressure. The HP absorber and LP generator operate at same intermediate pressure whereas the LP absorber and evaporator operate at same lowest system pressure. Following relationship exists among the pressures in these components:

$$(P_{g_h} = P_c) > (P_{g_l} = P_{a_h}) > (P_{a_l} = P_e)$$

The refrigerant (water) is circulated through the evaporator, LP absorber, LP generator, HP absorber, HP generator and condenser. After water vapour has condensed in the condenser, it returns to the evaporator through an expansion valve. However, the absorbent lithium bromide aqueous solution is circulated within two separate stages i.e. a LP stage between the LP absorber and the LP generator, and a HP stage between the HP absorber and the HP generator. Compared to a single-stage absorption refrigeration system, there are two additional components viz. HP absorber and LP generator in a half effect system. These are used to concentrate the lithium bromide aqueous solution in the LP stage cycle.

## THERMODYNAMIC ANALYSIS

Following assumptions are made for the analysis : Heat losses through the system components are negligible; and reference enthalpy ($h_o$) and entropy ($s_o$) used for calculating exergy of the working fluid are the values for water at an environmental temperature and pressure of 25°C and 1 bar respectively. For the computing the optimum parameters of half effect VAR system, the principles of mass and material conservation, energy balance (First law of thermodynamics) and exergy balance

(Second law of thermodynamics) are applied to each component of the system. Each component has been treated as a control volume with inlet and outlet streams, heat transfer and work interactions. The application of above mentioned principles is presented in the following equations.

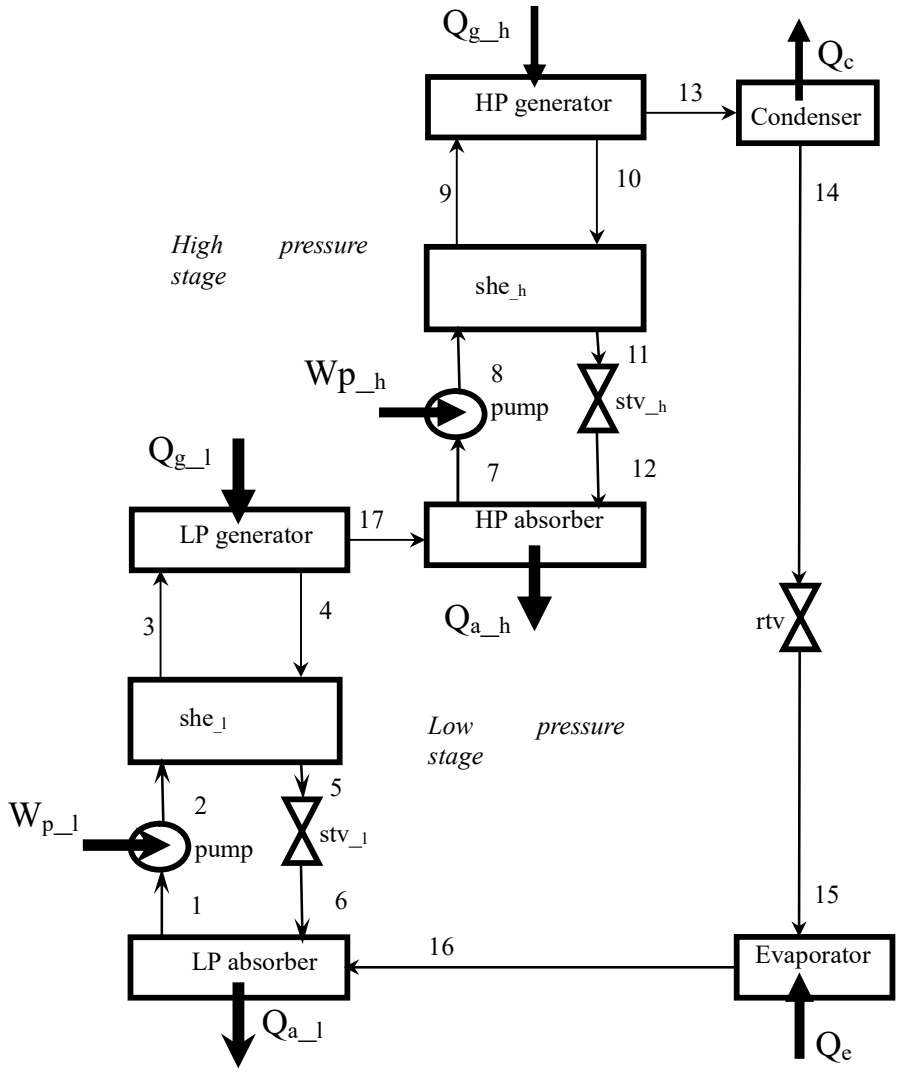


**Fig. 1** Schematic diagram of a half effect water lithium bromide VAR system

***Mass balance***

The governing equations of mass and material conservation for a steady state and steady flow system are given below:

$$\sum \dot{m}_i = \sum \dot{m}_e \tag{1}$$

The equations of mass balance in a Half Effect system are specified below.

*LP generator or LP absorber*

$$\dot{m}_{g,l} = \dot{m}_{w,l} + \dot{m}_r \tag{2}$$

*HP generator or HP absorber*

$$\dot{m}_{g,h} = \dot{m}_{w,h} + \dot{m}_r \tag{3}$$

The mass flow rate of refrigerant through evaporator is $\dot{m}_r$.

***Material Balance***

*LP generator or LP absorber*

$$\dot{m}_{s,l} X_{s,l} = \dot{m}_{w,l} X_{w,l} \quad (4)$$

*HP generator or HP absorber*

$$\dot{m}_{s,h} X_{s,h} = \dot{m}_{w,h} X_{w,h} \quad (5)$$

**Energy Balance**

The first law of thermodynamics yields the energy balance of each component of the VAR system as follows:

$$\sum(\dot{m}_e h_e) - \sum(\dot{m}_i h_i) + \sum \dot{Q}_i = \dot{W} \quad (6)$$

The energy in each component of a Half Effect system is given by the following equations:

$$\dot{Q}_{a,l} = \dot{m}_r h_{16} + \dot{m}_{w,l} h_6 - \dot{m}_{s,l} h_1 \quad (7)$$

$$\dot{Q}_{g,l} = \dot{m}_r h_{17} + \dot{m}_{w,l} h_4 - \dot{m}_{s,l} h_3 \quad (8)$$

$$\dot{Q}_{a,h} = \dot{m}_r h_{17} + \dot{m}_{w,h} h_{12} - \dot{m}_{s,h} h_7 \quad (9)$$

$$\dot{Q}_{g,h} = \dot{m}_r h_{13} + \dot{m}_{w,h} h_{10} - \dot{m}_{s,h} h_9 \quad (10)$$

$$\dot{Q}_c = \dot{m}_r (h_{13} - h_{14}) \quad (11)$$

$$\dot{Q}_e = \dot{m}_r (h_{16} - h_{15}) \quad (12)$$

$$\dot{Q}_{shx,l} = \dot{m}_{s,l} (h_3 - h_2) = \dot{m}_{w,l} (h_4 - h_5) \quad (13)$$

$$\dot{Q}_{shx,h} = \dot{m}_{s,h} (h_9 - h_8) = \dot{m}_{w,h} (h_{10} - h_{11}) \quad (14)$$

$$\dot{W}_{p,l} = \dot{m}_{s,l} (h_2 - h_1) \quad (15)$$

$$\dot{W}_{p,h} = \dot{m}_{s,h} (h_8 - h_7) \quad (16)$$

$$Energy\ input = \dot{Q}_{g,l} + \dot{Q}_{g,h} + \dot{Q}_e + \dot{W}_{p,l} + \dot{W}_{p,h} \quad (17)$$

$$Energy\ output = \dot{Q}_{a,l} + \dot{Q}_{a,h} + \dot{Q}_c \quad (18)$$

The coefficient of performance (COP) of the Half Effect VAR system is defined as the ratio of the cooling capacity obtained at the evaporator divided by energy input into the high and low pressure generators and pumps. Accordingly, COP is given by Eq. (19).

$$COP = \frac{\dot{Q}_e}{\dot{Q}_{g,l} + \dot{Q}_{g,h} + \dot{W}_{p,l} + \dot{W}_{p,h}} \quad (19)$$

The solution circulation ratio (SCR) is defined as the ratio of the mass flow rate of the strong solution to the mass flow rate of the refrigerant. The solution circulation ratio of the low pressure and high pressure stages are given by the equations (20) and (21) respectively.

$$SCR_l = \frac{\dot{m}_{s,l}}{\dot{m}_r} = \frac{x_{w,l}}{x_{w,l} - x_{s,l}} \quad (20)$$

$$SCR_h = \frac{\dot{m}_{s,h}}{\dot{m}_r} = \frac{x_{w,h}}{x_{w,h} - x_{s,h}} \quad (21)$$

**Exergy Balance**

Exergy destruction in each component of a Half Effect Generation VAR system is furnished below:

$$\dot{E}D_{a_l} = \dot{m}_r (h_{16} - T_o s_{16}) + \dot{m}_{w_l} (h_6 - T_o s_6) - \dot{m}_{s_l} (h_1 - T_o s_1) \quad (22)$$

$$\dot{E}D_{g_l} = \dot{m}_{s_l} (h_3 - T_o s_3) - \dot{m}_{w_l} (h_4 - T_o s_4) - \dot{m}_r (h_{17} - T_o s_{17}) + \dot{Q}_{g_l} (1 - T_0 / T_{g_l}) \quad (23)$$

$$\dot{E}D_{a_h} = \dot{m}_r (h_{17} - T_o s_{17}) + \dot{m}_{w_h} (h_{12} - T_o s_{12}) - \dot{m}_{s_h} (h_7 - T_o s_7) \quad (24)$$

$$\dot{E}D_{g_h} = \dot{m}_{s_h} (h_9 - T_o s_9) - \dot{m}_{w_h} (h_{10} - T_o s_{10}) - \dot{m}_r (h_{13} - T_o s_{13}) + \dot{Q}_{g_h} (1 - T_0 / T_{g_h}) \quad (25)$$

$$\dot{E}D_c = \dot{m}_r ((h_7 - h_8) - T_o (s_7 - s_8)) \quad (26)$$

$$\dot{E}D_e = \dot{m}_r ((h_9 - h_{10}) - T_o (s_9 - s_{10})) + Q_e \left(1 - \frac{T_o}{T_r}\right) \quad (27)$$

$$\dot{E}D_{she_l} = \dot{m}_{s_l}((h_2 - h_3) - T_o(s_2 - s_3)) + \dot{m}_{w_l}((h_4 - h_5) - T_o(s_4 - s_5)) \quad (28)$$

$$\dot{E}D_{she_h} = \dot{m}_{s_h}((h_8 - h_9) - T_o(s_8 - s_9) + \dot{m}_{w_h}((h_{10} - h_{11}) - T_o(s_{10} - s_{11})) \quad (29)$$

$$\dot{E}D_{rtv} = \dot{m}_r T_o(s_{15} - s_{16}) \quad (30)$$

$$\dot{E}D_{stv_l} = \dot{m}_{w_l} T_o(s_6 - s_5) \quad (31)$$

$$\dot{E}D_{stv_h} = \dot{m}_{w_h} T_o(s_{12} - s_{11}) \quad (32)$$

$$\dot{E}D_t = \dot{E}D_{a_l} + \dot{E}D_{a_h} + \dot{E}D_{g_l} + \dot{E}D_{g_h} + \dot{E}D_c + \dot{E}D_e + \dot{E}D_{she_l} + \dot{E}D_{she_h} + \dot{E}D_{rtv} + \dot{E}D_{stv_l} + \dot{E}D_{stv_h} \quad (33)$$

**Exergetic Efficiency**

$$\eta_{e_x} = \frac{\dot{Q}_e\left|(1 - T_0/T_r)\right|}{\dot{Q}_{g_l}\left(1 - T_0/T_{g_l}\right) + \dot{W}_{p_l} + \dot{Q}_{g_h}\left(1 - T_0/T_{g_h}\right) + \dot{W}_{p_h}} \quad (34)$$

The base parameters considered for computation of results are evaporator temperature ($T_e$) = 7°C, condenser temperature ($T_c$) = 37.8°C, absorber temperature in low and high pressure stages ($T_{a_l} = T_{a_h}$) = 37.8°C, effectiveness of solution heat exchangers = 0.7, mass flow rate of refrigerant (water) = 1 kg/s.

## RESULTS AND DISCUSSION

The results of the present analysis have been compared with the results of Ma and Deng (1996). It is observed that the COP in the present work is about 5% higher than the value obtained in their work. The difference in values is due to the fact that the properties of water lithium bromide have been taken from McNeely (1985) whereas in the present study the water lithium bromide properties are referred from Pa´tek and Klomfar (2006). Moreover, the values of heat exchanger effectiveness have not been reported by them whereas in the present work the same have been considered as 0.7.

Figure 2 presents the effect of variation in LP and HP generator temperatures on COP and exergetic efficiency of the Half Effect Generation VAR system. A small increase in the generator temperatures above 60.5°C causes the COP and exergetic efficiency values to increase abruptly. With further increase in HP and LP generator temperatures, the COP becomes constant whereas exergetic efficiency shows a decreasing trend. The initial values of COP and exergetic efficiency are nearly zero since the solution circulation ratio in HP stage is very high and consequently heat duty rate in HP generator is high. The maximum values of COP and exergetic efficiency obtained are about 0.41 and 9.5% respectively.

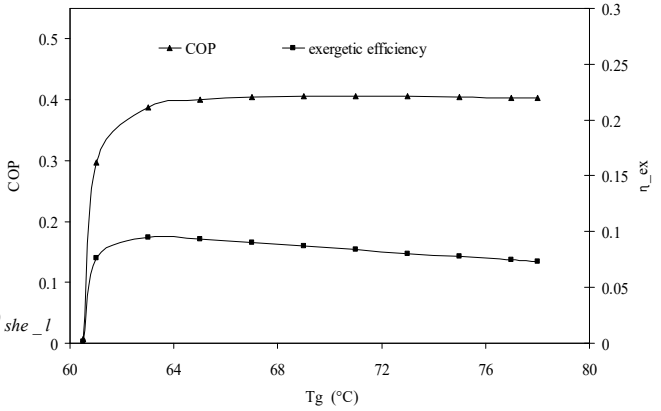


**Fig. 2** Variation of COP and exergetic efficiency with generator temperature ($T_e$ = 7°C, $T_{al} = T_{ah} = T_c$ = 37.8°C, $T_{gl} = T_{gh}$, $\varepsilon_she_l = \varepsilon_she_h$ =0.7)

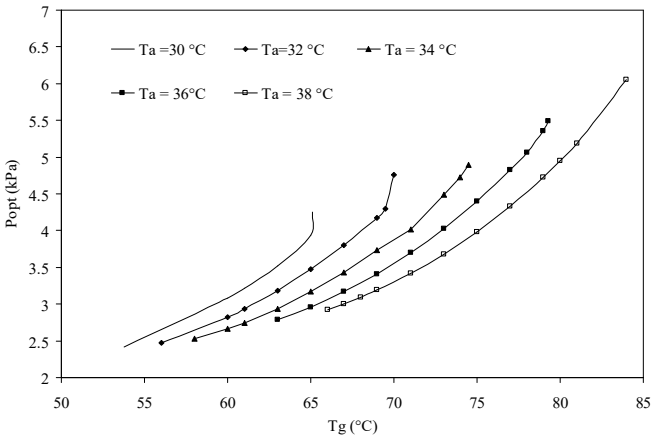


**Fig. 3** Variation of optimum intermediate pressure ($T_e$ = 7°C, $T_{a,l} = T_{a,h} = T_c$, $T_{g,l} = T_{g,h}$, $\varepsilon_{she,l} = \varepsilon_{she,h}$ =0.7)

Figure 3 illustrates the effect of generator temperature on optimum intermediate pressure for different absorber temperatures. For a constant absorber temperature, it is observed that with increase in generator temperature the optimum intermediate pressure increases. When generator temperature is increased beyond the value corresponding to maximum COP and maximum exergetic efficiency, then the requirement of heat in the generator increases resulting in fall of both COP and exergetic efficiency. Thus, in order to obtain the point of maximum COP and maximum exergetic efficiency corresponding to the increased generator temperature (at constant absorber temperature) the intermediate pressure has to be increased. Hence, optimum intermediate pressure increases

with increase in the generator temperature. For a constant value of generator temperature, the increase in absorber temperature is responsible for increase in solution circulation ratios and this causes the heat supply to increase in HP and LP generators. In order to maximize the COP and exergetic efficiency, the intermediate pressure should be reduced. So, optimum intermediate pressure decreases as absorber temperature increases.

Figure 4 presents the effect of generator temperature on maximum value of COP. It is observed that the maximum COP nearly remains constant with increase in generator temperature. This happens because the optimum pressure is adjusted in such a way that small reduction in heat supply in HP stage generator is observed whereas there is small increase in heat supply in LP generator. These two effects negate each other and hence maximum COP remains nearly constant.
As specified in previous paragraph that with increase in absorber temperature the optimum intermediate pressure is achieved for higher values of solution circulation ratios, hence more heat is to be supplied for the same generator temperature. Further, it is also observed that increase in condenser temperature causes more flashing during throttling in refrigerant throttle valve, hence cooling effect reduces marginally. Thus, increase in heat duty in generators and decrease in cooling effect in evaporator result in a decrease of COP when absorber and condenser temperatures increase. The maximum value of maximum COP achieved is about 0.438 (corresponding to $T_{a,h}$ = $T_{a,l}$ = $T_c$ = 30ºC) whereas minimum value of maximum COP achieved is about 0.415(corresponding to $T_{a_h}$ = $T_{a_l}$ = $T_c$ = 38ºC)

The variation of maximum exergetic efficiency is shown in Fig. 5. It is observed that with increase in HP and LP generator temperatures, maximum exergetic efficiency reduces. This happens because of increase in total irreversibility. The irreversibility in generators increase, since the temperature difference between the solution exiting the solution heat exchanger and generator increases. The irreversibility in absorbers also increase because of the weak solution which leaves the solution heat exchangers is at a temperature higher than before and hence the temperature difference between refrigerant and weak solution increases causing an increase in entropy generation and consequently higher exergy destruction is observed in absorbers. The irreversibility in condenser also increases because of increase in average temperature of condenser. The change in exergy destruction in valves is negligible. Thus increase in total exergy destruction is observed for the same output exergy and hence maximum exergetic efficiency decreases. The increase in absorber temperature causes increase in solution circulation ratio in LP and HP stages and consequently exergy destruction increase causing the maximum exergetic efficiency to reduce. The maximum and minimum values of maximum exergetic efficiency obtained are 13.74% and 6.96% under identical set of conditions as specified in previous paragraph.

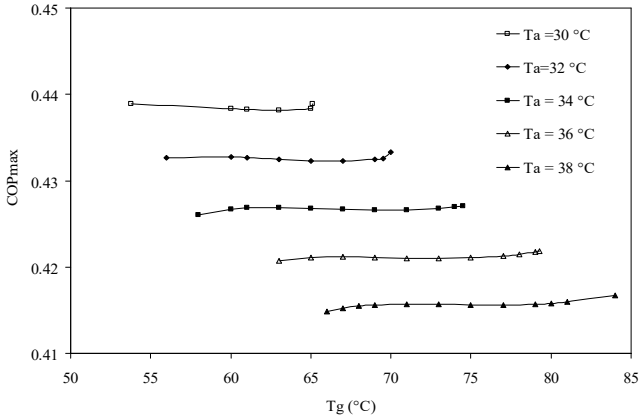


**Fig. 4** Variation of maximum COP with generator temperature ($T_e$ = 7°C , $T_{a,l}$ = $T_{a,h}$ = $T_c$, $T_{g,l}$ = $T_{g,h}$, $\varepsilon_{she,l}$ =$\varepsilon_{she,h}$ =0.7, $P_{g,l}$ = $P_{a,h}$ = $P_{opt}$)

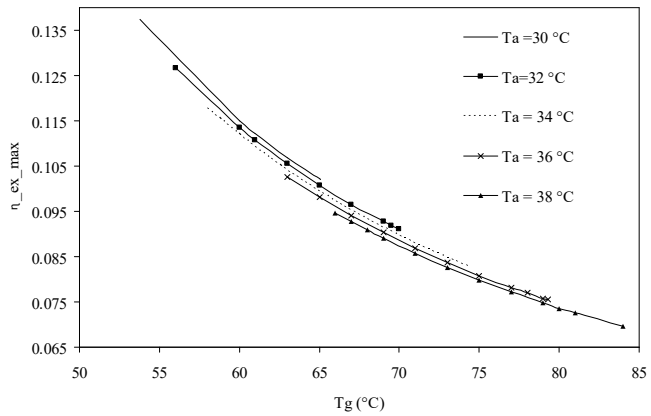


**Fig. 5** Variation of maximum exergetic efficiency with generator temperature ($T_e$ = 7°C, $T_{a,l}$ = $T_{a,h}$ = $T_c$, $T_{g,l}$ = $T_{g,h}$, $\varepsilon_{she,l}$ =$\varepsilon_{she,h}$ =0.7)

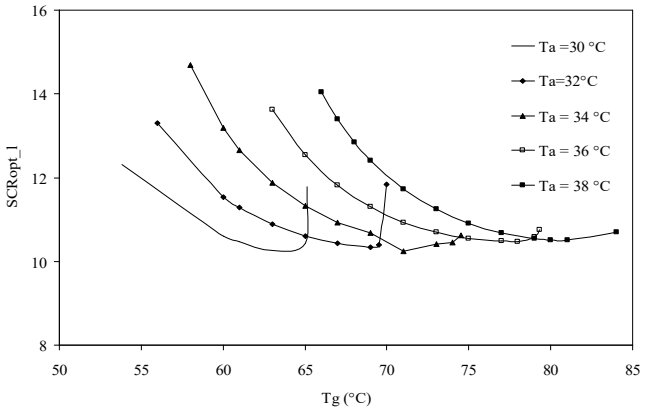


**Fig. 6** Variation of optimum solution circulation ratio in LP stage with generator temperature ($T_e$ = 7 °C, $T_{a,l}$ = $T_{a,h}$ = $T_c$ , $T_{g,l}$ = $T_{g,h}$, $\varepsilon_{she,l}$ =$\varepsilon_{she,h}$ =0.7)

Figures 6 and 7 illustrate the variation in optimum solution circulation ratio in LP and HP stages with generator temperature. It is observed that the optimum solution circulation ratio reduces with increase in generator temperature in HP stage up to a specific value of generator temperature and further increase in generator temperature causes the solution circulation ratio to drop suddenly. This can be explained on the basis that with increase in HP generator temperature the *'$Xw_h$'* keeps on increasing whereas *'$Xs_l$'* keeps on decreasing and correspondingly mass flow rates of weak as well as strong solution keeps on reducing in HP stage. Finally a limit reaches where the mass flow rate of weak solution is negligible and the mass of strong solution leaving the absorber is unity.

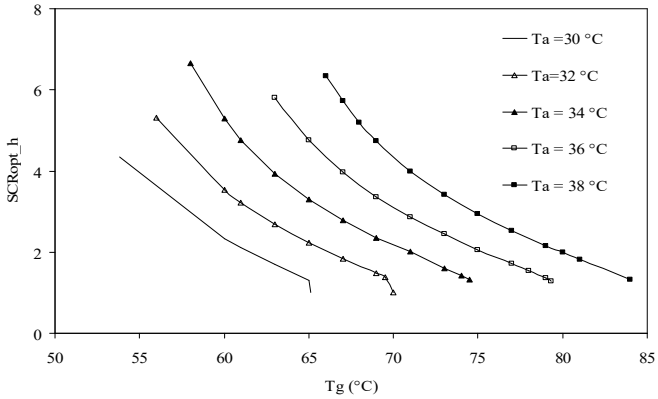


**Fig. 7** Variation of optimum solution circulation ratio in HP stage with generator temperature *(*$T_e$ = 7 °C, Tal = $T_{ah}$ = $T_c$ , $T_{gl}$ = $T_{gh}$, $\varepsilon_she_l$ =$\varepsilon_she_h$ =0.7)

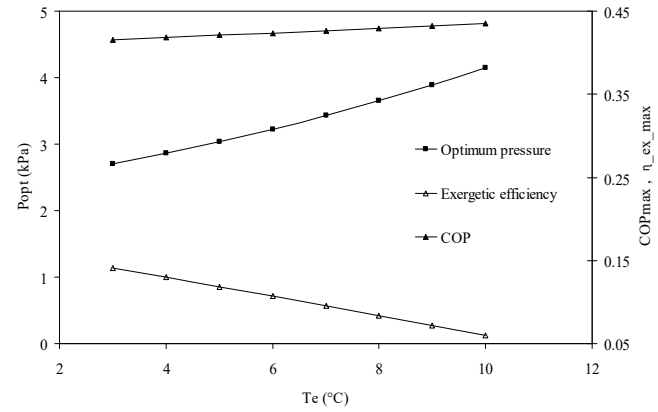


**Fig. 8** Variation of optimum pressure, maximum COP and maximum exergetic efficiency with evaporator temperature ($T_{ah}$ = $T_{al}$ = $T_c$ = 34°C, $T_{gh}$ = $T_{gl}$ = 67°C)

Thus the solution circulation ratio is nearly unity. Hence system can't be operated above this particular value of the solution circulation ratio since this is the minimum value which can be attained. Further it is also observed that the at this specific generator temperature, the optimum intermediate pressure (i.e. optimum pressure in HP absorber or LP generator) approaches condenser pressure. This is the reason for abrupt increase in the value of solution circulation ratio in LP stage.

Figure 8 illustrates the effect of evaporator temperature on optimum intermediate pressure, $COP_{max}$ and maximum exergetic efficiency. It is observed that with increase in evaporator temperature, evaporator pressure increases and consequently optimum intermediate pressure also increases. The $COP_{max}$ increases with increase in evaporator temperature because of reduction in solution circulation ratio in both LP and HP stages which causes heat supply rates to decrease in generators. The maximum exergetic efficiency reduces with increase in evaporator temperature. The results show a drop in both input and output exergies. However the rate of drop in output exergy per unit increase in evaporator temperature is found to be higher in comparison to rate of drop in input exergy per unit increase in evaporator temperature, hence exergetic efficiency, being a ratio of output exergy to input exergy, reduces.

Figure 9 shows the variation of optimum intermediate pressure in LP generator or HP absorber, $COP_{max}$ and maximum exergetic efficiency versus effectiveness of solution heat exchangers. It is seen that the optimum intermediate pressure, $COP_{max}$ and maximum exergetic efficiency increase with increase in effectiveness of solution heat exchangers. The $COP_{max}$ and maximum exergetic efficiency increase because with increase in effectiveness of solution heat exchangers the heat supply at generators is reduced. Secondly, the irreversibility reduces as the temperature difference between the solution exiting the solution heat exchangers and generators reduce and it contributes in increasing the exergetic efficiency.

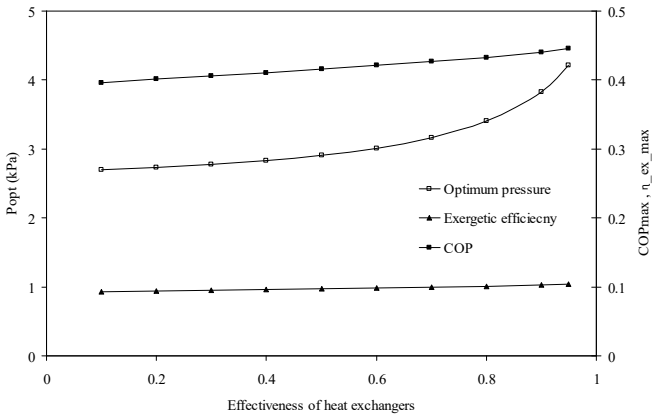


**Fig. 9** Variation of optimum pressure, maximum COP and maximum exergetic efficiency with effectiveness of heat exchangers ($T_{ah}$ = $T_{al}$ = $T_c$ = 34°C, $T_{gh}$ = $T_{gl}$ = 65°C, $T_e$ = 7°C)

The variation of optimum intermediate pressure with variation in effectiveness of one of the solution heat exchanger (when the effectiveness of other heat exchanger is kept constant) is indicated in Fig. 10. The results indicate that when effectiveness of LP heat exchanger is assumed constant while effectiveness of HP heat exchanger is varied, the optimum intermediate pressure reduces and trends reverse when effectiveness of HP heat exchanger is assumed constant while effectiveness of LP heat exchanger is varied.

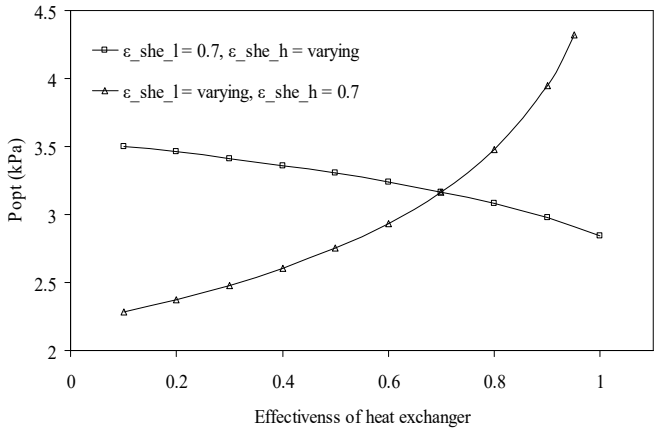


**Fig. 10** Variation of optimum pressure with effectiveness of heat exchangers keeping the effectiveness of one heat exchanger constant ($T_{ah} = T_{al} = T_c = 34°C$, $T_{g,h} = T_{g,l} = 65°C$, $T_e = 7°C$)

Moreover, the effect of varying the effectiveness of LP heat exchanger is higher on both $COP_{max}$ and maximum exergetic efficiency since the rate of rise of $COP_{max}$ and maximum exergetic efficiency with increase in effectiveness of LP heat exchanger is higher in comparison to corresponding effect of increase in effectiveness of HP heat exchanger as shown in Fig. 11.

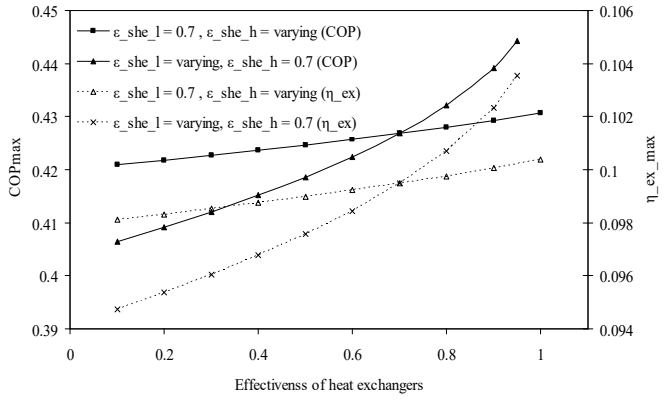


**Fig. 11** Variation of maximum COP with effectiveness of heat exchangers ($T_{ah} = T_{al} = T_c = 34°C$, $T_{gh} = T_{gl} = 65°C$, $T_e = 7°C$)

Figure 12 shows the effect of HP generator temperature on COP and exergetic efficiency when it is taken higher and lower than the LP generator temperature. The results indicated in this Fig. show that it is better to have HP generator temperature lower than the LP generator temperature since maximum COP and maximum exergetic efficiency are higher when LP generator temperature is higher than HP generator temperature.

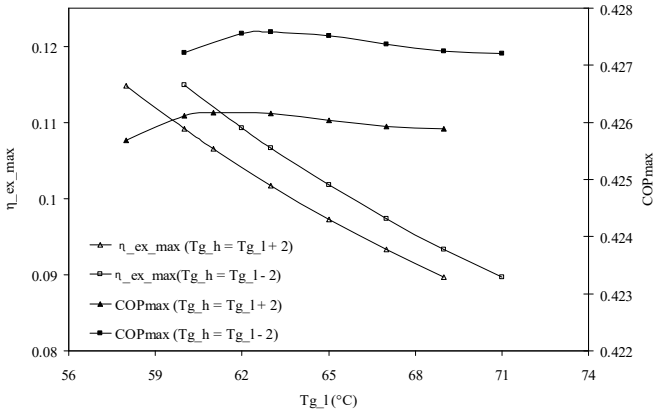


**Fig. 12** Variation of maximum COP and maximum exergetic efficiency with generator temperature in LP stage ($T_{al} = T_{ah} = T_c = 34°C$, $T_e = 7°C$, $\varepsilon_she_l = \varepsilon_she_h = 0.7$, $P_{g,l} = P_{a,h} = P_{opt}$)

## CONCLUSIONS

The main conclusions drawn on the basis of the analysis are listed below**:**

1. There exists a specific generator temperature below which a half effect system ceases to work. The COP and exergetic efficiency are zero corresponding to this value. In the present case, this value is found to be 60.5ºC corresponding to an intermediate pressure of 2 kPa (for Tc = Ta_l =Ta_h = 37.8C and Tg_h = Tg_l). The maximum value of COP achieved is about 0.41 and maximum exergetic efficiency attained is 9.5%. Such a trend of COP and exergetic efficiency is obtained only when the intermediate pressure (Pa_h or Pg_l) is not optimum.
2. There exists an optimum intermediate pressure (Pa_h_opt or Pg_l_opt) corresponding to which COP and exergetic efficiency are maximum. The optimum intermediate pressure increases with increase in LP or HP generator temperatures and evaporator temperature (at a particular absorber temperature) and decreases with increase in absorber temperature (at a particular generator temperature).
3. The variation in maximum COP (corresponding to optimum intermediate pressure) is negligible with increase in generator temperatures (for a particular absorber temperature) whereas maximum exergetic efficiency is found to decrease under identical set of conditions. The maximum COP and maximum exergetic efficiency reduce with increase in absorber temperature.
4. With the increase in evaporator temperature, the increase in maximum COP is negligible. The maximum exergetic efficiency reduces under identical conditions.
5. The increase in effectiveness of solution heat exchangers causes optimum intermediate pressure, maximum COP and

maximum exergetic efficiency to increase. Also, the influence of effectiveness of lower heat exchanger is more pronounced than that of higher heat exchanger.

6. The maximum COP and maximum exergetic efficiency are higher when LP generator temperature is higher in comparison to HP generator temperature.

## NOMENCLATURE

| | |
|---|---|
| COP | Coefficient of performance |
| e | Specific exergy (kJ/kg) |
| $\dot{E}$ | Exergy rate of fluid (kW) |
| $\dot{E}D$ | Exergy destruction rate (kW) |
| $\dot{E}F$ | Exergy rate of fuel (kW) |
| $\dot{E}P$ | Exergy rate of product (kW) |
| h | Enthalpy (kJ/kg) |
| HP | High pressure |
| LP | Low pressure |
| $\dot{m}$ | Mass flow rate (kg/s) |
| P | Pressure (kPa) |
| $\dot{Q}$ | Rate of heat transfer (kW) |
| s | Entropy (kJ/kg K) |
| SCR | Solution circulation ratio |
| T | Temperature (°C) |
| VAR | Vapour Absorption Refrigeration |
| $\dot{W}$ | Work transfer rate (kW) |
| X | LiBr mass fraction |
| **Subscripts** | |
| a | Absorber |
| c | Condenser |
| e | Evaporator |
| ex | Exergetic |
| g | Generator |
| h | High temperature stage |
| l | Low temperature stage |
| max | Maximum |
| opt | Optimum |
| p | Pump |
| r | Refrigerant, room |
| rtv | Refrigerant throttle valve |
| s | Strong |
| she | Solution heat exchanger |
| t | Total |
| w | Weak |
| 0 | Dead state |
| **Greek letters** | |
| ε | Effectiveness |
| η | Efficiency |
| ∑ | Sum of |

## ACKNOWLEDGMENTS

The support of Ministry of New and Renewable Energy (MNRE), Government of India is duly acknowledged.

## REFERENCES

[1] Vliet G.C., Lawson, M.B., Lithgow, R.A., 1982. Water-Lithium Bromide double effect absorption cooling system analysis. ASHRAE Transactions HO-82-5(2), 811-823.

[2] Fallek M., 1985. Parallel flow Chiller- heater. ASHRAE Transactions HI-85-41(5), 2095-2102.

[3] Kaushik S. C. and Chandra S., 1985. Computer modeling and parametric study of a double effect generation absorption refrigeration cycle. Energy Conversion Management 25(1), 9-14.

[4] Iyer, P. S. A, Murthy S. S. and Murthy M. V. K., 1988. Correlations for evaluation of the performance characteristics of vapour absorption refrigeration cycles. Solar & Wind Technology 5 (2), 191-197.

[5] Gommed K. and Grossman, G., 1990. Performance analysis of staged absorption heat pumps: water-lithium bromide systems. ASHRAE Transactions 30(6), 1590-1598.

[6] Riffat, S. B. and Shankland, N., 1993. Integration of absorption and vapour-compression systems. Applied Energy 46(4), 303-316.

[7] Oh M. D., Kim S. C., Kim Y. L. and Kim Y. I., 1994. Cycle analysis of an air-cooled LiBr/$H_2O$ absorption heat pump of parallel-flow type. International Journal of Refrigeration 17(8), 556- 565.

[8] Xu G. P., Dai Y. Q., Tou K. W. and Tso C. P.,1996. Theoretical analysis and optimization of a double-effect series-flow-type absorption chiller. Applied Thermal Engineering 16(12), 975-987.

[9] Xu G. P. and Dai Y.Q., 1997. Theoretical analysis and optimization of a double-effect parallel flow type absorption chiller. Applied Thermal Engineering 17(2), 157-170.

[10] Arun M.B., Maiya M.P., Murthy S. S, 2000. Equilibrium low pressure generator temperatures for double effect series flow absorption refrigeration systems. Applied Thermal Engineering 20, 227-242.

[11] Elsafty A and Al-Daini A.J., 2000. Theoretical Investigation of a water-lithium bromide vapour absorption cooler, Renewables: The Energy for the 21st Century World Renewable Energy Congress VI, Brighton, UK, 2202-2205.

[12] Arun M.B., Maiya M.P., Murthy S. S, 2001. Performance comparison of double effect parallel flow and series flow water lithium bromide absorption systems. Applied Thermal Engineering 21, 1273-1279.

[13] Lee, S.F., Sherif, S.A., 1999. Second law analysis of multi effect Lithium Bromide/Water absorption chillers. ASHRAE Transactions Ch-99-23(3), 1256- 1266.

[14] Izquierdo M., Vega M. D, Lecuona A., Rodríguez P., 2000. Entropy generated and exergy destroyed in lithium bromide thermal compressors driven by the exhaust gases of an engine. International Journal of Energy Research 24(13), 1123 – 1140.

[15] Lee, S.F., Sherif, S.A., 2001. Second law analysis of various double effect Lithium Bromide/Water absorption chillers. ASHRAE Transactions AT-01-9(5), 664-673.
[16] Gebreslassie B.H., Medrano M., Boer D., 2010. Exergy analysis of multi-effect water LiBr/absorption systems: From half to triple effect. Renewable Energy 35, 1773–1782.
[17] Izquierdo M., Marcos J.D., Palacios M.E., González-Gil A., 2012. Experimental evaluation of a low-power direct air-cooled double-effect LiBr-H2O absorption prototype. Energy 37, 737-748.
[18] Farshi L.G., Mahmoudi S.M.S., Rosen M.A., Yari M., Amidpour M., 2013. Exergoeconomic analysis of double effect absorption refrigeration systems. Energy Conversion and Management 65, 13–25.
[19] Li Z., Ye X., Liu J., 2014. Performance analysis of solar air cooled double effect LiBr/$H_2O$ absorption cooling system in subtropical city. Energy Conversion and Management 85, 302-312.
[20] Arcaklıoğlu E., Cavuşoğlu A. and Erişen A, 2005. An algorithmic approach towards finding better refrigerant substitutes of CFCs in terms of the second law of thermodynamics. Energy Conversion and Management 46, 1595-1611.
[21] Bejan, A., Tsatsaronis, G., Moran, M., 1996. Thermal Design and Optimization. John Wiley and Sons Inc., USA, 143–156.
[22] Klein S.A., Alvarado F., 2005. Engineering Equation Solver, Version 7.441, F-Chart software, Middleton, WI.
[23] Pátek J., Klomfar J., 2006. A computationally effective formulation of the thermodynamic properties of LiBr/H2O solutions from 273 to 500 K over full composition range. International Journal of Refrigeration 29, 566-578.

Journal of Statistical Theory and Applications, Vol. 14, No. 4 (December 2015), 399-412

# Dynamic Cumulative Residual and Past Inaccuracy Measures

Vikas Kumar*
*Department of Applied Sciences, UIET, M. D. University,*
*Rohtak-124001, India*
*vikas_iitr82@yahoo.co.in*

H. C. Taneja
*Department of Applied Mathematics, Delhi Technological University,*
*Delhi-110042, India*
*hctaneja@rediffmail.com*

Received 15 April 2014

Accepted 12 March 2015

In this paper, we have developed measures of dynamic cumulative residual and past inaccuracy. We have studied characterization results under proportional hazard model in case of dynamic cumulative residual inaccuracy and under proportional reversed hazard model in case of dynamic cumulative past inaccuracy measure. We have characterized certain specific lifetime distributions using the measures proposed. Some generalized results have also been considered.

*Keywords*: Shannon entropy; Cumulative residual entropy; Cumulative inaccuracy measure; Mean residual life function; Proportional hazard model.

2000 Mathematics Subject Classification: 62N05, 90B25

## 1. Introduction

Let $X$ and $Y$ be two non-negative random variables representing time to failure of two systems with p.d.f. respectively $f(x)$ and $g(x)$. Let $F(x) = P(X \leq x)$ and $G(y) = P(Y \leq y)$ be failure distributions, and $\bar{F}(x) = 1 - F(x)$, $\bar{G}(x) = 1 - G(x)$ be survival functions of $X$ and $Y$ respectively. Shannon's (1948) measure of uncertainty associated with the random variable $X$ and Kerridge measure of inaccuracy (1961) are given as

$$H(f) = -\int_0^\infty f(x) \log f(x) dx \,, \tag{1.1}$$

and

$$H(f;g) = -\int_0^\infty f(x) \log g(x) dx \,, \tag{1.2}$$

*Corresponding Author.


Copyright: the authors

respectively. In case $g(x) = f(x)$, then (1.2) reduces to (1.1).

The measures (1.1) and (1.2) are not applicable to a system which has survived for some unit of time, say $t$. Ebrahimi (1996) considered the entropy of the residual lifetime $X_t = [X - t|X > t]$ as a dynamic measure of uncertainty given by

$$H(f;t) = -\int_t^\infty \frac{f(x)}{\bar{F}(t)} \log \frac{f(x)}{\bar{F}(t)} dx \,. \tag{1.3}$$

Extending the dynamic measure of information, a dynamic measure of inaccuracy, refer to Taneja et al. (2009) is given as

$$H(f,g;t) = -\int_t^\infty \frac{f(x)}{\bar{F}(t)} \log \frac{g(x)}{\bar{G}(t)} dx \,. \tag{1.4}$$

Rao et al. (2004) introduced an alternate measure of entropy called *cumulative residual entropy (CRE)* of a random variable $X$ defined as

$$\xi(F) = -\int_0^\infty \bar{F}(x) \log \bar{F}(x) dx \,, \tag{1.5}$$

where $\bar{F}(x) = 1 - F(x)$ is the survival function of $X$.
This measure is based on cumulative distribution function (CDF) rather than probability density function, and is thus, in general more stable since the distribution function is more regular because it is defined in an integral form unlike the density function which is defined as the derivative of the distribution function. Some general results regarding this measure have been studied by Rao (2005), Drissi et al. (2008) and Navarro et al. (2010).

Asadi and Zohrevand (2007) have defined the dynamic cumulative residual entropy (DCRE) as the cumulative residual entropy of the residual lifetime $X_t = [X - t|X > t]$. This is given by

$$\xi(F;t) = -\int_t^\infty \frac{\bar{F}(x)}{\bar{F}(t)} \log \frac{\bar{F}(x)}{\bar{F}(t)} dx \,. \tag{1.6}$$

In this paper we propose dynamic cumulative residual and past inaccuracy measures and study their characterization results. The paper is organized as follows. In Section 2, we consider cumulative residual inaccuracy measure and derive a lower bound to it. Section 3 contains the dynamic cumulative residual inaccuracy. In Section 4, we study characterization results concerning dynamic cumulative residual inaccuracy measure and also characterize a few specific lifetime distributions. Section 5 considers dynamic cumulative past inaccuracy measure and its characterization result. Finally we give some conclusions and comments.

## 2. Cumulative Residual Inaccuracy Measure

If $\bar{F}(.)$ and $\bar{G}(.)$ are survival functions of lifetime random variables $X$ and $Y$ respectively, then the cumulative residual inaccuracy is defined as

$$\xi(F;G) = -\int_0^\infty \bar{F}(x) \log \bar{G}(x) dx \,. \tag{2.1}$$

Here and throughout this communication, we consider the random variables $X$ and $Y$ with the same support.


Copyright: the authors

When the two distributions $F$ and $G$ coincide, the measure (2.1) reduces to the cumulative residual entropy (1.5). Even if the two random variables $X$ and $Y$ satisfy the proportional hazard model (PHM), refer to Cox (1972) and Efron (1981), that is, if $\lambda_G(x) = \beta\lambda_F(x)$, or equivalently

$$\bar{G}(x) = [\bar{F}(x)]^{\beta}, \tag{2.2}$$

for some constant $\beta > 0$, then obviously the cumulative residual inaccuracy (2.1) reduces to a constant multiple of the cumulative residual entropy (1.5).

**Example 2.1** Let a non-negative random variable $X$ be uniformly distributed over $(a,b)$, $a < b$, with density and distribution functions respectively given by

$$f(x) = \frac{1}{b-a} \text{ and } F(x) = \frac{x-a}{b-a},\ a < x < b.$$

If the random variables X and Y satisfy the proportional hazard model (PHM), then the distribution function of the random variable $Y$ is

$$\bar{G}(x) = [\bar{F}(x)]^{\beta} = \left[\frac{b-x}{b-a}\right]^{\beta},\ a < x < b\ ,\ \beta > 0.$$

Substituting these in (2.1) and simplifying we obtain the cumulative inaccuracy measure as

$$\xi(F;G) = \frac{\beta(b-a)}{4}\ .$$

### 2.1. *A lower bound to* $\xi(F;G)$

Before deriving the lower bound to $\xi(F;G)$, we define the *log-sum inequality* given as follows: Let $m$ be a sigma finite measure. If $f$ and $g$ are positive and $m$-integrable, then

$$\int \log\left(\frac{f}{g}\right) dm \geq \left[\int f dm\right] \log\frac{\int f dm}{\int g dm}\ . \tag{2.3}$$

We prove the following result.

**Theorem 2.1.** *If $X$ and $Y$ are non-negative random variables with finite means $E(X)$ and $E(Y)$ respectively and CRE $\xi(F)$ is finite, then*

$$\xi(F;G) \geq \int_0^{\infty} F(x)\bar{F}(x)dx + E(X) - E(Y). \tag{2.4}$$

**Proof** We have

$$\begin{aligned}\xi(F;G) &= -\int_0^{\infty} \bar{F}(x)\log\bar{G}(x)dx\ ,\\ &= -\int_0^{\infty} \bar{F}(x)\log\bar{F}(x)dx + \int_0^{\infty} \bar{F}(x)\log\frac{\bar{F}(x)}{\bar{G}(x)}dx\ .\end{aligned}$$


Copyright: the authors

Using the log-sum inequality (2.3), we have

$$\begin{aligned}\xi(F;G) &\geq \xi(F) + \left(\int_0^\infty \bar{F}(x)dx\right) \log \frac{\int_0^\infty \bar{F}(x)dx}{\int_0^\infty \bar{G}(x)dx}\,, \\ &\geq \xi(F) + E(X) \log \frac{E(X)}{E(Y)}\,.\end{aligned} \tag{2.5}$$

Next, using the inequality $x \log \frac{x}{y} \geq x - y$ for non-negative $x$ and $y$ in (2.5), we obtain

$$\begin{aligned}\xi(F;G) &\geq \int_0^\infty \bar{F}(x)F(x)dx + E(X) \log \frac{E(X)}{E(Y)}\,, \\ &\geq \int_0^\infty \bar{F}(x)F(x)dx + E(X) - E(Y)\,.\end{aligned}$$

This proves the result.

## 3. Dynamic Cumulative Residual Inaccuracy

In life-testing experiments normally the experimenter has information about the current age of the system under consideration. Obviously the cumulative residual inaccuracy measure (2.1) defined above is not suitable in such a situation and should be modified to take into account the current age also. Further, if $X$ is the lifetime of a component, which has survived upto time $t$, then the random variable $X_t = [X - t | X > t]$, called the residual lifetime random variable, has the survival function

$$\bar{F}_t(x) = \begin{cases} \frac{\bar{F}(x)}{\bar{F}(t)} & ; \quad \text{if } x > t \\ 1 & ; \quad \text{otherwise} \end{cases}$$

and similarly for $\bar{G}_t(x)$. Further we know that the mean residual life function $\delta_F(t) = E[X - t | X > t] = \frac{\int_t^\infty \bar{F}(x)dx}{\bar{F}(t)}$ and the hazard rate $\lambda_F(t) = \frac{f(t)}{\bar{F}(t)}$ characterize the distribution function $F(.)$, and the relation between the two is given by

$$\lambda_F(t) = \frac{1 + \delta_F'(t)}{\delta_F(t)}\,, \tag{3.1}$$

where $\delta_F'(t) = \frac{d}{dt}\delta_F(t)$.

Analogous to the measure (2.1) the cumulative inaccuracy measure for the residual lifetime $X_t = [X - t | X > t]$, is given by

$$\xi(F,G;t) = -\int_t^\infty \bar{F}_t(x) \log \bar{G}_t(x)dx\,,$$

$$= -\int_t^\infty \frac{\bar{F}(x)}{\bar{F}(t)} \log \frac{\bar{G}(x)}{\bar{G}(t)} dx\,. \tag{3.2}$$

We define the measure (3.2) as the *dynamic cumulative residual inaccuracy* measure. Obviously when $t = 0$, then (3.2) becomes (2.1).


Copyright: the authors

**Example 3.1** Let $X$ be a non-negative random variable with p.d.f.

$$f_X(x) = \begin{cases} 2x & ; \text{ if } 0 \leq x < 1 \\ 0 & ; \text{ otherwise} \end{cases}$$

and the suvival function $\bar{F}(x) = 1 - F(x) = (1 - x^2)$, and let the random variable $Y$ be uniformly distributed over $(0,1)$ with density and survival functions given respectively by $g_Y(x) = 1$ and $\bar{G}_Y(x) = 1 - x$ , $0 < x < 1$.
Substituting these values in (3.2), we obtain the dynamic cumulative residual inaccuracy measure as

$$\xi(F,G;t) = \begin{cases} \frac{9(1-t)-2(1-t)^2}{18(1+t)} & ; \text{ if } 0 \leq t < 1 \\ 0 & ; \text{ otherwise} \end{cases}$$

The behaviour of the dynamic cumulative residual inaccuracy measure $\xi(F,G;t)$ for $t \in (0,\ 1)$ is shown in Fig. 3.1.

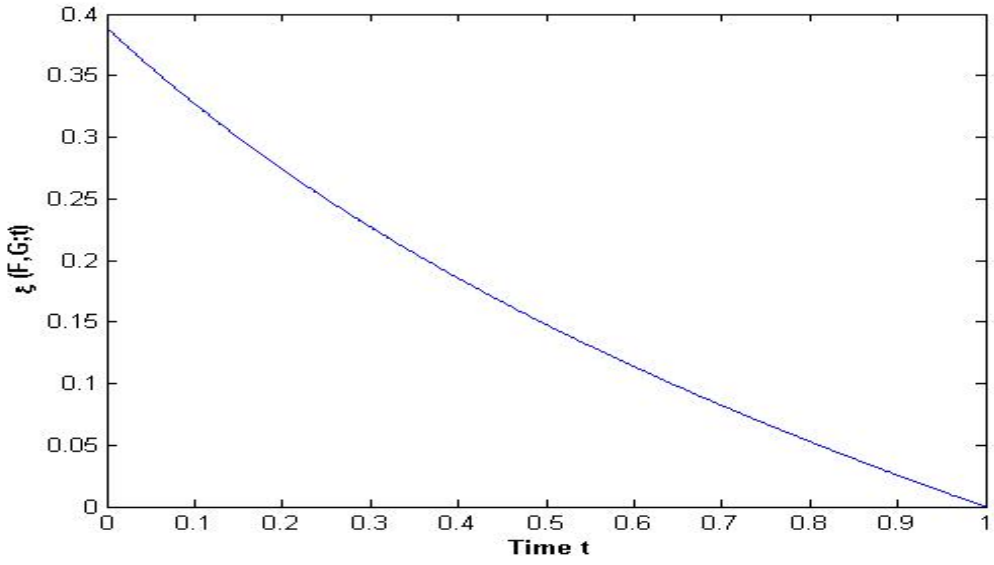


**Fig. 3.1:** Plot of $\xi(F,G;t)$ against $t \in [0\ ,1]$ .

## 4. Characterization Problem

The general characterization problem is to determine when the proposed dynamic cumulative residual inaccuracy measure (3.2) characterizes the distribution function uniquely. We study the characterization problem under the proportional hazard model (2.2).


Copyright: the authors

**Theorem 4.1.** *Let X and Y be two non negative random variables with survival functions $\bar{F}(x)$ and $\bar{G}(x)$ satisfying the proportional hazard model (2.2). Let $\xi(F,G;t) < \infty, \forall\, t \geq 0$ be an increasing function of t, then $\xi(F,G;t)$ uniquely determines the survival function $\bar{F}(x)$ of the variable X.*

**Proof** Rewriting (3.2) as

$$\xi(F,G;t) = -\frac{1}{\overline{F}(t)} \int_t^\infty \bar{F}(x) \log \bar{G}(x) dx + \delta_F(t) \log \bar{G}(t) \,, \tag{4.1}$$

where $\delta_F(t)$ is the mean residual life function. Substituting (2.2) into (4.1) gives

$$\xi(F,G;t) = -\frac{\beta}{\overline{F}(t)} \int_t^\infty \bar{F}(x) \log \bar{F}(x) dx + \beta\, \delta_F(t) \log \bar{F}(t) \,.$$

Differentiating this w.r.t. $t$ both sides, we obtain

$$\xi'(F,G;t) = \beta \log \bar{F}(t)[1 + \delta_F'(t)] - \beta \lambda_F(t) \int_t^\infty \frac{\bar{F}(x)}{\overline{F}(t)} \log \bar{F}(x) dx - \beta \lambda_F(t) \delta_F(t) \,, \tag{4.2}$$

where $\lambda_F(t)$ is hazard rate function. Substituting (3.1) and (4.1) in (4.2) we obtain

$$\xi'(F,G;t) = \lambda_F(t) \{ \xi(F,G;t) - \beta\, \delta_F(t) \} \,. \tag{4.3}$$

Let $F_1, G_1$ and $F_2, G_2$ be two sets of the probability distribution functions satisfying the proportional hazard model, that is, $\lambda_{G_1}(x) = \beta \lambda_{F_1}(x)$, and $\lambda_{G_2}(x) = \beta \lambda_{F_2}(x)$, and let

$$\xi(F_1,G_1;t) = \xi(F_2,G_2;t) \;\forall\; t \geq 0 \,. \tag{4.4}$$

Differentiating it both sides w.r.t. $t$, and using (4.3), we obtain

$$\lambda_{F_1}(t) \{ \xi(F_1,G_1;t) - \beta\, \delta_{F_1}(t) \} = \lambda_{F_2}(t) \{ \xi(F_2,G_2;t) - \beta\, \delta_{F_2}(t) \}. \tag{4.5}$$

If for all $t \geq 0,\ \lambda_{F_1}(t) = \lambda_{F_2}(t)$, then $\bar{F}_1(t) = \bar{F}_2(t)$ and the proof will be over, otherwise, let

$$A = \{ t : t \geq 0, \text{and } \lambda_{F_1}(t) \neq \lambda_{F_2}(t) \} \tag{4.6}$$

and assume the set A to be non empty . Thus for some $t_0 \in A$, $\lambda_{F_1}(t_0) \neq \lambda_{F_2}(t_0)$. Without loss of generality suppose that $\lambda_{F_2}(t_0) > \lambda_{F_1}(t_0)$. Using this, (4.5) for $t = t_0$ gives

$$\xi(F_1,G_1;t_0) - \beta\, \delta_{F_1}(t_0) > \xi(F_2,G_2;t_0) - \beta\, \delta_{F_2}(t_0),$$

which implies that

$$\delta_{F_1}(t_0) < \delta_{F_2}(t_0),$$

a contradiction. Thus the set A is empty set and this concludes the proof.

In the next result, based on dynamic cumulative residual inaccuracy measure (3.2), we characterize some specific lifetime distributions.


Copyright: the authors

**Theorem 4.2.** *Let $X$ and $Y$ be two non-negative continuous random variables satisfying the proportional hazard model (2.2). If $X$ is with mean residual life $\delta_F(t)$, then the dynamic cumulative residual inaccuracy measure*

$$\xi(F,G;t) = c\ \delta_F(t),\ \ c>0 \tag{4.7}$$

*if, and only if*

*(i) $X$ follows the exponential distribution for $c=\beta$ ,*
*(ii) $X$ follows the Pareto distribution for $c>\beta$ ,*
*(iii) $X$ follows the finite range distribution for $0<c<\beta$.*

**Proof** First we prove the 'if' part.
(i) If $X$ has an exponential distribution with survival function $\bar{F}(x)=\exp(-\theta x), \theta>0$, then the mean residual life function $\delta_F(t)=\frac{1}{\theta}$. The dynamic cumulative residual inaccuracy measure (3.2) under PHM (2.2) is given as

$$\xi(F,G;t) = \frac{\beta}{\theta} = c\delta_F(t),$$

for $c=\beta$.

(ii) If $X$ follows a Pareto distribution with p.d.f.

$$f(x) = \frac{ab^a}{(x+b)^{a+1}},\ \ a>1,\ b>0,$$

then the survival function is

$$\bar{F}(x) = 1-F(x) = \left(1+\frac{x}{b}\right)^{-a} = \frac{b^a}{(x+b)^a}\ ,$$

and the mean residual life is

$$\delta_F(t) = \frac{\int_t^\infty \bar{F}(x)dx}{\bar{F}(t)} = \frac{t+b}{a-1}\ . \tag{4.8}$$

The dynamic cumulative inaccuracy measure (3.2), under PHM (2.2) is given by

$$\xi(F,G;t) = \frac{\beta a(t+b)}{(a-1)^2} = c\delta_F(t)\ ,$$

for $c=\frac{\beta a}{a-1}>\beta$.


Copyright: the authors

(iii) In case $X$ follows a finite range distribution with p.d.f.

$$f(x) = a(1-x)^{a-1}, \quad a > 1, \ 0 \leq x \leq 1,$$

then the survival function is

$$\bar{F}(x) = 1 - F(x) = (1-x)^a,$$

and the mean residual life is

$$\delta_F(t) = \frac{1-t}{a+1}.$$

The inaccuracy measure (3.2) under PHM (2.2) is given by

$$\xi(F,G;t) = \frac{\beta a(1-t)}{(a+1)^2} = c\delta_F(t) \ ,$$

for $c = \frac{\beta a}{a+1} < \beta$.
This proves the 'if' part.

To prove the $'$ only if $\backslash$ part, consider (4.7) to be valid. Using (4.1) under PHM, it gives

$$-\frac{\beta}{\bar{F}(t)} \int_t^\infty \bar{F}(x) \log \bar{F}(x) dx + \beta \delta_F(t) \log \bar{F}(t) = c\delta_F(t) \ .$$

Differentiating it both sides w.r.t. $t$, we obtain

$$\begin{aligned} \frac{c}{\beta}\delta_F'(t) = \ & \delta_F'(t)\log\bar{F}(t) - \lambda_F(t)\delta_F(t) + \log\bar{F}(t) \\ & -\lambda_F(t)\frac{1}{\bar{F}(t)}\int_t^\infty \bar{F}(x)\log\bar{F}(x)dx \end{aligned}$$

$$= \delta_F'(t)\log\bar{F}(t) - \lambda_F(t)\delta_F(t) + \log\bar{F}(t) + \lambda_F(t)[\frac{c}{\beta}\delta_F(t) - \delta_F(t)\log\bar{F}(t)] \ .$$

From (3.2) put $\delta_F'(t) = \lambda_F(t)\delta_F(t) - 1$ and simplify, we obtain

$$\lambda_F(t)\delta_F(t) = \frac{c}{\beta} \ ,$$

which implies

$$\delta_F'(t) = \frac{c}{\beta} - 1 \ .$$

Integrating both sides of this w.r.t. $t$ over $(0, x)$ yields

$$\delta_F(x) = \left(\frac{c}{\beta} - 1\right)x + \delta_F(0). \tag{4.9}$$

The mean residual life function $\delta_F(x)$ of a continuous non-negative random variable $X$ is linear of the form (4.9) if, and only if the underlying distribution is exponential for $c = \beta$, Pareto for $c > \beta$, or finite range for $0 < c < \beta$, refer to Hall and Wellner (1981). This completes the theorem.


Copyright: the authors

Theorem 4.2 can be extended by taking $c$ as a function of $t$. We state the following result:

**Theorem 4.3.** *Let X and Y be two non-negative continuous random variables satisfying the proportional hazard model (2.2). If*

$$\xi(F,G;t) = c(t)\delta_F(t) \text{ ,for } t \geq 0, \tag{4.10}$$

*then*

$$\delta_F(t) = \left[k + \left(\int_0^t \left\{\frac{c(x)-\beta}{\beta}\right\} e^{\frac{c(x)}{\beta}} dx\right)\right] e^{-\frac{c(t)}{\beta}}, \tag{4.11}$$

*where* $k = \delta_F(0)e^{\frac{c(0)}{\beta}}$.

**Proof** Substituting (4.10) in (4.3), we obtain

$$\xi'(F,G;t) = \lambda_F(t)\delta_F(t)\{c(t)-\beta\}\,. \tag{4.12}$$

Differentiating (4.10) w.r.t. $t$ and substituting from (4.12), we obtain

$$c'(t)\delta_F(t) + c(t)\delta_F'(t) = \lambda_F(t)\delta_F(t)\{c(t)-\beta\}\,.$$

Substituting $\lambda_F(t)\delta_F(t) = 1 + \delta_F'(t)$ from (3.2) and simplifying, we obtain

$$\delta_F'(t) + \frac{c'(t)}{\beta}\delta_F(t) = \frac{c(t)-\beta}{\beta}, \tag{4.13}$$

a linear differential equation in $\delta_F(t)$. Solving this we obtain (4.10).

For $c(t) = at + b$, $t > 0$ and $a > 0$, from (4.10), we obtain the general model with mean residual life function

$$\delta_F(t) = ke^{\frac{-(at+b)}{\beta}} + \frac{at - 2\beta + b}{a} - \frac{(b-2\beta)e^{\frac{-at}{\beta}}}{a}. \tag{4.14}$$

If $a = 0$, we obtain the characterization results given by Theorem 4.2.

Further for $\beta = 1$, (4.14) reduces to

$$\delta_F(t) = k\,e^{-at-b} + \frac{b-2+at}{a} - \frac{(b-2)e^{-at}}{a},$$

a result given by Navarro J. et al. (2010) in context with the cumulative residual entropy (1.3).

## 5. Dynamic Cumulative Past Inaccuracy Measure

Measures of uncertainty in context with past lifetime distributions have been studied extensively in the literature, refer to, Di Crescenzo and Longobardi (2002, 2004) Nanda and Paul (2006), Kumar et al. (2010). For instance if at time $t$, a system which is observed only at certain preassigned inspection times, is found to be down, then the uncertainty of the system's life relies on the past, that is, at which instant in $(0,\ t)$ the system has failed. In this situation, the random variable ${}_tX = [X|X \leq t]$ is suitable to describe the time elapsed between the failure of a system and the time when it is found


Copyright: the authors

to be 'down'. The past lifetime random variable ${}_tX$ is related with two relevant ageing functions, *the reversed hazard rate* defined by $\mu_F(x) = \frac{f(x)}{F(x)}$, and *the mean past lifetime* (MPT) defined by $\delta_F^*(t) = E(t-X|X<t) = \frac{1}{F(t)}\int_0^t F(x)dx$, which are further related as follows

$$\mu_F(t) = \frac{1-\delta_F'^*(t)}{\delta_F^*(t)}\ , \tag{5.1}$$

where $\delta_F'^*(t) = \frac{d}{dt}\delta_F^*(t)$. For further results on reversed hazard rate function refer to Gupta and Nanda (2001).

In analogy with the cumulative residual entropy (CRE) measure (2.1), Di Crescenzo and Longobardi (2009) introduced and studied the cumulative entropy, defined as

$$\xi^*(F) = -\int_0^\infty F(x)\log F(x)dx. \tag{5.2}$$

A dynamic version of the cumulative entropy (5.2) given as

$$\xi^*(F;t) = -\int_0^t \frac{F(x)}{F(t)}\log\frac{F(x)}{F(t)}dx\ , \tag{5.3}$$

was also studied by Di Crescenzo and Longobardi (2009).

Analogous to the Kerridge measure of inaccuracy (1.2), we propose a cumulative inaccuracy measure as

$$\xi^*(F;G) = -\int_0^\infty F(x)\log G(x)dx\ , \tag{5.4}$$

where $F(x)$ is the baseline distribution function and $G(x)$ can be considered as some reference distribution function. When these two distributions coincide, the measure (5.4) reduces to the measure (5.2) the cumulative entropy.

In case the two random variables $X$ and $Y$ satisfy the *proportional reversed hazard model* (PRHM), refer to Gupta et al. (2007) , that is, if $\mu_G(x) = \beta\ \mu_F(x)$, or equivalently

$$G(x) = [F(x)]^\beta\ , \beta > 0\ , \tag{5.5}$$

then obviously the cumulative inaccuracy measure (5.4) reduces to a constant multiple of the cumulative information measure (5.2).

The distribution function of the past lifetime random variable $[X|X \le t]$ is given by

$$F_{tX}(x) = \begin{cases} \frac{F(x)}{F(t)} & ;\ \text{if } x<t \\ 1 & ;\ \text{otherwise} \end{cases}$$

and similarly for $\bar{G}_t(x)$. Thus the cumulative inaccuracy measure analogous to the inaccuracy measure (5.4), for the past lifetime distribution is given by

$$\xi^*(F,G;t) = -\int_0^t F_{tX}(x)\log G_{tX}(x)dx\ ,$$

$$= -\int_0^t \frac{F(x)}{F(t)}\log\frac{G(x)}{G(t)}dx\ . \tag{5.6}$$


Copyright: the authors

We define the measure (5.6) as the *dynamic cumulative past inaccuracy* measure. When $t \to \infty$, the measure (5.6) reduces to (5.4).

**Example 5.1** Let $X$ and $Y$ be two nonnegative random variables having distribution functions respectively

$$F(x) = \begin{cases} \frac{x^2}{2}, & \text{for } 0 \le x < 1 \\ \frac{x^2+2}{6}, & \text{for } 1 \le x < 2 \\ 1 & \text{for } x \ge 2 \end{cases}$$

and

$$G(x) = \begin{cases} \frac{x^2+x}{4}, & \text{for } 0 \le x < 1 \\ \frac{x}{2}, & \text{for } 1 \le x < 2 \\ 1 & \text{for } x \ge 2 \end{cases}$$

The cumulative past inaccuracy measure is given by

$$\xi^*(F,G;t) = \begin{cases} \frac{2t}{9} - \frac{(t-2)}{6t} - \frac{1}{3t^2}\log(t+1), & \text{for } 0 < t < 1 \\ \frac{t}{9} + \frac{16t}{9(t^2+2)} - \frac{17}{18(t^2+2)} - \frac{18\log 2 + 24\log t}{18(t^2+2)}, & \text{for } 1 \le t < 2 \\ \log 2 + \frac{1}{6}\log 5 - \frac{41}{54} - \frac{8}{3}\tan^{-1}(\frac{1}{2}) & \text{for } t \ge 2 \end{cases}$$

Analogous to Theorem 4.1, the characterization problem in case of the dynamic measure (5.6) under the proportional reversed hazard rate model (5.5) is given as follows.

**Theorem 5.1.** *Let $X$ and $Y$ be two non-negative random variables with distribution functions $F(.)$ and $G(.)$ satisfying the proportional reversed hazard rate model (5.5). Let $\xi^*(F,G;t) < \infty, \forall\, t \ge 0$ be an decreasing function of $t$, then $\xi^*(F,G;t)$ uniquely determines the distribution function $F(.)$ of the variable $X$.*

The proof is silmilar to that of Theorem 4.1 . Hence omitted.

Next, we characterize a specific distribution by using the dynamic cumulative past inaccuracy measure. The result is stated as follows.

**Theorem 5.2.** *If $F(.)$ and $G(.)$ are two distribution functions satisfying the proportional reversed hazard model (5.5), then the dynamic cumulative past inaccuracy measure*

$$\xi^*(F,G;t) = c\,\delta_F^*(t)\ ,\ 0 < c < \beta\ . \tag{5.7}$$

*if, and only if $t\,F(x) = \left(\frac{x}{b}\right)^{\frac{c}{\beta-c}}$ , $b > 0$ .*

**Proof** Rewriting (5.6) as

$$\xi^*(F,G;t) = -\frac{1}{F(t)}\int_0^t F(x)\log G(x)dx + \delta_F^*(t)\log G(t)\ , \tag{5.8}$$

Substituting (5.5), this gives

$$\xi^*(F,G;t) = -\frac{\beta}{F(t)}\int_0^t F(x)\log F(x)dx + \beta\,\delta_F^*(t)\log F(t)\ . \tag{5.9}$$


Copyright: the authors

Differentiating this w.r.t. $t$ both sides, we obtain

$$\xi'^*(F,G;t) = \beta \log F(t)[\delta_F'^*(t) - 1] + \beta \mu_F(t) \int_0^t \frac{F(x)}{F(t)} \log F(x) dx + \beta \mu_F(t) \delta_F^*(t) \,, \tag{5.10}$$

Substituting (5.1) and (5.9) in Eq. (5.10), we obtain

$$\xi'^*(F,G;t) = \mu_F(t)\{\beta \delta_F^*(t) - \xi^*(F,G;t)\} \,. \tag{5.11}$$

Let us take that (5.7) is valid, then differentiate both side w.r.t. $t$, we get

$$\xi'^*(F,G;t) = c\delta_F'^*(t) \,. \tag{5.12}$$

Put these value to (5.11) , we get

$$c\delta_F'^*(t) = (\beta - c)\mu_F(t)\delta_F^*(t) \,. \tag{5.13}$$

Using(5.1)and simplify, we obtain

$$\delta_F'^*(t) = \left(\frac{\beta - c}{\beta}\right) = 1 - \frac{c}{\beta}. \tag{5.14}$$

This gives

$$\delta_F^*(t) = \left(\frac{\beta - c}{\beta}\right) t \,. \tag{5.15}$$

Divide (5.14) by (5.15), we obtain

$$\frac{1 - \delta_F'^*(t)}{\delta_F^*(t)} = \mu_F(t) = \left(\frac{c}{\beta - c}\right) \frac{1}{t} \,. \tag{5.16}$$

We know the relationship between reversed hazard rate and distribution function is given by

$$F(x) = \exp\left[\int_0^x \mu_F(t) dt\right] \,,$$

this gives

$$F(x) = \left(\frac{x}{b}\right)^{\frac{c}{\beta - c}} \,,\ b > 0. \tag{5.17}$$

The reverse part is straightforward and easy to prove.

**Example 5.2** Let $X$ and $Y$ be two non-negative random variables satisfying the proportional reversed hazard model (PRHM) and let

$$f_X(x) = \begin{cases} ax^{a-1} & ; \quad \text{if } 0 \le x < 1,\ a > 0 \\ 0 & ; \quad \text{otherwise} \end{cases}$$

The distribution function $F(x) = x^a$, and $G(x) = [F(x)]^\beta$, $\beta > 0$.
Substituting these values in (5.6), after simplification we get

$$\xi^*(F,G;t) = \frac{t}{(a+1)^2} = c\delta_F^*(t) \,,$$

where $c = \frac{1}{a+1}$ and mean past lifetime is $\delta_F^*(t) = \frac{t}{a+1}$ .


Copyright: the authors

Next, we extend the result (5.7) to a general case taking $c$ as a function of $t$. We state the following result:

**Theorem 5.3.** *If $X$ and $Y$ satisfy the PRHM (5.5) and*

$$\xi^*(F,G;t) = c(t)\delta_F^*(t) \text{ ,for } t \geq 0, \tag{5.18}$$

*then*

$$\delta_F^*(t) = \left( \int_0^t \left\{ \frac{\beta - c(x)}{\beta} \right\} e^{\frac{c(x)}{\beta}} dx \right) e^{-\frac{c(t)}{\beta}}. \tag{5.19}$$

The proof is similar to that of Theorem 4.3. Hence omitted.

For $c(t) = at + b$, $t > 0$ and $a > 0$, from (5.19), we obtain the general model with mean past lifetime function

$$\delta_F^*(t) = \frac{2\beta - at - b}{a} + \frac{(b - 2\beta)e^{\frac{-at}{\beta}}}{a}. \tag{5.20}$$

Further for $\beta = 1$, (5.20) reduces to

$$\delta_F^*(t) = \frac{2 - at - b}{a} - \frac{(b-2)e^{-at}}{a},$$

a result given by Di Crescenzo and Longobardi (2009) in context with cumulative entropy.

**Conclusions and Comments:** The cumulative distribution function based measures of entropy $\xi(F)$ and $\xi^*(F)$ are in general more stable in comparison to probability density function based measure $H(f)$ given by Shannon (1948). The concept of cumulative entropy is extended to cumulative inaccuracy and further to their dynamic versions viz. cumulative residual inaccuracy $\xi(F,G;t)$ and cumulative past inaccuracy $\xi^*(F,G;t)$ . The characterization results concerning, when these inaccuracy measures determine the underlying distributions uniquely, have been studied and a few specific lifetime distributions have been characterized. It is expected that dynamic inaccuracy measures introduced in this paper will encourage the researchers to explore this concept further.

## References


[1] A. Di Crescenzo, M. Longobardi, Entropy- based measure of uncertainty in past lifetime distributions, *Journal of Applied Probability*, **39** (2002) 434-440.

[2] A. Di Crescenzo, M. Longobardi, A measure of discrimination between past lifetime distributions, *Statistics and Probability Letters*, **67** (2004) 173-182.

[3] A. Di Crescenzo, M. Longobardi, On cumulative entropies, *Journal of Statistical Planning and Inference*, **139** (12) (2009) 4072-4087.

[4] A. K. Nanda, P. Paul, Some properties of past entropy and their applications, *Metrika*, **64** (1) (2006) 47-61.

[5] B. Efron, Censored data and the bootstrap, Journal of the American Statistical Association, **76** (1981) 312-319.

[6] C. E. Shannon, A mathematical theory of communication, *Bell System Technical Journal*, (1948) 279-423 and 623-656.

[7] D. F. Kerridge, Inaccuracy and inference, *Journal of Royal Statistical Society, Series B*, **23** (1961) 184-194.



Copyright: the authors

[8] D. R. Cox, Regression models and life tables, *Journal of Royal Statistical Society, Series B* , **34** (1972) 187-220.
[9] H. C. Taneja, V. Kumar, R. Srivastava, A dynamic measure of inaccuracy between two residual lifetime distributions, *International Mathematical Fourm*, **4**(25) (2009) 1213-1220.
[10] J. Navarro, Y. D. Aguila, M. Asadi, Some new results on the cumulative residual entropy, *Journal of Statistical Planning and Inference*, **140**(1) (2010) 310-322.
[11] M. Asadi, Y. Zohrevand, On the dynamic cumulative residual entropy, *Journal of Statistical Planning and Inference*, **137** (2007) 1931-1941.
[12] M. Rao, More on a new concept of entropy and information, *Journal of Theoretical Probability*, **18** (2005) 967-981.
[13] M. Rao, Y. Chen, B.C. Vemuri, F. Wang, Cumulative residual entropy: a new measure of information, *IEEE Transactions on Information Theory*, **50** (2004) 1220-1228.
[14] N. Drissi, T. Chonavel, J. M. Boucher, Generalized cumulative residual entropy for distributions with unrestricted supports, Research letters in signal processing, (2008)
[15] N. Ebrahimi, How to measure uncertainty about residual lifetime, *Sankhya A*, **58** (1996) 48-57.
[16] R. C. Gupta, R.D. Gupta, Proportional reversed hazards models and its applications, *Journal of Statistical Planning and Inference*, **137** (2007) 3525-3536.
[17] R. D. Gupta, A. K. Nanda, Some results on reversed hazard rate ordering, *Communications in Statistics: Theory and Methods*, **30** (2001) 2447-2457.
[18] V. Kumar, H.C. Taneja, R. Srivastava, A dynamic measure of inaccuracy between two past lifetime distributions, *Metrika*, **74**(1) (2010) 1-10.
[19] W. J. Hall, J. A. Wellner, Mean residual life, In Statistics and Related Topics (Csrg, et al. eds), North-Holland, Amsterdam, (1981) 169-184.


Copyright: the authors

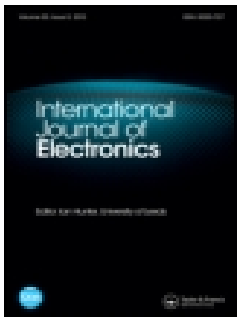

International Journal of Electronics

ISSN: 0020-7217 (Print) 1362-3060 (Online) Journal homepage: http://www.tandfonline.com/loi/tetn20

# Dynamic Positive-Feedback Source-Coupled Logic (D-PFSCL)

Kirti Gupta, Neeta Pandey & Maneesha Gupta

**To cite this article:** Kirti Gupta, Neeta Pandey & Maneesha Gupta (2016): Dynamic Positive-Feedback Source-Coupled Logic (D-PFSCL), International Journal of Electronics, DOI: 10.1080/00207217.2016.1138519

**To link to this article:** http://dx.doi.org/10.1080/00207217.2016.1138519

Accepted author version posted online: 07 Jan 2016.

Submit your article to this journal

Article views: 4

View related articles

View Crossmark data

Full Terms & Conditions of access and use can be found at http://www.tandfonline.com/action/journalInformation?journalCode=tetn20

**Download by:** [Delhi Technological University] **Date:** 13 January 2016, At: 23:11

**Publisher:** Taylor & Francis

**Journal:** *International Journal of Electronics*

**DOI:** 10.1080/00207217.2016.1138519

Downloaded by [Delhi Technological University] at 23:11 13 January 2016

# Dynamic Positive-Feedback Source-Coupled Logic (D-PFSCL)

Kirti Gupta[1], Neeta Pandey[1], Maneesha Gupta[2]

[1] Dept. of Electronics and Communication Engineering, Delhi Technological University, Delhi, India
[2] Dept. of Electronics and Communication Engineering, Netaji Subhas Institute of Technology, Delhi, India

kirtigupta22@gmail.com, n66pandey@rediffmail.com, maneeshapub@gmail.com

Corresponding Author: Dr. Neeta Pandey
Associate Professor,
Dept. of Electronics and Communication Engineering,
Delhi Technological University,
Delhi, India
Email: n66pandey@rediffmail.com
Mob: +91-9868780900

Date of submission: 2/7/14

ACCEPTED MANUSCRIPT

# Dynamic Positive-Feedback Source-Coupled Logic (D-PFSCL)

This paper presents dynamic positive-feedback source coupled logic (D-PFSCL) style which is derived from positive feedback source coupled logic (PFSCL). The proposed logic style uses dynamic current source in contrast to constant current source of PFSCL to attain lower power consumption. Two techniques for D-PFSCL style based multi-stage applications are suggested. Several D-PFSCL gates are simulated and compared with the respective PFSCL counterparts through SPICE simulations by using TSMC 0.18 µm CMOS technology parameters. A maximum power reduction of 84 % is achieved for D-PFSCL gates. The effect of process variation on the power consumption of the D-PFSCL gates shows a maximum variation factor of 1.5 between the best and the worst cases.

Keywords: Single-ended SCL, PFSCL, low power, dynamic circuits, positive feedback.

## 1. Introduction

The emergence of high-resolution mixed-signal applications has led to an increase in the demand for high performance digital circuits. The traditional CMOS logic style is not suitable for mixed-signal applications as it generates large amount of switching noise (Allstot, Chee, Kiaei & Shristawa, 1993, Masui, 1992). The source-coupled logic (SCL) style has been proved to be a better alternative than the CMOS logic (Kiaei, Chee & Allstot, 1990). The SCL gates are classified as differential or single-ended (Musa, 2010, Alioto, Pancioni, Rocchi & Vignoli, 2004, Alioto, Fort, Pancioni, Rocchi & Vignoli, 2004, Alioto, Fort, Pancioni, Rocchi & Vignoli, 2005, Alioto, Pancioni, Rocchi & Vignoli, 2007, Alioto, Pancioni, Rocchi & Vignoli, 2006). The former is based on the series-gating approach (Alioto & Palumbo, 2005) whereas in later the transistors share a common source and drain terminal and are source-coupled to a transistor whose gate is connected to reference voltage source (Alioto, Pancioni, Rocchi & Vignoli, 2004).

An improved form of single-ended SCL style named as positive-feedback source-coupled logic (PFSCL) style has been suggested in literature (Alioto, Pancioni, Rocchi & Vignoli, 2004, Alioto, Fort, Pancioni, Rocchi & Vignoli, 2004, Alioto, Fort, Pancioni, Rocchi & Vignoli, 2005, Alioto, Pancioni, Rocchi & Vignoli, 2007, Alioto, Pancioni, Rocchi & Vignoli, 2006). The logic style replaces the reference voltage source used in traditional single-ended SCL gates with a positive feedback to improve their performance. The PFSCL gates consume static power which severely limits their use for low power applications. In this paper, a new dynamic positive-feedback source-coupled logic (D-PFSCL) style is proposed which has lower power consumption than the PFSCL style.

The paper first presents an overview of PFSCL style in section 2. Thereafter, the architecture of the proposed D-PFSCL style is described in section 3. The two techniques for multistage operation of D-PFSCL gates are also described. Several logic gates based on the D-PFSCL style are proposed and are compared with their PFSCL counterparts through SPICE simulations by using TSMC 0.18 µm CMOS technology parameters in section 4. The effect of process variation on the D-PFSCL gates is also studied. Finally, the conclusions are drawn in section 5.

Downloaded by [Delhi Technological University] at 23:11 13 January 2016

ACCEPTED MANUSCRIPT

## 2. Positive-Feedback Source-Coupled Logic (PFSCL)

A PFSCL circuit consists of three main parts: a pull-down network (PDN), a constant current source and a load circuit. A generic N-input PFSCL gate is shown in Fig. 1a. The inputs are applied to gates of N-NMOS transistors $M_i$ (i =1,2,….., N) which share common source and drain terminals. The input transistors are source-coupled with a feedback transistor $M_f$ whose gate is connected to the output node Q. The constant current source $M_S$ provides the bias current $I_{SS}$ while the load transistor $M_L$ determines the voltage swing. The circuit of a PFSCL inverter with input A is shown in Fig. 1b. It works on the principle of current steering. When the voltage at input A is high, the bias current $I_{SS}$ is steered to transistor $M_1$ and a low voltage ($V_{OL} = V_{DD} - V_L$) is obtained at the output where $V_L$ is the voltage drop across the load transistor (Alioto, Pancioni, Rocchi & Vignoli, 2004). Similarly, for low value of input A, the transistor $M_1$ is turned OFF and a high voltage ($V_{OH} = V_{DD}$) is obtained at the output. The voltage swing for PFSCL circuits ($V_{SWING}$) is defined as the difference between $V_{OH}$ and $V_{OL}$.

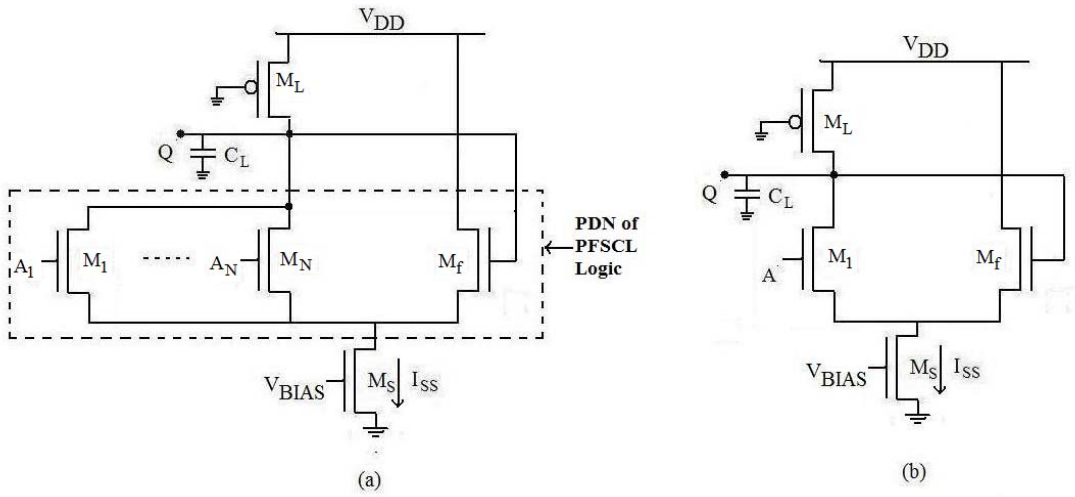


Fig. 1 (a) Basic N-input PFSCL circuit (b) PFSCL inverter

It can be noted that the bias current flows from the transistor $M_S$ throughout the operation and consumes power. Hence, these circuits are unsuitable for low-power applications. Therefore, in the next section we present a new logic style (D-PFSCL) that consumes lesser power than the PFSCL style.

## 3. Dynamic Positive-Feedback Source-Coupled Logic (D-PFSCL)

The basic architecture of dynamic positive-feedback source-coupled logic (D-PFSCL) style includes a PDN, a precharge transistor and a dynamic current source (Allam & Elmasry, 2001). The circuit of a D-PFSCL inverter is shown in Fig. 2. The PDN ($M_1$-$M_f$) is implemented in the similar manner as in PFSCL style. The precharge transistor ($M_P$) and the dynamic current source ($M_{DC1}$, $M_{DC2}$, $C_1$) are driven by a clock input (CLK). The operation of the circuit can be divided into two phases namely precharge and evaluation phase according to the clock signal value.

Downloaded by [Delhi Technological University] at 23:11 13 January 2016

ACCEPTED MANUSCRIPT

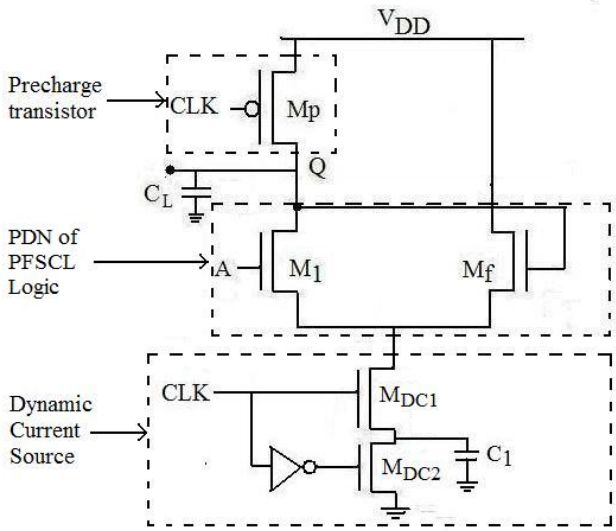


Fig. 2 Proposed D-PFSCL inverter

(1) Circuit operation in precharge phase

During the precharge phase, the CLK is low, the transistors $M_P$, $M_{DC2}$ are ON and the transistor $M_{DC1}$ is OFF. So, the output node Q is charged to the high level ($V_{OH} = V_{DD}$) through $M_P$ and the capacitor $C_1$ is discharged to the ground potential via transistor $M_{DC2}$. The input A is applied in this phase which does not cause any change in the output as the transistor $M_P$ is ON and the transistor $M_{DC1}$ is OFF.

(2) Circuit operation in evaluation phase

In the evaluation phase, the CLK goes high and makes the transistor $M_{DC1}$ ON; and transistors $M_P$ and $M_{DC2}$ OFF. The output is evaluated depending on the value of input A. For a low value of the input, the transistor $M_1$ is OFF and the inverter output remains high ($V_{OH} = V_{DD}$) as no path exists for the transfer of the charge stored on load capacitor $C_L$ to capacitor $C_1$. However, the capacitor $C_1$ gets charged through transistor $M_{DC1}$ and $M_f$. For a high value of the input A, the transistor $M_1$ is ON, the potential of the output node Q decreases to low level ($V_{OL} = V_{DD} - V_{SWING}$) as the result of the charge transfer from the load capacitor $C_L$ to capacitor $C_1$. The potential of capacitor $C_1$ increases until the source and drain terminals of transistor $M_{DC1}$ attain same potential. It is clear from the above discussion that the capacitor $C_1$ is charged irrespective of the input value and charging is continued until the potential of source and drain terminals of transistor $M_{DC1}$ becomes equal.

To demonstrate the functioning of the proposed D-PFSCL inverter, the SPICE simulations are carried out with a power supply, voltage swing and load capacitance of 1.8 V, 400 mV and 100 fF respectively. The voltage waveforms for different nodes of the inverter are shown in Fig. 3. It can be observed that the output node Q is precharged to a high level ($V_{OH}$ = 1.8V) in the precharge phase and the input is applied which remains constant in the evaluation phase. In Fig 3a during the evaluation phase with low value of input A, the output node remains at the high level ($V_{OH}$ = 1.8V) as no charge transfer take place and the capacitor $C_1$ gets charged. In Fig 3b for high value of the input A, the output node Q potential attains low level ($V_{OL}$= 1.4V) due to charge transfer and also charges the capacitor $C_1$.

Downloaded by [Delhi Technological University] at 23:11 13 January 2016

ACCEPTED MANUSCRIPT

Downloaded by [Delhi Technological University] at 23:11 13 January 2016

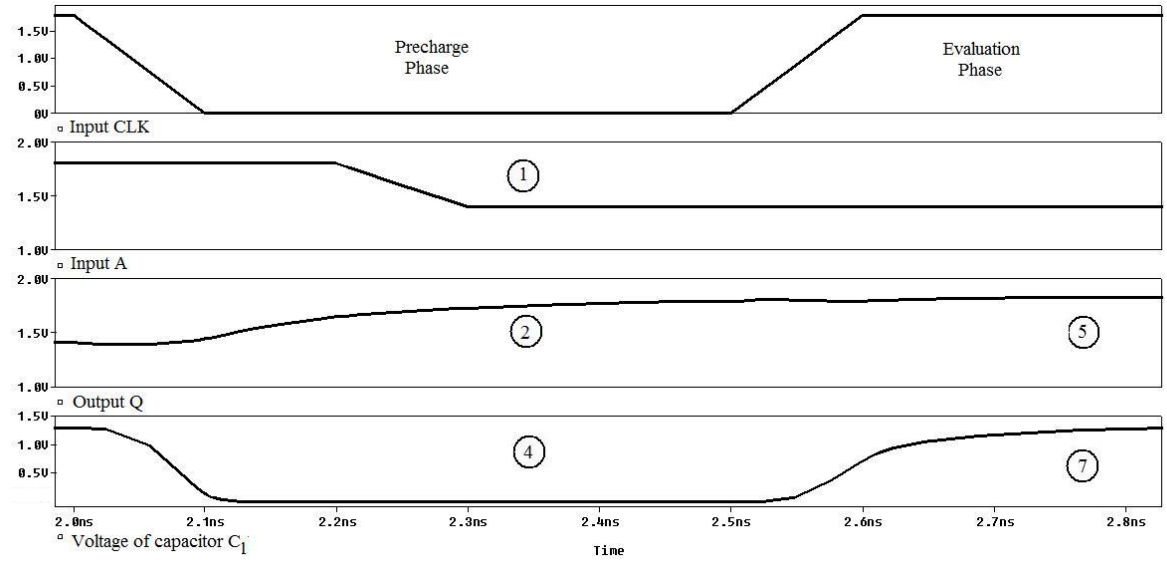


(a)

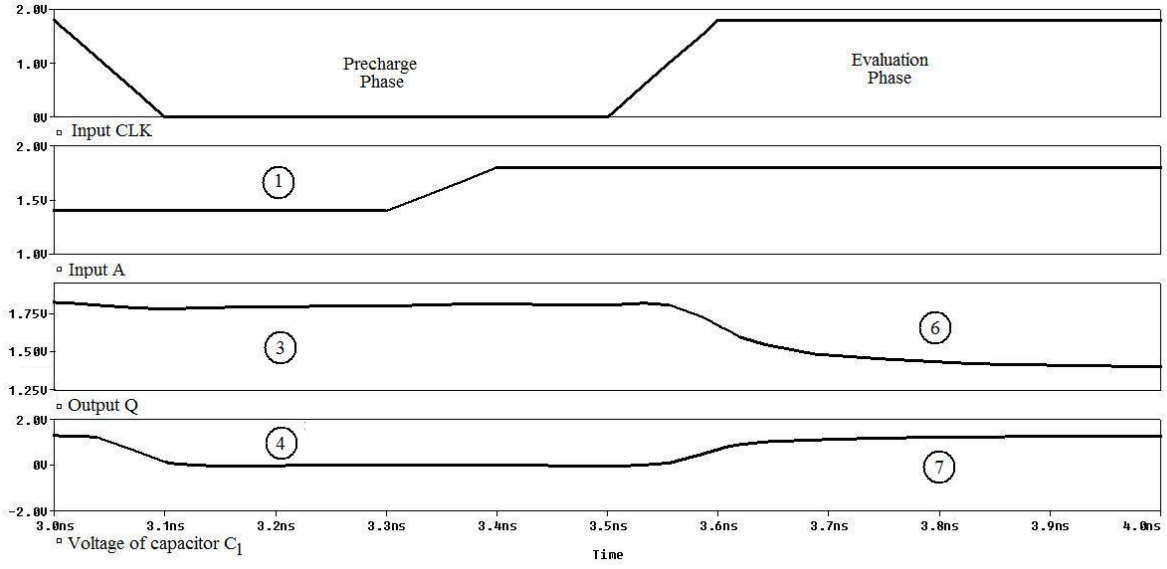


1. Precharge Phase: Input is applied
2. Precharge Phase: Output node is precharged
3. Precharge Phase: Output node already charged
4. Precharge Phase: Capacitor $C_1$ discharge
5. Evaluation Phase: No Change at the output node
6. Evaluation Phase: PDN is evaluating the output
7. Evaluation Phase: Capacitor $C_1$ is charged

(b)

Fig. 3 Voltages at different nodes in the D-PFSCL inverter (a) for low value of A (b) for high value of A

Based on the above discussion, some of the important characteristics of the proposed style can be summarized as:

1. The PDN of the proposed style is realized in the same manner as in PFSCL style.
2. The size of the precharge transistor $M_P$ does not determined the voltage swing of the circuit as in PFSCL style.
3. The capacitor $C_1$ is always charged in the evaluation phase irrespective of the inputs to the PDN.
4. The performance of the D-PFSCL gates is not affected by the charge sharing effect of dynamic circuits as they employ only one level of source-coupled transistors in their PDN.
5. The proposed logic style exhibits charge leakage during the evaluation phase because of the leakage currents. This can be overcome by driving the precharge transistor $M_P$ with a signal that makes it to remain in near cut-off during the evaluation phase as suggested in (Kang & Leblebici, 2006).

### *3.1 Design of capacitor value $C_1$ to achieve given voltage swing*

To achieve the required voltage swing $V_{SWING}$ during the evaluation, the capacitor $C_1$ is sized such that the output is discharged to the low level ($V_{DD}$-$V_{SWING}$). Using the charge conservation principle, we can write:

$$V_{DD} \times C_{OUT} = (C_{OUT} + C_1) \times (V_{DD} - V_{SWING}) \quad (1)$$

where $C_{OUT}$ is the total load capacitance at the output node which include the parasitic capacitances of the transistors and the external load capacitance $C_L$ (Alioto, Pancioni, Rocchi & Vignoli, 2004).

$$C_1 = \frac{V_{SWING} \times C_{OUT}}{V_{DD} - V_{SWING}} \quad (2)$$

In practice, the capacitor $C_1$ is realized by a dummy transistor with its source and drain terminals connected together. Therefore, by substituting, $C_1 = W_{C1} \times L_{C1} \times C_{ox}$, the size of dummy transistor can be calculated as:

$$W_{C1} \times L_{C1} = \frac{V_{SWING} \times C_{OUT}}{C_{ox} \times (V_{DD} - V_{SWING})} \quad (3)$$

where $W_{C1}$, $L_{C1}$ are the width and length of dummy transistor for $C_1$, $C_{ox}$ is the gate oxide capacitance per unit area.

### *3.2 D-PFSCL design for multi-stage applications*

There are restrictions in employing D-PFSCL stages for multi-stage applications. To elaborate this issue, a cascade of two D-PFSCL inverters, as depicted in Fig. 4a, is considered. During the precharge phase, the output of both the inverters (Q1, Q2) is high. Also, the external input (A1) is applied to the first stage inverter during this phase. At the beginning of evaluation phase, the output voltages Q1 and Q2 are high. Assuming high value of input A1, the output of the first stage (Q1) will drop to low level during the evaluation phase. As evaluation of both the inverters is done simultaneously, the output of the second stage inverter will be erroneously low as explained in Fig. 4b and remedy of this is not possible. Therefore the D-PFSCL stages cannot be connected directly. The problem in cascading two D-PFSCL inverters is due to the fact that both stages are evaluating simultaneously and output of the first stage makes a high to low transition.

Downloaded by [Delhi Technological University] at 23:11 13 January 2016

ACCEPTED MANUSCRIPT

This situation can be practically avoided - by ensuring a low to high transition at the output or by delaying the evaluation in second stage until output of first stage is obtained. These two techniques for multi-stage applications of D-PFSCL are discussed here.

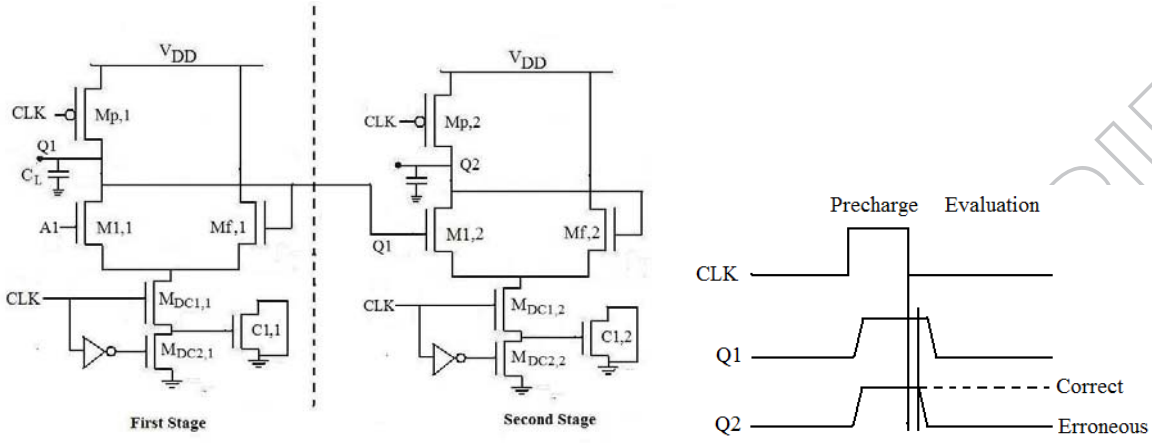


(a) (b)

Fig. 4 a) Cascading of two D-PFSCL inverters b) Output of the two stages with respect to the common clock (CLK)

Technique 1: Insertion of PFSCL inverter

The insertion of a PFSCL inverter between D-PFSCL stages can eliminate the above problem. During the precharge phase, the output node of the first stage D-PFSCL inverter is precharged to a high voltage level, such that the output of the PFSCL inverter becomes low. This condition ensures that a low to high transition at the output will occur and will avoid erroneous outputs of the subsequent stages.

This technique allows the implementation of multi-stage applications based on D-PFSCL logic style. The insertion of PFSCL inverter leads to static power consumption which contradicts the basic aim of the proposed logic style. Hence another technique is suggested.

Technique 2: Insertion of Self-timed buffer

The second technique involves the insertion of a self-timed buffer (Allam & Elmasry, 2001) between the stages. The self-timed buffer converts the voltage stored on the capacitor $C_1$ in the dynamic current source to a full swing output which can be used as clock input by the subsequent stage. The proposed scheme is illustrated by considering a cascade of two D-PFSCL inverters as shown in Fig 5. In this scheme, the external clock signal (CLK) is applied to the first stage. When the CLK goes low (precharge phase), the output of the first stage is precharged to a high level and the capacitor $C_{1,1}$ gets discharged simultaneously. This input condition makes the output of the self-timed buffer as low and ensures that the second stage is also in the precharge phase. When the CLK goes high (evaluation phase), the capacitor $C_{1,1}$ gets charged to high level and produces a high level at the output of the self-timed buffer. Thus, the evaluation of the second stage starts only after the evaluation of the first stage.

Downloaded by [Delhi Technological University] at 23:11 13 January 2016

ACCEPTED MANUSCRIPT

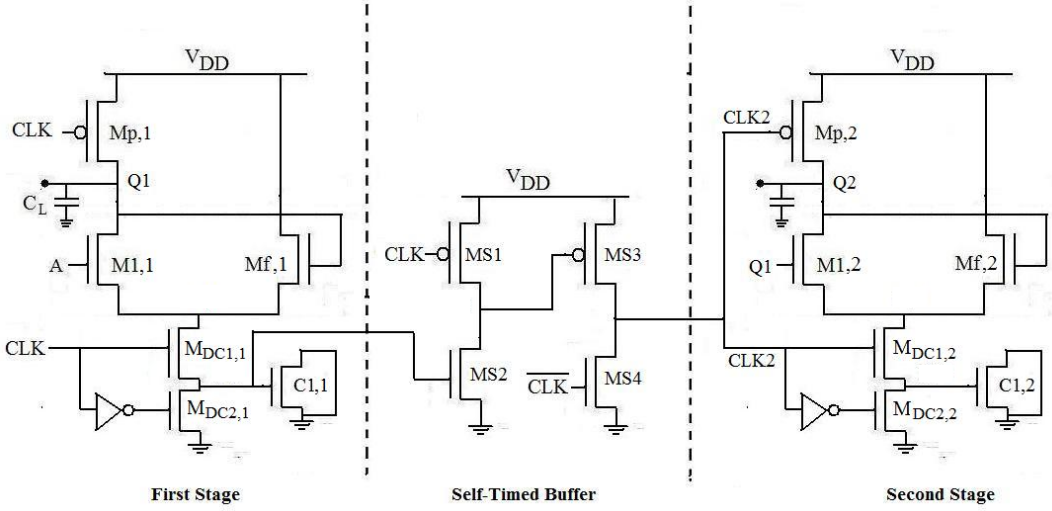


Fig. 5 Insertion of a self-timed buffer between the two D-PFSCL inverters

### *3.3 Power Consumption of D-PFSCL gates*

The D-PFSCL gates do not consume static power. This is due to the fact that there is no constant current path from the power supply to the ground because the transistor pairs $M_{DC1}$ and $M_{DC2}$ (Fig. 2) in the dynamic current source would never turn ON simultaneously. The D-PFSCL gates, however, consume dynamic power which is

$$P_{dyn} = C_{OUT}V_{DD}V_{SWING}f_{CLK} \tag{4}$$

for a single stage D-PFSCL gate. The $f_{CLK}$ represents the frequency of the clock signal (CLK).

The dynamic power consumption of the logic gates depend on the switching activity of the output node (Rabaey, Chandrakasan & Nikolic, 2003). The output node makes a low-to-high transition during the precharge phase, only if the output was discharged during the preceding evaluation phase. Hence it is necessary to determine the low-to-high transition probability for a D-PFSCL gate (Rabaey, Chandrakasan & Nikolic, 2003). It is already known that for uniformly distributed inputs, the low-to-high transition probability for an N-input gate is

$$\alpha_{L\to H} = \frac{N_0}{2^N} \tag{5}$$

where $N_0$ is the number of zero entries in the truth table of the logic function.

Thus, the power consumption of an N-input D-PFSCL gate with transition probability $\alpha_{L\to H}$ is given as:

$$P_{dyn} = \alpha_{L\to H}C_{OUT}V_{DD}V_{SWING}f_{CLK} \tag{6}$$

Downloaded by [Delhi Technological University] at 23:11 13 January 2016

ACCEPTED MANUSCRIPT

For the multi-stage D-PFSCL gate realized using technique 1 power can be computed as the sum of the power consumption of its constituent D-PFSCL gates and the PFSCL inverters used in the realization. The power consumption of the PFSCL inverter can be computed as the product of the supply voltage and bias current (Alioto, Pancioni, Rocchi & Vignoli, 2007).

The overall power consumption for multi-stage D-PFSCL gate based on technique 2 may be approximated as the sum of the power consumption of its constituent D-PFSCL gates. If identical gates are used in the realization of the multi-stage D-PFSCL gate then the power can be approximated as the product of the number of gates and the power consumption by one gate as given in eq. (6). Therefore, power consumption of a multi-stage D-PFSCL gate based on technique 2 and employing K number of identical D-PFSCL gates is given as:

$$P_{dyn} = K\,\alpha_{L\to H} C_{OUT} V_{DD} V_{SWING} f_{CLK} \tag{7}$$

## 4. Simulation Results

This section first presents the simulation results for different D-PFSCL gates such as 2-input NOR, 3-input NOR, 2-input XOR and 3-input XOR followed by the effect of parameter variations on the power consumption of D-PFSCL gates. Thereafter, the performance of the proposed D-PFSCL gates is compared with the PFSCL and dynamic CMOS gates. All the simulations are performed through SPICE simulations by using TSMC 0.18 µm CMOS technology parameters with a power supply of 1.8 V. The voltage swing of 400 mV is chosen and load capacitance of 100 fF is taken. The channel length of the transistors is taken as 0.18 µm uniformly. All the circuits have been simulated with a clock frequency of 1 GHz.

### 4.1 *Different D-PFSCL gates*

The circuit for a 2-input D-PFSCL NOR gate with inputs A and B is shown in Fig. 6a. The input A and B drives the transistor $M_1$ and $M_2$ respectively in the PDN and are further source-coupled to a feedback transistor $M_f$. The circuit of the 3-input D-PFSCL NOR gate can be implemented in a similar manner by adding a third transistor $M_3$ in the PDN of the 2-input D-PFSCL NOR gate as drawn in Fig. 6b. The output waveforms for the 2-input NOR gate is shown in Fig. 7. It can be observed that during the precharge phase, the CLK is low, the transistors $M_P$, $M_{DC2}$ are ON and the transistor $M_{DC1}$ is OFF. So, the output node Q is charged to the high level ($V_{OH}$ = 1.8 V) through $M_P$. The inputs A and B are applied in this phase which does not cause any change in the output as the transistor $M_P$ is ON and the transistor $M_{DC1}$ is OFF. In the evaluation phase, the CLK goes high and makes the transistor $M_{DC1}$ ON; and transistors $M_P$ and $M_{DC2}$ OFF. The proposed circuit exhibits the functionality of the NOR gate. The output is evaluated depending on the value of inputs A and B. For a low value of the inputs, the transistors $M_1$, $M_2$ are OFF and the gate output remains high

Downloaded by [Delhi Technological University] at 23:11 13 January 2016

ACCEPTED MANUSCRIPT

($V_{OH}$ = 1.8 V) as no path exists for the transfer of the charge stored on load capacitor $C_L$ to capacitor $C_1$. For the remaining three cases wherein at either one or both the inputs are high, the output node Q potential decreases to low level ($V_{OL}$= 1.4 V) due to charge transfer from the load capacitor $C_L$ to capacitor $C_1$. The simulation results for the power consumption by the single-stage D-PFSCL gates namely inverter, 2-input NOR, 3-input NOR are listed in Table I. In the table, the theoretical value of the power consumption by a particular gate is computed by using eq. (6). It can be observed that a maximum error of 12.6 % is obtained between the theoretical and the practical values. The waveforms for 3-input D-PFSCL NOR gate is not shown for the sake of brevity.

A 2-input D-PFSCL XOR gate can be implemented by using 2-input D-PFSCL NOR gates as shown in Fig. 8. The gate has three stages so the techniques suggested in sub-section 3.2 are used in the realization. Similarly, the 3-input D-PFSCL XOR gate is implemented by connecting two identical XOR gates. The simulation results for the power consumption by the XOR gates using the two techniques for multi-stage operations are listed in Table II. The theoretical value of the XOR gates realized using technique 1 has been calculated by adding the power consumption of all the D-PFSCL gates and the PFSCL inverter with bias current value of 10 µA. For the XOR gate realized using technique 2, the theoretical value of the power consumption is computed by using eq. (7). It can be observed that the simulation results are in close agreement with the theoretical values.

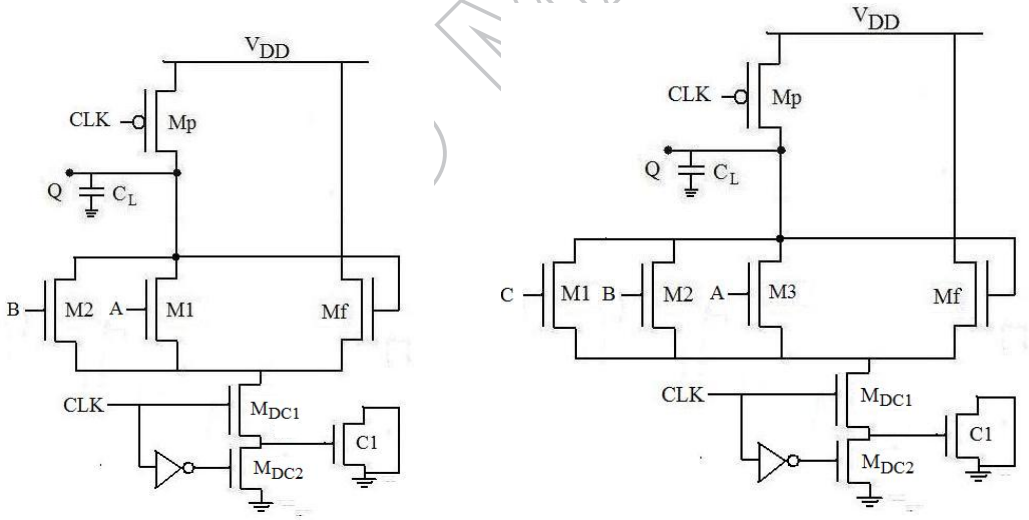


Fig. 6 Proposed D-PFSCL gates a) 2-input NOR gate b) 3-input NOR gate.

Downloaded by [Delhi Technological University] at 23:11 13 January 2016

ACCEPTED MANUSCRIPT

Downloaded by [Delhi Technological University] at 23:11 13 January 2016

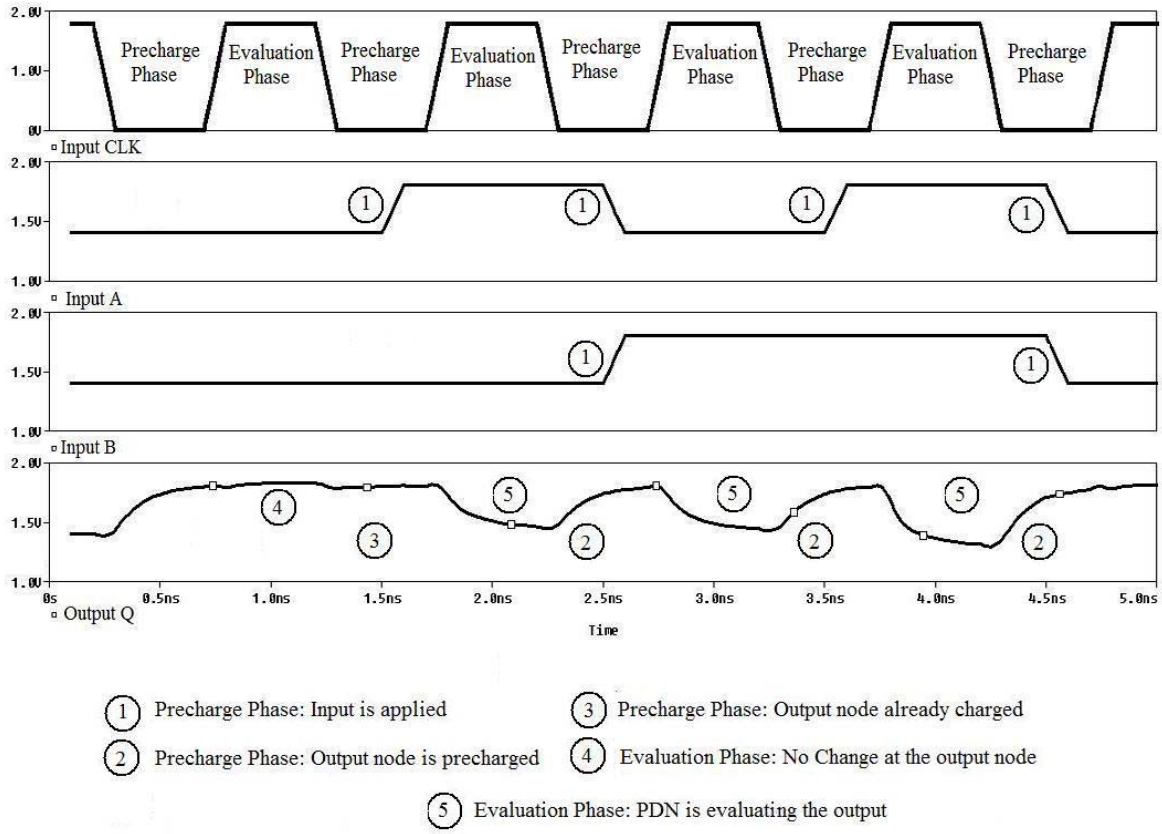


Fig. 7 Output waveforms of the 2-input D-PFSCL NOR gate

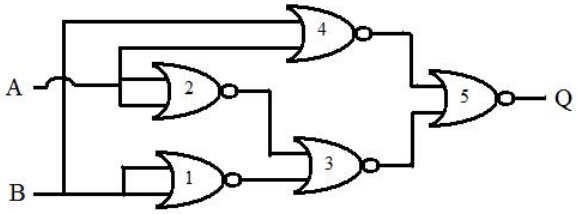


Fig. 8 A 2-input XOR gate using 2-input D-PFSCL NOR gates

The impact of parameter variation on power consumption of the proposed D-PFSCL gates is studied at different design corners. The results along with the power consumption variation between the best and the worst cases are listed in Table III. It is found that the power consumption of the D-PFSCL inverter, 2-input NOR, 3-input NOR, 2-input XOR and 3-input XOR gates varies by a factor of 1.5, 1.2, 1.1, 1.3 and 1.2 between the best and the worst cases respectively.

The performance of the proposed architecture is studied at 180 nm and 90 nm technology nodes by considering the same input conditions. The simulation results are listed Table IV. An enhancement in the performance of the circuits is observed. The values of the timing parameters

ACCEPTED

are reduced while moving from 180 nm technology node to 90 nm technology. Also, it is found that for the same value of voltage swing, the noise margin of the circuits is increased in the sub-nm CMOS technologies as established in (Alioto & Palumbo, 2006).

### *4.2 Performance Comparison*

Several logic gates such as inverter, 2-input NOR, 3-input NOR, 2-input XOR and 3-input XOR based on the proposed D-PFSCL, PFSCL and the dynamic CMOS styles are implemented for the purpose of comparison. The PFSCL circuits are designed using the approach suggested in (Alioto, Pancioni, Rocchi & Vignoli, 2007). The aspect ratios of the transistors in the PDN of the two styles are taken to be same. The simulation results of the gates based on both the logic styles is listed in Table V. It can be observed that a power saving of 11.2 % to 84 % is obtained by using the proposed D-PFSCL style. The speed performance of the proposed gates is studied by noting down different timing parameters such as propagation delay high-to-low transition ($t_{PHL}$), propagation delay low-to-high transition ($t_{PLH}$) and precharge time ($t_{pre}$) and is summarized in Table V. It may be noted that the output is high at the beginning of evaluation period and no switching at the output takes place for low values of the inputs thereby making $t_{PLH}$= 0. The results for $t_{PHL}$ in Table V indicate lower value of $t_{PHL}$ for the proposed gates which can be attributed to the process of charge transfer and absence of current steering mechanism of PFSCL gates. The waveforms for the parameters reported in Table V for inverter are included as Fig. 9. Similar waveforms are obtained for other gates but are omitted for the sake of brevity. The proposed gates include precharge time, $t_{pre}$ which is not applicable for PFSCL gates.

Apart, from having the advantages of better speed and power consumption, it is appropriate to compare the implementation area of proposed architecture with PFSCL. The D-PFSCL gate uses the dynamic current source in place of the constant current source of PFSCL. The implementation of the dynamic current source requires two transistors and capacitor $C_1$ in contrast to the simple current mirror in PFSCL style (Alioto, Pancioni, Rocchi & Vignoli, 2007). The PFSCL and D-PFSCL circuits are implemented in TSMC 0.18 µm CMOS technology with a load capacitance of 100 fF for the sake of comparison. Considering the same aspect ratios of the transistors in the PDN, a maximum increase of about 9% is observed for D-PFSCL circuits implementation in comparison to PFSCL inverter which can be traded off against speed and power consumption.

The results for the logic gates implemented using dynamic CMOS style are also listed in Table V. It is found that the D-PFSCL gates show significant reduction in power, high-to-low delay and precharge time in comparison to the respective dynamic CMOS counterparts. However, the D-PFSCL gates occupy much larger area than the dynamic CMOS ones.

Downloaded by [Delhi Technological University] at 23:11 13 January 2016

ACCEPTED MANUSCRIPT

Downloaded by [Delhi Technological University] at 23:11 13 January 2016

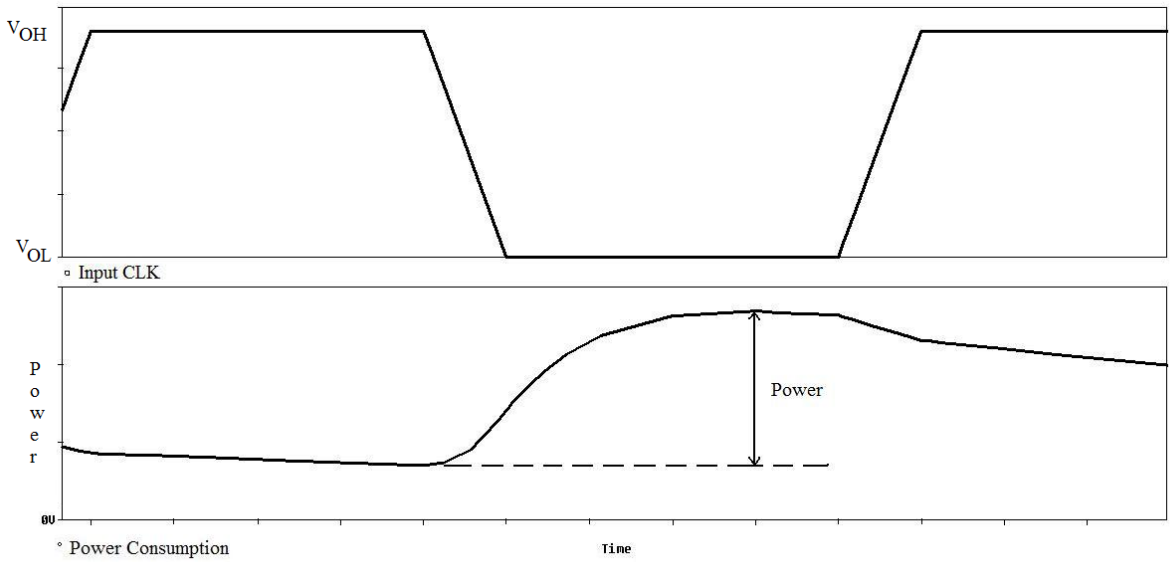


(a)

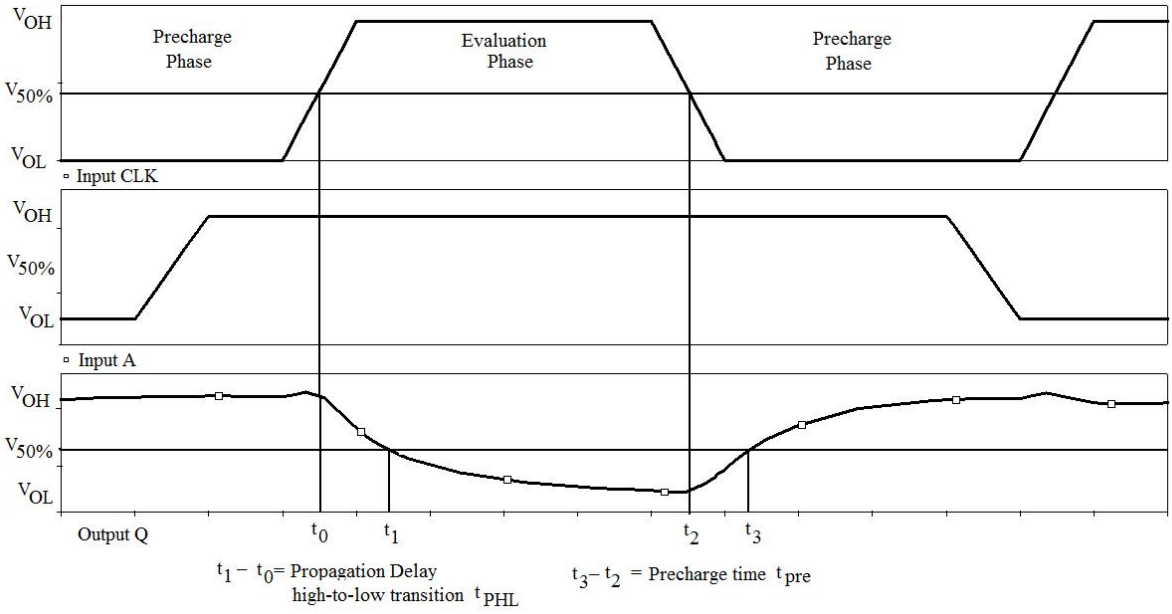


(b)

Downloaded by [Delhi Technological University] at 23:11 13 January 2016

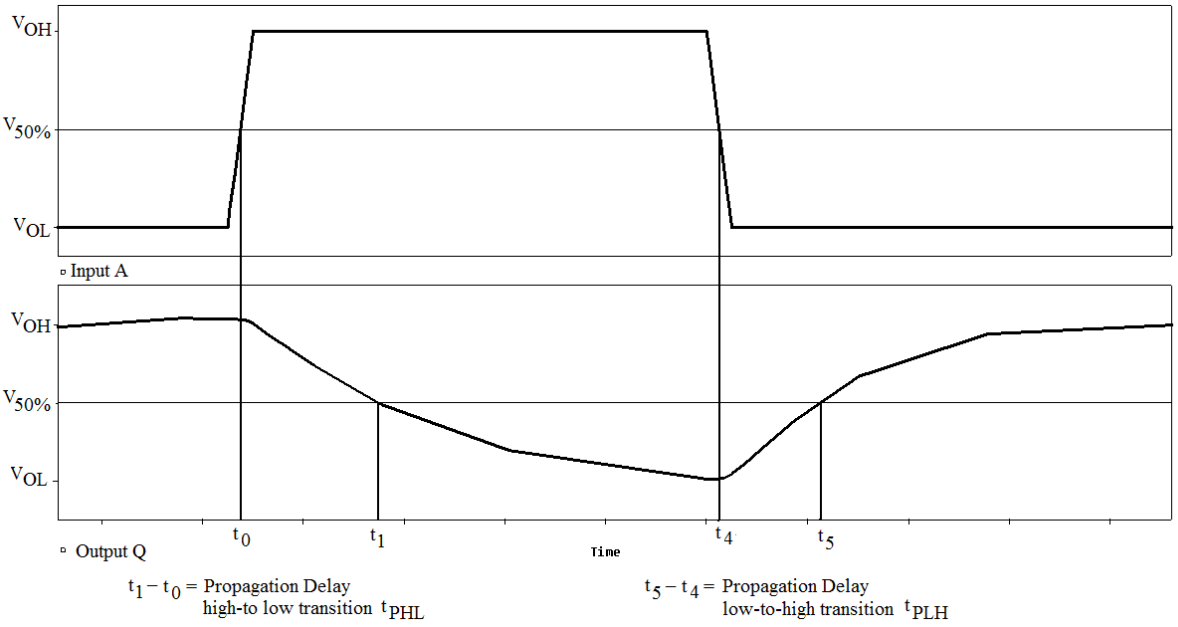


(c)

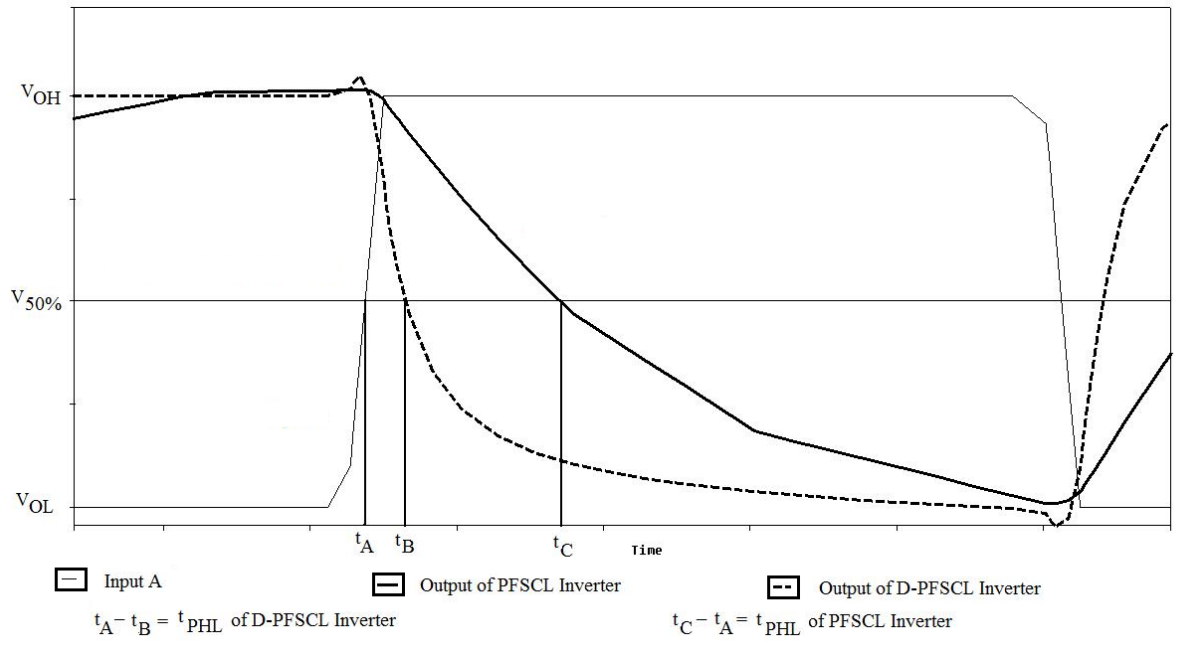


(d)

Fig. 9 (a) Power measurement (b) Timing parameters of a D-PFSCL inverter (c) Timing parameters of a PFSCL inverter (d) Comparison of high-to-low delay for the D-PFSCL and PFSCL inverter.

## 5. Conclusions

This paper proposes a new dynamic positive-feedback source-coupled logic (D-PFSCL) style that consumes lesser power than the PFSCL style. It employs a dynamic current source that eliminates the constant current flow in the circuit in contrast to the PFSCL style. Two techniques to implement multi-stage D-PFSCL application are suggested. Several logic gates based on the proposed D-PFSCL style are implemented and their performance is compared with the PFSCL gates. It is found that the proposed D-PFSCL circuits are more power efficient than the PFSCL ones. The effect of process variation on the power consumption of the D-PFSCL gates shows a maximum variation factor of 1.5 between the best and the worst cases.

## References


Allstot, D., Chee, S., Kiaei, S., & Shristawa, M. (1993). Folded source-coupled logic vs. CMOS static logic for low-noise mixed-signal ICs. *IEEE Transactions on Circuits and Systems-I, 40,* 553–563.

Masui, S. (1992). *Simulation of substrate coupling in mixed-signal MOS circuits. Proceedings of International Symposium on VLSI circuits, Seattle, WA, USA,* June 1992. IEEE.

Kiaei, S., Chee, S., & Allstot, D. (1990). *CMOS source-coupled logic for mixed-mode VLSI, Proceedings of International Symposium on Circuits and Systems, New Orleans,* May 1990, 1608–1611.

Alioto, M., & Palumbo, G. (2005). *Model and Design of Bipolar and MOS Current-Mode logic (CML, ECL and SCL Digital Circuits).*Netherlands: Springer.

Musa, O. (2010). An Efficient Delay Model for MOS Current-Mode Logic Automated Design and Optimization. *IEEE Transactions on Circuits and Systems-I, 57,* 2041-2052.

Alioto, M., Pancioni, L., Rocchi, S., & Vignoli, V. (2004). Modeling and evaluation of positive-feedback source-coupled logic. *IEEE Transactions on Circuits and Systems-I, Regular Papers, 51,* 2345–2355.

Alioto, M., Fort, A., Pancioni, L., Rocchi, S., & Vignoli, V. (2004). *Positive-Feedback Source-Coupled Logic: a Delay Model. Proceedings of International Symposium on Circuits and Systems,* May 2004, IEEE.

Alioto, M., Fort, A., Pancioni, L., Rocchi, S., & Vignoli, V. (2005). *An approach to the design of PFSCL gates. Proceedings of International Symposium on Circuits and Systems, May 2005,* IEEE.

Alioto, M., Pancioni, L., Rocchi, S., & Vignoli, V. (2007). Power-Delay-Area-Noise Margin Trade-offs in Positive-Feedback Source-Coupled Logic Gates. *IEEE Transactions on Circuits and Systems.-I, Regular Papers, 54,* 1916-1928.

Alioto, M., Pancioni, L., Rocchi, S., & Vignoli, V. (2006). Exploiting Hysteresys in MCML Circuits. *IEEE Transactions on Circuits and Systems-II, 53,* 1170-1174.



Downloaded by [Delhi Technological University] at 23:11 13 January 2016

ACCEPTED MANUSCRIPT

Allam, M. W., & Elmasry, M. (2001). Dynamic Current Mode Logic (DyCML): A New Low-Power High-Performance Logic Style. *IEEE Journal of Solid-State*, *36*, 550-558.

Kang, S. M., & Leblebici, Y. (2006). *CMOS Digital Integrated Circuits: Analysis and Design. 3rd ed*. New York:Tata Mcgraw Hills.

Rabaey, J. M., Chandrakasan, A., & Nikolic, B. (2003). *Digital Integrated Circuits*, India: Pearson Education, 2nd Edition.

Alioto, M., & Palumbo, G. (2006). Nanometer MCML Gates: Models and Design Considerations *Proceedings of International Symposium on Circuits and Systems, Island of KOS*, May 2006, IEEE.

Downloaded by [Delhi Technological University] at 23:11 13 January 2016

Table I. Power consumption of the single-stage D-PFSCL gates.

| Logic gate | Theoretical Value (μW) | Simulated Value (μW) | Percentage Error |
|---|---|---|---|
| Inverter | 36 | 38 | 5.2 % |
| 2-input NOR | 54 | 57 | 5.5 % |
| 3-input NOR | 63 | 71 | 12.6 % |

Table II. Power consumption of the multi-stage D-PFSCL XOR gates based on the two techniques

| Logic gate | Technique 1 | | | Technique 2 | | |
|---|---|---|---|---|---|---|
| | Theoretical Value (μW) | Simulated Value (μW) | Percentage Error | Theoretical Value (μW) | Simulated Value (μW) | Percentage Error |
| 2-input XOR | 342 | 385 | 12.5 % | 270 | 313 | 16 % |
| 3-input XOR | 684 | 778 | 13.7 % | 540 | 619 | 14.6 % |

Table III. Impact of parameter variation on power consumption (μW) of the different D-PFSCL gates

| NMOS / PMOS / Logic gate | T / T | F / F | S / S | F / S | S / F |
|---|---|---|---|---|---|
| Inverter | 38 | 51 | 33 | 43 | 41 |
| 2-input NOR | 58 | 70 | 57 | 67 | 66 |
| 3-input NOR | 71 | 75 | 66 | 74 | 71 |
| 2-input XOR | 313 | 344 | 272 | 324 | 319 |
| 3-input XOR | 619 | 662 | 555 | 636 | 619 |

where different design corners are denoted by T = Typical, F= Fast, S= Slow

ACCEPTED MANUSCRIPT

Table IV: Performance evaluation of D-PFSCL circuits at different technology nodes

| Technology node | Parameter / Logic gate | Power (μW) | $t_{PHL}$ (ps) | $t_{pre}$ (ps) | $NM_H$ (mV) | $NM_L$ (mV) |
|---|---|---|---|---|---|---|
| 180 nm | Inverter | 38 | 93 | 111 | 200 | 180 |
| | 2-input NOR | 57 | 145 | 112 | 200 | 300 |
| | 3-input NOR | 71 | 132 | 118 | 200 | 240 |
| | 2-input XOR | 313 | 450 | 250 | 200 | 280 |
| | 3-input XOR | 619 | 496 | 296 | 200 | 270 |
| 90 nm | Inverter | 38 | 38 | 103 | 200 | 220 |
| | 2-input NOR | 57 | 114 | 95 | 200 | 310 |
| | 3-input NOR | 71 | 73 | 114 | 200 | 290 |
| | 2-input XOR | 313 | 282 | 168 | 200 | 300 |
| | 3-input XOR | 619 | 297 | 188 | 200 | 290 |

Table V: Performance comparison of logic gates

| Logic gate / Style | Inverter | 2-input NOR | 3-input NOR | 2-input XOR | 3-input XOR |
|---|---|---|---|---|---|
| Power consumption (uW) | | | | | |
| PFSCL | 252 | 120 | 80 | 580 | 1110 |
| D-PFSCL | 38 | 57 | 71 | 313 | 619 |
| Dynamic CMOS | 177 | 267 | 284 | 364 | 762 |
| Propagation delay high-to-low transition, $t_{PHL}$ (ps) | | | | | |
| PFSCL | 518 | 473 | 445 | 1235 | 1290 |
| D-PFSCL | 93 | 145 | 132 | 450 | 496 |
| Dynamic CMOS | 203 | 191 | 147 | 464 | 510 |
| Propagation delay low-to-high transition, $t_{PLH}$ (ps) | | | | | |
| PFSCL | 329 | 371 | 254 | 1135 | 1210 |
| D-PFSCL | 0 | 0 | 0 | 0 | 0 |
| Dynamic CMOS | 0 | 0 | 0 | 0 | 0 |
| Precharge time $t_{pre}$ (ps) | | | | | |
| PFSCL | -- | -- | -- | -- | -- |
| D-PFSCL | 111 | 112 | 118 | 250 | 296 |
| Dynamic CMOS | 173 | 195 | 210 | 317 | 327 |
| Area ($um^2$) | | | | | |
| PFSCL | 17 | 18.3 | 19.6 | 91 | 183 |
| D-PFSCL | 18.5 | 19.8 | 21.1 | 99.45 | 198 |
| Dynamic CMOS | 16 | 14.25 | 15.40 | 42.75 | 86 |
| Power Saving (%) | | | | | |
| w. r. t. PFSCL | 84 | 52.5 | 11.2 | 46 | 44 |
| w. r. t. Dynamic CMOS | 78.5 | 78.6 | 75 | 14 | 18.7 |
| Propagation delay high-to-low transition, $t_{PHL}$ (ps) reduction (%) | | | | | |
| w. r. t. PFSCL | 82 | 69.3 | 70.3 | 63.5 | 61.5 |
| w. r. t. Dynamic CMOS | 54 | 24 | 10.2 | 3 | 2.7 |
| Precharge time reduction (%) | | | | | |
| w. r. t. Dynamic CMOS | 35 | 42.5 | 43.8 | 21.1 | 9.4 |
| Increase in Area (%) | | | | | |

Downloaded by [Delhi Technological University] at 23:11 13 January 2016

ACCEPTED MANUSCRIPT

| | | | | | |
|---|---|---|---|---|---|
| w. r. t. PFSCL | 9 | 7.5 | 7.6 | 8.4 | 8.1 |
| w. r. t. Dynamic CMOS | 15.6 | 40 | 37 | 132 | 130 |

**Summary of the additions**

1. The name of the software is added and highlighted in Cyan color.

**RESPONSE TO REVIEWERS**

**Title: Dynamic Positive-Feedback Source-Coupled Logic (D-PFSCL)**

**To Respected Reviewer # 3**

First of all may I gratefully appreciate your invaluable comments. It is certainly my pleasure to take advantage of the current opportunity to discuss subject of mutual interest with you. The response to your observations and suggestions are as follows:

I have not any real argument against publication this paper. I have only few questions.

**1. Question/suggestion/observation:** Page 10, last sentence before Figs. 6: "It can be observed that the simulation results are in close agreement with the theoretical values." Which approach has been used to obtain these theoretical values?

The approach used to determine the theoretical value of power consumption of the D-PFSCL gates is illustrated below:

The dynamic power consumption of a single stage D-PFSCL gate with a power supply $V_{DD}$, voltage swing $V_{SWING}$, and clock frequency $f_{CLK}$ (eqn. (6) of the original manuscript,) is given as:

$$P_{dyn} = \alpha_{L\to H} C_{OUT} V_{DD} V_{SWING} f_{CLK}$$

where $\alpha_{L\to H}$ and $C_{OUT}$ are the low-to-high transition probability and the total load capacitance at the output node. The computation of the power requires the determination of $\alpha_{L\to H}$ and $C_{OUT}$ for the gate. By assuming uniformly distributed inputs, the low-to-high transition probability for an N-input gate is given in eqn. (5) of the original manuscript and is reproduced here

$$\alpha_{L\to H} = \frac{N_0}{2^N}$$

where $N_0$ is the number of zero entries in the truth table of the logic function. The values of $\alpha_{L\to H}$ for the single stage D-PFSCL inverter, 2-input NOR, 3-input NOR gates are 0.5, 0.75 and 0.875 respectively. The total load capacitance $C_{OUT}$ includes the parasitic capacitances of the transistors

Downloaded by [Delhi Technological University] at 23:11 13 January 2016

ACCEPTED MANUSCRIPT

and the external load capacitance $C_L$. The calculation of the parasitic capacitances of the transistors is based on the approach suggested by (Alioto, Pancioni, Rocchi & Vignoli, 2004).

For multi-stage D-PFSCL gates realized using technique 1, the power consumption of the constituent D-PFSCL gates and the PFSCL inverters is added up. The power consumption of a PFSCL inverter is computed as the product of the supply voltage and the bias current (Alioto, Pancioni, Rocchi & Vignoli, 2007). The approach can be elaborated for a D-PFSCL 2-input XOR gate (Fig. 8 of the original manuscript) wherein five D-PFSCL NOR gates and four PFSCL inverters are needed. Therefore, the theoretical value of total power consumption is computed as sum of power consumption of these gates. Similarly, the multi-stage D-PFSCL gates realized using technique 2, the power consumption is approximated as the sum of the power consumption of its constituent D-PFSCL gates including the self-timed buffers. Equation (7) of the original manuscript is used to compute power of the D-PFSCL XOR gate. These approaches are used for all the multi-stage gates reported in the manuscript.

**2. Question/suggestion/observation:** Which simulation way has been used: which equations (relations (1)-(7) or other), which method of solution (algebraic transformation only)?

Answer: Thank you for pointing out the simulation way used in the paper. There was a miss on author's part for not putting the software name. SPICE simulations are been carried out for all the results reported in the manuscript and is now been mentioned in the revised manuscript. It is highlighted in cyan for ready reference. The simulation waveforms depicting the functional verification and measurement of different performance parameters are shown in Figs. 7 and 9 respectively in the original manuscript. The transient response is shown for functional verification and measurement of timing parameters. The power meter simulation is carried out for dynamic power measurement.

Yours Sincerely

N. Pandey

References:

Alioto, M., Pancioni, L., Rocchi, S., & Vignoli, V. (2004). Modeling and evaluation of positive-feedback source-coupled logic. *IEEE Transactions on Circuits and Systems-I, Regular Papers, 51,* 2345–2355.

Alioto, M., Pancioni, L., Rocchi, S., & Vignoli, V. (2007). Power-Delay-Area-Noise Margin Trade-offs in Positive-Feedback Source-Coupled Logic Gates. *IEEE Transactions on Circuits and Systems.-I, Regular Papers, 54*, 1916-1928.

Downloaded by [Delhi Technological University] at 23:11 13 January 2016

ACCEPTED MANUSCRIPT

Volume 3, Issue 4 (2015) 611-614 ISSN 2347 - 3258
International Journal of Advance Research and Innovation

# Economic Analysis of the Nisargruna Based Bio-Methanation Plant

Aftab Anjum *, Mohit Gupta, Aadish Jain
Department of Mechanical Engineering, Delhi Technological University, Delhi, India

**Article Info**

Article history:
Received 25 September 2015
Received in revised form
20 October 2015
Accepted 28 November 2015
Available online 15 December 2015

**Keywords**
Vapour Compression Refrigeration Systems,
Energy and Exergy Analysis,
First and Second Law Analysis,
Irreversibility Analysis,
VCR with Direct nano Particles Mixed Refrigerants

**Abstract**

In the present paper economic as well as technological aspects of the bio-methanation plant has been studied. Nisargruna technology converts almost any type of organic solid waste to bio methane as compared to the conventional cowdung/ animal faeces based biogas plants. The reduction in the size of the plant has attracted many institutions to erect it in a rather confined space with less setup time and reduced waste processing period along with enhanced output, this has greatly reduced the gestation period. A Nisargruna based plant has been installed at Delhi Technological University which handles 500 kg of organic solid waste per day aimed to supply the biogas to the university's canteen. About 60-65% biogas along with high quality manure which is completely organic in nature can be obtained from the plant. It can be inferred from the economical aspects that the plant has a gestation period between 2-3 years.

## Nomenclature

| | |
|---|---|
| COP | coefficient of performance (non-dimensional) |
| VCR | vapour compression refrigeration |
| CFC | chlorofluorocarbon |
| HCFC | hydrochlorofluorocarbon |
| Q | rate of heat transfer (kW) |
| W | work rate (kW) |
| T | temperature (K) |
| δ | efficiency defect (non-dimensional) |
| $\Delta T_{sc}$ | degree of subcooling |
| EP | exergy rate of product (kW) |
| EV | Expansion Valve |
| EP | Evaporator |

**Subscript**

| | |
|---|---|
| e | evaporator |
| comp | compressor |
| h | specific enthalpy (kJ/kg) |
| P | pressure (kPa) |
| IR | irreversibility (kW) |
| $E_x$ | exergy rate of fluid (kW) |
| m | mass flow rate (kg/s) |
| s | specific entropy (kJ/kgK) |
| EF | exergy rate of fuel (kW) |
| EL | exergy loss rate (kW) |
| η | efficiency (non-dimensional) |
| r | refrigerant, space to be cooled |
| ex | exergetic |
| ev | expansion valve |
| c | condenser |
| sc | subcooler |
| k | kth component |

## 1. Introduction

Refrigeration is a technology which absorbs heat at low temperature and provides temperature below the surrounding by rejecting heat to the surrounding at higher temperature. Simple vapour compression system which consists of four major components compressor, expansion valve, condenser and evaporator in which total cooling load is carried at one temperature by single evaporator but in many applications like large hotels, food storage and food processing plants, food items are stored in different compartment and at different temperatures. Therefore there is need of multi evaporator vapour compression refrigeration system. The systems under vapour compression technology consume huge amount of electricity, this problem can be solved by improving first law and second law performances of system.

Performance of systems based on vapour compression refrigeration technology can be improved by following:

- The performance of refrigerator is evaluated in term of COP which is the ratio of refrigeration effect to the net work input given to the system. The COP of vapour compression refrigeration system can be improved either by increasing refrigeration effect or by reducing work input given to the system.
- It is well known that throttling process in VCR is an irreversible expansion process. Expansion process is one of the main factors responsible for exergy loss in cycle performance because of entering the portion of the
- refrigerant flashing to vapour in evaporator which will not only reduce the cooling capacity but also increase the size of evaporator. This problem can be eliminated by adopting multi-stage expansion with flash chamber where the flash vapours is removed after each stage of expansion as a consequence there will be increase in cooling capacity and reduce the size of the evaporator.
- Work input can also be reduced by replacing multi-stage compression or compound compression with single stage compression.

**Corresponding Author,**
**E-mail address:** aftabanjum915@gmail.com
**All rights reserved:** http://www.ijari.org

- Refrigeration effect can also be increased by passing the refrigerant through subcooler after condenser to evaporator.
- Use of nano particles mixed with R718 in the secondary evaporator circuit
- Use of nano particles directly mixed with ecofriendly refrigerants in the primary circuit
- Use of nano particles coating in the VCR condenser tubes

## 2. Literature Review

Vapour compression refrigeration system based applications make use of refrigerants which are responsible for greenhouse gases, global warming and ozone layer depletion. Montreal protocol was signed on the issue of substances that are responsible for depleting Ozone layer and discovered how much consumption and production of ozone depletion substances took place during certain time period for both developed and developing countries. Another protocol named as Kyoto aimed to control emission of green house gases in 1997. The relationship between ozone depletion potential and global warming potential is the major concern in the field of GRT (green refrigeration technology) so Kyoto proposed new refrigerants having lower value of ODP and GWP. Internationally a program being pursued to phase out refrigerants having high chlorine content for the sake of global environmental problems .Due to presence of high chlorine content ,high global warming potential and ozone depletion potential after 90's CFC and HCFC refrigerants have been restricted. Thus, HFC refrigerants are used nowadays, showing much lower global warming potential value, but still high with respect to non-fluorine refrigerants. Lots of research work has been done for replacing "old" refrigerants with "new" refrigerants [1].

**Reddy et al. [2]** carried out numerical analysis of vapour compression refrigeration system using R134a, R143a, R152a, R404A, R410A, R502 and R507A , and discussed the effect of evaporator temperature, degree of subcooling at condenser outlet, superheating of evaporator outlet, vapour liquid heat exchanger effectiveness and degree of condenser temperature on COP and exergetic efficiency. They reported that evaporator and condenser temperature have significant effect on both COP and exergetic efficiency and also found that R134a has the better performance while R407C has poor performance in all respect.

**Selladurai et.al.[3]** compared the performance between R134a and R290/R600a mixture on a domestic refrigerator which is originally designed to work with R134a and found that R290/R600a hydrocarbon mixture showed higher COP and exergetic efficiency than R134a. In their analysis highest irreversibility obtained in the compressor compare to condenser, expansion valve and evaporator. **Nikolaidis et.al. [4]** studied the change in evaporator and condenser temperatures of two stage vapour compression refrigeration plant using R22 add considerable effect on plant irreversibility. They suggested that there is need for optimizing the conditions imposed upon the condenser and evaporator. **Kumar et. al. [5]** carried out energy and exergy analysis of vapour compression refrigeration system by the use of exergy-enthalpy diagram. They did first law analysis (energy analysis) for calculating the coefficient of performance and exergy analysis (second law analysis) for evaluation of various losses occurred in different components of vapour compression cycle using R11 and R12 as refrigerants. **Mastani Joybari et al.[6]** conducted experimental measurements on a domestic refrigerator originally manufactured to use of 145g of R134a and concluded the exergetic defect occurred in compressor was highest as compare to other components and through their analysis it has been found that instead of 145g of R134a if 60g of R600a is used in the considered system gave same performance which ultimately result into economical advantages and reduce the risk of flammability of hydrocarbon refrigerants. **Ahamed et al.[7]** performed experimental measurements of domestic refrigerator with hydrocarbons (isobutene and butane) by energy and exergy analysis. They reached to the results that energy efficiency ratio of hydrocarbons comparable with R134a but exergy efficiency and sustainability index of hydrocarbons much higher than that of R134a at considered evaporator temperature. It was also found that compressors shows highest system defect (69%) among components of considered in the system. **Bolaji et al. [8]** did experimentally comparative analysis of R32, R152a and R134a refrigerants in vapour compression refrigerator and concluded that R32 shows lowest performance whereas R134a and R152a showing nearly same performance but best performance was obtained of system using R152a. **Yumrutas et al. [9]** studied the exergy analysis based investigation of effect of condensing and evaporating temperature on vapour compression refrigeration cycle in terms of pressure losses, COP, second law efficiency and exergy losses. Variation in temperature of condenser as well as have negligible effect on exergy losses of compressor and expansion valve, also first law efficiency and exergy efficiency increase but total exergy losses of system decrease with increase in evaporator and condenser temperature. **Padilla et al. [10]** did exergy analysis **Getu and Bansal [11]** had optimized the design & operating parameters of like condensing temperature, subcooling temperature, evaporating temperature, superheating temperature and temperature difference in cascade heat exchanger R744-R717 cascade refrigeration system. A regression analysis was also done to obtain optimum thermodynamic parameters of same system. **Spatz and Motta [12]** had mainly focused on replacement of R12 with R410a through experimental investigation of medium temperature vapour compression refrigeration cycles. In terms of thermodynamic analysis, comparison of heat transfer and pressure drop characteristics, R410a gives best performance among R12, R404a and R290a.. **Han et al. [13] carried out** experimental tests under different working conditions experimental results revealed that there could be replacement of R407C in vapour compression refrigeration system having rotor compressor with mixture of R32/R125/R161 showing higher COP, less pressure ratio

and slightly high discharge compressor temperature without any modification in the same system. **Halimic et al. [14] had** compared performance of R401A, R290 and R134A with R12 by using in vapour compression refrigeration system, which is originally designed for R12.Due to similar performance of R134a in comparison with R12, R134A can be replaced in the same system without any medication in the system components. But in reference to green house impact R290 presented best results. **Xuan and Chen [15]** suggested the replacement of R502 by mixture of HFC-161 in vapour compression refrigeration system and conducted experimental study it was found that mixture of HFC-161 gives same and higher performance than R404A at lower and higher evaporative temperature respectively on the vapour compression refrigeration system designed for R404A. **Cabello et al. [16]** had analyzed the effect of operating parameters on first law efficiency (COP), work input and cooling capacity of single-stage vapour compression refrigeration system. There is great influence on energetic parameters due change in suction pressure, condensing and evaporating temperatures. **Cabello et al. [17] observed the** effect of condensing pressure, evaporating pressure and degree of superheating was experimentally investigated on single stage vapour compression refrigeration system using R22, R134a and R407C.It was observed that mass flow rate is greatly affected by change in suction conditions of compressor in results on refrigeration capacity because refrigeration capacity depended on mass flow rate through evaporator. It was also found that for higher compression ratio R22 gives lower COP than R407C.. Mishra [ 18 ] Simple VCR with liquid vapour heat exchanger, flash intercooler, flash chamber, water intercooler, liquid subcooler and stages in compression(double stage and triple stage) Mishra [19] conducted detailed analysis of vapour compression refrigeration systems using thirteen ecofriendly refrigerants Mishra [22 ] observed that there is a 12% to 19% improvement in the first law efficiency using nano particles mixed with R718 in the secondary evaporator circuit of VCR and suggested that higher improvement occurs using copper particles mixed with R718 and low improvement occurs using TiO2 in R134a Mishra [19 ] also observed the improvement in the second law thermal performance of vapour compression refrigeration system by mixing $Al_2O_3$ in R718 in secondary evaporator circuit and various ecofriendly refrigerants in the primary evaporator circuit. The lowest performance was observed by using R410a in the primary evaporator circuit Based on the literature it was observed that researchers have gone through detailed first law analysis in terms of coefficient of performance and second law analysis in term of exergetic efficiency of simple vapour compression refrigeration system with single evaporator. Researchers did not go through the nano mixed ecofriendly refrigerant in the secondary evaporator and R1234yf and R1234ze used in the primary circuit of evaporator in terms of improving first and second law efficiency of vapour compression refrigeration systems

## 3. Results and Discussions

**Table: (1—3)** gives the variation of first law efficiency in terms of coefficient of performance and second law efficiency using R1234ze refrigerant in the primary circuit and R-718 with nano mixed refrigerant in the evaporator circuit . It was observed that performance of R1234yf and R1234ze is acceptable as compared with R1234a. Even then mixing circuit, the performance of R1234yf gives better performance than R1234ze and R1234a. The worst performance is observed using R410a

**Table: 1.** performance evaluation of vapour compression refrigeration system using R1234 ze ecofriendly refrigerants in primary circuit and following nano materials mixed with R718 in the secondary circuit

| Nano materials | **COP** | **EDR** | **ETA_II** |
|---|---|---|---|
| Copper | 5.093 | 0.5199 | 0.4801 |
| Al oxide sapphire | 4.34 | 0.6239 | 0.3761 |
| TiO2 | 3.823 | 0.644 | 0.356 |

**Table: 2.** performance evaluation of vapour compression refrigeration system using R1234 yf ecofriendly refrigerants in primary circuit and following nano materials mixed with R718 in the secondary circuit

| Nano materials | **COP** | **EDR** | **ETA_II** |
|---|---|---|---|
| Copper | 5.293 | 0.5071 | 0.4929 |
| Al oxide sapphire | 4.36 | 0.5666 | 0.4334 |
| TiO2 | 3.832 | 0.6721 | 0.3279 |

**Table: 3.** performance evaluation of vapour compression refrigeration system using R134 a ecofriendly refrigerants in primary circuit and following nano materials mixed with R718 in the secondary circuit

| Nano materials | **COP** | **EDR** | **ETA_II** |
|---|---|---|---|
| Copper | 5.193 | 0.5194 | 0.4806 |
| Al oxide sapphire | 4.35 | 0.6239 | 0.3761 |
| TiO2 | 3.82 | 0.654 | 0.346 |

Similarly the effect of nucleate heat transfer in terms of enhancement factor is showing the percentage improvement in the first law efficiency as shown in Table-4-5 respectively**.** The effect of computed nano refrigerant property for enhancement factor and first law efficiency is shown in Table-5. It was observed the best performance is achieved using R1234yf which can replace R134a for low temperature and R1234ze for higher temperature applications

**Table: 4.** Nucleate heat transfer coefficient enhancement factor and First law improvement (COP enhancement) based on nanoparticle used in R718 and ecofriendly refrigerants in primary circuit

| **Refrigerant** | **Enhancement factor** | **COP_enhancement** |
|---|---|---|
| R1234yf | 3.54 | 23 % |
| R1234ze | 2.38 | 18% |
| R134a | 2.3 | 19% |

**Table: 5.** Effect of Computed nanorefrigerents property in terms of enhancement factor on first law improvement

| **Refrigerant** | **Enhancement factor** | **COPenhancement** |
|---|---|---|
| R1234 yf | 2.04 | 23 % |
| R 1234ze | 1.7 | 19% |
| R134a | 2.24 | 21 % |

## 4. Conclusions and Recommendations

The following conclusions have been drawn

a) Even in mixing of nano particles mixed with R718 in the secondary circuit and R1234yf for low temperature applications gives better first law and second law performance as compared to R134arefrigerant

b) Although the performance of R134a is better than R134a using nano particles mixing in R718 but R1234ze can replace R134a for higher temperature applications.

c) The best first law and second law performances have been found using copper nano materials mixed with R718 in secondary evaporator circuit as compared to TiO2 nano particles.

## References

[1] Johnson. E. Global warming from HFC. Environ. Impact Asses.1998, 18, 485-492

[2] V. Siva Reddy, N. L Panwar, S. C. Kaushik, Exergy analysis of a vapour compression refrigeration system with R134a, R143a, R152a, R404A, R407C, R410A, R502 and R507A. Clean Techn Environ Policy.2012, 14:47-53

[3] R. Saravanakumar, V. Selladurai, Exergy analysis of a domestic refrigerator using eco-friendly R290/R600a refrigerant mixture as an alternative to R134a.Int J Therm Anal Calorim.2013

[4] C. Nikolaidis, D. Probert, Exergy method analysis of a two-stage vapour-compression refrigeration-plants performance. Int J Applied Thermal Engineering, 1998, 60:241-256

[5] S. Kumar, M. Prevost, R. Bugarel, Exergy analysis of a vapour compression refrigeration system. Heat Recovery Systems & CHP.1989, 9, 151-157

[6] Mahmood Mastani Joybari, Mohammad Sadegh Hatamipour, Amir Rahimi, Fatemeh Ghadiri Modarres-Exergy analysis and optimization of R600a as a replacement of R134a in a domestic refrigerator system. International Journal of refrigeration, 2013, 36, 1233-1242.

[7] J. U. Ahamed, R. Saidur, H. H Masjuki, M.A Sattar-An analysis of energy, exergy and sustainable development of a vapour compression refrigeration system using hydrocarbon, International journal of Green energy, 2012, 9, 707-717.

[8] B. O. Bolaji, M. A. Akintunde, T. O. Falade. Comparative analysis of performance of three ozone-friends HFC refrigerants in a vapor compression refrigerator. Int J Sustainable Energy & Environment, 2011, 2, 61-64.

[9] RecepYumrutas, Mehmet Kunduz, Mehmet Kanoglu-Exergy analysis of vapor compression refrigeration systems. Exergy, An International Journal, 2002, 2, 266-272.

[10] M. Padilla, R. Revellin, J. Bonjour. Exergy analysis of R413A as replacement of R12 in a domestic refrigeration system. Int J Energy Conversion and Management, 2010, 51, 2195-2201.

[11] H. M Getu, P. K Bansal. Thermodynamic analysis of an R744-R717 cascade refrigeration system. Int J Refrigeration, 2008, 31, 45-54

[12] Mark W. Spatz, Samuel F. Yana Motta. An evaluation of options for replacing HCFC-22 in medium temperature refrigeration systems. Int J Refrigeration, 2004, 27, 475-483.

[13] X. H. Han, Q. Wang, Z. W. Zhu, G. M. Chen. Cycle performance study on R32/R125/R161 as an alternative refrigerant to R407C. Int J Applied Thermal Engineering, 2007, 27, 2559-2565

[14] E. Halimic, D. Ross, B. Agnew, A. Anderson, I. Potts. A comparison of the operating performance of alternative refrigerants. Int J Applied Thermal Engineering, 2003, 23, 1441-1451

[15] Yongmei Xuan, Guangming Chen. Experimental study on HFC-161 mixture as an alternative refrigerant to R502. Int J Refrigeration. Article in Press.

[16] R. Cabello, J. Navarro-Esbrı, R. Llopis, E. Torrella. Analysis of the variation mechanism in the main energetic parameters in a single-stage vapour compression plant. Int J Applied Thermal Engineering, 2007, 27, 167-176

[17] R. Cabello, E. Torrella, J. Navarro-Esbr, Experimental evaluation of a vapour compression plant performance using R134a, R407C and R22 as working fluids. Int J Applied Thermal Engineering, 2004, 24, 1905-1917

[18] R. S. Mishra, R. K. Jaiswal, Methods for Improving Thermodynamic Performance of Variable Speed Vapour Compression Refrigeration Systems Using Nanorefrigerent in Primary Circuit, Nature & Environment, 20(2), 2015, 26-47

[19] R. S. Mishra, Kapil Chopra, V. Sahni, Irreversibility Optimization Using Energy-Exergy Analysis of Three Stage Vapour Compression Refrigeration Systems with Flash-Intercooler Using Ecofriendly Refrigerants (R410a, R290, R600, R600a, R1234yf, R125, R717 And R134A) for Reducing Global Warming and Ozone Depletion, Nature & Environment, 20(2), 2015, 73-89

J Mater Sci
DOI 10.1007/s10853-016-9725-x

# Effect of ion beam irradiation on dielectric properties of $BaTiO_3$ thin film using surface plasmon resonance

**Savita Sharma[1,3,4] · Ayushi Paliwal[1] · Monika Tomar[2] · Fouran Singh[3] · Nitin K. Puri[4] · Vinay Gupta[1]**

Received: 28 September 2015 / Accepted: 4 January 2016
© Springer Science+Business Media New York 2016

**Abstract** The effects of swift heavy ions on the structure, surface morphology and dielectric behaviour of barium titanate ($BaTiO_3$, known as BTO) thin films have been investigated by irradiating the films with 100 MeV $Au^{+8}$ ions at an ion fluence of $1 \times 10^{12}$ ions $cm^{-2}$. BTO thin films were deposited on Pt/Si substrate by pulsed laser deposition technique. The structure of the film was crystalline with tetragonal phase. Surface topography was studied by atomic force microscope. The dielectric properties of BTO have been studied using surface plasmon resonance (SPR) technique in Otto configuration. SPR is a highly sensitive technique for investigating the dielectric and optical properties of dielectrics. Gold-coated glass prisms have been utilized to excite the surface plasmon waves (SPWs) at the metal–air interface. When BTO thin film is integrated with the surface of Au thin film, a significant shift in the SPR curve has been observed due to change in the propagation constant of SPW at metal–dielectric interface. The optical and dielectric parameters of BTO thin film were obtained by fitting the experimental SPR data with the Fresnel's equations. The observed increase in the dielectric constant of BTO thin film after irradiation may be attributed to packing density.

✉ Vinay Gupta
drguptavinay@gmail.com

[1] Department of Physics and Astrophysics, University of Delhi, Delhi 110007, India

[2] Physics Department, Miranda House, University of Delhi, Delhi 110007, India

[3] Inter University Accelerator Centre, Aruna Asaf Ali Marg, New Delhi 110067, India

[4] Department of Applied Physics, Delhi Technological University, Delhi 110042, India

## Introduction

Barium titanate ($BaTiO_3$) also well known as BTO is one of the most important ferroelectric materials and has attracted much attention for its remarkable properties such as high dielectric constant, good ferroelectric property and large electro-optic and nonlinear optic coefficients resulting in broad applications in the control systems [1, 2]. BTO thin films have been deposited by several methods like metal–organic chemical vapour deposition (MOCVD) [3], sol–gel method [4, 5], chemical solution deposition [6], radio frequency (RF) sputtering [7] and pulsed laser deposition [8, 9]. Among the various methods, pulsed laser deposition is an excellent method to fabricate the multicomponent thin films on various substrates with good stoichiometry [10].

Irradiation of materials with high-energy ion beams or 'swift heavy ion (SHI) irradiation', is one of such techniques that effectively induce micro-structural modifications in materials [11]. Irradiation with energetic ions leads to the creation of a wide variety of defect states in the material, which changes the structural, optical and electrical transport properties of the material [12, 13]. The changes are strongly dependent on the mass of the incident ion, the irradiation energy and fluence [14]. Thus, it is essential to study the effect of irradiation on the dielectric and optical properties of materials.

SPR technique has been widely accepted as a standard tool for the optical characterisation of interfaces and thin films. When electromagnetic radiation of the appropriate frequency is incident on the metals, it gives rise to an evanescent wave, and SPR reflectance reduces to a minimum value at resonance. The phenomena of SPR were first demonstrated by Zeenack in 1907 by formulating a special surface wave solution of Maxwell's equations for radio

Published online: 12 January 2016

frequency surface EM waves to propagate at the boundary of lossy medium and loss-free medium [15]. SPR phenomena can be studied using two configurations: Kretschmann configuration [16] and Otto configuration [17]. A glass prism is used as a coupler in Krestschmann configuration where a metal thin film is directly deposited on its surface and an evanescent wave is generated due to the light beam incident on the glass [18]. In Otto configuration, the light is shone on the wall of a prism and totally reflected. A thin metal film is positioned close enough such that the evanescent waves can interact with the plasma waves on the surface and excite the plasmons [17]. Otto configuration has unique advantages that the film deposited on specific substrate could be studied and hence it is used in the present work for SPR measurements. Noble metals like Gold (Au) and Silver (Ag) are capable of exciting an SP wave [18]. The SPR reflectance curve could be used to evaluate the value of dielectric constant of materials in the vicinity of noble metals. Dielectric properties of various metal oxides deposited on glass substrate have been examined by different workers exploiting SPR technique [19–22]. However, to the best of our knowledge no report is available on the study of dielectric property of metal oxides deposited on other substrates using SPR technique especially in the Otto configuration.

In the present work, an attempt has been made to investigate the dielectric properties of BTO thin films prepared by pulsed laser deposition on Si substrate and study the effect of SHI irradiation using SPR technique. An Otto prism coupler arrangement having air gap facility is designed.

## Experimental details

The single-phase ceramic target of BTO was prepared using conventional solid-state reaction method. The raw powders of $BaCO_3$ and $TiO_2$ (99.9 % pure) were used for the preparation of BTO target. The powders were ball-milled, pressed into discs of 25 mm diameter and sintered at 1250 °C to obtain the dense BTO target. The target face was polished and mounted on the target holders for deposition of thin film. The ceramic targets of BTO were ablated using the 4th harmonic of Nd:YAG pulsed laser ($\lambda = 266$ nm), and thin film of BTO was prepared on platinum (Pt)-coated Si (Pt/Ti/$SiO_2$/Si) substrate. The 70-nm thin layer of the Pt metal was deposited over the $SiO_2$-passivated Si ($SiO_2$/Si) substrate by e-beam evaporation technique. A buffer layer of Ti (20 nm) was deposited in situ over $SiO_2$/Si substrate prior to Pt deposition to improve the adhesion of Pt. Typical deposition conditions used for deposition of BTO thin films are summarized in Table 1. The as-grown BTO thin films were

**Table 1** PLD processing conditions for the growth of BTO thin film

| Parameters | Deposited conditions |
|---|---|
| Target | BTO |
| Substrate | Pt/Ti/$SiO_2$/Si |
| Substrate temperature | 750 °C |
| Deposition pressure | 200 mT |
| T–S distance | 4.5 cm |
| Laser type | Nd:YAG (266 nm) |
| Pulse repetition rate | 10 Hz |
| Fluence | 120 mJ |

irradiated using the 15 UD Pelletron accelerator at Inter University Accelerator Centre (IUAC), New Delhi, with 100 MeV $Au^{+8}$ at a fluence of $1 \times 10^{12}$ ions $cm^{-2}$. The beam current was maintained at 1 pnA (particle nanoampere) to avoid heating effects of the samples during irradiation. The ion beam incident normal to the surface of BTO thin film was made to scan over an area of 10 mm × 10 mm to achieve dose uniformity across the sample area.

Structural characterization of the prepared samples was carried out using X-ray diffraction (XRD) analysis (Bruker D8). Optical properties were studied using UV–Visible spectrophotometer (Perkin Elmer Lambda 35). Surface morphology was studied by atomic force microscopy (AFM) technique using Bruker Dimension Icon.

The details of the experimental setup used for studying the dielectric properties of BTO thin films using SPR technique have been explained elsewhere [23]. Figure 1 shows the schematic of SPR Otto configuration used to study the dielectric properties of BTO thin films (as-grown and after irradiation). The SPR reflectance curves were obtained for different prepared systems including prism/air-gap/Au/Pt/Ti/$SiO_2$/Si, prism/air-gap/Au/$BaTiO_3$ (as-grown)/Pt/Ti/$SiO_2$/Si and prism/air-gap/Au/$BaTiO_3$ (after radiation)/Pt/Ti/$SiO_2$/Si by varying the incident angle of laser beam ($\lambda = 633$ nm). The SPR measurements were

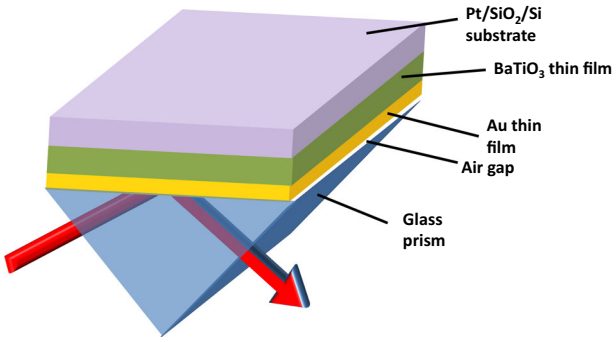


**Fig. 1** Schematic of SPR Otto configuration

carried out after depositing 40 nm thin Au layer on $BaTiO_3$ thin films using thermal evaporation technique. The thickness of Au thin film was controlled in situ using a quartz crystal thickness monitor, and the deposition was carried out at a slow rate of about 2.5 Å/s. The experimental SPR reflectance data were fitted with Fresnel's equations to calculate the complex dielectric constant and refractive index of BTO thin films using the fixed values of thickness of air gap and complex dielectric constant of Au layer [24].

## Results and discussion

The XRD patterns of the as-grown and irradiated BTO thin films with 100 MeV $Au^{+8}$ ions are presented in Fig. 2. The as-grown thin films (Fig. 2) exhibited peaks corresponding to the tetragonal phase of BTO [25]. No change in the phase of BTO thin film was observed after irradiation with 100 MeV $Au^{+8}$ ions (Fig. 2). The average crystallite size of the films was calculated using full width at half maxima (FWHM) of the most intense (110) peak obtained at $2\theta = 29.9°$ and the Scherrer's formula [26]:

$$D_{hkl} = 0.9\lambda/\beta\cos\theta, \quad (1)$$

where $\lambda$ and $\beta$ represent the X-ray wavelength and full width at half maxima (FWHM), respectively, of the XRD peak and $\theta$ is the Bragg's diffraction angle. Irradiated thin film of BTO exhibited a crystallite size of about 21 nm which is smaller than the corresponding value (30 nm) obtained for the as-grown thin film. The observed decrease in crystallite size is due to energy confinement in the sample leading to crystallite fragmentation in small volume when exposed to radiation [27]. Thus, irradiation increases the disorder structure in BTO. The dislocation density ($\delta$) and the strain in the films ($\varepsilon$) were also examined using XRD data and the following expressions [28]:

$$\delta_{hkl} = 1/D_{hkl}^2 \quad (2)$$

$$\varepsilon = \beta\,\mathrm{Cos}\,\theta/4, \quad (3)$$

where $d$ is the thickness of the film. The dislocation density and strain in the films increased from $1.1 \times 10^{15}$ lines $m^{-2}$ to $2.3 \times 10^{15}$ lines $m^{-2}$ and 1.36 to 1.45, respectively, after irradiation, indicating the increase of defects in the films upon exposure to irradiation. When SHI passes through the material, it deposits high energy to the system, which leads to the modification of the material. The modification can be explained by thermal spike formalism. The incident ion beam creates a transient temperature spike during which the temperature is not reached to molten state but is sufficient to produce point defects and interstitials, which cause strain in the film. During irradiation, the kinetic energy of the electrons ejected from the target atom gets transferred to the lattice by electron–phonon interaction causing an increase in the local lattice temperature over the melting point of the material resulting in defects and defect clusters [29]. Recognizing that the net accumulated damage will be influenced by the temperature pulse caused by the energy deposition in the BTO by the passing beam, the heat sinking to a temperature-controlled base is crucial.

SRIM software has been used to examine the electronic energy loss, nuclear energy loss and projectile range for detailed understanding, and it has been observed that electronic energy loss (23.38 keV/nm) is found to be much higher than nuclear energy loss (0.478 keV/nm). The creation of recoils is also studied by full TRIM calculations, and it is observed that 98 % energy is spent during the process of ionization, and only about 1 % in recoils (remaining in vacancies and phonons). Therefore, the effects of recoils may be ignored.

Figure 3a and b shows the AFM images of the surface morphology of the as-grown and irradiated BTO thin films, respectively (2 μm × 2 μm area scan). The surface morphology of the as-grown BTO thin films was found to be fine having uniformly distributed crystallinity (Fig. 3a). The crystallite size of the film diminishes and thus reduces their boundaries after irradiation (Fig. 3b). Particle fragmentation occurs in case of polycrystalline BTO samples as the spread of energy lost by the SHI is relatively large. The measured value of root-mean-square (RMS) surface roughness for 2 μm × 2 μm area scan is about 3.4 nm and 16.9 nm, respectively, for the as-grown BTO film and the BTO film irradiated at $1 \times 10^{12}$ ions $cm^{-2}$ (Fig. 3a and b). Thus, the RMS roughness increases with the irradiation of BTO film.

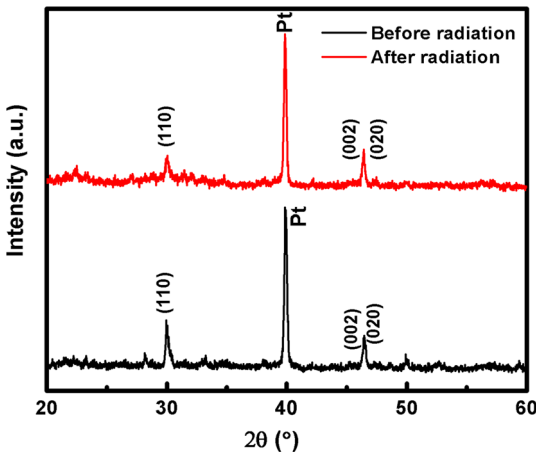


**Fig. 2** XRD pattern of $BaTiO_3$ thin films (as-grown and after irradiation) deposited on Pt/Ti/$SiO_2$/Si substrate

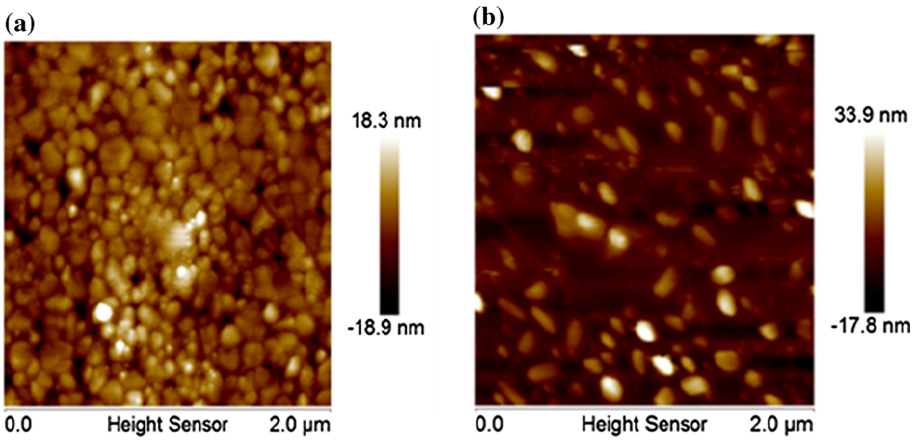


**Fig. 3** AFM images of **a** the as-grown and **b** irradiated $BaTiO_3$ thin films at $1 \times 10^{11}$ ions $cm^{-2}$

Figure 4 represents the UV–Visible reflectance spectra of both the as-grown and irradiated BTO thin films. It can be clearly seen from Fig. 4 that the reflectance of BTO thin film decreases significantly in the lower wavelength region (<400 nm) after irradiation with 100 MeV $Au^{+8}$ ions at $1 \times 10^{12}$ ions $cm^{-2}$ fluence.

## SPR reflectance measurements

The SPR reflectance curves obtained for prism/air-gap/Au/Pt/Ti/$SiO_2$/Si and prism/air-gap/Au/BTO/Pt/Ti/$SiO_2$/Si (with the as-grown BTO film) systems at an incident light of $\lambda = 633$ nm under Otto configuration are shown in Fig. 5. The SPR resonance angle ($\theta_{SPR}$) for prism/air-gap/Au/Pt/Ti/$SiO_2$/Si system observed at about 36.1° shifts towards higher resonance angle gap after integration of the as-grown BTO thin film with Pt/Ti/$SiO_2$/Si substrate (Fig. 5). In the SPR reflectance curves, the value of $\theta_{SPR}$ for prism/air-gap/Au/BTO/Pt/Ti/$SiO_2$/Si system is about

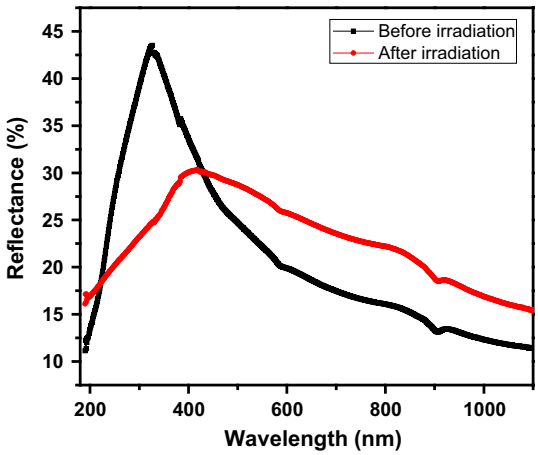


**Fig. 4** UV–Visible reflectance spectra of the as-grown $BaTiO_3$ film and the $BaTiO_3$ film irradiated with 100 MeV $Au^{+8}$ ions at $1 \times 10^{11}$ ions $cm^{-2}$

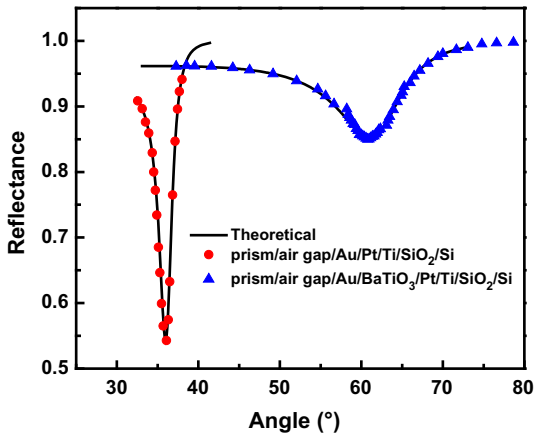


**Fig. 5** SPR reflectance curves for prism/air-gap/Au/Pt/Ti/$SiO_2$/Si and prism/air-gap/Au/$BaTiO_3$/Pt/Ti/$SiO_2$/Si systems

60.8°. The minimum value of reflectance ($R_{min}$), that is $\theta_{SPR}$, in the SPR curves drastically increases upon depositing BTO thin film on Si substrate (Fig. 5). As the BTO thin film is present on Pt/Ti/$SiO_2$/Si substrate, the backscattered field decreases which is in antiphase with that of the incoming light and thus increases the value of $R_{min}$ [2]. The full width at half maxima (FWHM) of the SPR reflectance curves corresponds to the absorption losses which increase for prism/air-gap/Au/BTO/Si system (Figure 5), in comparison to prism/air-gap/Au/BTO/Pt/Ti/$SiO_2$/Si system.

Figure 6 shows the SPR reflectance curves for prism/air-gap/Au/BTO/Pt/Ti/$SiO_2$/Si systems having the as-grown and irradiated BTO thin films. The $\theta_{SPR}$ for the system having the as-grown and irradiated BTO, respectively, is about 60.8° and 72.9°. The observed shift in SPR curve towards higher angle is related to the change in dielectric media from the as-grown BTO film to the irradiated BTO thin film, and hence the dielectric property of BTO thin film with exposure to radiation. Also, the increase in point of defects and the dislocation density in

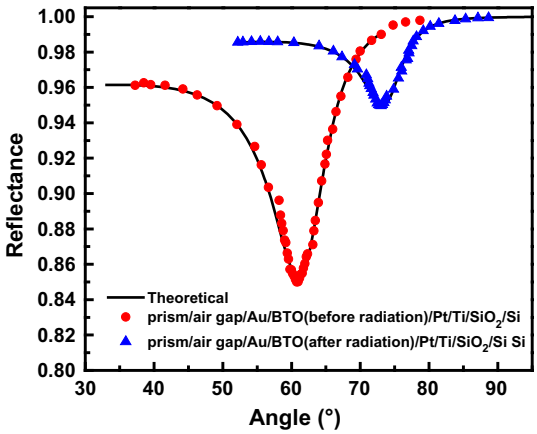


**Fig. 6** SPR reflectance curves for prism/air-gap/Au/BTO/Pt/Ti/$SiO_2$/Si system having both the as-grown and irradiated BTO thin films

BTO thin film after irradiation leads to an increase in the propagation constant of SPW and hence the resonance condition. The FWHM of SPR curve is related to the absorption losses in the dielectric film [30]. Therefore, losses in the BTO thin film decreases on exposure to radiation (Fig. 6).

### Complex dielectric constant and refractive index

The symbols in Figs. 5 and 6 represent the experimental SPR data, and the continuous line corresponds to the theoretically fitted curve. Fresnel's equations were utilized in order to evaluate the complex dielectric constant and refractive index of the BTO thin films [24]. The thickness of the air gap has been calculated by fitting the SPR reflectance curve for Au thin films (Fig. 5) using the known values of dielectric constant of prism $\varepsilon_0 = (1.517)^2$, dielectric constant of air $\varepsilon_1 = 1.0$ and the dielectric constant of Au [23]. The values of complex dielectric constant for both the as-grown and irradiated BTO thin films were estimated and further used to determine the values of complex refractive index $(n_i + ik_i)$ [19]. The complex dielectric constant of BTO thin film before and after radiation were found to be about 4.59 + i1 and 5.01 + i0.8, respectively, at $\lambda = 633$ nm. The corresponding values of refractive indices are 2.14 + i0.04 and 2.24 + i0.07, respectively. The obtained values of refractive index of both $BaTiO_3$ thin films were found to be slightly lower than the corresponding value (2.41) reported for bulk BTO [31]. The variation in refractive index is generally related to the presence of voids (porosity) and defects in the deposited thin films [32].

For both the prepared samples, it is observed that the value of packing density (0.88) obtained for irradiated BTO thin film is higher indicating more densification due to irradiation [23]. The observed enhancement in the packing density leads to an increase in dielectric constant and hence refractive index after irradiation [33, 34]. The increase in the packing density of BTO thin film after irradiation clearly indicates the denser packing of structures after irradiation. After irradiation with SHI beam, the atomic rearrangements of the constituent elements are suppressed leading to higher packing density. The increase in packing density shows amorphization due to irradiation [35]. As observed from the XRD spectra (Fig. 2), the crystallite size of the film decreases upon irradiation leading to an increase in the packing density.

The variation in the refractive index of thin films is related to the presence of voids in thin films, i.e. packing density. A linear dependence of refractive index on packing density has been observed by Tansley et al. for the as-grown sputtered ZnO film [36]. Many attempts have been made to correlate the packing density with refractive index of the material. Macleod et al. have summarized the relation between the packing density and refractive index utilizing Lorentz–Lorentz polarization theory [37]. Hence, a thin film free of voids shows higher packing density leading to an increase in its refractive index.

## Conclusion

The impact of SHI on the crystallographic structure, surface morphology and dielectric properties of barium titanate thin ($BaTiO_3$) films have been investigated after irradiation with 100 MeV $Au^{+8}$ ions at an ion fluence of $1 \times 10^{12}$ ions $cm^{-2}$. BTO thin film was deposited onto Pt/$SiO_2$/Si substrate using pulsed laser deposition technique. The as-deposited BTO thin film was a polycrystalline film with tetragonal phase. The dielectric properties of both the as-grown and irradiated BTO films have been studied using SPR technique under Otto configuration. Gold thin film was coated on the BTO thin films to excite the SPWs at the metal–dielectric (air) interface. When BTO thin films were integrated with the Pt/$SiO_2$/Si substrate, a significant shift in the SPR curve has been observed due to a change in the propagation constant of SPW at metal–dielectric interface leading to the determination of complex dielectric constant and refractive index. The dielectric parameters of BTO thin film were estimated by fitting experimental SPR data with the Fresnel's equations. The shift in dielectric constant of BTO thin film is associated with the packing density. The irradiation of BTO thin film results in an increase in the packing density to 0.88. The observed enhancement in the packing density leads to an

increase in dielectric constant and hence refractive index after irradiation.

**Acknowledgements** The authors are thankful to the Department of Science and Technology (DST) and the University of Delhi for the financial support (DST/IDP/SEN-NEW/25). One of the authors (SS) is thankful to the Delhi Technological University (DTU) for the teaching assistantship.

**Compliance with ethical standards**

**Conflict of Interest** All the authors declare that they have no conflict of interest.

## References

1. Roy D, Krupanidhi SB (1992) Pulsed excimer laser ablated barium titanate thin films. Appl Phys Lett 61:2057–2059
2. Yuan Z, Liu J, Weaver J, Chen CL, Jiang JC, Lin B, Giurgiutiu V, Bhalla A, Guo RY (2007) Ferroelectric $BaTiO_3$ thin films on Ni metal tapes using NiO as buffer layer. Appl Phys Lett 90:202901–220290
3. Terren AR, Belot JA, Edleman NL, Marks TJ, Wessels BW (2000) MOCVD of epitaxial $BaTiO_3$ films using a liquid barium precursor. Chem Vap Depos 6:175
4. Sharma HBK, Mansingh A (1998) Phase transition in sol-gel-derived barium titanate thin films. J Phys D Appl Phys 31:1527
5. Hu Z, Wang G, Huang Z, Meng X, Chu J (2003) Investigations on the infrared optical properties of $BaTiO_3$ ferroelectric thin films by spectroscopic ellipsometry. Semicond Sci Technol 18:449
6. Petzelt J, Ostapchuk T, Paskin A, Rychetsky I (2003) FIR and near-millimetre dielectric response of $SrTiO_3$, $BaTiO_3$ and BST films and ceramics. J Eur Ceram Soc 23:2627
7. Jia QX, Smith JL, Chang LH, Anderson WA (1997) Characteristics of $BaTiO_3$ thin films on Si deposited by rf magnetron sputtering. Philos Mag B 77:163
8. Schmitt H, Ziebert C, Sternberg A, Zauls V, Kundzins M, Kundzins K, Aulika I, Ehses KH, Krüger JK (2002) Nanocrystalline ferroelectric/relaxor multilayers. Ferroelectrics 268:193–198
9. George JP, Beeckman J, Woestenborghs W, Smet PF, Bogaerts W, Neyts K (2013) Preferentially oriented $BaTiO_3$ thin films deposited on silicon with thin intermediate buffer layers. Nanoscale Res Lett 8:62
10. Chinchamalatpure Ramkrishna V, Ghosh SA, Chaudhari GN (2010) Synthesis and electrical characterization of $BaTiO_3$ thin films on Si (100). Mater Sci Appl 1:187
11. Deng H, Yang D, Chen B, Lin CW (2008) Simulation of surface plasmon resonance of Au–$WO_{3-x}$ and Ag–$WO_{3-x}$ nanocomposite films. Sens Actuators B 134:502–509
12. Kumar P, Saxena N, Gupta V, Singh F, Agarwal A (2015) Correlation between surface phonon mode and luminescence in nanocrystalline CdS thin films: an effect of ion beam irradiation. J Appl Phys 116:043517
13. Gautam SK, Singh F, Sulania I, Singh RG, Kulriya PK, Pippel E (2014) Micro-Raman study on the softening and stiffening of phonons in rutile titanium dioxide film: competing effects of structural defects, crystallite size and lattice strain. J Appl Phys 115:143504
14. Singh F, Singh RG, Kumar V, Khan SA, Pivin JC (2011) Softening of phonons by lattice defects and structural strain in heavy ion irradiated nanocrystalline zinc oxide films. J Appl Phys 110:083520
15. Hui H, Fan Y, Wu BI, Kong F, Kong JA (2007) Surface modes at the interfaces between isotropic media and uniaxial plasma. Prog Electromagn Res 76:1–14
16. Kretschmann E, Raether H (1968) Notizen: radiative decay of non radiative surface plasmons excited by light. Zeitschrift Fur Naturforschung 23A:2135
17. Otto A (1968) Excitation of nonradiative surface plasma waves in silver by the method of frustrated total reflection. Zeitschrift für Physik 216:398–410
18. Yang D, Lu HH, Chen B, Lin CW (2010) Surface plasmon resonance of $SnO_2$/Au Bi-layer films for gas sensing applications. Sens Actuators B 145:832–838
19. Saha S, Mehan N, Sreenivas K, Gupta V (2009) Temperature dependent optical properties of (002) oriented ZnO thin film using surface plasmon resonance. Appl Phys Lett 95:071106
20. Shandilya S, Tomar M, Sreenivas K, Gupta V (2010) Temperature dependent optical properties of c axis oriented $LiNbO_3$ thin film using surface plasmon resonance. J Light Wave Technol 28:3004–3011
21. Das RR, Yuzyuk YI, Bhattacharya P, Gupta V, Katiyar RS (2004) Folded acoustic phonons and soft mode dynamics in $BaTiO_3$/$SrTiO_3$ superlattices. Phys Rev B 69:132302
22. Kanjilal D (2001) Swift heavy ion-induced modification and track formation in materials. Curr Sci-Bangalore 80:1560–1566
23. Paliwal A, Sharma A, Tomar M, Gupta V (2014) Optical properties of $WO_3$ thin films using surface plasmon resonance technique. J Appl Phys 115:043104
24. Gönül TS (2003) Temperature effects on surface plasmon resonance: design considerations for an optical temperature sensor. J Lightwave Technol 21:805
25. Lu SW, Lee BI, Wang ZL, Samuels WD (2000) Hydrothermal synthesis and structural characterization of $BaTiO_3$ nanocrystals. J Crystal Growth 219:269–276
26. Cullity BD, Stock SR (2001) Elements of x-ray diffraction. Prentice Hall, Inc., New Jersy
27. Kumar M, Singh F, Khan SA, Baranwal V, Kumar S, Agarwal DC, Siddiqui AM, Tripathi A, Gupta A, Avasthi DK, Pandey AC (2005) Swift heavy ion induced structural and optical modification in LiF thin film. J Phys D Appl Phys 38:637–641
28. Chandramohan S, Sathyamoorthy R, Sudhagar P, Kanjilal D, Kabiraj D, Asokan K, Ganesan V, Shripathi T, Deshpande UP (2009) High-energy heavy-ion induced physical and surface-chemical modifications in polycrystalline cadmium sulfide thin films. Appl Phys A 94:703–714
29. Gautam SK, Singh RG, Kumar VVS, Singh F (2015) Giant enhancement of the n-type conductivity in single phase p-type ZnO: N thin films by intentionally created defect clusters and pairs. Solid State Commun 218:20
30. Raether H (1986) Surface plasmons on smooth and rough surfaces and on gratings. Springer, Hiedelberg
31. Wemple SH, Didomenico M Jr, Camlibel I (1968) Dielectric and optical properties of melt-grown $BaTiO_3$. J Phys Chem Solids 29:1797–1803
32. Gupta V, Mansingh A (1996) Influence of post deposition annealing on the structural and optical properties of sputtered zinc oxide film. J Appl Phys 80:1063–1073
33. Calcagno L, Foti G (1987) Density enhancement in ion implanted polymers. Nucl Instrum Methods Phys Res Sect B 19–20:895–898
34. Bertino MF, Smarsly B, Stocco A, Stark A (2009) Densification of oxide nanoparticle thin films by irradiation with visible light. Adv Funct Mater 19(8):1235
35. Suryanarayana C (1999) Non equilibrium processing of materials. Elsevier, Oxford
36. Tansley TL, Neely DF, Foley CP (1983) Optical dispersion in zinc oxide. Phys Status Solidi A 77:491
37. Macleod HA (1986) Structure-related optical properties of thin films. J Vac Sci Technol A 4:418

Volume 3, Issue 4 (2015) 631-634 ISSN 2347 - 3258
International Journal of Advance Research and Innovation

# Estimation of Electrical Energy Generation from Waste to Energy using Incineration Technology

Shubham Gupta *, R. S. Mishra
Department of Mechanical Engineering, Delhi Technological University, New Delhi, India

**Article Info**

Article history:
Received 3 October 2015
Received in revised form
10 November 2015
Accepted 20 November 2015
Available online 15 December 2015

**Keywords**
Waste to Energy,
Incineration,
Roorkee City,
Municipal Solid Waste,
Solid Waste Management,
Electricity

**Abstract**

This paper mainly deals with viability of Waste to energy Incineration technology in Roorkee City, Uttarakhand by estimating the total municipal solid waste generated and evaluating the energy potential by using the incineration technology. Day to day increase in waste generation demands Renewable technology for solid waste management for an effective economic and social growth of the people. This paper focuses on technical feasibility only.

## 1. Introduction

There are several parts of the beginning of waste-to-energy technology in India. This technology of waste to energy (WTE) incineration is a renewable source of supplying electricity and also solves the problems of landfills. The current trend of economic growth and standard of living of people increases municipal solid waste (MSW) generation and effects on current landfill scenario, unavailability of land, open burning landfill causes pollution and has greatly effects on public health. There is urgency for an effective solid waste management due to all of these reasons. WTE incineration helps in reducing greenhouse gases (GHGs) by avoiding dumping to landfill, foils the methane emission from landfill and generating renewable energy in form of electricity which further helps in reducing dependency on fossil fuels. Currently largest source of GHGs emissions in the world are landfills with an assessment of almost21% of the total methane production. As a GHG Methane is 21 times stronger than carbon dioxide.

## 2. Literature Review

Mufeed Sharholy et.al (2007)[1]used ArcGIS technique which included MSW sample collection and questionary survey on randomly selected houses and concluded that 45.3% of organic matter and 40% miscellaneous material (glass, paper, plastics etc.) and mentioned the qualitative and quantitative characteristics of MSW for MSWM for developing GIS maps for city of Allahabad. He also explained MSWSM collection, storage and disposal methods. Tsai et.al (2014)[2]did content and chemical analysis of MSW from year 2008 to 2012 with the use of CHP technology and compared the efficiency of plants of Taiwan with different parts of Europe, Germany and Netherlands. He also classified plants on the basis of capacity of waste handling, power generation and efficiency was done and discussed use of district heating and cooling and its use and advantage. S Rathi et.al (2014)[3] used Dulong Formulae heat energy in incineration technology to calculate and analyse potential generation of electricity in Kanpur city of 33MW from MSW of 1200 tonnes/day by considering conversion efficiency, station allowance, unaccounted heat loss and net power generated and classified solid wastes on physical and chemical composition. NIE et.al (2008)[4] explained new technology of circulating fluidized bed and emission of reduction by using equipment such as house filtration, flue gas cleaning and activated carbon in incinerator, adopted by 30 plants for development of China. Biodegradable matter shares 31-36% of total MSW in big cities and 65% in small cities having calorific value of around 5000KJ/Kg. Dioxin emission was limited to 1.0ng TEQ/$Nm^3$. Ojha et.al (2011)[5] explained, classified and compared cities on the basis of population, MSW composition, total waste generated; very big city, big city, medium city, small city and calculated potential of 1700 MW electricity from WTE incineration with some solutions and suggestion to problems occurring in MSWM. Arena et.al (2015)[6] proposed the opinion to solve waste problem as using it as a resource. He explained WTE technology was successful and reliable because of thermal conversion, heat recovery and air pollution technique to reduce health and environmental risk, landfill substitute. Vikash Talyan et.al (2008)[8] discussed first incineration in Delhi, setup in 1989 at Timarpur to produce 3.7MW from 300 Tonnes of waste of calorific value higher 1000 Kcal/Kg but was closed in 21 days only due to falling of calorific value. First composting plant was setup in 1980 in Okhla and was shut down due to absence of market and high production cost. He explained three landfills in at Gazipur, Okhla and Bhalswa with LFG potential of energy generation $12.98*10^5$ Kwh/year. Ityona Amber et.al (2012)[7] calculated potential generation of 700KWh/tonne of electricity with calorific value of 17.23 MJ/Kg and conversion efficiency of 25% from incineration technology in Nigeria by considering methodology of analysing 5

**Corresponding Author,**
**E-mail address:** professor_rsmishra@yahoo.co.in
**All rights reserved:** http://www.ijari.org

samples of 10 Kg each of waste and evaluated that 43% of total MSW organic components are present while 8% are paper, cardboard, plastics. E. Autret et.al (2007)[10] overviewed design and operation of incineration plant on basis of composition of different type of wastes, suitable technique, avoiding environment effects and risk of human health. He described various incinerators techniques such as grate, fluidised bed and rotary kilns. He observed incineration plants replaced fossil fuel made of 50% natural gas and 50% oil in France. V G Sister (2006)[9] simulated plant model to improve the performance of waste incineration plant by considered gas turbine and steam cycle heat from outgoing fuel gases which resulted in efficiency of binary system gas incinerator of 42-45%. In addition he said Pyrolysis in incineration increases its efficiency by providing high yield of components of CO, $H_2$, and $CH_4$. Sieting Tan et.al (2014)[11] compared three WTE technologies i.e. incineration, landfill gas recovery and anaerobic digestion (AD) on environmental and economic basis which included includes transportation cost, carbon credit and sale of by-product of Taman Beringin, Malaysia landfill which can yield in 287% of increment in profit. CHG emission was checked on basis of Intergovernmental Pollution Climate Change (IPCC) guidelines. Incineration plants produced 1430 MW/day of heat and 480 MWh/day of electricity from 100 tonnes/day of waste. Hefa Cheng et.al (2007)[12]carried out methodology to study two incinerators of capacity each 250 tonnes/day having technology based on co-firing of MSW with coal in grate circulated fluidized producing 46.2 million KWh of electricity having calorific value of 3000-6700 KJ/Kg lower than developed countries of 8400-17000 KJ/Kg. In addition he calculated coal equivalent to MSW fuel ratio of 0.14, with saving of 0.2 million $m^3$ landfill yearly. Sudhanshu Kaushik et.al (2011)[13] studied the MSW generation during KumbMela 2010 at famous temples of Haridwar City; Mansa Devi &Chandi Devi located at Shiwalik Foothills on seven days of Hindu festival which includes Makar sakranti, Magh Purnima, Mahashivratri, Chaitra Amavasya and Full moon days by recording observations of individual composition of MSW according to days. 7615.0 Kg of Waste was produced at Mansa Devi Site and approximately 5000 Kg of waste was produced at Chandi Devi Site. He observed that 64.7% was biodegradable waste and 12.3% was non-biodegradable at Mansa Devi hillock and at Chandi Devi hillock 62.7% of biodegradable and 10.2% of non-biodegradable. C Liamsanguan et.al (2007)[14] compared incineration, landfill & conventional power plants using Life Cycle Assessment (LCA) methodology and declared that incineration had higher advantages for global warming & photochemical ozone formation over conventional power plants but from acidification and nutrient enrichment aspect incineration was not suitable. He described landfill with gas collection and flaring systems were much favourable than incineration technology. In addition he compared conventional plant's energy content which was much higher than of Municipal Solid Waste (MSW) and also conventional power plants had higher efficiency than incineration plants. Dioxins emissions from incineration plants cause health issues.

## 3. Comparison of Current Technologies

Mainly there are four technologies for WTE:

- **WTE Incineration:** MSW is combusted in presence of oxygen. Heat produced then utilized to produce steam which turns the turbine and then alternator to produce electricity. Harmful flue gases are treated and then released in atmosphere. By product is utilized in cement factory.
- **Landfill gas Recovery:** Anaerobic biodegradation results in methane production in landfill which is recovered to produce either electricity or heat.
- **Biomethanation:** Organic matter of MSW is converted to biogas by means of anaerobic digestion in presence of methanogenic bacteria. This biogas can further be utilized for cooking or electricity production.
- **Refuse Derived Fuel:** This technology fuses whole MSW irrespective of individual calorific value of organic and inorganic matter. It forms briquettes and pellets which can be used further as a fuel in many applications.

## 4. Case Study Undertaken

"Roorkee is a city in Haridwar district, Uttarakhand that is spread over a flat terrain with the grand spectacle of Himalayas ranges flanking it in the East and the North-east. It is on the banks of the Ganges canal on the national highway 58 (Delhi - Sri Badnrinath - Mana). The dominant feature of the city is the Upper Ganges Canal which flows north-south and bisects the city. Also known for Roorkee Cantonment, one of the country's oldest, and the headquarters of Bengal Engineer Group (Bengal Sappers) since 1853.The renowned IIT Roorkee is located in this city." [16]

## 5. Current MSW Methodology

Door to door primary collection by engaging private sweepers. Waste is mostly collected through community bins/containers and road sweeping. Sweepers and sanitary workers engaged by the Roorkee Nagar PalikaParishad (RNPP) sweep the streets. They accumulated the collected waste into small heaps and subsequently loaded manually or mechanically onto the community containers/bins or directly loaded onto the solid waste transportation vehicles for onward transportation to the disposal site. RNPP presently utilizes the vehicles and equipment for transportation of solid waste.

**Fig: 1.** MSW Methodology used in Roorkee City

## 6. Amount of waste generated

The city generates, on an average, about 250 MT of MSW per day. The major sources of MSW generation of the city are domestic, shops and commercial establishments, hotels, restaurants, dharamsalas and fruit and vegetable markets. Number of registered hotels, restaurants and dharamsalas in the city are 90, 50 and 52 respectively. In addition there are 3 fruit and vegetable markets. Out of which 1 market is excluded as it is not under RNPP. Following is the table shows type of vehicles used to collect the waste and dump in open landfill.

**Fig: 2a.** Dumping Vehicles

**Fig: 2b.** Dumping Vehicles

Table 1: Vehicle Carrying MSW

| S. No. | Vehicle | Amount of MSW(MT) | Quantity of Vehicle | Total Waste (MT) |
|---|---|---|---|---|
| 1. | TATA Ace | 1.6 | 11 | 17.6 |
| 2. | Tractor trolley | 2.5 | 7 | 17.5 |
| 3. | Compactor | 3.2 | 3 | 9.6 |
| 4 | Dumper | 5 | 1 | 5 |
| | **Total** | | | 49.7 |

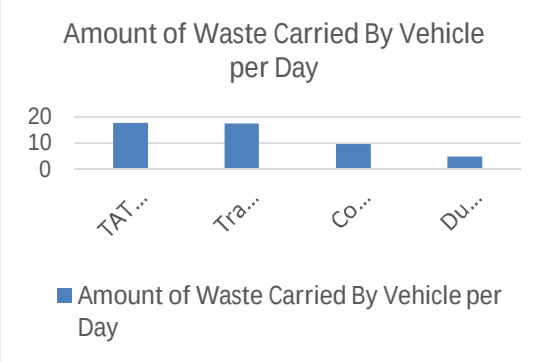


**Chart: 1.** Amount of waste carried by vehicle per day

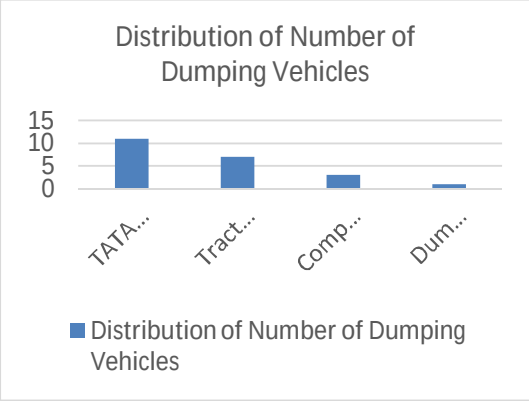


**Chart: 2.** Distribution number of dumping vehicles

These vehicles on average make 5 trips daily
So total MSW generated: 49.7*5 ≈250 MT

## 7. Computation of Energy Potential

Heat Energy (Dulong's Formula) to calculated heat energy generated by whole Roorkee
Dulong's formula:**HV(KJ/Kg) = 338.2*C + 1442.8*(H-O/8) + 94.2*S**
Where C, H, O and S are the % of these elements on dry ash free basis.
Considering Literature Review taking percentage by Mass theoretical calculations are as follows:
C= 31.22
H= 8.17
O= 55.68, Sulphur very small so neglected
Applying to formulae we get Heat Energy Generated = 12260.69 kJ/kg
First, heat energy generated is used to calculate steam energy which is 70% of heat energy.
Finally after steam energy calculation, net electric power generated by solid waste is calculated after accounting station service allowance and heat losses.
Steam energy available = 70% of heat energy
Steam energy available = (0.70 ×12,260 .69) kJ/kg
Steam energy available = 8,582.483 kJ/kg.
Above calculated steam energy is used to run the turbines, these turbines are coupled with generators which produces electricity. Heat rate is the heat input required to produce one unit of electricity (kWh).
1 kW = 3,600 kJ/h
But practically no energy conversion is 100% efficient, considering the conversion efficiency of 31.6% in a power plant heat input of 3600 ÷ 31.6% = 11395 kJ/kWh is required.
So, to produce 1kWh electrical energy 11395 kJ of steam energy is required.
Electric power generation = Steam energy ÷ 11395kJ/kWh
Electric power generation = (8,582.483 ÷ 11395) kWh/kg
Electric power generation = 0.753179728 kWh/kg
Total weight of solid waste collected from Roorkee city =250 tons/day
Total electric power generation = (0.753179728×250000) kWh/day
Total electric power generation = 188295 kWh/day

Station service allowance = 6% of total electric power generation
Station service allowance = (0.06 ×188295) kWh/day
Station service allowance = 11297.7 kWh/day
Unaccounted heat loss = 5% of electric power generation
Unaccounted heat loss = (0.05 × 188295) kWh/day
Unaccounted heat loss = 9414.75 kWh/day
Net electric power generation = Electric power generation – (station service allowance + unaccounted heat loss)
Net electric power generation = 188295 – (11297.7 + 9414.75)
Net electric power generation = 167582.55 kWh/day = 167.6 MWh/day
The above generated electricity is for one day and one day has 24 hours, so using this net electric power is calculated for per hour basis.
Net electric power generated = 167.6 MWh / 24h
Net electric power generated = 6.9 MW≈ 7 MW

## 8. Results & Discussion

The numerical computation has been carried out and following total energy potential is calculated which provides the feasibility of the WTE incineration in Roorkee City.

Total electricity production is 7 MW for 24hrs operation which can provides 5 Million units (MU) monthly, which fulfil the 16% of total energy need of Roorkee city as the demand of urban Roorkee is around 32 MU monthly.

## 9. Conclusion

None of the single solution is capable of solving the entire solid waste management problem, although by favourable use of methodology of combined technologies- decrease at source, reutilizing, composting and incineration can be supportive. Decreasing the waste generation at source level only. Recycling & reprocessing new materials from used matter like paper, plastics, metals, glass, etc. By decomposing organic matter like kitchen waste, food waste in aerobic or anaerobic way compost can be prepared which further can be utilized as a fertilizer for soil. Combustion of waste in presence of air at high temperatures in Incinerator technology, it lowers the volume of waste up to 90%. Therefore landfill can be avoided completely by above technologies. But from decades in India definition of energy means electricity and scarcity of electricity creates hindrance to growth and development so Waste to Energy Incineration technology should be used for solid waste management as it provides all kind of process- reduce, recycle and regeneration.

## References

[1] K. A. Mufeed Sharholy, Municipal solid waste characteristics and management in Allahabad, India. Waste Management, 2007, 490-496
[2] W.-T. Tsai, Analysis of Municipal solid waste incineration plants for promoting power generation efficiency in Taiwan. Master Cycles Waste Management, 2014
[3] D. P. S Rathi, Electrical Energy Recovery from Municipal Solid Waste of Kanpur City. International Journal of Scientific Research Engineering & technology (IJSRET), 2014, 923-929
[4] Y. NIE, Development and prospects of municipal solid waste (MSW) incineration in China. Environment Science Engineering China, 2008, 1-7
[5] K. Ojha, Status of MSW management system in northern India-an overview. Environmental Development Sustainable, 2011, 203-215
[6] U. Arena, From waste-to-energy to waste-to-resources: The new role of thermal treatments of solid waste in the Recycling Society Waste Management, 2015
[7] D. M. Ityona Amber, Generation, characteristics and energy potential of solid municipal waste in Nigeria. Journal of Energy in South Africa, 2012, 47-51
[8] R. P. VikashTalyan, Status of municipal solid waste management in Delhi, the capital of India. Waste Management, 2008, 1276-1287.
[9] L. V. V G Sister, Ways of improving the performance of energy producing equipment at waste incineration plant. Chemical and Petroleum Engineering, 2006, 3-4
[10] F. B. E Autret, Incineration of municipal and assimilated wastes in France: Assessment of latest energy and material recovery performances. Journal of Hazardous Materials, 2007, 569-574
[11] H. H. Sieting Tan, Economical and environmental impact of waste-to-energy (WTE) alternatives for waste incineration, landfill and anerobic digestion. Energy procedia, 2014, 704-708
[12] Y. Z. Hefa Cheng, Municipal Solid Waste Fueled Power Generation in China: A Case Study of Waste-to-Energy in Changchun City. Environmental Science Technology, 2007, 7509-7515.
[13] P. D. Sudhanshu Kaushik, A comparitve study of solid waste generation at Mansa Devi and Chandi Devi in the Shiwalik foothills, during the KumbMela, 2011
[14] S. H. C Liamsanguan, Environmental assessment of energy production from Municipal Solid Waste incineration. LCA Case Studies, 2007, 529-536
[15] http://en.wikipedia.org/wiki/Roorkee, 2015

# Finite Element Analysis of Silicon Gate All Around Nanowire Transistor with Different High-k dielectrics


Neel Chatterjee
*Electronics and Communication, Amity School of Engineering and Technology*
Amity University
Noida, India
neel.chatterjee95@gmail.com

Kshitij Chopra
*Electronics and Communication, Amity School of Engineering and Technology*
Amity University
Noida, India
chopra_kshitij@live.com

Kshitij Bhatia
*Applied Physics Department*
Delhi Technological University
New Delhi, India
kshitij2992@gmail.com

Sujata Pandey
*Electronics and Communication, Amity School of Engineering and Technology*
Amity University
Noida, India
spandey11@gmail.com



***Abstract*— Scaling down of the semiconductor devices from micro to Nano scale has now become the trend for the electronics industry and it is the only hope that can ensure lesser power consumption and also reliability. Ultra thin MOSFET's, Double Gate MOSFET's, FINFET and now the latest development is the Nanowire FET. The nanowire FET is a revolutionary device as the gate is all around the channel which provides better gate control and better switching applications. But as the devices are scaled down in size, the oxide layer which lies between the channel and the gate metal is also being reduced in thickness. In this process, when $SiO_2$ is scaled down to nanometer range leakage current is observed in the device which was not prevalent in the micrometer range devices. In this paper, we present the application of high-k dielectrics in use with the Nanowire Field Effect Transistor. The transfer characteristics of the device is studies with three different dielectrics along with the energy band diagrams and trap occupancy in the devices.**



***Keywords—Nanowire FET; High-k dielectrics;***


## I. INTRODUCTION

There have been a lot of developments in the domain of transistor designs. At first we had the conventional MOSFET's with the gate being located only at one side of the body and most of the space in the CMOS design was occupied by the substrate unnecessarily. Solutions were sought to reduce the area covered by the substrate and also to improve the capacitive coupling between the gate and the channel for better gate control over the channel. Strained structures and high k-dielectrics were used to boost the performance of the MOSFET's. Then the need of improving the overall transistor design and structure was looked into. Ultra thin body MOSFET's were introduced and then the Double Gate (DG) MOSFET's. The structure of the DG structure was quite a simple one. There were two rectangular slabs, perpendicular to each other in the shape of a fin. One of the fin included the source and the drain with a width of $W_{fin}$. Another was used for channel with a width of $L_g$. The problem that was faced after a long time was lowering of DIBL (Drain Induced Barrier Lowering), which has been an inherent problem of short channels. As the channel was being shortened, it was observed that $L_g/W_{fin} > 1.5 \sim 2$. This posed a problem for lithography and again new transistor designs were sought. Then the GAA Nanowire Transistors were introduced. At first, the structure was rectangular but slowly it was developed to cylindrical GAA NWT. The device can be scaled down incredibly and the biggest advantage is an excellent gate control. Since the gate is all around the channel, the current flow can be controlled very well. This ensures less power consumption and hence more efficiency which is now the cardinal idea behind the development of the electronic gadgets.

Since the electronics era began Silicon has been the fundamental material for semiconductor research after replacing Germanium in the early research. The reasons which supported Si as the backbone was its high temperature stability and inexpensive availability. Similarly, NWT has been studied with Silicon as its material in detail [1-4].

One of the main demands of electronics industry is scaling down of the device as has been discussed in an earlier section. The scaling down also needs the oxide thickness to be reduced. The conventional oxide that has been in use is SiO2. But one of the drawbacks encountered when scaling down the gate thickness is the leakage current in the case of SiO2 [5-9]. This problem has been proposed to be solved by using high k-dielectrics as the gate material. This can alleviate the problem of leakage current to a great extent.

In this paper, our study includes the study of Silicon GAA NWT with different dielectrics and has been compared with the conventional oxide material. The simulations have been carried out with three different surface trap densities. Surface traps are mechanical defects in the region under the gate in the channel. The energy band diagrams are studied in this paper along with


**978-1-4799-8641-5/15/$31.00 ©2015 IEEE**

the noticeable changes in the gate voltage vs drain characteristics.

## II. Device Structure

The figure below shows the 3-D figure of the device under consideration. The gate is wrapped all around the channel as evident in the name of the device GAA NWT. The length of the drain and source is 10nm with a donor concentration of 1026/m3. The channel is considered to be 20nm in length. It has been doped with an acceptor concentration of 1023/m3 and since the doping is quite less the channel can be said to be undoped. The gate thickness has been kept constant at 2nm for all the three gate materials namely, SiO2 (Silicon Dioxide), ZrO2 (Zirconium Oxide) and HfO2 (Hafnium Oxide). The reason for taking such a low thickness of the gate seems pragmatic in this paper since the effect of scaling down the gate size is considered here. Three different trap densities are considered here for our simulations. The reason for consideration of trap densities is again due to practical reasons. It is an inadvertent fact that any material can't be free of mechanical defects and this device under consideration is no exception. The simulations have been made to resemble the real situations as much as possible. Fermi-Dirac carrier characteristics have been considered. The simulations have been performed at room temperature of 293.15K. Fig 1 below shows the structure of the device simulated for the results.

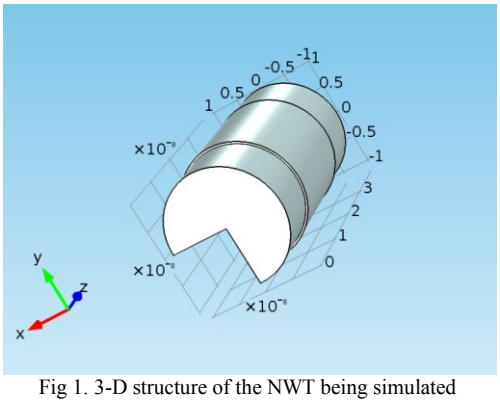


Fig 1. 3-D structure of the NWT being simulated

The Si NWT follows Poisson's equation and the same is modeled by it. The equation is solved for obtaining various parameters [10].

$$\frac{1}{r}\frac{\partial}{\partial r}\left(r\frac{\partial}{\partial r}\varphi_i(r,z)\right)+\frac{\partial^2}{\partial z^2}\varphi_i(r,z)=-\frac{qN_D}{\epsilon_j} \qquad (1)$$

Where r is the radial distance, z is the position along the channel, $\varphi_i(r,z)$ is the potential of the material depending on radius and position along the channel, $N_D$ is the doping concentration.

The boundary conditions used are:

$$\frac{\partial}{\partial r}\Phi(r,z)|_{r=0}=0 \qquad (2)$$

$$\Phi(r,z)|_{r=R}=\Phi_S \qquad (3)$$

Where $\Phi_S$ is the surface potential at radius R of the nanowire. Equation (3) explains that the potential at the centre of the nanowire is null because of the symmetry of the device.

Electric field is obtained by differentiating the surface potential as:

$$\frac{\partial}{\partial r}\Phi(r,z)|_{r=R}=\frac{C_{ox}}{\epsilon_j}\left[V_{gs}-V_{fb}-\Phi(r=R,z)\right] \qquad (4)$$

Where $V_{gs}$ is the gate to source voltage, $V_{fb}$ being the flatband voltage.

Numerous parameters were used in the simulation of the device. Table I tabulates the parameters involved in the simulations.

TABLE I PARAMETERS INVOLVED IN THE SIMULATION OF THE DEVICE

| Parameters Considered in the Simulation of Si GAA NWT | | |
|---|---|---|
| 1. | Radius of the nanowire FET | 10 nm |
| 2. | Length of channel | 20 nm |
| 3. | Length of source/drain | 10 nm |
| 4. | Oxide layer thickness | 2 nm |
| 5. | Acceptor concentration | $10^{23}/m^3$ |
| 6. | Donor concentration | $10^{26}/m^3$ |
| 7. | Trap density | Nt_0 |

## III. Simulation Results and Discussions

At first, the transfer characteristics (ID vs VG) of the three different gate materials will be considered. The dielectric constant of SiO2 is 3.9, ZrO2 is 25 and that of HfO2 is 20. As can be observed, the dielctric constants of ZrO2 and HfO2 is almost the same but the reason for their consideration is because they are the most promising materials for high k-dielectrics. Since three different trap densities are being considered the transfer characteristics of the three different gate materials will be shown differentl to avoid any confusion. Fig 2, 3 and 4 signify the drain current vs gate voltage for SiO2, ZrO2 and HfO2 as its gate material respectively.

The values 1, 6 and 21 are used to discretize the values of Gate Voltages in the graphs, the gate voltages range from -0.5V to 1.5V with a step size of 0.1V, thus -0.5V is denoted by 1, 0 V by 6 and 1.5V with 21.

978-1-4799-8641-5/15/$31.00 ©2015 IEEE

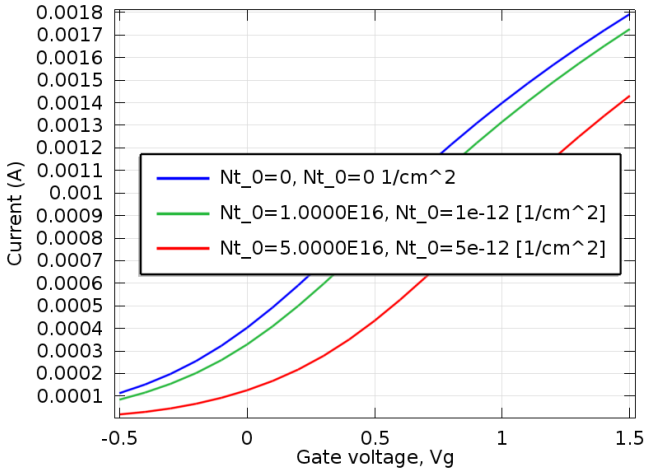


Fig 2. $I_D$ vs $V_G$ characteristics of Si NWT with $SiO_2$ as its gate material

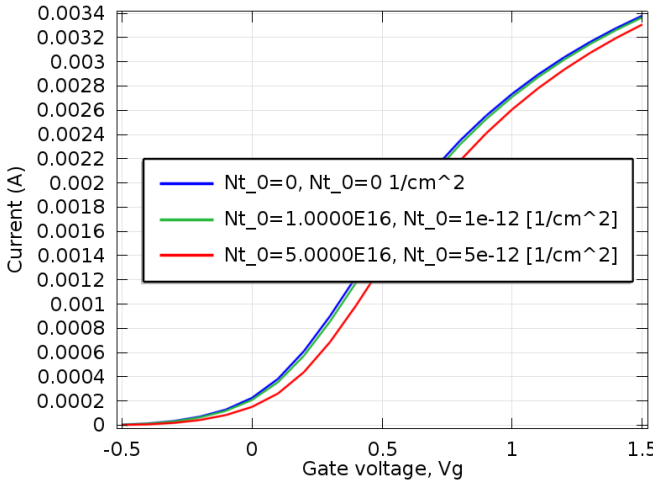


Fig 3. $I_D$ vs $V_G$ characteristics of Si NWT with $ZrO_2$ as its gate material

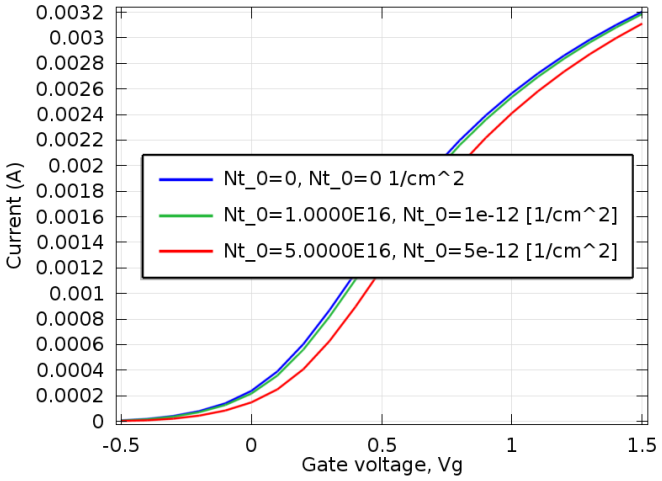


Fig 4. $I_D$ vs $V_G$ characteristics of Si NWT with $HfO_2$ as its gate material

The first noticeable difference between the first and second along with third is that, the current in at lower gate voltage is more in the device with SiO2 as its gate material but the trend reverses at higher gate voltages where the current is higher in the other two devices with high-k dielectrics. This trend shows that there exists high leakage current in the case of SiO2 which vanishes or can be said to be greatly reduced in the case of high-k dielectrics. For the higher gate voltages the high-k dielectrics give a favorable response by having a higher value of drain current than that in the device with SiO2 as its gate material. This would enable to lower the DIBL (Drain Induced Barrier Lowering) effect in the case of the nanoscale device which is an inherent problem of short channel devices as was discussed in the case of FINFET.

Next, we will be discussing the energy band diagrams of the devices. The energy band diagrams of HfO2 and ZrO2 is nearly the same and hence the band diagrams of ZrO2 and SiO2 is considered. The band diagrams are considered at zero trap density and a gate voltage of 1.5V. Fig 5 shows the energy band diagram of the Si NWT with SiO2 as its gate material and Fig 6 shows the band diagram with ZrO2 as its gate material.

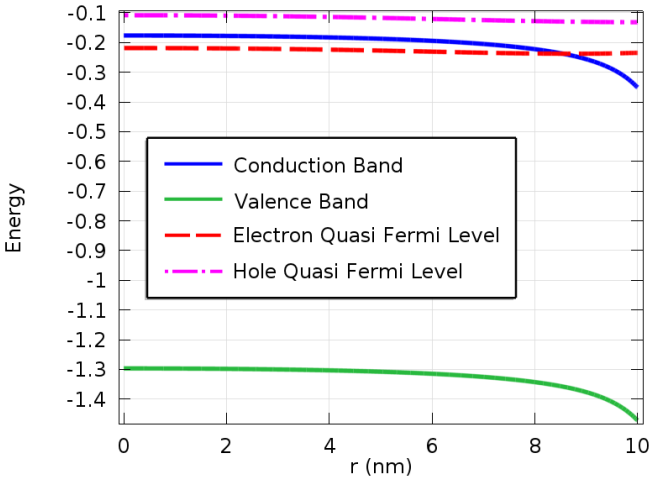


Fig 5. Energy band diagram of SI NWT with $SiO_2$ as its gate material

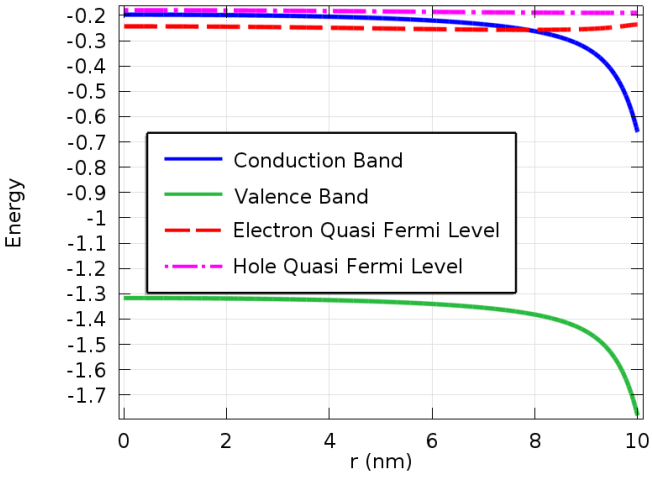


Fig 6. Energy band diagram of SI NWT with $ZrO_2$ as its gate material

978-1-4799-8641-5/15/$31.00 ©2015 IEEE

The energy band diagram shows the position of the energy bands along the radius of the nanowire. The position at zero represents the central axis of the cylindrical nanowire. The distance that increases along the x-axis denotes the increasing radius of the nanowire. When gate voltage is applied, the conduction band is moved below or near the electron quasi Fermi level. More the conduction band below the electron quasi Fermi level more is the electron density in that region and hence more the current. In both the cases, as the radius is increased it is observed that the distance between the electron quasi Fermi level and conduction band remains same till about 6nm and then it increases beyond that distance. The increase is more in the case of NWT with ZrO2 as its gate material than in SiO2. This tells us that the current towards the surface is more in the case of ZrO2 than in SiO2. This can be observed from the ID vs VG plot at 1.5V that the current is more in the case of ZrO2.

Next we will be discussing about the trap occupancy in the channel under the gate region. In our simulations, we have chosen our trap density to be 5 x 1016/m3. We will observe how much of the traps are occupied in terms of probability, where the highest value one (1) denotes that all traps are occupied. The trap density distribution will be observed in all the three devices. The total length of the material is about 40 nm including the source, drain and channel. The channel varies between 10nm and 30nm on the z-axis and hence only that region is considered in the trap occupancy as the gate is above the channel only and the traps are introduced by the coupling between the two. Fig 7 describes trap density with SiO2 as the gate material. Fig 8 and Fig 9 describe the trap density with ZrO2 and HfO2 as its gate material at three different gate voltages.

.....

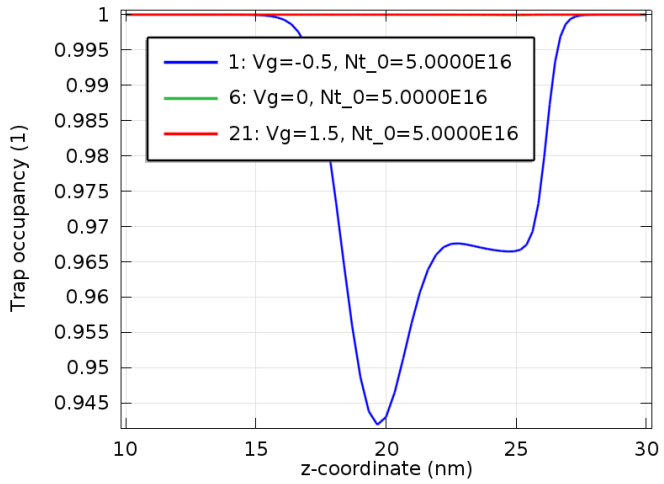


Fig 7. Trap density in NWT with $SiO_2$ as the gate material

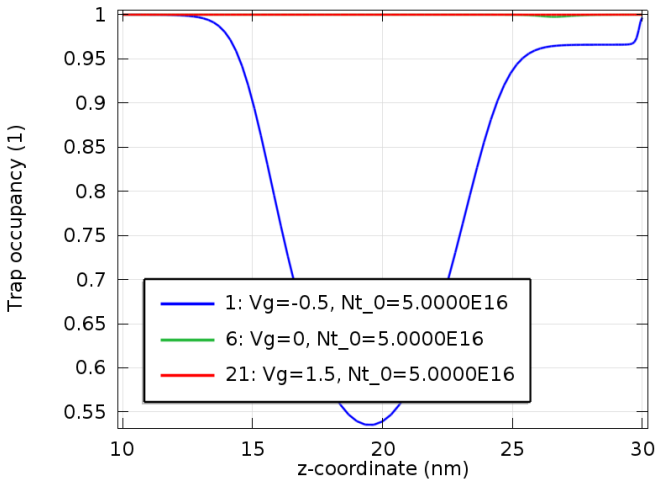


Fig 8. Trap density in NWT with $ZrO_2$ as the gate material

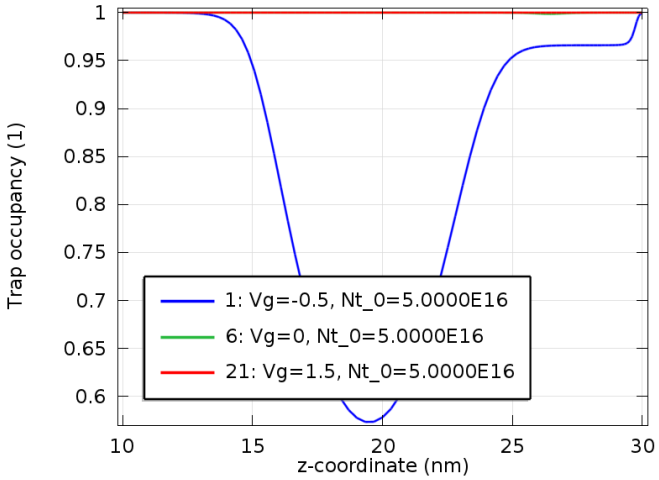


Fig 9. Trap density in NWT with $HfO_2$ as the gate material

The trap occupancy can be appreciated when considering the switching applications and when using these devices for CMOS where high speed switching is necessary. When the voltage is 0V or 1.5V it can be observed that almost all the traps are occupied. The reason can be attributed to the fact that at 0V the device is at dynamic equilibrium and hence all traps are occupied. At 1.5V, all the electrons in the channel travel along the channel and near the surface of the nanowire. This is the reason why all the traps are occupied at 1.5V, since traps are located under the gate and near the surface. Now, when a negative voltage is applied, the trap densities become more evident in all the three cases considered above. The reason for this phenomenon can be attributed to the fact that when a negative gate voltage is applied to the gate, electrons are 'pushed' away from the surface towards the centre of the nanowire from all the sides as the shape is cylindrical. Due to this phenomenon, trap occupancy goes down when negative voltage is applied. Now, the important fact to be noted here is that trap occupancy should be low when negative voltage is applied or else it defies the notion of switching where reverse voltage should drive the device to off state. Now, when comparing the above devices it can be observed that in the case

978-1-4799-8641-5/15/$31.00 ©2015 IEEE

of SiO2 as the gate material, the lowest trap density is 0.940 in the middle of the channel, which means that 94% of the traps are still occupied in the channel when the device is supposed to be in the off state. Now in the case of ZrO2 and HfO2 as its gate material the trap density is nearly 0.5 and 0.55 respectively. This is way lower than in the earlier case of SiO2. This points to the fact that electrons are actually not present in the channel region when the device is supposed to be off, which is a good sign. Thus it can be observed that high-k dielectrics are a good gate material for switching applications in the digital application where the switching efficiency is most important.

One of the biggest assumption made in the above case is that at 1.5V and at 0V, the trap occupancy is the same. But it is not exactly same. The contrast between the trap density of the two voltages as seen closely is shown below in Fig 10.

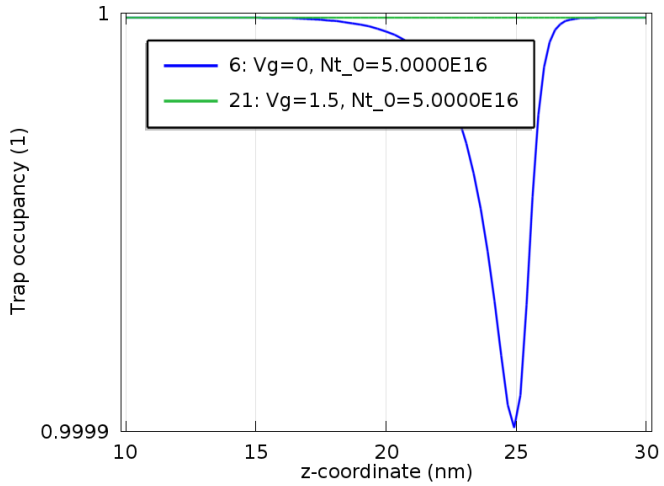


Fig 10. Trap density with $SiO_2$ at 0V and 1.5V of gate voltage

As can be observed, the traps are completely occupied in the case of 1.5V but not in the case of 0V.

## IV. Conclusions and Discussions

It can be observed from all the results that high-k dielectrics are favorable as the leakage current reduces and alleviates the problems of phenomenon occurring at low gate voltages such as DIBL. The current is also higher at higher gate voltages than the devices possessing the conventional gate material. The advantage of using it in devices used for digital applications has also been studied. Overall, high-k dielectrics are the future for the nanoscale devices to improve their efficiency and make them more reliable.

## References


[1] Kim, Dae Mann, Bomsoo Kim, and Rock-Hyun Baek. "Silicon Nanowire Field-Effect Transistor." *Nanowire Field Effect Transistors: Principles and Applications*. Springer New York, 2014. 63-87.

[2] Cui, Yi, et al. "High performance silicon nanowire field effect transistors." *Nano letters* 3.2 (2003): 149-152.

[3] Schmidt, Volker, et al. "Realization of a Silicon Nanowire Vertical Surround-Gate Field-Effect Transistor." *Small* 2.1 (2006): 85-88.

[4] D. M. Kim, B. Kim, and R.-H. Baek, "Silicon Nanowire Field-Effect Transistor," Nanowire Field Effect Transistors: Principles and Applications, pp. 63–87, Oct. 2013.

[5] Chan, T. Y., et al. "The impact of gate-induced drain leakage current on MOSFET scaling." *Electron Devices Meeting, 1987 International*. Vol. 33. IEEE, 1987.

[6] Timp, G., et al. "Low leakage, ultra-thin gate oxides for extremely high performance sub-100 nm nMOSFETs." *Electron Devices Meeting, 1997. IEDM'97. Technical Digest., International*. IEEE, 1997.

[7] Ribes, G., et al. "Review on high-k dielectrics reliability issues." *Device and Materials Reliability, IEEE Transactions on* 5.1 (2005): 5-19.

[8] Kang, Laegu, et al. "MOSFET devices with polysilicon on single-layer HfO/sub 2/high-K dielectrics." *Electron Devices Meeting, 2000. IEDM'00. Technical Digest. International*. IEEE, 2000.

[9] Kittl, J. A., et al. "High-k dielectrics for future generation memory devices."*Microelectronic engineering* 86.7 (2009): 1789-1795.

[10] Lin, S. H., et al. "A rigorous surface-potential-based IV model for undoped cylindrical nanowire MOSFETs." *Nanotechnology, 2007. IEEE-NANO 2007. 7th IEEE Conference on*. IEEE, 2007.


**978-1-4799-8641-5/15/$31.00 ©2015 IEEE**

IJIREEICE

ISSN (Online) 2321 – 2004
ISSN (Print) 2321 – 5526

*INTERNATIONAL JOURNAL OF INNOVATIVE RESEARCH IN ELECTRICAL, ELECTRONICS, INSTRUMENTATION AND CONTROL ENGINEERING*
*Vol. 3, Issue 12, December 2015*

# Grid Integration of Fuel Cell with MPPT under Variable Air Flow Rate

**Gitanjali Pandove[1], Mukhtiar Singh[2]**

Associate Professor, Electronics & Communication Engg, DCRUST, Murthal, Hrayana, India[1]

Registered Scholar at Dr. K. N. Modi University, Newai, Rajasthan, India[1]

Associate Professor, Electrical Engg, DTU, Delhi [2]

**Abstract:** In the proposed work a proton exchange membrane fuel cell (PEMFC) with variable air flow rate has been presented. Here, the main objective is to extract maximum power out of fuel cell at different air flow rates. The proposed scheme consists of DC-DC buck-boost converter with grid interfacing inverter. The DC-DC converter is controlled to perform maximum power point tracking under varying fuel cell conditions while grid interfacing inverter is controlled to evacuate the generated output power from fuel cell. It has also been demonstrated that the grid interfacing inverter may also be helpful in meeting the reactive power demand of nearby local loads so that grid always exchange power at unity power factor. Finally, detailed modelling and simulation results under MATLAB/SimPowerSystem environment have been presented to validate the proposed control algorithms.

**Keywords:** Fuel Cell, MPPT, Grid Integration, Inverter Control, DC-DC Converter, Renewable energy sources, Reactive power compensation.

## I. INTRODUCTION

There has been renewed interest in developing advanced technologies for the alternate energy sources due to various disadvantages related to conventional power generation [1-3]. Recently, the fuel cell based energy sources are gaining lot of popularity not only for automotive transportation but also as energy storage option in the form of hydrogen and then reconversion at desired location or site of use.

The output energy from FC depends on various parameters and system operating conditions, e.g. Cell temperature, gas flow rate, humidity, pressure at anode and cathode, dry gas mole fraction, stoichiometry etc. These parameters not only vary the output of fuel cell but also the voltage at its terminals. In order to extract maximum power under all these aforementioned conditions, it is very much important to have an efficient means of maximum power point tracking (MPPT).

The MPPT in fuel cell may be performed in two different stages: 1. Optimal control of fuel cell parameters such as gas flow, air flow and pressure, 2. Optimal control of fuel cell terminal voltage and current. In the proposed work, the second option of MPPT has been explored by controlling the buck-boost converter.

The output from Fuel cell may vary as per the load connected on its terminals. There is nonlinear relationship between terminal voltage and current drawn from fuel-cell, which further makes the output power as nonlinear function of loading current. Therefore, there is only one unique operating point at which the fuel cell may deliver maximum power. The maximum power point (MPP) may vary with system temperature, pressure, air and fuel flow rate. Therefore, it is a great challenge to perform MPPT under different operating conditions.

Lot of research have taken place in past and different MPPT algorithms are available in literature. Some of the common MPPT methods such as Hill-climbing/ Perturb and Observe (P&O), incremental conductance, fractional open-circuit voltage, fractional short-circuit current may be found in abundance. Further, the intelligent techniques based on fuzzy logic control, neural network, ripple correlation control, sliding mode control current etc. have also been proposed and all these techniques are generally implemented for photovoltaic system. Since, the output profile of photovoltaic systems is similar to fuel cell and hence, most of these MPPT techniques may be easily adopted for fuel cell also. MPPT methods vary in complexity, hardware implementation, convergence of speed and sensed parameters [4]. Some of the MPPT methods applied to fuel cells are primarily based on P&O [5-9], adaptive MPPT control [10], moto compressor based control technique [11], adaptive neuro-fuzzy logic controller and sliding mode [12-14], MPPT algorithm based on resistance matching between the direct methanol fuel cells internal resistance and the tracker's input resistance [15], voltage and current based MPPT [16], adaptive extreme seeking control [17].

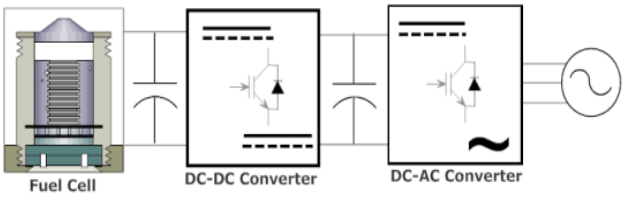


Fig.1 Block Diagram of Proposed Scheme

In the proposed work, the MPPT based on fuel cell terminal voltage and current has been implemented with the help of DC-DC converter. Besides this, the grid side inverter is also controlled to perform multiple roles simultaneously. The proposed scheme as shown in Fig. 1

Copyright to IJIREEICE

IJIREEICE
ISSN (Online) 2321 – 2004
ISSN (Print) 2321 – 5526
INTERNATIONAL JOURNAL OF INNOVATIVE RESEARCH IN ELECTRICAL, ELECTRONICS, INSTRUMENTATION AND CONTROL ENGINEERING
Vol. 3, Issue 12, December 2015

is able to extract maximum power under varying operating conditions. The main characteristics of the proposed approach are its good transition response, low tracking error, very fast dynamic system response against set point, fuel cell airflow rate, robustness as well as its low complexity. The rigorous simulation study has been carried out to evaluate the performance and accuracy of the proposed algorithm.

## II. FUEL CELL MODELLING

A fuel cell is a device that converts the chemical energy in to the electrical energy. The fuel cell in which chemical reaction takes place due to the combination of hydrogen with oxygen in the presence of suitable oxidizing agent is similar to battery. The major difference between them is the fuel cell's capability of producing electricity is dependent on continuity of fuel supply or in other words the continuity of electricity may be maintained as long as fuel is supplied. The fuel cell may be a promising technology for our future energy demand, and may be helpful in catering the heat and electricity requirements. The energy released from the chemical reaction between hydrogen and oxygen is the basic principle of the fuel cell [18-20]. At the anode of an electrolyte, the electrons are released by the ionization of hydrogen gas and $H^+$ ions are generated.

$$2H_2 \rightarrow 4H^+ + 4e^-$$

At the cathode, the combination of oxygen, electrons from electrode and $H^+$ions from electrolyte yields water as given below.

$$O_2 + 4H^+ + 4e^- \rightarrow 2H_2O$$

Thus for continuous chemical reaction, the electron from anode to cathode through electric circuits and hydrogen ions through electrolyte should keep on flowing. The typical model of PEMFC is shown in Fig.2.

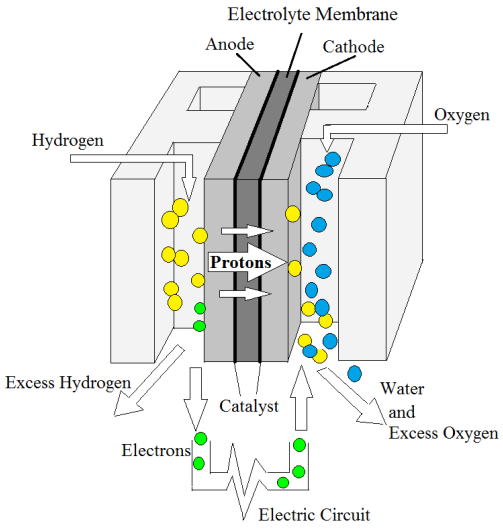


Fig.2. PEM Fuel Cell

Electrical Equivalent Model of Fuel Cell: The output voltage of fuel cell (V) mainly depends on four different kind of voltages and represented as

$$V = V_{rev} - V_{act} - V_{ohm} - V_{conc}$$

Where $V_{rev}$ represents the reversible voltage; $V_{act}$is the voltage drop due to the activation of the anode and cathode; $V_{ohm}$ is a measure of ohmic voltage drop; $V_{conc}$represents the voltage drop resulting from the concentration or mass transportation of the reacting gases. The theoretical reversible voltage which sometimes also referred as fuel cell's open circuit voltage may be calculated as

$$V_{rev} = V_{0,rev} + \frac{RT}{2F}\ln\left[P^*_{H_2} \times \sqrt{P^*_{O_2}}\right] - V_{d,rev}$$

Where R is a gas constant, T is temperature in Kelvin, F is Faraday's constant, and P* is the partial pressure of the noted species, all of which are positive. Further

$$V_{0,rev} = V^0_{0,rev} - k_E(T - 298)$$

where$V^0_{0,rev}$ is the reference potential at standard Temperature and pressure (298 K, 1 atm), and $k_E$ is a constant.

$$V_{d,rev}(t) = \lambda_e I(t)\left[1 - e^{-t/t_e}\right]$$

where$\lambda_e$ is a constant, I(t) is the cell current, and $t_e$ is fuel and oxidant flow delay.

Similarly, the activation voltage drop is nothing but loss of potential due to slow electrochemical reaction taking place at the electrode surface especially under low power demands and can be represented as

$$V_{act} = \eta_0 + a(T - 298) + bT\ln(I)$$

Where a, b and $\eta_0$ are constants.
The loss of potential due to electrical resistance exerted by polymer membrane between membrane and electrodes and among electrode themselves is known as ohmic voltage drop and may be represented as

$$V_{ohm} = IR_{ohm}$$

Where

$$R_{ohm} = R_{ohm\,0} + k_{RI}I - k_{RT}T$$

Here, $R_{ohm0}$, $k_{RI}$, and $k_{RT}$ are all positive constant.
The concentration voltage drop generally happens during high load current, where the system is unable to supply enough reactants and remove products at faster rate for the complete chemical reaction.

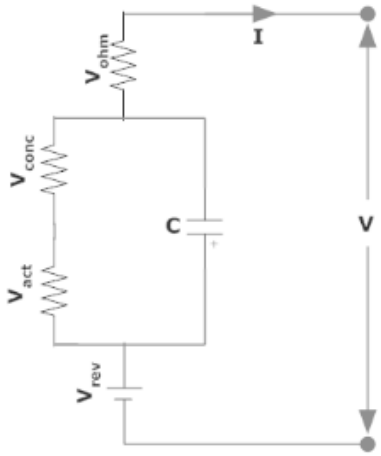


Fig.3 Electrical Eqv. Model of Fuel Cell

IJIREEICE
ISSN (Online) 2321 – 2004
ISSN (Print) 2321 – 5526
INTERNATIONAL JOURNAL OF INNOVATIVE RESEARCH IN ELECTRICAL, ELECTRONICS, INSTRUMENTATION AND CONTROL ENGINEERING
Vol. 3, Issue 12, December 2015

The concentration polarisation or potential loss is defined as

$$V_{conc} = -\frac{RT}{zF}\ln\left(1-\frac{I}{I_{lim}}\right)$$

Where, z is the no. of participating electrons and $I_{lim}$ is the maximum current limit. The fuel cells are normally designed to avoid during such operating conditions. The electrical equivalent model of Fuel Cell is shown in Fig. 3. [21-22]

## III. CONTROL DESCRIPTION

The power processing equipment are major components of proposed system consisting of DC-DC converter and grid interfacing inverter. The DC-DC converter is controlled to extract maximum power out of fuel cell while the grid interfacing inverter is controlled to evacuate the fuel cell generated power and inject it into the grid. The control of proposed system is divided into two parts: 1. Fuel Cell side control, 2. Grid side control.

A. Fuel Cell side control

The main role of DC-DC converter is to control the fuel cell output power as a function of its output current in compliance of P-I curve as shown in Fig. 4.

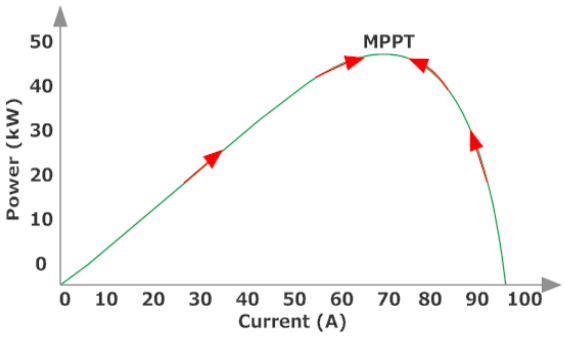


Fig.4. Power-Current curve of Fuel Cell

Since the output power is the function of fuel cell current, there is always one point at which maximum power can be extracted at a given condition.

Accordingly, under different operating points, the controller is designed to perform MPPT as per the flow chart shown in Fig. 5. Here, the output power and current are compared with their values at previous instant and as per their sign the operating modes are divided in to four categories. Depending on the mode of operation the amount of current drawn from fuel cell is decided and incremented/decremented as shown in Fig. 5.

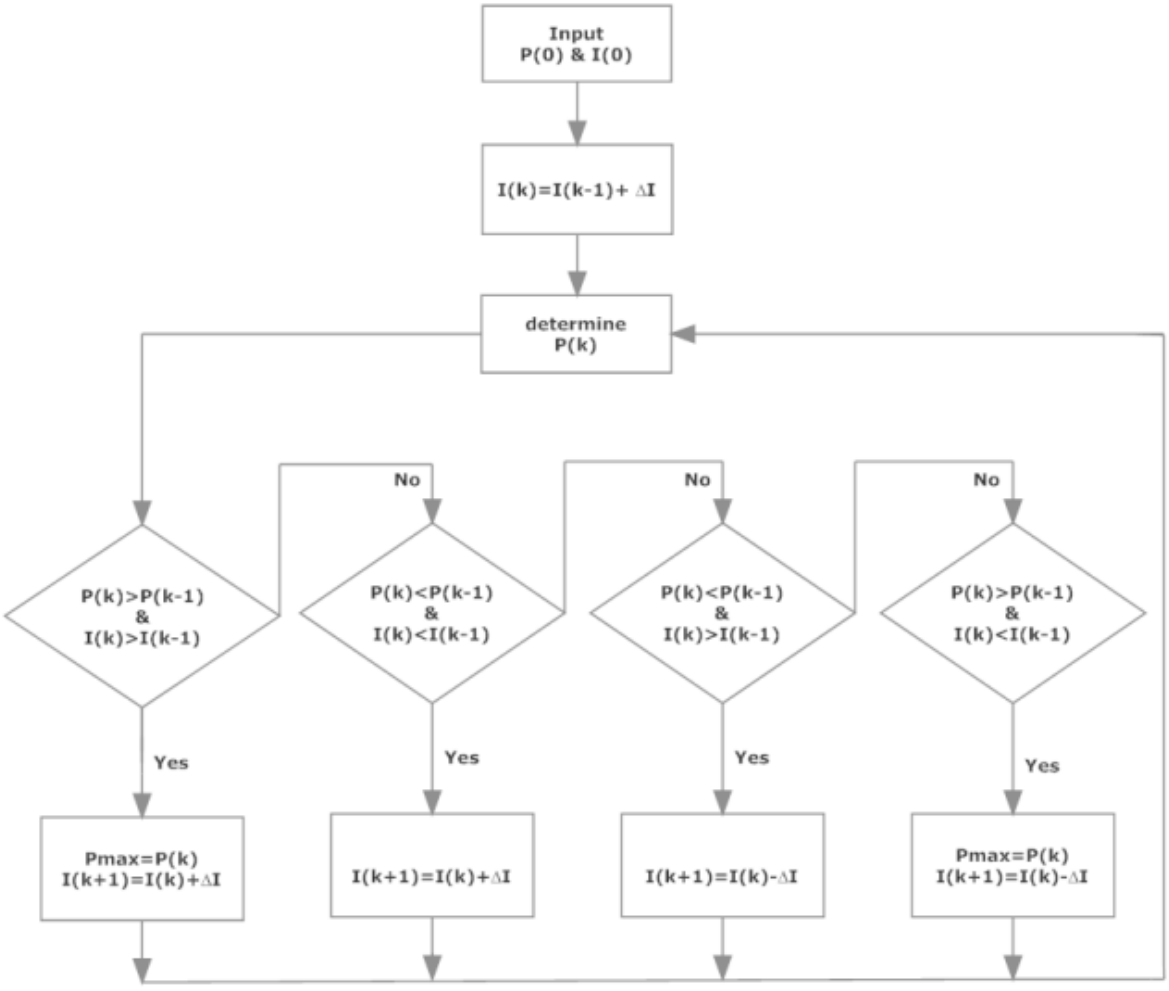


Fig.5. Flow Chart of MPPT Control Algorithm

IJIREEICE
ISSN (Online) 2321 – 2004
ISSN (Print) 2321 – 5526
INTERNATIONAL JOURNAL OF INNOVATIVE RESEARCH IN ELECTRICAL, ELECTRONICS, INSTRUMENTATION AND CONTROL ENGINEERING
Vol. 3, Issue 12, December 2015

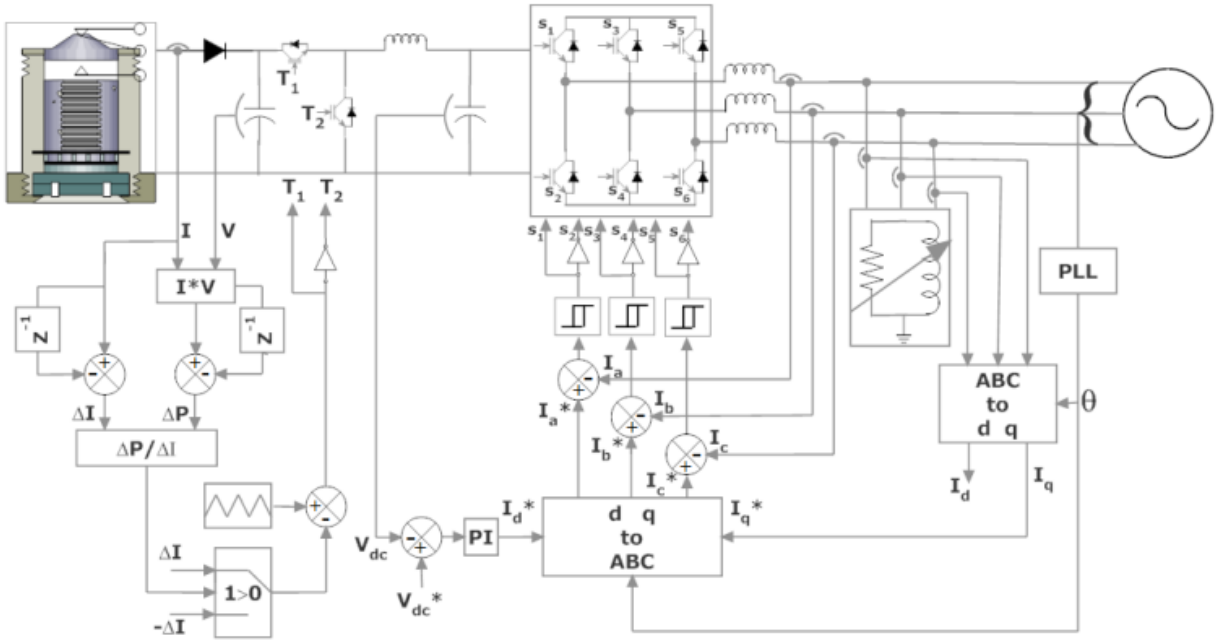


Fig .6 Control Diagram of proposed system

B. Grid Side Control

The main purpose of grid interfacing inverter is to inject the fuel-cell output power into the grid. However, in the proposed work the inverter is also utilised to feed the reactive power demand of local loads connected at point of common coupling (PCC). The control algorithm is mainly divided into two control loops: Outer Voltage loop and Inner current loop. The outer loop maintains the DC voltage close to its reference value and sets the reference active current demand for inverter current. The load reactive current is directly taken as reference reactive component of inverter current. Once, the active and reactive current components of Inverter are known then its equivalent 3-phase components may be easily determined with the help of Park's transformation which is also referred as d-q to ABC transformation. Here it is pertinent to mention that the phase lock loop (PLL) is utilised to determine synchronizing angle for the grid interfacing inverter. The complete control diagram is shown in Fig.6.

## IV. RESULTS AND ANALYSIS

The proposed system consisting of fuel cell, DC-DC converter and grid interfacing inverter is developed in MATLAB Simulink and extensive simulation study has been carried out to validate the proposed control algorithm. The simulations are carried out for variable input air flow with Resistive and Resistive-Inductive load at PCC.

A. Results with Resistive load

In Fig.7., the traces of active and reactive power for inverter, grid, load with variable air flow are shown. Initially, a load of 50kW with no reactive power demand has been connected in the system where the air flow rate is varied in between 1200-2000 m/s. Under the given circumstances, the fuel cell generates almost 42kW as evident from the active power injected by the inverter in to the grid and the reactive power is zero due to no

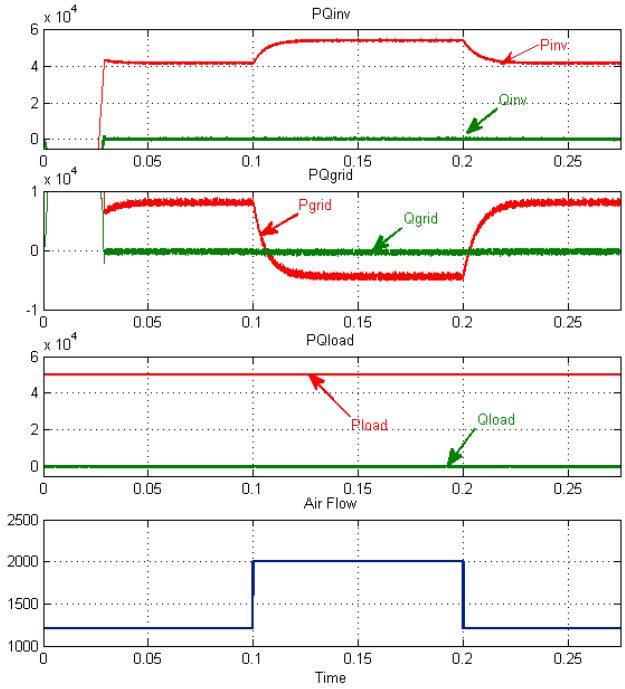


Fig.7. P-Q traces of Inverter, Grid and Resistive load

requirement of reactive power from load at PCC. Here it can be easily noticed that the deficit active power of 8kW is supplied from grid in order to meet the total load active power demand of 50kW. At 0.1Sec., the air flow is suddenly increased from 1200 to 2000m/s which results in increased power generation from Fuel cell and accordingly the power injected from inverter reaches up to 54kW. Since, the fuel cell generates the power in excess to the load power demand of 50kW at PCC, the rest of the power of 4kW is being absorbed by the grid as indicated by the profile of grid active power, where it suddenly changes its sign from 8kW to -4kW with sudden increase in air flow rate. At 0.2Sec., the air flow rate is dropped to its initial

IJIREEICE

ISSN (Online) 2321 – 2004
ISSN (Print) 2321 – 5526

*INTERNATIONAL JOURNAL OF INNOVATIVE RESEARCH IN ELECTRICAL, ELECTRONICS, INSTRUMENTATION AND CONTROL ENGINEERING*
*Vol. 3, Issue 12, December 2015*

value and the system again restores itself to its initial stage.

The traces of grid voltage, grid current, load current, inverter injected current and DC-link voltages are shown in Fig.8. Here, it can be easily noticed that the initially the current drawn by load is more than the current injected by inverter and hence, grid has to supply the deficit amount of current. Since, the load is resistive in nature, the grid voltage and currents are in same phase. However, at 0.1 Sec., the grid current becomes in opposite phase to grid voltages, which indicates the current is being injected in to grid as now the current supplied from inverter is more than the current drawn by load. At 0.2Sec., the grid current again changes its phase as the current supplied from inverter falls to its initial value due to drop in air flow supplied to fuel cell and consequently drop in its output power. Here, it may be noticed that the DC-link voltage is always maintained to its reference value of 1000 V, despite of variations in operating conditions of the whole system.

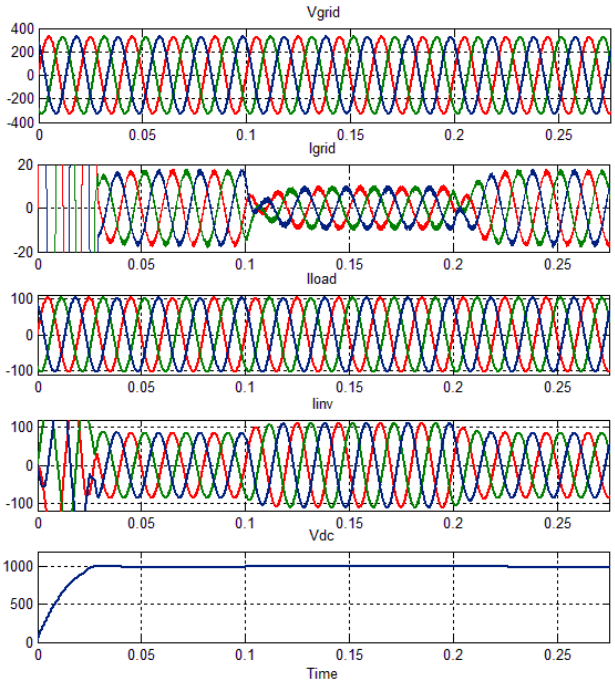


Fig.8. Traces of Grid Voltage, Grid, Inverter, Load Currents and DC-Link voltage with Resistive load

B. Results with Resistive-Inductive load

The Fig. 9 shows the traces of active and reactive power of grid, load and inverter with variable air flow rate applied to fuel cell having RL load connected at PCC. Here, the main purpose is to control the grid interfacing inverter to supply not only the active power generated from fuel cell but also the reactive power demand of load at PCC in order to have grid unity power factor (UPF) operation.

From Fig.9, it can be easily noticed that the load demands almost 50kW active power and 20kVAR of reactive power. The inverter supplies the whole reactive power demanded by load as also evident from grid side zero reactive power, while the load active power is shared by both inverter and grid as discussed in case of simulation results with resistive load.

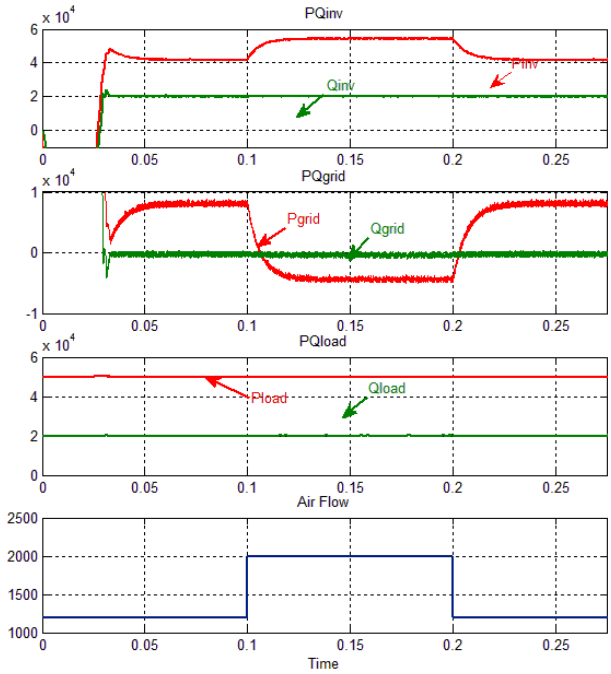


Fig.9. P-Q traces of Inverter, Grid and Resistive-Inductive load

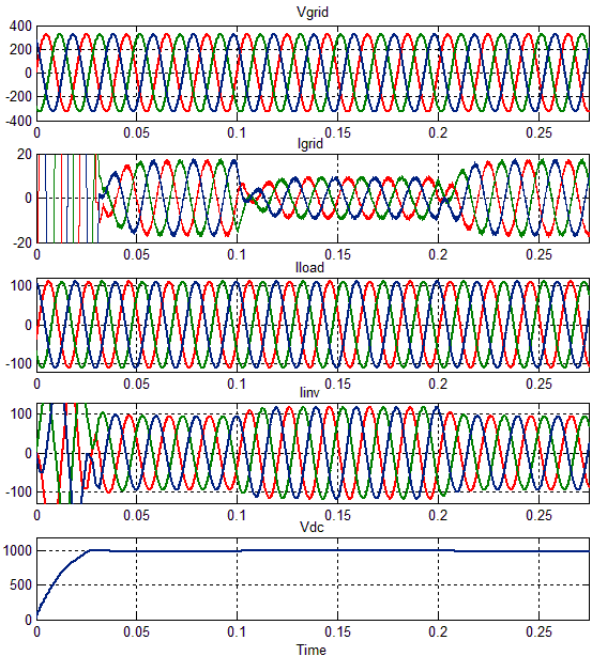


Fig.10. Traces of Grid Voltage, Grid, Load, Inverter Currents and DC-Link voltage with Resistive-Inductive load

Finally, the traces of grid voltage, grid current, load current, inverter current and DC-Link voltage are shown. Here it can be seen that the load current is lagging the grid voltage due to RL load, but grid current always remains in phase or out of phase depending on the active power being drawn from grid or being injected in to grid. Thus from grid side only exchange of active power takes place irrespective of nature of load (R, RL, RLC load etc.) as the reactive power demand is well taken cared by inverter while keep on supplying the generated active power from fuel cell, simultaneously. This confirms the UPF operation

Copyright to IJIREEICE
DOI 10.17148/IJIREEICE.2015.31203

of grid which is very much desirable considering the side effect of supplying reactive power demand to be fed from grid.

## V. CONCLUSION

In the proposed work, the detailed modeling of fuel cell with MPPT control algorithm has been presented. Besides this, the grid UPF operation has been achieved by controlling the grid interfacing inverter in such a way that it not only supplies the generated active power but also the reactive power demand of nearby loads connected at PCC. The detailed control algorithm with relevant diagrams has been provided to understand the proposed concept. Finally, the detailed simulation study has been carried out and validated by the analysis of simulation results.

## ACKNOWLEDGMENT

Many thanks to the D. C. R. University of Science & Technology, Murthal a Govt. of Haryana university for providing me an opportunity to pursue the current research work from Dr. K. N. Modi, University, Newai, Rajasthan.

## REFERENCES

[1] M. Singh, and A. Chandra, "Real Time Implementation of ANFIS Control for Renewable Interfacing Inverter in 3P4W Distribution Network," IEEE Trans. Industrial Electron, vol. 60, no.1, pp. 121-128, Jan. 2013.
[2] M. Singh, V. Khadkikar, A. Chandra, and R. K. Varma, "Grid-Interconnection of Renewable Energy Sources at Distribution Level with Power Quality Improvement Features," IEEE Trans. Power Delivery., vol.26, no. 1, pp. 307-315, Jan. 2011.
[3] G. Pandove, and M. Singh "High-Frequency DC-DC Boost Converter for Residential PV System with Power Factor Correction," in Proc. IEEE PICONF'2012, 19 –22 Dec. 2012, Murthal, Haryana, India.
[4] O. Wasynczuck, "Dynamic Behavior of a Class of PhotovoltaicPower Systems", IEEE Trans. Apparatus and Systems, 1983.
[5] M. Singh, A. Chandra and B. Singh, "Sensorless Power Maximization of PMSG based Isolated Wind-Battery Hybrid System Using Adaptive Neuro-Fuzzy Controller" In the Proc. of IEEEIASGM-2010, Houston, Texas, USA.
[6] N. Karami, R.Outbib and N.Moubayed, "Fuel Flow Control of a PEM Fuel Cell with MPPT," In the Proc. ofIEEE ISIC-2012, Croatia.
[7] Sarvi, M.; Barati, M.M.; , "Voltage and current based MPPT of fuelcells under variable temperature conditions," Universities PowerEngineering Conference, Sept. 2010.
[8] C.A. Ramos-Paja, G. Spagnuolo, G. Petrone, R. Giral, A. Romero,"Fuel cell MPPT for fuel consumption optimization," Circuits andSystems (ISCAS), Proceedings of 2010 IEEE InternationalSymposium, June 2010.
[9] K. Hussein, I.Muta, T.Hoshino, M. Osakada, "MaximumPhotovoltaic Power Tracking: An Algorithm for Rapidly ChangingAtmospheric Conditions", lEE Proc.-Generation, Transmission,Distribution, January, 1995.
[10] N. Bizon, "On tracking robustness in adaptive extremum seekingcontrol of the fuel cell power plants", Applied Energy 2010.
[11] M. Becherif, D. Hissel, "MPPT of a PEMFC based on air supplycontrol of the motocompressor group", International Journal ofHydrogen Energy, Vol: 35, Issue: 22, 2010.
[12] Sh. Abdi, K. Afshar*, N. Bigdeli, S. Ahmadi, "A Novel Approach for Robust Maximum Power Point Trackingof PEM Fuel Cell Generator Using Sliding Mode ControlApproach", Int. J. Electrochem. Sci., 7,4192 – 4209, 2012.
[13] J. Jiao, and X. Cui, "Adaptive Control of MPPT for Fuel Cell Power System," Journal of Convergence Information Technology(JCIT), Vol. 8, No. 4,Feb.-2013.
[14] M. ELSayed Youssef, Moataz H. Khalil, Khairia E. AL-NAdi, "Neural Network Modeling forProton Exchange Membrane Fuel Cell (PEMFC)", Advances in Information Sciences and ServiceSciences, Advanced Institute of Convergence Information Technology, vol. 2, no. 2, pp. 61-66,2010.
[15] C. Ramos Paja, C. Bordons, A. Romero, R. Giral and L. Martinez Salamero, "Minimum FuelConsumption Strategy for PEM Fuel cells", IEEE Transactions on Industrial Electronics, vol. 56,no. 3, pp. 685-696, 2009.
[16] Yan Minxiu, Fan Liping, Sun Ping, "Constant Voltage Output in Proton Exchange Membrane FuelCell under Fuzzy Sliding Mode Control", Advances in Information Sciences and Service Sciences,Advanced Institute of Convergence Information Technology, vol. 4, no. 20, pp. 180-187, 2012.
[17] ZhongZhidan, HuoHaibo, Zhu Xinjian, Cao Guangyi, Ren Yuan, "Adaptive Maximum PowerPoint Tracking Control of Fuel Cell Power Plants", Journal of Power Sources, vol. 176, no. 1, pp.259-269, 2008.
[18] J. M Correa, F. A Farret, L. N Canha, Marcelo G. Simoes, "An Electrochemical-Based Fuel-CellModel Suitable for Electrical Engineering Automation Approach", IEEE Transactions onIndustrial Electronics, vol. 51, no. 5, pp. 1103-1112, 2004.
[19] S. Pasricha, and S.R. Shaw, "A Dynamic PEM Fuel Cell Mode",IEEE Transactions on Energy Conversion, vol. 21, no. 2, June2006.
[20] R. OHayre, S.Cha, W. Colella, F. Prinz ,"Fuel cell fundamentals",John Wiley and Sons, New York, 2009.
[21] C. Wang, M. H. Nehrir, and S. R. Shaw, "Dynamic Models and ModelValidation for PEM Fuel Cells Using Electrical Circuits," IEEE Trans.Energy Conv., vol. 20, no. 2, pp. 442-451, June 2005.
[22] P. Famouri and R. S. Gemmen, "Electrochemical Circuit Model of aPEM Fuel Cell," at Power Eng. Soc. Gen. Meeting, pp. 1440-1444, July 2003.

## BIOGRAPHIES

**Gitanjali Pandove** has done her M.Tech from AMU Aligarh and B. Tech from Nagpur University. Presently, she is working as associate professor in Electronics and Communication Engineering dept. At Deenbandhu Chhotu Ram University of Science and Technology (D.C.R.U.S.T.) Murthal, Sonipat, Govt. of Haryana, India. Her research interest includes, Digital Control, power electronics, Renewable Energy, Optical communication, Image Processing and Digital signal processing.

**Mukhtiar Singh** received the B.Tech. and M.Tech. Degrees in electrical engineering from National Institute of Technology (formerly known as R.E.C. Kurukshetra), Kurukshetra, India, in 1999 and 2001, respectively. He has done his Ph.D. degree in 2010 from Ecolede Technologie Superieure, Universite du Quebec, Montreal, QC, Canada, under the National Overseas Scholarship, funded by the Government of India. Since 2002, he has been Assistant Professor in the Department of Electrical Engineering, Deenbandhu Chhoturam University of Science and Technology, Murthal, Sonepat, India. Currently, he is working as Associate Professor at Delhi Technological University (Formerly Delhi College of Engineering) Delhi. His research interests include renewable energy sources, power quality, energy storage systems, electric vehicles, and power electronics and drives.

Volume 3, Issue 4 (2015) 682-690 ISSN 2347 - 3258
International Journal of Advance Research and Innovation

# Identification, selection and evaluation of COTS selection criteria using Fuzzy Set Theory

Rakesh Garg [a, *], R. K. Sharma [a], Kapil Sharma [b]
[a] Department of Computer Science & Engineering, Al-Falah School of Engineering & Technology, Faridabad, Haryana, India
[b] Department of Computer Science and Engineering, Delhi Technological University, Delhi, India

**Article Info**
Article history:
Received 05 October 2015
Received in revised form
20 October 2015
Accepted 28 November 2015
Available online 15 December 2015

**Keywords**
Commercial Off-the-Shelf;
Fuzzy Set Theory;
Selection Criteria;
Component Based Software Engineering

**Abstract**
In the last decades, the development of the reliable and stable software with less development time and cost, has led to a great interest in CBSE (component based software engineering). The success of such component based systems mainly depends on the effective selection of COTS components among the various alternatives that meet the user's requirements. So, a set of predefined selection criteria must be obtained for the effective selection and evaluation of various COTS components. In this research paper, the identification of various criteria for the selection of COTS component is done, and then these selection criteria are ranked according to their local and global weights.

## 1. Introduction

A significant proportion of the IT portfolio now a day is comprised by the component based software development (CBSD). Component based software development focuses on the development of large software systems by integrating the already existing reusable software components named as COTS. Commercial-off-the-shelf (COTS) is defined as the software pieces that can be further reused by the software developers to build the new software systems. The COTS products are readymade and can be used by the software developers "as it is" and can be easily installed and incorporated with the existing system components. The use of COTS products provides many potential benefits as: (i) Reduction in development cost (ii) Reduction in development time and effort (iii) Improved quality of target software. In spite of many potential benefits, some disadvantages are also associated with the COTS products as (i) Incomplete knowledge of inner working code (ii) Compatibility issues (iii) Unavailability of correct and complete specifications. Unlike the other software development approaches, the success of component based software engineering is dependent on the identification, selection and evaluation of the COTS components. So, before the integration of the various COTS components in the final software there is a need of to qualify adapt these components. For the accurate evaluation of these COTS components, a set of the COTS selection criteria must be identified.

The rest of the paper is structured as follows: Section 2 review various COTS selection criteria available in open literature. The methodology of assigning priority weights to the identified criteria is explained in section 3. Ranking procedure for the COTS selection criteria based on fuzzy set theory is described in section 4. Priority weights and results of ranking of the COTS selection criteria and sub-criteria are provided in section 5. References used in the present research work are given at the end of the paper.

**Corresponding Author,**
**E-mail address:** rkgarg06@gmail.com
**All rights reserved:** http://www.ijari.org

## 2. Review of COTS selection criteria

COTS selection has become very crucial in the component based development approach for the developers and researchers. A lot of research has been done by various researchers to find the COTS selection criteria. Bertoa and Vallecillo [1] proposed a quality model for the component based software development (CBSD) based on ISO 9126, that defines a set of quality attributes as Functionality, Reliability, Usability, Efficiency, Maintainability, Portability etc. and their associated metrics for the effective selection and evaluation of COTS components. Wanyama and Homayoun [2] found that the COTS selection is a complex multi-criteria decision making (MCDM) problem characterized by uncertainty, complexity, multiple stakeholders and multiple objectives. In the contemporary work Rehman et al. [3] present vendor dependence as a major factor in COTS selection.

Huan-Jyh Shyur [4] presented cost, supplier's support, technological risk, closeness of fit to company's business, ease of implementation, flexibility to easy change as the company business change and system integration (CO, SS, TR, FB, EI, FC, SI) as the COTS selection criteria. Neubauer and Stummer [5] solved the problem of COTS selection by categorizing the different COTS selection factors mainly in functional criteria, quality criteria (defect rate, performance, usability, security etc.), strategic criteria (cost, available time etc.) and domain and architectural criteria. Wanyama and Far [6] had addressed the problem of COTS selection using reliability, maintainability, security, portability, compatibility, vendor ability, initial product price, initial hardware price, implementation costs, training costs, license conditions as selection criteria.

Basem Suleiman [7] has addressed the COTS selection problem using system integration interface, functionality aspects, COTS vendor maturity, conformity to system environment (consistency between system requirements, hardware, software application systems and COTS

component infrastructure), budget, time, vendor support as selection criteria. Ibrahim et al. [8] proposed the selection criteria for the COTS component such as usability, security, functionality, performance, recoverability and impact. Ravi chandran et al. [9] listed a large number of COTS selection attributes such as reliability, stability, portability, consistency, completeness, interface and structural complexity, understandability of software documents, security, usability, accuracy, compatibility, performance, serviceability and customizability.

Baharom et al. [10] introduced vendor characteristics such as vendor stability, vendor reputation, vendor supportability and organization characteristics as system platform, development environment, culture and financial characteristic for COTS component selection. Gupta et al. [11] used quality, cost, probability of failure on demand, average no. of invocations, no. of lines of code, execution time, delivery time and quality characteristics as selection criteria. Mittal and Bhatia [12] applied AHP technique for the COTS selection by considering the reusability as selection criteria. Faridi et al. [13] presented the COTS selection on the basis of software quality model ISO/IEC 25010. Faundes et al. [14] proposed PBEC-OTS technique by accounting six criteria as Coverage, Automation, Implementation, Cost, Collaboration, and Participation.

Kaur and Singh [15] used Promethee method for the COTS selection by considering performance, reliability, maintainability, cost and integrability as selection criteria. Khan et al. [16] presented a component based software engineering framework for software reusability. Shah et al. [17] presented various quality criteria as effectiveness, efficiency, satisfaction, safety and usability as component selection criteria. A review of different COTS component selection criteria [1-29] is given in table 1.

## 3. Methodology Adopted

In this research, Fuzzy set theory is used for the ranking of various COTS selection criteria. Fuzzy logic theory which was introduced by Zadeh [18] has proved to be essential for numerous applications. As compared to conventional scale in problems of researches exploratory in nature and where primary data is needed to be collected through surveys i.e. questionnaires, interviews, etc. It is capable to model the vagueness and impreciseness. In fuzzy set theory, the data is collected from the respondents in linguistic variables, qualitative in nature, i.e. Extremely Less Important, Very Less Important, Less Important, Important, More Important, Very More Important, Extremely More Important etc. these linguistic variable are then converted into crisp score, a single numerical value, through fuzzy numbers using membership functions. The algebraic functions can easily be applied on fuzzy numbers. The details on conversion of linguistic variables of a seven point fuzzy scale into corresponding crisp score values is explained in Table 2.

**Table: 1:** Review of COTS component selection criteria

| Criterion/ Sub-Criterion | Author(s) | Jung and Choi | Leung and Leung | Iribrane and Vallecillo | Beetoa and Vallecillo | Wanyama and Homayoun | Rehman et al. | Carvallo et al. | Cortellssa et al. | Sassi et al. | Huan- Jyh shyur | Mohamed et al. | Neubauer and Stummer | Wanyama and H. Far | Basem Suleiman | Rao and Rajesh | Ibrahim et al. | Kaur and Mann | Kwong et al. | Indumati et al. | Tang et al. | Ibrahim et al. | Ravichandran et al. | Baharom et al. | Gupta et al. | Gupta et al. |
|---|---|---|---|---|---|---|---|---|---|---|---|---|---|---|---|---|---|---|---|---|---|---|---|---|---|---|
| | Year | 1999 | 2002 | 2002 | 2002 | 2005 | 2005 | 2006 | 2006 | 2006 | 2006 | 2007 | 2007 | 2008 | 2008 | 2009 | 2009 | 2010 | 2010 | 2011 | 2011 | 2011 | 2012 | 2012 | 2012 | 2013 |
| Quality | | Y | | | | | | | | | | | Y | | | | | | | | | | | | | Y |
| Cost | | Y | | | | | Y | | Y | | Y | | Y | Y | Y | Y | | Y | | Y | | | | | Y | Y |
| Suitability | | | | Y | | | | | | | | | | | | | | | | | | | | | | Y |
| Functionality | | | Y | | Y | | | | | Y | | Y | Y | | Y | | | | Y | | | Y | | | | Y |
| Reliability | | | | | Y | | | | Y | | | | | Y | | | | | | | | | Y | | | Y |
| Reusability | | | | | Y | | | | | | | | Y | | | | | | | | Y | | Y | | | Y |
| Efficiency | | | | | Y | | | | | | | | | | | | | | | | | | | | | Y |
| Maintainability | | | | | Y | | | | | | | | | Y | | | | | | | | | | | | Y |
| Cohesion | | | | | | | | | | | | | | | | | | | Y | Y | | | | | | |
| Coupling | | | | | | | | | | | | | | | | | | | Y | Y | | | | | | |
| Compatibility | | | | | | | | | | | | | | Y | | | | | | | Y | | Y | | | |
| Recoverability | | | | | | | | | | | | | | | | | | | | | | Y | | | | |
| Delivery Time | | | | | | | | | Y | | | | Y | | | | | | | | | | | | Y | |
| Interoperability | | | | | | | | | | | | | | | | | | | | | | | | | | Y |
| Compliance | | | | | | | | | | | | | | | | | | | | | | | | | | Y |
| Maturity | | | | | | | | | | | | | | | | | | | | | | | | | | Y |
| Operability | | | | | | | | | | | | | | | | | | | | | | | | | | Y |
| Testability | | | | | | | | | | | | | | | | | | | | | | | | | | Y |
| Adaptability | | | | | | | | | | | | | | | | | | | | | | | | | | Y |
| Install-ability | | | | | | | | | | | | | | | | | | | | | | | | | | Y |
| Replace-ability | | | | | | | | | | | | | | | | | | | | | | | | | | Y |
| Time Behavior | | | | | | | | | | | | | | | | | | | | | | | | | | Y |
| Resource Behavior | | | | | | | | | | | | | | | | | | | | | | | | | | Y |
| Conformance | | | | | | | | | | | | | | | Y | | | | | | | | | | | Y |
| Technological Risk | | | | | | | | | | | Y | | | | | Y | | | | | | | | | | |
| Closeness of Fit | | | | | | | | | | | Y | Y | | | | Y | | | | | | | | | | |
| Ease of Implementation | | | | | | | | | | | Y | | | | | Y | | | | | | | | | | |
| Flexibility to Change | | | | | | | Y | | | | Y | | | | | Y | | Y | | | | | | | | Y |
| Development Environment | | | | | | | | | | | | | | | | | | | | | | | | Y | | |
| POF on Demand | | | | | | | | | | | | | | | | | | | | | | | | | Y | |
| Line of Code | | | | | | | | | | | | | | | | | | | | | | | | | Y | |
| No. of Invocations | | | | | | | | | | | | | | | | | | | | | | | | | Y | |
| Execution Time | | | | | | | | | | | | | | | | | | | | | | | | | Y | |
| Customizability | | | | | | | | | | | | | | | | | | | | | | | Y | | | |
| Schedule | | | | | | | Y | | | | | | | | | | | | | | | | | | | |
| Multiple Objectives | | | | | | Y | | | | | | | | | | | | | | | | | | | | |
| Impact | | | | | | | | | | | | | | | | | | | | | | Y | | | | |
| Stability | | | | | | | | | | | | | | | | | | | | | | | Y | | | |
| Consistency | | | | | | | | | | | | | | | | | | | | | | | Y | | | |
| Completeness | | | | | | | | | | | | | | | | | | | | | | | Y | | | |
| Interface Complexity | | | | | | Y | | | | | | | Y | | | | | | | | | | Y | | | |
| Understandability | | | | | | | | | | | | | | | | | | | | | | | Y | | | Y |
| Accuracy | | | | | | | | | | | | | | | | | | | | | | | Y | | | Y |
| Compatibility | | | | | | | | | | | | | | | | | | | | | | | Y | | | |
| Serviceability | | | | | | | | | | | | | | | | | | | | | | | Y | | | |
| Vendor Stability | | | | | | | | | | | | | | | Y | | | | | | | | | Y | | |

**Table: 2.** Linguistic terms representation using triangular fuzzy numbers

| Qualitative measures of selection criteria/sub-criteria (Linguistic Variables) | Fuzzy number | Membership function $\mu(x)$ | Right score $\mu_R(M_1)$ | Left score $\mu_L(M_1)$ | Crisp score $\mu_T(M_1)$ |
|---|---|---|---|---|---|
| Extremely Less Important | $M_1(0, 0, 0)$ | $\mu_{M_1}(x) = 1, x = 0$ | 0 | 1 | 0 |
| Very Less Important | $M_2$ (0, 0. 1, 0. 2) | $\mu_{M_2}(x) = \begin{cases} (x-0)/(0,1)\ 0 \le x \le 0.1 \\ (0.2-x)/(0,1)\ 0.1 \le x \le 0.2 \end{cases}$ | 0.1818 | 0.9091 | 0.1364 |
| Less Important | $M_3$ (0.2, 0.3, 0.4) | $\mu_{M_3}(x) = \begin{cases} (x-0.2)/(0,1)\ 0.2 \le x \le 0.3 \\ (0.4-x)/(0,1)\ 0.3 \le x \le 0.4 \end{cases}$ | 0.3636 | 0.7273 | 0.3182 |
| Important | $M_4$(0.4, 0.5, 0.6) | $\mu_{M_4}(x) = \begin{cases} (x-0.4)/(0,1)\ 0.4 \le x \le 0.5 \\ (0.6-x)/(0,1)\ 0.5 \le x \le 0.6 \end{cases}$ | 0.5455 | 0.5455 | 0.5 |
| More Important | $M_5$(0.6, 0.7, 0.8) | $\mu_{M_5}(x) = \begin{cases} (x-0.6)/(0,1)\ 0.6 \le x \le 0.7 \\ (0.8-x)/(0,1)\ 0.7 \le x \le 0.8 \end{cases}$ | 0.7273 | 0.3636 | 0.6818 |
| High/ Very More Important | $M_6$(0.8, 0.9, 1) | $\mu_{M_6}(x) = \begin{cases} (x-0.8)/(0,1)\ 0.8 \le x \le 0.9 \\ (1-x)/(0,1)\ 0.9 \le x \le 1 \end{cases}$ | 0.9091 | 0.1818 | 0.8636 |
| Very high/ Extremely More Important | $M_7$ (1, 1, 1) | $\mu_{M_7}(x) = 1, \quad x = 1$ | 1 | 0 | 1 |

## 4. Ranking Procedure

In this section, a ranking procedure for the ranking of various COTS selection criteria based on their local and global weights is described as:

### 4.1 Ranking Criteria: Identification and Selection

The COTS components can be compared by means of several criteria, collectively termed as ranking criteria. An exhaustive list of such ranking criteria available in open literature has been tabulated in previous section. The major emphasis of the researchers for the selection of COTS components is on the quality characteristics, cost, vendor issues etc. However, each of the ranking criteria relates to some particular aspect of the COTS considered important to the objective of present research work. Using the experience gained from the literature and peer group discussions, seventeen ranking criteria are identified and grouped in four major categories namely (i) Quality characteristics (ii) Technology factors (iii) Domain and architectural factors and (iv) Strategic factors. A hierarchical structure of these ranking criteria is given in Figure 1.

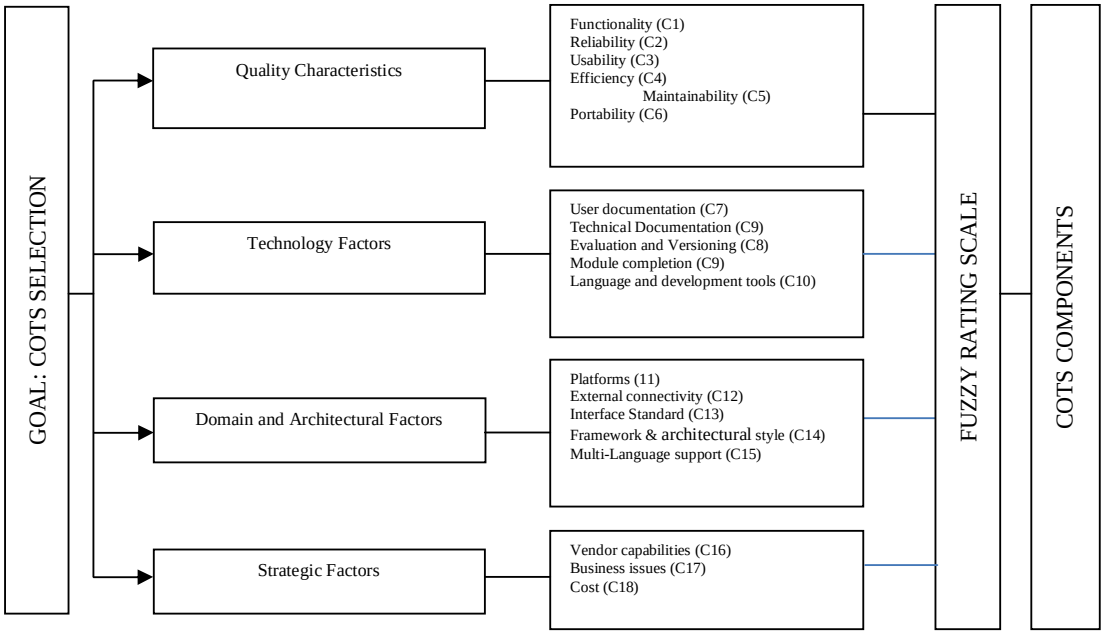


**Fig: 1.** Hierarchal structure of COTS selection criteria

### 4.2 Experts Identification and Selection

There exists a lack of maturity in this field and it is impossible to identify secondary data in the open literature that could constitute the basis for ranking the various COTS selection criteria. Consequently, there is only an alternate to collect primary data and under such circumstances, reliance on expert opinion is the only optimal approach for collection of data. A single expert is sufficient for an expert elicitation process if possesses infinite knowledge and never errs meaning thereby perfect in the field of specialization. The chances of making a mistake or due to limited and inadequacy of the knowledge, it is always better to have more than one expert.

For the present research work, the researchers prepared a list of twenty five potential experts taking experts dependencies' into consideration. Finally, ten experts are selected based on their expertise, subject knowledge going

through brain storming, experience and current position in academia/industry.

### 4.3 Questionnaire Design

The present research is exploratory in nature. Questionnaire is considered to be the best way of collection of data in survey researches which are exploratory in nature. Since, no secondary data is available in the open literature and hence questionnaires are used to collect primary data. A questionnaire is designed to estimate the weights of the various COTS selection criteria identified in this research from the literature. The weights by the experts are provided on a seven point fuzzy scale. The questionnaire is designed in three parts: First part of each questionnaire contains a covering letter which explains the purpose of the research study and statement of confidentiality. Second part consists of demographic details e.g. name of the organization, field of expertise (software development, software design, software purchasing and procurement, etc.); length of experience, qualification and designation, etc. Third part of the questionnaire consists of assigning weights to the selection criteria of the COTS components on a predetermined seven point fuzzy scale.

### 4.4 Data Collection

In this research, the data to calculate the weights for the various selection criteria is provided by the ten experts through a well designed questionnaire, then these linguistic terms are converted in triangular fuzzy numbers and corresponding crisp values by using table 2 as given in section 3.

A statistical analysis was performed on the data obtained from the experts using SPSS. The Cronbach's alpha value, so obtained, was more than 0.8 in case of importance of the ranking criteria. Such a value of Cronbach's alpha indicates higher reliability and internal consistency among the values assigned by the different experts. Aggregation of expert opinions is necessary irrespective of the method of aggregation i.e. Arithmetic or geometric averages being consistently better than the opinions of individual experts. Keeping in consideration that all experts are equally competent, qualified and experienced, and no significant difference was observed in terms credibility and importance, hence all experts are weighted equally and arithmetic averaging aggregation method is adopted going through in-depth analysis of the responses of the experts.

The weights for the various selection criteria in linguistic terms on a seven point fuzzy scale provided by the ten experts are given in Appendix 1. The linguistic terms are converted into corresponding crisp scores on a scale of 0-1 and the average values of the experts rating are done using fuzzy aggregation methods. The corresponding crisp scores and average aggregation values are provided in Table 3.

**Table: 3.** Crisp scores and average values of priority weights of COTS selection criteria

| S. No. | Criterion/Sub-Criterion | E1 | E2 | E3 | E4 | E5 | E6 | E7 | E8 | E9 | E10 | Average |
|---|---|---|---|---|---|---|---|---|---|---|---|---|
| A | Quality Characteristics | | | | | | | | | | | |
| 1 | Functionality | | | | | | | | | | | |
| 1.1 | Accuracy | 1.00 | 1.00 | 1.00 | 0.86 | 0.86 | 0.68 | 1.00 | 1.00 | 0.68 | 0.86 | 0.895 |
| 1.2 | Compliance | 0.68 | 0.50 | 0.50 | 0.86 | 0.50 | 0.68 | 0.86 | 0.50 | 0.50 | 0.68 | 0.627 |
| 1.3 | Interoperability | 0.68 | 0.50 | 0.86 | 0.86 | 0.50 | 0.68 | 0.86 | 0.68 | 0.50 | 0.50 | 0.664 |
| 1.4 | Security | 1.00 | 1.00 | 0.68 | 0.86 | 0.68 | 0.68 | 0.86 | 1.00 | 0.68 | 0.86 | 0.832 |
| 1.5 | Suitability | 0.50 | 0.50 | 0.50 | 0.68 | 0.31 | 0.50 | 0.68 | 0.50 | 0.50 | 0.68 | 0.536 |
| 2 | Reliability | | | | | | | | | | | |
| 2.1 | Fault Tolerance | 0.68 | 0.50 | 0.86 | 0.68 | 0.86 | 0.50 | 0.50 | 0.68 | 0.68 | 0.86 | 0.682 |
| 2.2 | Maturity | 0.50 | 0.31 | 0.68 | 0.50 | 0.50 | 0.31 | 0.68 | 0.31 | 0.31 | 0.50 | 0.464 |
| 2.3 | Recoverability | 0.50 | 0.68 | 1.00 | 0.86 | 0.68 | 0.68 | 0.50 | 1.00 | 0.50 | 0.50 | 0.691 |
| 3 | Usability | | | | | | | | | | | |
| 3.1 | Learn-ability | 0.31 | 0.50 | 0.13 | 0.31 | 0.50 | 0.13 | 0.13 | 0.00 | 0.31 | 0.31 | 0.268 |
| 3.2 | Operability | 0.86 | 1.00 | 0.68 | 0.68 | 0.50 | 0.68 | 0.86 | 0.86 | 0.68 | 1.00 | 0.782 |
| 3.3 | Understandability | 0.68 | 0.68 | 1.00 | 0.68 | 0.50 | 0.68 | 0.50 | 0.86 | 0.50 | 0.68 | 0.677 |
| 4 | Efficiency | | | | | | | | | | | |
| 4.1 | Resource Behavior | 0.50 | 0.31 | 0.86 | 0.50 | 0.68 | 0.31 | 0.50 | 0.50 | 0.31 | 0.68 | 0.518 |
| 4.2 | Time Behavior | 0.68 | 0.50 | 0.86 | 0.86 | 0.68 | 0.68 | 0.50 | 0.68 | 0.50 | 0.50 | 0.645 |
| 5 | Maintainability | | | | | | | | | | | |
| 5.1 | Analyzability | 0.31 | 0.31 | 0.68 | 0.31 | 0.50 | 0.50 | 0.68 | 0.50 | 0.31 | 0.31 | 0.445 |
| 5.2 | Changeability | 0.50 | 0.50 | 0.86 | 0.68 | 0.50 | 0.50 | 0.68 | 0.31 | 0.50 | 0.31 | 0.536 |
| 5.3 | Stability | 1.00 | 0.68 | 0.86 | 0.68 | 0.68 | 0.86 | 1.00 | 0.86 | 0.86 | 0.68 | 0.818 |
| 5.4 | Testability | 0.86 | 1.00 | 1.00 | 0.68 | 0.86 | 0.68 | 0.86 | 0.86 | 1.00 | 1.00 | 0.882 |
| 6 | Portability | | | | | | | | | | | |
| 6.1 | Adaptability | 0.68 | 0.68 | 0.86 | 0.68 | 0.50 | 0.68 | 0.68 | 0.86 | 0.86 | 0.50 | 0.700 |
| 6.2 | Conformance | 0.50 | 0.50 | 0.50 | 0.31 | 0.68 | 0.50 | 0.31 | 0.31 | 0.50 | 0.50 | 0.464 |
| 6.3 | Installability | 0.68 | 0.86 | 0.86 | 0.50 | 0.50 | 0.68 | 0.68 | 0.86 | 0.50 | 0.68 | 0.682 |
| 6.4 | Replaceabilty | 0.31 | 0.50 | 0.31 | 0.31 | 0.13 | 0.31 | 0.50 | 0.31 | 0.31 | 0.50 | 0.355 |
| B | Technology Factors | | | | | | | | | | | |
| 7 | User Documentation | 0.68 | 0.68 | 0.50 | 0.31 | 0.50 | 0.50 | 0.68 | 0.31 | 0.31 | 0.50 | 0.500 |
| 8 | Technical Documentation | 0.86 | 0.68 | 0.86 | 0.50 | 0.50 | 0.50 | 0.68 | 0.86 | 0.86 | 0.68 | 0.700 |
| 9 | Evaluation and Versioning | 0.50 | 0.68 | 1.00 | 0.68 | 0.86 | 0.68 | 0.68 | 0.50 | 0.86 | 0.68 | 0.714 |
| 10 | Module completion | 0.68 | 0.68 | 0.68 | 0.50 | 0.50 | 0.31 | 0.68 | 0.50 | 0.68 | 0.31 | 0.555 |

| | | | | | | | | | | | | |
|---|---|---|---|---|---|---|---|---|---|---|---|---|
| 11 | Language and Development Tools | 0.31 | 0.68 | 0.86 | 0.68 | 0.68 | 0.50 | 0.31 | 0.31 | 0.50 | 0.68 | 0.555 |
| C | Domain And Architectural Factors | | | | | | | | | | | |
| 12 | Platforms | 0.68 | 0.50 | 0.86 | 0.50 | 0.68 | 0.86 | 0.31 | 0.50 | 0.68 | 0.68 | 0.627 |
| 13 | External Connectivity | 0.68 | 0.68 | 0.86 | 0.68 | 0.50 | 0.50 | 0.68 | 0.86 | 0.68 | 0.50 | 0.664 |
| 14 | Interface Standard | 0.86 | 0.68 | 0.68 | 0.50 | 0.50 | 0.68 | 0.86 | 0.86 | 0.68 | 0.50 | 0.682 |
| 15 | Framework and Architectural Style | 0.68 | 0.68 | 0.86 | 0.68 | 0.86 | 0.86 | 0.50 | 0.86 | 0.68 | 0.68 | 0.736 |
| 16 | Multi-Language Support | 0.31 | 0.50 | 0.86 | 0.50 | 0.68 | 0.31 | 0.31 | 0.50 | 0.68 | 0.50 | 0.518 |
| D | Strategic Factors | | | | | | | | | | | |
| 17 | Vendor Capabilities | | | | | | | | | | | |
| 17.1 | Market Trends | 0.50 | 0.31 | 0.86 | 0.50 | 0.50 | 0.68 | 0.31 | 0.31 | 0.50 | 0.68 | 0.518 |
| 17.2 | Training and Support | 0.68 | 0.31 | 0.50 | 0.50 | 0.50 | 0.68 | 0.68 | 0.68 | 0.31 | 0.50 | 0.536 |
| 17.3 | Vendor Reputation | 0.68 | 0.50 | 0.68 | 0.31 | 0.31 | 0.50 | 0.68 | 0.50 | 0.50 | 0.31 | 0.500 |
| 17.4 | Vendor Location | 0.50 | 0.50 | 0.68 | 0.50 | 0.50 | 0.50 | 0.31 | 0.68 | 0.31 | 0.50 | 0.500 |
| 17.5 | R & D Technology | 0.50 | 0.50 | 0.31 | 0.50 | 0.50 | 0.31 | 0.68 | 0.31 | 0.31 | 0.31 | 0.427 |
| 17.6 | Financial Condition | 0.86 | 0.68 | 0.68 | 0.50 | 0.50 | 0.68 | 0.86 | 0.68 | 0.68 | 0.50 | 0.664 |
| 17.7 | Implementation and Serviceability | 0.68 | 0.68 | 0.86 | 0.50 | 0.50 | 0.50 | 0.50 | 0.68 | 0.86 | 0.68 | 0.645 |
| 18 | Business Issues | | | | | | | | | | | |
| 18.1 | Licensing Arrangements | 0.86 | 0.86 | 0.50 | 0.68 | 0.68 | 0.50 | 0.86 | 0.68 | 0.50 | 0.50 | 0.664 |
| 18.2 | Organizational Policies | 1.00 | 0.68 | 0.86 | 0.68 | 0.68 | 0.68 | 1.00 | 0.68 | 0.86 | 0.68 | 0.782 |
| 18.3 | Risk factors | 0.86 | 0.86 | 0.68 | 0.86 | 0.86 | 0.86 | 0.68 | 0.86 | 0.68 | 0.68 | 0.791 |
| 19 | Cost | | | | | | | | | | | |
| 19.1 | Production Cost | 0.68 | 0.68 | 1.00 | 0.86 | 0.68 | 0.86 | 0.86 | 0.68 | 0.50 | 0.68 | 0.750 |
| 19.2 | Installation and Implementation Cost | 0.86 | 0.68 | 0.68 | 0.50 | 0.68 | 0.50 | 0.86 | 0.68 | 0.50 | 0.50 | 0.645 |
| 19.3 | License Cost | 0.86 | 0.50 | 0.31 | 0.50 | 0.50 | 0.68 | 0.31 | 0.31 | 0.50 | 0.50 | 0.500 |
| 19.4 | Upgradation And Maintenance Cost | 0.68 | 0.50 | 0.86 | 0.50 | 0.68 | 0.68 | 0.50 | 0.86 | 0.86 | 0.50 | 0.664 |

### 4.5 Calculation of Criteria Weights

The weights (local and global) of the ranking criteria are estimated using the adopted methodology as explained in previous sections and are summarized in Table 4.

**Table: 4:** Weights (Local and Global) for ranking criteria

| S. No. | Criterion/Sub-Criterion | Local Wt. | Global Wt. | S. No. | Criterion/Sub-Criterion | Local Wt. | Global Wt. |
|---|---|---|---|---|---|---|---|
| **Quality Characteristics** | | 0.470 | 0.470 | **Domain & architectural factors** | | 0.115 | 0.115 |
| C1 | Functionality | 0.270 | 0.127 | C12 | Platforms | 0.194 | 0.022 |
| C2 | Reliability | 0.131 | 0.066 | C13 | External connectivity | 0.206 | 0.024 |
| C3 | Usability | 0.131 | 0.062 | C14 | Interface standard | 0.211 | 0.024 |
| C4 | Efficiency | 0.088 | 0.042 | C15 | Framework & architectural style | 0.228 | 0.026 |
| C5 | Maintainability | 0.204 | 0.096 | C16 | Multi-language support | 0.161 | 0.019 |
| C6 | Portability | 0.167 | 0.079 | **Strategic Factors** | | 0.307 | 0.307 |
| **Technology Factors** | | 0.108 | 0.108 | C17 | Vendor capabilities | 0.442 | 0.135 |
| C7 | User Documentation | 0.165 | 0.018 | C18 | Business Issues | 0.261 | 0.080 |
| C8 | Technical Documentation | 0.232 | 0.025 | C19 | Cost | 0.298 | 0.091 |
| C9 | Evaluation and versioning | 0.236 | 0.026 | | | | |
| C10 | Module completion | 0.184 | 0.020 | | | | |
| C11 | Language and development tools | 0.184 | 0.020 | | | | |

### 4.6 Ranking of Criteria Weights

Finally, the various selection criteria and sub-criteria identified in this research are ranked on the basis of their global weights as given in tables 5 and 6 respectively.

**Table: 5.** Ranking of selection criteria

| S. No. | Criterion | Global Weight | Ranking |
|---|---|---|---|
| 1 | Quality Characteristics | 0.470 | 1 |
| 2 | Technology Factors | 0.108 | 4 |
| 3 | Doman and Architectural Factors | 0.115 | 3 |
| 4 | Strategic Factors | 0.307 | 2 |

**Table: 6.** Ranking of selection sub-criteria

| S. No. | Sub-Criterion | Global Weight | Ranking |
|---|---|---|---|
| 1 | Vendor capabilities | 0.135 | 1 |
| 2 | Functionality | 0.127 | 2 |
| 3 | Maintainability | 0.096 | 3 |
| 4 | Cost | 0.091 | 4 |

| | | | |
|---|---|---|---|
| 5 | Business Issues | 0.08 | 5 |
| 6 | Portability | 0.079 | 6 |
| 7 | Reliability | 0.066 | 7 |
| 8 | Usability | 0.062 | 8 |
| 9 | Efficiency | 0.042 | 9 |
| 10 | Evaluation and versioning | 0.026 | 10 |
| 11 | Framework & architectural style | 0.026 | 11 |
| 12 | Technical Documentation | 0.025 | 12 |
| 13 | External connectivity | 0.024 | 13 |
| 14 | Interface standard | 0.024 | 14 |
| 15 | Platforms | 0.022 | 15 |
| 16 | Module completion | 0.02 | 16 |
| 17 | Language and development tools | 0.02 | 17 |
| 18 | Multi-language support | 0.019 | 18 |
| 19 | User Documentation | 0.018 | 19 |

## 5. Results and Conclusion

According to the methodology adopted in the illustrated example, the higher value of global weight of selection criteria depicts the better ranking. The comparative rankings of all four criteria namely quality characteristics, technology factors, domain and architectural factors and strategic factors are given in Fig: 2.

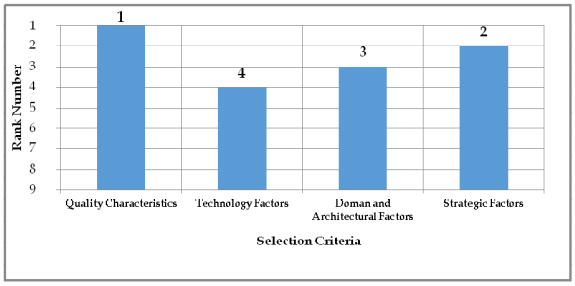


**Fig: 2.** Ranking of COTS selection criteria

Figure depicts that 'Quality Characteristics' selection criteria is ranked at number 1 based on global weights and is followed by 'Strategic Factors' and 'Domain and Architectural Factors'. 'Technology Factors' selection criterion is ranked at the last position or at number 4. Ranking of sub-criteria based on their global weights is shown in figure 3.

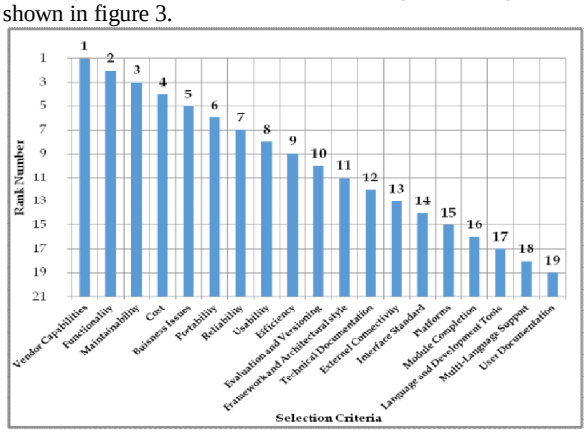


**Fig: 3.** Ranking of COTS selection sub-criteria

Figure depicts that 'Vendor Capabilities' is ranked at number 1 followed by 'Functionality' at number 2 and 'Maintainability' at number 3. The 'User Documentation' selection criterion is of least importance and ranked at number 19 or at last position.

From the above discussions, it is well established that expert opinion is a better method to determine the priority weights of the various COTS selection criteria and sub-criteria. Fuzzy method is suitable to overcome the fuzziness of the data and vagueness of the mind while estimating the priority weights of the criteria or sub-criteria.

## References

[1] F. Manuel, Y Bertoa, Antonio Vallecillo, Quality Attributes for COTS Components, 2002

[2] Tom Wanyama, and BehrouzHomayoun Far, Towards Providing Decision Support for COTS Selection, Canda, IEEE, 0-7803-8886-0/05 CCECE/CCGEI, Saskatoon, 2005.

[3] Maree Mujeeb-u-Rehman, Xiaohu Yang, Jinxiang Dong and Memon Abdul Ghafoor, Prioritized Selecting COTS Vendor in cots-based software development process, China, IEEE, 0-7803-8886-0/05 CCECE/CCGEI, Saskatoon, 2005.

[4] Huan-JyhShyur, COTS evaluation using modified TOPSIS and ANP, Applied Mathematics and Computation, 177, 2006, 251–259

[5] Thomas Neubauer and Christian Stummer, Interactive Decision Support for Multi-objective COTS Selection, IEEE, Proceedings of the 40th Annual Hawaii International Conference on System Sciences (HICSS'07) 0-7695-2755-8/07, 2007.

[6] Tom Wanyama and Behrouz H. Far, AN EMPIRICAL STUDY TO COMPARE THREE METHODS FOR SELECTING COTS SOFTWARE COMPONENTS, International Journal of Computing and ICT Research, 1(2), 2008, 34 - 46

[7] Basem Suleiman, Commercial-Off-The-Shelf Software Development Framework, Australia, IEEE, 19th Australian Conference on Software Engineering 1530-0803/08 DOI 10.1109/ASWEC.2008.73, 2008.

[8] Hamdy Ibrahim, Behrouz H. Far and Armin Eberlein, Tradeoff and Sensitivity Analysis of a Hybrid Model for Ranking Commercial Off-The-Shelf Products,

UAE, 16th Annual IEEE International Conference and Workshop on the Engineering of Computer Based Systems, 978-0-7695-3602-6/09, DOI 10.1109/ECBS.2009.47.

[9] K. S. Ravichandran, P. Suresh, K. R. Sekr, ANFIS Approach for Optimal Selection of Reusable Components, India, Research Journal of Applied Sciences, Engineering and Technology, 4(24), 2012, 5304-5312

[10] Fauziah Baharom, Feras Tarawneh, Jamaiah Hj. Yahaya, AzidaZainol, NurnasranPuteh, HaslinaMohd, NoridaMuhdDarus, ZaharinMarzuki Matt and AzmanYasin, The Vendor and User Organizations Characteristics for COTS Software Evaluation and Selection, Malaysia, Knowledge Management International Conference (KMICe), 2012

[11] P. Gupta, Hoang Pham, Mukesh Kumar Mehlawat, Shilpi Verma, A Fuzzy Optimization Framework for COTS Products Selection of Modular Software Systems, International Journal of Fuzzy Systems, 15(2), 2013

[12] Framework for Evaluating and Ranking the Reusability of COTS Components based upon Analytical Hierarchy Process, Sonu Mittal, Pardeep kumar Bhatia, International journal of innovations in engineering and technology, 2(4), 2013

[13] M. Shakeel Faridi, Zahid Javed, M. Haris Abid, Mudassar Ahmed, Md Asri Bin Ngadi, IROTS: A Proposed COTS evaluation & selection methodolgy for component based software engineering in under developemnt countries, 2nd International Conference on Advances in Computer Science and Engineering (CSE 2013)

[14] Maria Jesus Faundes, Hernan Astudillo and Bernhard Hitpass, Process based evaluation and comarison of OTS software alternatives, Federated Conference on Computer Science and Information Systems 2013.

[15] Kulbir Kaur, Harshpreet Singh, Quantifying COTS Components Selection using Multi Criteria Decision Analysis Method PROMETHEE, Global Journal of Computer Science and Technology: Software & Data Engineering, 2014

[16] Adnan Khan, Khalid Khan, Muhammad Amir, M. N. A. Khan, Shaheed Zulfikar Ali, A component-based framework for software reusability, International Journal of Software Engineering and Its Applications, 8(10), 2014, 13-24

[17] Shah Nazir, Sajid Anwar, Sher Afzal Khan,Sara Shahzad, Muhammad Ali, Rohul Amin, Muhammad Nawaz, Pavlos Lazaridis, John Cosmas, Software component selection based on quality criteria using analytic network process,. Abstract and Applied Analysis, 2014

[18] Ho-Won Jung, Byoungju Choi, Optimization models for quality and cost of modular software systems, South Korea, European Journal of Operational Research, 112, 1999, 613-619

[19] P. Gupta, Mukesh Kumar Mehlawat and ShilpiVerma, COTS selection using fuzzy interactive approach, India, Springer, 2012

[20] R. V. Rao, T. S. Rajesh, Software Selection in Manufacturing Industries Using a Fuzzy Multiple Criteria Decision Making Method, PROMETHEE, Surat, India,Intelligent Information Management, 2009, 1, 159-165.

[21] Arvinder Kaur and Kulvinder Singh Mann, Component Selection for Component based Software Engineering, International Journal of Computer Applications (0975 – 8887), 2(1), 2010

[22] Indumati, Vijay M. Ghantasalaand P. C Jha, Optimal Component Selection of COTS based Modular Software System under Cohesion & Coupling Quality Metrics with Budgetary Constraint, Proceedings of the 5th National Conference; INDIA Com, 2011.

[23] Luis Iribarne, Jos´e M. Troya and Antonio Vallecillo, Selecting Software Components with Multiple Interfaces, IEEE, Proceedings of the 28th Euromicro Conference (EUROMICRO'02) 1089-6503/02, 2002

[24] R. P. Karl, H. Leung, Hareton K. N. Leung, On the efficiency of domain-based COTS product selection method, China, Information and Software Technology, 44, 2002, 703–715

[25] Sihem Ben Sassi, Lamia Labed, Jilani Henda Hajjami, Ben Ghezala, Towards a COTS-Based Development Environment, Tunisia, IEEE, Proceedings of the Fifth International Conference on Commercial-off-the-Shelf (COTS)-Based Software Systems (ICCBSS 2006) 0-7695-2515-6/06, 2006

[26] Abdallah Mohamed, Guenther Ruhe and Armin Eberlein, COTS Selection: Past, Present, and Future, Canada, IEEE, Proceedings of the 14th Annual IEEE International Conference and Workshops on the Engineering of Computer-Based Systems (ECBS'07) 0-7695-2772-8/07.

[27] C. K. Kwong, L. F. Mu, J. F. Tang, X. G. Luo, Optimization of software components selection for component-based software system development, China, , Computers & Industrial Engineering 58 (2010) 618–624.

[28] J. F. Tang, L.F. Mu, C. K. Kwong, X.G. Luo, An optimization model for software component selection under multiple applications development, China, European Journal of Operational Research, 212, 2011, 301–311

[29] G. Grau, J. P. Carvallo, X. Franch, C. Quer, Des COTS: A Software System for Selecting COTS Components," in EUROMICRO'04, Rennes, France, 2004, 118-126.

[30] Hamdy Ibrahim, Abdel-Halim H. Elamy, Behrouz H. Far, Armin Eberlein, Un HOS: A Method for Uncertainty Handling in Commercial Off-The-Shelf (COTS) Selection, International Journal of Energy, Information and Communications, 2(3), 2011

APPENDIX – 1

Priority weights of COTS selection criteria and sub-criteria assigned by Experts in linguistic terms

| S. No. | Criterion/Sub-Criterion | E1 | E2 | E3 | E4 | E5 | E6 | E7 | E8 | E9 | E10 |
|---|---|---|---|---|---|---|---|---|---|---|---|
| A | Quality Characteristics | | | | | | | | | | |
| 1 | Functionality | | | | | | | | | | |

| | | | | | | | | | | | |
|---|---|---|---|---|---|---|---|---|---|---|---|
| 1.1 | Accuracy | EMI | EMI | EMI | VMI | VMI | MI | EMI | EMI | MI | VMI |
| 1.2 | Compliance | MI | I | I | VMI | I | MI | VMI | I | I | MI |
| 1.3 | Interoperability | MI | I | VMI | VMI | I | MI | VMI | MI | I | I |
| 1.4 | Security | EMI | EMI | MI | VMI | MI | MI | VMI | EMI | MI | VMI |
| 1.5 | Suitability | I | I | I | MI | LI | I | MI | I | I | MI |
| 2 | Reliability | | | | | | | | | | |
| 2.1 | Fault Tolerance | MI | I | VMI | MI | VMI | I | I | MI | MI | VMI |
| 2.2 | Maturity | I | LI | MI | I | I | LI | MI | LI | LI | I |
| 2.3 | Recoverability | I | MI | EMI | VMI | MI | MI | I | EMI | I | I |
| 3 | Usability | | | | | | | | | | |
| 3.1 | Learnability | LI | I | LI | LI | I | VLI | LI | ELI | LI | LI |
| 3.2 | Operability | VMI | EMI | MI | MI | I | MI | VMI | VMI | MI | EMI |
| 3.3 | Understandability | MI | MI | EMI | MI | I | MI | I | VMI | I | MI |
| 4 | Efficiency | | | | | | | | | | |
| 4.1 | Resource Behavior | I | LI | VMI | I | MI | LI | I | I | LI | MI |
| 4.2 | Time Behavior | MI | I | VMI | VMI | MI | MI | I | MI | I | I |
| 5 | Maintainability | | | | | | | | | | |
| 5.1 | Analyzability | LI | LI | MI | LI | I | I | MI | I | LI | LI |
| 5.2 | Changeability | I | I | VMI | MI | I | I | MI | LI | I | LI |
| 5.3 | Stability | EMI | MI | VMI | MI | MI | VMI | EMI | VMI | VMI | MI |
| 5.4 | Testability | VMI | EMI | EMI | MI | VMI | MI | VMI | VMI | EMI | EMI |
| 6 | Portability | | | | | | | | | | |
| 6.1 | Adaptability | MI | MI | VMI | MI | I | MI | MI | VMI | VMI | I |
| 6.2 | Conformance | I | I | I | LI | MI | I | LI | LI | I | I |
| 6.3 | Installability | MI | VMI | VMI | I | I | MI | MI | VMI | I | MI |
| 6.4 | Replaceabilty | LI | I | LI | LI | VLI | LI | I | LI | LI | I |
| B | Technology Factors | | | | | | | | | | |
| 7 | User Documentation | MI | MI | I | LI | I | I | MI | LI | LI | I |
| 8 | Technical Documentation | VMI | MI | VMI | I | I | I | MI | VMI | VMI | MI |
| 9 | Evaluation and Versioning | I | MI | EMI | MI | VMI | MI | MI | I | VMI | MI |
| 10 | Module completion | MI | MI | MI | I | I | LI | MI | I | LI | LI |
| 11 | Language and Development Tools | LI | MI | VMI | MI | MI | I | LI | LI | I | MI |
| C | Domain And Architectural Factors | | | | | | | | | | |
| 12 | Platforms | MI | I | VMI | I | MI | VMI | LI | I | MI | MI |
| 13 | External Connectivity | MI | MI | VMI | MI | I | I | MI | VMI | MI | I |
| 14 | Interface Standard | VMI | MI | MI | I | I | MI | VMI | VMI | MI | I |
| 15 | Framework and Architectural Style | MI | MI | VMI | MI | VMI | VMI | I | VMI | MI | MI |
| 16 | Multi-Language Support | LI | I | VMI | I | MI | LI | LI | I | MI | I |
| D | Strategic Factors | | | | | | | | | | |
| 17 | Vendor Capabilities | | | | | | | | | | |
| 17.1 | Market Trends | I | LI | VMI | I | I | MI | LI | LI | I | MI |
| 17.2 | Training and Support | MI | LI | I | I | I | MI | MI | MI | LI | I |
| 17.3 | Vendor Reputation | MI | I | MI | LI | LI | I | MI | I | I | LI |
| 17.4 | Vendor Location | I | I | MI | I | I | I | LI | MI | LI | I |
| 17.5 | R & D Technology | I | I | LI | I | I | LI | MI | LI | LI | LI |
| 17.6 | Financial Condition | VMI | MI | MI | I | I | MI | VMI | MI | MI | I |
| 17.7 | Implementation and Serviceability | MI | MI | VMI | I | I | I | I | MI | VMI | MI |
| 18 | Business Issues | | | | | | | | | | |
| 18.1 | Licensing Arrangements | VMI | VMI | I | MI | MI | I | VMI | MI | I | I |
| 18.2 | Organizational Policies | EMI | MI | VMI | MI | MI | MI | EMI | MI | VMI | MI |
| 18.3 | Risk factors | VMI | VMI | MI | VMI | VMI | VMI | MI | VMI | MI | MI |
| 19 | Cost | | | | | | | | | | |
| 19.1 | Production Cost | MI | MI | EMI | VMI | MI | VMI | VMI | MI | I | MI |
| 19.2 | Installation and Implementation Cost | VMI | MI | MI | I | MI | I | VMI | MI | I | I |
| 19.3 | License Cost | VMI | I | LI | I | I | MI | LI | LI | I | I |
| 19.4 | Upgradation And Maintenance Cost | MI | I | VMI | I | MI | MI | I | VMI | VMI | I |

Hindawi Publishing Corporation
International Journal of Medicinal Chemistry
Volume 2016, Article ID 2741038, 13 pages
http://dx.doi.org/10.1155/2016/2741038

*Research Article*

# *In Silico* Designing and Analysis of Inhibitors against Target Protein Identified through Host-Pathogen Protein Interactions in Malaria

**Monika Samant,[1] Nidhi Chadha,[2] Anjani K. Tiwari,[2] and Yasha Hasija[1]**

[1]*Department of Biotechnology, Delhi Technological University, Main Bawana Road, Shahbad Daulatpur, Delhi 110042, India*
[2]*Division of Cyclotron and Radiopharmaceutical Sciences, Institute of Nuclear Medicine and Allied Sciences, Brig. S. K. Mazumdar Road, Delhi 110054, India*

Correspondence should be addressed to Yasha Hasija; yashahasija@gmail.com

Received 9 October 2015; Revised 13 November 2015; Accepted 17 November 2015

Academic Editor: Armando Rossello

Copyright © 2016 Monika Samant et al. This is an open access article distributed under the Creative Commons Attribution License, which permits unrestricted use, distribution, and reproduction in any medium, provided the original work is properly cited.

Malaria, a life-threatening blood disease, has been a major concern in the field of healthcare. One of the severe forms of malaria is caused by the parasite *Plasmodium falciparum* which is initiated through protein interactions of pathogen with the host proteins. It is essential to analyse the protein-protein interactions among the host and pathogen for better understanding of the process and characterizing specific molecular mechanisms involved in pathogen persistence and survival. In this study, a complete protein-protein interaction network of human host and *Plasmodium falciparum* has been generated by integration of the experimental data and computationally predicting interactions using the interolog method. The interacting proteins were filtered according to their biological significance and functional roles. $\alpha$-tubulin was identified as a potential protein target and inhibitors were designed against it by modification of amiprophos methyl. Docking and binding affinity analysis showed two modified inhibitors exhibiting better docking scores of −10.5 kcal/mol and −10.43 kcal/mol and an improved binding affinity of −83.80 kJ/mol and −98.16 kJ/mol with the target. These inhibitors can further be tested and validated *in vivo* for their properties as an antimalarial drug.

## 1. Introduction

Malaria, one of the most distressing diseases, is caused by the parasitic protozoan *Plasmodium falciparum*. It takes away millions of lives with the rate increasing each growing year. According to WHO's Factsheet on the World Malaria Report 2013, 1.2 billion people out of a total of an estimated 3.4 billion are at a high risk of malaria. Malaria is highly prevalent in sub-Saharan Africa where 90% of all malaria deaths occur (WHO 2013). A lot of research has been going on in the field of malarial therapeutics. Nowadays, there are a wide variety of antimalarial drugs, such as chloroquine and artemisinin, and strategies available for the control and treatment of malaria [1–3].

Despite clinical researches in the field of infectious diseases, it remains to be a major problem in the worldwide health issue [4–6]. Exploring the infection process in detail can help in deciphering the mechanisms that govern and control it. In the process of evolution, pathogens have evolved an infection mechanism and humans have evolved immune responses as defense mechanism. A majority of host-pathogen interactions are governed by specific protein-protein interactions [7–9]. To obtain a deep understanding of the infection process, specific interactions between the host and pathogen need to be studied [10–15]. Host-pathogen protein interactions are typically studied using conventional small-scale methods which focuses on single protein at a time. Few methods for large-scale discovery have also been developed such as yeast two-hybrid experiments which allow more comprehensive identification but are expensive and time consuming. Computational methods are less time consuming and cost-effective and hence are a better alternative for the prediction of protein interactions [10, 16–20].

Several studies in the field of computational prediction of host-pathogen interactions and drug discovery have shown significant results. Dyer et al. developed a computational

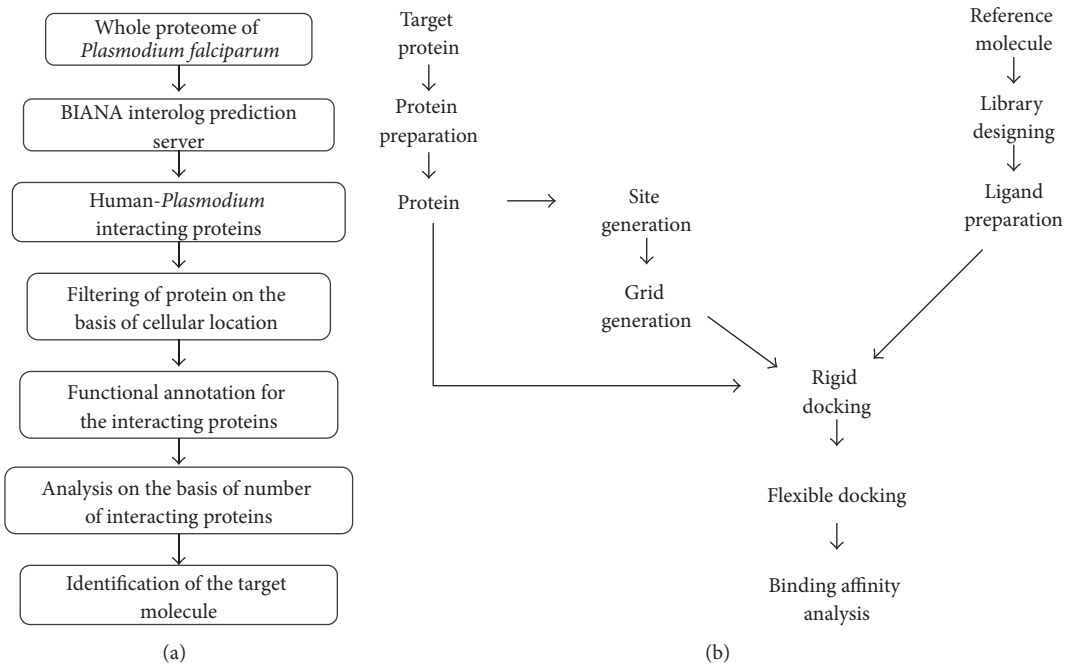


Figure 1: Flowchart of methodology. (a) Identification of the target molecule by filtering and analysis of the protein interactions predicted by BIPS. (b) Docking and binding affinity analysis of the target protein and modified inhibitors.

method to identify protein interactions which uses known PPIs to identify functional domains in interacting pairs and Bayesian statistics for assessing the probability of interaction of two proteins. In this study they observed that interacting pairs were coexpressed [10]. Krishnadev and Srinivasan adopted a homology based approach for identification of protein interactions between *Plasmodium falciparum* and its human host [21]. Lee et al. used an ortholog approach to predict protein interactions in human-*Plasmodium* system. They compared these interactions with Bayesian and structure based approaches [22]. Durmuş Tekir et al. created Pathogen-Host Interaction Search Tool (PHISTO), a web accessible tool that provides up-to-date information of experimentally verified data on protein interactions. The tool offers integrated visualization of pathogen-host interaction networks, BLAST search, text mining for detecting missing experimental methods, and graph-theoretical analysis of targeted human proteins [23]. Rapanoel et al. adopted interolog method for prediction of protein interactions between *Mycobacterium tuberculosis* and its human host. This method predicted interactions using experimentally known intraspecies and interspecies interactions and filtered proteins on several parameters, such as cellular location and cellular function, to confirm the practicality of the predictions. Function analysis of the predicted interactions is carried out to analyse the role of proteins in infection process [24]. These studies have contributed to the knowledge of protein interactions through different methods, but a lot is still unknown in the field of malarial therapeutics.

In this study, a complete protein interaction network between human host and *Plasmodium falciparum* has been developed by integration of experimental and computational methods. Experimental interactions are obtained from PHISTO and STRING. Interolog method is adopted, which hypothesizes that a set of two proteins, each from different species, can be predicted as possible interactions if their respective homologs are found to be interacting in any single species. Interaction network is used as a platform for identification of potential drug target.

Microtubule is a heterodimer consisting of two subunits, that is, $\alpha$-tubulin and $\beta$-tubulin. These subunits bind to each other and make a small subunit which polymerizes to make complete microtubule. It is very important for structural integrity of cells [25, 26]. After the analysis of predicted protein interactions, $\alpha$-tubulin, a validated target in the malarial infection [27], was found to be one of the highest interacting proteins in malarial infection. The eventual aim of this study is to design an efficient drug molecule for the target. Several tubulin mitotic inhibitors such as benzimidazole, dinitroanilines are already present in the literature which interact with these proteins and hinder the infection process. We have included the study in Figures 10(a) and 10(b). Amiprophos methyl prevents erythrocytic schizogony and blocks mitosis in *Plasmodium falciparum* infection and results in abnormal microtubule accumulation. This suggests that amiprophos methyl is worthy of investigation for its antimalarial potential. Amiprophos methyl is a validated tubulin inhibitor in reference studies and is found to have least mammalian toxicity [27, 28]. Therefore, derivatives of amiprophos methyl were designed by carrying out modifications at preferred locations with several functional groups. Finally, a molecule is identified which has better binding

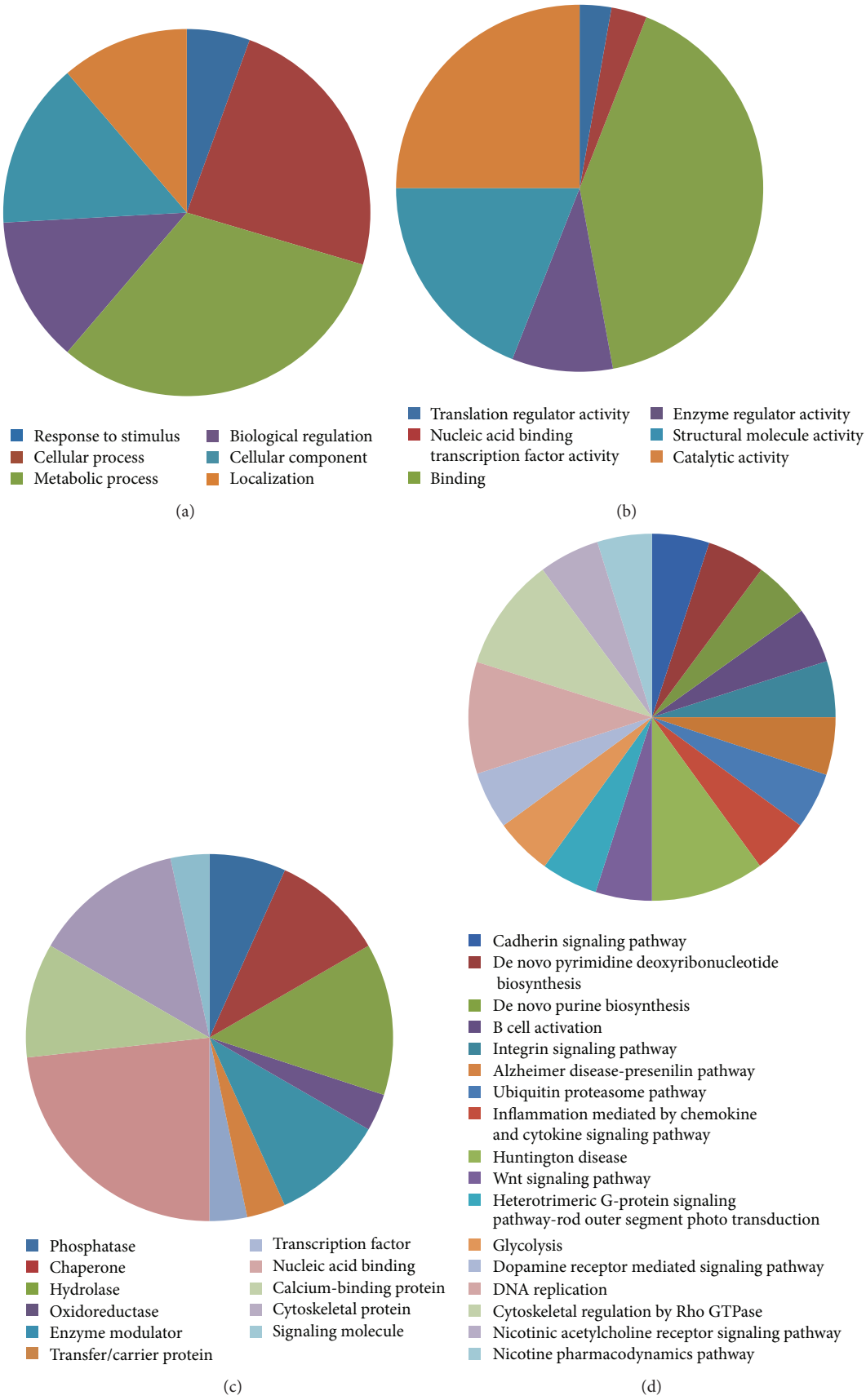


Figure 2: Pie chart representation of pathogen protein classified on the basis of (a) biological process, (b) molecular function, (c) protein class, and (d) pathway.

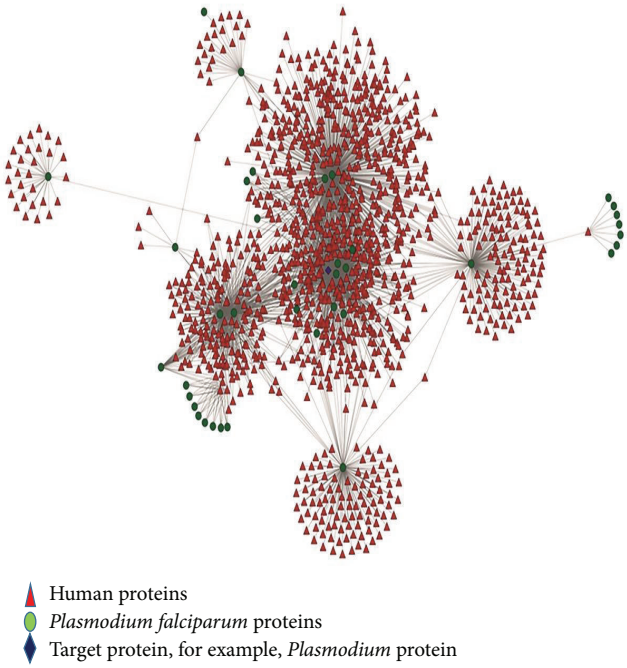


Figure 3: Protein-protein interaction network of human host and *Plasmodium falciparum*. Different colours and shapes are representing proteins of different species.

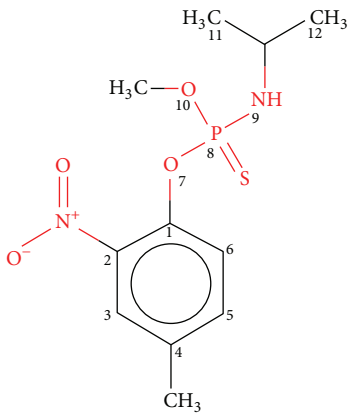


Figure 4: Molecular structure of amiprophos methyl.

affinity than the reference molecule which can be considered as a novel drug molecule.

## 2. Methodology

Whole methodology is divided into two major parts as shown in Figure 1. First part includes identification of target molecule through protein interaction network while the second part involves docking analysis of the target with designed inhibitors.

*2.1. Host-Pathogen Interactions.* The complete protein interaction network was developed by integration of experimentally found interactions, interaction data fetched from protein interaction database STRING, and computationally predicted interactions.

The computational prediction of host-pathogen protein interactions was carried out through BIPS, that is, BIANA interolog prediction server (http://sbi.imim.es/web/index.php/research/servers/bips) [29]. The whole proteome of *Plasmodium falciparum*, downloaded from UniProt (http://www.uniprot.org/), was taken as an input by the server and the predicting protein partner was restricted to *Homo sapiens*. The predicted interactions were annotated for their cellular location, gene ontologies, and functional processes, using the Database for Annotation, Visualization, and Integrated Discovery (DAVID), Functional Annotation Chart tool [30, 31], and Panther [32]. These protein

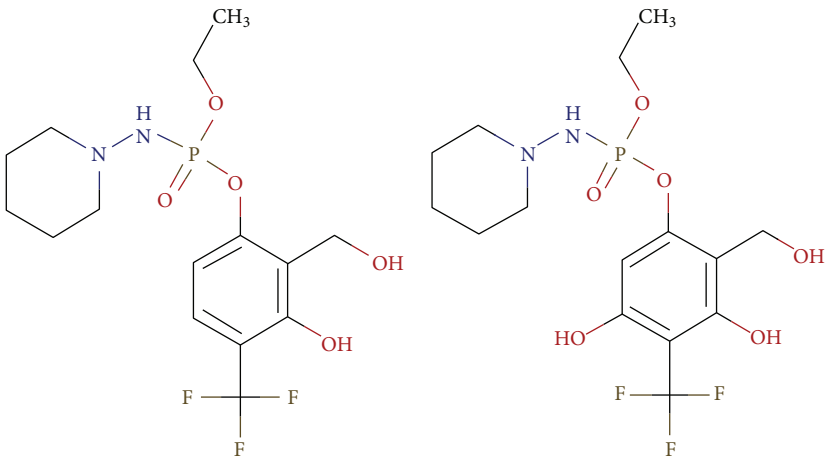


Figure 5: Molecular structure of final shortlisted molecules.

interactions were then functionally annotated for the functional processes and pathways involved.

The experimental protein interactions were obtained from PHISTO, that is, Pathogen-Host Interaction Search Tool (http://www.phisto.org/). The PHISTO server has a drop-down menu where one can select the type of pathogen for which experimentally known interactions with human are desired [23].

STRING (Search Tool for the Retrieval of Interacting Genes/Proteins) is a database for known and predicted protein interactions for a large number of organisms. The complete database was downloaded and data mining was performed in the following two steps:

(1) The interactions with a sum score more than 900 were filtered.

(2) Interacting proteins were then filtered on the basis of participating organism (*Homo sapiens-Plasmodium falciparum* interactions).

Protein interactions from the three sources were integrated to develop a complete human-*Plasmodium* interaction network. Protein interactions were analysed to find most significant proteins involved in the infection process. Pathogen proteins were then shortlisted on the basis of the number of their interacting partners. Highest interacting pathogen proteins were shortlisted for further analysis. The shortlisted proteins were then studied in literature for their functionality, role in the pathogen, and the infection mechanism. A potential drug target was found on the basis of above-mentioned analysis.

*2.2. Ligand Dataset Preparation.* Finalized drug target is a known target for cancer; hence it was searched for its present inhibitors in literature. Out of all already known inhibitors, the one with least known toxicity and highest absorption was finalized and its derivatives were designed by addition of specific chemical groups at the preferred positions according to the present literature. Reference inhibitor molecule chosen was amiprophos methyl. A library of the designed inhibitors was prepared by MarvinSketch. Designing of inhibitors was performed by addition of specific functional groups at single and multiple locations in many combinations [33].

*2.3. Docking Studies.* Rigid docking was carried out between protein target and designed inhibitors using GLIDE docking program of Schrödinger (*Schrödinger Release 2014-2*). The results of docking were analysed followed by prioritization of functional groups and positions on the chemical structure. More molecules were designed by combining the prioritized position and functional groups. Prime docking molecules were then taken for flexible docking by induced fit docking in Schrödinger (*Schrödinger Release 2014-2*) (Figure 9). Most suitable docking inhibitor is considered as a potential drug molecule [34–37].

The final molecule is checked for its binding affinity and ADME properties [38] (Table 2).

## 3. Result and Discussion

The whole proteome of *Plasmodium falciparum* was downloaded from UniProt which contained 5353 proteins; 157 reviewed and 5196 unreviewed proteins. From BIPS, a total of 2381 interspecies interactions were obtained. These interactions were annotated for their cellular location, gene ontology, and functional role and then filtered upon these parameters. Functional annotation of the predicted pathogen proteins was carried out using DAVID and Panther. Panther identified 31 pathogen proteins and classified them on the basis of biological process, molecular function, pathways, and protein class. It was observed that most of the interacting pathogen proteins are involved in metabolic processes and have binding as their molecular function. These proteins fall into nucleic acid binding class of proteins and thus it was concluded that they have an important function in DNA replication and cell survival. There was no majority observed

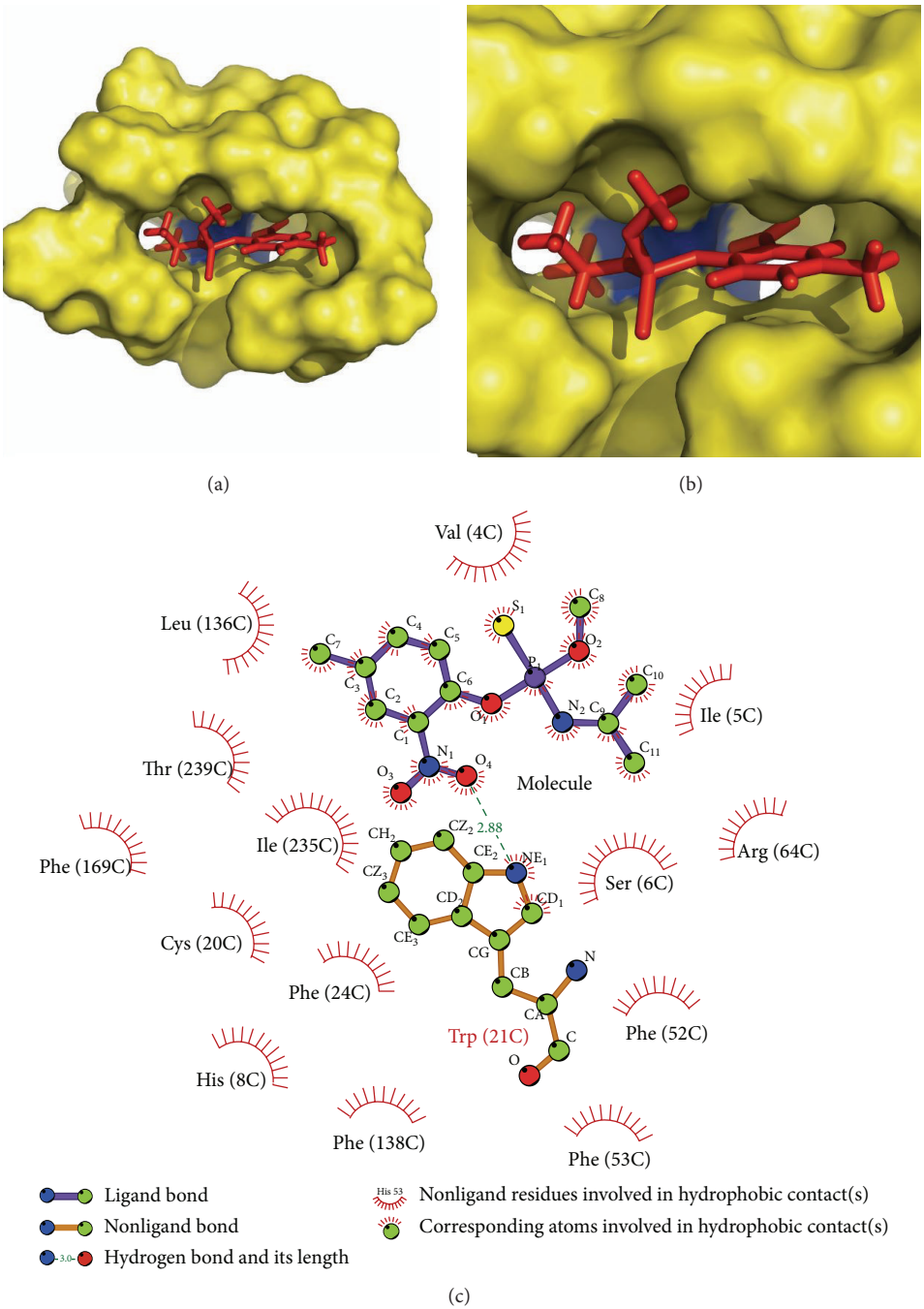


Figure 6: Interaction of amiprophos methyl with target protein at site II (a) and (b) docked reference molecule in the target protein at the site II with blue colour showing hydrogen bind between ligand and Tyr(21) of protein. (c) LigPlot analysis of protein and ligand interactions.

in the pathway classification of these proteins but there was a similarity: they all were involved in signalling and disease pathways (Figure 2).

The predicted protein interactions were used to generate host-pathogen interaction network (Figure 3). The predicted interactions were then analysed for the number of interacting partners of pathogen. Out of all the protein interactions, highly interacting proteins were shortlisted. Human proteins were not considered as a drug target because those proteins might have a role as an essential component in the biological processes. So, targeting human proteins have a high risk of drug toxicity. Human proteins which were interacting with more than three pathogen proteins were usually structural and assembly proteins such as actin, tubulin, and histone. Most of these human proteins were histone proteins. This shows that parasite infection affects mostly nuclear and cell assembly proteins in humans. Therefore, these proteins were left out because they are important proteins in human cells. If

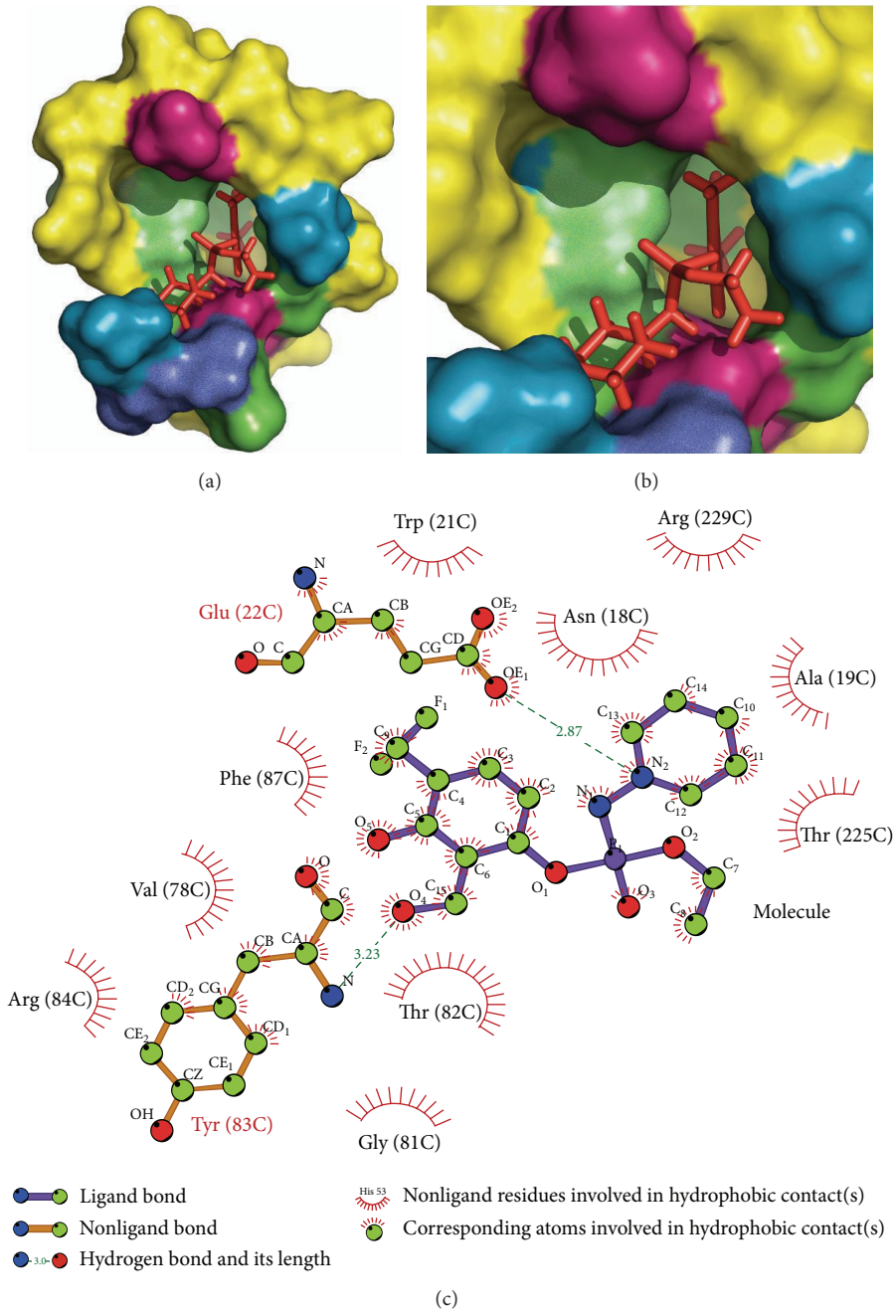


FIGURE 7: Interaction of 3-({ethoxy[(piperidin-1-yl)amino]phosphoryl} oxy)-2-(hydroxymethyl)-6-(trifluoromethyl) phenol with target protein at site II (a) and (b) docked molecule in the target protein at the site II with different colours showing different polarity and charges. Pink, blue, green, and cyan represent negative charge and positive charge and hydrophobic and polar residues, respectively. (c) LigPlot analysis of protein and ligand interactions.

human proteins or proteins similar to human proteins are targeted, the problem of drug toxicity after drug delivery might persist. Hence, pathogen proteins are considered for drug targeting to remove the possibility of negative effects in the host [39]. It was observed that most of the highly interacting proteins were involved in structural assembly of the pathogen such as actin, tubulin, and histone. Already present literatures of these proteins were studied to understand their functional role in the pathogen.

As a result of this analysis, $\alpha$-tubulin was finalized as an important protein involved in the infection process. $\alpha$-tubulin is a monomer unit which polymerizes to carry out several critically important roles throughout parasite life cycle [40, 41]. In parasite, they form mitotic spindle during

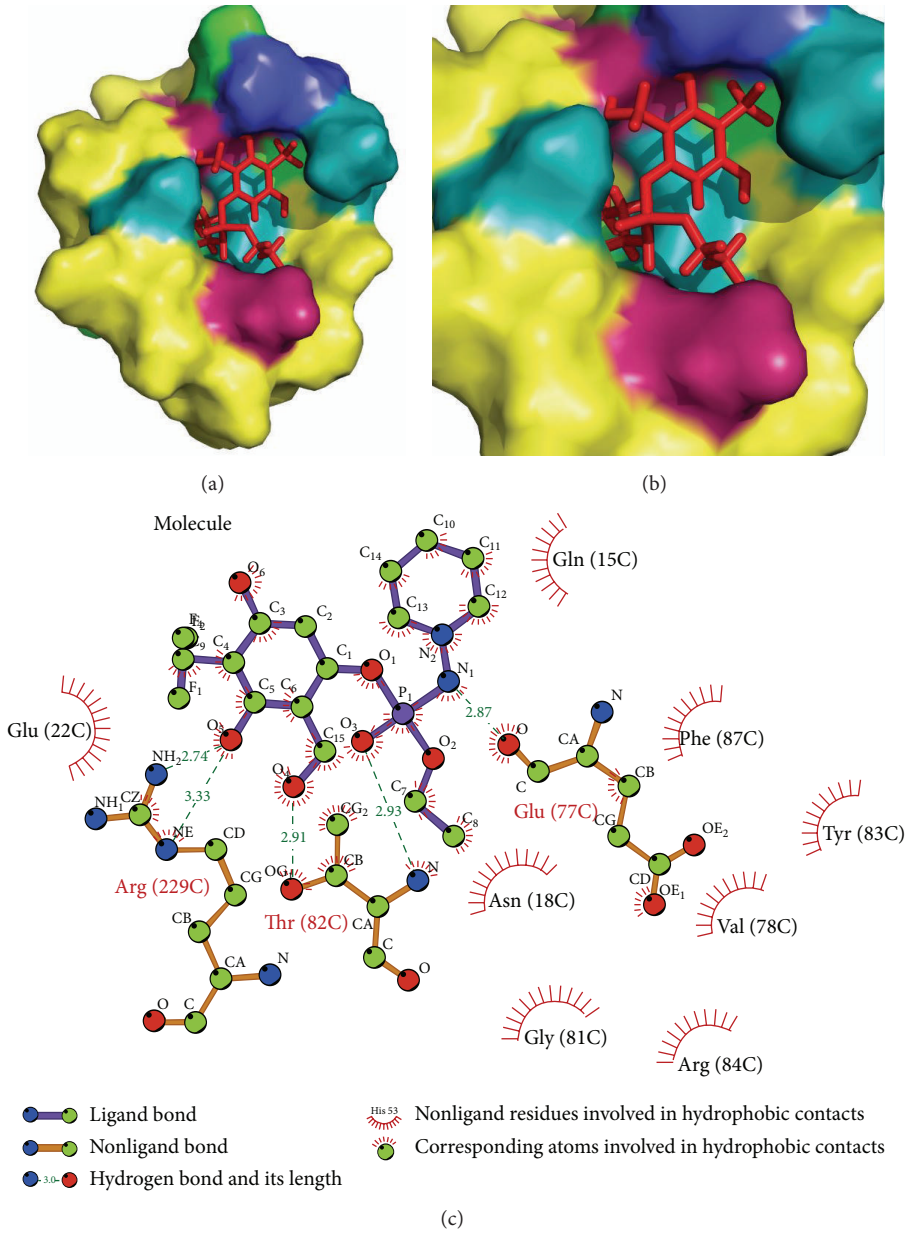


Figure 8: Interaction of 5-({ethoxy[(piperidin-1-yl)amino]phosphoryl} oxy)-4-(hydroxymethyl)-2-(trifluoromethyl) benzene-1,3-diol with target protein at site II (a) and (b) docked molecule in the target protein at the site II with different colours showing different polarity and charges. Pink, blue, green, and cyan represent negative charge, positive charge and hydrophobic and polar residues, respectively. (c) LigPlot analysis of protein and ligand interactions.

cell division and even slight disruption of microtubule causes a severe impact on the viability of parasite. *Plasmodium falciparum* infects the host and an initial contact occurs between merozoite and erythrocyte. $\alpha$-tubulin is also present in humans but tubulins of humans and plasmodium have significant differences in their mode of function. Present studies have shown that antitubulins show very low or no cross-reactivity to mammalian tubulins [28]. In experimental studies it was confirmed that invasion was decreased and eventually stopped when merozoites were exposed to tubulin inhibitors [27]. Experimental studies have demonstrated that microtubules were disrupted on exposure to antitubulin agent indicating the role of intact microtubule in merozoite invasion. Microtubule is found in many stages of malaria parasite, validating it as a potential drug target. Detailed examination of merozoites in erythrocyte invasion identified targeting $\alpha$-tubulin as a potential approach for malaria therapy [42–44].

Amiprophos methyl (Figure 4) is an antimitotic herbicide and a known inhibitor for $\alpha$-tubulin. It is found to be a promising molecule because of its low mammalian toxicity. It was reported in reference studies that amiprophos methyl has

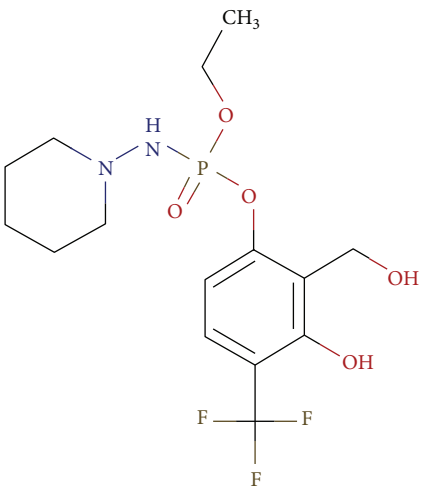

Molecule 1

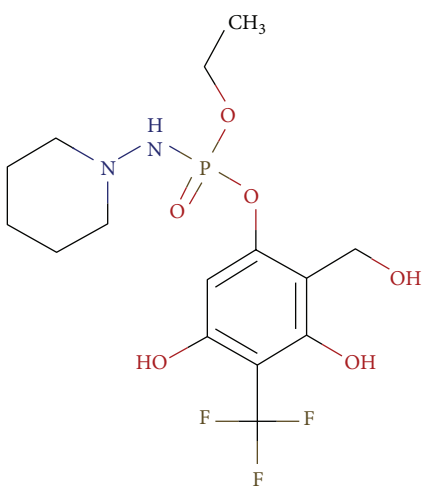

Molecule 2

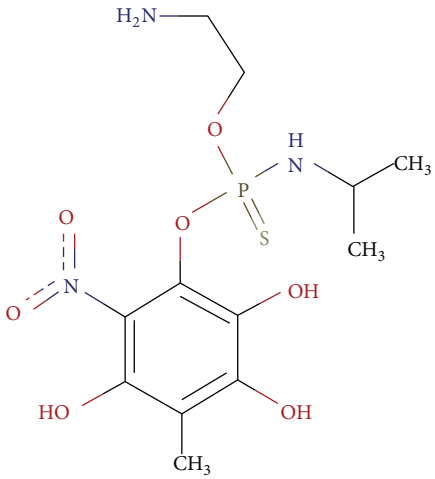

Molecule 3

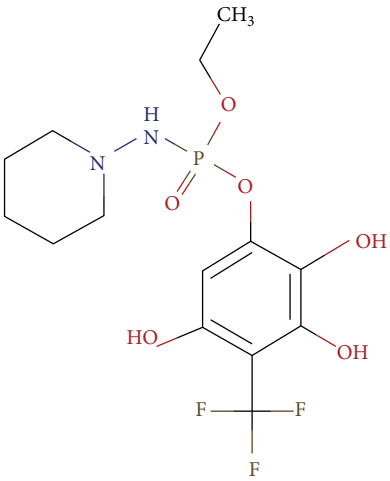

Molecule 4

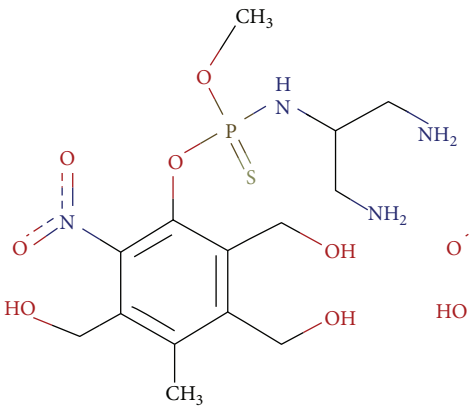

Molecule 5

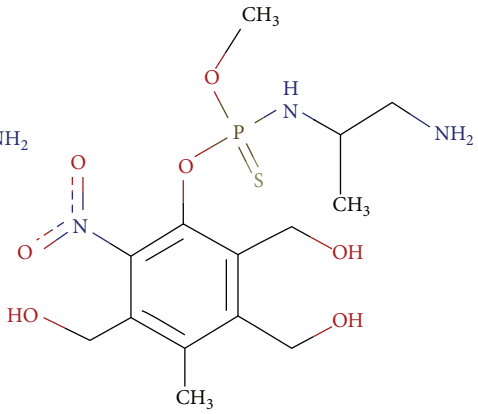

Molecule 6

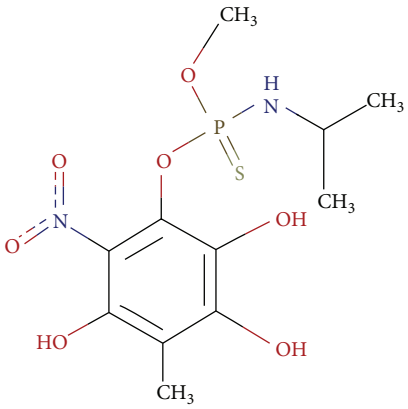

Molecule 7

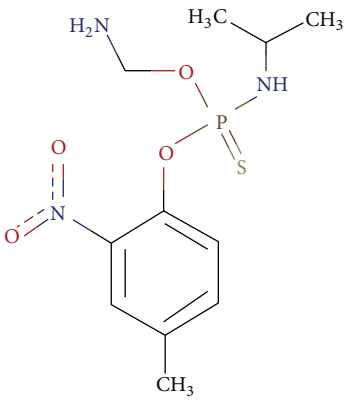

Molecule 8

Figure 9: Continued.

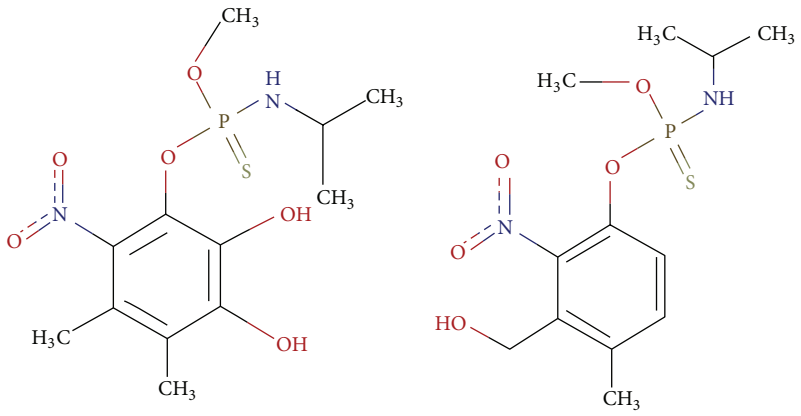


Molecule 9 Molecule 10

Figure 9: Molecular structure of the molecules shortlisted for flexible docking and binding affinity analysis.

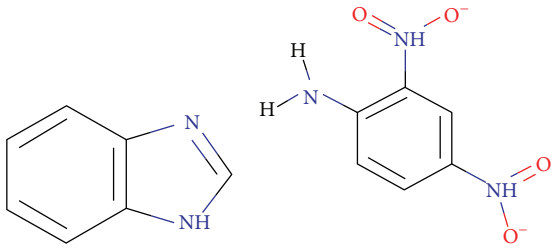


(a) (b)

Figure 10: (a) Chemical structure of benzimidazole. (b) Chemical structure of dinitroanilines.

better specificity for pathogen proteins and has no binding site in human tubulin protein [29, 30, 44–46].

Glide docking analysis of the target protein with the designed inhibitors and reference molecule was carried out. Glide docking performs significantly better than other docking programs with accuracy of more than 90% [34–37]. *Amiprophos methyl* was considered as a reference molecule with a docking score of 4.43. Among the designed inhibitors, molecules with best docking score were analysed for the functional molecules and their positions in that molecule. Molecules were then designed with the functional groups in combinations at the preferred positions. It was found that electronegative groups at positions 2, 3, and 9 showed significant improvements in docking score. A molecule with $CF_3$ at position 4, piperidine at position 9, and OH at position 3 showed the best docking score of −8.14 at site 2. This molecule had 83% better docking score than the reference molecule. The molecules with the best docking score were shortlisted and flexible docking was carried out (Figure 5). Highest docking score of −10.5 kcal/mol and −10.43 kcal/mol was obtained in flexible docking (Table 3).

These final molecules are analysed for their interaction with residues at site II using LigPlot [46]. 3-({Ethoxy[(piperidin-1-yl)amino]phosphoryl} oxy)-2-(hydroxymethyl)-6-(trifluoromethyl)phenol forms two hydrogen bonds with Glu(22) and Tyr(83). 5-({Ethoxy[(piperidin-1-yl)amino]phosphoryl} oxy)-4-(hydroxymethyl)-2-(trifluoromethyl) benzene-1,3-diol forms four hydrogen bonds with surrounding residue, that is, two with Arg(229), two with Thr(82), and one with Glu(77). The reference molecule was forming only a single hydrogen bond with Trp(21). The hydrogen bonds of these molecules with surrounding residues govern their stability and hence new molecules have better stability than reference molecule (Figures 6, 7, and 8).

The two final listed molecules have the highest docking score and low binding energy than the reference molecule which shows that it has better binding properties (Table 1). From ADME property analysis of the two molecules, it was observed that these have high values of human oral absorption, zero violations in Lipinski's rule of five, and zero violation in Jorgensen's rule of three and all the drug-ability determining properties lie under range (Table 2).

Better binding affinity and ADME property analysis of the final molecule confirm its potential to be used as a drug molecule for further analysis and trials.

## 4. Conclusion

From the predicted host-pathogen PPIs, the present study concludes that most of the host proteins with which pathogen protein interactions are structural proteins such as actin, tubulin, and histone. Most of the pathogen proteins involved in the infection process are structural and assembly proteins and most of the host proteins are either structural proteins or nuclear assembly proteins. Hence, the pathogen caused

Table 1: Comparison of binding energy scores of reference and potential drug molecules.

| Mol. number | H-bonding energy | Coulomb energy | Covalent binding energy | Pi-pi packing energy | Lipophilic energy | Binding energy | Electrosolvation energy | Van der Waals energy |
|---|---|---|---|---|---|---|---|---|
| Ref. | −0.33 | 3.52 | 4.77 | −0.17 | −42.46 | −80.96 | 5.05 | −51.35 |
| A | −2.35 | −19.23 | 2.09 | −3.63 | −37.46 | −83.79 | 21.08 | −44.34 |
| B | −3.78 | −66.20 | 5.94 | 0 | −32.50 | −98.16 | 37.69 | −39.30 |

Table 2: Comparison between QikProp scores of final molecules and reference molecule for analysis of ADME properties.

| Mol. number | # stars | MW | Human oral absorption | Percent human oral absorption | Rule Of five | Rule Of three |
|---|---|---|---|---|---|---|
| Ref. mol. | 0 | 304.3 | 3 | 100 | 0 | 0 |
| A | 0 | 398.32 | 3 | 80.59 | 0 | 0 |
| B | 0 | 414.32 | 3 | 69.87 | 0 | 0 |

Table 3: Glide scores and induced fit scores of the short listed molecules for flexible docking and binding affinity analysis.

| Mol. number | Glide score | IFD score |
|---|---|---|
| 1 | −10.5 | −762.72 |
| 2 | −10.43 | −762.29 |
| 3 | −10.24 | −766.93 |
| 4 | −9.65 | −768.15 |
| 5 | −9.25 | −761.87 |
| 6 | −8.99 | −760.97 |
| 7 | −8.46 | −764.92 |
| 8 | −7.61 | −767.01 |
| 9 | −6.68 | −757.47 |
| 10 | −6.65 | −763.28 |

infection by targeting nuclear assembly proteins and thereby inhibiting the host cell to function properly. $\alpha$-tubulin of pathogen is targeted for development of antimalarial agent for malarial treatment. Derivatives of herbicide having antimalarial property were developed and molecule with better binding affinity and ADME property was obtained. It was observed that molecules with electronegative groups have better binding properties than original molecule.

3-({Ethoxy[(piperidin-1-yl)amino]phosphoryl} oxy)-2-(hydroxymethyl)-6-(trifluoromethyl)phenol and 5-({ethoxy[(piperidin-1-yl)amino]phosphoryl} oxy)-4-(hydroxymethyl)-2-(trifluoromethyl)benzene-1,3-diol were the two best molecules which can be considered as drug molecules for *in vivo* analysis and validation.

## Conflict of Interests

The authors declare that there is no conflict of interests regarding the publication of this paper.

## Acknowledgment

The authors would like to thank Kirti Bhadhadhara for scientific discussions.

## References

[1] M. H. Gelb, "Drug discovery for malaria: a very challenging and timely endeavor," *Current Opinion in Chemical Biology*, vol. 11, no. 4, pp. 440–445, 2007.

[2] T. N. C. Wells, "Discovering and developing new medicines for malaria control and elimination," *Infectious Disorders—Drug Targets*, vol. 13, no. 4, pp. 292–302, 2013.

[3] K. G. Le Roch, D.-W. D. Chung, and N. Ponts, "Genomics and integrated systems biology in *Plasmodium falciparum*: a path to malaria control and eradication," *Parasite Immunology*, vol. 34, no. 2-3, pp. 50–60, 2012.

[4] R. W. Snow, C. A. Guerra, A. M. Noor, H. Y. Myint, and S. I. Hay, "The global distribution of clinical episodes of *Plasmodium falciparum* malaria," *Nature*, vol. 434, no. 7030, pp. 214–217, 2005.

[5] W. P. O'Meara, J. N. Mangeni, R. Steketee, and B. Greenwood, "Changes in the burden of malaria in sub-Saharan Africa," *The Lancet Infectious Diseases*, vol. 10, no. 8, pp. 545–555, 2010.

[6] S. Foster and M. Phillips, "Economics and its contribution to the fight against malaria," *Annals of Tropical Medicine and Parasitology*, vol. 92, no. 4, pp. 391–398, 1998.

[7] K. I. Barnes, D. N. Durrheim, F. Little et al., "Effect of artemether-lumefantrine policy and improved vector control on malaria burden in KwaZulu-Natal, South Africa," *PLoS Medicine*, vol. 2, no. 11, article e330, 2005.

[8] A. Casadevall and L.-A. Pirofski, "Host-pathogen interactions: redefining the basic concepts of virulence and pathogenicity," *Infection and Immunity*, vol. 67, no. 8, pp. 3703–3713, 1999.

[9] A. Casadevall and L.-A. Pirofski, "Host-pathogen interactions: basic concepts of microbial commensalism, colonization, infection, and disease," *Infection and Immunity*, vol. 68, no. 12, pp. 6511–6518, 2000.

[10] M. D. Dyer, T. M. Murali, and B. W. Sobral, "Computational prediction of host-pathogen protein-protein interactions," *Bioinformatics*, vol. 23, no. 13, pp. i159–i166, 2007.

[11] J. Mufunda, P. Nyarango, A. Usman et al., "Roll back malaria—an African success story in Eritrea," *South African Medical Journal*, vol. 97, no. 1, pp. 46–50, 2007.

[12] E. A. Franzosa, S. Garamszegi, and Y. Xia, "Toward a three-dimensional view of protein networks between species," *Frontiers in Microbiology*, vol. 3, article 428, 2012.

[13] J. Zahiri, J. H. Bozorgmehr, and A. Masoudi-Nejad, "Computational prediction of protein-protein interaction networks: algorithms and resources," *Current Genomics*, vol. 14, no. 6, pp. 397–414, 2013.

[14] N. Yosef, M. Kupiec, E. Ruppin, and R. Sharan, "A complex-centric view of protein network evolution," *Nucleic Acids Research*, vol. 37, no. 12, article e88, 2009.

[15] P. Uetz, L. Glot, G. Cagney et al., "A comprehensive analysis of protein-protein interactions in *Saccharomyces cerevisiae*," *Nature*, vol. 403, no. 6770, pp. 623–627, 2000.

[16] J. Mendez-Rios and P. Uetz, "Global approaches to study protein-protein interactions among viruses and hosts," *Future Microbiology*, vol. 5, no. 2, pp. 289–301, 2010.

[17] P. V. Desai, A. Patny, J. Gut et al., "Identification of novel parasitic cysteine protease inhibitors by use of virtual screening. 2. The available chemical directory," *Journal of Medicinal Chemistry*, vol. 49, no. 5, pp. 1576–1584, 2006.

[18] L. R. Matthews, P. Vaglio, J. Reboul et al., "Identification of potential interaction networks using sequence-based searches for conserved protein-protein interactions or 'interologs'," *Genome Research*, vol. 11, no. 12, pp. 2120–2126, 2001.

[19] Y. Qi, O. Tastan, J. G. Carbonell, J. Klein-Seetharaman, and J. Weston, "Semi-supervised multi-task learning for predicting interactions between HIV-1 and human proteins," *Bioinformatics*, vol. 26, no. 18, Article ID btq394, pp. i645–i652, 2010.

[20] S. Wuchty, "Computational prediction of host-parasite protein interactions between *P. falciparum* and *H. sapiens*," *PLoS ONE*, vol. 6, no. 11, Article ID e26960, 2011.

[21] O. Krishnadev and N. Srinivasan, "A data integration approach to predict host-pathogen protein-protein interactions: application to recognize protein interactions between human and a malarial parasite," *In Silico Biology*, vol. 8, no. 3-4, pp. 235–250, 2008.

[22] S.-A. Lee, C.-H. Chan, C.-H. Tsai et al., "Ortholog-based protein-protein interaction prediction and its application to inter-species interactions," *BMC Bioinformatics*, vol. 9, supplement 12, article S11, 2008.

[23] S. Durmuş Tekir, T. Çakir, E. Ardiç et al., "PHISTO: pathogen-host interaction search tool," *Bioinformatics*, vol. 29, no. 10, pp. 1357–1358, 2013.

[24] H. A. Rapanoel, G. K. Mazandu, and N. J. Mulder, "Predicting and analyzing interactions between Mycobacterium tuberculosis and its human host," *PLoS ONE*, vol. 8, no. 7, Article ID e67472, 2013.

[25] J.-C. Barale, T. Blisnick, H. Fujioka et al., "Plasmodium falciparum subtilisin-like protease 2, a merozoite candidate for the merozoite surface protein 1–42 maturase," *Proceedings of the National Academy of Sciences of the United States of America*, vol. 96, no. 11, pp. 6445–6450, 1999.

[26] G. S. Dow, A. Armson, M. R. Boddy et al., "Plasmodium: assessment of the antimalarial potential of trifluralin and related compounds using a rat model of malaria, Rattus norvegicus," *Experimental Parasitology*, vol. 100, no. 3, pp. 155–160, 2002.

[27] B. J. Fennell, J. A. Naughton, E. Dempsey, and A. Bell, "Cellular and molecular actions of dinitroaniline and phosphorothioamidate herbicides on *Plasmodium falciparum*: tubulin as a specific antimalarial target," *Molecular and Biochemical Parasitology*, vol. 145, no. 2, pp. 226–238, 2006.

[28] C. Mara, E. Dempsey, A. Bell, and J. W. Barlow, "Synthesis and evaluation of phosphoramidate and phosphorothioamidate analogues of amiprophos methyl as potential antimalarial agents," *Bioorganic and Medicinal Chemistry Letters*, vol. 21, no. 20, pp. 6180–6183, 2011.

[29] J. Garcia-Garcia, S. Schleker, J. Klein-Seetharaman, and B. Oliva, "BIPS: BIANA Interolog Prediction Server. A tool for protein-protein interaction inference," *Nucleic Acids Research*, vol. 40, no. 1, pp. W147–W151, 2012.

[30] D. W. Huang, B. T. Sherman, and R. A. Lempicki, "Bioinformatics enrichment tools: paths toward the comprehensive functional analysis of large gene lists," *Nucleic Acids Research*, vol. 37, no. 1, pp. 1–13, 2009.

[31] D. W. Huang, B. T. Sherman, and R. A. Lempicki, "Systematic and integrative analysis of large gene lists using DAVID bioinformatics resources," *Nature Protocols*, vol. 4, no. 1, pp. 44–57, 2009.

[32] H. Mi, A. Muruganujan, and P. D. Thomas, "PANTHER in 2013: modeling the evolution of gene function, and other gene attributes, in the context of phylogenetic trees," *Nucleic Acids Research*, vol. 41, no. 1, pp. D377–D386, 2013.

[33] G. Madhavi Sastry, M. Adzhigirey, T. Day, R. Annabhimoju, and W. Sherman, "Protein and ligand preparation: parameters, protocols, and influence on virtual screening enrichments," *Journal of Computer-Aided Molecular Design*, vol. 27, no. 3, pp. 221–234, 2013.

[34] R. A. Friesner, J. L. Banks, R. B. Murphy et al., "Glide: a new approach for rapid, accurate docking and scoring. 1. Method and assessment of docking accuracy," *Journal of Medicinal Chemistry*, vol. 47, no. 7, pp. 1739–1749, 2004.

[35] R. A. Friesner, R. B. Murphy, M. P. Repasky et al., "Extra precision glide: docking and scoring incorporating a model of hydrophobic enclosure for protein-ligand complexes," *Journal of Medicinal Chemistry*, vol. 49, no. 21, pp. 6177–6196, 2006.

[36] D. A. Gschwend, A. C. Good, and I. D. Kuntz, "Molecular docking towards drug discovery," *Journal of Molecular Recognition*, vol. 9, no. 2, pp. 175–186, 1996.

[37] T. A. Halgren, R. B. Murphy, R. A. Friesner et al., "Glide: a new approach for rapid, accurate docking and scoring. 2. Enrichment factors in database screening," *The Journal of Medicinal Chemistry*, vol. 47, no. 7, pp. 1750–1759, 2004.

[38] J. C. Shelley, A. Cholleti, L. L. Frye, J. R. Greenwood, M. R. Timlin, and M. Uchimaya, "Epik: a software program for $pK_a$ prediction and protonation state generation for drug-like molecules," *Journal of Computer-Aided Molecular Design*, vol. 21, no. 12, pp. 681–691, 2007.

[39] H. N. Chua, W.-K. Sung, and L. Wong, "Exploiting indirect neighbours and topological weight to predict protein function from protein-protein interactions," *Bioinformatics*, vol. 22, no. 13, pp. 1623–1630, 2006.

[40] D. J. Rawlings, H. Fujioka, M. Fried, D. B. Keister, M. Aikawa, and D. C. Kaslow, "$\alpha$-Tubulin II is a male-specific protein in *Plasmodium falciparum*," *Molecular and Biochemical Parasitology*, vol. 56, no. 2, pp. 239–250, 1992.

[41] N. Gerald, B. Mahajan, and S. Kumar, "Mitosis in the human malaria parasite *Plasmodium falciparum*," *Eukaryotic Cell*, vol. 10, no. 4, pp. 474–482, 2011.

[42] T. W. A. Kooij, C. J. Janse, and A. P. Waters, "Plasmodium post-genomics: better the bug you know?" *Nature Reviews Microbiology*, vol. 4, no. 5, pp. 344–357, 2006.

[43] C. Mara, E. Dempsey, A. Bell, and J. W. Barlow, "Synthesis and evaluation of phenoxyoxazaphospholidine, phenoxyoxazaphosphinane, and benzodioxaphosphininamine sulfides and

related compounds as potential anti-malarial agents," *Bioorganic and Medicinal Chemistry Letters*, vol. 23, no. 12, pp. 3580–3583, 2013.

[44] E. Lacey, "Mode of action of benzimidazoles," *Parasitology Today*, vol. 6, no. 4, pp. 112–115, 1990.

[45] L. M. MacDonald, A. Armson, R. C. A. Thompson, and J. A. Reynoldson, "Characterisation of benzimidazole binding with recombinant tubulin from *Giardia duodenalis*, *Encephalitozoon intestinalis*, and *Cryptosporidium parvum*," *Molecular and Biochemical Parasitology*, vol. 138, no. 1, pp. 89–96, 2004.

[46] A. C. Wallace, R. A. Laskowski, and J. M. Thornton, "LIGPLOT: a program to generate schematic diagrams of protein-ligand interactions," *Protein Engineering*, vol. 8, no. 2, pp. 127–134, 1995.

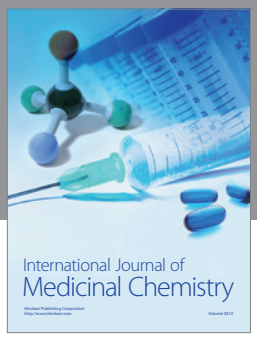

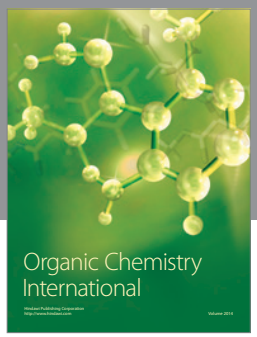

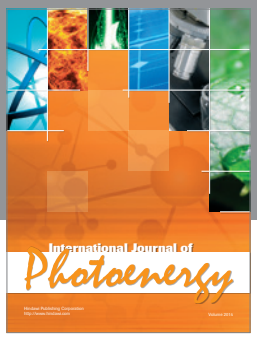

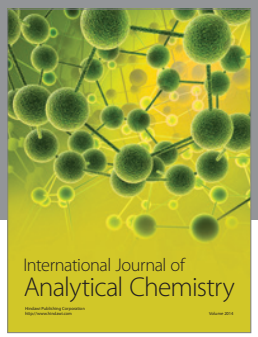

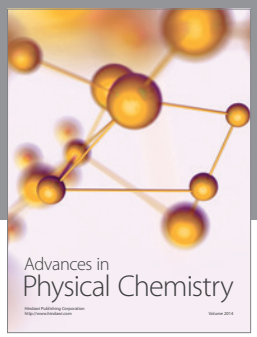

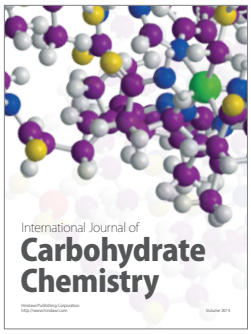

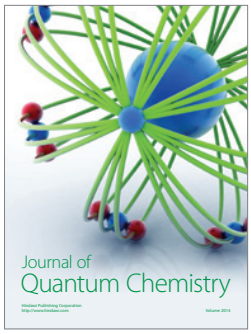

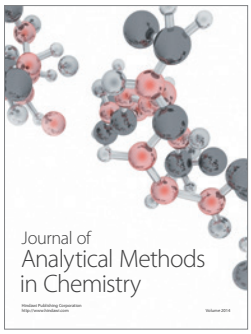

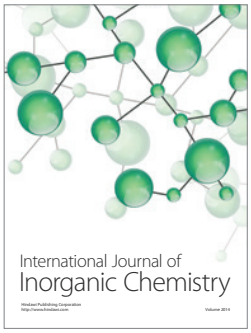

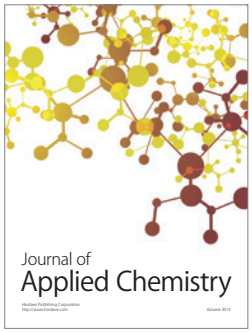

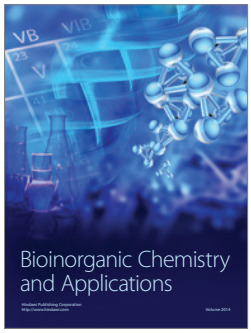

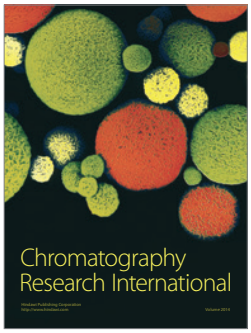

Hindawi
Submit your manuscripts at
http://www.hindawi.com

Indian Journal of Pure & Applied Physics
Vol. 54, January 2016, pp. 60-65

# Microwave device jig characterization for ferromagnetic resonance induced spin Hall effect measurement in bilayer thin films

Saood Ahmad[1]*, Jyoti Shah[1], Anurag K Katiyar[1], Rishu Chaujar[2], Nitin K Puri[2], P S Negi[1] & R K Kotnala[1]

[1]CSIR-National Physical Laboratory, New Delhi, India

[2]Department of Applied Physics, Delhi Technological University, Delhi, India

*E-mail: ahmads@mail.nplindia.org

*Received 21 April 2015; revised 17 September 2015; accepted 23 October 2015*

Microwave device jig for evaluating magnetic thin films consists of two symmetrical radial copper pad sections each having panel mounted *RF* connector. A non resonant measurement method for obtaining spin Hall voltage across magnetic thin films using ferromagnetic resonance was developed, based on electrical impedance of thin film and copper pads of the microwave device jig both in contact with each other. A geometry is introduced, which provides good impedance match characteristics and is optimised for maximum power transmission. It also gives the flexibility in measurements for any orientation of thin film with respect to applied magnetic field. In this geometry, a quantitative study of the microwave device jig has been done by measuring spin Hall voltages in the frequency range 0.1-10 GHz for bilayer thin films. The experimentally recorded voltages can be fully ascribed to SHE detection due to microwave induced FMR.

**Keywords:** Microwave magnetics, Spin Hall effect, Ferromagnetic resonance

## 1 Introduction

Spin Hall effect (SHE) aims to explore the role of electron spin in building the next generation electronic devices. Using electron spin rather than electron charge may allow faster, lower energy cost devices. The SHE originally presented by Dyakonov and Perel[1], can be described as an accumulation of spin generated by an electric current at the edges of a non magnetic metal. Ferromagnetic resonance is the most widely used technique for characterizing thin films[2] and a pure source of spin currents for spintronic applications[3,4]. Spin electronics does not just exploit electric charge of electrons but also their spin, which leads to development of new approaches for industrial applications. The research work in this area of spintronics has been focused on thin film characterization and phenomenon that will make it possible to control both spin orientation and spin flow. It is very important and will have major impact in understanding fundamental research as well as modern spin based technological applications. A discrepancy in SHE measurement result clearly shows that accurate measurements, understanding and analysis are essential in the area of spintronics.

The use of microwave device jig is experimentally demonstrated based on non resonant method with an optimized geometry to detect spin Hall voltage due to microwave induced FMR in a magnetic hetrostructures. An alternate microwave device jig is a cavity based resonant method where sample is placed in a resonant waveguide cavity[12-15]. The limitation for the cavity based device is that it is dependent on frequency. The study of SHE has been further extended as a function of orientation of thin film with respect to applied magnetic field, frequency and microwave power using specially designed microwave device jig. A geometry is introduced, which provides good impedance match characteristics and is optimised for maximum power transmission. A vector network analyzer (VNA) is used for evaluating the S parameters of microwave device jig using calibration kit. A vector network analyzer is a swept frequency reflectometer system used to measure the magnitude and phase angle of reflection and transmission coefficients for one port or two port network (S-parameters). The signal transmitted through or reflected from the unknown device is compared in amplitude and phase with a reference signal. The reflection coefficient ( $|S_{11}|$ or $|S_{22}|$ ) in general ( $|S_{nn}|$ ) of a device is measured in terms of return loss ($RL = -20 \log(1/|S_{nn}|)$ against a zero dB return loss standard.

This method allows us to tune the magnetization dynamics regardless of film size by applying microwave current directly to the magnetic layer.

Studies of the resonance frequencies, amplitudes, line widths, and line shapes as a function of microwave power, frequency and magnetic field shall provide detailed additional information about the exchange, damping and spin transfer torques that govern dynamics in magnetic hetrostructures[5-7].

## 2 Microwave Device Jig: Design and Fabrication

Spin current related phenomenon is an important aspect of modern magnetism, like spin currents which is nothing but a flow of angular momentum without a charge current and it can propagate in magnetic hetrostructures. Using microwave device jig along with its assembly, spin-Hall effect was studied in magnetic thin films to control both spin orientation and spin flow. Microwave device jig for evaluating magnetic thin films consists of two symmetrical radial copper pad sections designed and fabricated on a double sided teflon laminated copper foil plated board. These double sided teflon laminated copper foil plated board with the following specifications : teflon thickness 1.6 mm, copper thickness 35 μm both sides, teflon dielectric constant 2.55, *RF* connector SMA panel mount has been used for fabricating the microwave device jig. This is a high quality laminate with controlled dielectric constant. The layout details of microwave device jig are shown in Fig. 1. A non-resonant measurement method for obtaining spin Hall voltage across magnetic thin films using FMR was developed based on electrical impedance of thin film and copper pads of the microwave device jig both in contact with each other. In this geometry, a quantitative study of the microwave device jig has been done by measuring spin Hall voltages in the frequency range 0.1-10 GHz for bilayer thin films. The microwave device jig has a mounting section on which a thin film sample is mounted and a *RF* connector section which connects the device to an external microwave source using panel mount *RF* connectors.

The microwave device jig is designed using radial fan type structure in the form of microstrip conductor, a teflon substrate, a ground plane and coaxial *RF* connectors as shown in Fig. 2. In this method, a bilayer thin film is in contact with the radial microstrip conductor; propagating high frequency EM wave hence, the electric field generated has the maximum interaction with the sample. The microwave device jig is designed in such away to have a good impedance match with the 50 ohm microwave source and optimised for maximum power transmission. A radial stub is used as good impedance matching device in the form of a microstrip line[8]. It is used in many microwave circuits for impedance matching or as an *RF* ground. As known radial stub has three characteristic parameters: the radius $R_L$, angle $\alpha$ and the inner radius $R_i$. The theoretically characteristic impedance $Z_o$ of the microwave device jig is calculated[8] using the Eq. (1):

$$Z_0(R_1) = \frac{120\pi}{\sqrt{\varepsilon_r}}[J_0^2(K_{R1}) + N_0^2(K_{R1})]^{1/2} \times [J_1^2(K_{R1}) + N_1^2(K_{R1})]^{-1/2} \quad \ldots(1)$$

$$K = 2\pi\frac{\sqrt{\varepsilon_r}}{\lambda_0} \quad \ldots(2)$$

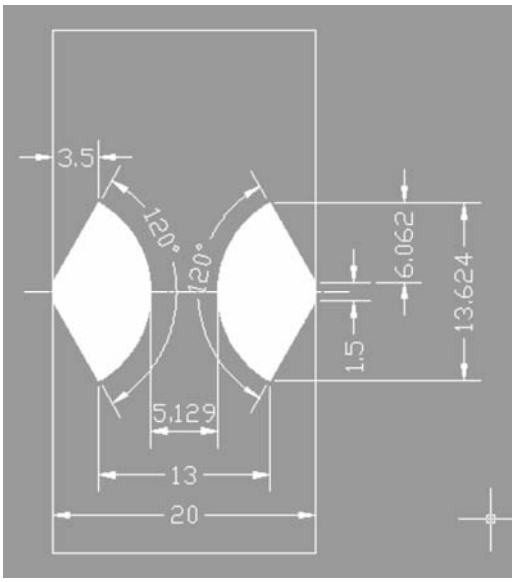


Fig. 1 — Layout details of a microwave device jig

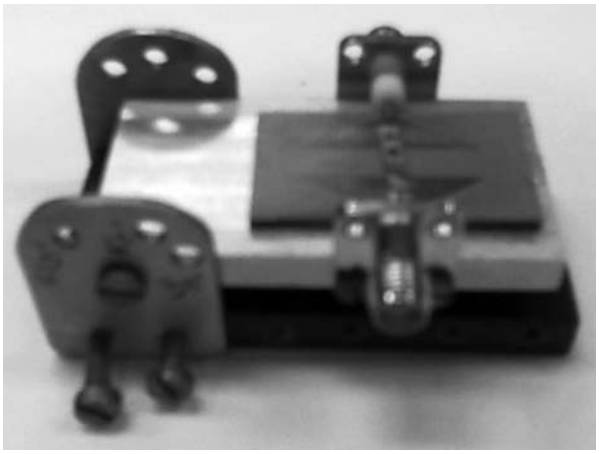

Fig. 2 — Microwave device jig assembly

$J_n$ is the Bessel function of the first kind of order $n$ and $N_n$ is the Bessel function of the second kind of order $n$. Finally, $k$ is the wave number, $\lambda_o$ the wavelength and $\varepsilon_r$ is the dielectric constant. In our case, the radius $R_L$=7.5 mm, angle $\alpha$=120°and the inner radius $R_i$=2.0 mm. Dielectric constant of teflon used is 2.55 with an operating frequency of 1 GHz. Using Eqs (1 and 2), along with the tables of Bessel's function, we get the characteristic impedance $Z_o$ as 52.13 ohm.

The assembly is designed and developed indigenously in our central workshop. The non magnetic material has been used with all the screw alignment for having different orientations. It also gives the flexibility in measurements for any orientation of thin film with respect to applied magnetic field as shown in Fig. 2.

The layout of microwave device jig was simulated using SONNET as an electromagnetic simulator to analyze its *RF* characteristics. The schematic of the microwave device jig under EM simulation is shown in Fig. 3. Sonnet as a 3D planar high frequency electromagnetic simulation software is used to analyze the designs in the complete frequency range. It provides a full-wave EM solution for planar structure having benefit of fast and efficient. The Sonnet develops precise *RF* models (S-, Y-, Z-parameters or extracted SPICE model) for planar circuits. It requires a physical description of your circuit (arbitrary layout and material properties for metal and dielectrics) and employs a rigorous Method-of-Moments EM analysis based on Maxwell's equations that include all parasitic, cross-coupling, enclosure. Sonnet maintains a single, dedicated focus on providing the most accurate and reliable high frequency planar EM software. The simulated input impedance in terms of return loss for the fabricated microwave device jig using vector network analyzer (VNA) is shown in Fig. 4. The microwave device jig was fabricated based on the optimum simulation

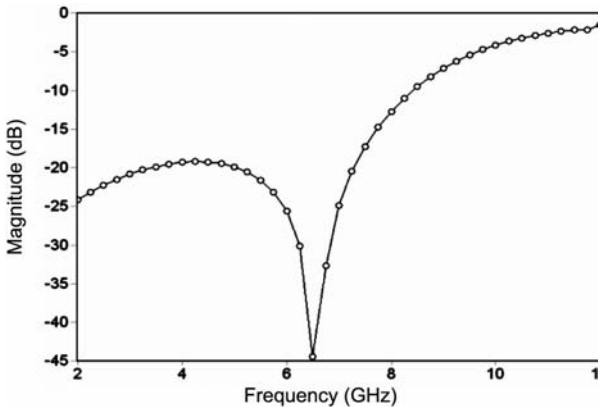


Fig. 3 — Schematic: Microwave device jig for EM simulation using SONNET

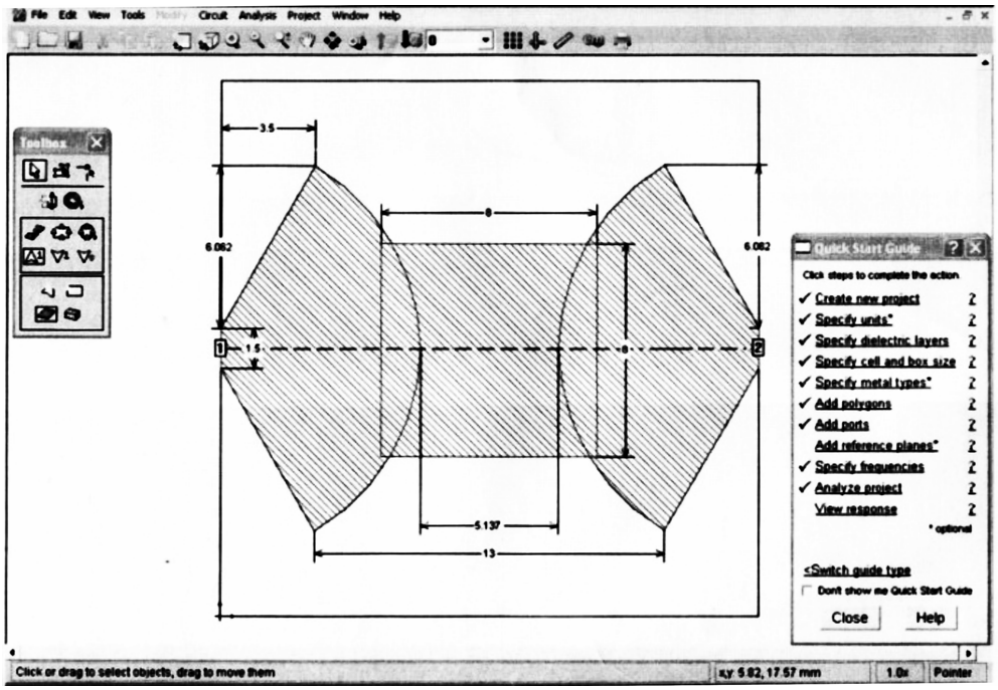


Fig. 4 — Simulation result (S11 in dB) using SONNET

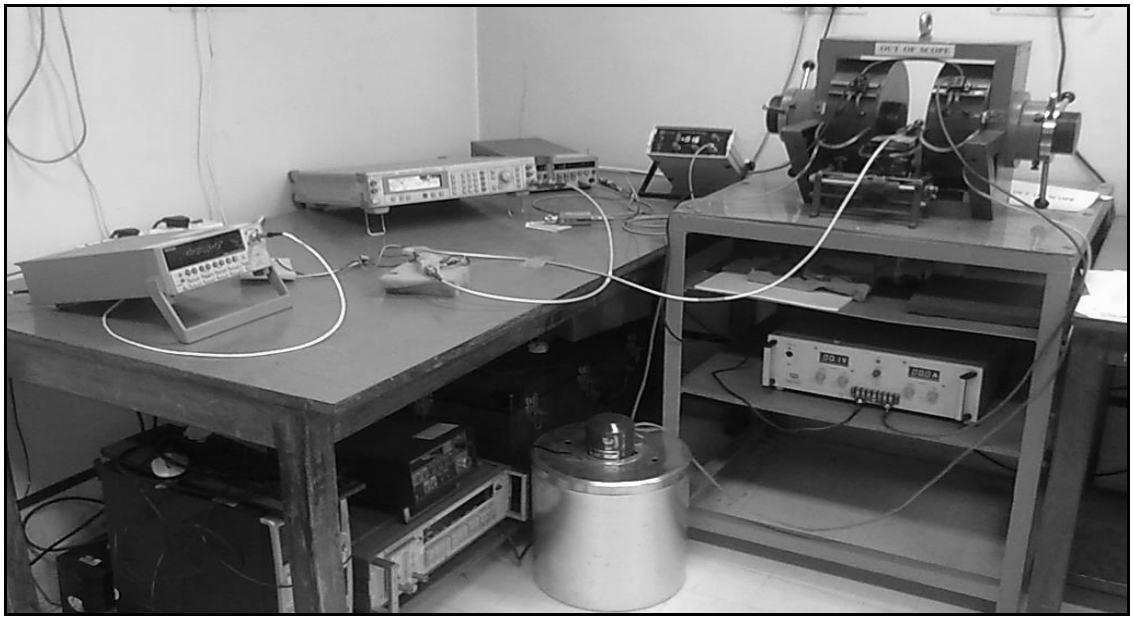

Fig. 5 — FMR measurement set-up

results and used for electrical characterization of magnetic thin film hetrostructures[9-11]. The simulated layout pattern was fabricated on the substrate using lithography.

## 3 Results

Ferromagnetic resonance is the absorption of microwave power by a magnetic film, measured as a function of applied sweeping *dc* magnetic field. The FMR measurement system is composed of a microwave device jig along with its assembly, an electromagnet, a *dc* power supply, a network analyzer, *RF* source and bias tee as shown in Fig. 5. Thin film samples are characterized using microwave device jig, which have electrodes having a gap of 5 mm for the contact. In this broadband experiment, a sweeping magnetic field is applied in film plane and microwave power from the synthesized signal generator varied up to 20 dBm (100 mW). A *dc* voltage signal is generated across the sample from the interaction of microwave power and oscillating resistance[12-15]. With the help of the microwave device jig and FMR measurement set-up, one can perform SHE measurements either in the direction of applied microwave signal or in the direction perpendicular to the applied signal. Using microwave device jig, bilayer thin film is in contact with the radial microstrip conductor of the device; propagating high frequency EM wave hence, the electric field

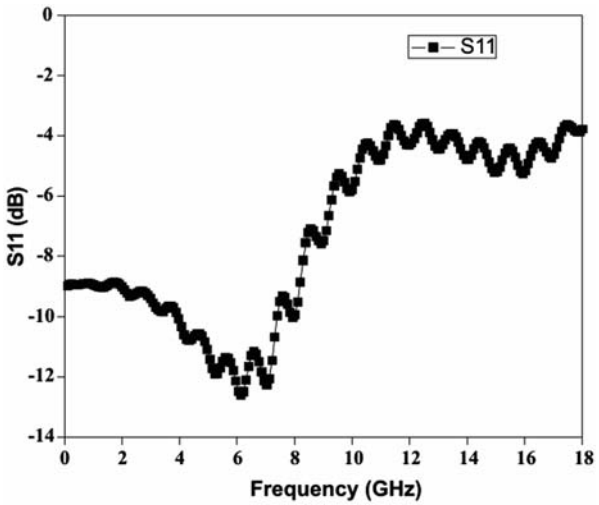


Fig. 6 — Measurement results of microwave device jig on VNA

generated has the maximum interaction with the thin film sample. We can also have the flexibility of measurements in any orientation of thin film with respect to the applied magnetic field. All measurements are performed at room temperature[16-21].

Vector network analyzer is used for impedance measurements that is calibrated and connected to one port of the sample holder as the other end is shorted to *RF* ground. VNA excites the port of the microwave device jig and measures the reflected power due to the impedance mismatch at thin film interface to calculate

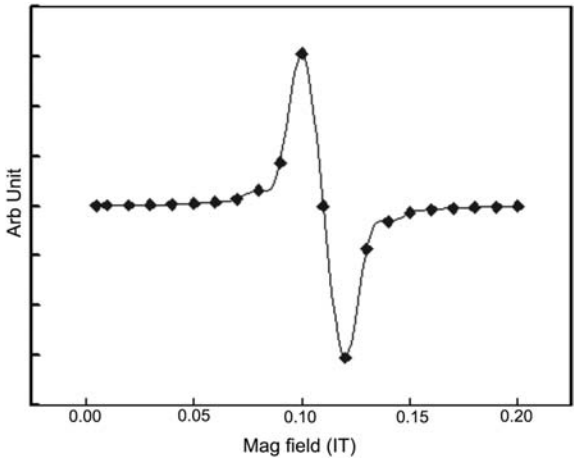


Fig. 7 — FMR Plot for a bilayer thin film

the return loss in dB. The measured return loss of the microwave device jig is shown in Fig. 6. FMR technique is implemented based on impedance of the magnetic film in contact with electrical conductors pad. An alternate method is a resonant method where sample is placed in a resonant waveguide cavity[13-16]. Although it is a good method for FMR measurements but the major disadvantage of this method is that one can perform the experiment at a single resonant frequency, where as in non-resonant method one can sweep the entire frequency range. The spin Hall voltage for a bilayer thin film was evaluated by the proposed method[4]. The FMR voltage spectra has been measured at the applied microwave frequencies and plotted as shown in Fig. 7.

## 4 Discussion

The simulated return loss and measured return loss in broadband frequency are different, which is a characteristic for the impedance mismatch. The measured values are low as compared to simulated results because of losses involved in microwave measurements. In simulation, software assumes perfect match between the film and layout, but in practical situation the match depends upon the geometrical dimensions of thin film. Though, the measured values are low as compared to the simulated results but both have identical pattern in the frequency range 0.1-10 GHz. Furthermore, the differences between measured and the simulated input impedance values may be because the magnetic film was driven by the high frequency current, and hence, high frequency losses are involved. The measured input impedance shows a good impedance match up to 9.0 GHz as return loss ($S_{11}$) greater than-10.0 dB with an uncertainty of ± 0.07 dB is a good practical realization[22-27].Spin electronics does not just exploit electric charge of electrons but also their spin, and should therefore, lead to development of new approaches for industrial applications. It is very important and will have major impact in understanding fundamental research as well as for modern spin based technological applications.

## 5 Conclusions

A non-resonant method has been successfully implemented for detecting spin Hall voltage using FMR technique. In this method of measurement, spin current generated due to spin-Hall effect in non-magnetic thin film is injected into the adjacent ferromagnetic thin film to study the voltage developed across the film. It is demonstrated microwave device jig geometry, its design, simulation and measurement results in terms of return loss, which allows broadband detection of spin Hall effect. The design of microwave device jig and its assembly gives the flexibility of measurements in any orientation of thin film with respect to the applied magnetic field. Electromagnetic simulator SONNET has been used to optimize *RF* layout of the microwave device jig for good impedance match, having maximum electric field interaction with the sample. An alternate method is a cavity based resonant method, though it is a good one for FMR measurements but its drawback is frequency limitation, where as in non-resonant method one can sweep the entire frequency range. The experimental investigation of in-plane *dc* voltage signal generated in bilayer thin film under the microwave excitation and sweeping magnetic field have been shown and discussed.

## Acknowledgement

Special thanks to Director, CSIR-National Physical Laboratory India for his kind support and motivation to carry out this work.

## References

1 Hirsch J E, *Physical Rev Lett*, 83 (1999) 1834.
2 Wolf S A, *Magnetism & Materials*, 294 (2001) 1488.
3 Czeschka F D, *Physical Rev Lett*, 107 (2011) 046601.
4 Ahmad Saood, *Appl Phys Lett*, 103 (2013) 032405.
5 Shu-Juan Yuan, *J of Shanghai Univ*, 11(3) (2007).
6 Nakayama H, *J of Phys*, 266 (2011) 012100.
7 Luqiao Liu, *Physical Rev Lett*, 106 (2011) 036601.
8 Weijun Luo, *Chinese J of Semicon*, 27 (2006).
9 Mosendz O, *Physical Rev Lett*, 104 (2010).

10 Ando K, *Physical Rev Lett*, 101 (2008) 036601.
11 Kimura T, *Physical Rev Lett*, 98 (2007) 156601.
12 Inoue H Y, *J Appl Phys*, 102 (2007) 083915.
13 Fuchs G D, *Appl Phys Lett*, 91 (2007) 062507.
14 Valenzula S O, *J Appl Phys*, 101 (2007) 09B103.
15 Sankey Jack C, *Physical Rev Lett*, 96 (2006) 227601.
16 Saitoh E, *Appl Phys Lett*, 88 (2006) 182509.
17 Harii K, *J Appl Phys*, 103 (2006) 07F311.
18 Yoshino T, *Appl Phys Lett*, 98 (2011) 132503.
19 Viela-Laeo L H, *J Appl Phys*, 109 (2011) 116105.
20 Harii K, *J Appl Phys*, 109 (2011) 07C910.
21 Nakajima N, *Phys Rev Lett*, 81 (1998) 5229.
22 Shu-Juan Yuan, *J of Shanghai Univ*, 11(3) (2007).
23 Inoue H Y, *J Appl Phys*, 102 (2007) 083915.
24 Oogane M, *J Appl Phys*, 45 (2006) 5A.
25 Valenzula S O, *Nature Lett*, 442 (2006) 04937.
26 Azevedo A, *J Appl Phys*, 97 (2005) 10C715.
27 Tserkovnyak Y, *Phys Rev Lett*, 88 (2002) 117601.

Volume 3, Issue 4 (2015) 615-618 ISSN 2347 - 3258
International Journal of Advance Research and Innovation

# Mixing of Various Renewable Energy Technologies towards Development of Village Energy Need

Shubham Gupta, R. S. Mishra*
Department of Mechanical Engineering, Delhi Technological University, Delhi, India

**Article Info**

Article history:
Received 25 September 2015
Received in revised form
20 October 2015
Accepted 28 November 2015
Available online 15 December 2015

**Keywords**
Hybrid Energy Optimization,
Mixing of Technology,
Rural Electrification,
Solar & Biomass

**Abstract**

This paper mainly deals with mixing of various Renewable energy technologies towards development of the village energy need. Main technologies are: solar & biomass. The energy crisis and environmental degradation are currently two vital issues for global sustainable development. Smart Village means Electricity 24 hr as electricity is the key factor for the development. Need, Methodology & Vision of this study is sustainable development as it is believed to develop India starts with developing Rural India first. This paper focuses on technical feasibility only.

## 1. Introduction

Energy is one of the main sources for the advancement of human civilization and is required for every activity and therefore plays a vital role in the development of society. India is facing an energy crisis and at least 500 million rural residents lack access to consistent electricity supply due to insufficient Grid Infrastructure. These household still use kerosene and wood to cook their food due to lack of fuel supply for cooking applications. In many villages, there is Lack of Education as absolutely no power is available during nights, therefore children cannot study. Providing access to electricity in rural areas of India is a major challenge. The current power supply is unreliable and access is limited. The unsustainable use of locally sourced biomass and an increasing dependence on fossil fuels are causing environmental degradation, lack of communication media, education and health services. Fuels used for cooking all over India are LPG, kerosene, fire wood, crop residue, cow dung cake and coal.

## 2. Power Scenario in India

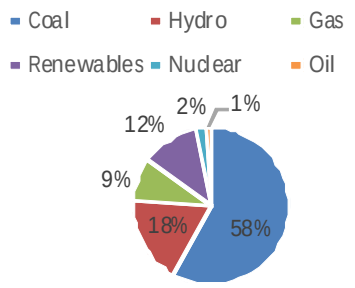


**Fig: 1.** Power Sources Distribution (Source: CEA, Ernst & Young analysis; as on 31 March 2013[10])

India has the 5th largest power generation portfolio worldwide. Coal and Gas are the popular sources and account for 58% and 9%, share, respectively. The country transitioned from being the world's 7th largest energy consumer in 2000 to the 3rdlargest one within a decade. Subsidies, Tax benefits, attractive bank loans scheme and foreign direct investment are favouring and promoting renewable energy sector. Energy demand is pacing at high rate because of need of economic growth & rapid industrialization.

**Corresponding Author,**
**E-mail address:** professor_rsmishra@yahoo.co.in
**All rights reserved:** http://www.ijari.org

## 3. Literature Review

Panda (2007) [1] focusses on the importance of electricity supply strategy resulted by domination of demand of rural electrification in India. In Addition, Rehman et al. (2012) [2] highlight the problems faced by electrification of rural India by enhancing on the demand–supply gap. Khandker et al. (2010) [3], discuss the co-relation of electricity and poverty of rural India, stated the problem faced by villages because of insufficient energy supply which disrupts their day to day work, also added the doubt whether energy leads to economic development or vice versa. In this framework, Panda (2007) [1] explained there are opportunities for consumers to earn incomes by integration of utility facility. Modi et al. (2005) [4] describe one of the goals of UN's Millennium Development modern is providing access to energy provision. Though, Cook (2011) [5] states that increased stress on rural electrification results in the more focus on poverty eradication rather than electrification. (Chaurey et al. 2004) [6] States in India 90 per cent of electrification is attained by nine states only and rest are at only 50% or below. (Palit and Chaurey 2011) [7] Discuss problems and challenges in fulfilling the rural electrification target such as more importance to urban development, inappropriate infrastructure, ineffectual implementation technique and low quality of power. (Balachandra 2012) [8]Discuss about the 1950-1980 planning period when prominence was more to irrigation in support of green revolution rather than providing households access to electricity and Kutir Jyoti scheme of government of India also focused on single line connection only. Nitesh Dutt et.al (2011)[9] analysed, compared renewable source technology i.e. biomass waste including solid waste, sewage waste, and waste cooking oil in IIT

Roorkee campus to calculate potential generation of total 396870 KWh annually of electricity out of which 180000 KWh from MSW, 72,000 KWh from kitchen waste, 870 KWh by Waste cooking oil and 144000 KWh from sewage treatment from 1.3 million litres per day of sewage water from MSW of 2190 Tonnes/ year and 238 tonnes per year of kitchen waste. He carried out cost assessment of cost per KWh without subsidy which was Rs 3.70 for Kitchen waste, Rs 2.80 for MSW and Rs 38.80 from Sewage treatment.

## 4. Problem Faced by Rural India

According to India's census 2011 data, fire wood is predominantly used as a cooking fuel in the households especially in rural parts Out of 168 million rural households; 63% use firewood, 11% use LPG, 24% use crop residues, cow dung cakes and coal, 1% use kerosene, 1% use biogas or electricity.

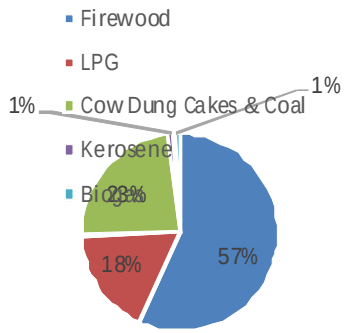


**Fig: 2.** Cooking Fuel Usage Distribution (Source: India Census 2011) [11]

Fire wood and traditional methods of cooking have various challenges such as Firewood is collected by villagers either from their own plantations or from government forests, results in deforestation. Gathering fire wood involves a lot of hard work in walking long distances and carrying head loads. These efforts are carried out mostly by women and girls in the villages which results in their underdevelopment. The women and children suffer respiratory diseases, which is an obvious impact of using fire wood and traditional methods of cooking. Using dried cow dung cakes would utilize only 10% of its total energy. Use of LPG also has challenges; People normally travel to distant place, high steep hills to get the LPG cylinder; hence the landed cost of cylinder increases. Typical reasons why villagers are not willing to entirely switch over to modern energy sources like LPG are either the fuel is very expensive or it is not easily available.

## 5. Solution Solar-Biogas Hybrid Model

Solar- Biogas Hybrid model is proposed for the Solution to problems discussed earlier. Since no single technology is capable of switching to renewable energy and moreover in Villages main activities are agriculture and Cattle feeding. We are utilizing the Cattle Dung & Agriculture waste to run Biogas Plant and installing Solar Panels on Houses to build Solar PV Plant. The tariff structure can be set to make the project viable economically by selling excess power to nearby industries. There is the possibility of paying back the capital cost over a short term period. Financial structure involves the participation of local bodies of villages, investors, NGO's. It will create employment opportunities for the village residents as they will be trained to operate and maintain the plant and revenue generated from gas and slurry can make projects viable by providing salaries and payback installments for investors and provide social-economic, educational & environmental benefits. Financing of these projects will need long term capital at favorable terms. The project is a helping held in Hon'ble PM Narendra Modi's vision: "Swach Bharat Mission".

## 6. Case Study Undertaken

A case study is done of 7 Villages near Roorkee. In Combined it consists of on an average 700 houses. Considering each house has 4 members. So total population is 700*4= 2800. Considering each house has 2 cattle and 1hectare of agriculture land. So in total cattle there are 2*700 = 1400 and 1*700=700 Hectare of agriculture land. On an average 100 water pumps have been taken into account. Village consists of 2 Health Centre, 1 Community Centre, 1 Senior Sec. School, 1 Primary School &1 post office.

### 6.1 Computation of energy need

Following numerical computation has been carried out for Villages near by Roorkee, Uttarakhand has shown in Table 1 & Table 2 respectively. Similarly the pie chart is also shown in figure 3.

**Table: 1.** Load calculation of 7 villages that have been under consideration

| Type | Items (per type) | Watts | Quantity( per type) | Total (Watts ) |
|---|---|---|---|---|
| House | Tube Light | 40 | 2 | 80 |
| | Fan | 80 | 1 | 80 |
| | Television | 140 | 1 | 140 |
| | | | Total | 300*700 Houses = 210 KW |
| School | | | | |
| Senior Secondary | Tube Light | 40 | 20 | 800 |
| | Fan | 80 | 20 | 1600 |
| | Miscellaneous | 400 | | 400 |
| | | | | |
| Primary | Tube Light | 40 | 35 | 1400 |
| | Fan | 80 | 35 | 2800 |
| | Miscellaneous | 800 | | 800 |

| | | | | |
|---|---|---|---|---|
| | | | **Total** | **7 KW** |
| | | | | |
| Post Office | Tube Light | 40 | 4 | 160 |
| | Fan | 80 | 5 | 400 |
| | | | **Total** | **0.66 KW** |
| | | | | |
| Community Centre | | | | **2 KW** |
| Health Centre | | | | **3 KW** |
| Pumps | | 1500 | 100 | **150 KW** |
| Miscellaneous | | 500000 | | **500 KW** |
| | | | **Total Wattage** | **873 KW** |

Miscellaneous load is taken which includes machines such as flour milling, reaper, threshing, milk processing, etc.

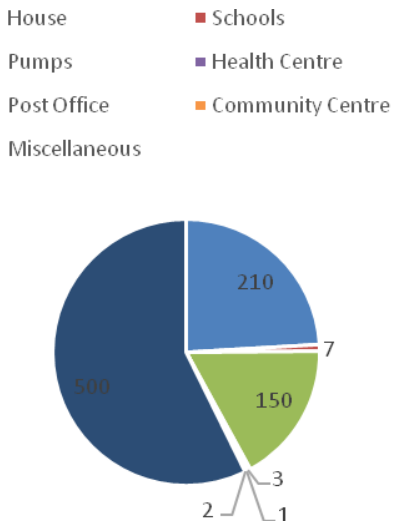


**Fig: 3.** Load Distribution in KW

**Table: 2.** Calculation total units requirement by considering optimal operational hours

| Type | Load (KW) | No. of Operational Hours | Units (KWh) |
|---|---|---|---|
| Houses | 210 | 12 | 2520 |
| Schools | 7 | 8 | 54 |
| Post Office | 1 | 8 | 8 |
| Community Centre | 2 | 3 | 6 |
| Health Centre | 3 | 18 | 54 |
| Miscellaneous | 50 | 8 | 400 |
| | | **Total** | **3042** |

### 6.2 Biomass Potential

The biomass potential for villages near Roorkee, Uttarakhand have been calculated by considering cattle dung and agricultural waste as a biogasifier feed.

#### 6.2.1 Cattle Dung

- Dung Produced= 3 Kg/Cattle/ Day
- Total Dung produced = 3*1500= 4500 Kg/Day
- Biogas produced = .07 $m^3$/Kg (with engine efficiency 28%, Generator efficiency 93%)
- Total Biogas produced = 315 $m^3$/Day
- Gas required to produce 1 KWh/day = .72$m^3$
- Total power produced= 315/.72 = 450 Kwh/ Day

#### 6.2.2 Agricultural Waste

- Agriculture waste produced= 30 % of Total Production
- Total Cultivation land= 700 Hectare
- Production in 1Hectare= 3 Ton/ 3Months
- Total production= 2100 Ton/ 3months
- Daily Production= 2100/90= 23.33 Ton
- Waste produced = .3*23.33 = 7 Ton
- Biogas produced = 140 $m^3$/Ton
- Total gas produced = 980 $m^3$
- .72$m^3$ gas generate 1KWh
- Total Power Generation = 1350 Kwh/ Day
- Total Power produced from Biogas = 450+1350 = 1800KWh/Day
- Plant Capacity = 100KW, taking 18 Hours of operation

### 6.3 Solar Potential

- Installing 2 Solar modules of 250 Wp on each house
- This gives total 700*250*2 = 350Kwp
- Taking Sun Hours = 4.5
- Total Electricity produced = 525*4.5 = 1575 KWh

## 7. Results & Discussion

The numerical computation has been carried out and following total load need is calculated which provides the feasibility of the Mixing technologies proposed as given below.

Total Peak Load Calculated = 3042 KW, Total Base load (considering 50 % of total peak load)= 1521 KW for 24hrs operation, Therefore Biogas plant can satisfy alone on Base Load demand which will produce 1800 units and for the Peak load demand Solar will alone contribute 1575 units. So in total the solution Solar Biomass hybrid modal produces 4300 Units and requirement is 3042 units.

## 8. Conclusion

It is seen electrification plays major role in economic development of the community and higher electrification rate more income is generated per capita. No single technology is capable to switch to renewable energy but by mixing the technologies we can utilize benefits of both the technologies. This solution involves in community participation of local village bodies, Village residents, NGO's, and investors. Training programme will be conducted to provide awareness of the project benefits; waste management, living standard, education, access to electricity to villages. Volunteers will be trained to operate and maintain the plant. This training can be replicated to near-by villages and locations. Community biogas plant, biogas grid and Solar Plant appears as sustainable solutions to cater to the village cooking, agriculture, health and education energy needs. In addition to availability of raw material (cattle dung) for biogas plant, willingness and commitment of villagers is a key to success.

## References

[1] H. Panda, Governance of rural electricity systems in India: An overview of Indian scenario. In Governance of Rural Electricity Systems in India (ed. Haribandhu Panda). New Delhi: Academic Foundation, 2007, 23–52
[2] I. H. Rehman, A. Kar, M. Banerjee, P. Kumar, M. Shardul, J. Mohanty, I. Hossain, Understanding the political economy and key drivers of energy access in addressing national energy access priorities and policies. Energy Policy, 47, Supplement 1, 2012
[3] S. R. Khandker, D. F. Barnes, H. A. Samad, Energy poverty in rural and urban India: Are the energy poor also income poor? Policy Research Working Paper Series 5463. The World Bank, 2010
[4] V. Modi, Improving Electricity Services in Rural India. Available at <http:/ / www.me. columbia.edu/fac-bios/modi/resources/Rural Energy_India.pdf>, 2014, 2005
[5] P. Cook, Infrastructure, rural electrification and development. Energy for Sustainable Development, 15(3), 2011, 304–313.
[6] A. Chaurey, M. Ranganathan, P. Mohanty, Electricity access for geographically disadvantaged rural communities: Technology and policy insights. Energy Policy, 32(15), 2004, 1693–1705.
[7] D. Palit, R. Malhotra, A. Kumar, Sustainable model for financial viability of decentralized biomass gasifier based power projects. Energy Policy, 39, 2011, 4893–4901
[8] P. Balachandra, Universal and sustainable access to modern energy services in rural India: An overview of policy-programmatic interventions and implications for sustainable development. Journal of the Indian Institute of Science, 92: 1, 2012
[9] M. P. Siddharthjain, Power generation from MSW of Haridwar City: A Feasibility study. Renewable and Sustainable Energy Reviews, 69-90, 2011
[10] CEA, Ernst & Young analysis; as on 31 March 2013 report.
[11] Source: India Census 2011 report.

*Nature & Environment*
Vol. 20 (2), 2015: 73-89
Website: www.natureandenvironment.com

ISSN (Print) : 2321-810X
ISSN (Online) : 2321-8738

RESEARCH ARTICLE

# Irreversibility Optimization Using Energy-Exergy Analysis of Three Stage Vapour Compression Refrigeration Systems with Flash-Intercooler Using Ecofriendly Refrigerants (R410a, R290, R600, R600a, R1234yf, R125, R717 And R134A) for Reducing Global Warming and Ozone Depletion

**R.S. Mishra, Kapil Chopra and V. Sahni**
Mechanical Engineering Department, Delhi Technological University, Delhi, India
Email: professor_rsmishra@yahoo.co.in, Rsmishra1651956@yahoo.co.in

Received: 9th March 2015, Revised: 14th May 2015, Accepted: 25th May 2015

## ABSTRACT

*In this analysis comparison and impact of environmental friendly refrigerants on multiple stage vapour compression refrigerator with flash intercooler and individual throttle valves (system-1) and multiple stage vapour compression refrigerator with flash intercooler and multiple throttle valves (system-2) has been investigated on the basis of energetic and exergetic approach. It has been observed that for all selected refrigerants energy and exergy efficiency of system-1 lower than sytem-2. For both systems R125 showed poor performance in terms of energetic efficiency, second law efficiency and irreversibility whereas performances of R600 and R717 is better in comparison of other selected refrigerants As R717 is toxic in nature and restricted to limited applications, so R600 is suggested for both systems. Thermodynamic performance of R134a is only 2-3% lesser than R600.Also R134A is easily available, therefore R134a may also be used for practical applications than R600 without taking of any safety precautions.*

***Key words:*** *Energy-Exergy Analysis, Flash-Intercooler, Ecofriendly Refrigerants, Global Warming*

## INTRODUCTION

Nowadays most of the energy utilize in cooling and air conditioning in industrial as well as for domestic applications, in addition to energy consumption, using of refrigerants in cooling and air conditioning having high GWP and ODP which are responsible for increasing global warming and ozone depletion. The primary requirements of ideal refrigerants are having good physical and chemical properties. Due to good physical and chemical properties such as non-corrosiveness, non-toxicity, non- flammability, low boiling point, Chlorofluorocarbons (CFCs) have been used over the last many decades, but hydrochlorofluorocarbons (HCFCs) and Chlorofluorocarbons (CFCs) having large amount chlorine content as well as high global warming potential and ozone depletion potential, so after 90s refrigerants under these categories these kinds of refrigerants are almost prohibited [1].Most of the study has been carried out for the performance evaluation of vapour compression refrigeration system using energetic analysis, but with the help of first law analysis irreversibility destruction or losses in components of system unable to determined [2], so exergetic analysis is the advanced approach for thermodynamic analysis which gives an additional practical view of the processes [3-5]. The utility of second law analysis on vapour compression refrigeration systems is well defined because it gives the idea for improvements in efficiency due to modifications in existing design in terms of reducing exergy destructions in the components. In

addition to this second law analysis also provides new thought for development in the existing system [6].

**Nomenclature:**

| | | | |
|---|---|---|---|
| LTE | low temperature evaporator | $\Phi$ | specific enthalpy (kJ/kg) |
| ITE | intermediate temperature evaporator | $\Psi$ | irreversibility rate(kW) |
| THE | high temperature evaporator | C | compressor |
| TR | ton of refrigeration | X | exergy rate of fluid (kW) |
| P | power (kJ/s) | $\dot{m}$ | mass flow rate (kg/s) |
| f | flash intercooler | S | specific entropy (kJ/kgK) |
| $\dot{Q}$ | rate of heat transfer (kW) | $\dot{EP}$ | exergy rate of product (kW) |
| $\dot{W}$ | work rate (kW) | | |
| T | temperature (°C) | | |
| TV | throttle valve | | |
| x | dryness fraction(non-dimensional) | | |

*Subscript*

| | | | |
|---|---|---|---|
| e | evaporator | tv | throttle valve |
| c | compressor | lsc | liquid subcooler |
| o | dead state | k | kth component |
| f | flash intercooler | gen | generation |
| r | refrigerant | cond | condenser |

Xuan and Chen [7] presented in this manuscript about the replacement of R502 by mixture of HFC-161.Through experimental study it was found that mixture of HFC-161 gives same and higher performance than R404A at lower and higher evaporative temperature respectively on the vapour compression refrigeration system designed for R404A.Cabello et al.[8] effect of condensing pressure, evaporating pressure and degree of superheating was experimentally investigated on single stage vapour compression refrigeration system using R22, R134a and R407C.It was observed that mass flow rate is greatly affected by change in suction conditions of compressor in results on refrigeration capacity because refrigeration capacity depended on mass flow rate through evaporator. It was also found that for higher compression ratio R22 gives lower COP than R407C.Spatz and Motta [9] focused on replacement of R12 with R410a through experimental investigation of medium temperature vapour compression refrigeration cycles. In terms of thermodynamic analysis, comparison of heat transfer and pressure drop characteristics, R410a gives best performance among R12, R404a and R290a.Han et al. [10] under different working conditions experimental results revealed that there could be replacement of R407C in vapour compression refrigeration system having rotor compressor with mixture of R32/R125/R161 showing higher COP, less pressure ratio and slightly high discharge compressor temperature without any modification in the same system. Cabello et al [11] had studied about the effect of operating parameters on COP, work input and cooling capacity of single-stage vapour compression refrigeration system.

There is great influence on energetic parameters due change in suction pressure, condensing and evaporating temperatures. Arora and Kaushik [12] developed numerical model of actual vapour compression refrigeration system with liquid vapour heat exchanger and did energy and exergy analysis on the same in the specific temperature range of evaporator and condenser. They concluded that R502 is the best refrigerant compare to R404A and R507A, compressor is the worst and liquid vapour heat exchanger is best component of the system. Getu and Bansal [13] had optimized the design and operating parameters of like condensing temperature, subcooling temperature, evaporating temperature, superheating temperature and temperature difference in cascade heat exchanger R744-R717 cascade refrigeration system. A regression analysis was also done to obtain optimum thermodynamic parameters of same system. Mohanraj et al [14] through experimental investigation of domestic refrigerator they arrived on conclusions that under

different environmental temperatures COP of system using mixture of R290 and R600a in the ratio of 45.2: 54.8 by weight showing up to 3.6% greater than same system using R134a, also discharge temperature of compressor with mixture of R290 and R600a is lower in the range of 8.5-13.4K than same compressor with R134a.Padilla et al [15] exergy analysis of domestic vapour compression refrigeration system with R12 and R413A was done. They concluded that performance in terms of power consumption, irreversibility and exergy efficiency of R413A is better than R12. In this paper great emphasis put on saving of energy and using of ecofriendly refrigerants due to increase of energy crises, global warming and depletion of ozone layer. In this investigation the work input required running the vapour compression refrigeration system reduced by using compound compression and further decreased by flash intercooling between compressors. COP of system can also be enhanced by compressing the refrigerant very close to the saturation line this can be achieved by compressing the refrigerants in more stages with intermediate intercoolers. The refrigeration effect can be increase by maintaining the condition of refrigerants in more liquid stage at the entrance of evaporator which can be achieved by expanding the refrigerant very close to the liquid line. The expansion can be brought close to the liquid line by subcooling the refrigerant and removing the flashed vapours by incorporating the flash chamber in the working cycle. The evaporator size can be reduced because unwanted vapours formed are removed before the liquid refrigerant enters in the evaporator. Multi-stage vapour compression with flash intercooler and individual throttle valves (system-1) consists of three compressors arranged in compound compression, individual throttle valves, condenser and evaporators as shown in Fig.1. Multiple evaporators at different temperatures with compound compression, flash intercooler and multiple throttle valves (system-2) consists of three compressors arranged in compound compression, multiple throttle valves, condenser and evaporators as shown in Fig.2.

**Table 1:** Physical and environmental characteristics of considered refrigerants

| Refrigerant | Chemical formula | Molecular mass(g/mol) | NBP ($^oC$) | $T_{cri}$ ($^oC$) | $P_{cri}$(MPa) | ASHRAE safety code |
|---|---|---|---|---|---|---|
| R410A | R-32/125 | 72.58 | -60.9 | 72.5 | 4.95 | A1 |
| R290 | $CH_3CH_2CH_3$ | 44.1 | -42.2 | 96.7 | 4.25 | A3 |
| R600A | $C_4H_{10}$ | 58.122 | -11.74 | 134.661 | 3.62 | A3 |
| R1234YF | $C_3H_2F_4$ | 114.04 | -29.4 | 94.85 | 3.38 | A2L |
| R600 | $C_4H_{10}$ | 58.122 | -0.49 | 151.98 | 3.79 | A3 |
| R134A | $CH_2FCF_3$ | 102.03 | -26.1 | 101.1 | 4.06 | A1 |
| R125 | $C_2HF_5$ | 120.02 | -48.09 | 66.023 | 3.61 | A1 |
| R717 | $NH_3$ | 17.03 | -33.327 | 132.25 | 11.33 | B2 |

## ENERGY AND EXERGY ANALYSIS

For carrying out energetic and exergetic analysis, computational models of system-1 and system-2 has been developed and impact of chosen refrigerants on these systems has been analyzed using Engineering Equation Solver software[16].In this investigation following assumptions are made:

1. Load on the low, intermediate and high temperature evaporators are 10TR, 20 TR and 30 TR respectively.
2. Dead state temperature ($T_0$): 25 $^oC$
3. Difference between evaporator and space temperature ($T_r$-$T_e$):5 $^oC$.
4. Adiabatic efficiency of compressor: 76%.

5. Dead state enthalpy ($\Phi_0$) and entropy ($s_0$) of the refrigerants have been calculated corresponding to the dead state temperature ($T_0$) of 25 °C.
6. Variation in kinetic and potential energy is negligible.
7. Expansion process is adiabatic
8. Temperature of low, intermediate and high temperature evaporators are -10 °C,0 °C and 10 °C respectively.
9. Condenser temperature : 40 °C
10. Degree of sub cooling : 10 °C

**Fig.1:** Schematic diagram of multiple evaporators with compound compression, flash intercooler and individual throttle valves

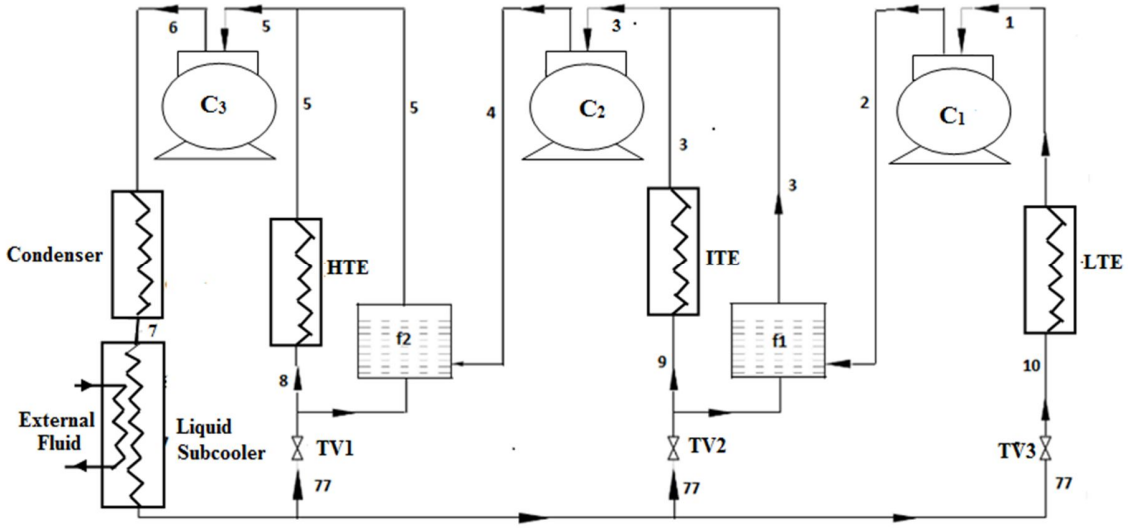


**Fig.2:** Schematic diagram of multiple evaporators with compound compression, flash intercooler and multiple throttle valves

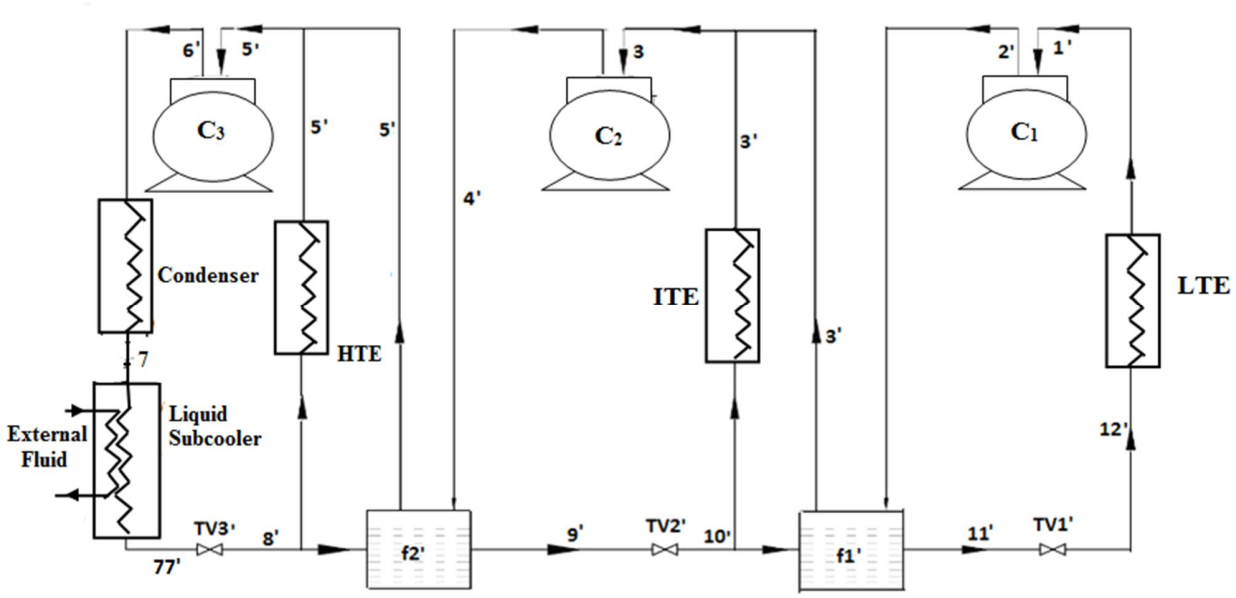

*Exergy at any state is given as*

$$X = (\Phi - \Phi_0) - T_0(s - s_0) \quad (1)$$

*Energy analysis*

First law of thermodynamic gives the idea of energy balance of system.

**Mass flow analysis of system-1**

$$\dot{m}_{c1} = \dot{m}_{e1} = \frac{\dot{Q}_{e1}}{(\Phi_1 - \Phi_{10})} \quad (2)$$

$$\dot{m}_{e2} = \frac{\dot{Q}_{e2}}{(\Phi_3 - \Phi_9)} \quad (3)$$

$$\dot{m}_{f1} = \frac{\dot{m}_{c1}(\Phi_2 - \Phi_3)}{(\Phi_3 - \Phi_9)} \quad (4)$$

$$\dot{m}_{c2} = \dot{m}_{c1} + \dot{m}_{e2} + \dot{m}_{f1} \quad (5)$$

$$\dot{m}_{e3} = \frac{\dot{Q}_{e3}}{(\Phi_5 - \Phi_8)} \quad (6)$$

$$\dot{m}_{f2} = \frac{\dot{m}_{c2}(\Phi_4 - \Phi_5)}{(\Phi_5 - \Phi_8)} \quad (7)$$

$$\dot{m}_{c3} = \dot{m}_{c2} + \dot{m}_{e3} + \dot{m}_{f2} \quad (8)$$

**Energy consumption for sytem-1**

$$P_{c1} = \frac{\dot{m}_{c1}(\Phi_2 - \Phi_1)}{60} \quad (9)$$

$$P_{c2} = \frac{\dot{m}_{c2}(\Phi_4 - \Phi_3)}{60} \quad (10)$$

$$P_{c3} = \frac{\dot{m}_{c3}(\Phi_6 - \Phi_5)}{60} \quad (11)$$

**Energetic efficiency of system-1**

$$COP = \frac{\dot{Q}_e}{P_c * 60} \quad (12)$$

***Rate of exergy loss due to irreversibility*** $(T_o\dot{S}_{gen})$ ***in various components of system-1***

The concept of exergy was given by second law of thermodynamics, which always decreases due to thermodynamic irreversibility. Exergy is defined as the measure of usefulness, quality or potential of a stream to cause change and an effective measure of the potential of a substance to impact the environment [12].

*Compressors*

$$(T_o\dot{S}_{gen})_{c1} = \dot{W}_{c1} + \dot{m}_{c1}(X_2 - X_1) \quad (13)$$

$$(T_o\dot{S}_{gen})_{c2} = \dot{W}_{c2} + \dot{m}_{c2}(X_4 - X_3) \quad (14)$$

$$(T_o\dot{S}_{gen})_{c3} = \dot{W}_{c3} + \dot{m}_{c3}(X_6 - X_5) \quad (15)$$

$$\dot{\Psi}_c = (T_o\dot{S}_{gen})_{c1} + (T_o\dot{S}_{gen})_{c2} + (T_o\dot{S}_{gen})_{c3} \quad (16)$$

*Evaporators*

$$(T_o\dot{S}_{gen})_{e1} = \dot{m}_{e1}(X_1 - X_{10}) - \dot{Q}_{e1}\left(1 - \frac{T_0}{T_{r1}}\right) \quad (17)$$

$$\left(T_o\dot{S}_{gen}\right)_{e2} = \dot{m}_{e2}(X_3 - X_9) - \dot{Q}_{e2}\left(1 - \frac{T_0}{T_{r2}}\right) \quad (18)$$

$$(T_o\dot{S}_{gen})_{e3} = \dot{m}_{e3}(X_5 - X_8) - \dot{Q}_{e3}\left(1 - \frac{T_0}{T_{r3}}\right) \quad (19)$$

$$\dot{\Psi}_e = (T_o\dot{S}_{gen})_{e1} + (T_o\dot{S}_{gen})_{e2} + (T_o\dot{S}_{gen})_{e3} \quad (20)$$

*Condenser*

$$\dot{\Psi}_{cond} = \left(T_o\dot{S}_{gen}\right)_{cond} = \dot{m}_{c3}(X_6 - X_7) - \dot{Q}_e\left(1 - \frac{T_0}{T_r}\right) \quad (21)$$

*Throttle Valves*

$$(T_o\dot{S}_{gen})_{tv1} = \dot{m}_{e1}(X_{77} - X_{10}) \quad (22)$$

$$\left(T_o\dot{S}_{gen}\right)_{tv2} = (\dot{m}_{e2} + \dot{m}_{f1})(X_{77} - X_9) \quad (23)$$

$$(T_o\dot{S}_{gen})_{tv3} = (\dot{m}_{e3} + \dot{m}_{f2})(X_{77} - X_8) \quad (24)$$

$$\dot{\Psi}_{tv} = (T_o\dot{S}_{gen})_{tv1} + (T_o\dot{S}_{gen})_{tv2} + (T_o\dot{S}_{gen})_{tv3} \quad (25)$$

*Liquid subcooler*

$$\dot{\Psi}_{lsc} = (T_o\dot{S}_{gen})_{sc} = \dot{m}_{c3}(X_7 - X_{77}) \quad (26)$$

*Flash intercoolers*

$$(T_o\dot{S}_{gen})_{f1} = \dot{m}_{f1}(X_9 - X_3) + \dot{m}_{c1}(X_2 - X_3) \quad (27)$$

$$(T_o\dot{S}_{gen})_{f2} = \dot{m}_{f2}(X_8 - X_5) + \dot{m}_{c1}(X_4 - X_5) \quad (28)$$

$$\dot{\Psi}_f = (T_o\dot{S}_{gen})_{f1} + (T_o\dot{S}_{gen})_{f2} \quad (29)$$

**Total irreversibility destruction in system-1**

$$\sum \dot{\Psi}_k = \dot{\Psi}_e + \dot{\Psi}_c + \dot{\Psi}_{cond} + \dot{\Psi}_{tv} + \dot{\Psi}_{lsc} + \dot{\Psi}_f \quad (30)$$

$$\dot{m}_{c1'} = \dot{m}_{e1'} = \frac{\dot{Q}_{e1'}}{(\Phi_{1'} - \Phi_{12'})} \quad (31)$$

$$\dot{m}_{e2'} = \frac{\dot{Q}_{e2'}}{(\Phi_{3'} - \Phi_{10'})} + \dot{m}_{c1'}\left(\frac{x_{10'}}{1 - x_{10'}}\right) \quad (32)$$

$$\dot{m}_{f1'} = \frac{\dot{m}_{c1'}(\Phi_{2'} - \Phi_{3'})}{(\Phi_{3'} - \Phi_{10'})} \quad (33)$$

$$\dot{m}_{c2'} = \dot{m}_{c1'} + \dot{m}_{e2'} + \dot{m}_{f1'} \quad (34)$$

$$\dot{m}_{e3'} = \frac{\dot{Q}_{e3'}}{(\Phi_{5'} - \Phi_{8'})} + \dot{m}_{c2'}\left(\frac{x_{8'}}{1 - x_{8'}}\right) \quad (35)$$

$$\dot{m}_{f2'} = \frac{\dot{m}_{c2'}(\Phi_{4'} - \Phi_{5'})}{(\Phi_{5'} - \Phi_{8'})} \quad (36)$$

**Power required for running the compressors**

$$P_{c1'} = \frac{\dot{m}_{c1'}(\Phi_{2'} - \Phi_{1'})}{60} \quad (37)$$

$$P_{c2'} = \frac{\dot{m}_{c2'}(\Phi_{4'} - \Phi_{3'})}{60} \quad (38)$$

$$P_{c3'} = \frac{\dot{m}_{c3'}(\Phi_{6'} - \Phi_{5'})}{60} \quad (39)$$

$$\text{Energetic efficiency} = \frac{\dot{Q}_{e'}}{P_{c'} * 60} \quad (40)$$

**Rate of exergy loss due to irreversibilties ($T_o\dot{S}_{gen}$) in various components of system-2**

*Compressors*

$$(T_o\dot{S}_{gen})_{c1'} = \dot{W}_{c1'} + m_{c1'}(X_{2'} - X_{1'}) \quad (41)$$

$$(T_o\dot{S}_{gen})_{c2'} = \dot{W}_{c2'} + m_{c2'}(X_{4'} - X_{3'}) \quad (42)$$

$$(T_o\dot{S}_{gen})_{c3'} = \dot{W}_{c3'} + m_{c3'}(X_{6'} - X_{5'}) \quad (43)$$

$$\dot{\Psi}_{c'} = (T_o\dot{S}_{gen})_{c1'} + (T_o\dot{S}_{gen})_{c2'} + (T_o\dot{S}_{gen})_{c3'} \quad (44)$$

*Evaporators*

$$(T_o\dot{S}_{gen})_{e1'} = \dot{m}_{e1'}(X_{1'} - X_{12'} - \dot{Q}_{e1'}\left(1 - \frac{T_0}{T_{r1'}}\right) \quad (45)$$

$$(T_o\dot{S}_{gen})_{e2'} = \dot{m}_{e2'}(X_{3'} - X_{10'}) - \dot{Q}_{e2'}\left(1 - \frac{T_0}{T_{r2'}}\right) \quad (46)$$

$$(T_o\dot{S}_{gen})_{e3'} = \dot{m}_{e3'}(X_{5'} - X_{8'}) - \dot{Q}_{e3'}\left(1 - \frac{T_0}{T_{r3'}}\right) \quad (47)$$

$$\dot{\Psi}_{e'} = (T_o\dot{S}_{gen})_{e1'} + (T_o\dot{S}_{gen})_{e2'} + (T_o\dot{S}_{gen})_{e3'} \quad (48)$$

*Condenser*

$$\dot{\Psi}_{cond'} = (T_o\dot{S}_{gen})_{cond'} = \dot{m}_{c3'}(X_{6'} - X_{7'}) - \dot{Q}_{e'}\left(1 - \frac{T_0}{T_{r'}}\right) \quad (49)$$

**Throttle Valves**

$$(T_o\dot{S}_{gen})_{tv1'} = \dot{m}_{e1'}(X_{11'} - X_{12'}) \quad (50)$$

$$(T_o\dot{S}_{gen})_{tv2'} = \dot{m}_{c2'}(X_{9'} - X_{10'}) \quad (51)$$

$$(T_o\dot{S}_{gen})_{tv3'} = \dot{m}_{c3'}(X_{77'} - X_{8'}) \quad (52)$$

$$\dot{\Psi}_{tv'} = (T_o\dot{S}_{gen})_{tv1'} + (T_o\dot{S}_{gen})_{tv2'} + (T_o\dot{S}_{gen})_{tv3'} \quad (53)$$

*Liquid subcooler*

$$\dot{\Psi}_{lsc'} = (T_o\dot{S}_{gen})_{lsc'} = \dot{m}_{c3'}(X_{7'} - X_{77'}) \quad (54)$$

*Flash intercoolers*

$$(T_o\dot{S}_{gen})_{f1'} = \dot{m}_{f1'}(X_{10'} - X_{3'}) + \dot{m}_{c1'}(X_{2'} - X_{3'}) \quad (55)$$

$$(T_o\dot{S}_{gen})_{f2'} = \dot{m}_{f2'}(X_{8'} - X_{5'}) + \dot{m}_{c2'}(X_{4'} - X_{5'}) \quad (56)$$

$$\dot{\Psi}_{f'} = (T_o\dot{S}_{gen})_{f1'} + (T_o\dot{S}_{gen})_{f2'} \quad (57)$$

**Total irreversibility destruction in system-1**

$$\sum \dot{\Psi}_{k'} = \dot{\Psi}_{e'} + \dot{\Psi}_{c'} + \dot{\Psi}_{cond'} + \dot{\Psi}_{tv'} + \dot{\Psi}_{lsc'} + \dot{\Psi}_{f'} \quad (58)$$

**Exergetic efficiency**

Exergetic efficiency

$$= \frac{\text{Exergy of cooling load of evaporators}}{\text{Compressors work}} = \frac{\dot{E}P}{\dot{W}} \quad (59)$$

**Exergetic efficiency of system − 1**

$$= \frac{(\dot{Q}_{e1} + \dot{Q}_{e2} + \dot{Q}_{e3}) - T_o\left(\frac{\dot{Q}_{e1}}{T_{r1}} + \frac{\dot{Q}_{e2}}{T_{r2}} + \frac{\dot{Q}_{e3}}{T_{r3}}\right)}{P_c * 60} \quad (60)$$

**Rational efficiency of system − 2**

$$= \frac{(\dot{Q}_{e1'} + \dot{Q}_{e2'} + \dot{Q}_{e3'}) - T_o\left(\frac{\dot{Q}_{e1'}}{T_{r1'}} + \frac{\dot{Q}_{e2'}}{T_{r2'}} + \frac{\dot{Q}_{e3'}}{T_{r3'}}\right)}{P_{c'} * 60} \quad (61)$$

## RESULTS AND DISCUSSION

Variation in low, intermediate and high temperature evaporator with coefficient of performance for considered refrigerants of system-1 and system-2 is shown by Fig.3-5 and Fig.6-8 respectively. Both systems (system-1& system-2) were analytically analyzed and it was observed that COP (energetic efficiency) of system-2 is higher than system-1.

**Fig.3:** Variation of low temperature evaporator of system-1 with energetic efficiency

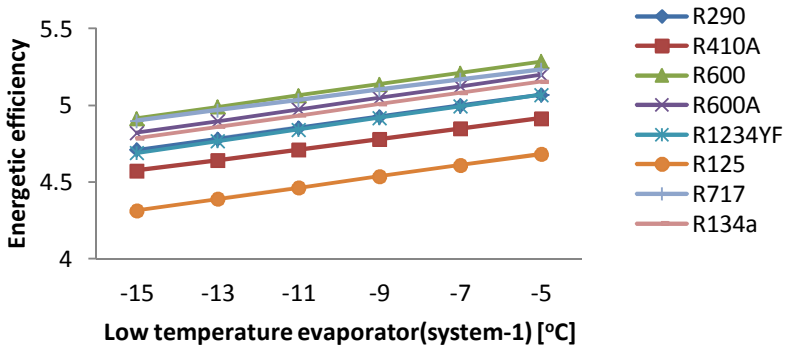


**Fig.4:** Variation of intermediate temperature evaporator of system-1 with energetic efficiency

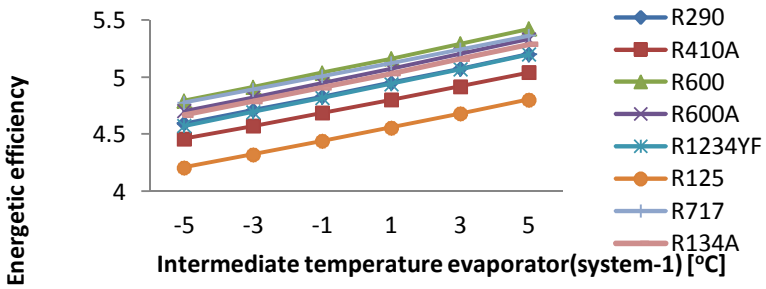

The COP of both system-1 and system-2 increase with increase in evaporator temperature for chosen refrigerants. It was also observed that R600 and R717 show better performance and R125 gives poor performance in term of energetic efficiency than other refrigerants for both systems. The maximum percentage difference of COP was observed in high temperature evaporator of system-2 and system-1 is 9.59% for R125 at 15 °C ,

**Fig.5:** Variation of high temperature evaporator of system-1 with energetic efficiency

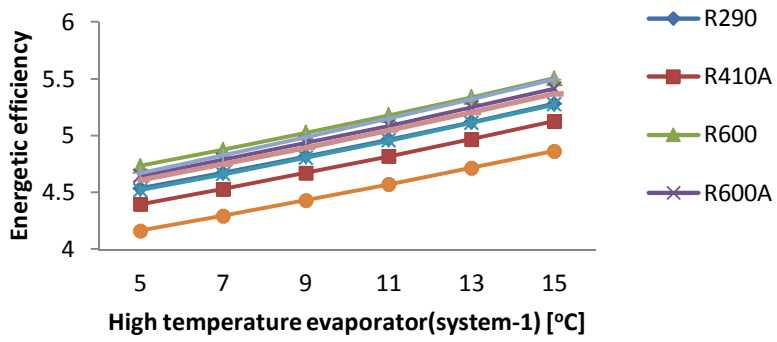


**Fig.6:** Variation of low temperature evaporator of system-2 with energetic efficiency

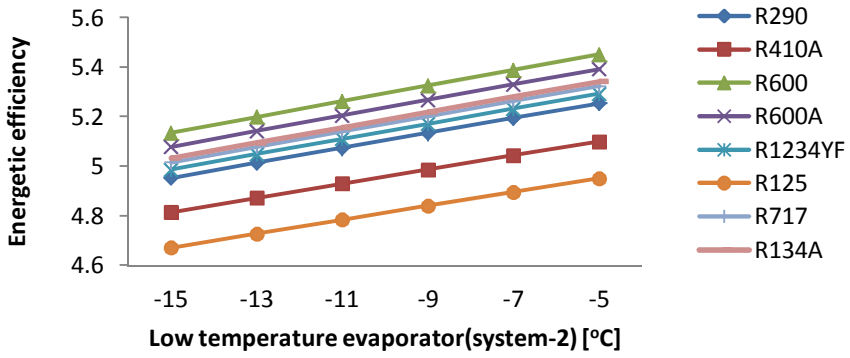


**Fig.7:** Variation of intermediate temperature evaporator of system-2 with energetic efficiency

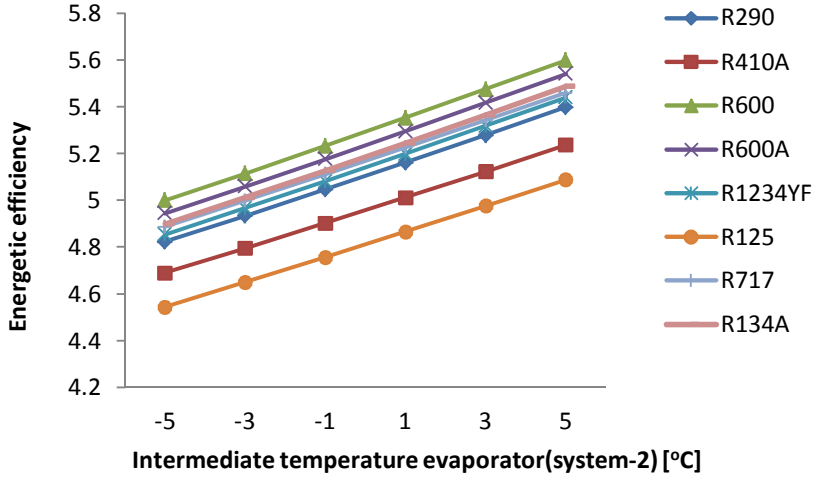

**Fig.8:** Variation of high temperature evaporator of system-2 with energetic efficiency

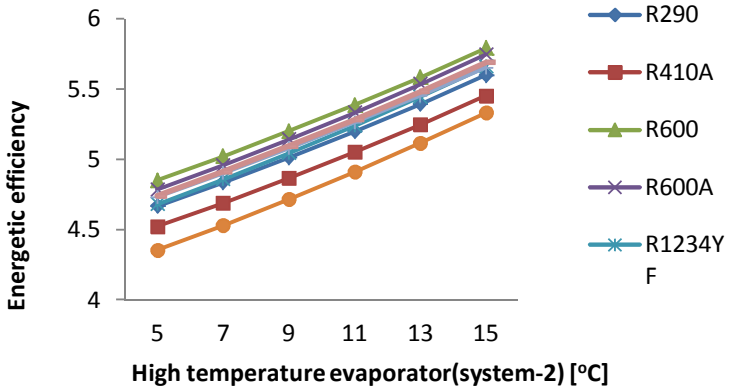


**Fig.9:** Variation of low temperature evaporator of system-1 with exergetic efficiency

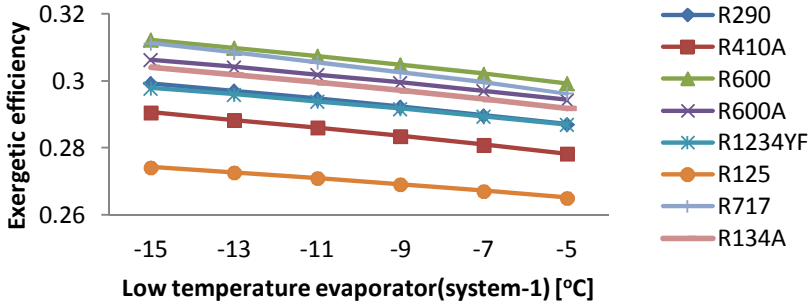


The impact on second law efficiency (exergetic efficiency) with change in temperature of low, intermediate and high temperature evaporator of system-1 and system-2 shown by Fig.9-11and Fig.11-14 respectively. As variation in second law efficiency is reciprocal to coefficient of performance. It is also observed that second law efficiency decrease with increase in evaporator temperature. R600 and R125 have maximum and minimum second law efficiency for both systems similar to performance evaluation in terms of energetic efficiency. It was also found that temperature variation in low and intermediate evaporator put great impact on second law efficiency in comparison with high temperature evaporator, for both systems

**Fig.10:** Variation of intermediate temperature evaporator of system-1with exergetic efficiency

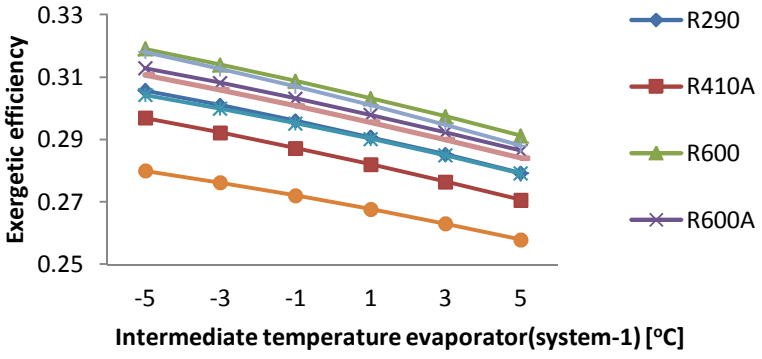

**Fig.11:** Variation of high temperature evaporator of system-1with exergetic efficiency

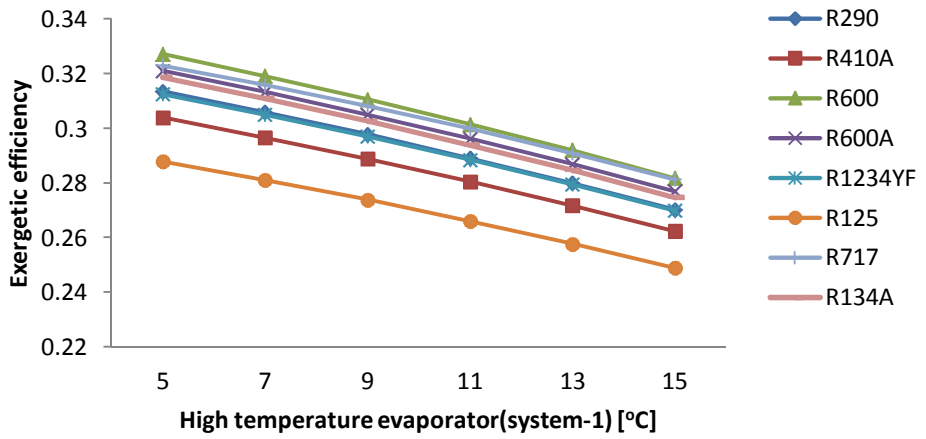


**Fig.12:** Variation of low temperature evaporator of system-2 with exergetic efficiency

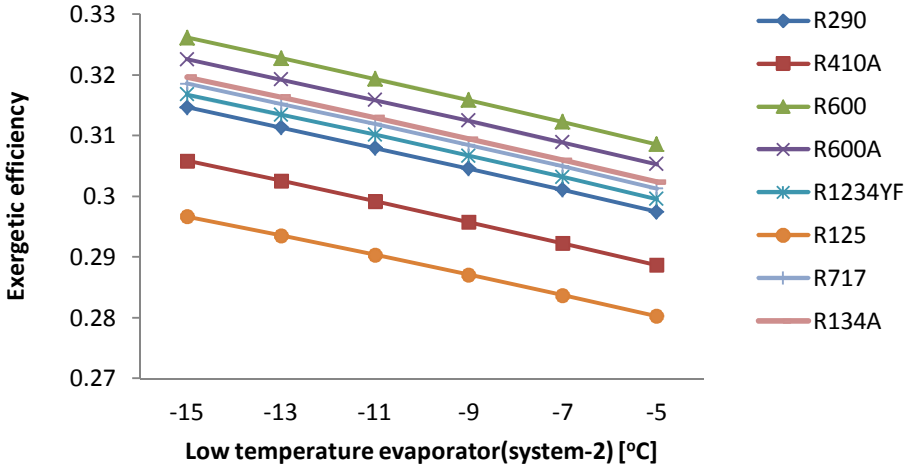


**Fig.13:** Variation of intermediate temperature evaporator of system-2 with exergetic efficiency

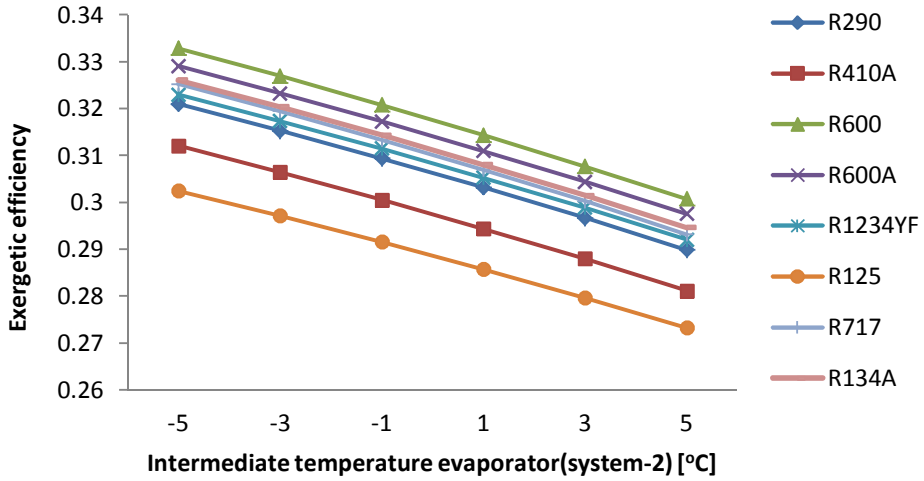

**Fig.14:** Variation of high temperature evaporator of system-2 with exergetic efficiency

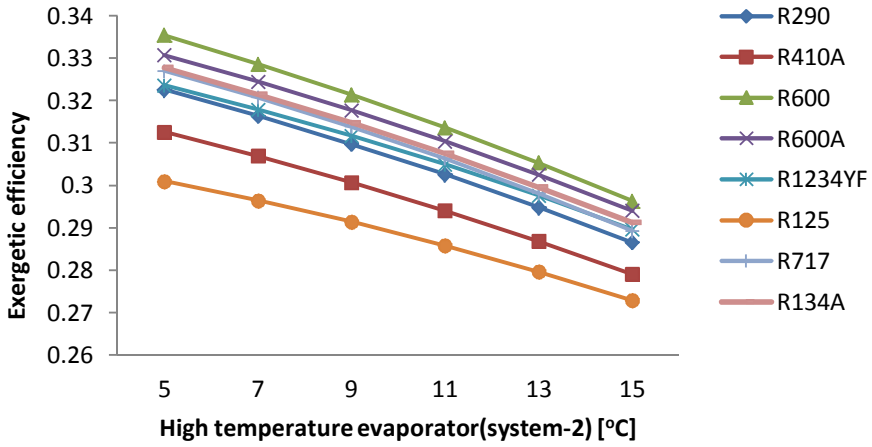


**Fig.15:** Variation of low temperature evaporator with irreversibility of sytem-1

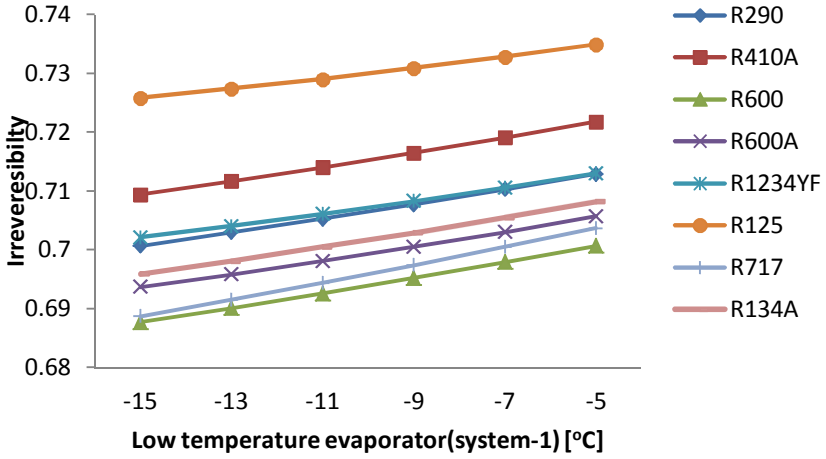


**Fig.16:** Variation of intermediate temperature evaporator with irreversibility of sytem-1

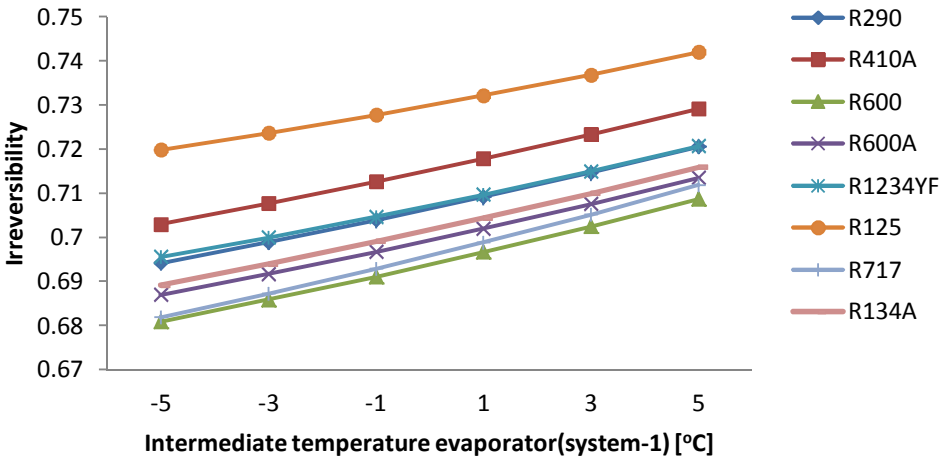

**Fig.17:** Variation of high temperature evaporator with irreversibility of sytem-1

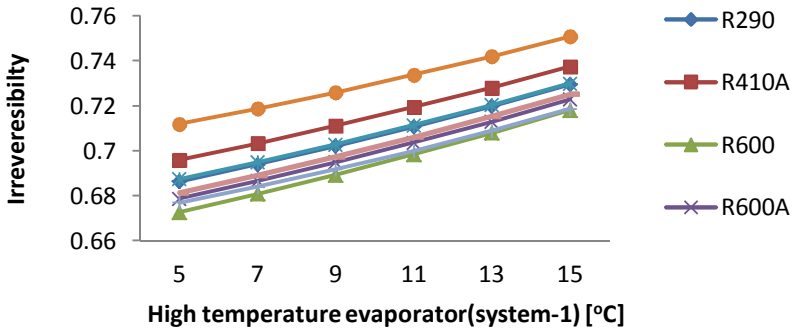


**Fig.18:** Variation of low temperature evaporator with irreversibility of sytem-2

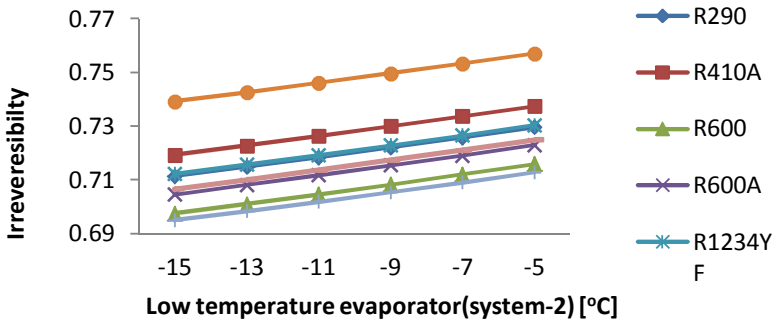


Irreversibility in system is work required to displace the atmosphere or lost work during the process. The irreversibility analysis of system-1 and system-2 is presented by Figs.15-17 and Figs.18-20 respectively. It was experienced that irreversibility of both system-1 and system-2 increase with increase in temperature of evaporator.R125 shows maximum irreversibility, on the other hand R600 and R717 show minimum irreversibility in systems compared with another selected refrigerants. It is also observed that irreversibility in system-1 is 1.4-2.1%, 1.3-2.2% and 1.6-2.0% using R600 and 1.8-3%, 1.7-3.1%, 2.2-2.7% using R125 is lower than system-2 for low, intermediate and high temperature evaporator respectively. This marginal irreversibility differences between system-1 and system-2 could be neglected.

**Fig.20:** Variation of high temperature evaporator with irreversibility of sytem-2

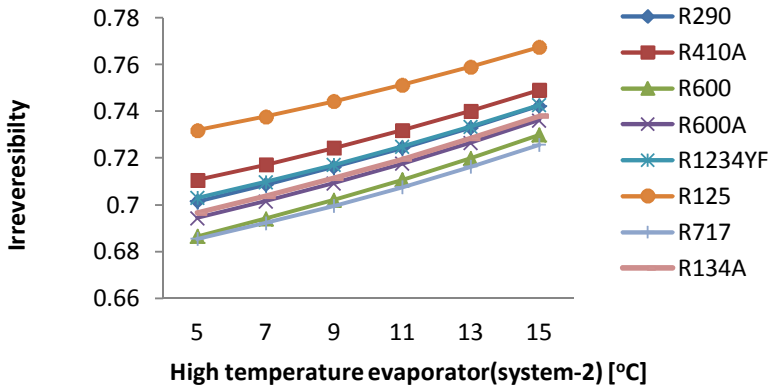

**Fig.19:** Variation of intermediate temperature evaporator with irreversibility of sytem-2

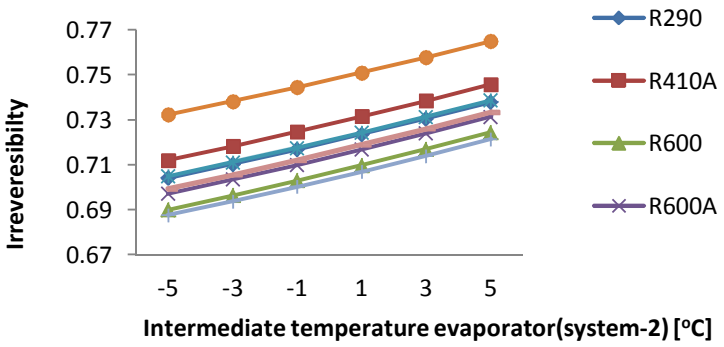


The impact of change in condenser temperature in range of 25 °C to 45 on coefficient of performance, second law efficiency and system irreversibility is shown in Figs.21-26 for sytem-1 and system-2 using ecofriendly refrigerants. This analysis reveals that COP and second law efficiency decreases with increase in condenser temperature on the other hand exergy destruction (system irreversibility) increase with increase in condenser temperature for system-1 & sytem-2.

**Fig.21:** Variation of condenser temperature with energetic efficiency of sytem-1

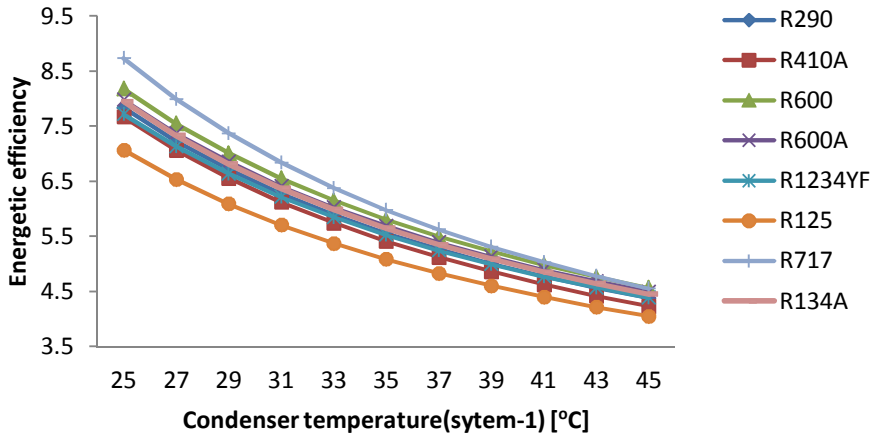


**Fig.22:** Variation of condenser temperature with energetic efficiency of sytem-2

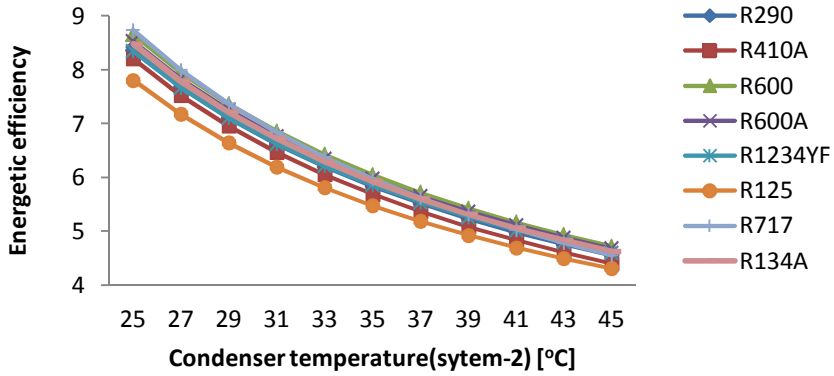

**Fig.23:** Variation of condenser temperature with exergetic efficiency of sytem-1

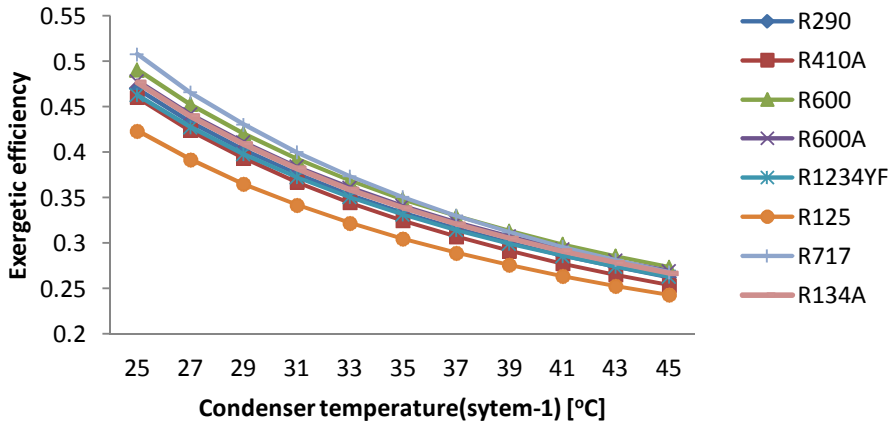


**Fig.24:** Variation of condenser temperature with exergetic efficiency of sytem-2

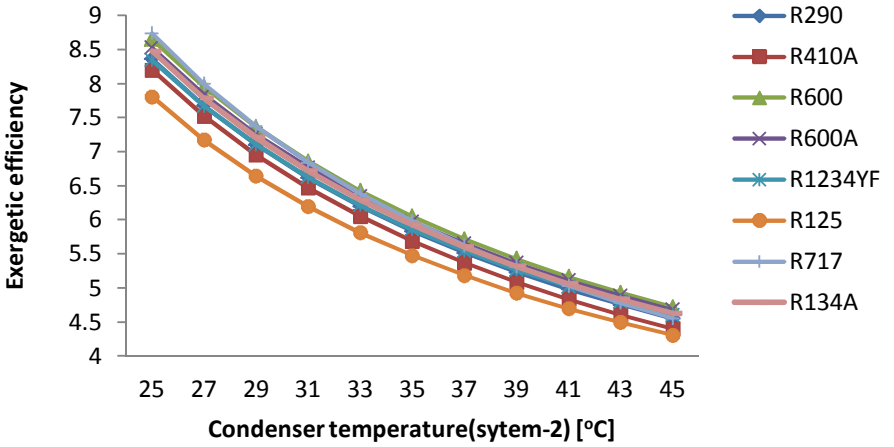


**Fig.25:** Variation of condenser temperature with irreversibility of sytem-1

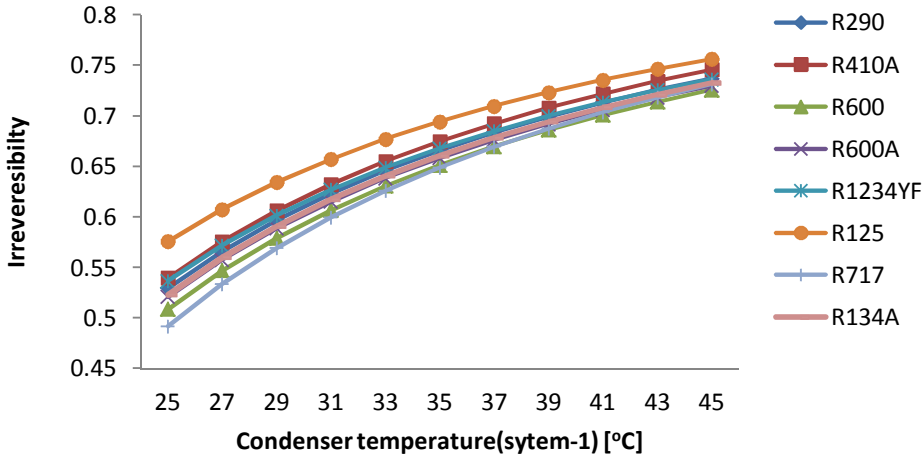

**Fig.26:** Variation of condenser temperature with irreversibility of sytem-2

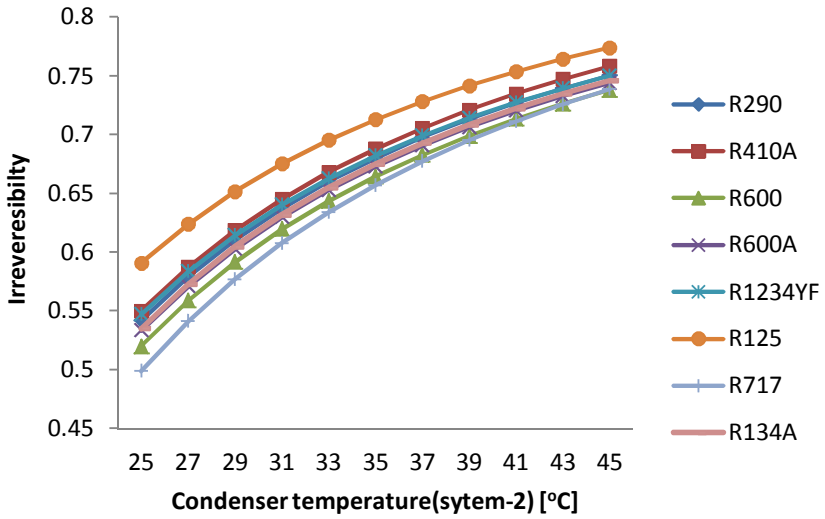


## CONCLUSION

Analysis of multi-stage vapour compression refrigerator and flash intercooler with individual or multiple throttle valves has been done in terms of COP, second law efficiency and irreversibility destruction.From the current study following conclusions were made:

1. Energetic and exergetic performance of system-2 is higher than system-1 for selected temperature range of condenser and evaporators with chosen ecofriendly refrigerants.
2. For both systems R125 shows minimum performance in terms of COP, second law efficiency and irreversibility.
3. Performances of R600 and R717 better in comparison of other selected refrigerants for system-1 and system-2. AS R717 is toxic and limited to industrial applications, therefore R600 is recommended for both systems by taking safety precautions. Performance of R134a is slighly lesser than R600, therefore R134a can also be used for practical applications without taking of any safety precautions.
4. The maximum percentage difference of COP between system-2 and system-1 is 9.59% for R125 at 15 °C , high temperature evaporator. Irreversibility in system-1 is 1.4-2.1%, 1.3-2.2% and 1.6-2.0% using R600 and 1.8-3%, 1.7-3.1%, 2.2-2.7% using R125 is lower than system-2 for low, intermediate and high temperature evaporator respectively. This marginal irreversibility differences between system-1 and system-2 can be neglected.

## REFERENCES

1. Camelia Stanciu,Adina Gheorghian,Dorin Stanciu, Alexandru Dobrovicescu(2011)-Exergy analysis and refrigerant effect on the operation and performance limits of a one stage vapour compression refrigeration system,Termotehnia, 36-42.
2. V. Siva Reddy,N. L. Panwar ,S. C. Kaushik(2011)-Exergetic analysis of a vapour compression refrigeration system with R134a, R143a, R152a, R404A, R407C, R410A, R502 and R507A,Clean Techn Environ Policy,14:47–53.
3. J.U. Ahamed , R. Saidur, H.H. Masjuki(2011)-A review on exergy analysis of vapor compression refrigeration system, Renewable and Sustainable Energy Reviews,15: 1593–1600.
4. Szargut D, Petela R, Egzergia(1965),WNT.
5. Szargut J, Morris D, Steward F(1998)-Exergy analysis of thermal, chemical and metallurgical processes.,New York: Hemisphere Publishing Corporation.

6. Saidur R, Masjuki HH, Jamaluddin MY(2007)-An application of energy and exergy analysis in residential sector in Malaysia. Energy Policy, 35: 1050–63.
7. Yongmei Xuan, Guangming Chen. Experimental study on HFC-161 mixture as an alternative refrigerant to R502. Int J Refrigeration. Article in Press.
8. R.Cabello a, E.Torrella b, J.Navarro-Esbr. Experimental evaluation of a vapour compression plant performance using R134a, R407C and R22 as working fluids. Int J Applied Thermal Engineering.2004; 24:1905-1917.
9. Mark W. Spatz, Samuel F. Yana Motta. An evaluation of options for replacing HCFC-22 in medium temperature refrigeration systems. Int J Refrigeration.2004; 27:475-483.
10. X.H. Han, Q. Wang, Z.W. Zhu, G.M. Chen. Cycle performance study on R32/R125/R161 as an alternative refrigerant to R407C. Int J Applied Thermal Engineering.2007; 27:2559-2565.
11. R. Cabello, J. Navarro-Esbrı, R. Llopis, E. Torrella. Analysis of the variation mechanism in the main energetic parameters in a single-stage vapour compression plant. Int J Applied Thermal Engineering.2007; 27:167-176.
12. AkhileshArora, S.C. Kaushik. Theoretical analysis of a vapour compression refrigeration system with R502, R404A and R507A. Int J Refrigeration.2008; 31:998-1005.
13. H.M Getu, P.K Bansal. Thermodynamic analysis of an R744-R717 cascade refrigeration system. Int J Refrigeration.2008; 31:45-54.
14. M. Mohanraj, S. Jayaraj, C. Muraleedharan, P. Chandrasekar.Experimental investigation of R290/R600a mixture as an alternative to R134a in a domestic refrigerator. Int J Thermal Sciences.2009; 48:1036-1042.
15. M. Padilla, R. Revellin, J. Bonjour. Exergy analysis of R413A as replacement of R12 in a domestic refrigeration system. Int J Energy Conversion and Management.2010; 51:2195-2201.
16. Klein, S.A., Alvarado, F., 2005. Engineering Equation Solver, Version 7.441. F Chart Software, Middleton, WI.

# Accepted Manuscript

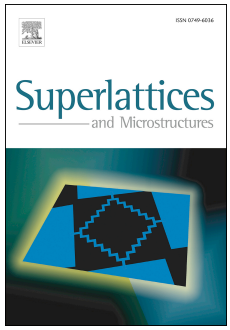


Power gain assessment of ITO based Transparent Gate Recessed Channel (TGRC) MOSFET for RF/Wireless Applications

Ajay Kumar, Neha Gupta, Rishu Chaujar

PII: S0749-6036(16)30026-X

DOI: 10.1016/j.spmi.2016.01.027

Reference: YSPMI 4162

To appear in: *Superlattices and Microstructures*

Received Date: 7 August 2015

Revised Date: 18 January 2016

Accepted Date: 20 January 2016

Please cite this article as: A. Kumar, N. Gupta, R. Chaujar, Power gain assessment of ITO based Transparent Gate Recessed Channel (TGRC) MOSFET for RF/Wireless Applications, *Superlattices and Microstructures* (2016), doi: 10.1016/j.spmi.2016.01.027.

This is a PDF file of an unedited manuscript that has been accepted for publication. As a service to our customers we are providing this early version of the manuscript. The manuscript will undergo copyediting, typesetting, and review of the resulting proof before it is published in its final form. Please note that during the production process errors may be discovered which could affect the content, and all legal disclaimers that apply to the journal pertain.

ACCEPTED MANUSCRIPT

# Power gain assessment of ITO based Transparent Gate Recessed Channel (TGRC) MOSFET for RF/Wireless Applications

Ajay Kumar[1], Neha Gupta[2] and Rishu Chaujar[3]

Microelectronics Research Lab, Department of Engineering Physics,
Delhi Technological University, Bawana Road, Delhi-110042, India
E-Mail: ajaykumar@dtu.ac.in[1],nehagupta@dtu.ac.in[2] and rishu.phy@dce.edu[3]

**Abstract-** In this work, power gain assessment and intrinsic delay of Transparent Gate Recessed Channel (TGRC) MOSFET have been observed for RF applications and the results so obtained have been compared with Conventional Recessed Channel (CRC) MOSFET. Simulation results show that TGRC architecture has significantly improved the power gains in terms of maximum available power gain (Gma), maximum transducer power gain ($G_{MT}$), maximum stable power gain (Gms) and appreciable reduction in intrinsic delay as compared to CRC-MOSFET owing to indium tin oxide (ITO) in recessed channel as a conducting gate material and thus providing its efficacy for low power switching applications. Further, effect of gate length scaling has also been observed on TGRC MOSFET and it has been found that the cut-off frequency ($f_T$) and maximum oscillator frequency ($f_{MAX}$) enhances by 66% and 36% respectively as channel length scales down to 20 nm. Further, the effect of negative junction depth, oxide thickness and substrate doping have also been investigated for TGRC-MOSFET. This TCAD assessment has been done at frequencies of several THz which fortify its use for high frequency RF/wireless applications.

**Keywords—** CRC-MOSFET, intrinsic delay, ITO, power gains, RF, TGRC-MOSFET.

## 1. Introduction

Continuous downscaling of MOSFET dimensions into sub-30 nm regime leads to undesirable effects such as Short channel effects (SCEs), leakage current, hot carrier effects (HCEs) and parasitic capacitances resulting in poor device performance and characteristics such as voltage gains, subthreshold slope and transconductance making it undesirable for RF and wireless communications [1]. However, as the feature size of CMOS technology shrinks to nm range, leads to excellent RF performance in terms of cut-off and maximum oscillator frequency. As a result, the MOS transistors have now replaced the technology which was previously governed by bipolar and Bi-CMOS technologies [2] in the field of RF and mobile communication applications. Numerous device engineering schemes and novel device structures have been reported in literature to overcome the problems arising from downscaling of device dimensions. Further scaling has faced serious limitations with respect to fabrication technology and device performances.

Many solutions are proposed to overcome these limitations. Some of the solutions include such as SOI MOSFET [3], multi-gate MOSFET [4], Recessed Channel (RC) MOSFET [5], GAA MOSFET [6], Silicon Nanowire MOSFET [7] etc. RC MOSFET improves the short channel effects (SCEs) and HCEs appreciably because of the presence of groove which splits the source and drain regions. The two potential barriers created at the two corners due to high-density field lines and carriers in the channel now requires more energy to surmount these barriers, which limits its carrier transport efficiency and hence, current driving capabilities of the device. To overcome this limitation, there is need of integrating device engineering scheme onto RC MOSFET. Previous work on RC MOSFET has demonstrated that gate engineering schemes improve the current driving capability of RC MOSFET [8].

Transparent conducting oxide (TCO) [9, 10] semiconductor is essential to use in optoelectronic devices such as flat panel display. ITO is one of the most promising TCO semiconductors which is used in optoelectronic device applications. ITO is not frequently available in the market because of cost and scarcity of indium, the principle material of ITO [11]. ITO is a solid solution of indium oxide ($In_2O_3$) and tin oxide ($SnO_2$). It is transparent and colorless in thin layers. ITO is one of the most widely used TCO because of its two chief properties, its electrical conductivity and optical transparency as well as the ease with which it can be deposited as a thin film [12]. ITO has a very low resistivity of the order of $10^{-5}\Omega$-cm and high concentration of the order of $10^{21}$ $cm^{-3}$ with higher Hall mobility of 53.5 $cm^2$ $V^{-1}s^{-1}$. In the conventional MOSFET, as the channel length scale-down, the gate control over the channel gets reduced due to the increased source/drain capacitances [13]. To incorporate the advantage of TCO, we proposed a novel device

structure called TGRC-MOSFET [14]. This work emphasise the TCAD assessment of TGRC-MOSFET for high-performance RF applications in terms of figure of merits such as Gma, Gms, $G_{MT}$, $f_T$, $f_{MAX}$ and intrinsic delay. In TGRC-MOSFET, the metal gate is replaced by a transparent conducting oxide (TCO) [10, 15] called ITO. Moreover, due to the increased demand for high-speed electronics products, there is need of accurate simulation analysis of the MOSFET at high frequencies (HF) to represent the behavior of the device in microwave circuits and systems [16].

## 2. Device structure and its description

The simulated device structure i.e. Transparent Gate Recessed Channel MOSFET consists of gate which is made by transparent conducting material ITO as shown in Fig 1. All simulations have been performed using ATLAS and DEVEDIT 3D device simulator. The Source/Drain region is heavily doped with n-type impurity of a length of 30 nm. While the substrate is doped with a p-type impurity and $t_{ox}$ thick oxide layer is exemplified in it is shown in Fig. 1. Design parameters of TGRC-MOSFET and CRC-MOSFET are properly tabulated in Table 1.

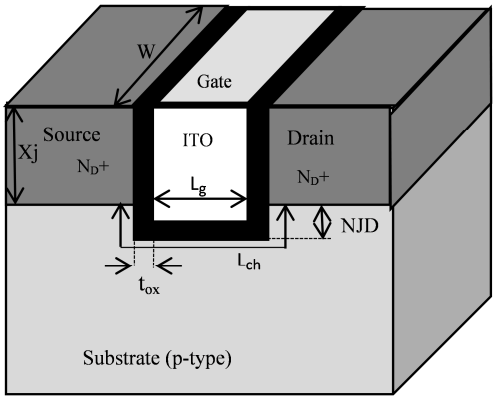


Fig. 1: Structure of Transparent Gate Recessed Channel MOSFET.

**Table 1:** Design parameters of TGRC-MOSFET and CRC-MOSFET

| Device Parameters | Value with unit |
|---|---|
| Gate Length ($L_g$) | 30 nm |
| Channel Length ($L_{ch}$) | 50 nm |
| Length of the Source and the Drain region | 30 nm |
| Device Width (W) | 200 nm |
| Groove Depth | 38 nm |
| Negative Junction Depth (NJD) | 10 nm |
| Substrate Doping ($N_A$) | $1x10^{17}$ $cm^{-3}$ |
| Source/Drain Doping ($N_D^+$) | $1x10^{19}$ $cm^{-3}$ |
| Physical Oxide Thickness ($t_{ox}$) | 2 nm |
| Work function for TGRC-MOSFET ($\Phi_{ITO}$) | 4.7 eV |
| Work function for CRC-MOSFET ($\Phi_M$) | 4.2 eV |

## 3. Simulation Methodology and Calibration

All the simulations have been performed using following models [17] as shown in Table II.

**Table II:** Simulations Model

| Physical Models | Description |
|---|---|
| Mobility Models | Lombardi CVT and constant low field mobility model. |
| Recombination Model | Shockley Read Hall (SRH) Recombination is included to incorporate minority recombination effects with carrier lifetime=$1\times10^{-7}$s. |
| Statistics | Boltzmann Transport model, the use of Boltzmann statistics is normally justified in semiconductor device theory, but Fermi-Dirac statistics are necessary to account for certain properties of very highly doped (degenerate) materials. |
| Energy Transport Model | Hydrodynamic Model is used as it includes all nonlocal effects and is more accurate than the drift-diffusion method. Drift-diffusion Model shows shortcomings as channel length scales down to 50nm |

Calibration of model parameters used in simulation has been performed according to the published results obtained by R. Chaujar et al [18] using above models and calibrated results shown in Fig. 2 in order to validate the simulations. The data has been extended [18] and then plotted.

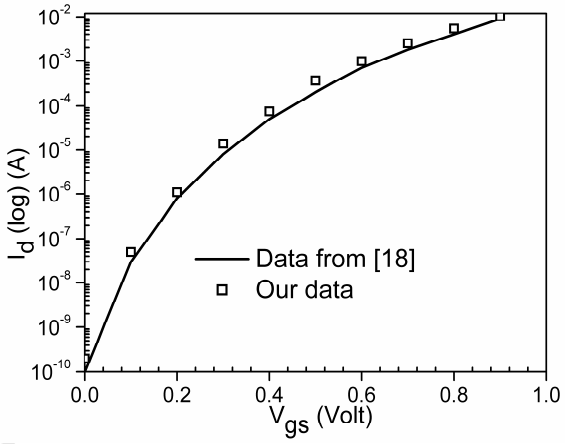


Fig. 2: Calibration with the published result, $I_{ds}$-$V_{gs}$ characteristics of 40 nm gate length TGRC-MOSFET.

## 4. RF performance metrics appraisement

### *4.1. Device comparison*

In this section, we perform the device comparison of CRC and TGRC-MOSFET in terms of RF metrics. Fig. 3 shows the enhanced performance of TGRC-MOSFET in comparison to CRC-MOSFET in terms of Gma and Gms which reflects the maximum theoretical power gain that we want from device. Gma of a two port network is defined as maximum power available at load to the maximum power available at the source and it is given as in equation 1. These two parameters should be larger for high frequency applications of the device thus; TGRC-MOSFET shows significant improvement due to the advantageous electrical property of ITO.

$$G_{ma} = \frac{P_{load,\max}}{P_{source,\max}} \qquad \text{..... (1)}$$

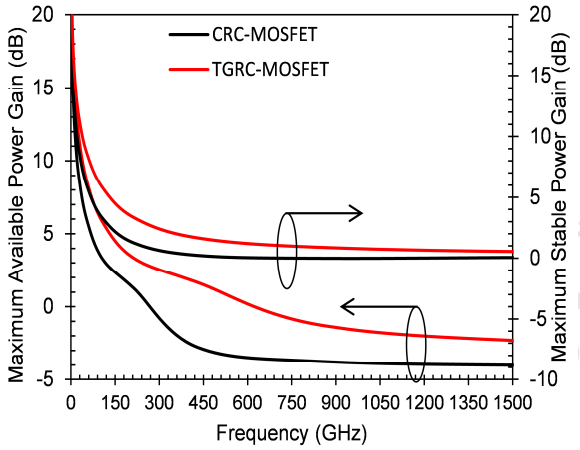


Fig. 3: Maximum Available Power Gain (Gma) and Maximum Stable Power Gain (Gms) for CRC-MOSFET & TGRC-MOSFET.

The cut-off frequency $f_T$ is calculated when current gain is unity and maximum oscillator frequency $f_{MAX}$ is calculated when power gain is unity [19] and it is defined as-

$$f_T = \frac{g_m}{2\pi(C_{gs} + C_{gd})} \qquad \text{..... (2)}$$

$$f_{MAX} = \frac{f_T}{\sqrt{4R_g(g_{ds} + 2\pi f_T C_{gd})}} \qquad \text{..... (3)}$$

where $g_m$ is the transconductance, $C_{gs}$ and $C_{gd}$ are parasitic capacitances, $R_g$ is gate resistance, $g_{ds}$ is drain conductance.

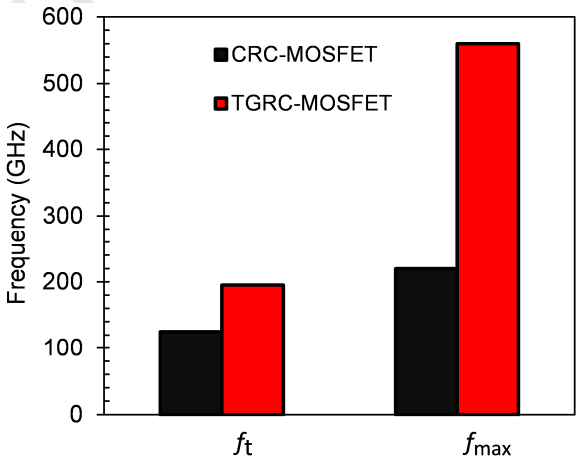


Fig. 4: Cut-off frequency and Maximum oscillator frequency for CRC-MOSFET and TGRC-MOSFET.

Fig. 4 reflects the higher cut-off frequency in TGRC-MOSFET as compared to CRC-MOSFET due to enhanced ON current and transconductance in TGRC-MOSFET owing to incorporation of ITO in which the concentration of charge carriers increased because, at the time of diffusion of Sn some oxygen vacancies are created by $SnO_2$ which gives some free electron to increase the carrier concentration. Thus, if the number of charge carriers will be more, they will contribute towards high current and hence ON current will increase. For high speed and high switching, maximum frequency should be high and thus, TGRC-MOSFET is suitable for high-speed digital circuits.

Further, TGRC-MOSFET shows the enhanced performance as compared to CRC-MOSFET in terms of maximum oscillator frequency. As we incorporate ITO on to recessed channel, the electron temperature decreases as is already reported in our previous [14] work, due to which, carrier mobility in the channel is enhanced which results in reduction of gate resistance. As a consequence from equation (3), $f_{MAX}$ improves as compared to CRC-MOSFET. As maximum oscillator frequency directly depends on transconductance and is inversely proportional to gate resistance [20], this proves its efficacy for switching and wireless applications. Fig. 5 reflects the device performance in terms of maximum transducer power gain ($G_{MT}$). $G_{MT}$ is a measure of the efficacy of the two ports and it is defined as the ratio of average power delivered to the load by a source to a maximum available power from the source.

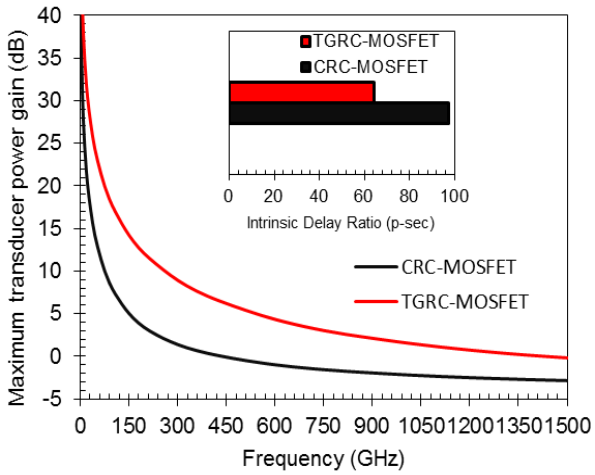


Fig. 5: Maximum Transducer Power Gain for CRC-MOSFET and TGRC-MOSFET. Inset: Intrinsic Delay Ratio for CRC and TGRC MOSFET

As is evident from the results that $G_{MT}$ is improved in TGRC-MOSFET in comparison to CRC-MOSFET due to incorporation of transparent conducting oxide at gate instead of metal by which the current driving capability of device is increased as evident from equation (4) [19] and results in higher power at the load end making the device suitable for RF/wireless applications. Inset of Fig. 5 shows the comparison between TGRC-MOSFET and CRC-MOSFET in terms of intrinsic delay which is defined as-

$$\tau = \frac{C_{gg}.V_d}{I_{ON}} \qquad \text{…….. (4)}$$

where $C_{gg}$ is the parasitic gate capacitance, $V_d$ is the bias voltage applied to drain and $I_{ON}$ is the on-current.

It is evident from Fig. 5 that there is 36.7% reduction in intrinsic delay of TGRC-MOSFET than CRC-MOSFET, due to the reduction of parasitic capacitance and improvement in current driving capability owing to the transparent gate instead of a normal metal gate. Thus, TGRC-MOSFET proves to be a most promising candidate in RF amplifier and high-speed switching applications [21].

*4.2 Effect of Gate Length ($L_g$)*

In this sub-section, we studied the influence of gate length from 20 nm to 40 nm on the high-frequency performance of TGRC MOSFET. Fig. 6 represents the cut-off frequency and maximum oscillator frequency respectively at different gate lengths for TGRC-MOSFET. It is evident from Fig. 6 that the cut-off frequency enhances when the gate length is reduced. When gate length reduces

from 40 nm to 30 nm, the cut-off frequency increases by 33.33% and when $L_g$ is further reduced to 20 nm, the cut-off frequency is increased by 25%. This increase in the cut-off frequency makes TGRC-MOSFET suitable for radio recievers

. Fig. 6 represents the maximum oscillator frequency, which enhances when the gate length reduces. If the gate length is reduced from 40 nm to 30 nm, maximum oscillator frequency is increased by 16% and further reduction in the gate length enhances $f_{MAX}$ by 18.96%. This increase in the maximum oscillator frequency reflects the device's suitability for high speed and high switching RF applications. Thus, we observed that if we reduce the gate length from 40 nm to 20 nm, TGRC-MOSFET gives enhanced performance in terms of $f_T$ and $f_{MAX}$.

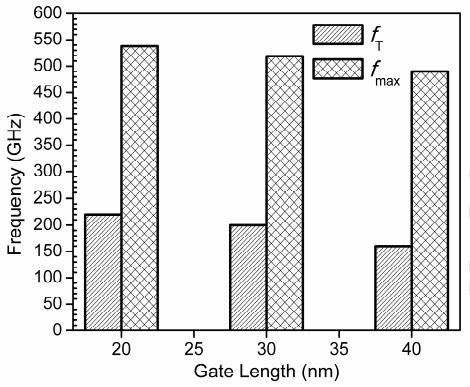


Fig. 6: Cut-off frequency and Maximum Oscillator Frequency for TGRC-MOSFET at different gate lengths.

Fig. 7(a) reflects the enhanced performance of TGRC-MOSFET in terms of Gma and Gms which also reflects the maximum theoretical power gain that is desired from the device. Gma and Gms are two most important parameters for RF amplifier design. Fig. 7(a) shows that, when the gate length reduces from 40 nm to 20 nm, both Gma and Gms is enhanced. Fig. 7(b) shows the $G_{MT}$ at different gate lengths and it is evident that $G_{MT}$ enhances like Gma and Gms as gate length decreases from 40 to 20 nm

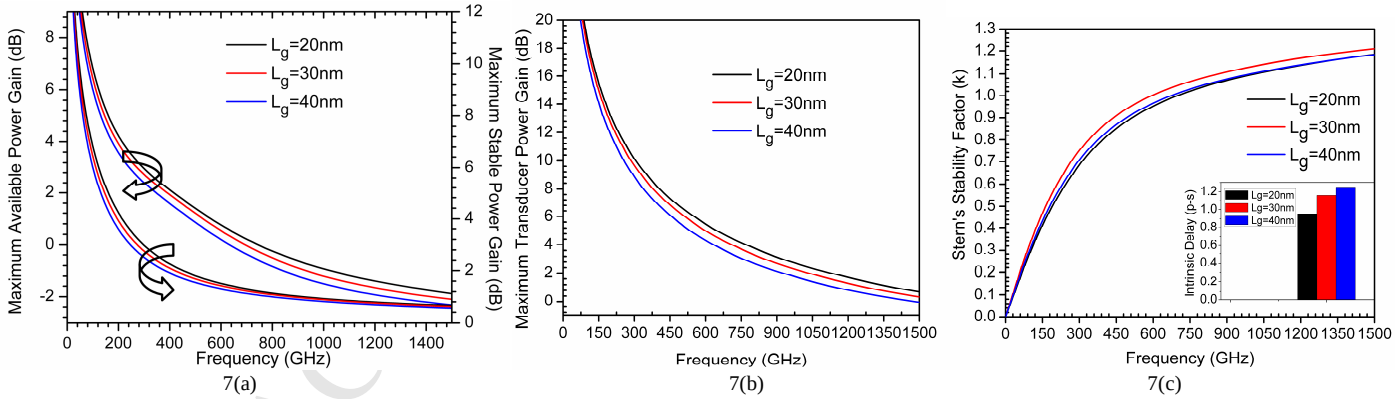


Fig. 7(a): Maximum Available Power Gain (Gma) and Maximum Stable Power Gain (Gms). (b) Maximum Transducer Power Gain ($G_{MT}$). (c) Stern's Stability Factor. Inset: Intrinsic Delay, for TGRC-MOSFET at different gate lengths.

. Moreover, for the designing of RF amplifiers, power gains play an important role. Stability is one of the major criterions for designing low-noise amplifiers (LNA). Basically, stability measures the ability of LNA to oscillate at very high frequencies. Our aim is to avoid any oscillation when designing an amplifier for high frequency range. Sometimes this stability is called Stern stability factor (K) and its value is usually less than one at low frequency and greater than one at high frequency [22, 23]. K is defined as the following equation-

$$K = \frac{1+|\Delta|^2-|S_{11}|^2-|S_{22}|^2}{2.|S_{12.}\cdot S_{21}|} \qquad \text{..... (5a)}$$

where $S_{11}$ and $S_{22}$ are the reflection coefficients and $S_{12}$ and $S_{21}$ are transmission coefficients and s-matrix Δ is defined as

$$\Delta = S_{11} \times S_{22} - S_{12} \times S_{21} \quad \text{..... (5b)}$$

Stern's stability factor has been investigated at different gate lengths. Stability factor is greater than one at high frequency and less than one at low frequency which is good for designing of RF amplifiers. Fig. 7(c) reflects the high stability factor at 30 nm gate length. When reducing the gate length, intrinsic delay also reduces which makes device faster for RF performances as shown in Fig. 7(c) (Inset).

*4.3 Effect of Negative Junction Depth (NJD)*

This section examines the efficacy of NJD on RF performance of TGRC MOSFET. The RF performance in terms of Gma and Gms enhances as we reduces NJD to 5 nm. The results are plotted w.r.t. frequency, which is taken from few Hz to several GHz. When NJD reduces from 15 nm to 10 nm, then Gma increases to 13.33%, also, when NJD reduces from 10 nm to 5 nm, Gma further enhances to 17.64% as shown in Fig. 8(a). Also, Gms increases to 9.6% as NJD reduces from 15 to 10 nm. If we further reduce it to 5 nm, Gms increases to 6.95% as is evident from Fig. 8 (b). Further, $G_{MT}$ has been investigated for different NJD and it is clearly evident from Fig. 8 (c) that when NJD reduces from 15 nm to 10 nm and then from 10 nm to 5 nm, then $G_{MT}$ increases appreciably. The analog performance of TGRC-MOSFET is enhanced when NJD increases while RF performance is enhanced when NJD is reduced and hence, there is a trade-off between RF and analog for optimized performance depending upon the application.

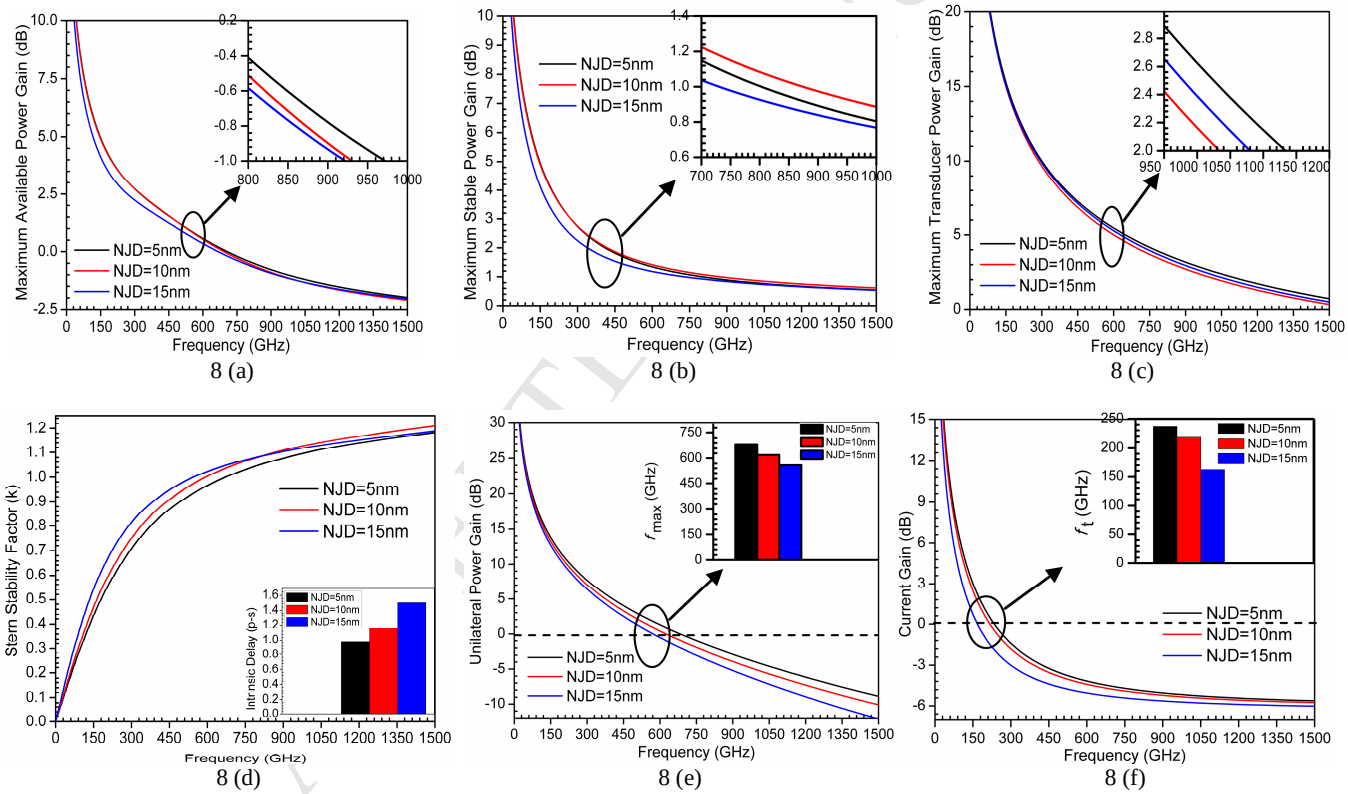


8 (a) 8 (b) 8 (c)

8 (d) 8 (e) 8 (f)

Fig. 8: (a) Maximum Available Power Gain (Gma). (b) Maximum Stable Power Gain (Gms). (c) Maximum Transducer Power Gain ($G_{MT}$). (d) Stern's Stability Factor. Inset: Intrinsic delay. (e) Unilateral power gain. Inset: Maximum Oscillator Frequency. (f) Current gain. Inset: Cut-off frequency, for TGRC-MOSFET at different values of NJD.

Fig. 8(d) shows the variation of stability factor as a function of frequency for different NJD. It is clearly evident from Fig. 8(d) that stability factor is less than one for low frequency and greater than one for high frequency. When NJD increases from 10 nm to 15 nm then stability factor is also enhanced and thus, TGRC-MOSFET is highly stable at 15 nm of NJD is reliable for the designing of LNA for high-frequency applications. Further, Intrinsic delay has been investigated at different NJDs and it is clearly evident from Fig 8 (d) (Inset) that when NJD reduces from 15 to 5 nm, intrinsic delay reduces due to reduction of parasitic capacitances according to

equation (4) and also due to decrease in channel length, carriers are required less time to reach from source to drain in TGRC-MOSFET having 5 nm NJD. Moreover NJD variation is also observed in terms of $f_{MAX}$ and $f_T$ which enhances when NJD is reduced from 10 nm to 5 nm but reduces when NJD increases from 10 nm to 15 nm as shown in Fig. 8(e) and 8(f) respectively, thus TGRC-MOSFET with 10 nm of NJD is more suitable for high-frequency RF applications. All the parameters are enhanced when NJD reduces from 15 to 5nm, due to enhancement in electron velocity at the source side [24], which improves the current driving capability and hence, increases the transconductance thereby results in improvement in power gains.

### *4.4 Effect of Oxide Thickness ($t_{ox}$)*

This section studies the impact of oxide thickness on RF metrics. The variation of oxide thickness from 1 to 3nm shows the irregular variation on RF matrices, such as Gma, Gms, $G_{MT}$, Stern's stability factor, $f_{MAX}$ and $f_T$. Fig. 9(a) shows the variation of Gma for different oxide thickness and it is clearly evident that Gma reduces when oxide thickness decreases, this is the drawback of TGRC-MOSFET, but when oxide thickness is 2 nm, it gives the enhanced performance as TGRC-MOSFET which we proposed designed with 2 nm oxide thickness. Further, when oxide thickness varies from 2 nm to 3 nm and from 2 nm to 1 nm, then Gms decreases in both the cases. If gate length is scaled down to 25 nm with 1.6 nm oxide thickness then, $I_{OFF}$ is a (70 nA) while if gate length reduced to below 20 nm (18 nm) with oxide thickness of below 1.5 nm (1.3 nm), then $I_{OFF}$ increases above 100 nA due to quantum effects and tunneling of electron occurs and causes SCEs (mainly increase in $I_{OFF}$) [25, 26] as mentioned in ITRS and to overcome this drawback, gate stack engineering can be used. Hence, for this device the optimum gate length is taken as 20 nm and oxide thickness is taken as 2 nm. Moreover, $G_{MT}$ observed for different oxide thickness and the results reflect that when oxide thickness reduces, $G_{MT}$ reduces. At 2 nm oxide thickness, $G_{MT}$ is less as compared to 3 nm of oxide thickness while greater than as compared to 1 nm oxide thickness. Stern's stability factor is also enhanced when oxide thickness is reduced from 3 to 1 nm as shown in Fig. 9(d) and it is also evident that that stability factor is less than 1 at low frequencies and greater than 1 for higher frequencies which is necessary to avoid oscillations for high-frequency RF applications.

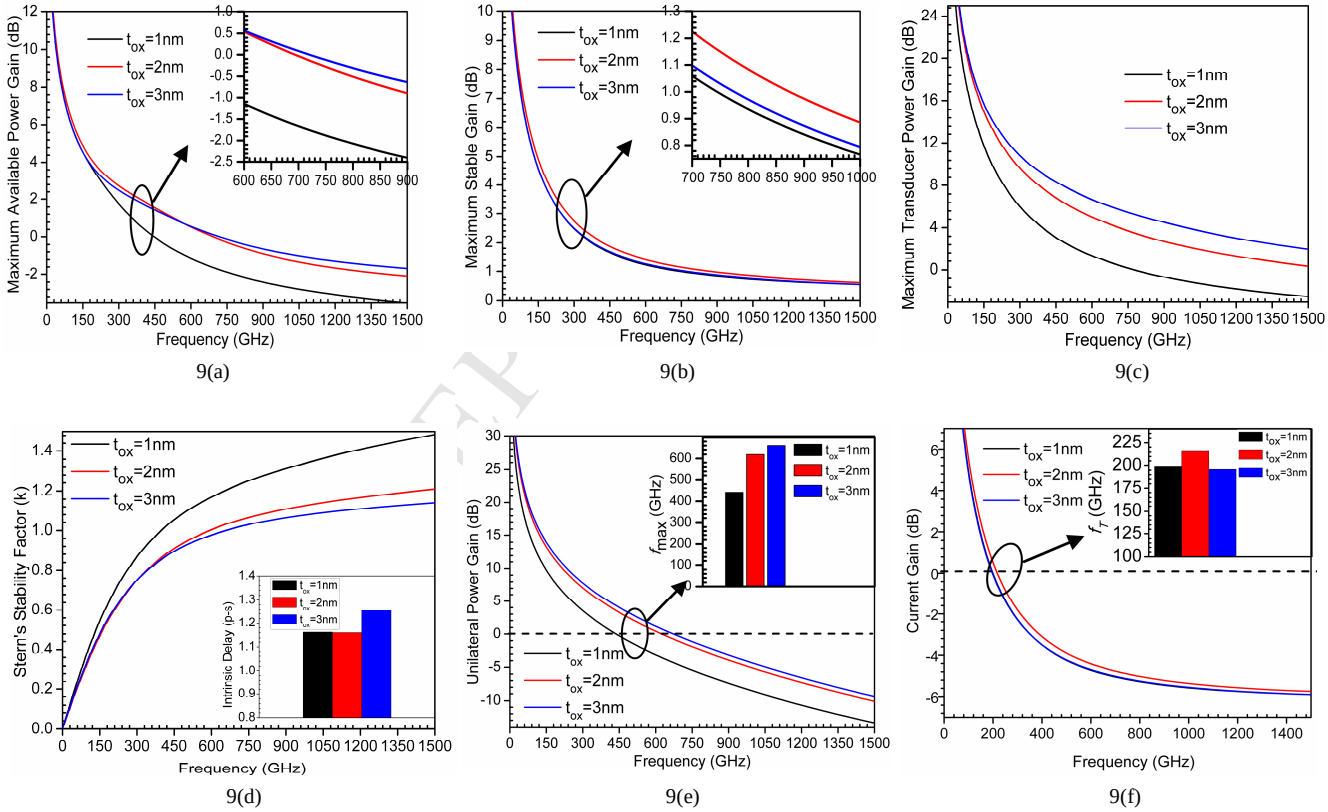


Fig. 9: (a) Maximum Available Power Gain (Gma). (b) Maximum Stable Power Gain (Gms). (c) Maximum Transducer Power Gain ($G_{MT}$). (d) Stern's Stability Factor. Inset: Intrinsic delay. (e) Unilateral power gain. Inset: Maximum Oscillator Frequency. (f) Current gain. Inset: Cut-off frequency, for TGRC-MOSFET at different values of $t_{ox}$.

Further, intrinsic delay has been investigated at different oxide thickness and it is evident from Fig. 9(d) (inset) that when oxide thickness reduces from 3 to 1 nm, intrinsic delay reduces due to the reduction of parasitic capacitances in TGRC-MOSFET. Moreover, $f_{MAX}$ and $f_T$ have been investigated for different oxide thickness. Fig. 9(e) reflects that when oxide thickness is increased, $f_{MAX}$ enhances at high frequencies while $f_T$ is reduced when oxide thickness reduces from 2 nm to 1 nm and further reduces, when oxide thickness increases from 2 nm to 3 nm. Thus, we conclude that TGRC-MOSFET gives best results at 2 nm of oxide thickness for high frequency applications.

*4.5 Effect of Substrate Doping*

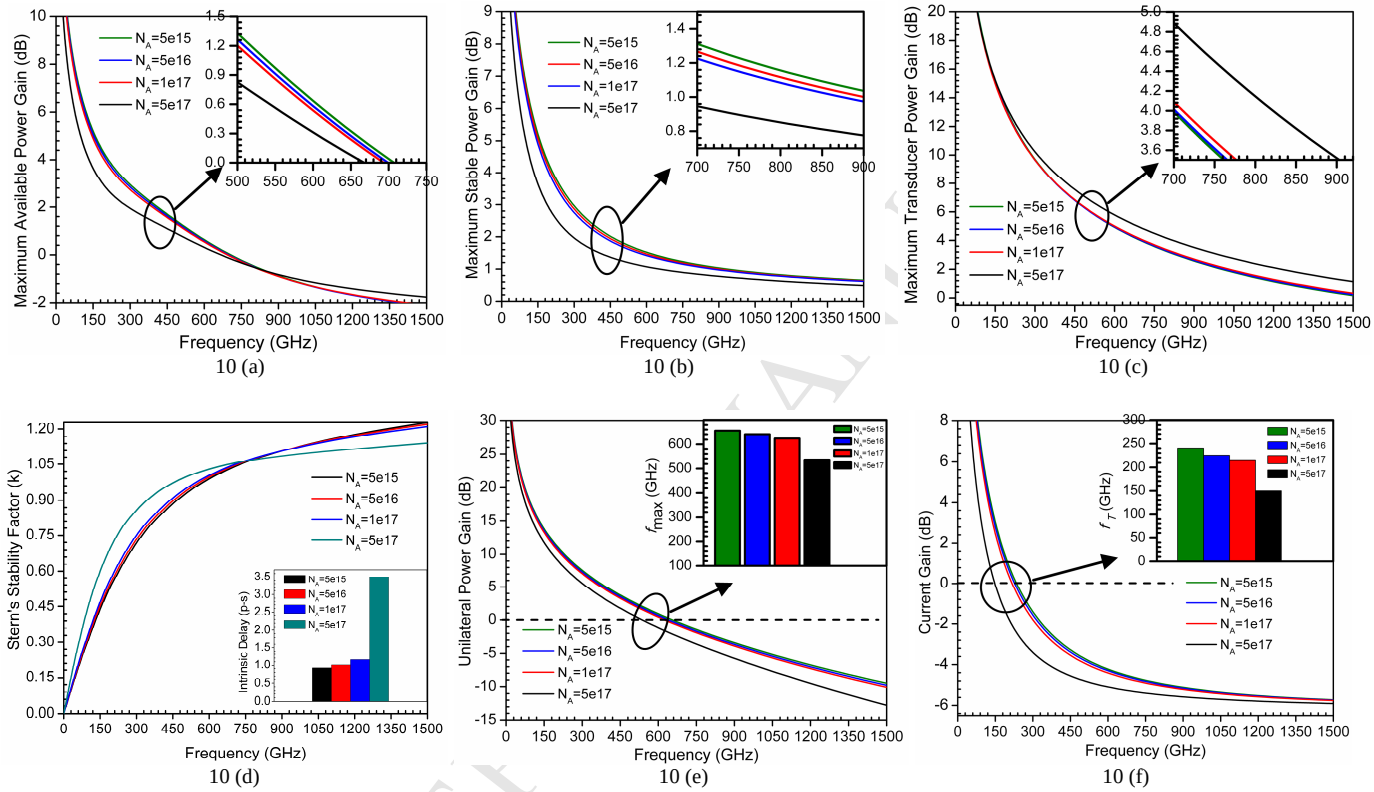


Fig. 10: (a) Maximum Available Power Gain (Gma). (b) Maximum Stable Power Gain (Gms). (c) Maximum Transducer Power Gain ($G_{MT}$). (d) Stern's Stability Factor. Inset: Intrinsic delay. (e) Unilateral power gain. Inset: Maximum Oscillator Frequency. (f) Current gain. Insrt: Cut-off frequency, for TGRC-MOSFET at different values of substrate doping.

In this section, the efficacy of substrate doping on RF performance of TGRC-MOSFET has been studied. Fig. 10(a) shows that when substrate doping of TGRC-MOSFET decreases, Gma enhances due to enhancement in transconductance. In the same manner, if substrate doping decreases, Gms increases as show in Fig. 10(b), while $G_{MT}$ reduces as substrate doping reduces from 5e17 to 5e15 $cm^{-3}$ as shown in Fig 10(c). Further Stern's stability factor has been investigated for different substrate doping and it is evident from Fig. 10(d) that at high frequency, K > 1 when substrate doping is reduced. Further, intrinsic delay has been investigated at different values of substrate doping and it is clearly evident from Fig. 10(d) (inset) shows that when substrate doping reduces from 5e17 to 5e15 $cm^{-3}$, intrinsic delay reduces due to reduction in acceptor atoms and increment in donor atoms. As a result, $C_{gg}$ gets reduced and hence the intrinsic delay. Moreover both $f_{MAX}$ and $f_T$ have been investigated for different substrate doping. For better RF performance these two parameters should be as high as possible; and $f_{MAX}$ and $f_T$ reflects superior enhancement with the reduction of substrate doping. These RF metrics are enhanced with the reduction of substrate doping of TGRC-MOSFET. Thus, TGRC-MOSFET with less substrate doping is suitable for the designing of LNA for high frequency RF performances.

ACCEPTED MANUSCRIPT

## 5. Conclusion

In this paper, we have investigated the effect of transparent gate architecture on the recessed channel MOSFET for improved RF/microwave performance. It has been observed that TGRC-MOSFET enhanced the cut-off frequency by 56% and maximum oscillator frequency by 154% with an appreciably low intrinsic delay. It also significantly improves Gma, Gms and maximum transducer power gain; hence, TGRC-MOSFET is suitable for RF applications and mobile wireless communications. Further, the device parameter variation has also been investigated in terms of gate length, NJD, oxide thickness and substrate doping. TGRC-MOSFET improves the maximum power transfer from source to load and the gate controllability. Simulation results show that TGRC-MOSFET technology is a better solution for high-performance System-On-Chip, low noise and RF applications in nm range.

## Acknowledgments

The authors would like to express gratitude to Microelectronics Research Lab, Department of Engineering Physics, Delhi Technological University and Department of Science & Technology (DST) to carry out this work.

## References

[1] Q. B. Chen, "Design of Prognostic Circuit for Electromigration Failure of Integrated Circuit" *IEEE International Wireless Symposium*, pp.353-356, **2013.**

[2] H. P. Woerlee, M. J. Knitel, R. V. Langevelde, D. B. M. Klaassen, L. F. Tiemeijer, A. J. Scholten, A. T. A. Zegers-van Duijnhoven, *IEEE Trans. Elec. Dev*. Vol. 48, pp. 1776–1782, **2001**.

[3] X. An, R. Huang, B. Zhao, X. Zhang and Y. Wang, "Design guideline of an ultra-thin body SOI MOSFET for low-power and high-performance applications". *Semicond. Sci. Technol. (IOP)* Vol.19, pp.347–350, **2004**.

[4] R.M. Barsan, "Analysis and Modeling of Dual-Gate MOSFETs", *IEEE Transactions on Electron Device*, Vol. 28(5),pp. 523-534, **1981**

[5] R. Chaujar, R. Kaur, M. Saxena, M. Gupta and R. S. Gupta, "TCAD Assessment of Gate Electrode Workfunction Engineered Recessed Channel (GEWE-RC) MOSFET and Its Multilayered Gate Architecture—Part I: Hot-Carrier-Reliability Evaluation" *IEEE Trans. Electron Devices*, vol. 55, no. 10, pp.2602-2612, **2008**.

[6] C. P. Auth and James D. Plummer, "Scaling Theory for Cylindrical, Fully-Depleted, Surrounding-Gate MOSFET˝s", *IEEE Electron Device Letters*, 18(2), pp. 74-76, **1997.**

[7] N. Gupta, A. Kumar and R. Chaujar, "Impact of Device Parameter Variation on RF performance of Gate Electrode Workfunction Engineered (GEWE)-Silicon Nanowire (SiNW) MOSFET", *Journal of Computation Electronics, Springer*, Vol. 14, **2015**.

[8] R. Chaujar, R. Kaur, M. Saxena, M. Gupta and R. S. Gupta "On-state and RF performance investigation of sub-50 nm L-DUMGAC MOSFET design for high-speed logic and switching applications" Semicond. Sci. Technol. Vol.23, pp.1-8, **2008**

[9] S. K. Sinha, S. Chaudhury "Impact of Oxide Thickness on Gate Capacitance—A Comprehensive Analysis on MOSFET, Nanowire FET, and CNTFET Devices", *IEEE Transactions on Nanotechnology*, Vol. 12, pp. 958-964, **2013.**

[10] P. P. Edwards, A. Porch, M.O. Jones, D.V. Morgan, R .M. Perks, "Basic materials physics of transparent conducting oxides", *Dalton Trans*. Vol.19, pp. 2995–3002, **2004**.

[11] T. Minami "Transparent Conducting Oxide Semiconductor for Transparent Electrodes" *Semiconductor Science Technology*. Vol.20, S35-S44, **2005**.

[12] S. V.N. Pammi, H.J. Jung, and S.G. Yoon. "Low-Temperature Nanocluster Deposition (NCD) for Improvement of the Structural, Electrical, and Optical Properties of ITO Thin Films" *IEEE Transactions on Nanotechnology*, Vol.10, pp.1059-1065, **2011**.

[13] R. Murali, J.D. Meindle, "Modeling the effect of source/drain junction depth on bulk-MOSFET scaling", *Solid-State Electronics*. Vol.51, pp.569-574, **2004**.

[14] A. Kumar, N. Gupta, R. Chaujar "Analysis of Novel Transparent Gate Trcessed Channel (TGRC) MOSFET for Improved Analog Behaviour", *Microsystem Technologies*. Vol.21 (5), **2015**.

[15] H. Kawazoe, K. Ueda, "Transparent conducting oxides based on the spinel structure". J. Am. Ceram. Soc., 82, pp.3330–3336, **1999**.

[16] C.H. Doan, S. Emami, A.M. Niknejad, R.W. Brodersen , "Millimeter-wave CMOS design", *IEEE J Solid-State Circuits*, , vol. 40, pp. 144–5, **2005**.

[17] ATLAS User's Manual *SILVACO Int., Santa Clara, CA*, **2011**.

[18] R. Chaujar, R. Kaur, M. Saxena, M. Gupta, R. S. Gupta, "Investigation of multi-layered-gate electrode Workfunction engineered recessed channel (MLGEWE-RC) sub-50 nm MOSFET: A novel design", *International Journal of Numerical Modelling: Electronic Networks, Devices and Fields*, Vol.22, pp.259-278, **2008**.

[19] B. Nae, A. Lazaro, B. Iniguez, "High Frequency and Noise Model of Gate-All Around MOSFETs" *Spanish Conference on Electron Devices*, pp. 112-115, **2009**.

[20] A. Sarkar, S. De, A. Dey, C. K. Sarkar, "Analog and RF performance investigation of cylindrical surrounding-gate MOSFET with an analytical pseudo-2D model". *Journal of Computational Electronics*, Vol.11, pp.182-195, **2012.**

ACCEPTED MANUSCRIPT

[21] P. Malik, R.S. Gupta, R. Chaujar and M. Gupta. "AC analysis of nanoscale GME-TRC MOSFET for microwave and RF applications". *Microelectronics Reliability*. Vol.52, pp. 151-158, **2012**.

[22] S. K. Pati, , K. Koley, A. Dutta, N. Mohankumar, and C. K. Sarkar, "Study of body and oxide thickness variation on analog and RF performance of underlap DG-MOSFETs". *Microelectronics Reliability*. Vol.54, pp. 1137-1142, **2014.**

[23] E. Dastjerdy, R. Ghayour, and H. Sarvari, "Simulation and analysis of the frequency performance of a new silicon nanowire MOSFET structure". *Physica E*. Vol. 45, pp.66-71, **2012**.

[24] A. Kumar, N. Gupta and R. Chaujar, "Impact of Parameter Variation on the Hot-Carrier-Effect Immunity for Transparent Gate Recessed Channel (TGRC) MOSFET", *2nd International Conference on Microelectronics, Circuits and Systems MICRO-2015*, Vol. 1, pp.36-39, **2015**.

[25] C. Hu, "Modern Semiconductor Device for Integrated Circuit" *Prentice Hall*, pp. 261-274, **2009**.

[26] H. Iwai, "Roadmap for 22 nm and beyond", *Microelectronics Engineering*, Doi: 10.1016/j.mee.2009.03.129, **2009**.

ACCEPTED MANUSCRIPT

ACCEPTED MANUSCRIPT

***HIGHLIGHTS***

- We proposed a novel 3-D Transparent Recessed Channel (TGRC) MOSFET for high frequency applications.
- We examined its RF performance in terms of power gains, intrinsic delay, RF FOMs such as cut-off and maximum oscillator frequency
- Cut-off frequency and maximum oscillator frequency enhances by 56% and 154% respectively with an appreciably low intrinsic delay compared to its conentional device.
- With change in gate length, NJD, oxide thickness and substrate doping, TGRC-MOSFET's RF performance improves.
- TGRC-MOSFET technology is better solution for high performance System-On-Chip, low noise and RF applications in nm range.

ACCEPTED MANUSCRIPT

ISSN: 2319-5967
ISO 9001:2008 Certified
International Journal of Engineering Science and Innovative Technology (IJESIT)
Volume 4, Issue 6, November 2015

# Prediction of Heat Affected Zone and Effect of Heat Input in GTA Welded Al Alloy 6061

Pawan Kumar[1], Kishor P Kolhe[2], Sham H Mankar[3], Sanjay Kumar[4]

***Abstract*— Aluminum Alloy 6061 is an Al-Mg-Si alloy employed in aircraft, automobiles, road containers and high speed trains due to their low density, high specific strength and excellent corrosion resistance. In this paper, the effects of heat input on Gas Tungsten Arc (GTA) welded Aluminium Alloy 6061 have been studied at various combinations of pulse parameters with sinusoidal AC wave. Also the effect of heat input on the microstructure, heat affected zone (HAZ) width, grain size and other mechanical properties of the weld joint has been studied.***

***Index Terms*— AA6061, GTAW, Heat Input, Microstructure of welded joints.**

## I. INTRODUCTION

Aluminium alloy 6061 (Al–Mg–Si alloy) is widely used in the fabrication of food processing equipment, chemical containers, passenger cars, road tankers and railway transport systems due to its high strength, excellent weldability and resistance to corrosion. As these Al alloys (6xxx series) are precipitation-hardened, they suffer from a strength reduction in heat affected zone (HAZ) and like most face-centered cubic metals, they do not exhibit clear endurance limit [1].

Welding of aluminium is generally performed either by gas metal arc welding (GMAW) or gas tungsten arc welding (GTAW). Lots of difficulties are associated with this kind of joining process, mainly related to the presence of a oxide layer, high thermal conductivity, high coefficient of thermal expansion, solidification shrinkage and, above all, high solubility of hydrogen in the molten state. Further problems occur when attention is focused on heat-treatable alloys, since heat, provided by the welding process, is responsible for the decay of mechanical properties, due to phase transformations and softening.

GTAW is an arc welding process, where arc is produced between non-consumable tungsten electrode and base metal. Pulsed GTA welding process is frequently used for welding of aluminium alloys as heat input during welding can be precisely controlled. This process is strongly characterized by bead geometry, which plays an important role in determining mechanical properties of the weld [2]. Pulse process variables are controlling factor for heat input, which in turn leads to grain refinement in fusion zone, width reduction of HAZ, segregation of alloying elements, reducing hot cracking sensitivity and residual stresses [3, 4].

Improved mechanical properties of weld are achieved by using current pulsing due to the grain refinement occurring in the fusion zone. The main aim of pulsing is to achieve maximum penetration without excessive heat built-up. The use of high current pulses is to penetrate deep and cater for longer arc period at lower current. Deep penetration in pulsed current welding is produced by arc pressure at peak for longer durations [4]. In addition to this argon – helium gas mixture offers certain advantages by increasing heat input of the arc during welding. Argon is known for stable arc with better arc ignition whereas helium provides higher thermal conductivity. There exists a linear relationship between heat input of a weld and maximum temperature at a given distance from the weld centre line. It shows that pulsed arc welds are cooler and exhibit less thermal distortion than conventional GTA welds of the same penetration [5]. Heat input is typically calculated as follows: H = [60EI]/1000S, Where H = Heat Input (kJ/mm), E = Arc Voltage (Volts), I = Current (Amps) and S = Travel Speed (mm/min).

The evolution of microstructure in weld fusion zone is influenced by current pulsing and cyclic variations of energy input into the weld pool causing thermal fluctuations. Consequently this leads to periodic interruption in solidification process. As pulse current decays, solid–liquid interface advances towards the arc and becomes susceptible for disturbances in the arc formation. As current increases again in the subsequent pulse, the growth of

ISSN: 2319-5967
ISO 9001:2008 Certified
International Journal of Engineering Science and Innovative Technology (IJESIT)
Volume 4, Issue 6, November 2015

dendrites can also occur. Current pulsing also results in periodic variations of the arc forces resulting in additional fluid flow, which lowers the temperature in front of the solidifying interface. Furthermore, the temperature fluctuations inherent in pulsed welding leads to a continual change in the weld pool size and shape favoring growth of new grains. It is to be understood that effective heat input for unit volume of weld pool should be considerably less in pulse current welds and thus expecting the average weld pool temperatures to be low [6].

A weldment basically consists of five micro structurally distinct regions normally identified as fusion zone, unmixed region, partially melted region, HAZ and unaffected base metal. The HAZ is the portion of weld joint which experiences peak temperatures high enough to produce solid-state micro structural changes but they are too low to cause any melting. Every point of the weldment in the HAZ relative to the fusion line is subjected to unique thermal experience during welding, in terms of both maximum temperature and cooling rate. Thus, each point has its own micro structural features and corrosion susceptibility. Partially melted region extends usually one or two grains into the HAZ relative to the fusion line. It is characterized by grain boundary liquation, which may result in liquation cracking. An increase in the pulse frequency refines grain structure of weld metal using pulses of short duration. At a given frequency, long pulse duration produces coarser grain structure than shorter pulse duration. Further increase in the peak current leads to coarseness of grain structure [7].

## II. EXPERIMENTAL PROCEDURE

In this study, five Al alloy 6061 GTA welded 5.0 mm thick samples were undertaken. These samples were welded with AA5356 filler rods. The chemical compositions of the base metals and filler rod are shown in Table 1. Samples were machined to the required dimensions (300 x 150 x 5 mm) and edges were prepared for butt welding. Welding of the samples was carried out using an automatic Pulse TIG welding machine (TRITON 220V AC/DC). Samples were welded at the parameters shown in Table 2. Specimens were separated out from the transverse section of the weld joint and polished using a standard metallographic procedure, which consisted of molding, polishing and etching. Specimens were etched with Keller's reagent. The following welding conditions were maintained constant during the welding:

a) Electrode : Tungsten with 2% Zirconium
b) Electrode size : 2.4 mm diameter
c) Shielding gas : 30% helium + 70% argon
d) Shielding gas flow rate : 8 Litre /min
e) Filler diameter : 3.15 mm
f) Welding speed : 4.16 mm/sec
g) Electric voltage : 16.8 V
h) AC Balance % : 0 (sinusoidal)

**Table 1: Chemical Composition of Base and Filler Metal (Weight %)**

| Alloy | Al | Mg | Si | Others |
|---|---|---|---|---|
| 6061 | 96.8 | 1.10 | 0.70 | Rest |
| 5356 | 95.2 | 4.8 | - | |

**Table 2: Pulse GTA Welding Parameters**

| Process Parameters | Unit | Sample | | | | |
|---|---|---|---|---|---|---|
| | | 1 | 2 | 3 | 4 | 5 |
| Pulse Current | A | 150 | 150 | 180 | 195 | 210 |
| Base Current | A | 105 | 135 | 75 | 105 | 90 |
| Pulse Frequency | Hz | 100 | 150 | 100 | 50 | 50 |
| Pulse Duty Cycle | % | 60 | 90 | 90 | 75 | 90 |

## III. TESTING AND ANALYSIS

The microstructures of the specimens were studied under optical microscope (GX51 N-233U, Olympus). Image analysis of micrographs of the weld metal was carried out using image analyzing software .The calculation of heat input for the pulse current welding process can be done by mean current using the relationship. Im = $[I_p t_p + I_b t_b]/t_T$ on heat input equation, where Im is mean current, $I_p$ is pulse current, $t_p$ is time on peak current, $I_b$ is base current, $t_b$ is time on base current, $t_T$ is total time. The heat input for various samples are tabulated in the Table 3.

ISSN: 2319-5967
ISO 9001:2008 Certified
International Journal of Engineering Science and Innovative Technology (IJESIT)
Volume 4, Issue 6, November 2015

**Table 3: Heat Input, HAZ width and ASTM Grain Size Number of Samples**

| Sample No | Tp sec | Tb sec | I mean (A) | Heat Input (J/mm) | HAZ Width (µm) | ASTM Grain Size No (Weld Zone) |
|---|---|---|---|---|---|---|
| 1 | 0.006 | 0.0040 | 132.0 | 31.9 | 1124.80 | 10.72 |
| 2 | 0.006 | 0.0007 | 148.4 | 35.9 | 1246.12 | 10.18 |
| 3 | 0.009 | 0.0010 | 169.5` | 41.0 | 1299.04 | 10.04 |
| 4 | 0.015 | 0.0050 | 172.5 | 41.8 | 1355.18 | 09.12 |
| 5 | 0.018 | 0.0020 | 198.0 | 48.0 | 1598.61 | 08.48 |

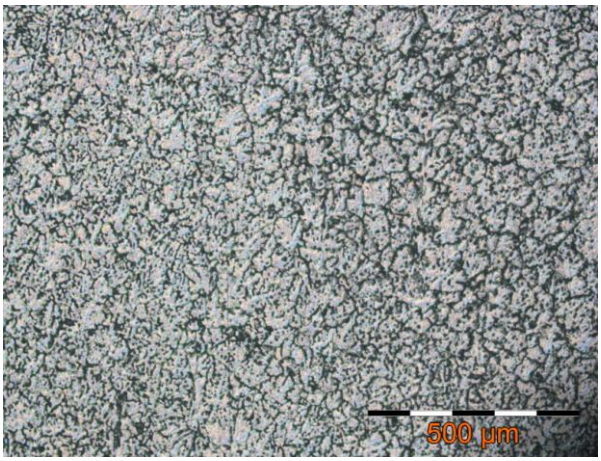


**Fig 1(a): Microstructure of Weld Zone**

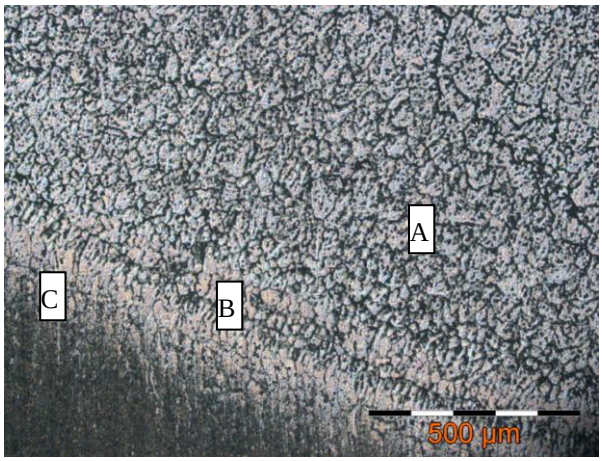


**Fig 1 (b): Microstructure of Welded AA6061 (A–Weld Zone, B–Fusion Boundary and C–HAZ)**

**1) Micro structural Study:** The microstructure of welded AA6061 is shown in Fig 1, in which weld zone (WZ), fusion boundary (FB) and HAZ are clearly visible. The grains in weld zone are coarser due to as cast nature of the weld and fine equiaxed grains are present at the fusion boundary. HAZ has large columnar grains (columnar grains generally occur in directional solidification or cold worked elongated grains in metal) near fusion boundary and the size reduces towards the unaffected base metal. With the help of image analyzer system, HAZ width and ASTM grain size number were calculated from microstructures of samples. The microstructural quantity known as the ASTM micro grain size number (n), is defined by the following relationship: $N = 2^{n-1}$, where N is the number of grain per square inch at 100x.

The effect of heat input on HAZ width and ASTM grain size number are shown in Fig 2 and 3. The data available from Table 3, Fig 2 and 3 clearly shows as heat input increases the HAZ width and ASTM grain size also increases. Fig 4 and 5 shows the variation of grain size from weld centre to unaffected base metal for samples 1 to 5. Here ASTM grain number is smallest in weld zone and increases at fusion boundary since it is having finer grains.

**2) Microhardness Study:** Microhardness (Vickers) was measured from the one fusion boundary to another fusion boundary with a load of 200 gf as shown in Fig 5. Microhardness testing is an indentation method for measuring the hardness of a material on a microscopic scale. A precision diamond indenter is impressed into the material at load. The impression length, measured microscopically and the test load are used to calculate a hardness value. The variations of micro hardness from the weld centre were given in Fig 6.

## IV. DISCUSSION

**Microstructures:** Welds in heat treatable alloys generally exhibit four micro structural zones (weld zone, fusion boundary, HAZ and unaffected base metal as explained in Fig 1 [8]. The weld zone is a mixture consisting of melted base plate and 5356 filler metal with an as-cast dendritic structure. The grain size in the cast metal did not vary significantly in the various weldments. The fusion zone, an area in which inter-granular melting occurred, a butted the weld metal and contained portions of the original parent structure with partially melted and re-solidified eutectic at the grain boundaries resulting from temperatures between the liquidus and solidus. The HAZ is the area where temperatures were below the solidus of the alloy but high enough to dissolve the precipitates that were originally present in the parent plate. Temperatures in this area during welding were $600^0$F or higher, resulting in

ISSN: 2319-5967
ISO 9001:2008 Certified
International Journal of Engineering Science and Innovative Technology (IJESIT)
Volume 4, Issue 6, November 2015

partial or complete solution heat treatment. The microstructure varied from fine precipitates, associated principally with the grain boundaries, to coarse precipitates dispersed throughout the grain matrix.

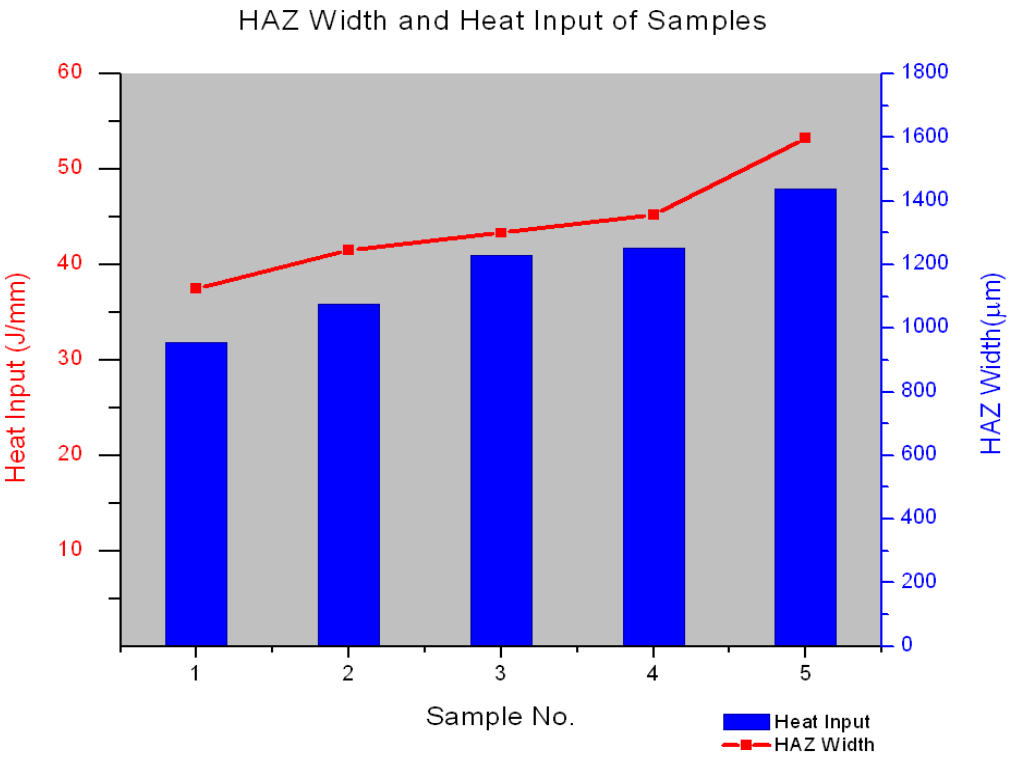


**Fig 2: Variation of HAZ Width and Heat Input of Samples**

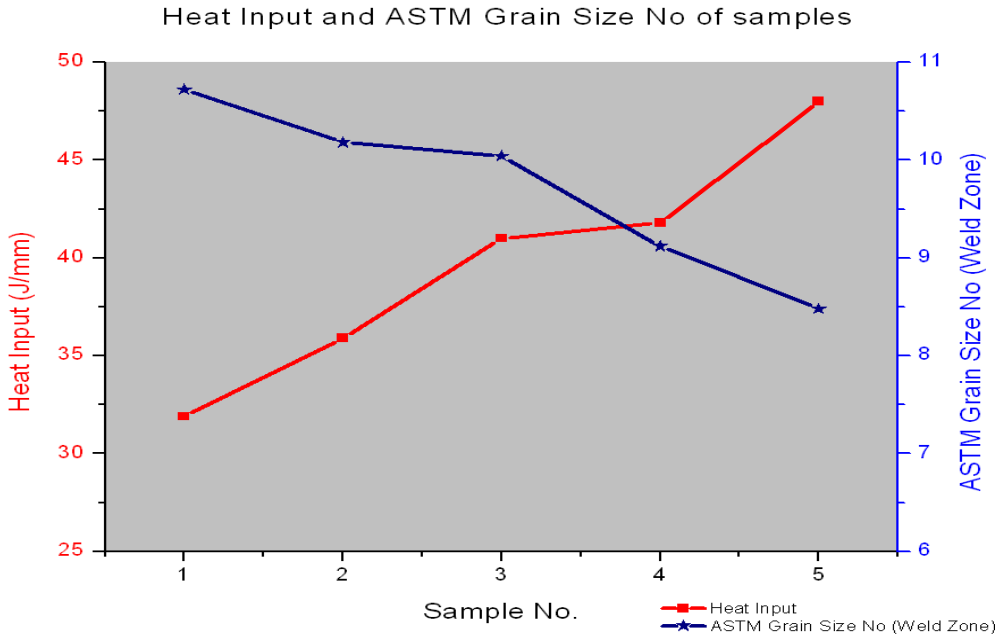


**Fig 3: Variation of Heat Input and ASTM Grain Size Number of samples**

ISSN: 2319-5967
ISO 9001:2008 Certified
International Journal of Engineering Science and Innovative Technology (IJESIT)
Volume 4, Issue 6, November 2015

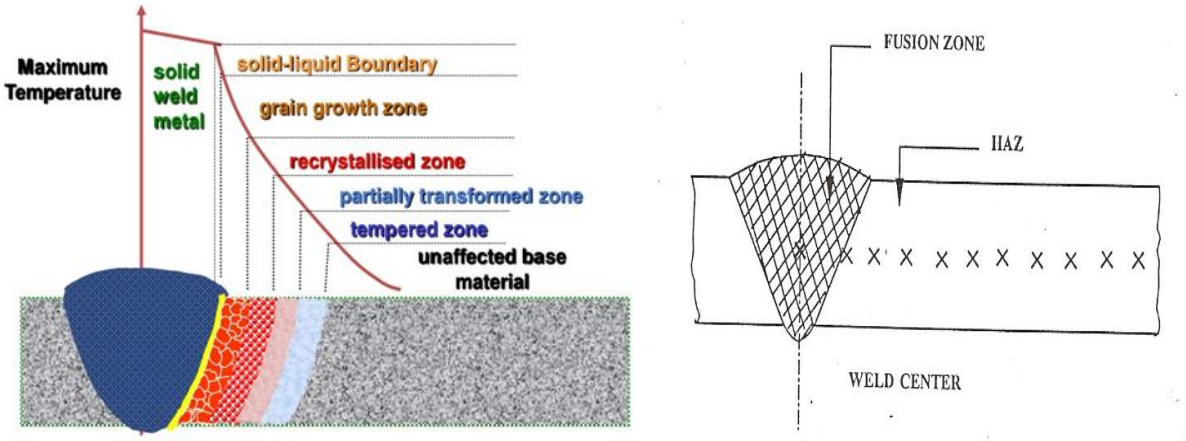


**Fig 4: (a) Geometry of Weld, (b) Schematic Diagram for Measurement of Grain Size and Microhardness**

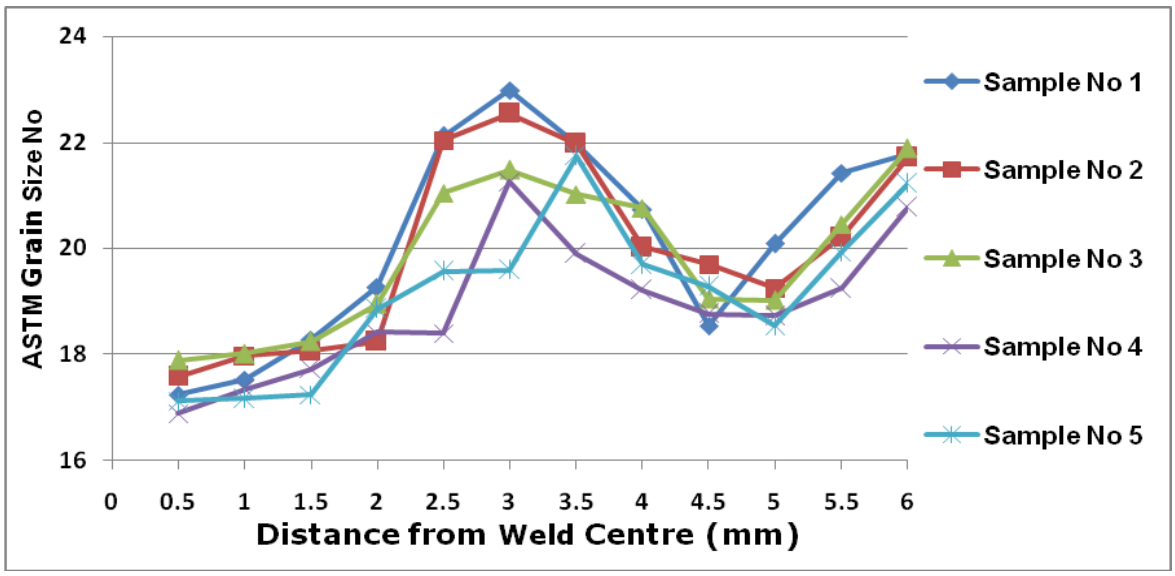


**Fig 5: Grain Size Number of Samples from the Weld Centre**

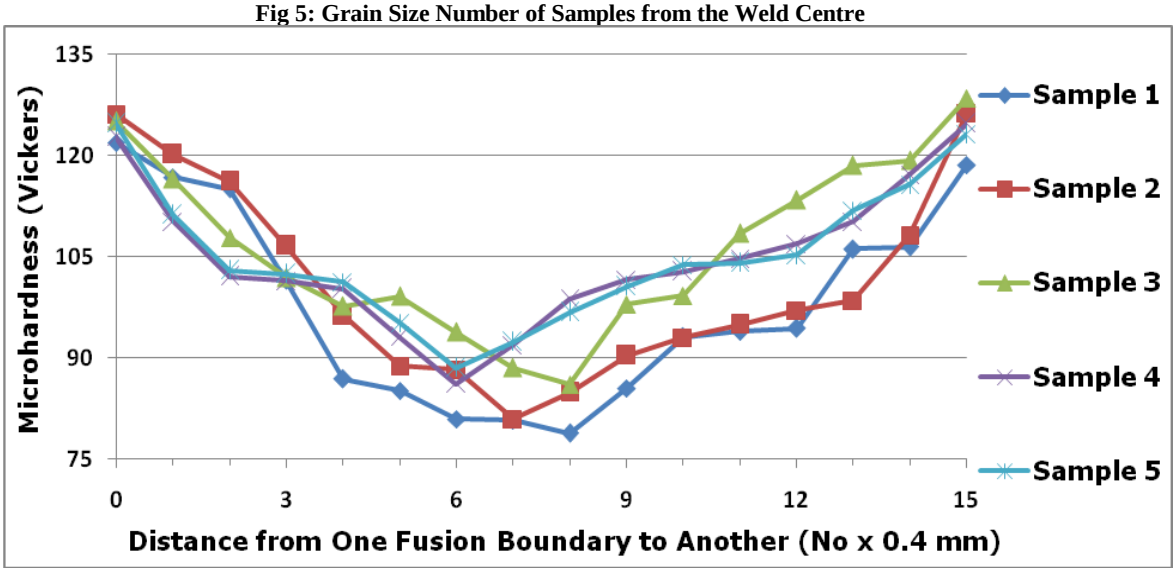


**Fig 6: Microhardness of Samples from One Fusion Boundary to Another**

ISSN: 2319-5967
ISO 9001:2008 Certified
International Journal of Engineering Science and Innovative Technology (IJESIT)
Volume 4, Issue 6, November 2015

**Grain size:** From Fig 5 and Table 3, weld zone of all samples are occupied by coarse due to as-cast nature of microstructure, which has low hardness (almost 40% less than the parent metal) and lack strengthening phases. The grain in the centre of weld is of largest size due to the slow cooling rate at centre and this size reduces towards the fusion boundary. As heat input increases, the width of weld zone becomes wider and generates coarse grains, which is very much unfavorable for both mechanical properties of weld joint as well as strength.

**Heat Input**: The rate of heat input per inch of weld in arc welding is proportional to the welding voltage and current and inversely proportional to the welding speed. Most of the heat of welding will be dissipated by conduction through the adjacent metal, although a small amount will be lost by radiation and convection to the surrounding environment. From Table 4 it is sure that higher heat input generates wider HAZ due to high thermal conductivity of the base metal. In heat treatable aluminium alloys, microstructure distribution of HAZ exhibits a complicated distribution due to temperature variations. Parent material properties appear to be unaffected in locations where temperature during welding does not exceed $400^0$F. Metal heated in the 400-$600^0$ F temperature range undergoes hardness reductions which are not restored by natural or artificial post-weld aging. This is HAZ softening zone. The width of the soft zone depends on the peak temperature heating / cooling rate, dissolution and / or growth of precipitates and formation of stable phases. Loss of hardness and strength in HAZ is due to the dissolution and coarsening of $Mg^2Si$ phase, the main strengthening phase in Al-Mg-Si alloys. Wider HAZ is also unfavorable for the mechanical properties of the weld joint, due to presence of coarse grains. Metal heated to above $600^0$F shows the greatest reduction in hardness immediately after welding, but it cab be gradually recovered by increasing its hardness according to the time elapsed after welding due to excellent natural age hardening.

**Microhardness:** There is a general correlation between hardness and tensile strength for aluminum alloys having similar chemical composition. Therefore, microhardness in the HAZ provided a convenient and simple means of studying the effect of heat input during welding on strength. There were mainly three regions in which microhardness shows significant change, the weld zone; fusion boundary and HAZ. From Fig 6, we can see that weld zone is having very low microhardness for all samples. As it moves from the weld centre microhardness increases at fusion boundary due to fine grains as it gets lesser time for solidification and then decreases at HAZ due to coarser elongated grains. Microhardness varies at a range of 70 VHN to 130 VHN from weld centre to parent metal. Also it was observed that the fall in microhardness moves away from weld centre from sample 1 to 5. This shows clearly the effect of heat input on microhardness.

## V. CONCLUSION

From the above results we can conclude that:
a) Mechanical properties of the weld zone depend on the grain size. The unfavorable mechanical properties of the weld joints are due to coarse grains.
b) High heat input generates wider weld zone and HAZ, which reduces the joint strength and weld hardness.
c) Metal heated in the 400-$600^0$F temperature range undergoes hardness reductions which are not restored by natural or artificial post-weld aging. Therefore minimum heat input, which can be controlled by optimum process parameters, should be used in welding of aluminium alloys.

## ACKNOWLEDGMENT

The author wishes to thank Vehicles Research & Development Establishment (VRDE), Ahmednagar for providing all the facilities for carrying out the experiments, and the scientists / staff of VRDE for their support and assistance.

## REFERENCES

[1] T. Senthilkumar, V. Balasubramanian and M. Y. S. Babu, “Effect of pulsed current GTAW parameters on fusion zone microstructure of AA6061”, International Journal of Metals & Materials, Vol. 13, No. 4, 2007, pp. 345–351.

[2] S.C. Juang and Y.S. Tarng, “Process parameter selection for optimizing the weld pool geometry in the TIG welding of stainless steel”, Journal of Material Process Technology, Vol. 122, 2002, pp. 33–37.

[3] A. A. Mohamed, “Optimisation of weld bead dimensions in GTAW of Al-Mg alloy”, Materials and Manufacturing Processes, Vol. 16 No. 5, 2001, pp 725–736.

ISSN: 2319-5967
ISO 9001:2008 Certified
International Journal of Engineering Science and Innovative Technology (IJESIT)
Volume 4, Issue 6, November 2015

[4] M. Balasubramanian, V. Jayabalan and V. Balasubramanian, "Optimizing the pulsed current GTAW parameters to attain maximum impact toughness", Materials and Manufacturing Processes, Vol. 23, 2008, pp. 69–73.

[5] R. E. Leitner, H. Mcelhinney and E. I. Pruitt, "An investigation of pulsed welding variables", Welding Journal, Vol. 52, No. 9, 1973, pp. 405-410.

[6] G. M. Reddy, A. A. Gokhale and K. P. Rao, "Optimization of pulse frequency in pulsed current gas tungsten arc welding of aluminium – lithium alloy sheets", Journal of Material Science and Technology, Vol. 14, 1998, pp. 61–66.

[7] R. Manti & D. K. Dwivedi and A. Agarwal, "Microstructure and hardness of Al-Mg-Si weldments produced by pulse GTA welding", International Journal of Advance Manufacturing Technology, Vol. 36, 2008, pp. 263–269.

[8] Brooks, Carson, "The Effect of Weld Heat in Arc Welding Aluminum," Light Metal Age, Vol. 24, Nos. 5-6, June, 1966, pp. 10-12.

## AUTHOR BIOGRAPHY

**Dr. Pawan Kumar** is working as Scientist in VRDE Ahmednagar since Dec 2007. He has done B.E (Mechanical Engg) from Nagpur University in 1995 with Ist Div, M.E (Production Engineering) from Delhi College of Engg, Delhi in 2004 with Ist Div and Ph.D (Welding Technology) from Delhi College of Engg, Delhi. He is Fellow & Chartered Engineer of "The Institution of Engineers (I)" Kolkata and Life Member of "The Indian Institute of Welding" Kolkata. He has published 27 research papers out of which 11 papers are in International Journal. He has also worked as Associate Professor in KIET, Ghaziabad for 8.5 years and also has 4 years industrial experience. In VRDE, he has developed Shock Resistant Seat for Mine Protected Vehicles and working in the research and development of defence projects.

Dr. Kishor P. Kolhe is working as a Professor at JSPM Imperial College of Engg & Research, Pune since 2013. He has done BE (Production Engg from Amaravati University in 1998 with Ist Division, ME (Mechanical Eng) from RGPV, Bhopal in Jan 2002 with Ist Division and PhD (Welding Technology) from Delhi University. He is Member of "The Institution of Engineers (I)" Kolkata, "The Indian Institute of Welding" Kolkata and "Indian Society for Agricultural Engineers", New Delhi. He has worked many research Project funded by Govt of India/State Govt/University. He has designed, developed and commercialized Tractor Mounted Hydraulic Elevator, Tractor Mounted & Self Propelled Coconut climber etc. Three Recommendations/patents are in his account. He has published more than 100 Research Papers in various National/Internal Journal/ Symposium. He has shouldered as responsibility of Principal at STC Khamgaon. He has guided 15 PG students and more than 50 UG students. Presently guiding for 10 ME student and 02 PhD students.

ISSN: 2319-5967
ISO 9001:2008 Certified
International Journal of Engineering Science and Innovative Technology (IJESIT)
Volume 4, Issue 6, November 2015

Sham H. Mankar is working as Assistant Professor at Trinity College of Engineering and Research, Pune since 2011. He has done B.E (Production Engineering) from Amravati University in 1998, M.E (Mechanical Engineering) with 1st division from R.G.P.V. Bhopal in 2002 and pursuing Ph.D from S.G.B.A.U. Amravati. He is Life Member of ISTE. He has published 25 research papers in various journals and symposium. He has guided more than 60 UG students and 10 PG students. His total work experience is more than 16 years.

**Sanjay Kumar** is working as Assistant Professor at Delhi Technological University, Delhi since Sep 2008. He has done B.Sc (Engg) from MIT Muzaffarpur in 1998 with Ist Div, M.Tech (Machine Design) from I.I.T. BHU, Varanasi in 2000 with Ist Div, and pursuing Ph.D from IIT Delhi. He is Life Member of ISTE. . He has published more than 6 Research Papers in various National/International Journal/ Symposium. He has also worked as Assistant Professor in KIET, Ghaziabad for 8 years. He has guided 2 PG students and more than 30 UG students.

BUT

Iranica Journal of Energy & Environment

Journal Homepage: www.ijee.net

IJEE an official peer review journal of Babol Noshirvani University of Technology, ISSN:2079-2115

# Production of Biodiesel from a mixture of Karanja and Linseed oils: Optimization of process parameters

Sanjay Mohite[1], Sudhir Kumar[1], Sagar Maji[2], Amit Pal[2]

[1] *Department of Mechanical Engineering, National Institute of Technology, Kurukshetra, India*
[2] *Department of Mechanical Engineering, Delhi Technological University, New Delhi, India*

*P A P E R I N F O*

*Paper history:*
Received 27 October 2015
Accepted in revised form 23 December 2015

*Keywords*:
Biodiesel production
Oil mixture
Process yield
Transesterification reaction

*A B S T R A C T*

Karanja and linseed are the potential non-edible oil crops which can be used for the biodiesel production. The main objective of this study is to find out the feasibility of using a mixture of karanja oil and linseed oil to produce biodiesel. Karanja oil has high amount of free fatty acid in it and linseed oil has low amount of free fatty acid content. Karanja biodiesel is produced by two step esterification/transesterification process which is costly, health hazardous & corrosive due to use of concentrated acids. Linseed biodiesel can be produced by alkali-base transesterfication which is much faster and gives higher yield than acid-base transesterification. A production method is developed to produce biodiesel from the mixture of karanja and linseed oil which is faster, safer and non-corrosive. The yields in the range of 68.2 to 78.9% have been achieved with varying different parameters like molar ratio, stirring time, mixture ratio and amount of catalyst. Optimum parameters are also established to achieve maximum biodiesel yield from the transesterification of a mixture of linseed and karanja oils.

***doi**: 10.5829/idosi.ijee.2016.07.01.03*

## INTRODUCTION

Biodiesel is considered as a carbon neutral fuel because all the carbon dioxide released during its combustion segregate from the atmosphere for the growth of biodiesel plants [1]. In developing countries, edible vegetable oils can not be used as fuel because it may cause starvation and other environmental problems by utilizing much of the arable land. Therefore, non-edible vegetable oils become more attractive for biodiesel production. Feedstock which contains free fatty acids and triglyceride such as vegetable oils, waste oils, animal fats and waste greases can be converted into biodiesel by transesterification process [2, 3]. Depending upon the various properties of feedstocks, the production processes may have their own advantages and disadvantages. Biodiesel is produced as fatty acid methyl esters from the transesterification process in vegetable oils and animal fats with methanol [4]

Karanja seeds contain 30-40% oil [5]. It belongs to nitrogen fixing trees [6]. Karanja tree is widely available because it can grow in humid as well as subtropical regions with annual rainfall ranging from 500 to 2500mm [7, 8]. Oleic (C18:1) and linoleic (C18:2) acids are the major fatty acids of karanja oil with oil content varies from 9 to 46% [9]. Karanja biodiesel has lower emissions, higher the cetane number, higher flash point temperature, lower sulfur content and lower calorific value as compared to diesel. It has good lubrication property, anti-knocking property, biodegradable, renewable and non-toxic [10].

It was also reported that the alkali catalyzed transesterification process cannot be used effectively for biodiesel production for high free Faty acid (FFA) feedstock like karanja oil [11]. Canakci and Gerpan informed that the oils having high FFA value like Karanja oil cannot be converted into biodiesel by the direct trasesterification process as it results in the formation of soaps causing reduction in conversion efficiency to a

* Corresponding author: S. Mohite
E-mail: smohite001@yahoo.com, Mobile: +919953190067

Please cite this article as: S. Mohite, S. Kumar, S. Maji, A. Pal, 2016. Production of Biodiesel from a mixture of Karanja and Linseed oils: Optimization of process parameters, Iranica Journal of Energy and Environment 7(1): 12-17.

large extent. In this case, two step process, i.e esterification followed by transesterification is required [12].

Linseed seeds can yield from 33- 44% oil content under optimum conditions. Linseed oil has the disadvantage of low volatility and high viscosity due to the long chain structure [13]. It is available world wide. It is less water consuming crop for its growth as it is naturally grown [14]. Demirbas observed that Linseed oil has higher linolenic acid content in fatty acid compositions [15]. Linseed oil contains three double bonds linolenic (47.4%), two bonds Linoleic (24.1%) and one double bond oleic (19%) fatty acids [16]. Linseed oil contains 60% linolenic acid, which is the most unsaturated acids. This linolenic acid affects the drying property of oil to make it suitable for drying in alkyd paints [17]. The comparison of fatty acid composition of linseed oil and karanja oil are given in Table 1 [18]. Iyer informed the possibility of polymerization and oxidation for linseed biodiesel due to two double bonds between the reactive methylene groups in diesel engine when its temperature is $900^0$C in running condition [16].

Biodiesel can be produced from Linseed oil from the transesterification process by using methanol and potassium hydroxide as an alkali catalyst. After transesterification process, the viscosity of Linseed oil biodiesel decreases to a large extent. 88% yield of biodiesel was obtained using 20% methanol, 0.5% NaOH and $55^0$C reaction temperature [14].

**TABLE 1**: Comparison of fatty acid composition of karanja and linseed oil [18]

| S.N | Fatty acid | Linseed Oil (% wt) | Karanja Oil (% wt) |
|---|---|---|---|
| 1 | Myristic | 0.045 | 3.7-7.7 |
| 2 | Palmitic | 6.21 | 44.5-71.3 |
| 3 | Oleic | 20.17 | 2.4-8.9 |
| 4 | Stearic | 5.63 | 2.4-8.9 |
| 5 | Linoleic | 14.93 | 10.8-18.3 |
| 6 | Linolenic | 51.12 | 00 |

## General concept of mixing oils for biodiesel production

Mahua oil and Simarouba oil with FFA levels of 13 and 1.43%, respectively were mixed in equal proportions to reduce the consumption of methanol in the production of biodiesel. The FFA of mixed oil was observed at 7.19%. A two step process, an acid pretreatment followed by base transesterification was followed to bring down the FFA level at around 1% to produce biodiesel [19]. It was reported that dual biodiesel blends of Pongamia pinnata oil and mustard oil with diesel can be used in a single cylinder diesel engine. It was also found that calorific values of dual biodiesel blends with diesel were found to be close to diesel, which was more than single biodiesel blend with diesel [20].

It was mentioned that the use of blends of biodiesel could be an alternative to improve the oxidation stability of biodiesel instead of using antioxidants. It was stated that the composition of unsaturated fatty acids in oil was proportional to the oxidation instability of biodiesel and therefore, biodiesel blends of opposite properties (low and high content of unsaturated fatty acids) can be used to get a final biodiesel with improved oxidation stability [21]. Studies of blends of palm biodiesel with jatropha biodiesel had been carried out to cut the cost of antioxidants. It was also stated that palm biodiesel had good oxidation stability because of presence of saturated fatty acids causing resistance to autoxidation. It was concluded that when jatropha biodiesel blended with palm biodiesel, it gave a final biodiesel, which was having good oxidation stability and improved low temperature property. It was also stated that jatropha biodiesel had good low temperature properties as compared to palm biodiesel, which was having poor low temperature properties [22].

The yield of biodiesel obtained from the base catalyzed transesterification of mixtures of castor oil and soybean oil in the presence of ethanol increased as the proportion of castor oil decreased, but no significant substrate preference was observed. Ethanolysis of vegetable oil mixtures containing up to 25 wt% of castor oil yielded biodiesels that were more easily purified than those obtained from neat castor oil and hence, relatively high process yields could be obtained [23]. The major hurdles in the successful commercialization of biodiesel are high feedstock cost and conversion technology to reduce viscosity. The choice of raw material and biodiesel production method must depend upon techno-economical view. It is investigated that hybrid biofuels could be prepared from local crude vegetable oils i.e. Gmelina arborea Roxb (GAO), Mimusops elengi Linn (MEO), Acer laurinum Hasskarl (ALO), Thevetia peruviana Schum (TPO) and Mesua Ferrea Linn (MFO) which does not involve any chemical reaction thus reducing the production cost of biofuels [24]. It is also investigated that soapnut oil methyl esters (SNME) and jatropha oil methyl esters (JME) showed complimentary fuel properties and hence a blending ratio of 35:65 by weight of SNME-JME can improve high cold filter plugging point (CFPP) of SNME and poor oxidation stability of JME to satisfy all specifications of biodiesel[25]. Mixture of biodiesel blends of soybean (25%), canola (25%), palm (25%) with diesel (25%) were found to give acceptable fuel properties like kinematic viscosity 4.3$mm^2$/s, cetane number 53 and pour point -$4^0$C[26]. It was informed that biodiesel produced by two step acid transesterification from a mixture of karanja oils and jatropha oils can meet the requirements of diesel fuels in near future[27].

## MATERIAL AND METHODS

### Materials

The biodiesel was prepared from the mixture of oils of Karanja and linseed by alkali based transesterification. Different proportions of oils (50-50, 75-25 and 25-75%) have been taken to mix for biodiesel production. The biodiesels were produced by different molar ratio of 4.5:1 and 6:1 with change in the amount of KOH catalyst as 1, 1.5 and 2 g for every sample. The stirring time was also changed for these samples from 30 to 60 minutes and the yields of biodiesel were observed.

### Experimental Set Up & Alkali based Transesterification

Experiments were conducted in a 250ml glass vessel. Mixtures of karanja oil and linseed oil were taken and preheated to $110^0$C to remove any moisture content and then cool down to room temperature. Methanols were taken as per the molar ratio and mix with required amount of KOH catalyst and allow stirring at $50^0$C temperature till KOH dissolve completely. Now this methanol containing dissolved KOH mixed with 100ml mixed karanja and linseed oils and allow to stir for 30, 45 and 60 minutes at $60^0$C. After completion of reaction, it was cool and then allowed to settle down overnight. Next day, the upper layer of biodiesel was separated from lower layer of glycerol in a separating funnel. The biodiesel was water washed by hot water and then again, pure biodiesel were separated by physical separation method and the biodiesel was heated to $110^0$C to remove any moisture content. The biodiesel was weighed and the yields were estimated.

## RESULTS AND DISCUSSION

The various physico-chemical properties like specific gravity, density, kinematic viscosity and calorific value of raw oils and biodiesel produced from mixture of oils were determined by using ASTM methods and compared with diesel properties as shown in Table 2.

### Calorific value of fuels

The digital bomb calorimeter is used to determine the calorific value of fuels. The karanja oil and linseed oil have very low calorific value as compared to diesel. But, after transesterification, calorific values of biodiesel of mixture of these oils are found to be nearer to that of diesel. It varies in the range of 37.89 to 39.06 MJ/kg for biodiesel in the different mixing ratio of oils whereas it is 42.47 MJ/kg for diesel.

### Specific Gravity of fuels

Specific gravity of biodiesel is measured by precision hydrometer. The specific gravity of biodiesel of mixture of oils in different mixing ratio varies from 0.89 to 0.90 whereas for diesel it is 0.822.

### Viscosity of fuels

Redwood Viscometer is used to determine the kinematic viscosity. ASTM D0445 procedure is followed. The viscosity of karanja and linseed oil are very high as compared to diesel. Viscosity of Karanja oil and Linseed oil are found to be 27.32 and 29.2 cSt, respectively. The viscosities of mix oil biodiesel are reduced to a great extent by a transesterification reaction which varies in the range of 5.61 to 6.76 cSt whereas it is found to be 2.54 cSt for diesel.

### Effect of parameters for biodiesel production

The important factors which affect the quantity of biodiesel yield are oil to methanol molar ratio, quantity of catalyst used, time of reaction, and proportions of mixed oils.

### Effect of molar ratio (Methanol to oil ratio)

The molar ratio is one of the important factors which affect the yield of biodiesel. Effect of two different molar ratio of 4.5:1 and 6:1 are investigated in transesterification reaction. It is observed that maximum yields are obtained when molar ratio was 6:1 as compared to 4.5:1. The obtained data are shown in Figures 1 to 6.

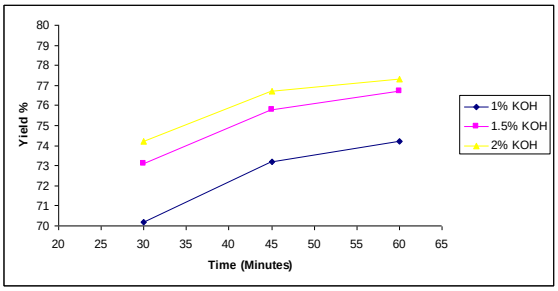


**Figure 1.** Effect of molar ratio 4.5:1 for biodiesel from mixture of 50% karanja and 50% linseed oil

### Effect of alkali catalyst concentration

The effect of alkali catalyst is investigated for 1, 1.5 and 2 wt% KOH with methanol to oil molar ratio of 4.5:1 and 6:1 at $60^0$C with different reaction time of 30, 45 and 60 minutes. It is observed that the biodiesel yields are found to be higher when 2% catalyst amount is used. Insufficient amount of catalyst does not give proper results during the transesterification reaction and higher amount of catalyst (more than 2 wt%) results in the saponification leading to decrease in yield. Obtained data are shown in Figures 1 to 6.

### Effect of reaction time

The effect of reaction time influences the quantity of biodiesel yield. It is observed that 60 minutes duration gives an optimum yield of biodiesel as compared to 30 and 45 minutes. Results are shown in Figures 1 to 6.

**Effect of proportions of oils for biodiesel production**

It is also observed that a mixture of 75% linseed oil with 25% karanja oil give higher yield of biodiesel as compared to 50% each of linseed oil and karanja oil mixture and 25% linseed oil and 75% karanja oil mixture. It is shown in Figures 1 to 6.

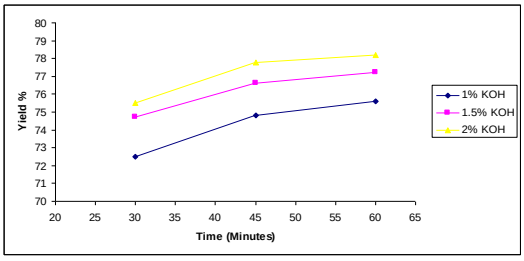


**Figure 2** Effect of molar ratio 6:1 for biodiesel from mixture of 50% karanja and 50% Linseed oil

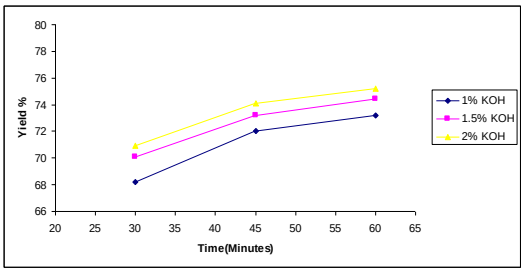


**Figure 3.** Effect of molar ratio 4.5:1 for biodiesel from mixture of 75% karanja and 25% linseed oil

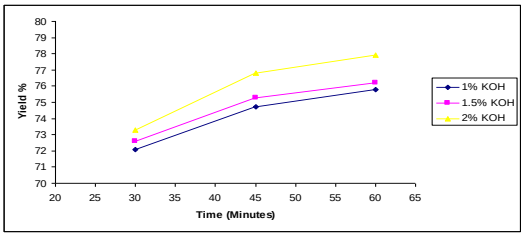


**Figure 4.** Effect of molar ratio 6:1 for biodiesel from mixture of 75% karanja and 25% linseed oil

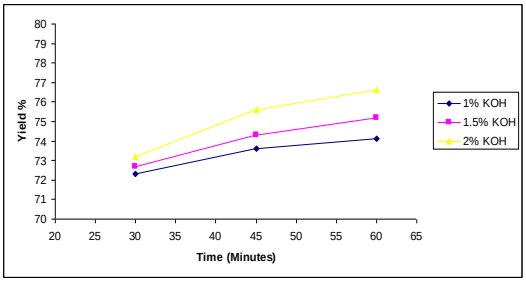


**Figure 5** Effect of molar ratio 4.5:1 for biodiesel from mixture of 25% karanja and 75% linseed oil

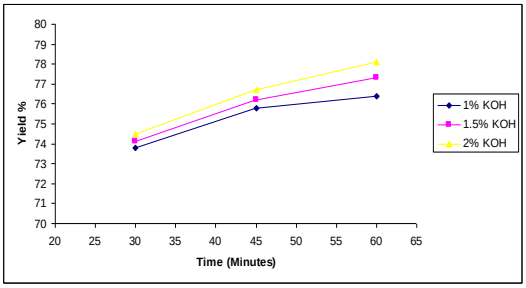


**Figure 6.** Effect of molar ratio 6:1 for biodiesel from mixture of 25% karanja and 75% linseed oil

## CONCLUSION

Karanja oil has high FFA content and, therefore, it requires two steps, acid esterification followed by an alkali catalyzed transesterification reaction which is costly and corrosive production method. Linseed oil has low FFA content and it can be converted into biodiesel by the alkali catalyzed transesterification reaction. An efficient biodiesel production method is developed by mixing proper proportion of karanja and linseed oils using the alkali catalyzed transesterification process.

This process is single step, simpler, safer, faster, non-corrosive and economically and therefore, it is very useful for biodiesel production from a mixture of non-

**TABLE 2**: Comparison of Physico-Chemical Properties

| S.N | Properties | KO | LO | D | A BD | B BD | C BD |
|---|---|---|---|---|---|---|---|
| 1 | Kinematic Viscosity cSt | 27.32 | 29.2 | 2.54 | 5.61 | 6.76 | 6.35 |
| 2 | Calorific Value MJ/kg | 34.12 | 30.6 | 42.47 | 37.89 | 38.53 | 39.06 |
| 7 | Specific Gravity | 0.913 | 0.9 | 0.822 | 0.8934 | 0.9001 | 0.8974 |
| 8 | Density $kg/m^3$ | 912.4 | 926.3 | 840 | 892.59 | 899.33 | 896.6 |

Abbreviations: KO: Karanja Oil, LO: Linseed Oil, D: Diesel, A BD: Biodiesel obtained from a mixture of 50%KO:50% LO, B BD: Biodiesel obtained from a mixture of 25%KO:75% LO, C BD: Biodiesel obtained from a mixture of 75%KO:25% LO

edible oils like karanja and linseed oils. The biodiesel yields are obtained in the range of 68.2 to 78.9%, which is satisfactory from the point of view of single step transesterification process. The following points may be concluded:-

1. Higher yield has been achieved with molar ratio of 6:1 in comparison to 4.5:1 molar ratio.
2. Higher yield has been achieved with 2 wt% KOH catalytic concentration in comparison to 1 wt% KOH and 1.5 wt% KOH catalytic concentration.
3. Higher yield has been achieved with 60 minutes reaction time in comparison to 30 and 45 minutes reaction time.
4. Higher yield has been achieved from mixing ratio of 75% linseed oil and 25% karanja oil in comparison to mixing ratio of 50% linseed oil and 50% karanja oil and 25% linseed oil and 75% karanja oil
5. Maximum yield of 78.9% has been achieved with a mixing ratio of 75% linseed oil and 25% karanja oil, 60 minutes reaction time, 6:1 molar ratio and 2 wt% catalytic concentration.

## REFERENCES


1. Barnwal, B. and M. Sharma, 2005. Prospects of biodiesel production from vegetable oils in India. Renewable and sustainable energy reviews, 9(4): 363-378.
2. Janaun, J. and N. Ellis, 2010. Perspectives on biodiesel as a sustainable fuel. Renewable and Sustainable Energy Reviews, 14(4): 1312-1320.
3. Manjunath H., O. Hebbal, H. K. Reddy, 2015. Process optimization for biodiesel production from Simarouba, Mahua, and waste cooking oils. International Journal of Green Energy, 12(4): 424-430.
4. Zhang, Y., M. Dube, D. McLean and M. Kates, 2003. Biodiesel production from waste cooking oil: 1. Process design and technological assessment. Bioresource technology, 89(1): 1-16.
5. Borugadda, V.B. and V.V. Goud, 2012. Biodiesel production from renewable feedstocks: status and opportunities. Renewable and Sustainable Energy Reviews, 16(7): 4763-4784.
6. Agarwal, A.K. and K. Rajamanoharan, 2009. Experimental investigations of performance and emissions of Karanja oil and its blends in a single cylinder agricultural diesel engine. Applied Energy, 86(1): 106-112.
7. Sharma, Y., B. Singh and S. Upadhyay, 2008. Advancements in development and characterization of biodiesel: a review. Fuel, 87(12): 2355-2373.
8. Amarnath, H., P. Prabhakaran, S.A. Bhat and R. Paatil, 2014. A Comparative Analysis of Thermal Performance And Emission Characteristics of Methyl Esters of Karanja And Jatropha Oils Based on A Variable Compression Ratio Diesel Engine. International Journal of Green Energy, 11(7): 675-694.
9. Issariyakul, T. and A.K. Dalai, 2014. Biodiesel from vegetable oils. Renewable and Sustainable Energy Reviews, 31: 446-471.
10. Dhingra, S., G. Bhushan and K.K. Dubey, 2013. Development of a combined approach for improvement and optimization of karanja biodiesel using response surface methodology and genetic algorithm. Frontiers in Energy, 7(4): 495-505.
11. Thiruvengadaravi, K., J. Nandagopal, P. Baskaralingam, V.S.S. Bala and S. Sivanesan, 2012. Acid-catalyzed esterification of karanja (Pongamia pinnata) oil with high free fatty acids for biodiesel production. Fuel, 98: 1-4.
12. Canakci, M. and J. Van Gerpen, 2001. Biodiesel production from oils and fats with high free fatty acids. Transactions-American Society of Agricultural Engineers, 44(6): 1429-1436.
13. Dixit, S, S. Kanakraj. and A. Rehman, 2012. Linseed oil as a potential resource for bio-diesel: A review. Renewable and Sustainable Energy Reviews, 16(7): 4415-4421.
14. Salvi, B. and S. Jindal, 2013. A comparative study of engine performance and exhaust emissions characteristics of linseed oil biodiesel blends with diesel fuel in a direct injection diesel engine. Journal of The Institution of Engineers (India): Series C, 94(1): 1-8.
15. Demirbas, A., 2009. Production of biodiesel fuels from linseed oil using methanol and ethanol in non-catalytic SCF conditions. Biomass and Bioenergy, 33(1): 113-118.
16. Iyer, R., 2011. Comments on the use of fatty acid methyl esters of linseed and castor oil as biodiesel. Journal of the American Oil Chemists' Society, 88(8): 1271-1273.
17. Juita, B.Z. Dlugogorski, E.M. Kennedy and J.C. Mackie, 2012. Low temperature oxidation of linseed oil: a review. Fire science reviews, 1(1): 1-36.
18. Puhan, S., R. Jegan, K. Balasubbramanian and G. Nagarajan, 2009. Effect of injection pressure on performance, emission and combustion characteristics of high linolenic linseed oil methyl ester in a DI diesel engine. Renewable Energy, 34(5): 1227-1233.
19. Raheman, H., P.C. Jena and S.S. Jadav, 2013. Performance of a diesel engine with blends of biodiesel (from a mixture of oils) and high-speed diesel. International Journal of Energy and Environmental Engineering, 4(1): 1-9.
20. Srithar, K., K.A. Balasubramanian, V. Pavendan and B.A. Kumar, 2014. Experimental investigations on mixing of two biodiesels blended with diesel as alternative fuel for diesel engines. Journal of King Saud University-Engineering Sciences.
21. Serqueira, D.S., D.M. Fernandes, R.R. Cunha, A.L. Squissato, D.Q. Santos, E.M. Richter and R.A. Munoz, 2014. Influence of blending soybean, sunflower, colza, corn, cottonseed, and residual cooking oil methyl biodiesels on the oxidation stability. Fuel, 118: 16-20.
22. Sarin, R., M. Sharma, S. Sinharay and R.K. Malhotra, 2007. Jatropha–palm biodiesel blends: an optimum mix for Asia. Fuel, 86(10): 1365-1371.
23. da Costa Barbosa, D., T.M. Serra, S.M.P. Meneghetti and M.R. Meneghetti, 2010. Biodiesel production by ethanolysis of mixed castor and soybean oils. Fuel, 89(12): 3791-3794.
24. Bora, P., L.J. Konwar, J. Boro, M.M. Phukan, D. Deka and B.K. Konwar, 2014. Hybrid biofuels from non-edible oils: A comparative standpoint with corresponding biodiesel. Applied Energy, 135: 450-460.
25. Chen, Y.-H., T.-H. Chiang and J.-H. Chen, 2012. An optimum biodiesel combination: Jatropha and soapnut oil biodiesel blends. Fuel, 92(1): 377-380.
26. Ozcanli, M. and H. Serin, 2011. Evaluation of soybean/canola/palm biodiesel mixture as an alternative diesel fuel. Journal of Scientific & Industrial Research, 70: 466-470.
27. Yogish, H., K. Chandrashekara and M.P. Kumar, 2012. Optimization of experimental conditions for composite biodiesel production from transesterification of mixed oils of Jatropha and Pongamia. Heat and Mass Transfer, 48(11): 1955-1960.


**Persian Abstract**

*DOI: 10.5829/idosi.ijee.2016.07.01.03*

**چکیده**

این مقاله

Decision Science Letters 5 (2016) 201–210

Contents lists available at GrowingScience

Decision Science Letters

homepage: www.GrowingScience.com/dsl

# Ranking and selection of commercial off-the-shelf using fuzzy distance based approach

**Rakesh Garg[a,b], R. K. Sharma[a*] and Kapil Sharma[b]**

[a]*Department of Computer Science & Engineering, Al-Falah School of Engineering & Technology, Faridabad, Haryana, India*
[b]*Department of Computer Science and Engineering, Delhi Technological University, Delhi, India*

**C H R O N I C L E**

*Article history*:
Received June 25, 2015
Received in revised format:
October 12, 2015
Accepted December 15, 2015
Available online
December 17 2015

*Keywords*:
*Commercial Off-the-Shelf (COTS)*
*Fuzzy Distance Based Approach (FDBA)*
*Selection Criteria*
*CBSE*

**A B S T R A C T**

There is a tremendous growth of the use of the component based software engineering (CBSE) approach for the development of software systems. The selection of the best suited COTS components which fulfils the necessary requirement for the development of software(s) has become a major challenge for the software developers. The complexity of the optimal selection problem increases with an increase in alternative potential COTS components and the corresponding selection criteria. In this research paper, the problem of ranking and selection of Data Base Management Systems (DBMS) components is modeled as a multi-criteria decision making problem. A 'Fuzzy Distance Based Approach (FDBA)' method is proposed for the optimal ranking and selection of DBMS COTS components of an e-payment system based on 14 selection criteria grouped under three major categories i.e. 'Vendor Capabilities', 'Business Issues' and 'Cost'. The results of this method are compared with other Analytical Hierarchy Process (AHP) which is termed as a typical multi-criteria decision making approach. The proposed methodology is explained with an illustrated example.

© 2016 Growing Science Ltd. All rights reserved.

## 1. Introduction

It was the late 70's when the concept of reusable components was introduced in structured programming by the software developers to maintain and develop software systems and it led the development of object oriented software systems in 80's. However, it is today's growing complexity of systems that forces us to turn this idea into practice. Component-Based Software Engineering (CBSE) is concerned with designing, selecting and composing components (Crnkovic & Larsson, 2002). CBSE is emerged as new approach to solve the development of complex problem. CBSE is concerned with the assembly of off the shelf components using well defined system architecture. CBSE is about building software through composition. The main purpose of using CBSE is that it allows reusability for selecting the components, adapting the components and then integrating them using a pre-defined architecture. A component once developed can be used further to develop new software systems which

* Corresponding author. Tel: 91-9992995488
E-mail address: rkgarg06@gmail.com (R. K. Sharma)

© 2016 Growing Science Ltd. All rights reserved.
doi: 10.5267/j.dsl.2015.12.004

will result in the less development effort. The main success factor while implementing the CBSE approach is the component selection that mainly depends on the optimization of (i) software requirements satisfaction and (ii) development cost.

The component-based software engineering emphasises mainly on the integration of existing COTS component into the target system. So the component selection and their integration become the two main issues, which play a vital role in the growth and development of the component based systems. Component selection is very important factor in component selection problem because there is a chance that more than one component satisfy the target requirements. The use of COTS component leads to the better software quality and reduces development time and the cost. The development of component-based software needs reuse of the components which interacts mutually as well as with the architecture of the system. No standard method exists in the past to describe, define and compose these COTS components or third party components in the final system. The development of the software which is based on COTS is one demanding process that offers the potential reuse of existing components with the reduction of software complexity (Tran et al., 1997). Due to a number of major benefits such as better software quality, less development effort etc. provided by the COTS based development approach has become more and more popular in the IT sector (Kontio, 1996; Alves & Castro, 2001; Phillips & Polen, 2002; Ncube & Maiden, 1999; Ibrahim et al., 2007; Erdogmus, 2001). However, development of software based on COTS is a nontrivial task. Such tasks are associated with major challenges e.g. uncertainty, information lack, standards etc.; (Gashi et al., 2007; Mohamed et al., 2007; Ziv et al., 1997; Mead, 2008; Ibrahim et al., 2008, 2009). The software developed by adopting the component based Software engineering approach is generally the integration of commercial off the shelf (COTS) components provided by various vendors that fulfill the desired technical and non-technical requirements of the target system. In the COTS– based software development, the complicated system is decomposed into the various that support the identification of multiple COTS components for evaluation. Although, the use of the COTS component lead to the great benefits such as time and cot development, there arises the problem of the COTS evaluation and selection due to the lack of information, high uncertainty etc.

The paper is organized as follows: in Section 2, the component selection problem and multi criteria decision making analysis are described. A review of the existing COTS selection methods is provided in Section 3. The proposed methodology for COTS component selection is provided in Section 4. A case study on E-payment system is provided in Section 5 to show the applicability of proposed methodology. The results and comparison with other existing methodologies are analyzed in Section 6 and Section 7 contains the conclusion of the methodology presented in this paper.

## 2. Problem Formulation and Research Motivation

The primary focus of the CBSE approach is on the integration of various COTS components to produce the target system or software. The major problem in CBSE approach is the selection and integration of components in the final target system such that the final system satisfy all the requirements which were stated at earlier stages of the software development. If a set of components is provided then the component selection problem may be categorized into two main selection problems based on the objectives and the criteria for selection. These two categories are shown in Fig. 1.

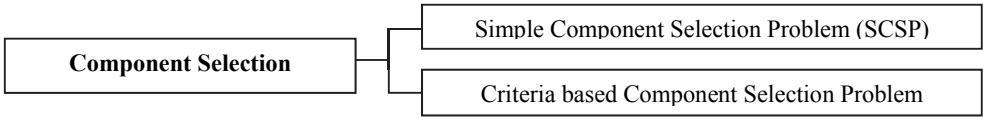


**Fig. 1.** Classification of the problem of component selection

### *2.1 Simple Component Selection problem (SCSP)*

The problem, which involves the selection of a subgroup of software components among a given large group of such software components or from repository in such a manner that the chosen subset of

software components is capable enough to satisfy the predetermined set of objectives of the problem is defined as Simple Component Selection Problem (SCSP).

*2.2 Criteria Based Component Selection problem (CCSP)*

Criteria-based Component Selection Problem (CCSP) may be defined as the problem of selection of a subgroup of software components among a given large group of such software components or from repository in a way that the composition of the chosen subset of software components fulfils the set of objectives of the problem and using various criteria.

The schematic selection procedure of components based on multiple criteria is given in Fig. 2.

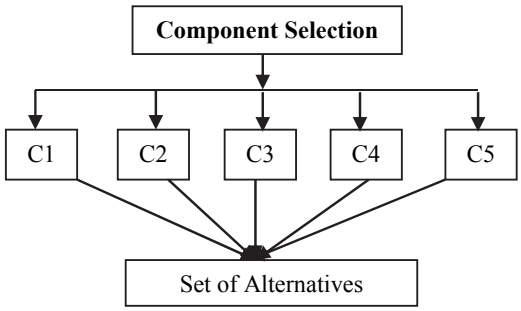


**Fig. 2.** Criteria based component selection problem

*2.3 Multi Criteria Decision Analysis (MCDA)*

A Multi Criteria Decision Analysis (MCDA) method helps the decision makers to select the optimal or best suitable alternative solution or component among a large number of potentially viable alternative solutions or components. The selection is based on particular requirements and ratings of these alternatives based on criteria to be taken under consideration. The basic activities involved in MCDA are as follows:

1. Establishment of various criteria that the selected component should fulfill.
2. Assigning a weight to each to represent the relative importance.
3. Evaluating the fitness of each component against defined selection.
4. Finally, Rank the components based on how well they fit the criteria.

## 3. Previous Related Work

Kontio (1995) developed a method of OTSO for the selection and evaluation of the components based on the product quality characteristics. Finkelstein et al. (1996) addressed the problem of the requirement specficataion and their deployment in an accuurate manner whereas. Wong and Jeffery (1996) proposed a method based on the gutman's means-end chain model for evaluation of software quality by considering the importnace of non ISO-9126 chracterstics in the software quality evaluation. Gaedke et al. (1999) proposed web components repository as a tool that supports the reuse of code of existing component to develop a new system. The repository introduced by the researchers in this study mainly consists of three parts as (i) component store (ii) metadata store and (iii) search tool.

Ncube and Dean (2002) compared various existing approaches for the component selection and developed a more effective approach based on requirement-driven. Phillips and Polen (2002) provided an approach for COTS selection that mainly stresses on the creation and maintenance of a data repository that can help the developers select the appropriate component for the software development. Rus et al. (2001) built the web based repository by extracting information from research articles published in journal, conference proceedings and project reports. Morisio et al. (2000, 2002) provided a new process and the proper guidelines for the selection and evaluation of COTS components by identifying the main differences as requirements definition, high level design, testing etc. in comparison to the traditional approach for the software development.

Ruhe (2003) addressed the COTS selection problem with a high uncertainty and lack of information and developed a software namely COTS-DSS for the selection and evaluation of COTS. Kunda (2003) presents an approach incoroporating the non technical isues associated in the selection of COTS components and is named as social technical approach. Ducik and Boegh (2003) present a framework that helps the software developer in the quality evaluation process of the COTS software product. Mohamed et al. (2004) provide a conceptual model for the component selection and evaluation that was implemented by using the agent technologies incorporated by toe knowledge bases as COTS KB and methods KB. Mancebo and Andrews (2005) present a component selection and evaluation approach based on the existing techniques by considering the archietecture of the components as a major aspect. Mohamed et al. (2005) proposed a two level mainly process level and activity level customization process for the selection process by considering the attributes related to the project domain such as project effort. In the contemporary work, Mohamed et al. (2007) addressed the problem of COTS selection and evaluation and provide a survey on the contribution of the most significant eighteen existing COTS selection approaches provided by various researchers.

Gesellensetter and Glesner (2007) developed a unified approach for the development of component based systems using methods from code optimization which further helps the software developer to select the optimal components for the target system. Haghpanah et al. (2007) presented the problem of component selection and evaluation as NP-complete problem and proposed a method based on the greedy approach and the genetic algorithm by taking the computational complexity of this problem into account.

Saltelli et al. (2008) introduced the concept of sensitivity analysis which provides the basis for obtaining the useful information about the selection parameters which can contribute up to a large extent to the uncertainties in the output of the model. Ibrahim et al. (2009) present a hybrid approach for the selection and evaluation of COTS components by combining two approaches as analytical hierarchy processing and the bayesian-belief network and the selection criteria uncertainty was considered in this research.

Mittal and Bhatia (2013) considered reusability as a major selection criterion for the component selection and solved the problem of COTS component selection and evaluation by applying analytic hierarchy processing technique. Faridi et al. (2013) presented the characteristics described in the software quality codes for the component selection and evaluation. Faundes et al. (2013) proposed a method process based evaluation and comparison for the selection of OTSS by accounting six criteria as Coverage, Automation, Implementation, Cost, Collaboration, and Participation.

Kaur and Singh (2014) solved the problem of component selection and evaluation by applying Promethee method and they considered performance, reliability, maintainability, cost and inerrability as COTS selection criteria. Nazir et al. (2014) presented effectiveness, efficiency, satisfaction, safety and usability as the major selection criteria for the COTS component selection and evaluation. Vinay et al. (2014) developed a W-shaped framework for component selection by considering the problem of component selection and evaluation problem as NP-complete problem due to the high availability of the selection parameters in literature. As the reusability approach in the software development leads to the great benefits such as reduction in cost and time, a framework based on the component based software engineering for the reusability was developed (Khan et al., 2014).

## 4. Proposed Methodology

Fuzzy Distance Based Approach (FDBA) is used for ranking and evaluation of COTS components for the first time. Fuzzy set theory is used for assigning weights to the selection criteria and performance ratings of the COTS components. Fuzzy operators are used to determine average aggregated weights and performance ratings. Distance Based Approach is further applied to determine the composite distance of the alternative COTS components from the optima, which is an imaginary component having all ideal values for each selection criteria. The ranking of the COTS components is done on the ascending/descending order of the values of the composite distance of the COTS components from the optimal value i.e. zero. The DBA has already been applied for the evaluation, selection and ranking of

robots and software engineering metrics, etc. (Kumar and Garg, 2010). The composite distance value is:

$$CD_{OP-Alt} = \left[ \sum_{j=1}^{m} (Z_{OPj} - Z_{ij})^2 \right]^{1/2} \quad (1)$$

where $Z_{ij} = \frac{r_{ij} - \bar{r}_j}{S_j}$, $\bar{r}_j = \frac{1}{n}\sum_{i=1}^{n} r_{ij}$; $S_j = \left[ \frac{1}{n}\sum_{i=1}^{n} (r_{ij} - \bar{r}_j)^2 \right]^{1/2}$

$$[r] = \begin{bmatrix} r_{11} & r_{12} & \cdots & r_{1j} \\ r_{21} & r_{22} & \cdots & r_{2j} \\ \vdots & \vdots & \vdots & \vdots \\ r_{i1} & r_{i2} & \cdots & r_{ij} \\ r_{b1} & r_{b2} & \cdots & r_{bj} \end{bmatrix};$$

Here, $i, j$ represent COTS components and selection criteria, respectively. $r_{bj}$ is the best (optimal) value for a particular selection criteria among all alternate COTS components.

## 5. An Empirical Study

In the past decades, as the software development increases rapidly, management of data has become a very crucial issue. Generally for the purpose of management of data software developers use the concept of Databases. The power of the databases comes from a body of knowledge and technology that has developed and is embodied in the software applications known as database management systems (DBMS). Database management systems (DBMS) are computer software applications that make interaction with the user, other applications and the database itself to capture and analyze data.

In this study, a group of ten experts from various software companies according to their vast knowledge in this field was established. As the data that can contribute a lot to the COTS selection and evaluation present in the open literature is not sufficient due to lack of maturity, expert's opinion approach was adopted in this research to collect the data that is relevant to the COTS selection and evaluation problem. Firstly, a team of experts from academia as well as IT companies having wide experience in the area of component based software engineering was formed. The experts search for DBMS COTS candidates and finally, provide a number of DBMS candidates as COTS (i) Oracle (ii) SQL-Express (iii) MYSQL (iv) Ms-Access (v) Postgreys. The DBMS COTS components identified by experts can be compared by the mean of (i) Quality Characteristics (ii) Technology factors (iii) Domain and Architectural Factors (iv) Strategic Factors, named as ranking criteria. The main focus in this study is on strategic factors as shown in Fig. 3.

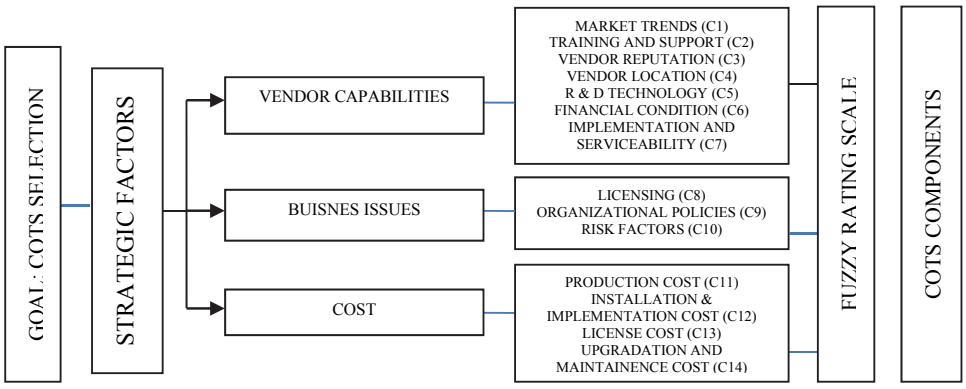


**Fig. 3.** COTS ranking criteria

The main motive of this research is to design a framework that provides the functionality to rank the various COTS components on the basis of various relevant COTS selection criteria/sub-criteria. An example of the selection of COTS components of a Data Base management System for an E-payment

system has been taken for ranking of five COTS components based on 14 selection criteria grouped in three broad categories namely 'Vendor capabilities', 'business issues' and 'cost' which fall under the category of Strategic Factors for the selection of COTS. The example will demonstrate and validate the proposed method. The present research is exploratory in nature. Questionnaire is considered to be the best way of collection of data in survey researches which are exploratory in nature. Since, no secondary data is available in the open literature and hence questionnaires are used to collect primary data. Two questionnaires were prepared. The first questionnaire is related to estimate the weights of the COTS selection criteria and the second questionnaire is used to get the performance ratings of the COTS components based on each selection criteria. The weights and ratings are obtained on a seven point fuzzy scale. The questionnaires are designed in three parts: First part of each questionnaire contains a covering letter which explains the purpose of the research study and statement of confidentiality. Second part consists of demographic details e.g. name of the organization, field of expertise (software development, software design, software purchasing and procurement, etc.); length of experience, qualification and designation, etc. Third part of the questionnaire consists of assigning weights to the selection criteria/performance ratings of the COTS components on a predetermined seven point fuzzy scale. The weights (Local and Global) of the selection criteria using the expert opinion are estimated and given in Table 1.

**Table 1**
Weights (Local and Global) for ranking criteria

| S. No. | Criterion/Sub-Criterion | Local Wt. | Global Wt. | S. No. | Criterion/Sub-Criterion | Local Wt. | Global Wt. |
|---|---|---|---|---|---|---|---|
| Vendor Capabilities | | - | 0.4415 | Business Issues | | - | 0.2605 |
| C1 | Market Trends | 0.1367 | 0.06035 | C8 | Licensing Arrangements | 0.2967 | 0.0772 |
| C2 | Training and Support | 0.1415 | 0.06247 | C9 | Organizational Policies | 0.3496 | 0.0910 |
| C3 | Vendor Reputation | 0.1319 | 0.05823 | C10 | Risk factors | 0.3837 | 0.0999 |
| C4 | Vendor Location | 0.1319 | 0.05823 | Cost | | - | 0.2980 |
| C5 | R & D Technology | 0.1127 | 0.04975 | C11 | Production Cost | 0.2931 | 0.0873 |
| C6 | Financial Condition | 0.1751 | 0.07730 | C12 | Installation & Implementation Cost | 0.2522 | 0.0751 |
| C7 | Implementation & Serviceability | 0.1703 | 0.07518 | C13 | License Cost | 0.1954 | 0.0582 |
| | | | | C14 | Upgradation & Maintenance Cost | 0.2593 | 0.0772 |

A summary of the aggregated average performance ratings assigned by the experts for each criterion is presented in Table 2.

**Table 2**
Aggregated average performance ratings of DBMS COTS components

| Criterion/ Sub-Criterion | | Oracle | SQL Express | MYSQL | MS-Access | Postgreys |
|---|---|---|---|---|---|---|
| Strategic Factors | | 0.3864 | 0.5079 | 0.7960 | 0.4246 | 0.7600 |
| Vendor Capability | | 0.4675 | 0.6042 | 0.7935 | 0.4117 | 0.7928 |
| C1 | Market Trends | 0.5909 | 0.6091 | 0.8363 | 0.3727 | 0.8182 |
| C2 | Training and Support | 0.2500 | 0.5545 | 0.8500 | 0.3546 | 0.8091 |
| C3 | Vendor Reputation | 0.7000 | 0.7727 | 0.7727 | 0.4636 | 0.7363 |
| C4 | Vendor Location | 0.3364 | 0.6818 | 0.6273 | 0.5000 | 0.6454 |
| C5 | R & D Technology | 0.5909 | 0.7363 | 0.8091 | 0.3182 | 0.8682 |
| C6 | Financial Condition | 0.2318 | 0.4636 | 0.8863 | 0.4091 | 0.8818 |
| C7 | Implementation and Serviceability | 0.5727 | 0.6636 | 0.7727 | 0.4636 | 0.7909 |
| Business Issues | | 0.4349 | 0.4879 | 0.6879 | 0.4758 | 0.5848 |
| C8 | Licensing Arrangements | 0.3364 | 0.4455 | 0.7909 | 0.4091 | 0.7909 |
| C9 | Organizational Policies | 0.2318 | 0.4636 | 0.5364 | 0.3909 | 0.3546 |
| C10 | Risk Factors | 0.7363 | 0.5545 | 0.7363 | 0.6273 | 0.6091 |
| Cost | | 0.2568 | 0.3955 | 0.9068 | 0.3864 | 0.9023 |
| C11 | Production cost | 0.2818 | 0.4818 | 0.9409 | 0.3909 | 0.9727 |
| C12 | Installation and Implementation cost | 0.2273 | 0.3727 | 0.9318 | 0.3364 | 0.8682 |
| C13 | License Cost | 0.2864 | 0.3364 | 0.9318 | 0.4091 | 0.9591 |
| C14 | Upgradation and Maintenance Cost | 0.2318 | 0.3909 | 0.8227 | 0.4091 | 0.8091 |

The adjusted matrix so formed can be given as:

$$[r_a] = \begin{bmatrix} 0.2182 & 0 & 0.2364 & 0 & 0.2727 & 0 & 0.1091 \\ 0.2364 & 0.3045 & 0.3091 & 0.3454 & 0.4181 & 0.2318 & 0.2 \\ 0.4636 & 0.6 & 0.3091 & 0.2909 & 0.4909 & 0.6545 & 0.3091 \\ 0 & 0.1046 & 0 & 0.1636 & 0 & 0.1773 & 0 \\ 0.4455 & 0.5591 & 0.2727 & 0.309 & 0.55 & 0.65 & 0.3273 \\ 0.4636 & 0.6 & 0.3091 & 0.3454 & 0.55 & 0.6545 & 0.3273 \end{bmatrix}$$

The average and standard deviation are 0.27274, 0.31364, 0.22546, 0.22178, 0.459867, 0.34634, 0.1891 and 0.190365, 0.266648, 0.129591, 0.141632, 0.219601, 0.295276, 0.137638 respectively. By using the Z-formula, the standardized matrix is obtainted.

Now, the distance matrix can be represented as:

$$[r_d] = \begin{bmatrix} 1.2891 & 2.2502 & 0.5610 & 2.4387 & 1.2627 & 2.2166 & 1.5853 \\ 1.1935 & 1.1082 & 0 & 0 & 0.6006 & 1.4315 & 0.9249 \\ 0 & 0 & 0 & 0.3848 & 0.2691 & 0 & 0.1322 \\ 2.4353 & 1.8579 & 2.3852 & 1.2836 & 2.5045 & 1.6161 & 2.3707 \\ 0.0951 & 0.1534 & 0.2809 & 0.2570 & 0 & 0.0152 & 0 \end{bmatrix}$$

Finally the resultant matrix having composite distance will be given as:

$$[r_c] = \begin{bmatrix} 1.6618 & 5.0632 & 0.3147 & 5.9474 & 1.5945 & 4.9132 & 2.5132 \\ 1.4244 & 1.2281 & 0 & 0 & 0.3608 & 2.0493 & 0.8554 \\ 0 & 0 & 0 & 0.1481 & 0.0724 & 0 & 0.0175 \\ 5.9308 & 3.4517 & 5.6892 & 1.6477 & 6.2727 & 2.6118 & 5.6548 \\ 0.0090 & 0.0235 & 0.0789 & 0.0661 & 0 & 0.0002 & 0 \end{bmatrix}$$

By using Eq. (1) it can be seen in Table 3 that the proposed methodology for COTS selection uses the basis of distance of each alternative COTS from the best or optimum hypothetical solution for quantitative comparison and ranking of COTS. This distance is termed as composite distance and overall ranking of COTS based on this composite distance value is shown in Table 3.

**Table 3**
Overall Ranking of DBMS COTS Component using FDBA

| COTS Components | Vendor Capabilities | | Business Issues | | Cost | | Strategic Concerns | |
|---|---|---|---|---|---|---|---|---|
| | Composite Distance | Rank | Composite Distance | Rank | Composite Distance | Rank | Composite Distance | Rank |
| ORACLE | 4.69127 | 4 | 3.36158 | 5 | 4.337614 | 5 | 3.725443 | 5 |
| SQL EXPRESS | 2.432702 | 3 | 2.816597 | 4 | 3.477869 | 3 | 2.700875 | 3 |
| MYSQL | 0.487837 | 2 | 0 | 1 | 0.4568 | 2 | 0 | 1 |
| MS-ACCESS | 5.590946 | 5 | 2.538834 | 3 | 3.528409 | 4 | 3.423775 | 4 |
| POSTGREYS | 0.421601 | 1 | 2.229029 | 2 | 0.19439 | 1 | 1.011105 | 2 |

In order to validate the methodology and the results obtained, the present COTS component selection problem using the same datasets is solved using AHP. The results so obtained are given in Table 4. The comparison shows that the results obtained using FDBA method and AHP are same for the selection criteria – cost and strategic concerns. In case of selection criteria namely ‘Vendor Capabilities’ and ‘Business Issues’ a minor differences in the rankings of two COTS components is observed. In case of AHP method MYSQL is ranked at #1 followed by POSTGREYS whereas the POSTGREYS is ranked

at #1 followed by MYSQL using FDBA method. The reason is quite obvious that there is a negligible difference in the ranking values (0.7971 and 0.7954) of these two components using AHP. Same pattern is observed in the ranking values of SQL EXPRESS and MS-ACCESS components for selection criterion namely 'Business Issues'. It is thus evident that the FDBA method is validated.

**Table 4**
Overall Ranking of DBMS COTS Component using AHP

| COTS Components | Vendor Capabilities | | Business Issues | | Cost | | Strategic Concerns | |
|---|---|---|---|---|---|---|---|---|
| | Composite Distance | Rank | Composite Distance | Rank | Composite Distance | Rank | Composite Distance | Rank |
| ORACLE | 0.4575 | 4 | 0.4412 | 5 | 0.2559 | 5 | 0.3962 | 5 |
| SQL EXPRESS | 0.6306 | 3 | 0.4903 | 3 | 0.4023 | 3 | 0.5276 | 3 |
| MYSQL | 0.7971 | 1 | 0.6826 | 1 | 0.9061 | 2 | 0.7997 | 1 |
| MS-ACCESS | 0.4146 | 5 | 0.4799 | 4 | 0.3854 | 4 | 0.4208 | 4 |
| POSTGREYS | 0.7954 | 2 | 0.5740 | 2 | 0.9401 | 1 | 0.7712 | 2 |

## 6. Results

According to methodology adopted in this empirical study, lower value of composite distance implies better ranking. The comparative rankings of all five COTS components based on vendor capabilities, Business issues and cost individually as well as taken altogether are given in Fig. 4. It is depicted that Postgreys has been ranked first on the basis of vendor capabilities and cost as selection criteria. MYSQL and SQL Express are ranked second and third, respectively and fall among top three DBMS cots components. Oracle is ranked at five based on Business issues, cost and Strategic factors whereas ranked at four based on vendor capabilities which shows the least use of this component. MYSQL is ranked at #1 based on strategic concern i.e. considering all three selection criteria namely vendor capabilities, Business issues and cost collectively, and is followed by Postgreys whereas Oracle is ranked at last.

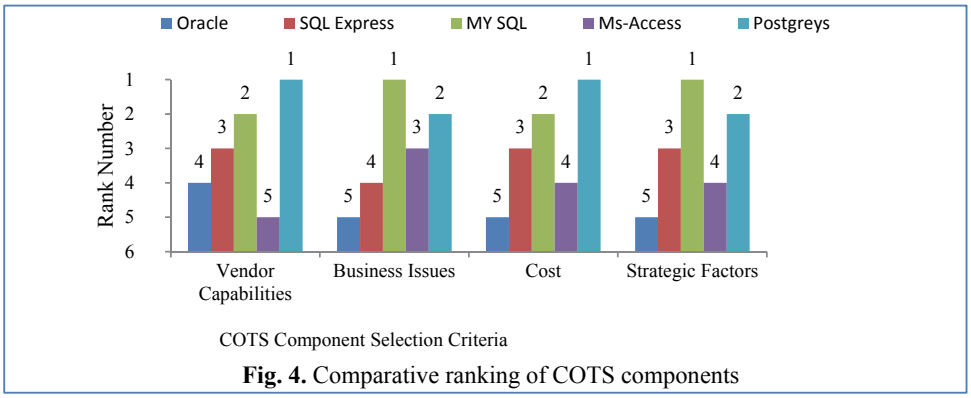


**Fig. 4.** Comparative ranking of COTS components

## 7. Conclusions

The aim of the research paper was to resolve the major problems of optimal selection of COTS components for DBMS of an e-payment system while implementing the concept of component based system development. The problem of ranking and selection of COTS components of database management system is modeled as a multi-criteria decision making problem. The selection component problem relates to an e-payment system. The alternative potential COTS components are ranked based on a number of mutually conflicting selection criteria using 'Fuzzy Distance Based Approach'. The developed approach had not been employed earlier and can be termed as a benchmark concept for the rapid solution of such type of component selection problems. The proposed 'Fuzzy Distance Based Approach' uses a very simple mathematics and is efficient enough to solve the problems which involve a large number of mutually interacting and dependent selection criteria. The proposed methodology is

validated comparing the results with the results obtained using a well-known AHP technique. The comparison of the results shows that the proposed FDBA method is in good agreement with the AHP technique with an additional advantage of easy, simple reduced mathematical calculations. In order to validate the proposed approach, the results so obtained can be compared with such other techniques such as TOPSIS, PROMETHEE, Matrix or Fuzzy Matrix methods.

## References


Alves, C., & Castro, J. (2001, October). CRE: A systematic method for COTS components selection. In *XV Brazilian Symposium on Software Engineering (SBES)*. Rio de Janeiro, Brazil.

Phillips, B. C., & Polen, S. M. (2002). Add decision analysis to your COTS selection process. *Software Technology Support Center Crosstalk*.

Crnkovic, I., & Larsson, M. P. H. (2002). *Building reliable component-based software systems*. Artech House.

Kunda, D. (2003). STACE: social technical approach to COTS software evaluation. In *Component-Based Software Quality* (pp. 64-84). Springer Berlin Heidelberg.

Beus-Dukic, L., & Bøegh, J. (2003). COTS software quality evaluation. In*COTS-Based Software Systems* (pp. 72-80). Springer Berlin Heidelberg.

Erdogmus, H. (2001). Management of License Cost Uncertainty in COTS-Based Software Development: A Real Options Approach.

Faridi, M. S., Javed, Z., Abid, M. H., Ahmed, M., & Ngadi, M. A. B. (2013). IROTS: A Proposed COTS Evaluation & Selection Methodology for Component Based Software Engineering in Under-Development Countries.

Faundes, M. J., Astudillo, H., & Hitpass, B. (2013, September). Process-based evaluation and comparison of OTS software alternatives. In *Computer Science and Information Systems (FedCSIS), 2013 Federated Conference on* (pp. 1093-1100). IEEE.

Finkelstein, A., Spanoudakis, G., & Ryan, M. (1996, March). Software package requirements and procurement. In *Software Specification and Design, 1996., Proceedings of the 8th International Workshop on* (pp. 141-145). IEEE.

Gaedke, M., Rehse, J., & Graef, G. (1999, May). A repository to facilitate reuse in component-based web engineering. In *International Workshop on Web Engineering at the 8th International World-Wide Web Conference (WWW8). Toronto, Ontario, Canada*.

Gashi, I., Popov, P., & Stankovic, V. (2009). Uncertainty explicit assessment of off-the-shelf software: A Bayesian approach. *Information and Software Technology*, *51*(2), 497-511.

Gesellensetter, L., & Glesner, S. (2007). Only the best can make it: Optimal component selection. *Electronic Notes in Theoretical Computer Science*,*176*(2), 105-124.

Haghpanah, N., Moaven, S., Habibi, J., Kargar, M., & Yeganeh, S. H. (2007, December). Approximation algorithms for software component selection problem. In *Software Engineering Conference, 2007. APSEC 2007. 14th Asia-Pacific* (pp. 159-166). IEEE.

Ibrahim, H., Far, B. H., & Eberlein, A. (2007, April). On Agent-Oriented Requirements Engineering for COTS-Based Software Development (CBSD). In *Electrical and Computer Engineering, 2007. CCECE 2007. Canadian Conference on* (pp. 690-693). IEEE.

Ibrahim, H., Far, B. H., & Eberlein, A. (2008, November). Towards Uncertainty Management in COTS-Based Development. In *Proc. of the 9th IASTED International Conference on Software Engineering and Applications SEA* (pp. 16-18).

Ibrahim, H., Far, B. H., & Eberlein, A. (2009). Weighted criteria hybrid model for ranking commercial off-the-shelf products. In *Proc. of the IASTED Int. Conf. on Software Engineering SE 2009* (pp. 49-56).

Kaur, K., & Singh, H. (2014). Quantifying COTS Components Selection using Multi Criteria Decision Analysis Method-PROMETHEE. *Global Journal of Computer Science and Technology*, *14*(2).

Khan, A., Khan, K., Amir, M., & Khan, M. N. A. (2014). A Component-Based Framework for Software Reusability. *International Journal of Software Engineering and Its Applications*, *8*(10), 13-24.

Kontio, J. (1995). OTSO: a systematic process for reusable software component selection.

Kontio, J. (1996, March). A case study in applying a systematic method for COTS selection. In *Software Engineering, 1996., Proceedings of the 18th International Conference on* (pp. 201-209). IEEE.

Kumar, R., & Garg, R. K. (2010). Optimal selection of robots by using distance based approach method. *Robotics and Computer-Integrated Manufacturing*, *26*(5), 500-506.

Mancebo, E., & Andrews, A. (2005, March). A strategy for selecting multiple components. In *Proceedings of the 2005 ACM symposium on Applied computing* (pp. 1505-1510). ACM.

Mead, W. J. (2008). Uncertainty in Decision Making. *Encyclopedia of Public Administration and Public Policy,*

Mittal, S., & Bhatia, P. K. (2013). Framework for Evaluating and Ranking the Reusability of COTS Components based upon Analytical Hierarchy Process.

Mohamed, A., Ruhe, G., & Eberlein, A. (2005, May). Decision support for customization of the COTS selection process. In *ACM SIGSOFT Software Engineering Notes* (Vol. 30, No. 4, pp. 1-4). ACM.

Mohamed, A., Ruhe, G., & Eberlein, A. (2007, March). COTS selection: past, present, and future. In *Engineering of Computer-Based Systems, 2007. ECBS'07. 14th Annual IEEE International Conference and Workshops on the*(pp. 103-114). IEEE.

Mohamed, A., Wanyama, T., Ruhe, G., Eberlein, A., & Far, B. (2004). COTS evaluation supported by knowledge bases. In *Advances in Learning Software Organizations* (pp. 43-54). Springer Berlin Heidelberg.

Morisio, M., Seaman, C. B., Basili, V. R., Parra, A. T., Kraft, S. E., & Condon, S. E. (2002). COTS-based software development: Processes and open issues. *Journal of Systems and Software*, *61*(3), 189-199.

Morisio, M., Seaman, C. B., Parra, A. T., Basili, V. R., Kraft, S. E., & Condon, S. E. (2000, June). Investigating and improving a COTS-based software development. In *Proceedings of the 22nd international conference on Software engineering* (pp. 32-41). ACM.

Nazir, S., Anwar, S., Khan, S. A., Shahzad, S., Ali, M., Amin, R., ... & Cosmas, J. (2014, January). Software component selection based on quality criteria using the analytic network process. In *Abstract and Applied Analysis*. Hindawi Publishing Corporation.

Ncube, C., & Dean, J. (2002). The Limitations of Current Decision-Making Techniques in the Procurement of COTS Software Components.

Ncube, C., & Maiden, N. A. (1999). Guiding parallel requirements acquisition and COTS software selection. In *Requirements Engineering, 1999. Proceedings. IEEE International Symposium on* (pp. 133-140). IEEE.

Ruhe, G. (2003). Intelligent support for selection of COTS products. In *Web, Web-Services, and Database Systems* (pp. 34-45). Springer Berlin Heidelberg.

Rus, I., Seaman, C., Lindvall, M., Basili, V., & Boehm, B. (2001). A Web Repository of Lessons Learned from COTS-Based Software Development1.*Notes*.

Saltelli, A., Ratto, M., Andres, T., Campolongo, F., Cariboni, J., Gatelli, D., ... & Tarantola, S. (2008). *Global sensitivity analysis: the primer*. John Wiley & Sons.

Tran, V., Liu, D. B., & Hummel, B. (1997, July). Component-based systems development: challenges and lessons learned. In *Software Technology and Engineering Practice, 1997. Proceedings., Eighth IEEE International Workshop on [incorporating Computer Aided Software Engineering]* (pp. 452-462). IEEE.

Vinay, M. K., & Johri, P. (2014). W-Shaped Framework for Component Selection and Product Development Process. *World Applied Sciences Journal*, *31*(4), 606-614.

Wong, B., & Jeffery, R. (2002). A framework for software quality evaluation. In *Product Focused Software Process Improvement* (pp. 103-118). Springer Berlin Heidelberg.

Ziv, H., Richardson, D., & Klösch, R. (1997). The uncertainty principle in software engineering. In *submitted to Proceedings of the 19th International Conference on Software Engineering (ICSE'97)*.

Artif Intell Rev
DOI 10.1007/s10462-015-9454-6

# Recent advances on multicue object tracking: a survey

**Gurjit Singh Walia**[1] · **Rajiv Kapoor**[2]

© Springer Science+Business Media Dordrecht 2016

**Abstract** The performance of single cue object tracking algorithms may degrade due to complex nature of visual world and environment challenges. In recent past, multicue object tracking methods using single or multiple sensors such as vision, thermal, infrared, laser, radar, audio, and RFID are explored to a great extent. It was acknowledged that combining multiple orthogonal cues enhance tracking performance over single cue methods. The aim of this paper is to categorize multicue tracking methods into single-modal and multi-modal and to list out new trends in this field via investigation of representative work. The categorized works are also tabulated in order to give detailed overview of latest advancement. The person tracking datasets are analyzed and their statistical parameters are tabulated. The tracking performance measures are also categorized depending upon availability of ground truth data. Our review gauges the gap between reported work and future demands for object tracking.

**Keywords** Object tracking · Multicue · Data set · Tracking evaluation · Computer vision

## 1 Introduction

The object tracking aims at analysis of video sequences for localization of object in sub sequences frames. It is foremost important due to its myriad of applications in field of computer vision such as driver assistance systems, video surveillance, man-machine interaction, autonomous robot, medical imaging, activity analysis, augmented reality, video indexing, traffic control and much more. However, object tracking in video is very challenging due to: dynamic environment conditions, conversions from 3D to 2D world, real time requirements, full or partial occlusion, clutter background, pose variations, abrupt object motion, appear-

✉ Rajiv Kapoor
rajiv.kapoor@dce.ac.in

1 Defense Research and Development Organization, Ministry of Defense, Delhi, India

2 Department of Electronics and Communication, Delhi Technological University (Formerly DCE), Bawana Road, Delhi, India

Published online: 09 January 2016

ance variability, noise in video (snow, fog, dust, fire etc.). In last two decade, a number of object tracking algorithms were proposed with the aim to cater for one or more of these listed challenges during tracking. The object tracking methods using cues (color, motion, orientation, spatial energy, shape, texture, infrared, and position, etc.) was extensively explored and discussed at length (Yilmaz et al. 2006; Yang et al. 2011; Smeulders et al. 2014). But, tracker based upon single cue can limitedly address tracking challenges. Hence, in last few years, there is paradigm shift of research work from single cue to multicue tracking methods. Under multicue object tracking, complementary cues are added in order to cater for different challenges. The multiple cues are extracted either from single-modal (one sensor) or from multi-modal (more than one sensor). In literature, it was well argued that cues which are good at one point of time may degrade at other instance during tracking process. Color cue being computationally efficient, invariant to scaling and handle partial occlusion cannot provide spatial information of target. Although, semi overlapping regions were used for embedding spatial information into color space (Maggio and Cavallaro 2005), single color cue cannot handle illumination changes, full occlusion, and texture changes of target. HSV color model is invariant to illumination changes but it cannot handle low saturation videos where hue channel is affected to large extent with small change in saturation (Hong et al. 2009). Motion feature can be detected from consequent frames but could not provide shape information of object. In order to augment motion cue, spatial appearance along with motion was extracted as spatial-temporal motion energy which is rich in texture information and can handle illumination changes and background clutters (Cannons et al. 2010). Texture cue representing fine level details of object can be extracted with low computational power. But, due to changes in texture from fine to coarse, tracker using only texture cue degrades performance as object moves away from the camera. Gradient cue being extracted from chromatic contents cater for tilting and deformation of object but tracker based upon only gradient cue degrade under heavy clutter environment. Shape cue being one of prominent feature for rigid object fails to track non rigid object or object whose shape changes with time. In addition, it is also greatly affected by change in view angle of sensing device. Depth cue extracted from Kinect source or stereo vision is illumination and color invariant but unable to provide motion information and degrade its performance when object lack texture information or under occlusion (Wang et al. 2014; Munoz-salinas et al. 2008). Apart from vision sensors, thermal sensors were extensively explored for object tracking. The thermal sensors are based upon thermal radiation from human superficial blood vessels or from any object thermal profile. Thermal sensors are insensitive to illumination changes, disguise and pose variation of object. However, thermal cue is affected by ambient temperature and it is difficult to distinguish thermal profile of different people in crowd. Thermal sensor has high image noise and low resolution as compared to vision sensors (Kong et al. 2005). In addition, inherent hallo effect and their inability to provide texture information limit their usage as single modality for object tracking (Conaire et al. 2008). Audio sensors can faithfully provide direction of moving object and are very discriminant when present but they are unreliable for object far away from sensors. Laser scanner has potential advantages such as low computational requirement, easy projection of laser data to rectangular coordinate system and insensitive to illumination changes but could not distinguish objects once track of objects is lost under heavy cluttered environments (Cui et al. 2008). Radio frequency sensors (i.e. radar, RFID) can provide accurate range information and locate object behind wall but mostly needs to be compensated with other modularity with rich information of object. In sum, single cue trackers are in general less reliable and less robust to environment conditions. The complimentary cues either from same or different sensors are fused for building robust tracking systems. In human sensory system, different cues are either suppressed or boosted depending upon their reliability for

achieving adaptive fusion of data from multisensory (Murphy 1996). The reliability of visual cues can be estimated either from correlation among cues or from ambiguity of cues (Jacobs 2002). Hence, in last few years, tracking researchers are motivated to shift their work towards either development of efficient cues or integration of multicue for robust tracking.

In 2006, review of object tracking techniques was addressed (Yilmaz et al. 2006). The review considered object representations for classification of object tracking methods. The object representation was classified into three categories as point correspondence, contour evolution or geometric models. In addition, object detection methods were briefly discussed. In similar line, various visual features descriptor for object representation along with visual tracking methods were reviewed (Yang et al. 2011). The feature descriptors for visual tracking were categorized as color, gradient, texture, spatio-temporal and multiple features. Further, the visual object tracking techniques were classified into Monte Carlo sampling, integration of context information and online learning. Sparse coding based visual tracking techniques were reviewed (Zhang et al. 2013c). But review was mainly focused on experimental analysis of some of representative work for sparse coding based appearance modeling and target tracking. In 2014, experimental survey for visual tracking was proposed (Smeulders et al. 2014). In this survey, algorithms that perform either matching or classification for object tracking were chosen for experiments. Nineteen trackers for which source code was available were evaluated for both qualitative and quantitative measures on large length of videos under various test scenarios. Also, survey on human detection techniques was proposed (Walia and Kapoor 2014a). But this review mainly focused on single-modal and multi-modal human detection methods. In last few years, object tracking work was extensively explored with main focus of research community on single-modal/multi-modal multicue tracking algorithms. Our survey mainly categorized and analyzed object tracking methods based upon single-modal and multi-modal multicue tracking.

With more than ten trackers being reported every year and also presence of flurry of work in literature, we feel time is ripe to summarize multicue tracking techniques as, in best of our knowledge, no such survey exists which exclusively categorizes multicue tracking methods. In order to gauge the gap in multi cue tracking work, we have limited our scope of this survey to object tracking based upon multiple different features extracted from either single-modal or multi-modal. We hope that our comprehensive survey on multicue object tracking will give seminal learning and new directions of research to academician, researchers and computer vision community. The remaining paper is organized as follows.

The aim of this survey is to characterize and summarize single-modal and multi-modal multicue techniques and analyse their merits and demerits. The single-modal multicue object tracking techniques are reviewed and tabulated in Sect. 2. In Sect. 3, multi-modal object tracking techniques are critically reviewed and tabulated. The different evaluation measures for tracking along with available online database for multicue object tracking are summarized in Sect. 4. The discussion of reported work is also followed in respective section in order to list out merit and demerits of work. In Sect. 5, concluding remarks and future directions in this field of multicue object tracking are sketched.

## 2 Multicue object tracking

The multicue object tracking aims at localization of object through processing of data acquired either from single-modal or from multi-modal sensors. The failure of single cue under different challenging scenarios is compensated by complementary cues. In general, multicue tracking framework can be illustrated as flow diagram Fig. 1. Where, sensors considered for

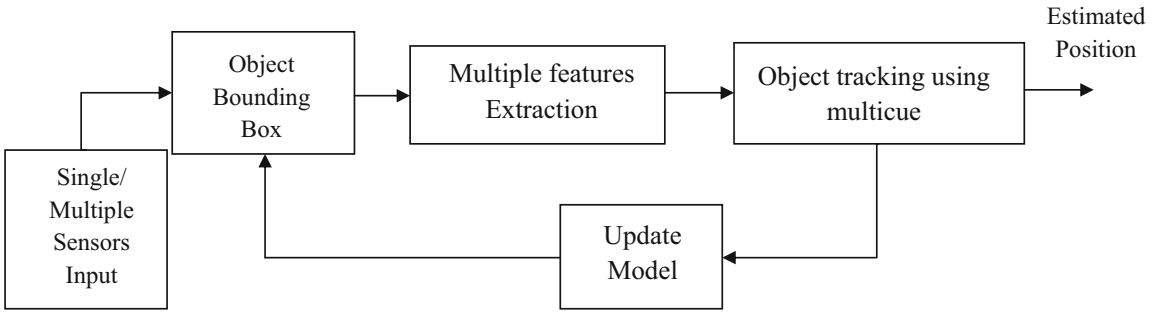


**Fig. 1** Flow chart of multicue object tracking

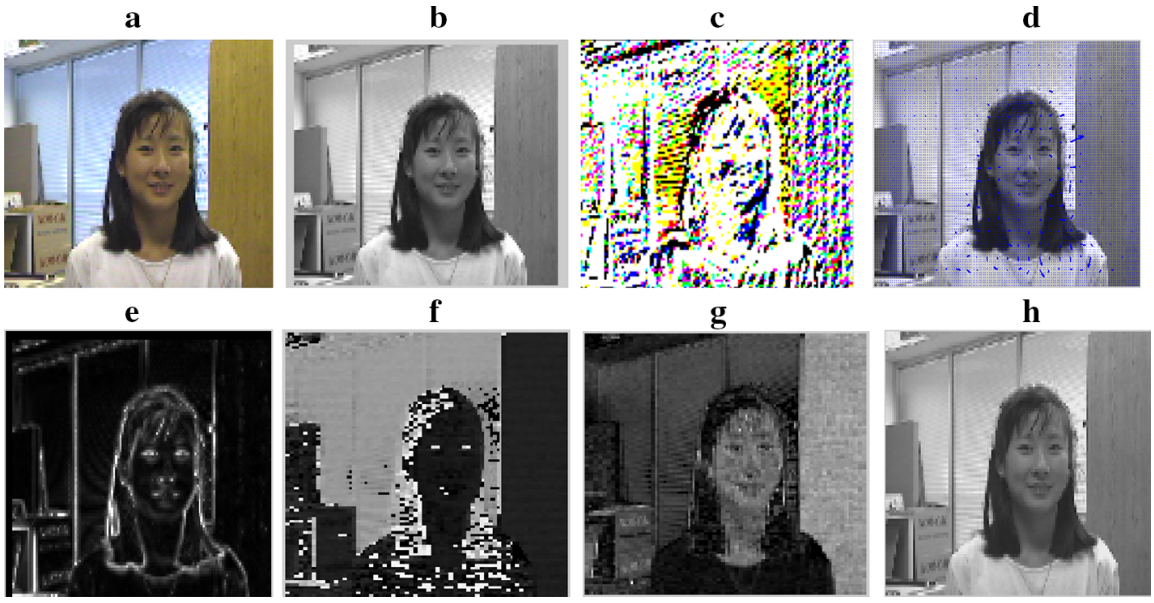


**Fig. 2** Features for multicue tracker from sample image for HTS dataset (HTS): **a** original image, **b** gray intensity, **c** gradient, **d** optical flow, **e** texture, **f** hue channel, **g** S channel, **h** Y channel

tracking are either single sensor such as vision, infrared, Kinect etc. or different combination of sensors such as vision, laser, radar, microphone, infrared, Microsoft Kinect, and RFID.

In general, cues used for object tracking are color, motion, orientation, spatial energy, shape, texture, infrared, and position, depth, disparity etc.. The different extracted cues from image taken from HTS dataset (HTS) are shown in Fig. 2. In tracking framework, cues are further processed using either deterministic or stochastic methods for estimation of object location. The deterministic methods were focused on minimization of cost function representing relationship between estimated object and ground truth object and hence reduced the search space. On the other hand, in stochastic methods, stochastic factors were added during object search operation. In addition, methods for handling target occlusion and clutters were included. In general, target model may be updated with new estimated parameters in order to cater for variation in target shape during tracking process.

In our review work, we have classified multicue object tracking work based upon data acquisition sources. One group of researchers considered moving or stationary sensor for data acquisition and tracking was performed by extracting different cues from single sensor. Another group of researchers used multiple sensors for data acquisition and tracking was performed by extracting one or more cues from different modularity. The classification of multicue object tracking work is illustrated in Fig. 3.

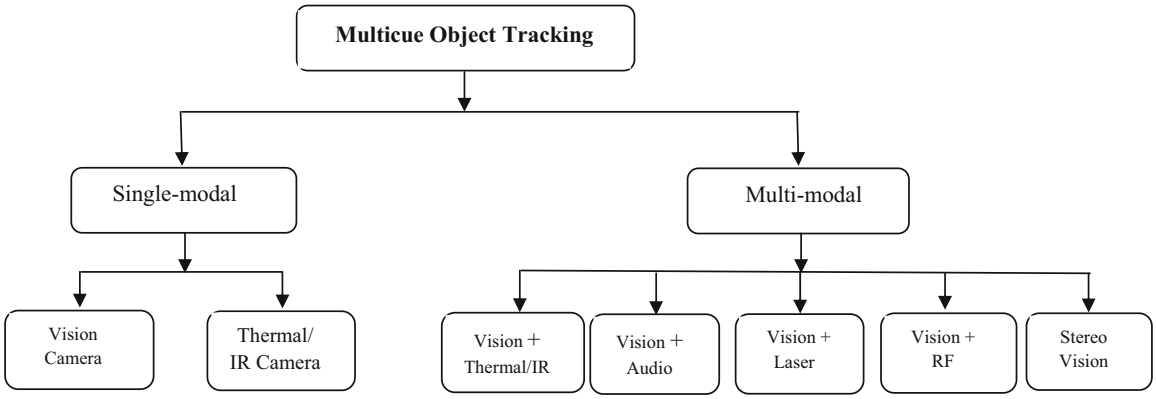


**Fig. 3** Classification of multicue object tracking techniques

Being rich source of information, vision or thermal camera were exploited for extracting multiple complementary cues for video tracking. On the other hand, RFID, radar, laser, audio sensors provide limited information for vision tracking. However, mostly, this information aids vision camera for robust object tracking. The stereo vision camera provides disparity information that was exploited for visual target tracking using multicues. Taking mode of data acquisition and operation performed as reference, we have classified multi cue object tracking work and examined these methods.

## 2.1 Single-modal multicue object tracking

The vision and thermal camera has abundant information contents which were exploited for deducing number of complementary cues. In this section, we have reviewed tracking methods based upon different multiple features extracted from single sensory. The section is concluded with discussion on reviewed techniques. The different cues such as shape, texture, color, intensity, motion, position and orientation, etc. were extracted from single sensor and fused for final state estimation. The representative works under multicue tracking using single sensory are reviewed in turn.

### *2.1.1 Vision camera*

In last decade, vision camera based multicue object tracking techniques were explored to a great extent. The cues extracted from vision camera were prone to degradation with changes in environment scenarios. However, orthogonal multiple cues were exploited for robust and reliable object tracking. In this review, we have categorized multicue object tracking work using single vision camera into techniques based upon operation performed on captured video sequences. The details of categorized work are discussed in turn.

Firstly, in general, deterministic methods mainly aimed at minimization of cost function representing relationship between centroid of tracked object and that of ground truth. The representation works for multicue tracking under deterministic methods using single sensory are detailed in turn. Multicue object tracking work gain momentum with the introduction of head tracking algorithm (Birchfield 1998). The authors used color cue extracted from head interior and intensity cue extracted from head perimeter for tracking head motion. The local search decided based upon score of two cues was used for locating person head in subsequent frames. The proposed algorithm claimed to be robust to head rotation, tilting, movement of camera and partial occlusion. However, under this work cues score were not fused in adaptive manner for catering complex motion under variable environment. Democratic integration of

five cues extracted from vision sensor was presented (Triesch and Malsburg 2001). Under democratic integration, adaptive mechanism boosts good cues and at the same time suppresses discordant cues. The motion, color, shape, position, contrast cues were used for locating object in subsequent frames. For each cue, saliency map was created by comparing each feature in current frame with reference frame. The reliability of each cue was estimated based upon its performance over previous frames. The saliency map of each cue was weighted with reliability factor for estimating overall saliency map and hence prediction of target position. However, two limitations of democratic integration: (a) incapability to multi hypothesis tracking, (b) false positive tracking was discussed (Spengler and Schiele 2003). In order to solve these problems, authors proposed a framework for robust object tracking using self-adaptions of cues and self-organization of integration method. The final estimated probability distribution of state was feedback to individual cues as well as integration unit for their adaptions. New quality measure along with occlusion handler for adaptive multicue integration using mean shift algorithm was proposed (Hong et al. 2009). Under this work, color cue along with orthogonal motion cue was extracted for handling low saturation object under full occlusion. In order to track objects which were lost in previous frames using mean shift algorithm, authors presented occlusion handler where size of search window changed if full occlusion was detected. Cue reliability in current frame was determined based upon its performance in previous frame and overall probability map was estimated as weighted sum of individual maps. The results were presented on thirteen sets of video sequence with different level of difficulties and revealed that proposed method can handle occlusion, clutter and low saturation video sequences. The edges along with color cues were exploited in centroid shifting framework for robust object tracking (Hong et al. 2015). The non-uniform quantization of color cue was performed for obtaining better image quality. The edges profile for object region was extracted using canny operator and motion based frame difference. The shift in edge color co-occurrence centroid was estimated without any iteration. The scaling of object was catered using edge-edge distance histogram which exploited smoothness of edges distance in consecutive frames. The proposed algorithm was tested on limited data set. The author claimed proposed algorithm to be robust to partial occlusion. As edge and color cues were both illumination dependent, performance of tracking under object rotation and illumination changes needs to be investigated. In sum, in most of deterministic methods, current state estimation depends upon estimated parameters from previous state which limit their ability to track occluded or lost targets.

Secondly, in another line of research, in recent past, multicue tracking is performed by introducing some stochastic factor during state prediction. The stochastic methods such as Kalman filter, Particle filter and its variants were preferred over contemporary methods due to their potential advantages such as fusion of multiple features, handling different level of uncertainty, and easy up-gradation for multiple object tracking. In order to reach global optimum location of targeted object, a stochastic factor was intentionally inserted during object search operation. In general, these techniques were covered under umbrella of Monte Carlo simulation where state PDF was represented by set of samples. The representation works for multicue tracking under stochastic methods using single sensory are detailed in turn. In order to compensate for variation in texture of object during tracking, texture cue and color cue in particle filter and Gaussian sum particle filter framework were combined (Brasnett et al. 2005). The color histogram was extracted from RGB color model and texture feature was recovered using discrete wavelet transform. The individual cue likelihood score in each frame was estimated by comparing current features with reference features using Bhattacharyya distance measure. The overall likelihood in the frame was determined as product of individual likelihoods. Inability of color histogram to provide spatial informa-

tion, spatial-color mixture of Gaussian for object color and proposed spatial histogram for object shape was introduced (Wang and David 2006). In this work, shape was represented by spatial distribution of edges, edge points and gradient intensity along edges. In particle filter framework, individual similarity measures for color and shape were estimated and used for finding overall likelihood as product of individual likelihood. However, proposed techniques (Brasnett et al. 2005; Wang and David 2006) were not using any adaptive fusion mechanism, tested on limited data set under control environment with no consideration of resources utilization. In order to efficiently allocate resources among multiple cues, particle filter and cue processor frameworks for 3D object tracking in video sequences was proposed (Loy et al. 2002). The authors used depth, skin color and radial symmetry cues for head tracking using particle filter framework. In multi hypothesis tracking, generated particles from particle filter were handed over to cue processor which determined cues likelihood and assigned resources to cues based upon their performance. The individual likelihood score for active cues were fused as product of their likelihoods for final state estimation. For sample impoverishment and degeneracy solution in particle filter framework, particle filter based upon particle swarm optimization for robust object tracking was proposed (Zheng and Meng 2008). The color and Haar histograms of reference object were compared with propagated particles histograms using Bhattacharya coefficient. The individual likelihood scores were combined using linear combination of individual likelihood score for final state estimation. However, no adaptive fusion of cues was considered in proposed work. Color and foreground cue for multiple objects tracking in particle filter framework was considered (Kumar et al. 2007). Likelihood of each particle was determined through likelihoods product for color cue and foreground cue. This work was extended for tracking multiple objects in video sequences captured through moving camera (Kumar et al. 2008). Further, for non-overlapping cameras, facial and color information was exploited for person detection (Kumar and Dogancay 2011). In an attempt towards adaptive fusion at likelihood level, color cue along with shape cue in modified particle filter framework was considered for tracking objects (Shen et al. 2003). The inability of color cue to provide shape information of tracked object was compensated by iincorporating shape cue in their algorithm. The cues were adaptively integrated before posterior state estimation by estimating L2 norm between the centroid of final state estimation and that of individual cue state estimation. Also, to cater time varying objects, authors introduced target updation model based upon average likelihood of particles. However, the results were tested on single video sequence and no quantitative performance metrics were evaluated. For efficient movement of particles during interferences, Camshift algorithm in particle filter framework was embedded (Yin et al. 2011). The color and motion probability distribution maps were extracted and combined map was estimated. The adaptive integration of cues was performed by proposed combined likelihood estimation where cues weights were in concurrence with their average similarity coefficient. Due to Brownian motion and Camshift iteration of particles, authors claimed that effectiveness of particles increased and hence small numbers of particles were required for tracking object under illumination changes and background clutters. However, reliability of cues was estimated based upon previous measurements rather than only current measurements. Difficulties in integrating motion cue with color cue for hand tracking was discussed and a multi stage framework for tracking complex motion of hand was proposed (Zhang et al. 2015). The feature points were (1) generated through color cue, (2) selected through representation, compact and diverse criteria, (3) tracked using motion cue. The integration of cues was performed in feature point selection process and tested for hand video sequences. As extension of previous work (Brasnett et al. 2005), estimation of reliability of each cue based upon current measurement rather than earlier approach of estimation of cue reliability from previous observations was discussed

(Brasnett et al. 2007). The authors combined color, texture and edge cues in particle filter framework. The overall likelihood score was determined as product of individual cue likelihoods which were separately weighted by reliability factor. Also, solution for automatic tuning of noise parameter for cues was presented. However, contribution of all particles was not considered for deciding entire cue reliability score. Inability of color cue to provide spatial information of object was compensated by orientation cue (Maggio et al. 2007). The orientation histogram representing shape and edges of object catered for illumination and clutters variations. In particle filter framework, cues were adaptively weighted by measuring spatial uncertainty based upon weighted covariance matrix. More uncertainty leads to less reliability of cues and hence less contribution in overall likelihood estimation. The more features can be added to proposed model for better robustness in tracking. A new multi feature re-sampling algorithm was introduced where number of particles for each cues were re-sampled based upon performance of cue. In order to cater for texture variation during tracking, adaptive combination of three complementary cues i.e. color, local binary pattern and histogram of oriented gradient extracted from vision camera was proposed (Dou and Li 2014). The histogram of oriented gradient along with color cue can faithfully estimate shape of object. In addition, local binary pattern recover texture features of object and cater for rotational error. In particle filter framework, individual cue likelihood scores were estimated using Bhattacharya distance. In each frame, the adaptive cue weights were estimated through measurement of Euclidean distance between estimated target position using individual cue and estimated target position using all cues. Further, overall likelihood score was determined as weighted linear combination of individual cue likelihood scores. Multi-graph based ranking method for fusing HOG,intensity and LBP features in particle filter framework were introduced (Yang et al. 2015). The candidate objects having highest ranking score was labeled as tracked object for current frame. Robustness of solution was introduced through consideration of temporal consistency in video sequences. Evolutionary particle filter framework for adaptively combining color cue with texture cue was considered (Zhang et al. 2013b). The HSV color model was used for creation of color histogram and local binary pattern was used for extraction of texture histogram. The cues were fused adaptively using two fusion methodology being decided based on re-sampling requirement in particle filter. In order to improve accuracy, adaptive genetic algorithm was used for performing re-sampling and hence to overcome particle degeneracy. However, proposed algorithm was tested on three self-generated video sequences. Due to its ability to distinguish moving object from background clutters, object motion energy along with other cues was explored extensively for object tracking. A combination of color and spatial temporal motion energy for human tracking using particle filter framework was presented (Zhou et al. 2014). The spatial temporal motion energy was a three dimensional feature extracted from orientated selective band pass filter and edge detector. It can effectively handle clutter, and variation in illumination and shape. The cues adaptive contribution was determined through measurement of Euclidean distance between centroid estimated using cues and that of final estimation. The reliability score of cue was estimated by hyperbolic tangent function of mean Euclidean distances over set of measurements. The cues were adaptively combined using estimated reliability scores. The applicability of proposed work for far away multiple objects need to be explored. For multiple people tracking, independent tracker for each of object in cluttered scene was discussed (Sun and Bentabet 2010). The problem was modeled in DSmT framework where hyper power set with elements as individual tracker, ignorance and conflict were predefined. The location and color cue provided confidence for each of elements of hyper power set and any conflict among cues due to clutter or occlusion was resolved using DSmT fusion. The individual masses were combined using combination rule and final belief about each particle

was determined. However, proposed method can only be applicable for resolving conflict among multiple targets not for single object tracking. Considering independent appearance and motion cues, multi hypothesis method for multiple objects tracking under closed vicinity was proposed (Ying et al. 2014). The overall likelihood was determined as weighted sum of dynamic and appearance confidences where optical flow confidence was deciding factor under constrained conditions. The authors also implemented dynamic updation of model and repulsion inertia model for avoiding local minimum traps. However, automatic adjustment of tracking parameters needs further investigations for scenarios where no data is available a prior.

Instead of adaptive fusion under single tracking model, switching among three interactive models for object tracking in video sequences was proposed (Dou and Jianxun 2014). In particle filter framework, authors considered three object models as: histogram of orientated gradient (HOG), completed local ternary patterns (CLTP), corrected background weighted histogram (CBWH). The switching between models was decided based upon model transition probability and model likelihood estimated in each frame. The results on three datasets revealed that proposed interactive multiple model particle filter (IMM_PF) was robust to clutter, rotation and partial occlusion.

Instead of fusing multiple cues, fusion of multiple likelihoods in multi feature PSO tracking algorithm was proposed (Ahmed et al. 2014). The authors performed study on different similarity measures and reported that Bhattacharya coefficient measure was rotation and scale invariant. On the contrary, similarity index measure (SIM) provided spatial information and easily computed. The likelihood measures were extracted sequentially and overall likelihood score was estimated as linear combination of individual scores. The authors claimed that proposed scheme was invariant to scaling, rotation and zooming. However, only single grey level cue was used for feature extraction.

In contrast to earlier approaches, feature level fusion for human detection and tracking was proposed (Liu et al. 2015). First, point ensemble image (PEI) was extracted from captured RGB-D data. In order to reduce search space, initial elimination of non-human candidates was performed using support vector machine trained using two features as histogram of height difference (HOHD) and joint height and color histogram (JHCH). After detecting plausible candidates, 3D JHCH was extracted and tracking was performed using Kalman filter where new similarity measure was used for associating each target with respective track. However, performance of proposed approach for non-human and maneuverings human needs further studies. Three cues i.e. gradient, color and local binary pattern for building robust appearance model was considered (Zeng et al. 2013). The authors claimed that using three independent cues lead to more discriminative appearance model which was used for updating classifier and hence estimation of object state. The multi feature joint descriptor (MFJD) based upon color and HOG was proposed as representation of object (Li et al. 2014c). The feature weights were adjusted using contrast and stability scores. The object tracking was performed using mean shift framework and author claimed that proposed joint feature could handle scale change and deformation of object.

Instead of using multiple cues in single Bayesian filer, multiple Bayesian filters tracking framework was introduced (Francesc et al. 2008). For each cue, separate Bayesian filter was used and integration among different filters was performed at hypothesis correction stage. The authors assumed dependence among estimation from different filters. The experiments were performed with proposed four cues tracker i.e. bounding box, fisher color map, color distribution and contour. The final object state at contour estimation was determined assuming its dependencies with previous filters outputs. However, as reported in Leichter et al.

(2014), dependencies of cues assumed (Francesc et al. 2008, 2005) were in fact independent measurement.

In sum, vision camera being extensively used for multicue object tracking due to their ability to provide rich source of information about targeted object. In this section, we have classified multicue tracking methods using vision camera into deterministic and stochastic methods. In addition to this, in order to explore other related domains, methods considering multiple models, multiple likelihood or cue with multiple features were reviewed. The multicue tracking methods using single vision camera are also tabulated in Table 1.

### *2.1.2 Thermal/IR camera*

With the advancement in thermal/infrared camera technologies, thermal/infrared cameras were considered to be a good alternative for night vision applications. The passive infrared and thermal cameras were insensitive to illumination changes, disguise and pose variation of targeted objects. In this section, we review multicue tracking methods using different multiple features extracted from thermal/infrared cameras (see Table 2). Pedestrian detection along with tracking in infrared video sequences was presented (Congxia et al. 2007). The pedestrian detection was performed at two stages: (a) shape cue discriminate pedestrian from non-pedestrian, (b) appearance cue aids in positioning of pedestrian in frame. The shot consisting of sequences of frames were segmented and within shot tracking was performed using graph matching approach. The shape and position cues were used for establishing associations among detected pedestrians. The weighted contributions of these cues were used in graph matching algorithm for final track establishment. The results were presented on OSU and WVU databases. The authors claimed that proposed framework can perform better under occlusion without prior knowledge of motion trajectory; however, tracking pedestrians missed during detection stage needed further investigation. In infrared video, inability of intensity cue to provide shape information was compensated by fusing edge information (Wang et al. 2012). The particle filter framework was used for tracking pedestrian in infrared video sequences. The cue discriminant ability measured based on position and size difference between reference and target model was introduced. At particle level, overall likelihood score was estimated as product of weighted likelihood score from both cues. Where weights were decided from new measure of discriminant ability named as relative discriminative coefficient. The results were presented on OTCBVS dataset. In similar line, joint grey and local binary pattern histogram was proposed for representation of object (Li et al. 2014b). The extracted joint feature was used in mean shift framework for efficiently object tracking in IR video sequences. The experiment results were presented on OTCBVS and VIVID database for tracking dim small objects. The use of evolutionary technique for optimum fusion of multiple cues was explored (Zhang et al. 2013a). The authors used intensity and gradient cues for tracking objects in infrared videos. In particle filter framework, particle swarm optimization was used not only for overcoming particle degeneracy but also for combining particle weights during particle updation stage. The performance was evaluated on limited OTCBVS and own infrared datasets.

Although, thermal camera found to be good alternative for night vision application, multicue tracking using only infrared sensor was limited to targets with thermal radiation profile. In addition, it was difficult to distinguish target having similar thermal profile under multicue tracking using single thermal/IR sensor. Hence, multicue tracking using infrared/thermal sensors needs to be augmented in Multi-modal framework where other modularity aids thermal/IR cues for building robust tracking platform.

**Table 1** Recent advances on singlemodal multicue object tracking

| Reference | Algorithm | Tracking cues | Integration of cues | Database | Description |
|---|---|---|---|---|---|
| *(A) Vision camera* | | | | | |
| Birchfield (1998) | Local search | Intensity gradient and color | Adding up percentage of gradient and color score | HTS | Robust to complex head motion, tilting and rotation |
| Triesch and Malsburg (2001) | Saliency map | Motion, color, shape, contrast, position | Weighted saliency map | Self-generated | Assume statistical dependencies of cues |
| Shen et al. (2003) | Modified particle filter | Color and shape | Adaptive integration where cue reliability by L2 norm | HTS | No quantitative analysis and tested on limited video |
| Brasnett et al. (2005) | PF, Gaussian sum PF | Color and texture | Product of individual likelihood but not adaptive | Synthetic and natural seq. | Robust and improved accuracy |
| Brasnett et al. (2007) | Particle filter | Color, texture and edge | Product of individual weighted likelihood | Six natural video seq. | Adaptive fusion with automatic tuning of parameter |
| Loy et al. (2002) | Particle filter | Depth, skin color and radial symmetry | Product of active cue likelihood | Self-generated | Adaptive allocation of resources for multi rate cues |
| Zheng and Meng (2008) | Particle filter | Color and local statistic feature | Linear combination of two likelihood | Self-generated | PSO overcome particle impoverishment |
| Yin et al. (2011) | Camshift and Particle filter | Color and motion | Adaptive based upon previous frame results | CAVIAR, PETS | CamShift aided particle filter for propagating particles |
| Hong et al. (2009) | Mean shift | Color and motion | Weighted combined probability map | Self-generated 13 video seq. | Quality measure based upon previous frame performance |
| Hong et al. (2015) | Modified Centroid shift | Color and edges | Centroid shift estimated from edge-color co-occurrence | CAVIAR, Supermarket | Proposed solution for scaling but no adaptive fusion |
| Zhang et al. (2013b) | Particle filter | Color, texture | Re-sampling adaptively decide fusion methods | Self-generated | Adaptive GA for re-sampling and multicue fusion |
| Maggio et al. (2007) | Particle filter | Color and orientation | Cue reliability used in linear combination of likelihood. | HTS,CAVIAR, PETS-2001 | Eliminate manual selection of feature |
| Dou and Li (2014) | Particle filter | Color, HOG and LBP | Euclidean distance measure for combining individual cue | HTS | Cater for illumination changes, camera motion and clutter |

**Table 1** continued

| Reference | Algorithm | Tracking cues | Integration of cues | Database | Description |
|---|---|---|---|---|---|
| Yang et al. (2015) | Particle filter | Intensity, LBP, HOG | Multi-graph ranking method | 6 online video sequences | Could run at 2–3 frames per second |
| Zhou et al. (2014) | Particle filter | Color, spatial temporal motion energy | Hyperbolic tangent function of Euclidean distances | HTS and in house data set | Cater for pose/illumination variation and occlusion |
| Dou and Jianxun (2014) | IMM particle filter | CLTP, HOG, CBWH | Model likelihood or model transition probability | PETS,HTS, CAVIAR | Robust to rotation, partial occlusion and clutter |
| Sun and Bentabet (2010) | Particle filter | Color and location | Combination rules for finding maximum belief | Self-generated single video | DSmT for resolving conflict among multiple targets |
| Liu et al. (2015) | Kalman filter | Height and color | JHCH, similarity function with location and color. | Office, mobile clothing store | PEI representation for better human detection and tracking |
| Ying et al. (2014) | Kalman filter | LBP, Optical flow and dynamics | Weighted sum of appearance and dynamic confidence | TRECVID and PETS | Handle close vicinity problems of multiple person tracking |
| Francesc et al. (2008) | Kalman and Particle filter | Color, contour, fisher space, bounding box | Product with hypothesis correction from previous stage | Self-generated | Assumed dependencies among cues at measurement level |
| Kumar et al. (2007) | Particle filter | Color, foreground cues | Product of color and foreground likelihood | CAVIAR | Demonstrated tracker for tracking multiple objects |
| Li et al. (2014c) | Mean shift | Color and HOG | Joint histogram generated at object representation level | Freeman and PETS2009 | Feature weights adaptive based upon contrast and stability |
| *(B) Thermal/IR camera* | | | | | |
| Congxia et al. (2007) | Graph matching | Shape and appearance and location | Shape and location cues are adaptively fused in tracking | OSU and WVU infrared | Pedestrian detection rate may affect accuracy |
| Wang et al. (2012) | Particle filter | Intensity and edges | Adaptive fusion at particle level using product of weighted likelihood | OTCBVS three thermal video seq. | Proposed new measure for cue discriminant ability |
| Zhang et al. (2013a) | PSO-particle filter | Intensity and gradient | PSO based optimum data fusion from cues | OTCBVS and self-generated | Demonstrated on infrared videos on limited set |
| Li et al. (2014b) | Mean shift | Gray and local binary pattern | Cues were fused at object model level as joint histogram | OTCBVS and VIVID | Efficiently track small dim object in IR sequences |

**Table 2** Recent advances on multi-modal multicue object tracking

| Reference | Algorithm | Tracking cues | Integration of cues | Database | Description |
|---|---|---|---|---|---|
| *(A) Vision + thermal/IR* | | | | | |
| Conaire et al. (2008) | Mean shift | YUV, thermal, edge orientation | Product of individual tracker likelihood score | OTCBVS, PETS, self | No adaptive fusion of cues |
| Treptow et al. 2005 | Particle filter | Color, thermal | Handover from thermal to vision sensor | Self-generated | Could detect and track human far away from robot |
| Erdem et al. (2012) | Particle filter | Color, motion and Infrared brightness | Weighted product of individual cue likelihood | OSU,BEHAVE, CAVIAR | Two stage integration of cues, adaptive for particle assign |
| Airouche et al. (2012) | Particle filter | Color, location and thermal | DSmH hybrid rules | Self-generated single video | Solve clutter and occlusion |
| Wang et al. (2014) | Part based matching | Optical flow, color and depth | Linear combination of depth, color and pixel count | Self-generated using Kinect | Illumination invariant |
| Susperregi et al. (2013) | Particle filter | Leg, vest and thermal detection | Weighted sum of three individual likelihoods | Self-generated video | Independent detections were combined in particle filter |
| Han et al. (2012) | ID matching | Depth and color | Linear combination of individual similarity score | Self-generated | Tested on indoor environment, cues given equal importance |
| Xu et al. (2014) | Level set evolution | Depth and color | Local adaptive weighted map at super pixel level | Self-generated | Demonstrated for active contour tracking in outdoor |
| Motai et al. (2012) | Kalman filter and optical flow | Infrared, optical flow, laser | Arbitration between two modularity | Self- generated from robot | Infrared for object detection and laser for obstacle detection |
| Stolkin et al. (2012) | Mean shift | Infrared and color | Adaptive fusion at pixel level | Self-generated | Cue importance was estimated from background relearning |
| Talha and Stolkin (2014) | Particle filter | Color and infrared | Adaptive fusion of cues at particle levels | Self-generated | background relearning decide modularity weight |

**Table 2** continued

| Reference | Algorithm | Tracking cues | Integration of cues | Database | Description |
|---|---|---|---|---|---|
| *(B) Vision + audio* | | | | | |
| Chen and Rui (2004) | Particle filter | Contour, sound source location, color | Product of individual likelihoods | Self-generated two video | Sensors data used for proposal estimation and verification |
| Strobel et al. (2001) | Decentralized Kalman filter | Audio and vision sensors | Decentralized Kalman filter but not adaptive | Nil | Fusion was applicable for independent measurements |
| Perez et al. (2004) | Particle filter | Color, motion and sound | Partitioned sampling with two stage integration | Self-generated | Main color cue was aided by either motion or sound cue |
| Hu et al. (2002) | Kalman filter | Color and audio | LMS method | Self-generated | Automatic calibration of audio and video sensors |
| Megherbi et al. (2005) | Kalman filter | Color, position and audio parameters | Dempster's rule, and pignistic probability | Self-generated | Multiple person tracking with focus on data association |
| Nickel et al. (2005) | Particle filter | Face, upper body and TDOA of audio | Weighted sum of individual likelihood | Self-generated video | Solution for Audio + Visual log creation of lecturer |
| Kılıç et al. (2015) | Particle filter | Color and TDOA from audio sensor array | Two stage particle weight estimation with two cues | AV 16.3 | Calibration and active speaker presence assumed |
| *(C) Vision + laser* | | | | | |
| Chakravarty and Jarvis (2006) | Particle filter | Color and laser data | Measurement from two sensor used for detection | Self-generated | Depth info. handle occlusion, can track multiple person |
| Spinello et al. (2009) | Extended Kalman Filter | Color and laser data | Kalman filter fuse independent measurements | Self-generated | Brownian and linear motion model for tracking |
| Cui et al. (2008) | Mean shift and Kalman filter | Laser data and color | Bayesian fusion at tracker level | Self-generated | Two stage framework, detection and tracking |
| Song et al. (2013) | Particle filter | Laser data, Intensity and Edge orientation | Laser for tracking and visual for online learning | Self-generated | Online learning aided during correlated target and merger |

**Table 2** continued

| Reference | Algorithm | Tracking cues | Integration of cues | Database | Description |
|---|---|---|---|---|---|
| Scheutz et al. (2004) | Local search | Distance and color | Leg tracker and face tracker perform independently | Self-generated single video | Failure during leg occlusion handled by vision tracker |
| Song et al. (2008) | PD-PF | Distance and HSV color | Product of individual likelihood map | Self-generated single video | Better estimation of MAP than multiple and joint particle filter |
| *(D) Vision + RF* | | | | | |
| Kim and Moongu (2014) | Kalman Filter | Radar and vision | Kalman filter along with MIPDA | Self-generated single video | Low computational for real time implementation |
| Germa et al. (2010) | Icondensation | RFID, skin and face | Product for individual measurements | Self-generated single video | Perception systems for online detection and avoidance ability |
| *(E) Stereo vision* | | | | | |
| Nickel and Stiefelhagen (2008) | Condensation | Motion, color, detector, stereo correlation | Weighted likelihood by cue quality measure | Self-generated | Combine layered sampling with democratic integration |
| Munoz-salinas et al. (2008) | Particle filter | Depth, color and gradient | Product of individual distribution | Self-generated video seq. | Joint probalistic distribution for color and depth |
| Gavrila and Munder (2007) | Hungarian Matrix | Stereo, shape, texture | Weighted comb.: Euclidian and chamfer distance | Self-generated via Protector | Proposed automatic tuning of parameter using ROC |
| Zoidi et al. (2014) | Kalman filter | Texture, color, disparity | Maximum average similarity for texture | Self-generated nine videos | 3D object tracking in a stereo video |

### 2.2 Discussion

In last decade, multicue object tracking using single-modal was extensively explored with the aim to develop robust and reliable tracking solution. The vision research under single-modal multicue target tracking was mainly focused towards development of new techniques for extracting robust features and also towards adaptive fusion of multicues. In general, deterministic methods were more accurate in state estimation than stochastic methods. However, deterministic methods performance degraded for lost target or heavily occluded target. On the other hand, stochastic methods can effectively fuse multiple features, and easily up-gradate for multiple objects tracking. Although, particle filter established its niche in estimation of non-Gaussian, non-linear state, it suffers from sample degeneracy and impoverishment problems for which solutions were proposed (Li et al. 2014a; Walia and Kapoor 2014b, c). However, most of reviewed papers using particle filter did not discuss problem of sample impoverishment. Only, orthogonal cues need to be fused so that they can complement each other during tracking process. The color cue being computational efficient could not provide shape information of target. For incorporating shape information in color model, spatial histogram was proposed (Wang and David 2006). The feature level fusion, histogram of height difference (HOHD) and joint height and color histogram (JHCH) were also introduced for augmentation of color cue (Liu et al. 2015). Color cue was also fused with spatial temporal motion energy for object tracking (Zhou et al. 2014). Similarly in IR sequences, inability of grey cue to provide shape information was compensated by extracting joint gray and local binary pattern histogram (Li et al. 2014b). The cue orthogonality was also established by dynamically selecting same feature from different region of object (Nickel and Stiefelhagen 2008). Hence, it needs to further investigate newly developed cues and establish their complementary nature for development of robust tracking solution. The integration of multicue was also considered imperative for adaptive multicue tracking system development. The democratic integration (Triesch and Malsburg 2001) can efficiently boost good cues and suppress non performing cues but suffer from false positives tracking. In order to estimate cues contribution for overall likelihood for state estimation, cues reliabilities were evaluated considering either previous observations or current observation (Brasnett et al. 2007). For real time implementation of multicue framework, cues resource allocation was decided based on their reliability (Loy et al. 2002). In addition, switching between different models based upon cues reliability was presented (Dou and Jianxun 2014). Hence, estimation of cue reliability and adaptive fusion of cues is another line of research that needs further research work. The infrared/thermal cameras are useful for tracking object for night vision applications. But single intensity cues needs to be compensated with other features extracted from captured sequences. In addition, thermal sensors are unable to distinguish objects with similar thermal profile. For low vision application, vision camera may be compensated with other modularity for robust tracking.

## 3 Multi-modal multicue object tracking

The multi-modal multicue tracking solutions are based upon two or more modularities from which different complementary cues were extracted. In general, vision camera was aided by other sensors such as laser, audio, radar, RFID, sonar etc. for catering different challenges of visual world. In this section we reviewed different multi-modal multicue object tracking methods in turn. The details of different reported work are also summarized (see Table 2). This section is concluded with discussion on reviewed techniques.

### 3.1 Vision + thermal/IR sensor

The thermal/IR sensor along with vision sensor is required for 24 × 7 targets tracking for night vision applications where vision sensor alone fails. The passive IR/thermal sensor can recover objects information during night or bad weather conditions but unable to distinguish objects with similar thermal profiles. Hence, vision camera along with thermal/IR camera was exploited for robust 24 × 7 object tracking. For tracking human face using mobile robot, switching to vision camera after initial detection of human from thermal sequence was proposed (Treptow et al. 2005). In particle filter framework, efficient detection of human from thermal sequences aided vision camera for tracking human face. RGB sensor along with IR sensor for efficiently tracking moving objects was proposed (Kumar et al. 2014). Under this template based tracking using RGB sensor, false negative and false positive were overcome through track level fusion of IR sensor data with RGB data. In addition, solution for temporal and spatial alignment of IR and RGB data was proposed. For catering sudden turn during motion, arbitration between optical flow and Kalman filter model was proposed (Motai et al. 2012). In addition, initial target was efficiently detected from infrared camera and obstacles were overcome using laser sensors. Proposed algorithm was tested on data captured from mobile robot with three mode of target walking. However, proposed methods considered switching from thermal to vision camera rather than adaptive fusion. In order to develop solution with low computational requirement, tracker level fusion for multiple features extracted from vision and thermal camera was presented (Conaire et al. 2008). In this work, spectrograms were used instead of histogram for feature extraction incorporating spatial information of bins. The final likelihood score was determined through product of individual likelihood score. Mean shift framework for estimating new position of object and similarity measure from different spatiograms was claimed as novel contribution in this direction. The algorithm was tested on five dataset using different combination of five features i.e. YUV, edge orientation and thermal brightness. However, no automatic adaptive integration of features was incorporated and also tracker was evaluated with limited metrics. Pixel level fusion of color and infrared modularity was considered (Stolkin et al. 2012). In mean shift algorithm, importance of cues was adaptively adjusted through relearning of background information in each frame. The proposed framework could be extended for new modularity. In extension of earlier work (Talha and Stolkin 2012), particle level fusion of color and infrared modularity was proposed (Talha and Stolkin 2014). In particle filter framework, color and thermal information was adaptively fused through continuous relearning of background model for each particle. This method is useful for tracking object under heavy occlusion and rapidly varying background. Context-sensitive integration of cues at two stages in particle filter framework was considered (Erdem et al. 2012). In this work, color, motion and infrared brightness cues were extracted from calibrated video recorded using vision and CCD camera. In each frame, cues reliabilities were determined considering their performance in current estimation and also past performance. The reliability of cue was used not only for estimation of final likelihood but also for assigning particles to proposal functions. The algorithm was tested on three data set and authors claimed that their framework was open for new cues. In order to adapt to target shape and align images from thermal and vision camera, geometric fusion for image alignment and two stage background models for accurate tracking was proposed (Zhao and Sen-ching 2014). As extension of earlier work (Sun and Bentabet 2010), multiple objects tracking with online conflict resolving, due to occlusion and clutter, from color and thermal sensor was proposed (Airouche et al. 2012). The author used position cue as prior knowledge and color and thermal cues as independent measurement from properly aligned sensors. The thermal cue detected presence of pedestrian and aided by color feature

which distinguish among pedestrian. The cues were fused in DSmT hybrid model which was defined using hyper power set. The DSm hybrid rules were used for combining measurements from individual cues and conflicts were resolved among cues. However, the algorithm was tested on single video sequence and also computational requirement increased with increase in number of tracked object. The Microsoft Kinect camera was also extensively explored for extracting depth information from video (Han et al. 2013; Kinect Camera). In general, for video tracking consistency of depth information was assumed in consecutive frames. Two phase framework for robust object tracking which was invariant to illumination changes and occlusion was presented (Wang et al. 2014). In first phase, optical flow was estimated from two adjacent frames which gave the approximate position of object. Further, the position of object was estimated with more precision through patch based search approach using color and depth information. The object search was divided into four parts. The color histogram of four parts was compared with reference target template using Bhattacharyya distance. Similarly, variation in depth mean and variance between target region and individual parts was exploited for estimating smoothness of depth information in consecutive frames. The experiments were performed on four video sequences which were captured using Kinect source having inbuilt color camera, infrared projector and IR camera. Authors claimed that proposed algorithm was robust to illumination changes due to fusion of depth information. Human tracking framework for indoor home environment was proposed (Han et al. 2012). Under this, from RGB-D camera, human presence and identification was carried out using complementary depth and color cues extracted from RGB-D camera. The tracking was performed through matching of detected ID with previous assigned human ID using depth and color cues. The similarity score from two cues were fused as linear combination of individual score. However, no adaptive fusion was discussed and both cues were given equal importance for final state estimation. Framework for estimating importance of depth cues from adaptive weighted map was proposed (Xu et al. 2014). The depth was considered as prominent cues when object was far away from background object. On the other hand, when object is close to background object, color cue dominates over depth cue and contribute more towards final state estimation in tracking framework based upon level set method. In similar line, vision and depth cues from Kinect source for 3D object tracking using extended Kalman filter was considered (Gedik and Alatan 2013). Cues adaptive fusion was proposed through variation of measurement noise variance in accordance with quality measure of cue. Recently, a mobile robot tracking solution using RGB-D Kinect camera, laser and thermal sensor was proposed (Susperregi et al. 2013). In this work, person leg detection, Kinect vest detection and thermal detection likelihoods were combined in particle filter as weighted sum of individual likelihood. The results revealed that weighted combination of modularity's improved angle and location estimation of person wearing yellow vest. However, results were presented on indoor environment on limited set. In sum, thermal/IR camera aids vision camera for tracking applications. Still, data fusion and calibration of independent source of information remains challenge for vision community.

### 3.2 Vision + audio sensor

Multi-modal tracking using audio and vision sensors are considered effective means of tracking during distributed meeting, automatic scene analysis and effective presentation during lectures. During lectures, Multi-modal solutions using audio and vision sensors were used for automatic zooming of object for effective view of presenter (Polycom). The audio sensors based tracking solutions were focused on person localization and limited to speaking persons. The vision camera based solutions were limited to object in camera field of view. Hence, in recent years, researchers were motivated to fuse audio sensors with vision sensors for robust

object localization and tracking. The problem of fusing data from audio and video sensors was addressed (Strobel et al. 2001). The authors introduced decentralized Kalman filter for fusing data from different modularities. The audio sensors estimated posterior range and bearing information of target using extended Kalman filter. The Cartesian coordinates were extracted from video sensor and posterior estimation was performed using linear Kalman filter. The posterior estimates from independent sensors were given to fusion centre which determine global estimate of object. However, assumption of linear motion needs further investigation for manoeuvring objects. Using belief theory, a solution for data association between audio and vision sensor was discussed (Megherbi et al. 2005). The frame of discernment was assumed to be set of targets in the scene. For each target, three masses were determined from similarity measure in line with target association to target, not association to target or ignorance. Similarity measures were estimated using position and video or audio measurements separately. The masses were further combined using Dempster's rules and Pignistic probability was estimated for making final decision about the target. Calibration of audio and vision sensors was considered a prior and work was mainly focused on data association. In an attempt to automatically calibrate audio and vision sensors, multicue tracking system using two microphones and vision camera was proposed (Hu et al. 2002). In this work, object was localized using microphone array where fractional delay was determined for delay in arrival among microphone array. The direction of arrival estimated using vision camera was feedback to microphone array for necessary correction of phase distortion. The solution can automatically calibrate sensors without requirement of prior audio training samples. In order to increase localization accuracy, triangular array of three microphones along with vision camera was proposed for object tracking (Lim et al. 2007). The time delay in arrival of sound was used for estimation of sound likelihoods and standard deviation between microphones was changed dynamically. The overall likelihood was simple product of color and sound likelihood. Considering complexity of visual world and inherent property of particle filter to fuse different independent sources, framework where color cue acts as main cue and aided by intermittent motion cue or sound cue depending upon application scenario was presented (Perez et al. 2004). Under this, histograms were extracted for color and motion cues from video sequences. Also time difference of arrival (TDOA) of audio signals from pair of microphones placed on line orthogonal to optical centre was exploited for estimating bearing of object. The generalized cross correlation function used for estimating TDOA and likelihood was determined using multiple hypotheses. The independent likelihood were determined and used in partitioned sampling framework where motion or sound cues with mixture proposal distribution estimate the approximate search region. The estimated search region aided color cue for efficient estimation of state with minimum number of particles. Two stage frameworks for tracking object using audio, contour and color cues was proposed (Chen and Rui 2004). In proposed particle filter based framework, each sensor consisted of tracker and verifier where tracker estimated proposal for fuser and verifier determined likelihood score for individual sensor. The contour tracker exploited contour smoothness and based upon unscented Kalman filter (UKF). The color tracker assumed stability of object color in interior region and used mean shift algorithm for proposal estimation. Similarly, audio tracker exploited delay in arrival at two microphones for estimating proposal. These proposals were given to the fusers which generated combined proposal distribution considering tracker reliability and sent sampled particles to verifier. The three verifiers estimated likelihood for each cue and determined final likelihood score which was given to fuser for final state estimation. The approach was adaptive with feedback mechanism from fuser output to tracker input. Similarly, multiple audio and vision sensors under reverberant environment was used (Talantzis et al. 2008). The authors proposed independent tracker for audio and

vision sensors and fused information for building robust solution. The vision sensor aided audio tracker for tracking person who stopped talking during tracking process. However, results were presented on limited set of data and performance for outdoor environment needs to be investigated for real time application. In order to create efficient log of lecture presentation, a solution using multiple video cameras along with multiple microphone for locating presenter during his/her presentation was proposed (Nickel et al. 2005). In this work, 3D projection of image from multi view was performed using particle filter instead of tribulation. The visual information was extracted using foreground segmentation and detectors for face, upper body. Similarly, from pair of microphones, TDOA was exploited for estimating audio observation likelihood. In particle filter, final likelihood was weighted sum of likelihoods where weights were adjusted in accordance to audio cue performance. However, multiple persons tracking along with adaptive selection of parameters were not addressed. In order to track multiple persons in indoor environments, audio sensors measurements at two stages in particle filter i.e. propagation and observation was considered (Kılıç et al. 2015). In addition, number of particles and noise variance were made adaptive depending upon tracker performance. The authors demonstrated that combining vision data with circular array of audio sensors measurements enhanced tracking performance over vision sensor based tracking for occluded active speaker. However, calibration of audio sensors and presence of active speaker was assumed for tracker proposed. In sum, audio sensors aided vision sensor for developing robust tracking solution, but most of studies were limited to coherent audio sources. Effect of coherent and non-coherent audio sources on image feature response was investigated and studies revealed that non-coherent sources degraded image features response (Chen et al. 2014). Hence, considering real world tracking scenarios, performance of tracking algorithms needs to be evaluated for both coherent and non-coherent audio sources.

### 3.3 Vision + laser sensor

The high scanning rate laser scanners along with vision camera are used for target detection and tracking for video surveillance applications. The laser scanner has potential advantages such as low computational requirement, easy projection of laser data to rectangular coordinate system and insensitive to environment changes. But, it could not distinguish objects during merger/split, correlated objects or object with lost track under heavy cluttered environment (Cui et al. 2008; Song et al. 2013). On the other hand, vision data was complex, illumination dependent but rich in information and easily distinguished objects. Hence, in last decade, reliable and robust solutions was proposed for tracking people using laser and vision sensors. For tracking indoor people, multi-modal framework where independent laser and vision tracker perform tracking under constrained environment was proposed (Scheutz et al. 2004). In this work, person face tracking was performed on vision data using face detection module which confirmed presence of face using eye detection, horizontal projection and height to width ratio. The leg tracking was performed considering gap between two legs and if not detected properly information was passed to vision sensor for further processing. The mutual sharing of information between two trackers overcame failure of laser tracker under occlusion. Using stationary robot, fusion of data from panoramic vision camera and laser sensor for multiple people tracking was discussed (Chakravarty and Jarvis 2006). In this work, Laser sensors were focused on upper part of body rather than legs. If person was detected by vision and laser sensor, particle filter based tracker was initialized for detected person. However, results were presented on limited dataset. For robust tracking of people in outdoor environment, multiple laser scanners for fast detection of people along with single vision camera was considered (Cui et al. 2008). In this work, once people were detected by laser scanners, people tracking

was performed using two independent trackers (a) mean shift algorithm for vision sensor using color histogram, (b) Kalman filter for laser sensors using people walking model. Also, authors recognized difficulty in fusing laser sensor with vision sensor at data and feature level and proposed decision level fusion of independent tracking results. However, swing feed model for people may change during tracking period. In addition, tracking of objects such as car, bus where swing was not available needs more research. For tracking multi class objects such as car, bus, person in outdoor environment, independent object detection in laser range scanner and vision camera and use of multiple motion models was proposed (Spinello et al. 2009). In this work, laser range scanner provided structural information of object using conditional random field where node features were enhanced using Adaboost. The object appearance features were extracted using modified implicit shape model. The tracking was performed using extended Kalman filter using Brownian and linear motion model in order to cater multi class object. Rather than placing laser scanner at feet height, laser scanner was placed at top of tripod and laser scanner based detection of human body was considered (Song et al. 2008). Once, vision tracker was initialized with laser detection center, HSV color histogram was extracted around body region and used for estimation of color likelihood in proposed probabilistic detection based particle filter (PD-PF). The individual likelihood score were determined from measurement and over all observation was determined through product of individual likelihood. Results revealed that occlusion and interaction among human could be handled by incorporating weighted detection information into proposal distribution. A probabilistic exemplar models for object appearance were trained independently from laser sensor and vision camera (Schulz 2006). During tracking, joint exemplar states were sampled using Rao-Blackwellized particle filter for estimation of state of object. However, approach used object contour feature which was affected by environment changes and occlusion. In order to handle object during merger/split or close interaction, a solution where tracking was performed along with online learning using vision and laser scanner was proposed (Song et al. 2013). During normal operation (non-correlated), independent laser scanner performed tracking using particle filter and vision data was used for online training of regression tree classifier. The intensity and edge orientated histograms were extracted from randomly located patches around laser tracker estimated center and used as features for training classifier. Once target merger/split was detected visual information aided laser tracker for classifying targets into respective class during split into non correlated objects. Also during correlated object detection, random patches were sampled around interacting region and subjected to respective classifier for finding score map being used as observation model for particle filter. The results were demonstrated on single video for tracking multiple interacting objects. However, rotation and scaling of object along with effect of environments on vision camera needs to be further explored.

### 3.4 Vision + radio frequency

The radio frequency based sensors provide accurate identification information about object but needs to be compensated by other sensors for robust tracking solution. Recently, due to availability of low cost radar, radar sensors were used for tracking object for video surveillance, robots and driver assistance. The radar signal provides radial information of object along with bearing that can be exploited for locating object on image plane. The radar signals were less affected by noises such as fog, dust, snow, wind etc. and can detect trapped objects. For tracking multiple objects, data association from low cost radar and vision camera was proposed (Kim and Moongu 2014). In this work, radar giving low resolution bearing information was compensated by vision camera for multiple object tracking. The measure-

ments from independent sensors were projected on common plane using homography which mainly focus on calibration of two sensors. The tracks management and clutter handling was performed using multiple object integrated probabilistic data association (MIPDA). The tracking of multiple objects was performed using multiple Kalman filters where data fusion and tracks updation was performed. Results revealed that combining radial information with complementary image information enhanced performance over single modularity framework. Data association problem in vehicular networks for awareness of situation to driver or vehicle was discussed (Thomaidis et al. 2013). In this work, long range radar signals captured from first vehicle were fused with measurements such as yaw rate, position, velocity and acceleration from second vehicle. Once association between radar and VANET message was established, global tracker using multiple hypothesis algorithms was initialized for estimating further states. The authors claimed that fusing additional measurement to radar based perception system enhanced tracking accuracy and robustness. A perception system based upon 8-Radio Frequency ID (RFID) antennas and vision camera for accurate identification and tracking of person with passive tag was proposed (Germa et al. 2010). The vision cues, skin color and face, were fused with RF identification at measurement and important sampling in Icondensation algorithm. The results were presented on single video sequences and revealed that obstacle avoidance performance with proposed robot control scheme was better than single modularity. However, performance needs to be investigated for multiple persons carrying RFID tags in a crowd.

### 3.5 Stereo vision

Due to its ability to capture object gesture and illumination invariant, stereo vision is extensively explored for 3D object tracking in the real world scenario. The layered sampling (Perez et al. 2004) and democratic integration (Triesch and Malsburg 2001) were combined in single framework using condensation algorithm (Nickel and Stiefelhagen 2008). In this work, independent trackers were initialized for each targeted object using four cues such as color, motion, detector and stereo correlation. Apart from selection of orthogonal cues, authors proposed orthogonality by dynamically selecting same feature from different region of object. First, disparity map was extracted for stereo cue which gave rough approximate location of target. The estimated position was further refined using other cues for robust tracking in two stage. The cues were adaptively fused using proposed quality measure based upon position error. However, experimental results were briefly discussed on single self-generated video sequences. For mobile platform, 3D multiple people tracking without need of background model was proposed (Munoz-salinas et al. 2008). In this work, from stereo vision camera, depth information was extracted and its contribution in particle weight assignment was decided based upon amount of disparity information. First, Adaboost classifier along with depth information was used for efficient detection of people in the scene. The independent particle filter tracker was initialized for each detected person and interaction among them was determined for handling occlusion due to similar color person. Two ellipses at torso and head were considered for features extraction. The author proposed estimation of joint color and depth probability distribution for two portions where standard deviation of depth distribution was modified in accordance of confidence of disparity measure. Further, gradient probability distribution was extracted in order to estimation of matching of ellipsoidal object. The final observation was product of three probability distributions without considering adaptive contribution. In similar lien, disparity information from stereo video for 3D object tracking was exploited (Zoidi et al. 2014). The targeted object was first passed through Kalman filter for new state prediction. The search region was established around new predicted centre. In

order to reduce search space, sub sampling was performed by measuring similarity of 2D color disparity histogram of candidate ROI with that of reference ROI. From reduced search space, texture cue was extracted and similarity index was calculated for both left and right channel of video by comparing candidate texture with that of reference model. The final position of object was determined based upon maximum of average similarity determined using cosine similarity. The results revealed that stereo tracker perform better than monocular tracker for slowly deforming articulated objects. In order to automatic tuning of various tracking and detection parameters, receiver operator characteristics (ROC) usage for close interaction among different detection modules was discussed (Gavrila and Munder 2007). In this work, pedestrian detection was performed in various stages such as stereo for coarse search region generation, shape based detection followed by classification by texture cue and finally verification by stereo module. The tracking of pedestrian was performed using Hungarian method where cost matrix was extracted using two similarity measures as Euclidian and chamfer distance. The results were presented using proposed mobile protector system.

### 3.6 Discussion

In recent past, in order to exploit potential advantages of different sensing technology, multimodal multicue object tracking has been extensively explored. In general, vision camera was aided by one of sensing technology for development of robust multi-modal tracking solutions. Being invariant to illumination changes, insensitive to pose variation, thermal/IR cameras could detect object for night vision applications and aided vision camera for continuous video surveillances. The fusion and synchronization of vision and thermal camera was major area of research which was addressed differently for robust tracking solution. The tracker level fusion of vision and thermal camera was addressed (Conaire et al. 2008). The fusion based on context sensitive reliability was discussed (Erdem et al. 2012). Cues from color and thermal cameras were fused using DSmT framework for resolving conflict from independent measurements, but, model could not handle tracking of single object (Airouche et al. 2012). For tracking single object using vision and thermal camera, DSmT based framework was proposed considering conflict resolving using proportional conflict redistribution rules, PCR-5 rules (Walia and Kapoor 2015). The Microsoft Kinect camera having synchronized infrared and vision camera could provide depth information used for handling occlusion (Susperregi et al. 2013). The audio sensors can locate person through efficiently extraction of range and bearing information of target, but, fail to locate silent person/object. Hence, combining audio sensors with vision sensor found its niche for applications such as distributed meeting, automatic scene analysis and effective presentation during lectures. Being insensitive to environment changes and computationally efficient, laser scanners combined with vision camera for handling occlusion, and merge/split for multicue tracking framework. The laser scanner were placed either above upper body or at legs positions for extracting different patterns of objects. The patterns such as walking pattern (Scheutz et al. 2004), swing model (Cui et al. 2008), motion models (Spinello et al. 2009) were extracted using laser scanner and combined with vision camera for distinguishing objects. In addition, detection of whole body using laser scanner was considered (Song et al. 2008) which aided vision camera for robust tracking solution. Due to its ability to locate hidden object, RF sensing such as radar and passive RF tags along with vision camera were explored for multi-modal tracking solution. However, tracking multiple persons with similar passive RFID tag needs further investigated. The stereo camera being able to provide disparity information about target was exploited extensively for 3D multicue object tracking. The depth information extracted from disparity map was combined with other cues for multicue tracking. In sum, similar to single-

modal, multi-modal tracking work was mainly focused towards either extraction of efficient features or fusion of different sensors data in efficient manner. In addition, calibration and synchronization of different sensors is another domain which needs further research for accurate tracking solution development. Our analyses of single-modal and multi-modal multicue techniques revealed that technology in this field has matured enough for real applications of these solutions.

## 4 Datasets and evaluation metrics for multicue object tracking

The object tracking is challenging task due to complex nature of real world and number of environments scenarios. In each year, in addition to work reported by different authors, Performance Evaluation of Tracking and Surveillance (PETS) workshop introduced new datasets and performance measures for evaluation of tracking algorithms. On the contrary, most of reported methods were evaluated on limited dataset for specific performance measures. Hence, in order to give reader a quick overview and new trends and also for sake of completion of multicue tracking survey, we have briefly summarized various reported multicue datasets and performance measures for object tracking.

### 4.1 Datasets for evaluation of multicue object tracking techniques

For evaluation of tracking algorithms, standard datasets are available publically. Some of these datasets provide ground truth data in the form of separate *.xml file. In addition, algorithms are tested on synthesis video sequences for catering different test scenarios. The overview of various datasets for object tracking is summarized in Table 3 and also sample image of each listed set is included in Fig. 4. The brief description of multicue datasets follows in turn.

(a) TUD-Stadmittee dataset sequences contained 178 images with resolution of $640 \times 480$ (Andriluka et al. 2010). The data was captured using stationary monocular camera. The dataset had multiple persons being self or fully occluded by different objects. The ground truth data was available which consist of different object ID along with corresponding coordinates in different frames.
(b) PETS 2014 workshop introduced ARENA dataset which had 22 scenarios categorized as 'something is wrong' 6 video sequences, 'potentially criminal' 6 video sequences, 'criminal behaviour' 7 video sequences and 'extra criminal scenarios' 3 video sequences (Patino and Ferryman 2014; PETS 2014). The data set was collected at university using four cameras mounted on vehicle. The aim was to provide benchmark data set for evaluation of algorithms for behaviour and abnormality analysis in a scene captured using multiple cameras.
(c) Head tracking sequences (HTS) included various challenges such as occlusion, rotation, zooming and distractions. The video sequences along with ground truth data representing coordinate of ellipse position were available at HTS. The resolution of bmp images are $128 \times 96$ pixels.
d) Audio visual people (AVP) dataset consisting of three vision sequences along with two microphone outputs was available online (MOTINAS project). The dataset consist of 3271 frames of $360 \times 288$ pixels size at 25 fps. The two audio channels were at 44.1 kHz. The data was recorded in closed rooms having reverberations. The ground truth data was also provided in the form of *.xml file. In addition, AV16.3 dataset consisted of 8 annotated sequences captured indoor with three cameras and 2 arrays (8 each) of microphones (Lathoud et al. 2004).

**Table 3** Recent advances on datasets for object tracking

| Data set | Web address | GT | Frame size, Number of videos, rate etc. | Description |
|---|---|---|---|---|
| *(A) Vision camera dataset* | | | | |
| Andriluka et al. (2010) | https://www.d2.mpiinf.mpg.de/node/428#name:cvpr10_videos | Yes | 640 × 480, 178 frames | Multi persons with occlusion, captured from stationary camera |
| PETS (2014) | Pets2014.net | No | 1280 × 960, 30 fps, 22 video sequences | Multi Camera capturing of scene classified into four levels |
| HTS | http://www.ces.clemson.edu/_stb/research/headtracker/seq/ | No | 128 × 64, 17 video sequences | Included Occlusion, Rotation, Zooming and Distractions |
| Blunsden and Fisher (2010) | http://groups.inf.ed.ac.uk/vision/BEHAVEDATA/INTERACTIONS/ | Yes | 640 × 480, 25 fps, 90000 frames with 4 video | Interaction of people in 10 types of group behaviour with limited GT |
| EC-CAVIAR | http://groups.inf.ed.ac.uk/vision/CAVIAR/CAVIARDATA1/ | Yes | 384 × 288, 25 fps, 54 video sequences in two sets | Included scaling, occlusion, illumination changes and interactions |
| Klein et al. (2010) | http://www.iai.uni-bonn.de/~kleind/tracking/index.htm | Yes | 320 × 240, 25 fps, 5 human video sequences in mpeg2 format | Included rotation, occlusion and captured using moving camera |
| Fleuret et al. (2008) | http://cvlab.epfl.ch/data/pom | Yes | 5 video sequences captured using multiple cameras, 25 fps | Multiple people with partial or full occlusion, Scaling indoor/ outdoor environment |
| PETS (2006a, b) | http://www.cvg.reading.ac.uk/PETS2006/data.html | Yes | 7 video sequences, 768 × 576 pixels, 25 fps and JPEG. | Captured using four cameras, different difficulty level with multiple persons |
| Ess et al. (2007) | http://www.vision.ee.ethz.ch/~aess/iccv2007/ | Yes | Two video sequences with 804 frames, 640 × 480 at 13–15 fps | Mobile chariots with two AVT Marlins camera mounted on it |
| Baltieri et al. (2011) | http://imagelab.ing.unimore.it/visor/3dpes.asp | Yes | Resolution 704 × 576, 8 cameras sequences, 15 fps, JPEG image | Large sequences provided in six parts included person captured using multi cameras |
| *(B) Thermal/IR camera dataset* | | | | |
| Davis and Keck (2005) | http://www.vcipl.okstate.edu/otcbvs/bench/Data/01/download.html | Yes | 360 × 240, 10 sequences 284 frames, 8 bit grey scale | Video under different environments such as cloudy, rainy, fair etc, with occlusion |
| Zheng et al. (2014) | http://csr.bu.edu/BU-TIV/BUTIV.html | Yes | 1024 × 640 and 512 × 512, 3 pedestrian sequences with 16 bit | Multiple camera used for capturing multi view for real world scenario |

**Table 3** continued

| Data set | Web address | GT | Frame size, Number of videos, rate etc. | Description |
|---|---|---|---|---|
| Portmann et al. (2014) | http://projects.asl.ethz.ch/datasets/doku.php?id=ir:iricra2014 | Yes | 324 × 256, 9 sequences at 20 Hz rate | Handheld camera from elevated position to capture different scenarios |
| *(C) Thermal/IR + vision camera dataset* | | | | |
| Torabi et al. (2012) | http://www.polymtl.ca/litiv/en/vid/ | Yes | 320 × 240, 9 sequences 6,236 frames upto 88 sec | Captured with vision (Sony XCD-710CR) and thermal (FLIR T A40M) camera |
| INO's video | http://www.ino.ca/en/examples/video-analytics-dataset/ | Yes | Variable resolution for 13 video sequences | Sequences with variable challenges captured under different weather |
| Davis and Sharma (2007) | http://www.vcipl.okstate.edu/otcbvs/bench/ | No | 340 × 240, 6 sequences at 30 fps | Having occlusion, shadow and number of objects to be targeted |
| *(D) Vision camera + audio sensor dataset* | | | | |
| MOTINAS project | ftp://motinas.elec.qmul.ac.uk/pub/av_people | Yes | 3271 frames of 360 × 288 pixels size at 25 fps | One vision and two microphones were placed in rooms with reverberation |
| Lathoud et al. (2004) | http://www.idiap.ch/dataset/av16-3 | Yes | Avi video 288 × 360, 25 fps, audio at 16 khz, 8 annotated sequences | One sequences consisted of three video and 16 audio files |
| *(E) Vision camera + laser scanner dataset* | | | | |
| Strigel et al. (2014) | http://www.uniulm.de/in/mrm/forschung/datensaetze.html | Yes | Monochrome 656 × 494, 25 fps, laser 12.5 Hz | Three sequence for public interaction with object label and reference data |
| *(F) Stereo vision camera* | | | | |
| Ess et al. (2007) | http://www.vision.ee.ethz.ch/~aess/iccv2007/ | Yes | Three video sequences, 640 × 480, 10–15 fps | Pair of AVT Marlins used for recording in platform, calibration data is given |
| *(G) Kinect sensor* | | | | |
| Klein | http://www.iai.unibonn.de/~martin/tracking.html | Yes | Five video sequences, 640 × 480, RGB 8 bit and depth 16 bit | Contains rotation, occlusions, illumination changes |
| Munaro et al. (2012) | http://www.dei.unipd.it/~munaro/KTP-dataset.html | Yes | 640 × 480 resolutions, 30 Hz and in total 8475 frames in 4 Seq. | 2D and 3D ground truth data, five people in each sequence |

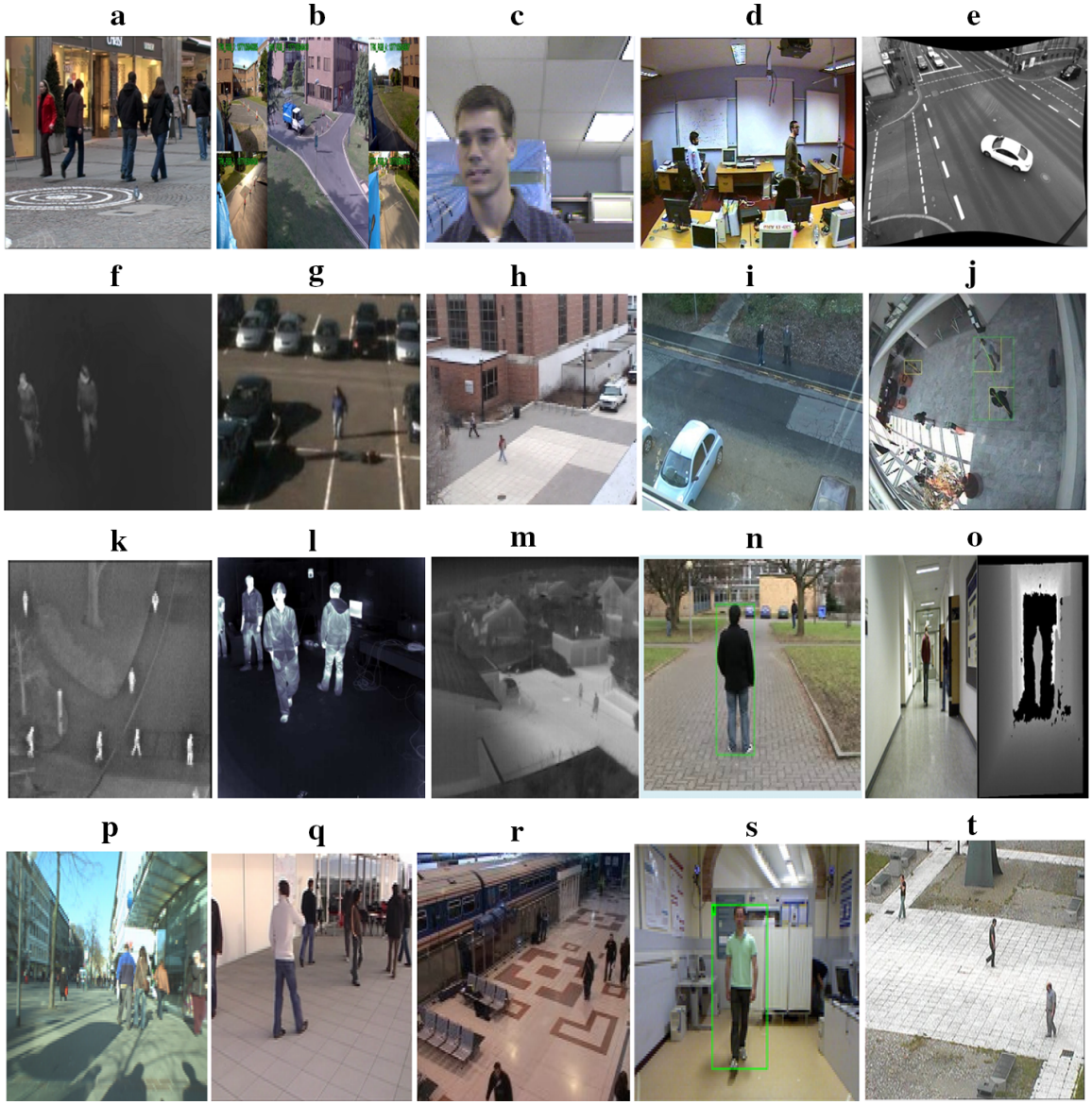


**Fig. 4** Sample image of datasets: **a** TUD-Stadmittee (Andriluka et al. 2010), **b** ARENA (PETS 2014), **c** HTS (HTS), **d** AVP (MOTINAS project), **e** Ko-PER (Strigel et al. 2014), **f** LITIV (Torabi et al. 2012), **g** INO (INO's Video), **h** OSU (Davis and Sharma 2007), **i** BEHAVE (Blunsden and Fisher 2010), **j** CAVIAR (EC CAVIAR), **k** OSU (Davis and Keck 2005), **l** TIV (Zheng et al. 2014), **m** ASL-TID (Portmann et al. 2014), **n** BoBoT (Klein et al. 2010), **o** BoBoT-D (Klein), **p** MSA (Ess et al. 2007), **q** EPFL (Fleuret et al. 2008), **r** PETS2006 (PETS 2006a, 2006b), **s** KTP (Munaro et al. 2012), **t** 3DPes (Baltieri et al. 2011)

(e) Under Ko-FAS, Ko-PER road interaction dataset was generated as benchmark dataset for evaluation of algorithms (Strigel et al. 2014). The dataset consist of three video sequences captured using eight monochrome cameras TXG-04 and laser scanner 14 SICK LD–MRS installed at height of 5m above ground level. The sequence 1 included object label and sequences 2 and 3 had reference data which was useful for evaluation of multiple object detection and tracking algorithms.

(f) LITIV Dataset included nine video sequences of visible and thermal video sequences captured under different conditions such zooming, position and occlusion (Torabi et al. 2012). The sequences were having resolutions of 320 $\times$ 240, variable frame rate and length ranging from 11 to 88 s. The ground truth data were provided separately for these sequences.

(g) INO's video analytics dataset consisted of video sequences captured using VIRxCam platform installed in outdoor with different weather conditions (INO's Video). The sequences with different resolution and duration were captured from calibrated thermal and color camera. The ground truth data was provided in form of images with extracted foreground.

(h) OSU Color-Thermal Database was created in three different locations at Ohio State University campus (Davis and Sharma 2007). The dataset consisted of 6 video sequences with 17,089 images captured from thermal and vision camera located on tripod above ground level. The sequences were captured in outdoor with different level of challenges. The tracking results were available in the form of *.cvml file.

(i) BEHAVE Interactions dataset (Blunsden and Fisher 2010) consisted of 4 video sequences captured at two different sites. The sequences capture 10 interaction behavior as in group, ignore, chase, fight, walk together, run together, approach, split, following, and meet. However, ground truth data for few video sequence was available online in the form of *.xml file. In totality, videos had approximately 90,000 frames with resolution of 640 × 480 at 25 fps.

(j) CAVIAR dataset consisted of 2 sets of video sequences captured at resolution of 384 × 288 with 25 fps. Set1: contained 28 video sequences representing six scenarios at INRIA lab. Set2: contained 26 video sequences, each with two views, representing 26 scenarios at shopping center Lisbon (EC CAVIAR). The sizes of videos were upto 21MB with MPEG2 compression. The ground truth data was available in the form of *.xml file.

(k) OSU dataset consisted of 10 thermal video sequences, 284 frames, captured at Ohio State University campus (Davis and Keck 2005). The ground truth (GT) data was provided for each sequence. The sequences were captured under different environmental conditions such as cloudy, rainy, fair etc.

(l) TIV dataset included three pedestrian thermal infrared (IR) video sequences at high resolution of 1024 × 640 and 512 × 512 (Zheng et al. 2014). The data was collected at variable frame rate with multiple cameras. The annotation of each sequence was provided along with Matlab code for reading data file.

(m) ASL-TID dataset had nine sequences captured at different outdoor locations (Portmann et al. 2014). The sequences were captured at fixed rate 20 Hz with resolution 324 × 256 with handheld FLIR Tau320 camera from elevated location.

(n) BoBoT benchmark dataset contained nine video sequences out of which five had presence of human (Klein et al. 2010). The sequences were captured at resolution of 320 × 240, 25 frame rate in mpeg2 format. The camera was in motion and scene had different video challenges such as distractions, occlusion, and rotation.

(o) BoBoT-D dataset included five RGB and depth sequences marked as 'Milk', 'Ball', 'Person', 'Tank', and 'Lunch Box'. The sequences were captured using Kinect sensor with color 3 channel 8 bit each and depth one channel 16 bit (Klein). The ground truth data is also available online.

(p) Mobile scene analysis (MSA) dataset consisted of two sequences, 804 frames, and recorded using pair of cameras mounted on mobile chariots (Ess et al. 2007). The images with resolution 640 × 480 were captured at rate 13–14 fps using AVT Marlins. The annotation along with calibration data was included for testing.

(q) Multiple people tracking EPFL dataset was created using multiple cameras (Fleuret et al. 2008). The dataset consisted of five video sequences captured at 25 fps with 2–4 camera mounted at height of 2 m above ground. The various challenges such as bad lighting, occlusion, scaling had been incorporated in these sequences. The ground truth data was provided for three video sequences.

(r) PETS series contained different sets of dataset depending upon scenarios and surveillance application domains. PETS2006 (PETS 2006a, 2006b) dataset consisted of 7 (S1–S7) video sequences captured using four cameras. The sequences had resolution of 768 × 576 pixels, 25 fps and JPEG compression. The different levels of difficulty were marked for each sequence and ground truth along with calibration data was provided.
(s) Kinect tracking precision (KTP) dataset consisted of 4 sequences captured at different position of mobile robot carrying Microsoft Kinect camera (Munaro et al. 2012). The images had 640 × 480 pixel resolutions, 30 Hz and in total 8475 frames. The 2D and 3D ground truth data was provided.
(t) 3DPes dataset contained video sequences in six parts with multiple cameras for surveillance (Baltieri et al. 2011). The eight cameras were installed with different zooming at different locations at University of Modena and Reggio Emilia. The resolution of cameras was fixed at 704 × 576 pixels with 15 frames/s. The sequences captured objects multiple times in one or more cameras.

In addition, there are datasets for which either public access is not present or cited in a few of multicue research papers. Additional details about datasets are available (CANTATA). In literature, it was well acknowledged that publically available datasets were preferred over self-generated datasets. However, for using public domain dataset, individuals are directed to read the license agreement/download instruction/reference citation for acknowledgement of sources. In addition to selection of datasets, performance measures are considered as critical parameters for evaluation of tracking algorithms. The brief introduction of various performance measures for multicue object tracking is discussed in following section.

## 4.2 Evaluation of multicue object tracking techniques

The tracker performance needs to be evaluated both quantitatively and qualitatively over a length of video sequences. In literature, tracking performance measures considered different aspects of video with aim to gauge robustness and efficiency of proposed technique. The aim of tracking performance measures is to estimate either deviation from track or false positive/false negative during tracking. In our review, we have categorized quantitative performance measures for single and multiple objects tracking depending upon availability of ground truth (GT) data. The brief introduction of various performance measures are examined in this section in turn:

### *4.2.1 Performance measure without using ground truth data*

Tracking performance measure without using GT data exploits abnormality in regular pattern of motion, appearance, shape etc. (Spampinato et al. 2012; Chau et al. 2009; Erdem et al. 2001b) or uses some prior knowledge of object trajectory (Wu et al. 2010). These measures are easily computed on real time but prone to errors under different tracking scenarios. Performance measure for evaluation of video segmentation and tracking without GT data was proposed (Erdem et al. 2001b). The spatial difference extracted from color, motion difference along boundary and temporal difference extracted from color histogram difference were used for deducing evaluation metrics. The color metrics were determined with the assumptions that intra frame color boundary coincides with object boundary and also that inter frame color histogram of object did not change. The motion metric was also determined with the assumption that motion vector of object does not coincide with background motion vector at object boundary. The individual metrics were combined with weighted contribution to get

final score in the range [0, 1]. As an extension of previous work, feedback mechanism for adjusting the weights assigned to features was considered (Erdem et al. 2001a). However, proposed technique was investigated for contour tracking. Similarly, appearance and motion smoothness for extracting performance measure scores was assumed (Wu and Zheng 2004). In this work, five features such as trajectory complexity, scale, motion smoothness, shape, and appearance similarity were considered to be consistent/smooth during tracking process. The individual scores were weighted to get final performance evaluation score. In order to make performance measure more adaptive and robust to variation in object scale and shape during tracking, seven features such as temporal length, exit zone, shape ratio, area, color along with their feature score at each frame were extracted (Chau et al. 2009). The final performance score of tracker was determined through weighted contribution of individual feature. The most of tracking performance metrics without GT were either application specific or algorithm specific. In order to test performance irrespective of tracker algorithms, physical motion reversibility of targeted object was exploited (Wu et al. 2010). The association between prior distribution at $t = 0$ and posterior distribution of time reversed Markov chain was used for evaluating performance of tracking algorithm. Also, fast approximation at different time interval was suggested for real time performance evaluation. Automatic exclusion of temporal state when target was lost and finally estimation of tracker performance when target was present was proposed (SanMiguel et al. 2012). In this work, tracker accuracy was measured by finding similarity between estimated target positions and time reversed tracker positions at each state. In similar lien, online evaluation of tracking algorithms using shape, appearance and motion features and Bayesian classifier was considered (Spampinato et al. 2012). In this work, Bayesian classifier classified tested frame features into good or bad tracking. The classifier was trained through features set extracted from training dataset. The final matching score was estimated from all features and used for deciding tracker performance metrics. In sum, performance measure without ground truth could evaluate tracker on real time during tracking but most of performance measures gave less reliable results due to variation in features with environment.

### *4.2.2 Performance measures using ground truth (GT) data*

The tracker performance measures using GT are evolved with the start of Performance Evaluation of Tracking and Surveillance (PETS) workshop. These measures gave more precise results and also independent of tracker algorithms. We have further categorized these metrics based upon how the ground truth data was used for comparison with tracker output.

First in trajectory based approach, ground truth trajectory was compared with estimated tracker trajectory. Apart from complete trajectory comparison, comparison of some discrete events in trajectory in order to reduce the effort for ground truth extraction was proposed (Pingali and Segen 1996). In similar line, establishment of correspondence between ground truth track and tracker estimated track before estimation of performance metrics was introduced (Senior et al. 2001). In this work, association of ground truth track with estimated track was established through threshold of $N_g \times N_t$ distance matrix. Where, $N_g$ was count of ground truth tracks and $N_t$ was count of estimated tracks. Distance matrix $D_T(K_1, K_2)$ between two tracks $K_1$ and $K_2$ was determined using Eqs. (1)–(3).

$$D_T(K_1, K_2) = \frac{1}{N_{12}^2} \left\{ \sum_{\substack{i:\exists K_1(t_i) \\ \& \exists K_2(t_i)}} \sqrt{p_x^2(i) + p_v^2(i)} \right\} \tag{1}$$

$$p_x(i) = |X_1(i) - X_2(i)| \tag{2}$$

$$p_v(i) = |V_1(i) - V_2(i)| \tag{3}$$

where $N_{12}$ is total number of states in two tracks, $p_x$ (i) and $p_v$ (i) were difference in centroid and velocity of object at time instant $t_i$. Using estimated $N_g \times N_t$ distance matrix, association between ground truth track and estimated tracks was established. Further, performance metrics for object tracking such as position error, area error, detection lab, incompleteness factor and track error rates were determined. Apart from track matching using association criteria, counting index was used and performance metrics such as object tracking accuracy, occlusion success rate, tracker detection rate, and tracking success rate, false alarm rate, track detection rate were considered (Black et al. 2003). Issues of spatial and temporal fragmentation/merging during object tracking were discussed (Brown et al. 2005). In this work, two stage evaluation of performance was proposed. Apart from measuring track false positive and negative, authors introduced metrics for measurement of fragmentation and merger errors. Temporal correspondence between GT track and tracker estimated track was measured (Yin et al. 2007) using Eq. (4).

$$\frac{L(GT_m \cap TT_n)}{L(GT_m \cup TT_n)} > \text{Threshold} \tag{4}$$

Under this work, function L () finds number of frames between GT track ($GT_m$) and target track ($TT_n$). When the above ratio was greater than threshold value, target track was associated with ground truth track. After establishment of association, various performance metrics such as track detection failure (TDF) track fragmentation (TF), latency of system track (LT), closeness of track (CT), false alarm track(FAT), track matching error (TME), ID change (IDC), correct detected track (CDT) and track completeness (TC) were determined for evaluation of tracker. Correspondence between ground truth track and tracker estimated track through estimation of Euclidean distance between centroid of ground truth bounding box and estimated bounding box was established (Bashir and Porikli 2006). After establishment of correspondence, different frame based metrics such as positive prediction, false alarm rate, tracker detection rate, detection rate etc. were determined based upon counting of number of true negative, true positive, false negative and false positive frames. In addition, authors proposed object tracking error (OTE), Eq. (5), as measure of average displacement of centroid of ground truth and estimated bounding box.

$$OTE = \frac{1}{N_{gt}} \left\{ \sum_{n \in T_g \cap T_t} \sqrt{(X_{ng} - X_{nt})^2 + (Y_{ng} - Y_{nt})^2} \right\} \tag{5}$$

where $X_{ng}$ and $X_{nt}$ were centroid of object in frame n for ground truth and tracker estimation. $N_{gt}$ was total number of frame where correspondence was established. For evaluating performance of mobile robot, visual contact rate (VCR) as measure of ratio of number of frames target was present in robot field of view to total number of frames processed was proposed (Germa et al. 2010). In (Bernardin and Stiefelhagen 2008; Zhang et al. 2015) CLEAR MOT matrix and multiple objects tracking accuracy (MOTA) was determined, Eq. (6), by counting number of false positive, miss detection and mismatches.

$$MOTA = 1 - \frac{\sum_{t=1}^{T} (M(t) + FP(t) + MM(t))}{\sum_{t=1}^{T} N(t)} \tag{6}$$

where at time t, M(t), FP(t), MM(t), and N(t) were number of miss, false positive, mismatch and object present respectively.

In order to measure more precise positional accuracy, performance measures considered area of overlap between ground truth bounding box and tracker estimated bounding box in subsequence frames. An area based measure of precision, recall, F measure and success rate was proposed (Kwon and Lee 2009). In this work, If GT bounding box area was $A_{GT}$ and that of tracker output as $A_{TO}$. The precision, recall, and F measure were determined using Eqs. (7)–(9) respectively. The F measure estimate area of overlap between ground truth bounding box and tracker estimated bounding box at each frame. Maximum value of F measure (max at 1) indicated best estimation results. Also, author defined success rate based upon estimated value of F measure at each frame. If F measure value was greater than 0.5, object was considered to be tracked correctly.

$$r = \frac{A_{GT} \cap A_{TO}}{A_{GT}} \tag{7}$$

$$p = \frac{A_{GT} \cap A_{TO}}{A_{TO}} \tag{8}$$

$$F = \frac{2\,r\,p}{r + p} \tag{9}$$

The success rate was determined as ratio of correctly tracked frame to total number of frame in video sequences.

The performance metrics based upon statistics of pixels in area of detected object and GT were introduced (Karasulu and Korukoglu 2011). Under this work, in each frame, pixel based precision and recall metrics were determined using Eqs. (10)–(11). Where, symbol || gives number of pixels in the area, $SUM_{GT}(k)$ and $SUM_{TO}(k)$ represent spatial union of bounding boxes of GT and detected object for kth fame in video sequence.

$$P_{pa} = \begin{cases} \text{undefined}, & \text{if } SUM_{TO}(k) = \text{empty} \\ 1 - \dfrac{\left|SUM_{TO}(k) \cap \overline{SUM_{GT}(k)}\right|}{SUM_{TO}(k)}, & \text{otherwise} \end{cases} \tag{10}$$

$$R_{pa} = \begin{cases} \text{undefined}, & \text{if } SUM_{GT}(k) = \text{empty} \\ 1 - \dfrac{\left|SUM_{GT}(k) \cap \overline{SUM_{TO}(k)}\right|}{SUM_{GT}(k)}, & \text{otherwise} \end{cases} \tag{11}$$

These measures for complete video sequences were estimated as weighted average over $N_{frame}$ where tracking was performed. Also, the authors introduced F1 measure as performance metric, Eq. (12), which was estimated from individual calculated values of pixel based precision and recall.

$$F1 = \frac{(1 + \beta)P_{pa} \times R_{pa}}{\beta(P_{pa} + R_{pa})} \tag{12}$$

where parameter β was determined by user depending upon application scenario. In order to give more weightage to frames with greater intersection area between ground truth object and tracker output, an error measure for estimation of tracker accuracy was proposed (Maggio et al. 2007). The error measure was determined using Eq. (13).

$$E(k) = 1 - \frac{2 \times TP(k)}{|A_{TO}(k)| + |A_{GT}(k)|} \tag{13}$$

where in frame k, TP(k) number of pixels matched in both ground truth and tracker output. $|A_{TO}(k)|$, $|A_{GT}(k)|$ were cardinality in the area of tracker output and ground truth. The error was estimated for all frames where target was present. Also, authors proposed estimation of

standard deviation of error under different run for probalistic tracker. A real time performance metric for object tracking was presented (Denman et al. 2009). The different object parameters such as position and area were explored for dynamically estimation of object detection and tracking metrics. For each of these metric, final performance score was determined while considering contribution of each frame with appropriate learning factor. Apart from quantitative measures, various qualitative measures such as ability to handle occlusion, multiple targets, rotation, scaling, deformation were investigated in different reported work. In sum, both quantitative and qualitative measures need to be considered for testing robustness and reliability of proposed algorithms.

### 4.3 Discussion

The different datasets for object tracking are summarized in Table 3 with listing of various parameters. The datasets are generated with incorporation of various environment challenges such as moving camera, clutter, occlusion, illumination changes etc. In general, for vision camera, tracking research works are published using standard dataset so that results can be reproduced for further study. But, for other sensing technologies, most of work was reported on self-generated data for which public access was not available. In addition, multi-modal synchronization and calibration of independent sensors is imperative for faithful tracking results. In line with this, experiment analysis was performed (Smeulders et al. 2014). Therefore, in our opinion newly reported methods need to be thoroughly evaluated on different sets of video sequences. Also, in our opinion video datasets may be assigned tracking difficulty levels which may be considered for performance metric. Mostly for vision dataset ground truth data is provided along with video sequences, but for most of multi-modal datasets ground truth needs to be extracted. The manual extraction of GT data is cumbersome task and subjected to human errors. Various challenges in extraction of ground truth data were investigated (Milan et al. 2013). A number of semi-automatic online tools such as VATIC (Vondrick et al. 2012) and multi-view annotation tool (Utasi and Benedek 2012), GTVT (Ambardekar et al. 2009), ViPER-GT (ViPER) etc. are available for extraction of GT. In another approach, in order to ease extraction of ground truth data, pseudo synthetic video sequences were generated for testing the robustness of tracking algorithms (Black et al. 2003; Schlogl et al. 2004). For prerecorded video, different challenges and complexities are intentionally introduced for generation of pseudo synthetic video.

In this review, we briefly categorized performance measures based upon availability of ground truth data. The performance measures without ground truth can be applied on real time. Performance metrics using ground truth data are more accurate and invariant to algorithm application domain. The measures based upon track similarity (Pingali and Segen 1996; Senior et al. 2001), object count (Yin et al. 2007; Bashir and Porikli 2006), area based (Kwon and Lee 2009) or pixel based performance metrics (Karasulu and Korukoglu 2011) may be considered for tracking performance evaluation. In an attempt to standardize evaluation methodology, various online tools such as ETISEO (Nghiem et al. 2007), VIVID (Collins et al. 2005), Video Analysis and Content Extraction (VACE; Kasturi et al. 2005), PETS (PETS 2006a, b) etc. are available for evaluation of performance of newly developed algorithm. Mostly, users need to submit online results and these tools provide complete performance reports. The CLEAR (CLEAR) performance evaluation workshop was mainly focused towards bringing VACE and CHIL (CHIL) program together under a common platform. The goal was to generate universal data set along with performance metrics which will help vision community for pursuing further research. However, most of performance measures do not consider system level changes in actual real system. Hence, in our view, con-

sidering overall tracking scenarios, system level performance metric needs to be investigated in future.

## 5 Concluding remarks and future direction

In this manuscript, we have reviewed recent advancement in single-modal and multi-modal multicue object tracking techniques. In general, combining orthogonal complementary cues not only enhance tracking accuracy over single cue techniques but also make algorithms more robust to environment challenges. Vision and thermal camera being rich source of information were extensively exploited for extracting different cues which were adaptively fused in multicue tracking framework. The thermal sensors are considered to be good alternative for vision sensor but cannot distinguish object with similar thermal profile. The laser, radar, sonar sensors are limited in extracting fine granularities of visual world. The audio sensors are good in locating object but unable to track silent person/object. Hence, vision camera was augmented by different modularity such as thermal, radar, sonar, laser, and RFID sensors for robust and reliable tracking solution development. The synchronization and calibration of different modularity is discussed to a limited extent and need further investigation. The Kinect sensor can give synchronized images from vision and thermal camera. The recent work on multicue tracking was mainly focused on either development of robust cues or integration of multiple cues in adaptive manner. Although, number of dataset for single-modal multicue are available online for testing of single-modal multicue techniques, multi-modal datasets are limitedly discussed in open literature. Although, it is well established that different independent modularity enhance tracking performance in multicue framework, sensors modularity such as seismic sensors, sonar etc. needs to be explored for tracking distance object. Considering our analysis of reviewed techniques, we conclude our survey with the following remarks:

1. Multi-modal and single-modal multicue techniques attained their advancement for real applications
2. Single-modal and multi-modal multicue methods can handle various tracking challenges more efficiently than single cue methods
3. Although, It was well established that multi-modal methods improve tracking performance, usage of more than two modularity needs more research
4. Calibrated and synchronized dataset for evaluating multi-modal techniques needs further research
5. Features with multiple cues for incorporating different tracking scenarios have promising research directions
6. Adaptive integration of cues with online cues conflict resolving solutions can be investigated

In sum, in this review we have investigated some of key single-modal and multi-modal multicue object tracking methods. Most recent developments are analyzed and compared in tabular form. We believe that our review will clear direction of research in ever growing field of multicue object tracking.

**Acknowledgments** The authors are grateful Defence Research and Development Organization and Delhi Technological University for financial support to this work. We would also like to thank anominous reviewers for their valuable suggestions.

## References


Ahmed M, Tawab A, Abdelhalim MB, Habib SED (2014) Efficient multi-feature PSO for fast gray level object tracking. Appl Soft Comput 14:317–337

Airouche M, Bentabet L, Zelmat M, Gao G (2012) Pedestrian tracking using color, thermal and location cue measurements: a DSmT-based framework. Mach Vis Appl 23:999–1010

Ambardekar A, Niclescu M, Dascalu S (2009) Ground truth verification Tool (GTVT) for video surveillance system. In: ACHI'09 second international conferences on advances in computer–human interactions

Andriluka M, Roth S, Schiele B (2010) Monocular 3D pose estimation and tracking by detection. In: IEEE conference on computer vision and pattern recognition (CVPR 2010), USA

Baltieri D, Vezzani R, Cucchiara R (2011) 3DPes: 3D people dataset for surveillance and forensics. In: Proceedings of international ACM workshop MA3HO, Scottsdale, AZ, USA, pp 59–64

Bashir F, Porikli F (2006) Performance evaluation of object detection and tracking systems. In: IEEE international workshop on performance evaluation of tracking and surveillance (PETS)

Bernardin K, Stiefelhagen R (2008) Evaluating multiple object tracking performance: the clear MOT metrics. EURASIP J IVP 2008(1):246–309

Birchfield S (1998) Elliptical head tracking using intensity gradients and color histogram. In: Proceedings of IEEE conference on computer vision and pattern reorganization, pp 232–237

Black J, Ellis T, Rosin P (2003) A novel method for video tracking performance evaluation. In: Joint IEEE international workshop on visual surveillance and performance evaluation of tracking and surveillance (VS-PETS), pp 125–132

Blunsden SJ, Fisher RB (2010) The BEHAVE video dataset: ground truth video for multi-person behavior classification. Ann BMVA 4:1–12

Brasnett P, Mihaylova L, Bull D, Canagarajah N (2007) Sequential Monte Carlo tracking by fusing multiple cues in video sequences. Image Vis Comput 25(8):1217–1227

Brasnett P, Mihaylova L, Canagarajah N, Bull D (2005) Particle filtering with multiple cues for object tracking invideo sequences. In: Proceedings of SPIE's 17th annual symposium on electronic imaging, science and technology, vol 5685, pp 430–441

Brown LM, Senior WA, Tian Y-l, Connell J, Hampapur A, Shu C-F, Merkl H, Max L, (2005) Performance evaluation of surveillance systems under varying conditions. In: IEEE internationl workshop on performance evaluation of tracking and surveillance, Colorado

Cannons K, Gryn J, Wildes R (2010) Visual tracking using a pixel wise spatio-temporal oriented energy representation. In: Proceedings of the11th European conference on computer vision, pp 511–524

CANTATA. http://www.multitel.be/cantata/

Chakravarty P, Jarvis R (2006) Panoramic vision and laser range finder fusion for multiple person tracking. In: Proceedings of IEEE/RSJ international conference on intelligent robots and systems, pp 2949–2954

Chau DP, Bremond F, Thonnat M (2009) Online evaluation of tracking algorithm performance. In: The 3rd international conference on imaging for crime detection and prevention

Chen Y, Nguyen TV, Kankanhalli M, Yuan J, Shuicheng Yan, Meng Wang (2014) Audio matters in visual attention. IEEE Trans Circuits Syst Video Technol 24(11):1992–2003

Chen Y, Rui Y (2004) Real-time speaker tracking using particle filter sensor fusion. In: Proceedings of the IEEE, vol 92(3)

CHIL—computers in the human interaction loop. http://chil.server.de/

CLEAR: classification of events, activities and relationships. http://www.clear-evaluation.org, 2008

Collins R, Zhou X, Teh SK (2005) An open source tracking test bed and evaluation web site. In: IEEE international workshop on performance evaluation of tracking and surveillance (PETS2005)

Conaire CO, O' Connor NE, Smeaton A (2008) Thermo-visual feature fusion for object tracking using multiple spatiogram trackers. Mach Vis Appl 19:483–494

Congxia Dai, Yunfei Zheng, Xin Li (2007) Pedestrian detection and tracking in infrared imagery using shape and appearance. Comput Vis Image Underst 106:288–299

Cui J, Zha H, Zhao H, Shibasaki R (2008) Multi-modal tracking of people using laser scanners and video camera. Image Vis Comput 26:240–252

Davis J, Keck M (2005) A two-stage approach to person detection in thermal imagery. In: Proceedings of IEEE workshop on applications of computer vision

Davis J, Sharma V (2007) Background-subtraction using contour-based fusion of thermal and visible imagery. IEEE OTCBVS WS Ser Bench Comput Vis Image Underst 106(2–3):162–182

Denman S, Fookes C, Sridharan S, Lakemond R (2009) Dynamic performance measures for object tracking systems. In: Proceeding of advanced video and signal based surveillance, IEEE

Dou JF, Jianxun Li (2014) Robust visual tracking based on interactive multiple model particle filter by integrating multiple cues. Neurocomputing 135:118–129

Dou J, Li J (2014) Robust visual tracking base on adaptively multi-feature fusion and particle filter. Optik 125:1680–1686
EC Caviar project/IST 2001 37540, found at http://homepages.inf.ed.ac.uk/rbf/CAVIAR/
Erdem CE, Sankur B, Tekalp AM (2001a) Non-rigid object tracking using performance evaluation measures as feedback. In: Proceedings of IEEE internationl conference on computer vision and pattern recognition, pp II-323–II-330
Erdem CE, Tekalp AM, Sankur B (2001b) Metrics for performance evaluation of video object segmentation and tracking without ground truth. In: Proceedings of international conference on image processing, vol 2, pp 69–72
Erdem E, Dubuisson S, Bloch I (2012) Visual tracking by fusing multiple cues with context-sensitive reliabilities. Pattern Reorgan 45:1948–1959
Ess A, Leibe B, van Gool L (2007) Depth and appearance for mobile scene analysis. In: Proceedings of ICCV
Fleuret F, Berclaz J, Lengagne R, Fua P (2008) Multi-camera people tracking with a probabilistic occupancy map. IEEE Trans Pattern Anal Mach Intell 30(2):267–282
Francesc MN, Sanfeliu A, Samaras D (2005) Integration of conditionally dependent object features for robust figure/background segmentation. In: Proceedings of IEEE international conference on computer vision (ICCV), vol 2, pp 1713–1720
Francesc MN, Sanfeliu A, Samaras D (2008) Dependent multiple cue integration for robust tracking. IEEE Trans Pattern Anal Mach Intell 30(4):670–685
Gavrila DM, Munder S (2007) Multicue pedestrian detection and tracking from a moving vehicle. Int J Comput Vis 73:41–59
Gedik OS, Alatan A (2013) 3-D rigid body tracking using vision and depth sensors. IEEE Trans Cybern 43(5):1395–1405
Germa T, Lerasle F, Quadah N, Cadenat V (2010) Vision and RFID data fusion for tracking people in crowds by a mobile robot. Comput Vis Image Underst 114:641–651
Han J, Pauwels EJ, de Zeeuw Paul M, de With Peter HN (2012) Employing a RGB-D sensor for real-time tracking of humans across multiple re-entries in a smart environment. IEEE Trans Consum Electron 58(2):1318–1334
Han J, Shao L, Xu D, Shotton J (2013) Enhanced computer vision with microsoft kinect sensor: a review. IEEE Trans Cybern 43(5):1318–1334
Hong Liu, Ze Yu, Hongbin Zha, Yuexian Zou, Lin Zhang (2009) Robust human tracking based on multicue integration and mean shift. Pattern Recognit Lett 30:827–837
Hong Lu, Zou WL, Li HS, Zhang Y, Fei SM (2015) Edge and color contexts based object representation and tracking. Optik 126:148–152
HTS. http://www.ces.clemson.edu/_stb/research/headtracker/seq/
Hu J, Su TM, Cheng CC, Liu, WH, Wu TI (2002) A self-calibrated speaker tracking system using both audio and video data. In: Proceedings of the 2002 IEEE international conference on control applications
INO's Video Analytics Dataset, found at URLwww.ino.ca/en/video-analytics-dataset/
Jacobs RA (2002) What determines visual cue reliability? Trends Cogn Sci 6(8):345–350
Karasulu B, Korukoglu S (2011) A software for performance evaluation and comparison of people detection and tracking methods in video processing. Multimed Tools Appl 55(3):677–723
Kasturi R, Goldgof D, Soundararajan P, Manohar V, Boonstra M, Korzhova V (2005) Performance evaluation protocol for text, face, hands, person and vehicle detection & tracking in video analysis and content extraction (VACEII). Technical report, University of South Florida
Kılıç V, Barnard M, Wang W, Kittler J (2015) Audio assisted robust visual tracking with adaptive particle filtering. IEEE Trans Multimed 17(2):186–200
Kim DY, Moongu Jeon (2014) Data fusion of radar and image measurements for multi-object tracking via Kalman filtering. Inf Sci 278:641–652
Kinect camera. http://www.xbox.com/en-US/kinect/default.htm
Klein DA BoBoT—Bonn benchmark on tracking. http://www.iai.uni-bonn.de/~kleind/tracking/index.htm
Klein DA, Schulz D, Frintrop S, Cremers AB (2010) Adaptive real-time video-tracking for arbitrary objects. In: Proceedings of IEEE IROS, Taipei, Taiwan, pp 772–777
Kong S, Heo BAJ, Paik J, Abidi M (2005) Recent advances in visual and infrared face recognitio—a review. Comput Vis Image Underst 97(1):103–135
Kumar P, Brooks MJ, Dick A (2007) Adaptive multiple object tracking using colour and segmentation cues. In: Asian conference on computer vision (ACCV 2007), Tokyo, Japan, Lecture notes in computer science, Springer, vol 4844, pp 853–863
Kumar P, Dick A, Brooks MJ (2008) Integrated Bayesian multicue tracker for objects observed from moving cameras. In: International conference on image and vision computing, New Zealand

Kumar P, Dogancay K (2011) Fusion of colour and facial features for person matching in a camera network. In: Seventh international conference on intelligent sensors, sensor networks and information processing, Adelaide

Kumar S, Marks TK, Jones M (2014) Improving person tracking using an inexpensive thermal infrared sensor. In: IEEE conference on computer vision and pattern recognition workshops

Kwon J, Lee KM (2009) Tracking of a non-rigid object via patch-based dynamic appearance modelling and adaptive basin hopping Monte Carlo sampling. In: Proceedings of IEEE CVPR, Miami, FL, USA

Lathoud G, Odobez JM, Gatica-Perez D (2004) AV16.3: an audio-visual corpus for speaker localization and tracking. In: Proceedings of the MLMI'04 workshop

Leichter I, Lindenbaum M, Rivlin E (2014) The cues in "dependent multiple cue integration for robust tracking" are independent. IEEE Trans Pattern Anal Mach Intell 36(3):620–621

Li T, Sun S, Sattar TP, Corchado JM (2014a) Fight sample degeneracy and impoverishment in particle filters: a review of intelligent approaches. Expert Syst Appl 41:3944–3954

Li Ying, Liang S, Bai B, Feng D (2014b) Detecting and tracking dim small targets in infrared image sequences under complex backgrounds. Multimed Tools Appl 71:1179–1199

Li Z, He S, Hashem M (2014c) Robust object tracking via multi-feature adaptive fusion based on stability: contrast analysis. Vis Comput 31:1432–2315

Lim YS, Jong S, Kim M (2007) Particle filter algorithm for single speaker tracking with audio-video data fusion. In: 16th IEEE international conference on robot and human interactive communication

Liu J, Liu Y, Zhang G, Zhu P, Chen YQ (2015) Detecting and tracking people in real time with RGB-D camera. Pattern Recognit Lett 53:16–23

Loy G, Fletcher L, Apostoloff N, Zelinsky A (2002) Adaptive fusion architecture for target tracking. In: IEEE international conference on automatic face and gesture recognition (FGR)

Maggio E, Smeraldi F, Cavallaro A (2007) Adaptive multi-feature tracking in a particle filtering framework. IEEE Trans Circuits Syst Video Technol 17(10):1–12

Maggio E, Cavallaro A (2005) Multi-part target representation for color tracking. In: Proceedings of IEEE international conference on image processing, Genoa, Italy, vol 1, pp 729–732

Megherbi N, Ambellouis S, Colot O, Cabestaing F (2005) Joint audio–video people tracking using belief theory. In: Proceeding of IEEE conference on advanced video and signal based surveillance

Milan A, Schindler K, Roth S (2013) Challenges of ground truth evaluation of multi-target tracking. In: Proceeding of IEEE conference on computer vision and pattern recognition workshops (CVPRW), pp 735–742

Motai Y, Jha SK, Kruse D (2012) Human tracking from a mobile agent: optical flow and Kalman filter arbitration. Signal Process Image Commun 27:83–95

MOTINAS project: courtesy of EPSRC funded MOTINAS project (EP/D033772/1). www.eecs.qmul.ac.uk/~andrea/avss2007_d.html

Munaro M, Basso F, Menegatti E (2012) People tracking within groups with RGB-D data. In: Proceedings of the international conference on intelligent robots and systems (IROS), Algarve (Portugal)

Munoz-salinas R, Miguel GS, Carnicer RM (2008) Adaptive multi-modal stereo people tracking without background modelling. J Vis Commun Image Represent 19:75–91

Murphy RR (1996) Biological and cognitive foundations of intelligent sensor fusion. IEEE Trans Syst Man Cybern A Syst Hum 26(1):42–51

Nghiem AT, Bremond F, Thonnat M, Valentin V, ETISEO (2007) Performance evaluation for video surveillance systems. In: IEEE international conference on advanced video and signal based surveillance (AVSS), London (UK)

Nickel K, Gehrig T, Ekenel H, Stiefelhagen R, McDonough J (2005) A joint particle filter for audio-visual speaker tracking. In: International conference on multimodal interfaces (ICMI05). Torento, Italy, pp 61–68

Nickel K, Stiefelhagen R (2008) Dynamic Integration of generalized cues for person tracking. ECCV 2008, Part IV, LNCS 5305:514–526

Patino L, Ferryman J (2014) PETS 2014: dataset and challenge. In: 11th IEEE international conference on advanced video and signal based surveillance (AVSS)

Perez P, Vermaak J, Blake A (2004) Data fusion for visual tracking with particles. In: Proceedings of the IEEE, vol 92(3)

PETS 2006. http://www.cvg.reading.ac.uk/PETS2006/data.html

PETS 2006 IEEE international workshop on performance evaluation of tracking and surveillance. http://www.pets2006.net/

PETS 2014 benchmark data. Multi camera sequences containing activity with different threat and difficulty levels. Pets2014.net

Pingali G, Segen J (1996) Performance evaluation of people tracking systems. In: Proceedings of IEEE workshop on applications of computer vision, pp 33–38

Polycom Worldwide [Online]. http://www.polycom.com/

Portmann J, Lynen S, Chli M, Siegwart R (2014) People detection and tracking from aerial thermal views. In: Proceedings of IEEE conference on robotics and automation

SanMiguel JC, Cavallaro A, Martinez JM (2012) Adaptive on-line performance evaluation of video trackers. IEEE Trans Image Process 21(5):1828–1837

Scheutz M, McRaven J, Cserey Gy (2004) Fast, reliable, adaptive bimodal people tracking for indoor environments. In: IEEE conference on robots system

Schlogl T, Beleznai C, Winter M, Bischof H (2004) Performance evaluation metrics for motion detection and tracking. In: Proceedings of the pattern recognition, 17th international conference on ICPR'04, 4: IEEE Computer Society, Washington, DC, USA, pp 519–522

Schulz D (2006) A probabilistic exemplar approach to combine laser and vision for person tracking. In: Robotics: science and systems (RSS), Philadelphia, USA

Senior A, Hampapur A, Ying-Li Tian, Brown L, Pankanti S, Bole R (2001) Appearance models for occlusion handling. In: IEEE international workshop on performance evaluation of tracking and surveillance, Kauai, HI

Shen C, Hengel AVD, Dick A (2003) Probabilistic multiple cue integration for particle filter based tracking. In: Sun C, Talbot H, Ourselin S, Adriansen T (eds) Proceedings of the VIIth digital image computing: techniques and applications

Smeulders AWM, Chu DM, Cucchiara R, Calderara S, Dehghan A, Shah M (2014) Visual tracking: an experimental survey. IEEE Trans Pattern Anal Mach Intell 36(7):1442–1468

Song X, Zhao H, Cui J, Shao X, Shibasaki R, Zha H (2013) An online system for multiple interacting targets tracking: fusion of laser and vision, tracking and learning. ACM Trans Intell Syst Technol 4(1):1–21

Song X, Cui J, Zhao H, Zha H (2008) Bayesian fusion of laser and vision for multiple people detection and tracking. In: Proceedings of IEEE international conference on instrumentation, control and information technology, pp 3014–3019

Spampinato C, Palazzo S, Giordano D (2012) Evaluation of tracking algorithms performance without ground truth data. In: Proceedings of 19th IEEE international conference on image processing (ICIP), Orlando, FL, pp 1345–1348

Spengler M, Schiele B (2003) Towards robust multicue integration for visual tracking. Mach Vis Appl 14(1):50–58

Spinello L, Triebel R, Siegwart R (2009) A trained system for Multimodal perception in urban environment. In: Proceedings of the IEEE ICRA, workshop on people detection and tracking

Stolkin R, Rees D, Talha M, Florescu I (2012) Bayesian fusion of thermal and visible spectra camera data for region based tracking with rapid background adaptation. In: Proceedings of IEEE international conference on multisensor fusion information and integration, pp 192–199

Strigel E, Meissner D, Seeliger F, Wilking B, Dietmayer K (2014) The Ko-PER intersection laser scanner and video dataset. In: IEEE 17th international conference on intelligent transportation systems (ITSC), pp 1900–1901

Strobel N, Spors S, Rabenstein R (2001) Joint audio-video object localization and tracking. IEEE Signal Process Mag 18:22–33

Sun Y, Bentabet L (2010) A particle filtering and DSmT based approach for conflict resolving in case of target tracking with multiple cues. J Math Imaging Vis 36:159–167

Susperregi L, Martinez-Otzeta JM, Ansuategui A, Aitorlbarguren Sierra B (2013) RGB-D, laser and thermal sensor fusion for people following in a mobile robot. Int J Adv Robot Syst 100:1–9

Talantzis F, Pnevmatikakis A, Constantinides AG (2008) Audio-visual active speaker tracking in cluttered indoors environments. IEEE Trans Syst Man Cybern B Cybern 39(3):799–807

Talha M, Stolkin R (2012) Adaptive fusion of infra-red and visible spectra camera data for particle filter tracking of moving targets. In: Proceedings of IEEE sensors conference, pp 1–4

Talha M, Stolkin R (2014) Particle filter tracking of camouflaged targets by adaptive fusion of thermal and visible spectra camera data. IEEE Sens J 14(1):151–166

Thomaidis G, Manolis Tsgas, Lytrivis P, Karaseitanidis G, Amditis A (2013) Multiple hypothesis tracking for data association in vehicular networks. Inf Fusion 14:374–383

Torabi A, Masse G, Bilodeau GA (2012) An iterative integrated framework for thermal-visible image registration, sensor fusion and people tracking for video surveillance applications. Comput Vis Image Underst 116:210–221

Treptow A, Cielniak G, Duckett T (2005) Active people recognition using thermal and grey images on a mobile security robot. In: Proceedings of the IEEE/RSJ international conference on intelligent robots and systems (IROS), Edmonton, Alberta

Triesch J, Malsburg CVD (2001) Democratic integration: self-organized integration of adaptive cues. Neural Comput 13:2049–2074
Utasi A, Benedek C (2012) A multi-view annotation tool for people detection evaluation. In: Workshop on visual interfaces for ground truth collection in computer vision applications, Capri, Italy
ViPER-GT, the ground truth authoring tool. http://vipertoolkit.sourceforge.net/docs/gt/
VIVID database. http://vision.cse.psu.edu/data/vividEval/datasets/datasets.html
Vondrick C, Patterson D, Ramanan D (2012) Efficiently scaling up crowd sourced video annotation. Int J Comput Vis (IJCV) 101:184–204
Walia GS, Rajiv K (2014) Human detection in video and images—a state-of-the-art survey. Int J Pattern Recognit Artif Intell 28(3):1–25
Walia GS, Rajiv K (2015) Robust object tracking based upon multi-cue integration for video surveillance. Multimed Tools Appl. doi:10.1007/s11042-015-2890-0
Walia Gurjit Singh, Kapoor Rajiv (2014) intelligent video target tracking using an evolutionary particle filter based upon improved cuckoo search. Expert Syst Appl 41:6315–6326
Wang JT, Chen DB, Chen HY, Yang JY (2012) On pedestrian detection and tracking in infrared videos. Pattern Recognit Lett 33(6):775–785
Wang Q, Fang J, Yuan Y (2014) Multicue based tracking. Neurocomputing 131:227–236
Wang H, David S (2006) Efficient visual tracking by probabilistic fusion of multiple cues. In: Proceedings of the 18th international conference on pattern recognition, pp 892–895
Wu H, Sankaranarayanan A, Chellappa R (2010) Online empirical evaluation of tracking algorithms. IEEE Trans Pattern Anal Mach Intell 32(8):1443–1458
Wu H, Zheng Q (2004) Self-evaluation for video tracking systems. Technical report, Department of Eletrical and Computer Engineering, Maryland University, College Park
Xu Y, Ye M, Zunhua Zhang X (2014) Locally adaptive combining color and depth for human body contour tracking using level set method. IET Comput Vis 8(4):316–328
Yang H, Shao L, Zheng F, Wang L, Song Z (2011) Recent advances and trends in visual tracking: a review. Neurocomputing 74(18):3823–3831
Yang X, Wang M, Tao D (2015) Robust visual tracking via multi-graph ranking. Neurocomputing 159:35–43
Yilmaz A, Javed O, Shah M (2006) Object tracking: a survey. ACM Comput Surv 38(4):1–45
Yin M, Zhang J, Sun H, Gu W (2011) Multicue based camshaft guided particle filter tracking. Expert Syst Appl 38(5):6313–6318
Ying L, Zhang T, Changsheng Xu (2014) Multi-object tracking via MHT with multiple information fusion in surveillance video. Multimed Syst 21:313–326
Yin F, Makris D, Velastin SA (2007) Performance evaluation of object tracking algorithms. In: 10th IEEE international workshop on performance evaluation of tracking and surveillance, PETS 2007
Zeng F, Xuan Liu, Huang Z, Ji Y (2013) Kernel based multiple cue adaptive appearance model for robust real-time visual tracking. IEEE Signal Process Lett 20(11):1094–1097
Zhang M, Ming X, Yang J (2013a) Adaptive multicue based particle swarm optimization guided particle filter tracking in infrared videos. Neurocomputing 121:163–171
Zhang X, Hong Liu, Xiaohong Sun (2013b) Object tracking with an evolutionary particle filter based on self-adaptive multi-features fusion. Int J Adv Robot Syst 10:1–11
Zhang S, Yao H, Sun X, Lu X (2013c) Sparse coding based visual tracking: review and experiment comparison. Pattern Recognit 46(7):1772–1788
Zhang X, Li Wei, Xiuzi Ye, Maybank S (2015) Robust hand tracking via novel multicue integration. Neurocomputing 157:296–305
Zhao J, Sen-ching Cheung S (2014) Human segmentation by geometrically fusing visible-light and thermal imageries. Multimed Tools Appl 73:61–89
Zheng W, Fuller N, Theriault D, Beltke M (2014) A thermal infrared video benchmark for visual analysis. In: IEEE conference on computer vision and pattern recognition workshops
Zheng Y, Meng Y (2008) Swarming Particles with multi-feature model for free-selected object tracking. In: IEEE international conference on Intelligent robots and systems, France
Zhou H, Fei M, Sadka A, Zhang Y, Li X (2014) Adaptive fusion of particle filtering and spatio-temporal motion energy for human tracking. Pattern Recognit 47:3552–3567
Zoidi O, Nikolaidis N, Tefas A, Pitas I (2014) Stereo object tracking with fusion of texture, color and disparity information. Signal Process Image Commun 29:573–589

**Journal of Atomic, Molecular, Condensate & Nano Physics**
Vol. 6, No. 3, pp. 195–206, 2015
ISSN 2349-2716 (online); 2349-6088 (print)
Published by RGN Publications

http://www.rgnpublications.com

# Role of Plasma and Doping Elements on the Growth and Field Emission Properties of Metallic Carbon Nanotube (CNT) Tip Placed over Cylindrical Surface

Research Article

Suresh C. Sharma*, Aarti Tewari and Ravi Gupta

*Department of Applied Physics, Delhi Technological University, Delhi, India*
***Corresponding author:** suresh321sharma@gmail.com

**Abstract.** Carbon nanotubes (CNTs) are currently attractive materials for a diverse range of applications because of their extra ordinary mechanical and electrical properties. Their application has already been demonstrated in field emission displays, nanoscale electronic devices, biosensors and hydrogen storage medium. The field emission properties of carbon nanotubes are an important field of study because they give very high values of current density as compared to the already existing field emission devices. The effect of various factors such as plasma parameters, substitutional atoms, dimensional effects, anode-cathode distance etc. on field emission from CNT has also been extensively studied. The present talk will cover the plasma production and effect of doping of hetero-atoms on the growth and field emission properties of Carbon Nanotubes (CNTs) tip placed over a cylindrical surface in complex plasma. A theoretical model incorporating kinetics of plasma species such as electron, ions and neutral atoms including doping elements like nitrogen (N), Boron (B), Potassium (K), Cesium (Cs) and energy balance of CNTs in complex plasma has been developed. The effect of doping elements of N, B, K, and Cs on the growth of CNTs namely the tip radius has been carried out for typical glow discharge plasma parameters. It is found that doping elements affect the radius of CNTs extensively. We obtained small radii for CNT doped with N and large radius for CNT doped with B. The field emission characteristics from CNTs have therefore been suggested on the basis of results obtained. Some of theoretical results are in compliance with the existing experimental observations.

**Keywords.** Carbon nanotubes; Doping; Field emission; Plasma

**PACS.** 61.48.De

**Received:** April 24, 2015 **Accepted:** November 26, 2015

Copyright © 2015 Suresh C. Sharma, Aarti Tewari and Ravi Gupta. *This is an open access article distributed under the Creative Commons Attribution License, which permits unrestricted use, distribution, and reproduction in any medium, provided the original work is properly cited.*

## 1. Introduction

Carbon nanotubes (CNTs) show excellent electron field emission properties because of their high aspect ratio, high chemical stability and thermal conductivity. The field emission from CNT is regarded as the most promising application of this nanostructure because they give very high values of current density as compared to the already existing field emission devices. Many extensive studies have been made by many researchers to study the field emission properties of CNTs [1–10]. Doping of CNT is an effective way to tailor the physical and chemical properties of CNTs. However, several groups have studied the field emission properties of doped CNTs [11–17].

Claye *et al.* [11] have achieved reversible insertion of lithium into purified single wall carbon nanotube electrochemically. They showed a continuous decrease in charge transfer resistance upon doping, consistent with the decrease in electronic resistivity of the electrodes. They also showed that the high lithium capacities are not due to double layer capacitance effects but to an actual ion insertion/extraction process in the bulk material.

Zhou *et al.* [12] have studied the p-type doped single wall Carbon nanotube (SWCNT) bulk samples by temperature dependent resistivity and thermo power, optical resistivity and Raman spectroscopy. All these give consistent results for Fermi level downshift ($\Delta E_F$) induced by doping. $\Delta E_F \approx 0.35$ eV and 0.50 eV for concentrated nitric and sulfuric acid doping, respectively. With these values, evolution in Raman spectra can be explained by variation in resonance condition as $E_F$ (Fermi energy level) moves down into the valance band.

Salvato *et al.* [13] have investigated the effect of potassium doping on the transport properties of the aligned single walled carbon nanotube fibers. The temperature dependence of the electrical resistance, current – voltage characteristics and the magneto resistance vs. external magnetic field of the fibers consistently shows that doping enhances the metallic characters of the fibers. In the framework of variable range of hopping theory they suggested that the increase in conduction with potassium doping is due to the increase of density of states.

Wadhawan *et al.* [14] have reported the effects of Cesium (Cs) deposition on the field emission properties of single walled carbon nanotube bundles. Cesium deposition decreases the turn on field for FE (field emission) by a factor of 2.1-2.8 and increases the FE current by six orders of the magnitude.

Xu *et al.* [1] have studied the enhance field emission mechanism by tip-flat emission mode. The results indicate that the radius of apex $r$ is an important factor in field emission with a relationship of field emission factor $\beta \propto r^{-\frac{1}{2}}$, while the tube length has little influence on $\beta$.

Levchenko *et al.* [18] have presented the results of hybrid numerical simulation of the growth kinetics of carbon nanowall like nanostructures in the plasma and neutral gas synthesis processes. Low temperature plasma based process was found to have a significant advantage over the purely neutral flux deposition in providing the uniform size distribution of nanostructure. It is shown that nanowall width uniformity is the best in the high density plasmas, worsens in lower density plasmas and is the worst in neutral gas based process.

Keidar *et al.* [19] suggested that length of SWNTs significantly increases (upto 4000 nm),

along with the purity of carbon deposit, when the magnetic field is applied to arc discharge. It is shown that nanotube charge with respect to the plasma as well as nanotube length depend on the plasma density and electric field in the inter electrode gap.

Wang *et al.* [20] have investigated the electron field emission (EFE) characteristics of vertically aligned carbon nanotubes (VACNTs) without and with treatment by the nitrogen plasma. The VACNTs with the plasma treatment showed a significant improvement in the EFE property compared to the untreated VACNTs. It is shown that the significant EFE improvement of the VACNTs after the nitrogen plasma treatment is closely related to the variation of the morphological and structural properties of the VACNTs.

Tewari and Sharma [21] presented the theoretical model to study the growth of carbon nanotube (CNT) on the catalyst substrate surface subjected to the reactive plasma. It is found that the height of the CNT increases with the ion density of the carbon ions and radius of CNT decreases with hydrogen ion density, hence field emission of electrons from the CNT increases.

Bonard *et al.* [2] reported the field emission properties of single-wall carbon nanotube films, with emphasis on current-versus-voltage (I-V) characteristics and current stability. The films are excellent field emitters, yielding current densities higher than 10 mA per $cm^2$ with operating voltage that are far lower than for other field emitters, but show a degradation of their performance with time.

Wong *et al.* [3] prepared the Silicon Carbide (SiC) nanowires on the silicon substrate using hot filament assisted chemical vapor deposition with solid silicon and carbon source. The silicon nanowire show good field emitting properties as revealed by the current-voltage characteristics.

Bonard *et al.* [4] have studied the emission behavior of single-wall, closed and opened arc discharge multiwall, and catalytically grown multiwall nanotubes, as single emitters and in film form. They suggested that to obtain good performances as well as long emitters lifetimes, the nanotube should be multi-walled and have closed, well-ordered tips.

Kenneth *et al.* [5] demonstrated that an individual nanotube exhibits current saturations above 100 nA of emission current and showed that this current saturation is a direct result of an adsorbate enhanced field emission mechanism. Current saturation results from the displacement of adsorbates from configurations of tunneling enhancement as electric field and current are increased.

Srivastava *et al.* [6] have shown the randomly oriented short and low density carbon nanotubes (CNTs) on silicon substrate. These films have superior emission characteristics compared to high density vertically aligned or randomly oriented bamboo shaped CNTs (BS-CNTs) films. These films were highly crystalline and had many open edges on the outer surface, particularly near the joints of the compartments.

In this paper, we have seen the role of different doping elements on the growth and field emission properties of a carbon nanotube (CNT) tip placed over cylindrical surface. A theoretical model is developed for spherical CNT tip placed over cylindrical surface, which is based on the charge neutrality of the CNT tip, kinetics of various species (electrons, positively charged ions, neutral atoms, and doping atoms) in plasma, number density of the CNT tip and the energy balance of various plasma species and CNT tip.

## 2. Model

Following the elegant models of the Sodha *et al.* [22, 23] and Tewari and Sharma [24], we consider the plasma containing electrons, positively charged ions and neutral atoms of three different types (1, 2 and 3) and CNT with spherical tip placed over cylindrical surface. We assume singly ionized positive charged ions. Atom 1 refers to the Carbon atom, 2 refers to the Neon, and 3 refers to the doped atoms i.e. Nitrogen (N), Boron (B), Potassium (K) and Cesium (Cs). The initial radius $a_0$ of the carbon nanotube (CNT) can be estimated by equating the accretion of electrons and positively charged ions on the CNT.

$$
\begin{aligned}
&4\pi a_0^2 n_e \left(\frac{T_e}{m_e}\right)^{\frac{1}{2}} \exp\left(\frac{-e^2}{a_0 k_B T_e}\right) + 2\pi a_0 h_0 n_e \left(\frac{T_e}{m_e}\right)^{\frac{1}{2}} \exp\left(\frac{eV_s}{k_B T_e}\right) \\
&= \pi a_0^2 \left(1 + \frac{e^2}{a_0 k_B T_e}\right) \left[ n_{i1} \left(\frac{T_{i1}}{m_{i1}}\right)^{\frac{1}{2}} + n_{i2} \left(\frac{T_{i2}}{m_{i2}}\right)^{\frac{1}{2}} + n_{i3} \left(\frac{T_{i3}}{m_{i3}}\right)^{\frac{1}{2}} \right] \\
&\quad + \left[ n_{i1} \left(\frac{T_{i1}}{m_{i1}}\right)^{\frac{1}{2}} + n_{i2} \left(\frac{T_{i2}}{m_{i2}}\right)^{\frac{1}{2}} + n_{i3} \left(\frac{T_{i3}}{m_{i3}}\right)^{\frac{1}{2}} \right] \\
&\quad \times \left[ \frac{2}{\sqrt{\pi}} \left(\frac{eV_s}{k_B T_i}\right) + \exp\left(\frac{eV_s}{k_B T_i}\right) erfc \left(\frac{eV_s}{k_B T_i}\right)^{\frac{1}{2}} \right],
\end{aligned}
$$

where

$h_0$ = height of the CNT,

$V_s$ = surface potential on the cylindrical surface,

$n_e$ = number density of electrons,

$T_e$ = electron temperature,

$k_B$ = Boltzmann's constant,

$T_i$ = ion temperature,

$n_{i1}$ = number density of ions of type 1,

$m_{i1}$ = mass of ions of type 1,

$n_{i2}$ = number density of ions of type 2,

$m_{i2}$ = mass of ions of type 2,

$n_{i3}$ = number density of ions of type 3,

$m_{i3}$ = mass of ions of type 3,

$e$ = electronic charge

**Charge neutrality equation**

$$
Q n_{cnt} + n_{i1} + n_{i2} + n_{i3} = n_e, \tag{2.1}
$$

where $Q$ = charge on CNT, $n_{cnt}$ = number density of CNT.

### Charging of the CNT

The charge is developed on the CNT due to accretion of electrons and positively charged ions on the surface of the CNT, which is given by the equation:

$$\frac{dQ}{d\tau} = I_{i1cnt} + I_{i1cntcyl} + I_{i2cnt} + I_{i2cntcyl} + I_{i3cnt} + I_{i3cntcyl} - \gamma_e \left(I_{ecnt} + I_{ecntcyl}\right), \quad (2.2)$$

where $I_{ecnt} = \pi a^2 \left(\frac{8k_B T_e}{\pi m_e}\right)^{\frac{1}{2}} n_e \exp[Q\alpha_e]$, is the electron collection current at the surface of spherical CNT tip and $\alpha_e = \left(\frac{e^2}{ak_B T_e}\right)$, $I_{ijcnt} = \pi a^2 \left(\frac{8k_B T_i}{\pi m_j}\right)^{\frac{1}{2}} n_{ij}[1 - Q\alpha_i]$, is the ion collection current due to the $j^{th}$ atom (1, 2 or 3) at the surface of spherical CNT tip.

$I_{ecntcyl} = \pi a h \left(\frac{2\pi k_B T_e}{m_e}\right)^{\frac{1}{2}} n_e \exp\left[\frac{eV_s}{k_B T_e}\right]$, is the electron collection current at the cylindrical surface of CNT.

$I_{ijcntcyl} = n_{ij} a h \left(\frac{2\pi k_B T_i}{m_{ij}}\right)^{\frac{1}{2}} \left(\frac{2}{\sqrt{\pi}} \left(\frac{eV_s}{k_B T_e}\right)^{\frac{1}{2}} + \exp\left[\frac{eV_s}{k_B T_e}\right] \mathrm{erfc}\left[\left(\frac{eV_s}{k_B T_e}\right)^{\frac{1}{2}}\right]\right)$, is the ion collection current due to $j^{th}$ type of atom (1, 2 or 3) at the cylindrical surface of CNT, $\alpha_i = \left(\frac{e^2}{ak_B T_i}\right)$, where a is the radius of the spherical tip of the CNT placed over cylindrical surface (i.e. radius at any instant of time), $\gamma_e$ is the sticking coefficient of the constituent electron at the surface of the spherical CNT tip.

### Growth rate equation of electrons

$$\frac{dn_e}{d\tau} = \left(\beta_1 n_1 + \beta_2 n_2 + \beta_3 n_3\right) - \left(\alpha_1 n_e n_{i1} + \alpha_2 n_e n_{12} + \alpha_3 n_e n_{i3}\right) - \gamma_e n_{cnt} \left(I_{ecnt} + I_{ecntcyl}\right), \quad (2.3)$$

where $\beta$ is the coefficient of ionization of the constituent neutral atoms i.e. atom 1, 2 or 3, $\alpha_j(T_e) = \alpha_{j0} \left(\frac{300}{T_e}\right)^k$ cm$^3$/sec, is the coefficient of recombination of electrons and positively charged ions due to $j^{\text{th}}$ atom i.e. atom 1 or 2 or atom 3.

First term on the RHS in this equation describes the rate of gain in electron density per unit time due to ionization of neutral atoms, second term describes the decaying rate of electron density due to electron-ion recombination, and third term describes the electron current at the surface of CNT.

### Growth rate equation of positively charged ions

$$\frac{dn_{i1}}{d\tau} = \beta_1 n_1 - \alpha_1 n_e n_{i1} - n_{cnt} \left(I_{i1cnt} + I_{i1cntcyl}\right), \quad (2.4)$$

$$\frac{dn_{i2}}{d\tau} = \beta_2 n_2 - \alpha_2 n_e n_{i2} - n_{cnt} \left(I_{i2cnt} + I_{i2cntcyl}\right), \quad (2.5)$$

$$\frac{dn_{i3}}{d\tau} = \beta_3 n_3 - \alpha_3 n_e n_{i3} - n_{cnt} \left(I_{i3cnt} + I_{i3cntcyl}\right), \quad (2.6)$$

First terms on the RHS describes the gain in ion density per unit time due to ionization of neutral atoms, second term describes the electron-ion recombination and third term describes the ion collection current to the surface of CNT.

**Growth rate equation of neutral atoms:**

$$\frac{dn_1}{d\tau} = \alpha_1 n_e n_{i1} - \beta_1 n_1 + n_{cnt}\left(1-\gamma_{i1}\right)\left(I_{i1cnt} + I_{i1cntcyl}\right) - n_{cnt}\gamma_1\left(I_{1cnt} + I_{icntcyl}\right), \tag{2.7}$$

$$\frac{dn_2}{d\tau} = \alpha_2 n_e n_{i2} - \beta_2 n_2 + n_{cnt}\left(I_{12cnt} + I_{i2cntcyl}\right), \tag{2.8}$$

$$\frac{dn_3}{d\tau} = \alpha_3 n_e n_{i3} - \beta_3 n_3 + n_{cnt}\left(1-\gamma_{i3}\right)\left(I_{i3cntcyl} + I_{i3cntcyl}\right) - n_{cnt}\gamma_3\left(I_{3cnt} + I_{3cntcyl}\right), \tag{2.9}$$

where $I_{jcnt} = \pi a^2\left(\frac{8k_BT_n}{\pi m_j}\right)^{\frac{1}{2}} n_j$, is the collection current due to $j^{\text{th}}$ type (1, 2 or 3) neutral atoms at the surface of spherical tip CNT, $I_{jcntcyl} = \pi ah\left(\frac{2k_BT_n}{m_j}\right)^{\frac{1}{2}} n_j$, is the collection current due to $j^{\text{th}}$ (1, 2 or 3) neutral atom at the cylindrical surface of CNT.

First term on the RHS describes the gain in neutral atom density per unit time due to electron-ion recombination, second term shows the decrement in neutral atom density due to ionization, third term describes the gain in neutral atom density due to neutralization of the atom collected at the surface of CNT, and the last term describes the accretion of neutral atoms of species 1 and 3 on CNT.

**Growth rate equation for the mass of CNT**

$$\begin{aligned}\frac{dm_{cnt}}{d\tau} &= m_1\gamma_1\left(I_{1cnt} + I_{1cntcyl}\right) + m_{i1}\gamma_{i1}\left(I_{i1cnt} + I_{i1cntcyl}\right) \\ &\quad + m_3\gamma_3\left(I_{3cnt} + I_{3cntcyl}\right) + m_{i3}\gamma_{i3}\left(I_{i3cnt} + I_{icntcyl}\right),\end{aligned} \tag{2.10}$$

where $m_{cnt} = \frac{4}{3}\pi a^3\rho_{cnt} + \pi a^2 h\rho_{cnt}$, is the mass of CNT and $\rho_{cnt}$ is the density of CNT.

These equations describe the gain in mass density due to collection of atoms of type 1 and 3.

**Energy balance equation for spherical CNT tip placed over cylindrical surface**

$$\begin{aligned}\frac{d\left(m_{cnt}C_pT_{cnt}\right)}{d\tau} &= n_{ecnt}\left[\gamma_e\varepsilon^s_{ec} + \left(1-\gamma_e\right)\delta_{ecnt}\left[\varepsilon^s_{ecnt} - \left(\frac{3}{2}k_B\right)T_{cnt}\right]\right] - \left(\frac{3}{2}k_B\right) \\ &\quad \times [n_{1cnt}(\gamma_1T_n + \delta_{1cnt}(1-\gamma_1)(T_n - T_{cnt})) + n_{2cnt}\delta_{2cnt}(T_n - T_{cnt}) \\ &\quad + n_{3cnt}(\gamma_3T_n + \delta_{3cnt}(1-\gamma_3)(T_n - T_{cnt}))] \\ &\quad + [(I_{i1cnt} + I_{i1cntcyl})(\varepsilon^s_{i1cnt} + \phi_1) + (I_{i2cnt} + I_{i2cntcyl})(\varepsilon^s_{i2cnt} + \phi_2) \\ &\quad + (I_{i3cnt} + I_{i3cntcyl})(\varepsilon^s_{i3cnt} + \phi_3)] \\ &\quad - \left(\frac{3}{2}k_B\right)[(1-\gamma_{1i})(I_{i1cnt} + I_{i1cntcyl}) + (I_{i2cnt} + I_{i2cntcyl}) \\ &\quad + (1-\gamma_{3i})(I_{i3cnt} + I_{i3cntcyl})]T_{cnt} - (4\pi a^2 + 2\pi ah) \\ &\quad \times \left[\varepsilon\sigma(T^4_{cnt} - T^4_a) + \left[n_1\left(\frac{8k_BT_n}{\pi m_1}\right)^{\frac{1}{2}} + n_2\left(\frac{8k_BT_n}{\pi m_2}\right)^{\frac{1}{2}} + n_3\left(\frac{8k_BT_n}{\pi m_3}\right)^{\frac{1}{2}}\right]k_B(T_{cnt} - T_n)\right],\end{aligned} \tag{2.11}$$

where $C_P$ is the specific heat of CNT at constant pressure, $\varepsilon$ is the emissivity of the material of CNT, $\sigma$ is the Stefan Boltzmann constant, $\varepsilon^s_{ijcnt}(Q) = \left(\left(\frac{(2-Q\alpha_{ji})}{(1-Q\alpha_{ji})}\right) - Q\alpha_{ji}\right) k_B T_i$, is the mean energy of $j^{th}$ type ion at the surface of CNT [25], $\varepsilon^s_{ecnt}(Q) = 2k_B T_e$, is the mean energy of electrons at the surface of CNT [25].

First, second and third term of the equation describes the rate of energy transferred to the CNT due to sticking accretion and elastic collision by constituent's species of the plasma. Fourth terms describes the energy per unit volume per unit time carries away from the surface of CNT by the neutral species generated due to recombination of the accreted ions and electrons. Fifth term describes the rate of energy dissipation in the form of radiation and conduction from the CNT to the host gas [26].

### Field Enhancement Factor

For the vertical CNT with cylindrical surface, Wang *et al.* [27] obtained an expression for field enhancement factor $\beta$ of the CNT.

$$\beta = \frac{h}{\rho} + 3.5,$$

where $h$ is the height of the CNT and $\rho$ is the radius of the CNT.

## 3. Results and Discussions

A theoretical model to study the effect of the hetero-atoms such as B, N, K and Cs on the growth of the CNTs in the complex plasma, is developed in this paper. The mass and energy balance of CNT, charging on CNT, kinetics of electrons, ions and neutral atoms have been incorporated in the present model. Growth of CNTs in complex plasma can occur in different ways like cluster formation, nucleation, coagulation and growth of embryonic nanotubes. We have studied the growth of embryonic nanotubes by condensation in complex plasma because we are willing to investigate the growth process of CNTs in the presence of hetero-atoms. These hetero-atoms act as different dopants on the surface of CNT. Neutral atoms are ionized by the electrons in plasma due to which positive ions and electrons are produced. Various processes are considered in the model like ionization process in which atom or molecule lose or gain electrons and acquire positive or negative charge, respectively, recombination process in which positive ions gain the free electrons or combine with negative ions and form the neutral atoms, sticking of plasma species on the surface of CNT.

To investigate the effect of different doping elements (N, B, K and Cs) on the growth of CNTs, numerical calculations have been carried out. Effect of addition of these dopants on the normalized radius of CNT have been investigated for the fixed number density of CNT ($n_{cnt}$), electron temperature ($T_e$), ion temperature ($T_i$), neutral atom temperature ($T_n$) and for variable number density of electrons ($n_e$), number density of ions ($n_i$), number density of neutral atoms ($n_n$) because when we change the doping element, number density of ions, electrons and neutral atoms changes. All physical quantities used are taken in CGS units.

Boundary conditions at $\tau = 0$ and all relevant parameters used are, number density of CNT ($n_{cnt}$) = $10^7$ cm$^3$, temperature of electron ($T_e$) = 0.6 eV, temperature of ion ($T_i$) = 2600 K,

temperature of neutral atom = temperature of CNT ($T_n = T_{cnt}$) = 2000 K, mass of neutral atom = mass of ion of type 1, i.e Carbon ($m_1 = m_{i1}$) = 12 amu, mass of neutral atom = mass of ion of type 2, i.e Neon ($m_2 = m_{i2}$) = 20 amu, mass of electron ($m_e$) = $9.31 \times 10^{-28}$ g, emissivity of the material of CNT ($\varepsilon$) = 0.6, specific heat of CNT at constant pressure ($C_P$) = $7 \times 10^6$ ergs/g K, density of CNT ($\rho_{cnt}$) = 4.2 g/cm$^3$, ionization energy of atom of type 1, i.e. Carbon ($\phi_1$) = 11.26 eV, ionization energy of atom of type 2, i.e. Neon ($\phi_2$) = 21.5 eV, sticking coefficient of ion and neutral atom of type 1 and 3 ($\gamma_i = \gamma_n$) = 1, initial height of CNT ($h_0$) = 10 $\mu$m.

Parameters and boundary condition at $\tau = 0$ used for undoped CNT are, number density of ions ($n_{i1} = n_{i2} = n_{i3}$) = $10^{10}$ cm$^{-3}$, number density of electrons ($n_e$) = $10^{10}$ cm$^{-3}$, number density of neutral atoms ($n_1 = n_2 = n_3$) = $10^{11}$ cm$^{-3}$, coefficient of recombination of electrons with ion of type 1 and 2 ($\alpha_{01} \approx \alpha_{02}$) = $10^{-7}$ cm$^3$/s, initial radius of CNT ($a_0$) = 1.1 nm.

Parameters and boundary condition at $\tau = 0$ used for Boron doped CNT are, number density of ions ($n_{i1} = n_{i2} = n_{i3}$) = $10^{10}$ cm$^{-3}$, number density of electrons ($n_e$) = $10^{10}$ cm$^{-3}$, number density of neutral atoms ($n_1 = n_2 = n_3$) = $10^{12}$ cm$^{-3}$, coefficient of recombination of electrons with ion of type 1 and 2 ($\alpha_{01} \approx \alpha_{02}$) = $1.08 \times 10^{-7}$ cm$^3$/s, initial radius of CNT ($a_0$) = 1.43 nm, ionization energy of atom of type 3, i.e., Boron ($\phi_3$) = 8.3 eV, mass of neutral atom = mass of ion of type 3 ($m_3 = m_{i3}$) = 10.8 amu.

Parameters and boundary condition at $\tau = 0$ used for Potassium doped CNT are, number density of ions ($n_{i1} = n_{i2} = n_{i3}$) = $10^{12}$ cm$^{-3}$, number density of electrons ($n_e$) = $10^{12}$ cm$^{-3}$, number density of neutral atoms ($n_1 = n_2 = n_3$) = $10^{11}$ cm$^{-3}$, coefficient of recombination of electrons with ion of type 1 and 2 ($\alpha_{01} \approx \alpha_{02}$) = $1.21 \times 10^{-7}$cm$^3$/s, initial radius of CNT ($a_0$) = 0.91 nm, ionization energy of atom of type 3, i.e., Potassium ($\phi_3$) = 4.3 eV, mass of atom = mass of ion of type 3 ($m_3 = m_{i3}$) = 39.08 amu.

Parameters and boundary condition at $\tau = 0$ used for Cesium doped CNT are, number density of ions ($n_{i1} = n_{i2} = n_{i3}$) = $10^{11}$ cm$^{-3}$, number density of electrons ($n_e$) = $10^{11}$ cm$^{-3}$, number density of neutral atoms ($n_1 = n_2 = n_3$) = $10^{10}$ cm$^{-3}$, coefficient of recombination of electrons with ion of type 1 and 2 ($\alpha_{01} \approx \alpha_{02}$) = $1.31 \times 10^{-7}$ cm$^3$/s, initial radius of CNT ($a_0$) = 0.84 nm, ionization energy of atom of type 3, i.e., Cesium ($\phi_3$) = 3.8 eV, mass of atom = mass of ion of type 3 ($m_3 = m_{i3}$) = 132.9 amu.

Parameters and boundary condition at $\tau = 0$ used for Nitrogen doped CNT are, number density of ions ($n_{i1} = n_{i2} = n_{i3}$) = $10^{11}$ cm$^{-3}$, number density of electrons ($n_e$) = $10^{11}$ cm$^{-3}$, Number density of neutral atoms ($n_1 = n_2 = n_3$) = $10^9$ cm$^{-3}$, coefficient of recombination of electrons with ion of type 1 and 2 ($\alpha_{01} \approx \alpha_{02}$) = $1.54 \times 10^{-7}$ cm$^3$/s, initial radius of CNT ($a_0$) = 0.73 nm, ionization energy of atom of type 3, i.e., Nitrogen ($\phi_3$) = 14.5 eV, mass of atom = mass of ion of type 3 ($m_3 = m_{i3}$) = 14 amu.

Figure 1(a) represents the growth of undoped CNT (Spherical tip placed over cylindrical surface) with respect to time. From the graph, we can interpret that normalized radius of the undoped CNT increases with time and get saturated after some time. This is because accretion of neutral atoms on the surface of CNT increases with time. The value of sticking coefficient of atom of type 1 is the important parameter for the growth of CNTs, as value of sticking coefficient increases, saturation region is achieved faster. When number of neutral atoms on the surface

of CNT increases, negative charge on the CNT decreases, which stops the further accretion of neutral atoms on the surface of the CNT and radius of the CNT attains the saturated value.

Figure 1(b) illustrates the variation of the normalized radius of the Boron doped carbon nanotube. Growth pattern is same as of undoped CNT but radius of the boron doped CNT is greater than the radius of the undoped CNT. Boron consumes electrons to form the covalent bonding with carbon to attain stability, thereby reducing the number density of electrons which reduces the ionization of neutral atoms and accretion of neutral atoms on the surface of CNT increases, hence radius of the CNT increases.

Figure 1(c) and Figure 1(d) show the variation of normalized radius of CNT when doped with alkali metals like Potassium (K) and Cesium (Cs), respectively. Growth pattern is same as of undoped CNT but radius of alkali metal doped CNT is less than the undoped CNT. Being a metal, Potassium and Cesium release electrons to form the stable bond with carbon. This increases the number density of electrons, thereby ionization of neutral atoms increases hence radius of the CNT decreases. But the radius of the Cesium doped CNT is less than the radius of Potassium doped CNT this is because, free electrons in Cesium are loosely bound than the Potassium therefore ionization of neutral atoms is more in Cesium doped CNT than the Potassium doped CNT hence accretion of neutral atoms in the case of Cesium doped CNT is less due to which radius is less than the Potassium doped CNT.

Figure 1(e) shows the time evolution of the normalized radius of the Nitrogen doped CNT. From all fives figs. we can see that radius of the Nitrogen doped CNT is least among all doped CNTs. Nitrogen is penta valent element i.e. contains five electrons in outer most shell, to attain the stability it requires three more electrons. Therefore ionization of neutral atoms is maximum in the case of Nitrogen doped CNT and accretion of neutral atoms on the surface of CNT is least and radius is minimum among all doped CNTs.

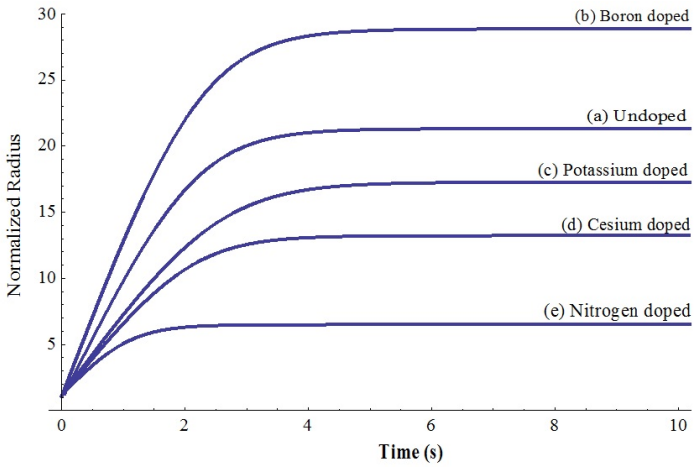


**Figure 1.** Illustrates the growth of normalized radius of spherical CNT tip placed over cylindrical surface for (a) boron doped CNT, (b) undoped CNT, (c) Potassium doped CNT, (d) Cesium doped CNT and (e) nitrogen doped CNT.

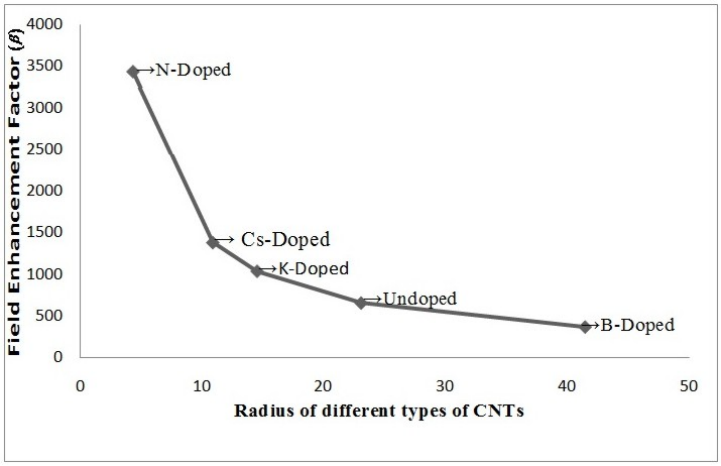


**Figure 2.** Shows the dependence of the field enhancement factor on the radius of different types of CNTs, i.e., undoped CNT, Boron doped CNT, Potassium doped CNT, Cesium doped CNT and Nitrogen doped CNT.

Figure 2 shows the variation of the field enhancement factor with respect to the radius of the CNT at constant height. From the results obtained, field enhancement factor for the different CNTs have been roughly estimated at the constant height, we have calculated the radius of all different types of CNTs and we get 23.1 nm for undoped CNT, 41.47 nm for boron doped CNT, 14.56 nm for potassium doped CNT, 10.92 nm for cesium doped CNT and 4.38 for nitrogen doped CNT, height of the CNT is considered to be 15 $\mu$m and field enhancement factor are obtained as 652.85, 365.20, 1033.71, 1377.12 and 3428.15 for undoped, boron doped, potassium doped, cesium doped and nitrogen doped CNTs, respectively. The graph between field enhancement factor and radius of the different CNTs shows that as radius (a) of the CNT decreases, field enhancement factor ($\beta$) of the CNT increases i.e. Nitrogen doped CNT has highest field emission factor and boron doped CNT has lowest field emission factor. The similar plot has been obtained experimentally by Xu *et al.* [1].

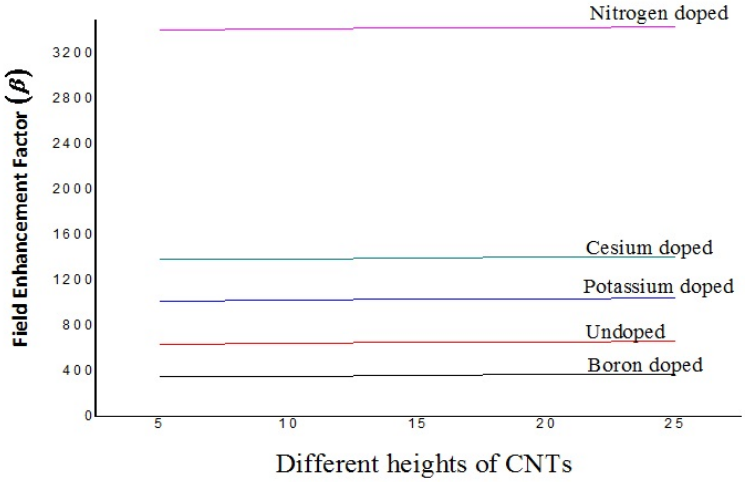


**Figure 3.** Displays the variation of the field enhancement factor with respect to the different heights of CNT for undoped CNT, Boron doped CNT, Potassium doped CNT, Cesium doped CNT and Nitrogen doped CNT.

Figure 3 shows the effect of height on the field enhancement factor of different CNTs. Radius and field emission properties of CNTs have been calculated corresponding to the different heights of CNTs. We found that the height of the CNT hardly effect the field enhancement factor of the CNT. Results obtained have also been experimentally verified by Xu *et al.* [1].

Similar results have been observed experimentally by Padya *et al.* [28], Srivastava *et al.* [8], Chan *et al.* [29], Zhang *et al.* [10], Ha and Lee [30] and Wadhawan *et al.* [14]. Therefore, doping of CNT tip with nitrogen atom can lead to enhance field emission properties. This has multiple applicative utilizations in the field of microelectronics, nanoscience and Technology.

## 4. Conclusion

A theoretical model has been developed for calculating the radius of spherical CNT tip placed over the cylindrical surface with different doping elements. The effect of different dopants has been studied with the help of an analytical model. The charging of CNT, charge neutrality, growth of electron density, neutral atom and positive ions density and energy balance of CNT with different doping elements are included in the model. It can be seen that decrease in the radius of the CNT is larger when CNT is doped with nitrogen. We conclude that radius of the CNTs has enormous effect of the field emission properties of the CNT whereas height of the CNTs does not play an important role to influence the field emission properties of the CNTs.

### Competing Interests

The authors declare that they have no competing interests.

### Authors' Contributions

All the authors contributed equally and significantly in writing this article. All the authors read and approved the final manuscript.

## References

[1] Z. Xu, X.D. Bai and E.G. Wang, *Appl. Phys. Lett.* **88** (2006), 133107.

[2] J.M. Bonard, J.P. Salvetat, T. Stockli, W.A. De Heer, L. Forro and A. Chatelain, *Appl. Phys. Lett.* **73** (1998), 918.

[3] K.W. Wong, X.T. Zhou, F.C.K. Au, H.L. Lai, C.S. Lee and S.T. Lee, *Appl. Phys. Lett.* **75** (1999), 2918.

[4] J.M. Bonard, J.P. Salvetat, T. Stockli, L. Forro and A. Chatelain, *Appl. Phys. A* **69** (1999), 245.

[5] K.A. Dean and B.R. Chalamala, *Appl. Phys. Lett.* **76** (1999), 375.

[6] S.K. Srivastava, V.D. Vankar and V. Kumar, *Nanosca le Res. Lett.* **3** (2008), 25.

[7] A.A. Koos, F. Dillon, E.A. Obraztsova, A. Crossley and N. Grobert, *Carbon* **48** (2010), 3033.

[8] S.K. Srivastava, V.D. Vankar, D.V.S. Rao and V. Kumar, *Thin Solid Films* **515** (2006), 1851.

[9] D.H. Lee, J.A. Lee, D.S. Choi, W.J. Lee and S.O. Kim, *J. Phys. Chem. C.* **114** (2010), 21184.

[10] G. Zhang, W. Duan and B. Gu, *Appl. Phys. Lett.* **80** (2002), 2589.

[11] A.S. Claye, J.E. Fischer, C.B. Huffman, A.G. Rinzler and R.E. Smalley, *J. Electrochem. Soc.* **147** (2000), 2845.

[12] W. Zhou, J. Vavro, N.M. Nemes and J.E. Fischer, *Phys. Rev. B* **71** (2005), 205423.

[13] M. Salvato, M. Lucci, I. Ottaviani and M. Cirillo, *Phys. Rev. B* **84** (2011), 233406.

[14] A. Wadhawan, R.E. Stallcup and J.M. Perez, *Appl. Phys. Lett.* **78** (2001), 108.

[15] S.Y. Choi, Y. Kanng, K.I. Cho, K.S. Choi and D. Kim, *J. Korean Phys. Soc.* **39** (2001), 193.

[16] Y.Y. Wang, S. Gupta, J.M. Garguilo, Z.J. Liu, L.C. Qin and R.J. Nemanich, *Diamond Relat. Mater.* **14** (2005), 714.

[17] J.M. Bonard, J.P. Salvetat, T. Stockli and W.A. De Heer, *Appl. Phys. Lett.* **73** (1998), 918.

[18] I. Levchenko, K. Ostrikov, A.E. Rider, E. Tam, S.V. Vladimirov and S. Xu, *Phys. Plasmas* **14** (2007), 0632502.

[19] M. Keidar, I. Levenchko, T. Arbel, M. Alexander, A.M. Waas and K.K. Ostrikov, *J. Appl. Phys.* **103** (2008), 094318.

[20] B.B. Wang, Q.J. Cheng, X. Chen and K. Ostrikov, *J. Alloys Compd.* **509** (2011), 9329.

[21] A. Tewari and S.C. Sharma, *Phys. Plasmas* **21** (2011), 063512.

[22] M.S. Sodha, S.K. Mishra and S. Srivastava, *J. Appl. Phys.* **107** (2010), 103307.

[23] M.S. Sodha, S.K. Mishra and S. Misra, *Phys. Plasmas* **16** (2009), 123701.

[24] A. Tewari and S.C. Sharma, *J. Plasma Phys.* **79** (2013), 939.

[25] M.S. Sodha and S. Guha, in *Physics of Colloidal Plasmas*, edited by A. Simon and W.B. Thomson (John Wiley & Sons, New York, 1971), p. 219.

[26] M. Rosenberg, D.A. Mendis and D.P. Sheehan, *IEEE Trans. Plasma Sci.* **27** (1999), 239.

[27] X.Q. Wang, M. Wang, P.M. He and Y.B. Xu, *J. Appl. Phys.* **96** (2004), 6752.

[28] B. Padya, D. Kalita, P.K. Jain, G. Padmanabham, M. Ravi and K.S. Bhat, *Appl. Nanosci.* **2** (2012), 253.

[29] L.H. Chan, K.H. Hong, D.Q. Xiao, W.J. Hsieh, S.H. Lai, H.C. Shih, T.C. Lin, F.S. Shieu, K.J. Chen and H.C. Cheng, *Appl. Phys. Lett.* **82** (2003), 4334.

[30] B. Ha and C.J. Lee, *Appl. Phys. Lett.* **90** (2007), 023108.

**Journal of Atomic, Molecular, Condensate & Nano Physics**
Vol. 2, No. 3, pp. 215–227, 2015
ISSN 2349-2716 (online); 2349-6088 (print)
Published by RGN Publications

http://www.rgnpublications.com

# Role of Plasma Parameters on the Growth and Field Emission Properties of 2D Graphene Sheet

Research Article

Neha Gupta, Aarti Tewari and Suresh C. Sharma*

*Department of Applied Physics, Delhi Technological University, Delhi, India*
***Corresponding author:** suresh321sharma@gmail.com

**Abstract.** The role of plasma parameters (electron density and temperature, ion density and temperature) on the growth and field emission properties of two dimensional graphene sheet has been theoretically investigated. A theoretical model of charge neutrality, including the kinetics of electrons, negatively and positively charged ions, neutral atoms and the energy balance of various species has been developed. Numerical calculations of the graphene for different plasma parameters (electron density and temperature, ion density and temperature) have been carried out for the typical glow discharge plasma parameters. It is found that the thickness of graphene sheet decreases with plasma parameters and hence the field emission of electrons from the graphene sheet increases. Some of our theoretical results are in compliance with the existing experimental observations.

**Keywords.** Graphene; Plasma parameters; Thickness; Field emission

**PACS.** 61.48.Gh

**Received:** February 13, 2015 **Accepted:** October 25, 2015

Copyright © 2015 Neha Gupta, Aarti Tewari and Suresh C. Sharma. *This is an open access article distributed under the Creative Commons Attribution License, which permits unrestricted use, distribution, and reproduction in any medium, provided the original work is properly cited.*

## 1. Introduction

Graphene is a two-dimensional nanostructure that has a flat monolayer of carbon atoms arranged in a honeycomb crystal lattice. It is the thinnest known material in the universe and exhibits various peculiar physical properties [1].

The graphene has been synthesized by various methods like using solid-phase based method, *micro wave plasma enhanced chemical vapor deposition* (MWPECVD), exfoliation of graphite,

different solid carbon sources, using ion implantation, via propane chemical vapor deposition, self organized growth etc.

Graphene nanowalls, nanosheets and few layer graphene have been grown in the presence of plasma atmosphere on a variety of substrates without the use of catalysts [2–9] as well as in the presence of catalyst [10–15].

Yuan *et al.* [2] have reported synthesis of high-quality graphene sheets (GSs) containing 1- or 2 - 3 layers of graphene using MWPECVD in a gas mixture of methane and hydrogen. They presented that preferential etching of the inter-planar carbon bonding by hydrogen atoms in the plasma is essential for the formation of graphene structure.

Malesevic *et al.* [3] have presented a possible route for the mass production of freestanding *few layer graphene* (FLG) by means of MWPECVD. This technique is most promising since it does not rely on the use of catalyst and only require substrates material to withstand temperatures up to 700 °C.

Yu *et al.* [4] have reported a patterned synthesis of vertical graphene nanosheets using plasma-enhanced chemical vapor deposition. Their results suggest that the electric field distribution above the substrate material plays a key role in the graphene coverage.

Soin *et al.* [5] have grown vertically aligned few layered graphene (FLG) nanoflakes on Si (100) substrates by MWPECVD method. They suggested that the growth of FLGs proceeds via the nucleation of highly stressed nanocrystalline graphite layers. They also studied the time dependent growth of FLG nanoflakes.

French *et al.* [6] have prepared carbon nanosheets using radio frequency plasma-enhanced chemical vapour deposition and studied the structure of graphene sheets at different substrate temperatures. Their results suggest that the average number of graphene layers reduces significantly with increase of temperature.

Hiramatsu *et al.* [7] have fabricated *carbon nanowalls* (CNWs) on Si, $SiO_2$ and sapphire substrates without catalyst and have also investigated the correlation between CNW growth and fabrication conditions.

Wang *et al.* [8] have synthesized carbon nanosheets on a variety of substrates by radio-frequency plasma-enhanced chemical vapor deposition without any catalyst or special substrate treatment. They highlighted that the nanosheets consist of one to three graphene layers with a large smooth surface topography, standing roughly vertical to the substrate.

Kondo *et al.* [9] have fabricated two-dimensional carbon nanostructures, *carbon nanowalls* (CNWs), on a Si substrate using radical injection plasma-enhanced chemical vapor deposition, employing fluorocarbon ($C_2F_6$) and hydrogen ($H_2$) mixtures. They suggested that the growth rate and morphology of grown CNWs were influenced by the surface conditions of the chamber wall.

Kim *et al.* [10] have demonstrated that methane alone can provide a sufficient amount of hydrogen species for single layer synthesis on Cu foil without explicit $H_2$ flow by PECVD. They have observed that as the plasma power (10-15 W) increases, the grain size increases and decreases at higher plasma power (greater than 50 W), showing a saturation behavior when the plasma power is higher than 120 W.

Vizireanu *et al.* [11] have shown that high quality CNW materials can be obtained by downstream PECVD in a radio frequency plasma generated beam generated in Ar, injected with a $H_2/C_2H_2$ mixture. They have revealed the importance of plasma species in the growth process by investigating the correlation between the material properties and the plasma characteristics measured at different points along the flow axis.

Nandmuri *et al.* [12] have grown single and multilayer graphene films on Ni substrate by RFPECVD using remote plasma configuration.The method employed eliminates the effect of plasma electrical field on the orientation of graphene films.

Recently, Kim *et al.* [13] have reported the synthesis of single layer graphene on Cu foil in the absence of $H_2$ flow by PECVD. In this case, they have observed that the average grain size is $\approx 0.4\,\mu$m when the plasma power is 10 W, but it sharply increases to $\approx 3\,\mu$m when the plasma power is increased to 50 W. It also sharply decreased to $\approx 0.8\,\mu$m at a plasma power of 170 W.

Lee *et al.* [14] have reported synthesis of graphene film by DC plasma on $SiO_2$ substrate coated with Ni thin film. They have found that in addition to the graphene film formed at the surface of catalyst layer, a second graphene film at the catalyst/$SiO_2$ interface was observed.

The highly desirable properties of graphene due to its unique energy-momentum dispersion relation have attracted tremendous interest for numerous fundamental studies [15]. Owing unique properties such as high mobility, atomic thickness, excellent electrical conductivity, and high aspect ratio qualify graphene as an ideal candidate for field emission applications. The electrons in graphene behave as massless Dirac fermions and display the half-integer quantum Hall effect. The presence of large number of edges renders graphene superior to CNTs for electron tunneling. In view of above properties of graphene, extensive studies on field emission properties of graphene have been carried out.

Field emission from single layer graphene films prepared by Electrophoretic deposition has been reported by Wu *et al.* [16]. Malesevic *et al.* [17] have shown the electron field emission from pristine FLGs synthesized by MPECVD and obtained field emission with a turn-on field as low as $1\,\mathrm{V}\mu\,\mathrm{m}^{-1}$. Soin *et al.* [18] and Palnitkar *et al.* [19] explained the field emission behavior of pristine and doped FLGs. They found that $N_2$ plasma treated FLGs showed significant improvement in field emission characteristics. Eda *et al.* [20] reported the field emission from graphene sheets oriented at some angles with respect to the substrate surface. Zhang *et al.* [21] showed that the field enhancement factor is strongly influenced by the height, tip shape and amorphous carbon content of FLGs.

However, relations between current density and applied field, estimation of field enhancement factor [18, 22] and expression for the dependence of field enhancement factor $\beta$ at the edge on the thickness, height and width [23] have also been established.

As far as author's knowledge is concerned nobody has studied the effect of plasma on the growth and field emission properties of graphene. Hence, in the present paper, we report the role of plasma on the growth and field emission properties of two dimensional graphene sheet. In Section 2, we develop a theoretical model for graphene based on the charge neutrality of graphene, including the kinetics of various species in plasma, i.e., electrons, neutral atoms, positively and negatively charged ions and number density of graphene and the energy balance of the plasma species and graphene. After that, results and discussions are presented in Section 3. Finally, the conclusion part is given in Section 4.

## 2. Model

Following the previous model of Sodha *et al.* [24] we consider plasma containing electrons, positively charged ions of type $A$ and $B$, neutral atoms of type $A$ and $B$, and graphene is grown in the presence of plasma. The positively charged ions are assumed to be singly ionized. $V_s$ is the surface potential on the plane metallic graphene. The surface potential $V_s$ can be estimated by equating the number of electrons striking on the graphene surface and number of ions striking on the graphene surface.

$$n_e\left(\frac{T_e}{m_e}\right)^{\frac{1}{2}}\exp\left(-\frac{eV_s}{k_BT_e}\right)=\left(1+\frac{eV_s}{k_BT_i}\right)\left[n_{iA}\left(\frac{T_i}{m_{iA}}\right)^{\frac{1}{2}}+n_{iB}\left(\frac{T_i}{m_{iB}}\right)^{\frac{1}{2}}\right]$$

or

$$\exp\left(-\frac{eV_s}{k_BT_e}\right)=\left(1+\frac{eV_s}{k_BT_i}\right)\left[\frac{n_{iA}}{n_e}\left(\frac{T_i}{T_e}\times\frac{m_e}{m_{iA}}\right)^{\frac{1}{2}}+\frac{n_{iB}}{n_e}\left(\frac{T_i}{T_e}\times\frac{m_e}{m_{iB}}\right)^{\frac{1}{2}}\right] \tag{1}$$

where

$n_e$ = number density of electron,
$T_e$ = electron temperature,
$T_i$ = ion temperature,
$k_B$ = Boltzmann's constant,
$n_{iA}$ = number density of ion $A$,
$m_{iA}$ = mass of ion $A$,
$n_{iB}$ = number density of ion $B$,
$m_{iB}$ = mass of ion $B$,
$e$ = electronic charge,

### A. Charge Neutrality Equation

$$Zn_{gn}+n_{iA}+n_{iB}=n_e, \tag{2}$$

where

$Z$ = charge on graphene,
$n_{gn}$ = number density of graphene.

### B. Charging of the Graphene

This equation describes the charge developed on the graphene due to accretion of electrons and positively charged ions on the surface of graphene.

$$\frac{dZ}{dt}=n_{iAgn}+n_{iBgn}-\gamma_e n_{egn}, \tag{3}$$

where

$n_{egn} = A\left(\frac{2\pi k_B T_e}{m_e}\right)^{\frac{1}{2}} n_e \exp\left[-\frac{eV_s}{k_B T_e}\right]$ is the electron collection current at the graphene surface and $A = a \times b$, where $a$ is the length and $b$ is the height of graphene.

$n_{ijgn} = A\left(\frac{2\pi k_B T_i}{m_j}\right)^{\frac{1}{2}} n_{ij}\left\{\frac{2}{\sqrt{\pi}}\left(\frac{eV_s}{k_B T_i}\right)^{\frac{1}{2}} + \exp\left(\frac{eV_s}{k_B T_i}\right)\mathrm{erfc}\left[\left(\frac{eV_s}{k_B T_i}\right)^{\frac{1}{2}}\right]\right\}$ is the ion collection current at the graphene surface, $j$ refers to either $A$ or $B$ positively charged ion and $\gamma_e$ is the sticking coefficient of constituent electron at the graphene surface.

### C. Growth Rate Equation of Electron Density

The equation describes the growth rate of electron density in the plasma

$$\frac{dn_e}{d\tau} = \left(\beta_A n_A + \beta_B n_B\right) - \left(\alpha_A n_e n_{iA} + \alpha_B n_e n_{iB}\right) - \gamma_e n_{gn} n_{egn}, \tag{4}$$

where $\beta_j$ is the coefficient of ionization of the constituent neutral atoms due to external agency, $\alpha_j(T_e) = \alpha_{j0}\left(\frac{300}{T_e}\right)^k \mathrm{cm}^3/\mathrm{sec}$ is the coefficient of recombination of electrons and positively charged ions. The first term in Eq. (4) is the rate of gain in electron density per unit time on account of ionization of neutral atoms and second term is the decaying rate of the electron density due to electron-ion recombination and the third term is the electron collection current at the surface of graphene.

### D. Growth Rate Equation of Positively Charged Ion Density

The equation describes the growth rate equation of positively charged ions in plasma

$$\frac{dn_{iA}}{d\tau} = \beta_A n_A - \alpha_A n_e n_{iA} - n_{gn} n_{iAgn}, \tag{5}$$

$$\frac{dn_{iB}}{d\tau} = \beta_B n_B - \alpha_B n_e n_{iB} - n_{gn} n_{iBgn}. \tag{6}$$

The first term in Eqs. (5) and (6) is the gain in ion density per unit time on account of ionization of neutral atoms, second term is the electron-ion recombination and third term is the ion collection current to the surface of graphene.

### E. Growth Rate Equation of Neutral Atoms

The equation describes the growth rate equation of neutral atoms in plasma

$$\frac{dn_A}{d\tau} = \alpha_A n_e n_{iA} - \beta_A n_A + n_{gn}\left(1 - \gamma_{iA}\right) n_{iAgn} - n_{gn}\gamma_A n_{Agn}, \tag{7}$$

$$\frac{dn_B}{d\tau} = \alpha_B n_e n_{iB} - \beta_B n_B + n_{gn} n_{iBgn}, \tag{8}$$

where $n_{jgn} = A\left(\frac{2\pi k_B T_n}{m_j}\right)^{\frac{1}{2}} n_j$ is the neutral collection current at the surface of graphene. The first term in Eqs. (7) and (8) is the gain in neutral atom density per unit time due to electron-ion recombination, second term is the decrease in neutral density due to ionization, third term is the gain in neutral density due to neutralization of the atoms collected at the surface of graphene and the last term in Eq. (7) is the accretion of neutral atoms of species $A$ on the surface of graphene.

### F. Growth Rate Equation of the Mass of Graphene

$$A\rho_s \frac{dz}{d\tau} = m_A \gamma_A n_{Agn} + m_{iA}\gamma_{iA} n_{iAgn}, \tag{9}$$

where $A = (a \times b)$ is area of two dimensional graphene, $\rho_s$ is the surface mass density of graphene and $z$ is the thickness of graphene. The terms are the gain in mass density due to collection of atomic and ionic species $A$.

### G. Energy Balance Equation of the Electrons

$$\begin{aligned}\frac{d}{d\tau}\left(\frac{3}{2}n_e k_B T_e\right) = {} & \left(\beta_A n_A \varepsilon_A + \beta_B n_B \varepsilon_B\right) - \left(\frac{3}{2}k_B\right)(\alpha_A n_e n_{Ai} + \alpha_B n_e n_{Bi})T_e \\ & - n_{gn} n_{egn}\left\{\gamma_e \varepsilon^{lh}_{egn} + \delta_{egn}\left(1-\gamma_e\right)\left[\varepsilon^{s}_{egn} - \left(\frac{3}{2}k_B\right)T_{gn}\right]\right\} \\ & - \left(\frac{3}{2}k_B\right)[f_{eA}\delta_{eA} + f_{eB}\delta_{eB}](T_e - T_n)n_e \\ & - \left(\frac{3}{2}k_B\right)(f_{eAi}\delta_{eAi} + f_{eBi}\delta_{eBi})(T_e - T_i)n_e,\end{aligned} \tag{10}$$

where $T_n$ is the temperature of neutral atoms, $T_{gn}$ is the temperature of graphene, $\varepsilon_j$ is the mean energy of electrons due to ionization of neutral atoms, $\varepsilon^{lh}_{egn}(Z) = \varepsilon^{s}_{egn}(Z) - eV_s$ is the mean energy of electrons (at large distance from the surface of graphene) collected by graphene, $\varepsilon^{s}_{egn}(Z) = 2k_B T_e$ is the mean energy of electrons collected by graphene, $f_{ej} = f_{ej0}\left(\frac{n_j}{n_{j0}}\right)\left(\frac{T_e}{T_{e0}}\right)^{\frac{1}{2}}$ is the electron collision frequency due to elastic collisions with neutral atom, and $f_{ej0} = (8.3\times10^5)\pi {r_j}^2 n_{j0} {T_{e0}}^{\frac{1}{2}}$, $f_{eji} = f_{eji0}\left(\frac{n_{ji}}{n_{ji0}}\right)\left(\frac{T_e}{T_{e0}}\right)^{-\frac{3}{2}}$ is the electron collision frequency due to elastic collisions with positively charged ions, and $f_{eji0} = \left(5.5\frac{n_{i0}}{T_{e0}^{\frac{3}{2}}}\right)\ln\left(\frac{220T_{e0}}{n_{i0}^{\frac{1}{3}}}\right)$, $\delta_{ej}\left[\approx 2\frac{m_e}{m_j}\right]$ is the fraction of excess energy of electron lost in a collision with the neutral atom, $\delta_{eji}\left[\approx 2\frac{m_e}{m_{ji}}\right]$ is the fraction of excess energy of electron lost in a collision with positively charged ion, $\delta_{egn}\left[\approx 2\frac{m_e}{m_{gn}}\right]$ is the fraction of excess energy of electron lost in a collision with graphene, $m_j$ is the mass of neutral atom, $r_j$ is the mean radii of atomic and ionic species, $n_j$ is the number density of neutral atoms, $T_{e0}$ is the temperature of electrons in the absence of graphene, $\frac{f_{ej0}}{f_{eij0}}$ is the electron collision frequency due to collisions with atoms/ions in the absence of graphene, $n_{e0}$ is the initial number density of electrons, and $n_{j0}$ is the initial number density of neutral atom.

The first term on the right hand side in Eq. (10) is the power gained per unit volume by electrons due to ionization of neutral atoms, second term is the energy loss per unit volume per unit time due to recombination with positively charged ions in plasma, third term is the energy loss per unit volume per unit time due to the sticking accretion and elastic collisions of electrons at the surface of graphene, fourth term is the energy loss per unit volume per unit time due to elastic electron - atom collision and fifth term is the energy loss per unit volume per unit time due to elastic electron- ion collision .

Substituting the value of $\frac{dn_e}{d\tau}$ from Eq. (4) in Eq. (10), we get

$$\begin{aligned}\left(\frac{3}{2}k_B\right)n_e\left(\frac{dT_e}{d\tau}\right) = &\left[\left(\beta_A n_A \varepsilon_A + \beta_B n_B \varepsilon_B\right) - \left(\frac{3}{2}k_B\right)\left(\beta_A n_A + \beta_B n_B\right)T_e\right] \\ &- n_{gn}n_{egn}\left\{\gamma_e\left[\varepsilon^l_{egn} - \left(\frac{3}{2}k_B\right)T_e\right]\right. \\ &\left.+\delta_{egn}\left(1-\gamma_e\right)\left[\varepsilon^s_{egn} - \left(\frac{3}{2}k_B\right)T_{gn}\right]\right\} - \left(\frac{3}{2}k_B\right) \\ &\times\left[f_{eA}\delta_{eA} + f_{eB}\delta_{eB}\right](T_e - T_n)n_e - \left(\frac{3}{2}k_B\right) \\ &\times\left[f_{eAi}\delta_{eAi} + f_{eBi}\delta_{eBi}\right](T_e - T_i)n_e. \end{aligned} \tag{11}$$

## H. Energy Balance Equation for Positively Charged Ions

$$\begin{aligned}\frac{d}{d\tau}\left[\frac{3}{2}(n_{iA}+n_{iB})k_B T_i\right] = &\left(\beta_A n_A \varepsilon_{iA} + \beta_B n_B \varepsilon_{iB}\right) + \left(\frac{3}{2}k_B\right) \\ &\times n_e\left[f_{eAi}\delta_{eAi} + f_{eBi}\delta_{eBi}\right](T_e - T_i) \\ &-\left(\frac{3}{2}k_B\right)(\alpha_A n_e n_{iA} + \alpha_B n_e n_{iB})T_i \\ &- n_{gn}\left[n_{iAgn}\varepsilon^l_{iAgn} + n_{iBgn}\varepsilon^l_{iBgn}\right] - \left(\frac{3}{2}k_B\right) \\ &\times\left[\left(f_{iAA}\delta_{iAA} + f_{iAB}\delta_{iAB}\right)n_{iA}\right. \\ &\left.+\left(f_{iBA}\delta_{iBA} + f_{iBB}\delta_{iBB}\right)n_{iB}\right](T_i - T_n), \end{aligned} \tag{12}$$

where $\varepsilon^l_{ijgn}(Z) = \left(2 - \frac{eV_s}{k_B T_i}\right)k_B T_i$ is the mean energy of positively charged ions (at large distance from the surface of graphene) collected by graphene, $\varepsilon_{ij}$ is the mean energy of positively charged ions produced by the ionization of neutral atoms, $f_{ijj'} = f_{ijj'0}\left(\frac{n_{j'}}{n_{j'0}}\right)\left(\frac{m_{j'}T_i + m_{ij}T_n}{(m_{j'}T_{i0} + m_{ij}T_{n0})}\right)^{\frac{1}{2}}$ is the collision frequency of a $j$ type of ion with $j'$ ion of neutral atom, $\delta_{ijj'} = \left[\frac{2m_{ij}}{(m_{j'}+m_{ij})}\right]$ is the fraction of excess energy of a $j$ type positively charged ion, lost in a collision with neutral $j'$ kind of neutral atom, $f_{ijj'0} = \left(\frac{8}{3}\right)(2\pi k_B)^{\frac{1}{2}}(r_{ij} + r_{j'})^2\left(\frac{n_{j'0}m_{j'}}{(m_{ij}+m_{j'})}\right)\left[\left(\frac{T_{i0}}{m_{ij}}\right) + \left(\frac{T_{n0}}{m_{j'}}\right)\right]^{\frac{1}{2}}$, $T_{i0}$ and $T_{n0}$ are the initial temperatures of positively charged ions and neutrals, respectively

The first term on the right hand side in Eq. (12) is the energy gained per unit volume per unit time by the positively charged ions due to ionization of atoms, second term refers to the energy gained per unit volume per unit time due to elastic collision of ions with electrons, third term is the energy loss per unit volume per unit time due to electron-ion recombination, fourth term is the energy loss per unit volume per unit time due to sticking accretion of ions at the surface of graphene and last term is the energy lost per unit volume per unit time on account of elastic collision with neutral species. Since both species of ions are assumed to be at the same temperature, the ion-ion collisions do not contribute to the energy balance.

Substituting the value of $\frac{dn_i}{d\tau}$ from Eq. (5) and Eq. (6) in Eq. (12), we get

$$\left(\frac{3}{2}k_B\right)(n_{iA}+n_{iB})\left(\frac{dT_i}{d\tau}\right)=\left[\left(\beta_A n_A\varepsilon_{iA}+\beta_B n_B\varepsilon_{iB}\right)-\left(\frac{3}{2}k_B\right)\left(\beta_A n_A+\beta_B n_B\right)T_i\right]$$
$$+\left(\frac{3}{2}k_B\right)n_e[f_{eAi}\delta_{eAi}+f_{eBi}\delta_{eBi}](T_e-T_i)$$
$$-n_{gn}\left[n_{iAgn}\left[\varepsilon^l_{iAgn}-\left(\frac{3}{2}k_B\right)T_i\right]+n_{iBgn}\left[\varepsilon^l_{iBgn}-\left(\frac{3}{2}k_B\right)T_i\right]\right]$$
$$-\left(\frac{3}{2}k_B\right)[(f_{iAA}\delta_{iAA}+f_{iAB}\delta_{iAB})n_{iA}$$
$$+(f_{iBA}\delta_{iBA}+f_{iBB}\delta_{iBB})n_{iB}](T_i-T_n). \tag{13}$$

## I. Energy Balance Equation for Neutral Atoms

$$\frac{d}{d\tau}\left[\frac{3}{2}(n_A+n_B)k_BT_n\right]=\left[\left(\frac{3}{2}k_B\right)(\alpha_A n_e n_{iA}+\alpha_B n_e n_{iB})(T_e+T_i)\right]$$
$$+\left(\alpha_A n_e n_{iA}I_{pA}+\alpha_B n_e n_{iB}I_{pB}\right)+\left(\frac{3}{2}k_B\right)[n_e(f_{eA}\delta_{eA}$$
$$+f_{eB}\delta_{eB})(T_e-T_n)+[(f_{iAA}\delta_{iAA}+f_{iAB}\delta_{iAB})n_{iA}$$
$$+(f_{iBA}\delta_{iBA}+f_{iBB}\delta_{iBB})n_{iB}](T_i-T_n)]$$
$$+\left(\frac{3}{2}k_B\right)n_{gn}\left[(1-\gamma_{iA})n_{iAgn}+n_{iBgn}\right]T_{gn}$$
$$-\left(\frac{3}{2}k_B\right)n_{gn}\left[n_{Agn}\left[\gamma_A T_n+\delta_{Agn}(1-\gamma_A)(T_n-T_{gn})\right]\right.$$
$$\left.+n_{Bgn}\delta_{Bgn}(T_n-T_{gn})\right]$$
$$-\left(\frac{3}{2}k_B\right)(\beta_A n_A+\beta_B n_B)T_n-E_{diss}, \tag{14}$$

where

$I_{pj}$ is the ionization energy of the constituent atomic species,

$E_{diss}=\left(E_{A,diss}+E_{B,diss}\right)$, $E_{j,diss}$ is the energy dissipated per unit volume per unit time by neutral atoms to the surrounding atmosphere, $\delta_{jgn}=\left[\frac{2m_j}{(m_j+m_{gn})}\right]$ is the fraction of excess energy of an atom lost in a collision with the graphene, $T_a$ is the ambient temperature. The dissipation energy may be assumed to be proportional to the difference between the temperatures of the neutral atomic species $T_n$ and the ambient temperature $T_a$.

$E_{j,diss}=E_{j,diss0}\left[\frac{(T_j-T_a)}{(T_{j0}-T_a)}\right]$.

The constant $E_{j,diss0}$ is easily obtained by imposing the ambient condition of the complex plasma system in Eq. (14) for both constituent neutral species.

The first term on the right hand side of Eq. (14) is the power gained per unit volume by the neutral species due to recombination of electron and positively charged ions, second term is

the rate of power gained per unit volume by neutral atoms in elastic collision with electrons and positively charged ions, respectively, third term is the energy gained per unit volume per second due to formation of neutrals at the surface of the graphene on account of electron and ion collection currents. The fourth term refers to the power loss per unit volume due to sticking accretion and elastic collisions with graphene. The next term refers to the thermal energy lost per unit volume per unit time by neutral atoms due to ionization. The last term is the energy dissipation rate per unit volume by neutral atoms to the surroundings

Substituting the value of $\frac{dn_A+n_B}{d\tau}$ from Eq. (7) and Eq. (8) in Eq. (14), we get

$$\begin{aligned}\frac{3}{2}(n_A+n_B)k_B\left(\frac{dT_n}{d\tau}\right) = &\left[\left(\frac{3}{2}k_B\right)(\alpha_A n_e n_{iA}+\alpha_B n_e n_{iB})(T_e+T_i-T_n)\right]\\ &+\left(\alpha_A n_e n_{iA} I_{pA}+\alpha_B n_e n_{iB} I_{pB}\right)\\ &+\left(\frac{3}{2}k_B\right)[(f_{iAA}\delta_{iAA}+f_{iAB}\delta_{iAB})n_{iA}\\ &+(f_{iBA}\delta_{iBA}+f_{iBB}\delta_{iBB})n_{iB}](T_i-T_n)\\ &+\left(\frac{3}{2}k_B\right)n_e(f_{eA}\delta_{eA}+f_{eB}\delta_{eB})(T_e-T_n)\\ &+\left(\frac{3}{2}k_B\right)n_{gn}[(1-\gamma_{iA})n_{iAgn}+n_{iBgn}](T_{gn}-T_n)\\ &-\left(\frac{3}{2}k_B\right)n_{gn}[n_{Agn}\delta_{gn}(1-\gamma_A)(T_n-T_{gn})\\ &+n_{Bgn}\delta_{Bgn}(T_n-T_{gn})]-E_{diss}\,. \end{aligned} \tag{15}$$

## J. Energy Balance for Metallic Graphene

$$\begin{aligned}\frac{d}{d\tau}\left(A\rho_s z C_p T_{gn}\right) = &\, n_{egn}\left[\gamma_e\varepsilon^s_{egn}+\left(1-\gamma_e\right)\delta_{egn}\left[\varepsilon^s_{egn}-\left(\frac{3}{2}k_B\right)T_{gn}\right]\right]+n_{Bgn}\delta_{Bgn}(T_n-T_{gn})]\\ &\times[n_{iAgn}(\varepsilon^s_{iAgn}+I_{pA})+n_{iBgn}(\varepsilon^s_{iBgn}+I_{pB})]\\ &-\left(\frac{3}{2}k_B\right)\left[n_{Agn}\left[\gamma_A T_n+\delta_{Agn}\left(1-\gamma_A\right)\left(T_n-T_{gn}\right)\right]\right.\\ &-\left(\frac{3}{2}k_B\right)\left[\left(1-\gamma_{Ai}\right)n_{iAgn}+n_{iBgn}\right]T_{gn}-A\left[\varepsilon\sigma\left({T_{gn}}^4-{T_a}^4\right)\right.\\ &+\left[n_A\left(\frac{8k_BT_n}{\pi m_A}\right)^{\frac{1}{2}}+n_B\left(\frac{8k_BT_n}{\pi m_B}\right)^{\frac{1}{2}}\right]k_B\left(T_{gn}-T_n\right)]\,, \end{aligned} \tag{16}$$

where $\varepsilon^s_{ijgn}(Z)=\left(\left(\frac{\left(2-\frac{eV_s}{k_BT_i}\right)}{\left(1-\frac{eV_s}{k_BT_i}\right)}\right)-\frac{eV_s}{k_BT_i}\right)k_BT_i$ is the mean energy collected by ions at the surface of graphene, $C_p$ is the specific heat of the material of the graphene at constant pressure, $\varepsilon$ is the emissivity of the material of the graphene, $\sigma$ is the Stefan-Boltzmann constant.

The first three terms in Eq. (16) are the rate of energy transferred to the graphene due to sticking accretion and elastic collision by constituent species of complex plasma. The fourth

term is the energy carried away by the neutral species (generated by the recombination of the accreted ions and electrons) from the graphene per unit volume per unit time. The last term is the rate of energy dissipation of the graphene through radiation and conduction to the host gas.

## 3. Results and Discussions

The calculations have been carried out to study the dependence of thickness of graphene on the plasma parameters, i.e., $n_e$, $T_e$, $n_i$, $T_i$.

We have solved the Eqs. (2), (3), (4), (5), (6), (7), (8), (9), (13), (15) and (16) simultaneously for charging of graphene, kinetics and energy balance of electrons, ions, neutrals and of graphene with appropriate boundary conditions, viz., at $\tau = 0$, graphene number density $(n_{gn}) = 10^4$ cm$^{-3}$, ion number density of type $A$ $(n_{iA0} = 0.8n_{e0})$, ion number density of type $B$ $(n_{iB0} = 0.2n_{e0})$, neutral atom number density of type $A$ and $B$ $(n_{A0}$ and $n_{B0}) = (1 \times 10^{10}$ cm$^{-3})$, electron number density $(n_{e0}) = (10^8$ cm$^{-3})$, electron temperature $T_{e0} = 0.8$ eV, ion temperature $T_{i0} = 2400$ K, neutral temperature $T_{n0}$ = graphene temperature $T_{gn} = 2000$ K, a (length of graphene) = 5 $\mu$m, $b$ (height of graphene) = 5 nm.

Other parameters used in the calculations are, e.g., mass of ion $A$ $(m_{iA}) \approx$ mass of neutral atom $A$ $(m_A) = 12$ amu (Carbon), mass of ion $B$ $(m_{iB}) \approx$ mass of neutral atom $B$ $(m_B) = 39.948$ amu (Argon), coefficient of recombination of electrons and positive ion of type $A$ and $B$ $(\alpha_{A0} \approx \alpha_{B0}) = 10^{-7}$ cm$^3$/sec, emissivity of material of graphene $(\varepsilon) = 0.6$, sticking coefficient of ion $A$ and neutral atom $A$ $(\gamma_A = \gamma_{iA}) = 1$, work function of graphene $\phi = 5$ eV (Carbon), specific heat of graphene $C_p = 7 \times 10^6$ ergs/gK, ionization energy of neutral atom $A$ $(I_{pA}) = 5.26$ eV, ionization energy of neutral atom $B$ $(I_{pB}) = 7$ eV, $\varepsilon_A = 4.69$ eV, $\varepsilon_B = 6.7$ eV, mean energy of positively charged ions produced by the ionization of neutral atom $A$ $(\varepsilon_{iA}) = 4.78$ eV, mean energy of positively charged ions produced by the ionization of neutral atom $B$ $(\varepsilon_{iB}) = 7.03$ eV, dissipation energy of neutral atom $A$ $(\varepsilon_{A,diss0}) = 1820.9$ eV, dissipation energy of neutral atom $B$ $(\varepsilon_{B,diss0}) = 799.6$ eV, $\kappa = -1.2$, initial thickness $z_0 = 4$ nm and density of graphene $\rho_{gn} = 2.2$ g/cm$^3$, surface potential $V_s = -400$ stat V.

Figure 1 illustrates the variation of normalized thickness of graphene sheet for different electron density and temperature (e.g., $n_{e0} = 10^7$ cm$^{-3}$ and $T_{e0} = 0.6$ eV, $n_{e0} = 10^8$ cm$^{-3}$ and $= T_{e0} = 0.7$ eV, $n_{e0} = 10^9$ cm$^{-3}$ and $T_{e0} = 0.8$ eV) and for other parameters are same as mentioned above. From Figure 1 it can be seen that the normalized thickness of graphene first increases with time and then attains a saturation value. It also shows the decrease of normalized thickness of graphene $z/z_0$ with electron density and temperature. The decrease of $z/z_0$ with electron density and temperatures is because with increase in electron densities and temperatures more and more neutral atoms ionizes to produce positively charged ions and electrons. Since, on the increase of electron density and temperature, the surface potential on graphene surface increases which corresponds to lesser number of ions and neutral atoms sticking to graphene surface, the decrease in its thickness is observed.

Figure 2 displays the variation of the normalized thickness of graphene $z/z_0$ with time for different ion number density and ion temperatures (e.g., $n_{i0} = 10^8$ cm$^{-3}$ and $T_{i0} = 2100$ K, $n_{i0} = 10^9$ cm$^{-3}$ and $T_{i0} = 2200$ K, $n_{i0} = 10^{10}$ cm$^{-3}$ and $T_{i0} = 2300$ K). From Figure 2 it can be seen that the thickness of graphene first increases with time and then attains a saturation

value. The thickness of graphene decreases with ion density $n_{i0}$ (in cm$^{-3}$) and temperature $T_i$ (in K) can also be seen. This happens because by increasing the ion density and temperatures, more and more neutral atoms ionize to produce positively charged ions and electrons. The reason behind the decrease in thickness of graphene with ion density and temperature is the increase of surface potential on graphene surface as explained for Figure 1.

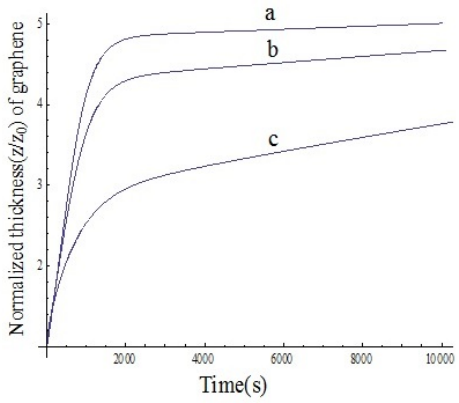


**Figure 1.** Shows the variation of the normalized thickness $z/z_0$ of graphene sheet for different electron number density and temperature where $a$, $b$ and $c$ corresponds to $n_{e0} = 10^7$ cm$^{-3}$ and $T_{e0} = 0.6$ eV, $n_{e0} = 10^8$ cm$^{-3}$ and $= T_{e0} = 0.7$ eV, $n_{e0} = 10^9$ cm$^{-3}$ and $T_{e0} = 0.8$ eV, respectively (the other parameters are given in the text).

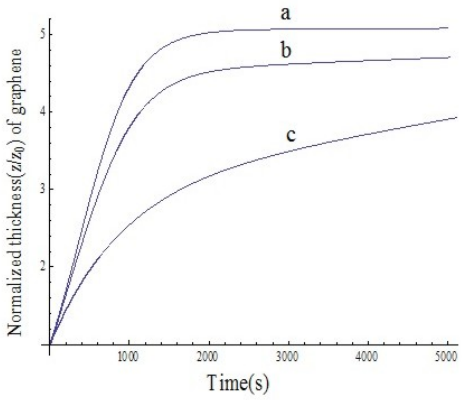


**Figure 2.** Shows the variation of the normalized thickness $z/z_0$ of graphene sheet for different ion number density and temperature where $a$, $b$ and $c$ corresponds to $n_{i0} = 10^8$ cm$^{-3}$ and $T_{i0} = 2100$ K, $n_{i0} = 10^9$ cm$^{-3}$ and $T_{i0} = 2200$ K, $n_{i0} = 10^{10}$ cm$^{-3}$ and $T_{i0} = 2300$ K, respectively (the other parameters are given in the text).

The variation of graphene's thickness in plasma has also been experimentally demonstrated by French *et al.* [6] where there is reduction in graphene's thickness with increasing substrate temperature. Our results are also consistent with Nang and Kim [28] and Kim *et al.* [13] where they have shown that graphene thickness decreases with increasing plasma power and growth time because of the etching by atomic H. Moreover, with increase in electron density and temperatures (plasma parameters), ions of $A$ type will decay faster leading to decrease in dimensions of nanostructures which is consistent with the experimental observations of Lee *et al.* [25] and Srivastava *et al.* [26].

Using the results obtained, the variation of the field emission factor with plasma parameters can be estimated. Since the field emission factor [23]

$$\beta_{edge} = 1.77\left(\frac{h}{t}\right)^{0.75}\left[1+0.09\left(\frac{h}{w}\right)\right][0.75+0.25\cos\phi]\left(\frac{d}{t}\right)^{-0.19},$$

where $h$ is the height of graphene and $t$ is the thickness of graphene) is inversely proportional to the thickness of graphene. From the above discussions, it is clear that the thickness of graphene decreases with increase of the plasma parameters (i.e., plasma density and temperatures) therefore, the increase in plasma parameters should lead to larger $\beta_{edge}$. The increase in field enhancement factor $\beta$, is proportional to the increase in the field emission current [18–22], so from our results it is clear that through varying plasma parameters, we can obtain larger $\beta$ or field emission current. The above observation have also been validated by Peltekis *et al.* [27] where graphene ribbons have electron and hole field-effect mobilities of 11.2 and 31.9 $cm^2/V_s$, respectively prior to treatment and 44.8 and 143.6 $cm^2/V_s$, respectively after treatment. The increased mobilities of electron and hole from plasma treated graphene imply increased current from graphene.

## 4. Conclusion

An analytical model for the growth kinetics of the graphene in complex plasma has been developed. The approach is based on the charge neutrality, number density of electrons, positively charged ions, neutral atoms and graphene. The energy balance of the participating species has also been considered because the accretion process gets significantly affected by the increase of electron and ion temperatures. It can be concluded from our study that on increasing the plasma parameters, the thickness of graphene sheet reduces and consequently the field emission factor increases. The present analysis presents the growth mechanism involved in growing graphene in plasma which has been widely reported and extending recent studies to correlate graphene's thickness in plasma with plasma parameters and estimating the field enhancement factor of graphene.

## Acknowledgement

This work has been partially supported by the Department of Science and Technology (DST), SERB, Government of India.

### Competing Interests

The authors declare that they have no competing interests.

### Authors' Contributions

All the authors contributed significantly in writing this article. The authors read and approved the final manuscript.

## References

[1] K.S. Novoselov, A.K. Geim, S.V. Morozov, D. Jiang, M.I. Katsnelson, I.V. Grigorieva, S.V. Dubonos and A.A. Firsov, *Nature* **438**, 197 (2005).

[2] G.D. Yuan, W.J. Zhang, Y. Yang, Y.B. Tang, Y.Q. Li, J.X. Wang, X.M. Meng, Z.B. He, C.M.L. Wu, I. Bello, C.S. Lee and S.T. Lee, *Chem. Phys. Lett.* **467**, 361 (2009).

[3] A. Malesevic, R Vitchev, K. Schouteden, A. Volodin, L. Zhang, G. Van Tendeloo, A. Vanhulsel and C.V. Haesendonck, *Nanotechnology* **19**, 305604 (2008).

[4] K. Yu, P. Wang, G. Lu, K.H. Chen and Z. Bo, *J. Chen. Phys. Chem. Lett.* **2**, 537 (2011).

[5] N. Soin, S.S. Roy, C. O'Kane, J.A.D. McLaughlin, T.H. Lim and C.J.D. Hetherington, *Cryst. Eng. Comm.* **13**, 312 (2011).

[6] B.L. French, J.J. Wang, M.Y. Zhu and B.C. Holloway, *J. Appl. Phys.* **97**, 114317 (2005).

[7] M. Hiramatsu, K. Shiji, H. Amano and M. Hori, *Appl. Phys. Lett.* **84**, 4708 (2004).

[8] J.J. Wang, M.Y. Zhu, R.A. Outlaw, X. Zhao, D.M. Manos, B.B. Holloway and V.P. Mammana, *Appl. Phys. Lett.* **85**, 1265 (2004).

[9] S. Kondo, M. Hori, K. Yamakawa, Shoji den, H. Kano and M. Hiramatsu, *J. Vac. Sci. Technol. B* **26**, 4 (2008).

[10] Y.S. Kim, J.H. Lee, Y.D. Kim, S.-K. Jerng, K. Joo, E. Kim, J. Jung, E. Yoon, Y.D. Park, S. Seo and S.-H. Chun, *Nanoscale* **5**, 1221 (2013).

[11] S. Vizireanu, S.D. Stoica, C. Luculescu, L.C. Nistor, B. Mitu and G. Dinescu, *Plasma Sources Sci. Technol.* **19**, 034016 (2010).

[12] G. Nandamuri, S. Roumimov and R. Solanki, *Appl. Phys. Lett.* **96**, 154101 (2010).

[13] K.Y. Seung, L.J. Hong, K.Y. Duck, J. Sahng-Kyoon, K. Joo, E. Kim, J. Jung, E. Yoon, P.Y. Daniel, S. Sunae and C. Seung-Hyun, *Nanoscale* **5**, 1221 (2013).

[14] C.S. Lee, L. Barton, Z.B. He, J.L. Maurice, D. Pribat and D. Cojocaru, *Phys. Rev.* **82**, 153412 (2010).

[15] A.K. Geim and K.S. Novoselov, *Nat. Mater.* **6**, 18 (2007).

[16] Z. Shuai, S. Pei, W. Ren, D. Tang, L. Gao, B. Liu, F. Li, C. Liu and H.M. Cheng, *Adv. Mater.* **21**, 1756 (2009).

[17] A. Malesevic, R. Kemps, A. Vanhulsel, M.P. Chowdhury, A. Volodin and C.V. Haesendonck, *J. Appl. Phys.* **104**, 084301 (2008).

[18] N. Soin, S.S. Roy, S. Roy, K.S. Hazra, D.S. Misra, T.H. Lim, C.J. Hetherington and J.A. McLaughlin, *J. Phys. Chem. C* **115**, 5366 (2011).

[19] U.A. Palnitkar, R.V. Kashid, M.A. More, D.S. Joag, L.S. Panchakarla and C.N.R. Rao, *Appl. Phys. Lett.* **97**, 063102 (2010).

[20] G. Eda, H.E. Unalan, N. Rupesinghe, G.A.J. Amaratunga and M. Chhowalla, *Appl. Phys. Lett.* **93**, 233502 (2008).

[21] Y. Zhang, J. Du, S. Tang, P. Liu, S. Deng, J. Chen and N. Xu, *Nanotechnology* **23**, 015202 (2012).

[22] T.T. Baby and S. Ramprahbu, *J. Appl. Phys.* **111**, 04311 (2012).

[23] S. Watcharotone, R.S. Ruoffa and F.H. Read, *Physics Procedia* **1**, 71 (2008).

[24] M.S. Sodha, S. Misra, S.K. Mishra and S. Srivastava, *J. Appl. Phys.* **107**, 103307 (2010).

[25] S.F. Lee, Y.-P. Chang and L.-Y. Lee, *J. Mater. Sci. Mater. Electron* **20**, 851 (2009).

[26] S.K. Srivastava, A.K. Shukla, V.D. Vankar and V. Kumar, *Thin Solid Films* **515**, 1851 (2006).

[27] N. Peltekias, S. Kumar, N. McEvoy, K. Lee, A. Weidlich and G. S. Duesberg, *Carbon* **50**, 395 (2012).

[28] L.V. Nang and E.T. Kim, *Journal of The Electrochemical Society* **159**, K-93 (2012).

International Journal on Textile Engineering and Processes, ISSN: 2395-3578
Vol 1, Issue 4,
October 2015

# Studies of Banana SAP used as mordant for natural dye

Shyam Barhanpurkar[1], Prabhakar Bhat[2] ,Alok Kumar[3], Roli Purwar[4].
Shyambarhanpurkar@yahoo.co.in
1 .Assistant professor, Dept of Textile Technology, SVITS indore
2. Director, Govt. college of Textile Institute, Kanpur
3. Assistant professor, Dept of Polymer Science, Delhi college of engineering Delhi

## INTRODUCTION

India has a rich biodiversity and it is not only one of the world's twelve mega diversity countries, but also one of the eight major center of origin and diversitification of domesticated places. It has approximately 490,000 plant species of which about 17,500 are angiosperms more than 400 are domesticated crop species and almost an equal number their wild relatives. Thus, India harbor a wealth of useful germplasm resources and there is no doubt that the plant kingdom is a treasure-house of diverse natural products. One such product from nature is the dye.

Natural dyes are dyes or colorants derived from plants, invertebrates, or minerals. The majority of natural dyes are vegetable dyes from plant sources – roots, berries, bark, leaves, flower and wood and other organic sources such as fungi and lichens. Natural dyes are known for their use in colouring of food substrate, leather, wood as well as natural fibers like wool, silk, cotton and flax as major areas of application since ancient times.

Natural dyes produce an extraordinary diversity of rich and colours that complement each other. Natural dyes from plants may also have dozens of compounds and their properties vary with soil type and dyes are one of the most important uses of the plants, as they are related with cultural practices, rituals, arts and crafts, fabrics and to satisfy personal embodiment, however, dye yielding plants have not received significant attention the weather. Synthetic dyes are produced at high temperature and pressure from chemicals isolated from petroleum derivatives. During the manufacturing process of dyes many carcinogenic chemicals are used which leads to formation of toxic by-products. These by- products are discharge in rivers and ponds or left in open. Hence cause severe water and atmospheric pollution. The production of synthetic chemical dyestuffs has become big business, but unfortunately the production and use of these synthetic dyes is one of the world's most polluting industries. Conventional synthetic dyes present health risks to those working with them and to those who wear them, as well as damaging the environment in a number of ways. The dyes in solution are absorbed by the fibers. The process of transferring the dye from the water to the fiber is called exhaustion or "fixation rate", with 100% exhaustion meaning there is no dye left in the dyebath solution. Most conventional dyes have an exhaustion rate of 80%, meaning the dyestuff which is not affixed to the fiber is flushed into our rivers with the spent process water. Each year the global textile industry discharges 40,000 – 50,000 tons of dye into our rivers, and more than 200,000 tons of salt. One of the most pressing issues today is the lack of fresh drinking water, and as one of the most polluting industries, textiles – and especially the dyeing of textiles – is responsible for many instances of pollution making fresh water undrinkable. The 40,000 to 50,000 tons of synthetic dyestuffs expelled into our rivers are complex chemical formulations containing some things that are very toxic to us, such as heavy metals (like lead, mercury, chromium, zinc, cobalt and copper), benzene and formaldehyde. Many certifications, such as the new Global Organic

## MORDANTS

A mordant is a substance used to set dyes on fabrics or tissue sections by forming a coordination complex with the dye which then attaches to the fabric or tissue. It may be used for dyeing fabrics, or for intensifying stains in cell or tissue preparations. The term is derived from the Latin *mordere*, to bite.

**Effects of Chemical Mordant**

## BANANA PSEUDOSTEM SAP AS MORDANT

In India, banana is cultivated on 5.65 lakh ha area and the leading states are Maharashtra (0.54 lakh ha), Gujarat (0.49 lakh ha), Tamil Nadu (0.82 lakh ha), Andhra Pradesh (0.56 lakh ha), Karnataka (0.42 lakh ha) and Kerala (0.59 lakh ha). In addition to fruit production, huge quantity of biomass (pseudostem, leaves, suckers etc.) is generated. Presently, this biomass is discarded as waste.

## ORIGIN OF BANANA

Alexander the Great discovered the taste of the banana in the valleys of India in 327 BC. The existence of an organized banana plantation could be found in China in 200 AD. The word banana is of West African origin, and passed into English via Spanish or Portuguese.

**Museceae**

Musaceae is a botanical name for a family of flowering plants. The family is native to the tropics of Africa and Asia. The plants have a large herbaceous growth habit with leaves with overlapping basal sheaths that form a pseudostem making some members appear to be woody trees.

**Genus Musa**

The genus *Musa* was first described by the pre-Linnean Rumphius. The name may derive from *mauz {mouz* or *moz)* the Arabic word for the banana fruit, but it was accepted by Linnaeus because it could have been in commemoration of Antonius Musa

## Review of Literature

### 6.Work done on Banana pseudostem

The banana pseudo stem has been reported to contain high quality starch (Shantha and siddappa, 1970). The banana Pseudo-stem show satisfactory physical properties, such as relatively high tensile strength and stiffness, which indicate its prospect as a promising fibre material. The application of natural fibers including banana Pseudo-stem has been proved promising in various technical fields, such as replacing synthetic fibers as reinforcement in various composites used in automobile parts (Pothan and Thomas ,2003) Ammayappan *et al.* (2004),studied the natural dye from pseudostem of banana for silk. The result revealed that pseudostem of banana contain 2-3% dye, which gives vanilla cream colour without mordanting and with mordants gave different colour only in pale and light shade on silk fabric. Each plant produces a single bunch of fruits.After harvesting, the bare Pseudo-stem are cut and thus, several tons of banana Pseudo-stem are produced daily on the plantations (Cordeiro *et al.*, 2004). In general, banana Pseudo-stem is an abundant natural resource in subtropical and tropical regions and has potential for providing profitable product such as manure(Ultra et at.2005). Anirudhan(2006) and Noeline (2005) studied new absorbent systems containing banana Pseudo-stem. These absorbent systems, which can remove phosphate from wastewater, exhibit high absorption potential and satisfactory recyclability. Zainudin (2009) studied the thermal behavior of banana Pseudo-stem (BSP) filled unplastisized polyvinyl chloride (UPVC) composites. From the study, the thermal stability of the composites was found to be higher than that of BPS fiber and the UPVC matrix. The physicochemical properties of plantain *(Musa paradisiaca)* and banana *(Musa sapientum)* pseudostem wastes have been determined. The results showed that the green plantain and banana pseudostem wastes contain high amount of carbohydrate which can be converted into sugar (glucose) by saccharification and fermentation into alcohol (biofuel), it can also be used in the paper making and in the preparation of cellulose derivatives; both samples have very high moisture content.( Akpabio *et al.*,2012)

## MATERIALS AND METHODS

### 7.1 Chemicals and Reagents

Iodine solution, Benedict's reagent, Barfoed's reagent, Seliwanoff's solution, Sulfuric acid, Acetic acid, Acetone, Sodium hydroxide, Fehling's reagent A, Fehling's reagent B, Cotton fabric, Alum, Myrobalan, *Butea* flowers dye, Folin Phenol reagent, Sodium carbonate solution.

### 7.2 Instrumentation

Hot air oven, Water bath, Desiccators, pH meter, Weighing machine, Spectrophotometer

### 7.3 Sample site

Banana plant pseudostem sap was collected from Raver Tehsil (Maharastra) just near Burhanpur (M.P.).

### 7.4 Sampling Process

The pointed end of the knife was pushed tangentially into the stem. The incision were left to bleed for 24 h and stored in a wide mouth plastic bottle in refrigerator until use.

### 7.5 Pseudostem sap colour:

Pseudostem sap is thick liquid and very light brown or dusty in colour.

Fig 1

### 8. Analysis of the composition of the Banana pseudostem sap:

Qualitative analysis for carbohydrate by Cole's method,(Cole,1933).

**Quantitative analysis of carbohydrate:**

**8.1Molisch's Test:** In a test tube, 2 ml. of the test solution and 2 drops of α-naphthol solution were added. The tube was carefully inclined and conc. $H_2SO_4$ were poured drop wise, using a dropper, along the sides of the tube. Violet colour at the junction of two liquids was observed.

**8.2 Fehling's Test:** In a test tube 2 ml. of the test solution and add equal volumes of Fehling A and Fehling B were added and placed it in a boiling water bath for few minutes. When the content of test tube started boiling, they were mixed together and observed for any change in colour or precipitate formation. The production of yellow or brownish –red precipitate of cuprous oxide indicated the presence of reducing sugars in the given sample.

**8.3 Benedict's Test:** To 2 ml. of Benedict's regent, 5 drops of the test solution were added and mixed well. The test tube were placed in a boiling water bath for 5 minutes after that the solution were cooled and observed for any change in colour or precipitate formation. The colour change from blue to green, yellow, orange or red (depending upon the amount of reducing sugar present in test sample) were observed.

**8.4 Barfoed's Test:** To 2 ml. of the test solution about 2 ml. Barfoed's reagent were added. Mixed well and boiled for one minute in the water bath. The solution were allowed to stand for few minutes. Formation of a red precipitate of cuprous oxide in the bottom and along the sides of the test tube immediately, indicated the presence of monosaccharide.Since Barfoed's reagent is weakly acidic, it is reduce only by monosaccharides.

**8.5 Seliwanoff 's Test:** To 2 ml. of Seliwanoff's reagent, two drops of test solution were added and mixture was heated to just boiling. A Cherry red condensation product was observed indicating the presence of ketoses in the test sample.

**8.6 Iodine Test:** 2 drops of iodine solution were added to about 2 ml. of the

test solution. A blue black colour was observed which is indicative of presence of polysaccharides.

**9. Chemical analysis**

**9.1 Sample preparation:**

A petriplate previously cleaned and dried in an oven was weighed on an analytical balance to 0.01 g. 30 gm of banana pseudostem sap was placed on the petriplate. The sap was dried in oven at 60°C for 24 hours with the cover off. Then the petriplate was removed and placed in the desiccator for 15 minutes to cool, before weighing. Procedure is referred from TAPPI Standard.

**9.2 Determination of Holocellulose content (TAPPI Standard T 222os – 74) :**

2 g of air dried sawdust was weighed accurately. The sawdust was transferred quantitatively to a 250 ml conical flask. 100 ml water, 1.5g sodium chloride and 5 ml of 10% acetic acid were added and the flask was placed in a water bath maintained at 70°C, swirling the content of the flask at least once every five minutes. The flask was kept closed with a small, inverted Erlenmeyer flask. 5 ml of 10% acetic acid was added after 30 minutes. 1.5g sodium chloride was added after further 30 minutes. Alternative acetic acid and sodium chloride at 30 minutes were continued, after last addition of sodium chloride. The mixture was heated for 30 minutes after last addition of sodium chloride. The suspension was cooled in an ice bath. Residue was filtered into a weighed fruited glass crucible (medium or coarse porosity) and washed with iced distilled water and finally washed with acetone. The residue was air-dried (allowed the residue to strand in the open laboratory for a day or two until it is free of acetone) Covered it with a perforated aluminium foil. The sample was transferred to a desiccator and weighed at daily intervals until the sample reached constant weight. The moisture content was determined on a 0.5 g sample which is afterward. The following formula was used to determine the holocellulose content in pseudostem: Holocellulose content in pseudostem sap (percent)

$$= \frac{W_4 - W_3}{100 \times W_2} \times (100 - W_1)$$

where,

$W_1$ = extractive free content (percent)

$W_2$ = weight of oven- dried extractive free sample (grams)

$W_3$ = weight of oven dried crucible (grams)

$W_4$= weight of oven- dried residue and crucible (grams)

**9.3 Determination of Cellulose content (TAPPI Standard T203 om- 93):**

Weigh 1 gm of a holocellulose sample and placed in 200 ml beaker. Add 25 ml of 17.5% sodium hydroxide and stir. After 4 minutes, smash for 5 minutes. After 16 minutes, add 25 ml of distilled water and stir for 1 minute. After 5 minutes, filter with a preweighed glass filtering crucible and wash with distilled water until neutral. Add 40 ml of 10% acetic acid and hold for 5 minutes. Weigh the residue to calculate the α-cellulose content.

α-cellulose content in pseudostem sap (percent)

$$= \frac{W_4 - W_3}{100 \times W_2} \times W_1$$

where,

$W_1$ = Holocellulose content (percent).

$W_2$ = weight of oven- dried holocellulose sample (grams).

$W_3$ = weight of oven dried cruicible (grams).

$W_4$ = weight of oven dried residue and crucible (grams).

**9.4 Determination of Hemicellulose:**

Hemicellulose was calculated by subtracting cellulose from holocellulose.

Hemicellulose content in banana pseudostem sap (percent) = $P_1 - P_2$

Where,

$P_1$= Holocellulose content (percent)

$P_2$ = Cellulose content (percent)

**9.5 Determination of Lignin content (TAPPI standard T 222 om – 06) :**

2 grams of sawdust was weighed out accurately in weighing bottle and transferred in a 100 ml beaker. 40 ml of cold (10-15 °C) 72% sulphuric acids was added carefully with a pipet and the mixture was stirred with a small glass rod. After the specimen is dispersed, cover the beaker with watch glass and keep it in a bath at 20 °C for 2 hours. Stir the materials frequently during this time to ensure complete solution. Add about 300 to 400 ml of water to a flask and transfer to material from the beaker to the flask. Rinse and dilute with water to 3% concentration of sulfuric acid, to a total volume of 1540 ml. Boil The solution for 4 hours, maintaining constant volume by addition of hot water. Allow the insoluble material (lignin) to settle keeping the flask in an inclined position. Without stirring up the precipitate, decant or siphon off the supernatant solution through a filtering crucible. Wash the lignin with hot water. Dry the crucible with lignin in an oven at 105°C to the constant weight. Cooled in a desiccator and weighed.

Lignin content in Banana pseudostem sap (percent)

$$= \frac{W_4 - W_3}{100 \times W_2} \times (100 - W_1)$$

where,

$W_1$ = extractive free content (percent).

$W_2$ = Weight of oven dried extractive- free sample (grams).

$W_3$ = weight of oven dried crucible (grams).

$W_4$ = weight of oven dried residue and crucible (grams).

**9.6 Tannin content:**

The tannins were determined by Folin and Ciocalteu method. 0.1 ml of the sample extract was added with 7.5 ml of distilled water and adds 0.5 ml of Folin Phenol reagent, 1 ml of 35% sodium carbonate solution and dilute to 10 ml with distilled water. The mixture was shaken well, kept at room temperature for 30 min and absorbance was measured at 725 nm. Blank was prepared with water instead of the sample. A set of standard solutions of gallic acid is treated in the same manner as described earlier and read against a blank.

**10. Dyeing procedure**

**10.1 Fabric sample**

Pure cotton fabric with plain weave is used. The fabric sample is used with 2 gm owf (oven weight of fabric)

**10.2 Dye extraction**

In this method, dye from flowers powder were extracted by preparing an aqueous solution of flowers (10 g in 100 ml distilled water) and the extraction process was carried out at a

temperature range of 80-85°C for 90 minutes. Extract was then filtered through a piece of cloth to yield the natural dye.

**Table 1**
CONDITION FOR EXTRACTION OF NATURAL DYE

| Solvent | Temperature (°C) | Time (minutes) |
|---|---|---|
| Distilled water | 80-85 | 90 |

Figure 2 *Butea* floewers

from Butea flowers

**10.3 Biomordanting**

The cotton fabric were mordanted using different amounts of banana pseudostem sap as mordant solution (10, 20, 30, 40 and 50 % owf) at 80 °C and M:L= 1:30 for 90 minute.

**10.4 Pre-mordanting:**

In this method, 5 cotton samples were pretreated with the Banana sap with different concentration 10, 20, 30, 40 and 50 % for 90 minutes at 80°C. The pretreated cotton fabric was introduced into the dye bath containing required amount of dye extract and water. The dyeing was carried out for 90 minutes at 80°C. The dyed samples were taken out, squeezed and dried at room temperature.

**TABLE 2**
CONDITION FOR DYEING

| Fabric | Mordant concentration | Dye concentration | Temperature (°C) | Time (min) | M:L ratio |
|---|---|---|---|---|---|
| Cotton | 10% | 20% | 80°C | 90 | 1:30 |
| | 20% | | | | |
| | 30% | | | | |
| | 40% | | | | |
| | 50% | | | | |

**10.5 Simultaneous Mordanting:**

Simultaneous Mordanting was done with the help of method in which , the 5 cotton samples were dyed with dye extract as well as the Banana sap with different percent 10, 20, 30, 40 and 50 % for 90 minutes at 80° c simultaneously. The dyed samples were taken out, squeezed and dried at room temperature.

**10.6 Post Mordanting:** 5 cotton fabrics was introduced into the dye bath containing required amount of dye extract and water for post mordanting method. The dyeing was carried out for90 minutes at 80°C. The dyed samples were taken out, squeezed and treated with the Banana sap with different percent 10, 20, 30, 40 and 50 % for 90 minutes at 80°C.

**Table 3**
**Qualitative tests used for carbohydrate analysis**

| No | Test | Observation | Inference |
|---|---|---|---|
| 1 | **Molisch's test** | Positve | Presence of carbohydrates |

| | | | |
|---|---|---|---|
| 2 | **Iodine test** | Negative | Absence of Starch |
| 3 | **Fehlings test** | Positive | Presence of reducing sugars |
| 4 | **Benedict's test** | Negative | Absence of reducing sugars |
| 5 | **Barfoed's test** | Positive | Presence of reducing sugars |
| 6 | **Seliwanoff's test** | Positive | Presence of ketose<br>Presence of aldoses |

The carbohydrate analysis test was shown positive results for presence of reducing sugars in table 3.

**4.2 pH test**

pH refers to acidity and alkalinity. It is measure of hydrogen ion ($H^+$) in the Banana pseudostem sap. Banana pseudostem sap pH was obtaining **6.2** .

**Table 4.2**
**Chemical composition of banana pseudostem sap**

| Content | Value(%) |
|---|---|
| Holocellulose | 5.51% |
| Hemicelluloses | 5.424% |
| Cellulose | 0.086% |
| Lignin | 1.44% |
| Tannin | 4.06% |

In table 4.2 Chemical composition of banana pseudostem sap was analysed and different contents calculated in percent basis. Holocellulose, hemicellulose, cellulose, lignin and tannin were main contents in banana pseudostem sap which was used as a mordant in dyeing process. Holocellulose includes alpha cellulose and hemicellulose. Cellulose content in banana pseudostem sap was very low. Cellulose is a homopolysaccharide composed of β-D-glucopyranose units which are linked together by (1→4)-glycosidic bonds. Cellulose molecules are completely linear and have a strong tendency to form intra- and intermolecular hydrogen bonds. Hemicelluloses are heterogeneous polysaccharides, like cellulose, most hemicelluloses function as supporting materials in the cell walls [Sjostrom 1981].

However banana pseudostem sap had lower lignin i.e. 1.44% content than wood but its glue like quality is important for dyeing process. Banana pseudostem sap has 2.06% of tannin. Tannin is defined as naturally occurring water soluble polyphenolic compounds of high molecular weight (about 500-3000) containing phenolic hydroxyl groups to enable them to form effective crosslink between proteins and other macromolecules.

**Discussion**

1. Chemical compositions confirm the presence of following contents on percent basis in banana pseudostem sap. They are holocellulose, hemicelllulose, cellulose, lignin and tannin. These compounds are the substances which can give the fixing properties to the banana pseudostem sap. Tannin are the most important ingredients which are the most important ingredients which are necessary for mordanting with natural dyes.
2. Fastness properties of cotton dyed sample will be explained and described in the next research paper because some further work related washing is going on. In banana pseudo stem sap it has been confirmed by laboratory research work that tannin content is present in banana sap mordant. Cotton is less suitable for natural dyes. There are some natural dyes that was work on cotton, however especially if mordanted with tannins.Cotton is the second most consumed fiber worldwide, behind polyester

***CONCLUSION***

In banana crop, after harvesting the bare pseudostem remains in several tons as a waste. Fiber can be produced for paper industry, fabrics or yarn industry etc. But usually they are disposed of by burning in fields which creates another air pollution problem. Larger amount of solid waste increases pollution load in environment. In this connection, present study deals with the use of banana pseudostem sap as a mordant to utilize a large quantity of biomass. The remaining material can be used as fiber, green manure, as a source of carbohydrate for production of starch, sugar and alcohol. Synthetic mordants cause many health hazards in society due to irruption of problems like skin and eye irritation, inflammation, more damage to wounds and abrasions, possibility to enter in blood stream etc. Analysis of chemical composition of banana pseudostem sap revealed the presence of holocellulose including hemicellulose and cellulose. Cellulosic material are homopolysaccharides and have a strong tendency to form intra and inter molecular hydrogen bonds which certainly responsible to improve the bonding capacity of

dye to fabric. On the other hand lignin and tannin contents are also present in banana pseudostem sap. Lignin's glue like property is acting as a binding agent in the dyeing process. If we talk about tannin content of pseudostem sap, then we can say it provides carboxylic group to cotton fabric to bind with dye molecule and thus increasing absorption capacity of fabric. The overall results show that banana pseudostem sap not only gives natural source of mordant but also improves the all qualities of dyeing process. The study carried out gives significant result use of because natural dyes helps to preserve the traditional art of dyeing and definitely will improve the popularity of natural material.The process of extraction of banana pseudostem sap and its use as a mordant was found to be cost effective as compared to the cost of chemical mordants in local market.If above concern has become fruitful it will give a way to grow more plants for greater use of dyes and mordants in textile industries, which will help to solve the problem of unemployment.The use of natural dyes and mordants in ecofriendly manner also giving conservation of plants as well as environment.

***References***

1. Anonymous, (1993). Technical Association of the Pulp and Paper Industry: (TAPPI Standard T203 om-93) Atlanta, USA.
2. Ammayappan et. al.,(2004): Natural Dye From Pseudostem Of Banana For Silk. Man-made Text India,47(6), 218-220
3. Cordeiro, N., Belgacem, M.N., Torres, I.C. and Moura, J.C.V.P. (2004) Chemical composition and pulping of banana pseudo-stems. Journal of Industrial Crop and Products 19: 147-154.
4. Dixit, S., and Jahan, S., (2005): Colourfastness properties of *Euphorbia continifolia* leaves dye on silk fabric. Man-made Text India, 58(5), 252-254
5. Ultra,V.U., Mendozam D.M., and Briones, A.M. (2005). "Chemical changes under aerobic composting and nutrient supplying potential of banana residue compost," Renewable Agriculture and Food Systems. 20(2), 113-125.
6. "Phosphate removal from wastewaters using a weak anion exchanger prepared from a lignocellulosic residue", Environmental Science and Technology 40(8), 2740-2745
7. Agarwal, R., Pruthi, N., and Singh (2007): Effect of Mordant on Printing with Marigold Flower Dye. Natural product Radiance, Vol. 6(4), pp.306-309
8. Adeel, S., Ali, S., Bhatti, I. A. And Zsila, F. (2009): Dyeing of Cotton Fabric Using Pomegranate (*Punica granatum)* Aqueous Extract. Asian J. Chem,. 21(5): 3493-3499.
9. Haslinda, W.H., Cheng, L.H., Chong, L.C. and Noor Aziah, A. A. (2009): Chemical composition and physiochemical properties of green banana (*Musa acuminate X balbisiana Colla cv. Awak*) flour. International Journal of Food Sciences and Nutrition 60(S4): 232-239.
10. Goodarzian, H and Ekrami, E. (2010): Extraction of Dye From Madder Plant (*Rubia tinctorium*) and Dyeing of wool.World Applied Sciences journal 9(4): 434-436
11. Haji, Aminoddin (2010): Functional Dyeing of Wool with Natural Dye Extracted From *Berberis vulgaris* Wood And *Rumex hymenosepolus* Root As Biomordant. *Iran. J. Chem. Chem. Eng. Vol. 29, No. 3*
12. Mohapatra, D., Mishra, S. and Sutar, N. (2010): Banana and its by-product utilization: an overview. Scientific and Industrial Research 69: 323-329.
13. Grover, N.,and Patni, V.,(2011) : Extraction And Application Of Natural Dye Preparations From The Floral Parts Of *Woodfordia fruticosa* . Indian Journal of Natural Products and Resources Vol. 2(4), pp 403-408
14. Akpabio, U.D., Udiong D.S. and Akpakpan A.E. (2012): The Physicochemical Characteristics Of Plantain *(Musa Paradisiaca)* And Banana *(Musa Sapientum)* Pseudostem Wastes. Advances in Natural and Applied Sciences, 6(2): 167-
15. Bose, S., and Nag, S.,(2012): Isolation Of Natural Dyes From The Flower Of *Hibiscus Rosa-sinensis.*Am. J. PharmTech Res.2(3)
16. Deshpande, R., and Chaturvedi, A.,(2012): Colourant Potential Of *Ricinus Communis* L. On Silk And Cotton Cloth. Science Research Reporter 2(3):302-306
17. Mahale et.al.,(2003): Acalypha leaves for silk dyeing. Indian J Fibre Text Res, 28,86-89
18. Mathur et.al.,(2003): Neem Bark As Wool Colourant. Indian J Fibre Text Res, 28,94-99
19. Mongkholrattanasit, R., Krystufek, J.,Wiener, J., and Viková M., (2011): Dyeing, Fastness, and UV Protection Properties of Silk and Wool Fabrics Dyed with Eucalyptus Leaf Extract by the Exhaustion Process Fibers and Textiles, 19(3):, 94-99.
20. Onal, A.,(1996): Extraction of Dyestuff From Madder Plant (Rubia tinctorum L.) and Dyeing of wool, Feathered-Leather and Cotton.Tr.J. of Chemistry 20, 204-213

Microelectronics Journal 49 (2016) 36–42

Contents lists available at ScienceDirect

Microelectronics Journal

journal homepage: www.elsevier.com/locate/mejo

# TCAD RF performance investigation of Transparent Gate Recessed Channel MOSFET

Ajay Kumar, Neha Gupta, Rishu Chaujar*

*Microelectronics Research Lab, Department of Engineering Physics, Delhi Technological University, Bawana Road, Delhi 110042, India*

ARTICLE INFO

*Article history:*
Received 4 February 2015
Received in revised form
24 November 2015
Accepted 3 December 2015

*Keywords:*
CRC-MOSFET
Cut-off frequency
Parasitic capacitance
Power gain
RF
TGRC-MOSFET

ABSTRACT

In this paper, analog/RF performance and small signal behavior of Transparent Gate Recessed Channel (TGRC) MOSFET has been investigated in terms of transconductance, DIBL, channel resistance parasitic capacitances, cut-off frequency and maximum oscillator frequency. Results so obtained are compared with Conventional Recessed Channel (CRC) MOSFET at THz frequency range, using ATLAS-3D device simulator. Furthermore, the impact of technology parameter variations in terms of gate length ($L_g$) has also been evaluated. Result shows that there is 42% enhancement in cut-off frequency, 132% increment in maximum oscillator frequency and significant improvement in parasitic capacitances for TGRC-MOSFET due to reduced short channel effects (SCEs) and enhanced on-current driving capabilities thus, reflecting its significance in high-frequency THz range applications.
© 2015 Elsevier Ltd. All rights reserved.

## 1. Introduction

In the era of sub-100 nm dimensions, continuing scaling of conventional MOSFET is done to develop opportunities for further high speed and low power applications. Highly scaled MOSFETs achieved cut-off frequencies in several THz range making CMOS technology appropriate for RF application and wireless communications [1–4]. In the conventional MOSFET, as the channel length diminishes, the gate control over the channel is reduced due to increased source/drain capacitances [5]. However, with scaling down of the device dimensions, the so-called SCEs arises such as mobility degradation, hot carrier effects, drain induced barrier lowering, parasitic capacitances etc, making the scaled devices inapt for high-frequency wireless applications [6]. To overcome such effects, numerous device engineering schemes such as gate engineering, channel engineering etc. and novel device structures such as SOI MOSFET [7], Dual Gate MOSFET [8], Recessed Channel (RC) MOSFET [9], GAA MOSFET [10], Silicon Nanowire MOSFET [11] etc. have been reported in the literature.

SCEs are mainly caused by drain barrier width extending into the source region, resulting in barrier lowering. Thus, in terms of both functionality and cost, grooved gate MOSFET is the most promising one to avoid this potential extension [12]. In RC MOSFET, two potential barriers are formed at the corners due to the high density of electric field lines at the corners, which leads to SCE immunity. Moreover, carriers in the channel now require more energy to surmount these hurdles, which bounds its electron transport efficiency and hence, on-current capabilities of the device [13]. To overcome this drawback, we incorporate the concept of gate transparency on RC MOSFET.

In TGRC-MOSFET, the metal (Al) gate is replaced with a transparent conducting oxide [14,15] called indium tin oxide (ITO). ITO is a solid solution of indium oxide ($In_2O_3$) and tin oxide ($SnO_2$). It is transparent and colorless in thin layers. ITO is one of the most widely used transparent conducting oxides because of its two chief properties: its electrical conductivity and optical transparency as well as the ease with which it can be deposited as a thin film [16–18]. Moreover, due to the increased demand for high-speed electronics products, the accurate modeling of the MOSFETs at high frequencies (HF) is necessary to represent the behavior of device in microwave circuits and systems [19]. Transparent conducting oxide (TCO) semiconductor is essential to use in optoelectronic devices such as flat panel display. ITO is one of the TCO semiconductors which are mostly used in optoelectronic device applications. ITO is not normally available in the market because of cost and shortage of indium, the principle material of ITO [20].

In this work, the analog performance of TGRC-MOSFET [21,22] has been observed in terms of transconductance ($g_m$), drain current ($I_D$), conduction band and valence band, which reflects that TGRC-MOSFET is suitable for AC applications. Further, the present work stresses on

* Corresponding author.
*E-mail addresses:* ajaykumar@dtu.ac.in (A. Kumar), nehagupta@dtu.ac.in (N. Gupta), rishu.phy@dce.edu (R. Chaujar).

http://dx.doi.org/10.1016/j.mejo.2015.12.007
0026-2692/© 2015 Elsevier Ltd. All rights reserved.

the TCAD assessment of TGRC-MOSFET for high-performance RF applications in terms of figure of merits such as cut-off frequency, maximum oscillator frequency and parasitic capacitances. The most suitable method to observe the small signal behavior of MOSFET at high frequencies involves *S*-parameter measurements. *S*-parameters are commonly employed for those networks that are operating at RF and microwave frequencies, where energy analysis and signal power are more easily computed as compared to voltages and currents, since, at high frequencies it is very difficult to estimate the current and voltages. Short and open circuits (used by definitions of most *n*-port parameters) are hard to realize at high frequencies. As a result, microwave engineers work with so-called *S* parameters, which utilize waves and matched terminations. This approach also minimizes the reflection problems [23].Thereafter, the impact of parameter variation in terms of gate length is observed with sufficient enhancement in terms of cut-off frequency, maximum oscillator frequency, and parasitic capacitances in TGRC-MOSFET.

## 2. Device structure and its parameters

A schematic cross-sectional view of simulated device i.e. TGRC-MOSFET is shown in Fig. 1, which consists of the gate made up of transparent conducting material indium tin oxide as shown in Fig. 1(a). The total gate length is 30 nm and thickness of oxide is 2.0 nm. In this case, substrate doping is p-type with a concentration of $1\times10^{17}$ cm$^{-3}$; source and drain are n-type with uniform doping profiles as $1\times10^{19}$ cm$^{-3}$. Table 1 shows the default parameters of the device structure.

Here, RF performance, which is determined by the figure of merits such as cut-off frequency, maximum oscillator frequency, parasitic capacitances, maximum available power gain and maximum stable power gain, are investigated by extensive device simulations for 30 nm gate length-CRC-MOSFET and TGRC-MOSFET. Further, the RF performance of CRC-MOSFET and TGRC-MOSFET has been studied under the bias condition ($V_{GS}=0.7$ V, $V_{DS}=0.5$ V and frequency range from 0 to 1.8 THz) and a comparative analysis has been performed.

## 3. Simulation methodology

All simulations have been performed using ATLAS and DEVEDIT 3D device simulator [24]. For the simulations, authors adopted physical models accounting for the electric field-dependent and concentration-dependent carrier mobilities, Shockley–Read–Hall recombination/generation with doping dependent carrier lifetime, inversion layer Lombardi CVT mobility model, wherein concentration-dependent mobility, high field saturation model are all included [24]. We have adopted the hydrodynamic energy transport model instead of drift-diffusion method which incorporates all non-local effects into account.

## 4. Calibration

Calibration of model parameters used in simulation has been performed according to the published results obtained by Chaujar et al. [25] using above models and the obtained calibrated results are shown in Fig. 2.

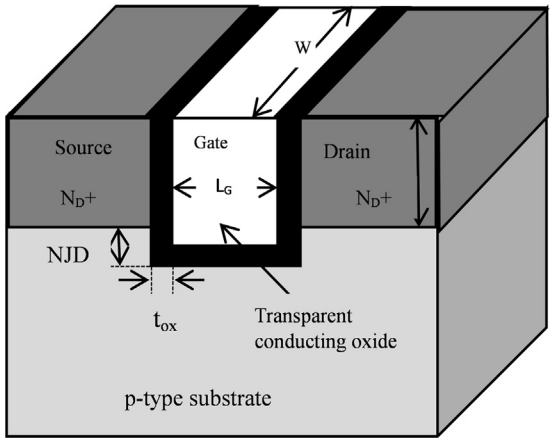


**Fig. 1.** Schematic structure of Transparent Gate Recessed Channel MOSFET.

**Table 1**
Design parameters of CRC-MOSFET and TGRC-MOSFET device designs.

| Parameters | Unit |
|---|---|
| Channel length ($L_G$) | 30 nm |
| Device width | 200 nm |
| Groove depth | 38 nm |
| Source/drain junction depth | 30 nm |
| Negative junction depth (NJD) | 10 nm |
| Substrate doping ($N_A$) | $1\times10^{16}$ cm$^{-3}$ |
| Source/drain doping ($N_D^+$) | $1\times10^{19}$ cm$^{-3}$ |
| Physical oxide thickness ($t_{ox}$) | 2 nm |
| Permittivity of $SiO_2$ | $\varepsilon_{ox}=3.9$ |
| Gate to source voltage ($V_{GS}$) | 0.7 V |
| Drain to source voltage ($V_{DS}$) | 0.5 V |
| Work function for TGRC-MOSFET ($\Phi_{ITO}$) | 4.7 eV |
| Work function for CRC-MOSFET ($\Phi_M$) | 4.2 eV |

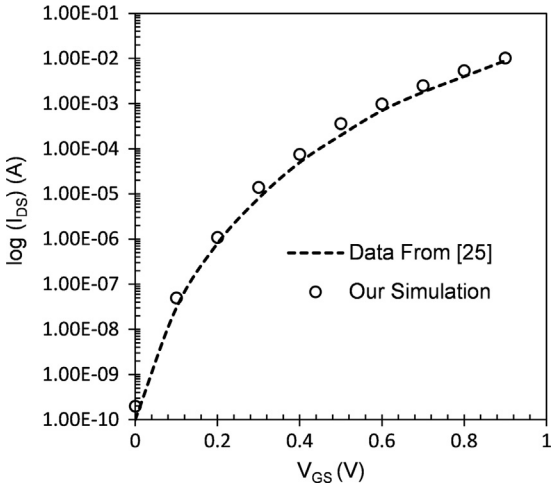


**Fig. 2.** Calibration with the published result, $I_{DS}-V_{GS}$ characteristics of 40 nm gate length TGRC-MOSFET.

## 5. Results and discussions

### 5.1. Analog performance metrics analysis

#### 5.1.1. Transfer characteristics and Transconductance

Fig. 3(a) and (b) shows the drain current and transconductance profile respectively, for CRC-MOSFET and TGRC-MOSFET. Transparent conducting oxide gate is used instead of a metal gate in TGRC-MOSFET, which enhances the drain current and hence the transconductance as shown in Figs. 3 and 4 respectively, due to improved

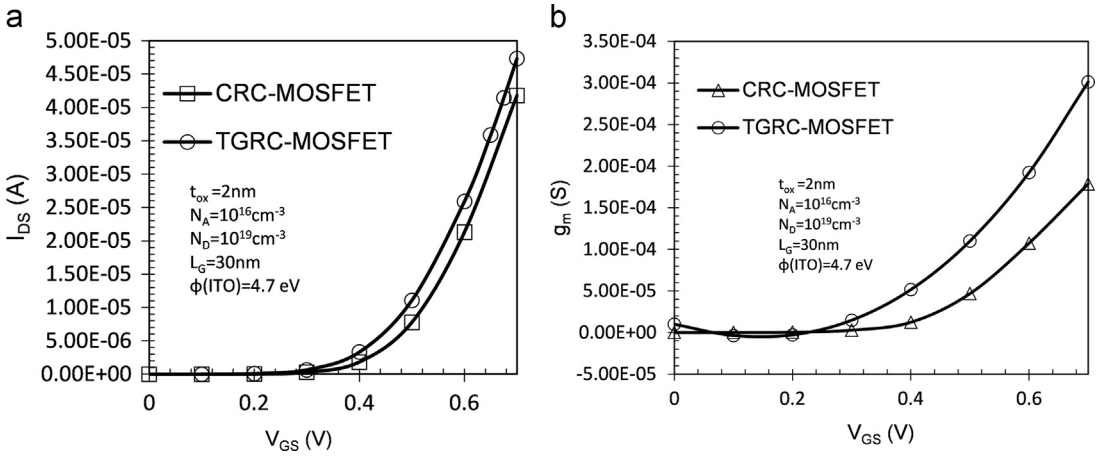


**Fig. 3.** (a and b) Transfer characteristics and transconductance of CRC-MOSFET and TGRC-MOSFET respectively at $V_{DS}$=0.5 V.

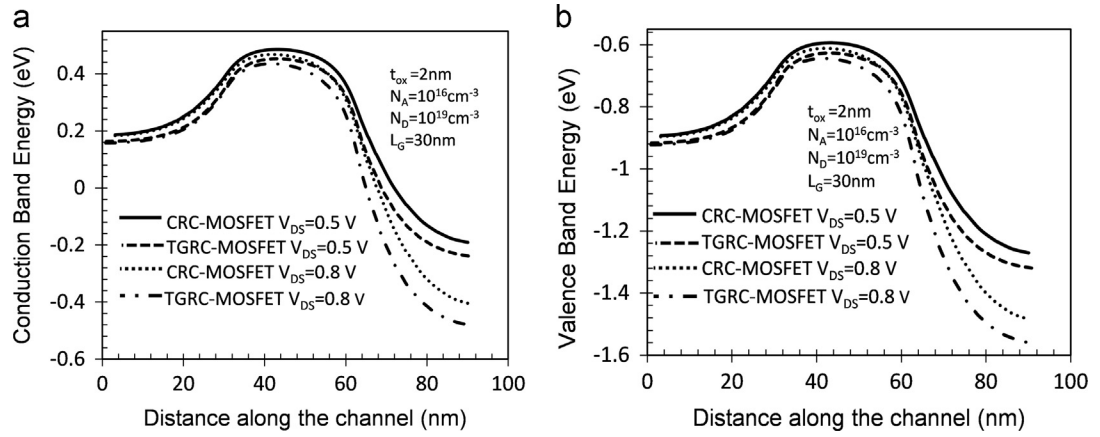


**Fig. 4.** (a) Conduction band energy as a function of position along the channel for CRC-MOSFET and TGRC-MOSFET, (b) valence band energy as a function of position along the channel for CRC-MOSFET and TGRC-MOSFET.

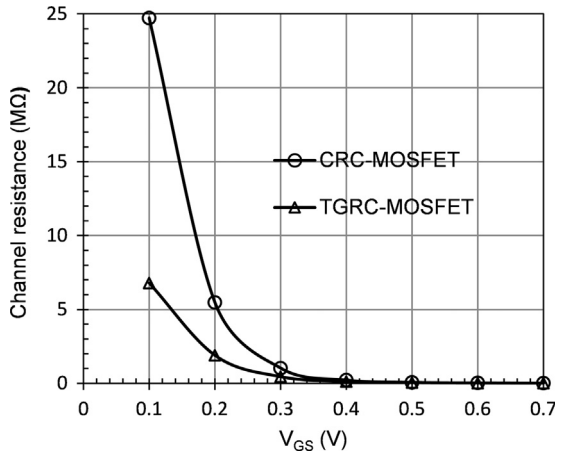


**Fig. 5.** Channel resistance distribution for CRC-MOSFET and TGRC-MOSFET.

gate control and hence reduces hot carrier and short channel effects for TGRC-MOSFET. $I_{DS}$ versus $V_{GS}$ characteristics curve is generated and it is done by obtaining solution when the drain bias is held at 0.5 V and gate bias is ramped from 0 to 1.0 V.

### 5.1.2. Conduction band and valence band profile

Fig. 4(a) and (b) indicates the conduction and valence band energy profiles along the channel length for CRC-MOSFET and TGRC-MOSFET. The lowering of barrier potential at source side indicates that the drain induced barrier lowering (DIBL) effect is less observed in the proposed device, as it is evident from the band diagram. DIBL is more pronounced in conventional MOSFET, which is calculated from the difference of conduction band energy between $V_{DS}$ of 0.5 and 0.8 V. The improvement in DIBL effect is due to the step in conduction band energy profile in the channel region, which is obtained as a result of incorporating the transparent gate onto the design [22].

### 5.1.3. Channel resistance

Fig. 5 demonstrates the distributed channel resistance of CRC-MOSFET and TGRC-MOSFET. The distributed channel resistance for CRC-MOSFET is much higher than TGRC-MOSFET. At $V_{GS}$=0.1 V, channel resistance decreases by 72.51% in TGRC-MOSFET as compared to CRC-MOSFET. For better performance of a device, channel resistance should be as low as possible because if channel resistance is low, the current flowing through the channel will be high and hence the device would be faster making it reliable for switching and high power applications. Thus, TGRC-MOSFET exhibits a promising device behavior for RF applications.

## 5.2. RF performance metrics analysis

### 5.2.1. Cut-off frequency and maximum oscillator frequency

A parameter generally described when comparing transistors for RF applications is the cut-off frequency, $f_T$ [26,27]. $f_T$ is a specification for high-speed digital applications (speed and high

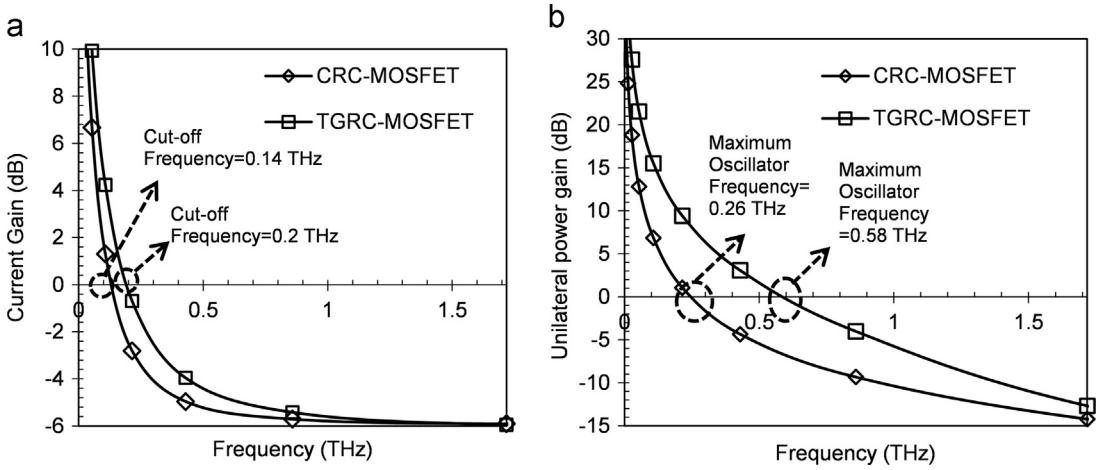


**Fig. 6.** (a) Cut-off frequency for CRC-MOSFET and TGRC-MOSFET, (b) maximum oscillator frequency for CRC-MOSFET and TGRC-MOSFET.

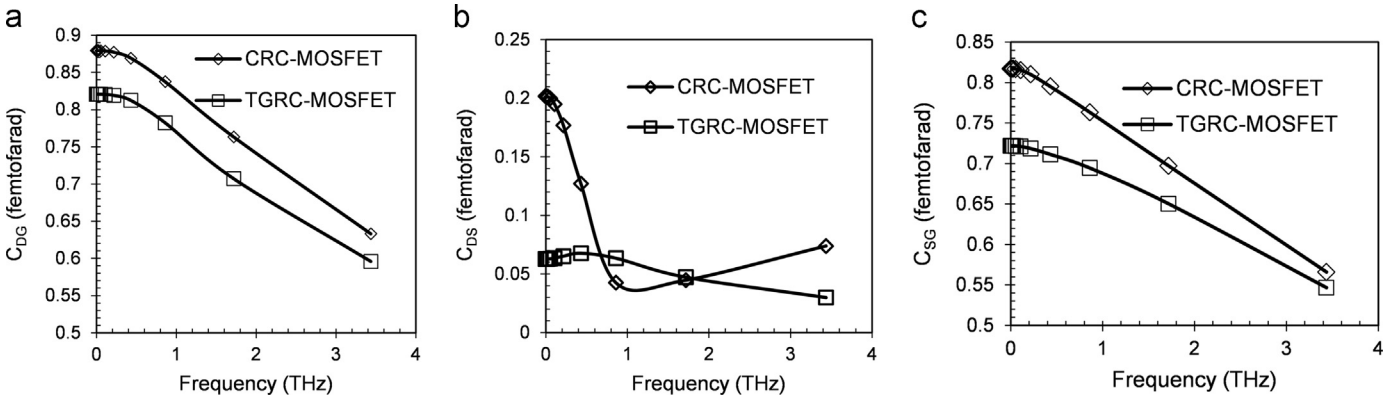


**Fig. 7.** (a–c) Parasitic capacitances (femto-Farad) for CRC-MOSFET and TGRC-MOSFET.

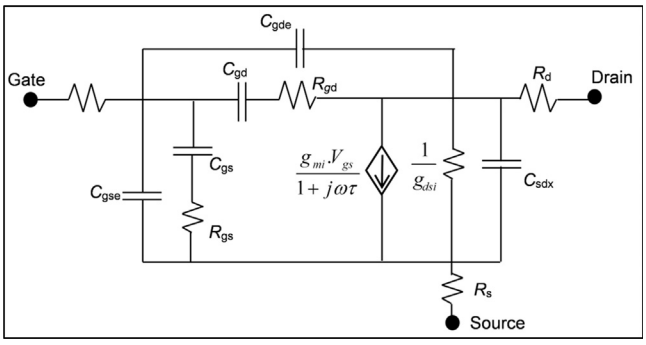


**Fig. 8.** NQS model of the RF MOSFET operating in the strong inversion region.

swing) and can be defined as follows:

$$f_T = \frac{g_m}{2\pi(C_{gs}+C_{gd})} \quad (1)$$

where $g_m$ is the transconductance, $C_{gs}$ and $C_{gd}$ are parasitic capacitances. Cut-off frequency $f_T$ is calculated when current gain is unity [28]. Fig. 6(a) reflects 42% higher cut-off frequency in TGRC-MOSFET as compared to CRC-MOSFET due to enhanced ON current and transconductance in TGRC-MOSFET owing to incorporation of transparent gate. For high speed and high switching, maximum frequency should be high and thus TGRC-MOSFET suitable for high speed digital circuits. Maximum oscillator frequency $f_{MAX}$ is calculated when power gain is unity [26]. Fig. 6(b) shows the 123% improved performance of TGRC-MOSFET as compared to CRC-MOSFET in terms of maximum oscillator frequency due to the enhancement in carrier mobility which results reduction in gate resistance and hence improves maximum oscillator frequency. As maximum oscillator frequency directly depends on transconductance and inversely proportional to gate resistance [26]. Thus it is providing efficacy for RF applications.

### 5.2.2. Parasitic capacitances

For the better performance of device in RF applications, parasitic capacitances should be as small as possible. Parasitic capacitances and resistance put an upper limit on the speed of a transistor [29], which causes a delay in logic-cell. When one logic cell drives another, the parasitic input capacitance of the driven cell becomes the load capacitance of the driving cell [30]. Fig. 7(a)–(c) shows that the parasitic capacitances in TGRC-MOSFET are less pronounced as compared to the CRC-MOSFET.

### 5.2.3. Small signal behavior of TGRC-MOSFET

Non-quasi-static (NQS) small-signal equivalent circuit is used to extract RF model parameters of TGRC-MOSFET and CRC-MOSFET operating in strong inversion regions as shown in Fig. 8. This is based on a conventional small-signal model of RF MOSFETs [31], where $R_s$ and $R_d$ are the source and drain resistances respectively; $C_{gde}$ and $C_{gse}$ are extrinsic gate-to-drain and gate-to-source capacitances respectively; $G_{dsi}$ and $g_{mi}$ are intrinsic gate-to-drain conductance and transconductance; $R_{gs}$ and $R_{gd}$ are distributed channel resistances; and $C_{ds}$ and $C_{gs}$ are intrinsic gate-to-drain and gate-to-source capacitances respectively.

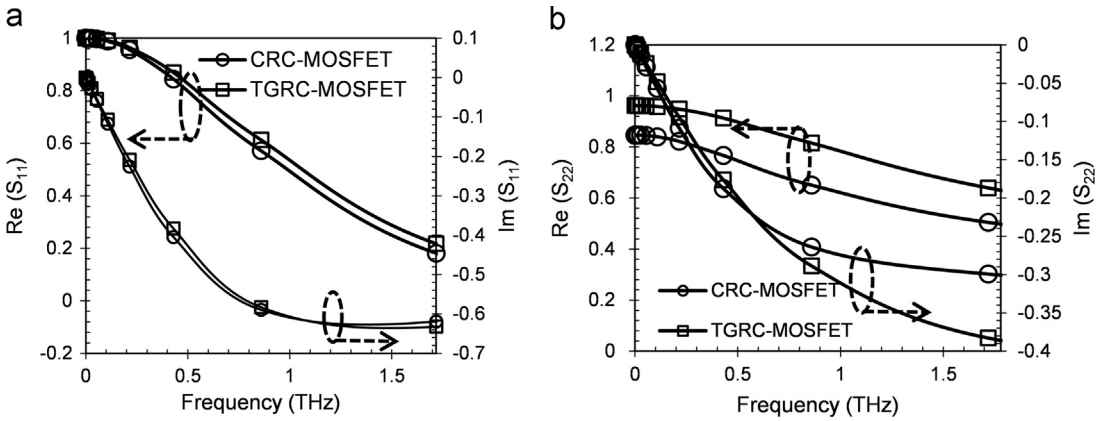


**Fig. 9.** (a and b) Real and imaginary part of input and output reflection coefficient as a function of frequency for CRC-MOSFET and TGRC-MOSFET at $V_{GS}=0.7$ V and $V_{DS}=0.5$ V.

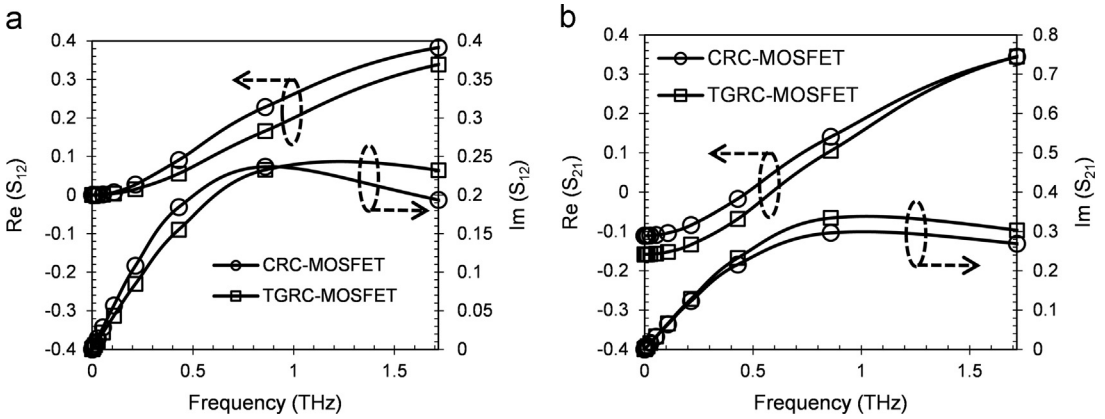


**Fig. 10.** (a and b) Real and imaginary part of reverse and forward transmission coefficient as a function of frequency for CRC-MOSFET and TGRC-MOSFET at $V_{GS}=0.7$ V and $V_{DS}=0.5$ V.

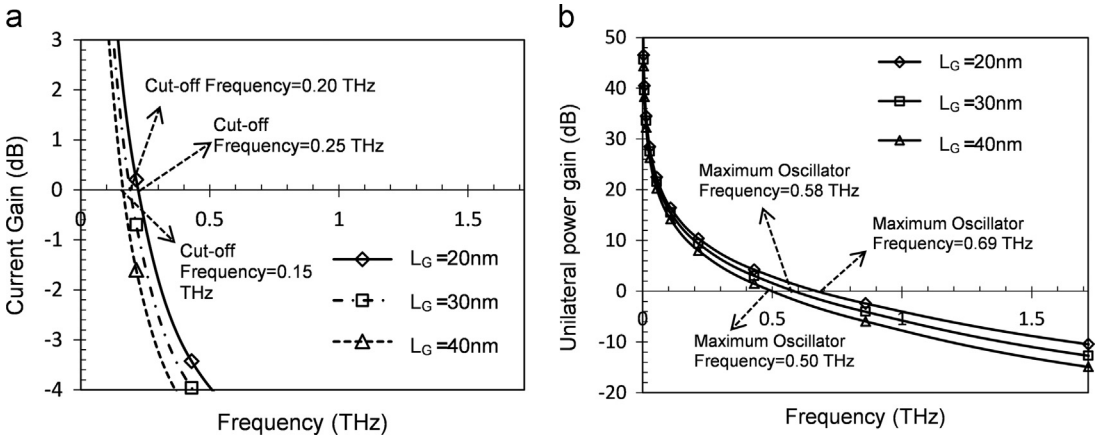


**Fig. 11.** (a) Cut-off frequency for TGRC-MOSFET at different gate lengths and (b) maximum oscillator frequency for TGRC-MOSFET at different gate lengths.

*5.2.4. S-parameters*

The most appropriate method to examine small signal behavior of MOSFET at high frequencies involves *S*-parameter measurements. *S*-parameters are commonly employed for those networks that are operating at RF and microwave frequencies where signal power and energy analysis are more easily computed than voltages and currents. Since, at high frequency it is very difficult to estimate current and voltages. Short and open circuits (used by definitions of most *n*-port parameters) are hard to realize at high frequencies. As a result, microwave engineers work with so-called *S*-parameters.

$S_{11}$ and $S_{22}$ are defined as input and output reflection coefficient at port 1 and port 2 respectively and is a measure of quality of match between the port and terminating impedance. $S_{11}$ is the most frequently used parameter to characterize small signal behavior of active device at very high frequency. Matching is generally required in RF circuits. When there is a perfect match, there is no reflected wave and reflection coefficient is zero.

Fig. 9(a) and (b) shows the real part of input and output reflection coefficients of CRC-MOSFET and TGRC-MOSFET. As is obvious from the figure, both input and output coefficient decreases with increase in frequency and decrement in reflection coefficient is more in TGRC-MOSFET as compared to its counterparts. Due to incorporation of transparent gate, current driving capability, and transconductance increases as shown in Fig. 3(a) and (b), leading to significant improvement in both input and output reflection coefficient. As the

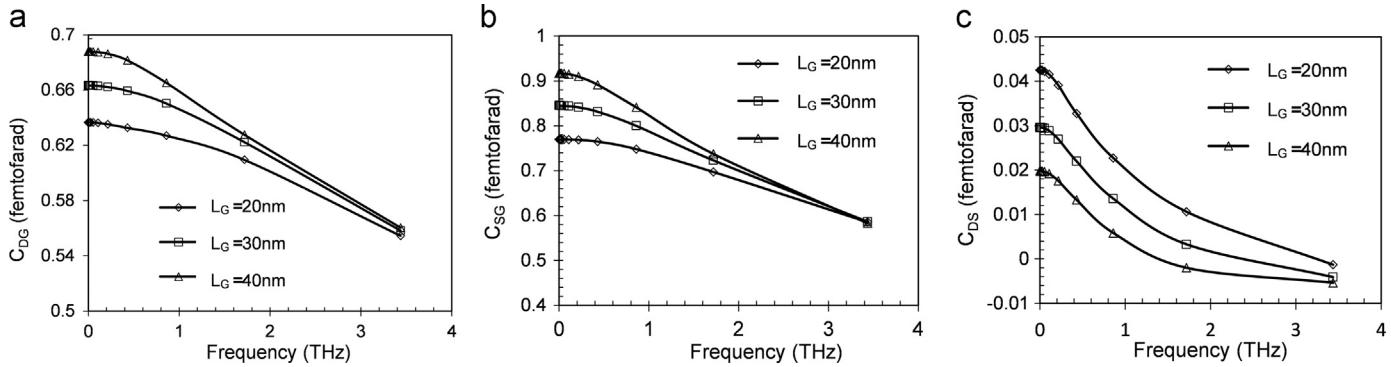


**Fig. 12.** (a–c) Parasitic capacitances (femto-Farad) for TGRC-MOSFET at different gate lengths.

**Table 2**
Summary of intrinsic small signal parameter and RF FOMs.

| Device | Parameters | | | | | | | | | | |
|---|---|---|---|---|---|---|---|---|---|---|---|
| | $g_m$ (S) | $R_{ch}$ (MΩ) | $f_T$ (THz) | $f_{MAX}$ (THz) | $C_{SG}$ (ff) | $C_{DG}$ (ff) | $C_{DS}$ (ff) | $S_{11}$ | $S_{12}$ | $S_{21}$ | $S_{22}$ |
| CRC-MOSFET | $1.5 \times 10^{-5}$ | 24.7 | 0.14 | 0.26 | 0.763 | 0.838 | 0.127 | 0.572 | 0.228 | 0.141 | 0.650 |
| TGRC-MOSFET | $3 \times 10^{-5}$ | 6.79 | 0.2 | 0.58 | 0.695 | 0.782 | 0.068 | 0.613 | 0.166 | 0.105 | 0.815 |

matching between the ports and characteristic impedance improves, reflection coefficient decreases due to smaller reflected power.

The reverse isolation parameter $S_{12}$ defines the measure of feedback from the output of an amplifier to the input and thus reigns its stability at high frequency [32]. Fig. 10(a) shows the variation of real part of reverse transmission coefficient of CRC-MOSFET and TGRC-MOSFET. The reverse transmission coefficient increases for TGRC-MOSFET compared to CRC-MOSFET devices as depicted in Fig. 10(a). This enhancement is due to transparent gate designs and transparent conducting oxide enhances device performance and alleviates SCEs. Fig. 10(b) shows the forward transmission coefficient as a function of frequency also defined as a forward gain of two port device. Fig. 10(b) unveils the enhancement in forward gain for TGRC-MOSFET due to augmentation of transconductance in comparison to CRC-MOSFET.

### 5.3. *Effect of scaling*

#### 5.3.1. *Cut-off frequency and maximum oscillator frequency*

For TGRC-MOSFET, Fig. 11(a) and (b) represents the cut-off frequency and maximum oscillator frequency respectively at different gate lengths. Fig. 11(a) shows that the cut-off frequency is enhanced when the gate length is reduced.

When gate length reduces from 40 nm to 30 nm then cut-off frequency is increased by 33.3% and when the gate length is further reduced from 30 nm to 20 nm then cut-off frequency is increased by 25.0%. Increase in cut-off frequency with scaling in TGRC-MOSFET makes it an ideal candidate for RF applications. Fig. 11(b) reflects the maximum oscillator frequency, which increases when the gate length is decreased. If the gate length reduces from 40 nm to 30 nm, the maximum oscillator frequency is increased by 16.0% and further reduction in gate length from 30 nm to 20 nm increases the maximum oscillator frequency by 18.96%. Hence, as the maximum oscillator frequency enhances in TGRC-MOSFET, the device becomes suitable for high switching applications.

#### 5.3.2. *Parasitic capacitances*

The parasitic capacitance at the inputs and outputs of the digital devices increases the rise and fall times. Thus, it is obligatory to investigate the parasitic capacitances at high frequency. Parasitic capacitance in RF amplifiers may cause these amplifiers to have low gain due to the parasitic loss. In some cases, it may cause these amplifiers to oscillate. In digital switching circuits, the rise time and fall time of the digital signal greatly affects the maximum speeds achievable [33]. It is reflected from Fig. 12(a)–(c) that TGRC-MOSFET exhibits smaller $C_{DG}$, $C_{SG}$ and $C_{DS}$ when the gate length is reduced from 40 nm to 20 nm at THz frequency due to transparent gate incorporation. Because of transparent gate, carrier mobility across the channel increases [34,35] thereby reducing the parasitic capacitances (Table 2).

## 6. Conclusion

This paper investigates the effectiveness of ITO as a transparent gate on CRC-MOSFET for improved analog and RF performance at THz frequency range. It has been observed that in TGRC-MOSFET, both cut-off and maximum oscillator frequency improves significantly owing to enhancement in transconductance, reduction in parasitic capacitances and reduction in SCEs such as DIBL as discussed in the work. Moreover, the small signal behavior of TGRC MOSFET is also studied in terms of S-parameters, and significant improvement is perceived both in reflection and transmission coefficients as compared to CRC-MOSFET. In addition, RF performance of TGRC-MOSFET further improves with device miniaturization down to 20 nm. Hence, TGRC-MOSFET is appropriate for high-performance System-On-Chip RF/microwave applications.

## Acknowledgment

The authors would like to express gratitude to Microelectronics Research Lab, Department of Engineering Physics, Delhi Technological University and Department of Science & Technology (DST) to carry out this work.

## References


[1] M. Saito, M. Ono, R. Fujimoto, H. Tanimoto, H. Nobuyuki, T. Yoshitomi, 0.15-m RF CMOS technology compatible with logic CMOS for low-voltage operation, IEEE Trans. Electron 45 (1998) 737–742.

[2] L.E. Larson, Silicon technology tradeoffs for radio-frequency/mixed-signal system-on-a-chip, IEEE Trans. Electron. 50 (2003) 683–699.

[3] V. Kilchytska, A. Neve, L. Vancaillie, D. Levacq, S. Adriaensen, H.V. Meer, K. D. Meyer, C. Raynaud, M. Dehan, J.P. Raskin, D. Flandre, Influence of device engineering on the analog and RF performances of SOI MOSFETs, IEEE Trans. Electron. 50 (2003) 577–588.

[4] J.Y. Yang, K. Benaissa, D. Crenshaw, B. Williams, S. Sridhar, J. Ai, G. Boselli, S. Zhao, S.P. Tang, N. Mahalingam, S. Ashburn, P. Madhani, T. Blythe, H. Shichijo, 0.1 pm RFCMOS on high resistivity. Substrate for system on chip (SOC) applications, IEDM Technol. (2002) 667–670.

[5] R. Murali, J.D. Meindle, Modeling the effect of source/drain junction depth on bulk-MOSFET scaling, Solid-State Electron. 51 (2004) 569–574.

[6] Q. (Brian) Chen, Compact modeling of multi-gate MOSFETs for RF designs, in: Proceedings of the IEEE International Wireless Symposium, 2013.

[7] A. Nakakubo, S. Yanagi, Y. Oniura, Proposal of sub 0.1 um SO1 MOSFET structure (partial-ground-plane SO1 MOSFET) for RF/digital applications, in: Proceedings of the IEEE International SO1 Conference, 2010, pp. 96–97.

[8] R.M. Barsan, Analysis and modeling of dual-gate MOSFETs, IEEE Trans. Electron Device 28 (5) (1981) 523–534.

[9] M. Chan, F. Assaderaghi, S.A. Parke, C. Hu, P.K. Ko, Recessed-channel structure for fabricating ultrathin SOI MOSFET with low series resistance, IEEE Electron Device Lett. 15 (1994) 22–24.

[10] C.P. Auth, James D. Plummer, Scaling theory for cylindrical, fully-depleted, surrounding-gate MOSFETs, IEEE Electron Device Lett. 18 (2) (1997) 74–76.

[11] N. Gupta, A. Kumar, R. Chaujar, Impact of device parameter variation on RF performance of gate electrode workfunction engineered (GEWE)-silicon nanowire (SiNW) MOSFET, J. Comput. Electron. 14 (2015).

[12] S. Kimura, J. Tdnaka, H. Noda, T. Toyabe, S. Ihara, Short-channel-effect-suppressed sub-0.1 pm grooved-gate MOSFET's with W gate, IEEE Trans. Electron Device 42 (1995) 94–110.

[13] R. Chaujar, R. Kaur, M. Saxena, M. Gupta, R.S. Gupta, On-state and RF performance investigation of sub-50 nm L-DUMGAC MOSFET design for high-speed logic and switching applications, Semicond. Sci. Technol. 23 (2008) 1–8.

[14] P.P. Edwards, A. Porch, M.O. Jones, D.V. Morgan, R.M. Perks, Basic materials physics of transparent conducting oxides, Dalton Trans. 19 (2004) 2995–3002.

[15] H. Kawazoe, K. Ueda, Transparent conducting oxides based on the spinel structure, J. Am. Ceram. Soc. 82 (1999) 3330–3336.

[16] R. Chaujar, R. Kaur, M. Saxena, M. Gupta, R.S. Gupta, TCAD assessment of gate electrode workfunction engineered recessed channel (GEWE-RC) MOSFET and its multilayered gate architecture—Part I: hot-carrier-reliability evaluation, IEEE Trans. Electron Devices 55 (10) (2008) 2602–2612.

[17] S.V.N. Pammi, H.J. Jung, S.G. Yoon, Low-temperature nanocluster deposition (NCD) for improvement of the structural, electrical, and optical properties of ITO thin films, IEEE Trans. Nanotechnol. 10 (2011) 1059–1065.

[18] R. Chaujar, R. Kaur, M. Saxena, M. Gupta, R.S. Gupta, Solution to CMOS technology for high performance analog applications: GEWE-RCMOSFET, Adv. Optoelectron. Mater. Devices (2008) 201–205.

[19] C.H. Doan, S. Emami, A.M. Niknejad, R.W. Brodersen, Millimeter-wave CMOS design, IEEE J. Solid-State Circuits 40 (2005) 144–145.

[20] T. Minami, Transparent conducting oxide semiconductor for transparent electrodes, Semicond. Sci. Technol. 20 (2005) S35–S44.

[21] A. Kumar, N. Gupta, R. Chaujar, Analysis of novel transparent gate trcessed channel (TGRC) MOSFET for improved analog behaviour, Microsyst. Technol. 21 (5) (2015).

[22] A. Kumar, R. Chaujar, N. Gupta, Novel design: transparent gate recessed channel (TGRC) MOSFET for improved reliability applications in: Proceedings of the IEEE 1st International Conference on Microelectronics, Circuits and Systems, vol. 1, 2014, pp. 1–5.

[23] J.J. Liou, F. Schwierz, RF MOSFET: recent advances, current status and future trends, Solid-State Electron. 47 (2003) 1881–1895.

[24] ATLAS Device Simulator, SILVACO International, 2011.

[25] R. Chaujar, R. Kaur, M. Saxena, M. Gupta, R.S. Gupta, Investigation of multi-layered-gate electrode workfunction engineered recessed channel (MLGEWE-RC) sub-50 nm MOSFET: a novel design, Int. J. Numer. Model.: Electron. Netw. Devices Fields 22 (2008) 259–278.

[26] A. Sarkar, S. De, A. Dey, C.K. Sarkar, Analog and RF performance investigation of cylindrical surrounding-gate MOSFET with an analytical pseudo-2D model, J. Comput. Electron. 11 (2012) 182–195.

[27] D.M. Pozar, Microwave Engineering, 4th ed., Wiley, 2011.

[28] B. Nae, A. Lazaro, B. Iniguez, Spanish Conference on Electron Devices, 2009, pp. 112–115.

[29] N.R. Mohapatra, Student, M.P. Desai, S.G. Narendra, V.R. Rao, Modeling of parasitic capacitances in deep submicrometer conventional and high-K dielectric MOS transistors, IEEE Trans. Electron Devices 50 (2003) 959–966.

[30] A.W. Longman, Application-specific Integrated Circuits, 1997.

[31] S. Cho, K.R. Kim, B.G. Park, I.M. Kang., RF performance and small-signal parameter extraction of junctionless silicon nanowire MOSFETs, IEEE Trans. Electron Device 58 (2011) 1388–1396.

[32] D.M. Pozar, Microwave Engineering, John Wiley and Sons, New York, 1998.

[33] P. Malik, R.S. Gupta, R. Chaujar, M. Gupta., AC analysis of nanoscale GME-TRC MOSFET for microwave and RF applications, Microelectron. Reliab. 52 (2012) 151–158.

[34] E.B. Ramayya, D. Vasileska, S.M. Goodnick, I. Knezevic., Electron mobility in silicon nanowires, IEEE Trans. Nanotechnol. 6 (2007) 113–116.

[35] M. Frey, A. Esposito, A. Schenk, Computational comparison of conductivity and mobility models for silicon nanowire devices, J. Appl. Phys. 109 (2011) 083707-1–083707-6; A.W. Longman, Application-specific Integrated Circuits.

**Journal of Atomic, Molecular, Condensate & Nano Physics**
Vol. 6, No. 3, pp. 169–178, 2015
ISSN 2349-2716 (online); 2349-6088 (print)
Published by RGN Publications

http://www.rgnpublications.com

# Terahertz Radiation Emission from A Surface Wave Pumped Free Electron Laser

Research Article

Jyotsna Panwar, Suresh C. Sharma* and Rinku Sharma

*Department of Applied Physics, Delhi Technological University* (*DTU*)*, Delhi, India*
***Corresponding author:** suresh321sharma@gmail.com

**Abstract.** We develop an analytical formalism for tunable coherent terahertz (THz) radiation generation from bunched relativistic electron beam (REB) counter -propagating to the surface wave in the vacuum region Compton backscatters the surface wave. Plasma supports the surface wave that acquires a large wave number around pump wave frequency. The surface wave extends into vacuum region that can be employed as a wiggler for the generation of terahertz radiation. As the beam bunches pass through the surface plasma wave wiggler, they acquire a transverse velocity, constituting a transverse current producing coherent THz radiation. It was found that the terahertz power increases with electric field as well as with the thermal velocity of electrons. It was also found that the growth rate and efficiency of the instability both increases with the modulation index of the density modulated beam.

**Keywords.** Terahertz radiation; FEL; SPW; Density modulation

**PACS.** 34.90.+q; 0.7.85Nc; 34.60.z; 34.50.Fa

**Received:** Junxxxxe 8, 2015 **Accepted:** October 4, 2015

Copyright © 2015 Jyotsna Panwar, Suresh C. Sharma and Rinku Sharma. *This is an open access article distributed under the Creative Commons Attribution License, which permits unrestricted use, distribution, and reproduction in any medium, provided the original work is properly cited.*

## 1. Introduction

Recently, there has been a great deal of interest in generation of high power terahertz radiation due to its non-ionizing behavior and good penetrating power and hence its applications in wide areas including medical imaging, chemical and security identification, spectroscopy analysis, remote sensing [1–3]. The main aspects of generating terahertz radiation of high power lies in

using a prebunched or a modulated electron beam interacting with the wiggler in a free electron laser where it exchanges the energy with the electromagnetic radiation. The beam transfers the energy to the radiation wave and the wave gets amplified [4–11]. The kind of the wave excited due to beam-plasma interaction depends on the parameters of beam and plasma, mainly the three parameters: wiggler period, beam velocity and the phase velocity of the radiation [6].

Chen et al. [7] investigated the generation of the radiation by the interaction of relativistic circularly polarized laser pulse with overdense plasma which allows large plasma density and high pump laser intensity.

Kumar and Tripathi [8] have studied the coupling of a relativistic electron beam, modulated by two laser beams with a magnetic wiggler. They observed that THz power increases with the beam velocity and varies linearly with the bunch length and scales as square of the bunch radius.

Neumann et al. [9] have experimentally demonstrated the generation of multiple sub picoseconds pulses repeated at the terahertz frequencies with a modified drive laser by creating the highly modulated electron beams at the photocathode.

Sharma et al. [10] have examined the growth rate, efficiency of the radiation by employing an interaction of an energy modulated electron beam with the surface plasma wave as wiggler at vacuum plasma interface. They observed that the phase velocity of the radiation can be reduced by plasma which helps in the decrease of beam energy required for generating the radiation.

Yugami et al. [11] have experimentally demonstrated the generation of the radiation by the coupling of the wake field with the magnetic field and observed that the relative power of the radiation varied with the square of the applied magnetic field strength and increases with the increase of the density. They also suggested that the frequency can be tuned by varying the pressure of the supersonic gas, used to create the vacuum-plasma interface.

Singh et al. [12] observed the coupling of an oscillatory velocity of electron beam produced by the laser beam incident on the metal surface with the density perturbation produced by the surface plasma wave propagating along a metal-free space boundary via the generation of nonlinear current and observed that power of the radiated beam increases monotonically with the frequency of the probing laser and the SPW field.

Kraft et al. [13] have studied the generation of the wave by injecting the beam at an angle to the magnetic field and concluded that the emission is very weak in case if parallel propagation and is not affected by the beam modulation where as the emission is improved upto 50% if incident obliquely.

For the generation of the radiation by the upper hybrid wave FEL, the plasma density must be greater than the beam density, otherwise the frequency of the upper hybrid wave will approach the cyclotron frequency and hence it will lead to cyclotron damping, investigated by Sharma and Tripathi [14].

Pathak et al. [15] have reported the generation of terahertz radiation using free electron laser in rippled density plasma and observed that the growth rate is affected by the plasma

density, amplitude, depth of density ripple and the transverse component of the ripple wave vector.

Liu and Tripathi [16] employed a layered dielectric with periodic permittivity in space as a wiggler for the generation of the radiation and observed that the beam energy requirement is considerably less as compared to one without dielectric.

Sharma and Singh [17] investigated that the two cross focused lasers in the presence of collisional plasma were able to produce nonlinear current at the terahertz frequency. They observed that the amplitude and power of the wave increases with the amplitude of the static electric field.

Leemans et al. [18] observed that the radiation is emitted at the plasma boundary when the pre-bunched beam is highly dense and scales quadratically with the density for larger wavelengths as compared to the bunch length.

In this paper, we study the Terahertz radiation emission from the surface wave pumped FEL and examine the growth rate and efficiency of the generated terahertz radiation by a density modulated relativistic electron beam counter-propagating surface plasma wave. The surface wave degrades as it moves away from the surface ($k_{ox} \ll k_{oz}$) and hence they have large amplitude at low powers. The SPW is a guided electromagnetic wave which propagates between the two media with different conductivities and dielectric properties along the boundary [19,20]. We have considered the vacuum-plasma interface and calculated the growth rate, power and efficiency of the generated wave in the later section.

## 2. Theoretical Dispersion Relation

We consider a relativistic pre-bunched electron beam which is density modulated traveling in the z-direction and a vacuum-plasma interface with a surface plasma wave (SPW) propagating above the interface. The interface is taken at y=0, with vacuum present above $x = 0$ and plasma below $x = 0$, both occupying half of the spaces. The vacuum has permittivity unity i.e. $\epsilon_0 = 1$ and plasma with effective permittivity, $\epsilon_{\text{eff}} = 1 - \frac{\omega_p^2}{\omega_0^2}$, where $\omega_p^2 = \frac{4\pi n_0 e^2}{m_e}$, $\omega_p$ being the plasma frequency, $\omega^0$ is the SPW frequency. The plasma is characterized by lattice dielectric constant $\epsilon_L$ and a.c conductivity $\sigma$, where $\sigma = \frac{n_0 e^2}{m_e \omega^0}$ ($n_0$ is the plasma density, $e$ is the electronic charge and $m_e$ is the mass of the electron).

The electric field of the SPW propagating along the interface is given as

$$E = E(x)e^{-i(\omega_0^0 t - k_{wz} z)}. \tag{2.1}$$

Electric field is polarized in the x-z plane. Using the Maxwell's III and IV equations, we obtain

$$\nabla^2 \vec{E} + \omega_0^{02}/c^2 \epsilon \vec{E} = 0 \tag{2.2}$$

which can be written as

$$\partial^2 E_z/\partial x^2 - k_p E_z = 0 \quad \text{for plasma} \tag{2.3}$$

and

$$\partial^2 E_z/\partial x^2 - k_v E_z = 0 \quad \text{for vacuum} \tag{2.4}$$

where $k_p^2 = k_{wz}^2 - \frac{\omega_0^{02}}{c^2}\epsilon$ and $k_v^2 = k_{wz}^2 - \frac{w_0^{02}}{c^2}$, $k_p$, $k_v$ is the plasma wave vector and vacuum wave vector respectively.

The solutions of above equations can be given as

$$E_z = A_p e^{(k_p x)} e^{-i(\omega_0^0 t - k_{wz} z)} \quad \text{for plasma} \tag{2.5}$$

and

$$E_z = A_v e^{-(k_v x)} e^{-i(\omega_0^0 t - k_{wz} z)} \quad \text{for vacuum.} \tag{2.6}$$

The dispersion relation for SPW can be obtained by applying the boundary conditions at $x = 0$ for $E_z$ and $\epsilon E_z$ continuous at the boundary

$$k_{wz}^0 = \omega^2 \epsilon / c^2 (1+\epsilon), \tag{2.7}$$

where $\epsilon = k_p/k_v$ .

In order to ensure that the surface wave is spatially damped away from the interface, we require $k_z^2 < 0$ i.e. $1+\epsilon < 0$ or $\omega < \omega_p/\sqrt{(1+\epsilon)}$ or $\omega < \omega_p/\sqrt{2}$ such that $k_p, k_v \to \infty$ as 1+ $\epsilon < 0$. Thus the waves are strongly localized near the surface.

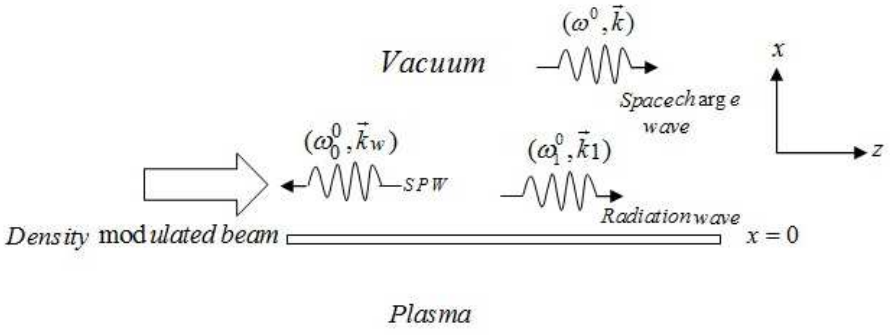


**Figure 1.** Schematic diagram of SPW-pumped FEL.

## 3. Beam Wiggler Interaction

The density modulated pre bunched electron beam interacts with the surface plasma wave which acts as a wiggler in the present case. The initial parameters of the beam are $n_b^0$ as the beam density, velocity $\vec{v}_b^0$. In the free electron laser, we have considered the propagation of surface wave over a wiggler with wave vector $k_{wz}$ and frequency $\omega^0$. The electron beam when interacts with the SPW, acting as a wiggler acquires an oscillatory velocity $\vec{v}_0^0$. This velocity can be obtained by using the equation of motion for an electromagnetic wave as

$$m_e \left[ \frac{\partial(\gamma \vec{v}_0^0)}{\partial t} + (\vec{v}_b^0 \cdot \nabla)(\gamma \vec{v}_0^0) \right] = -e\left( \vec{E} + \frac{1}{c} \vec{v}_0^0 \times \vec{B} \right) \tag{3.1}$$

On solving this equation with $\vec{B} = \frac{c}{w_0^0}(\vec{k}_w \times \vec{E})$ and taking different components of velocity, we obtain the x-component of oscillatory velocity as

$$v_{0x}^0 = \frac{eE_{0z}}{m_e\omega_0^0\gamma_0}\left[\frac{k_{wz}}{k_{0v}} + \frac{k_{0v}v_b^0}{(\omega_0^0 - k_{wz}v_b^0)}\right], \tag{3.2}$$

where $m_e$, $e$ are the electronic mass and charge, respectively, $c$ is the speed of light and $k_z$, $\omega_0^0$ being the SPW wave vector and frequency, respectively.

The equilibrium can be perturbed by applying the electromagnetic perturbation with perturbed values as

$$E_{1x} = A_1 e^{-i(\omega_1^0 t - k_{1z}z)}, \quad \vec{B}_1 = \frac{c}{\omega_1^0}(\vec{k}_1 \times \vec{E}_1), \quad \vec{v}_1^0 = \frac{e\vec{E}_1}{im\omega_1^0\gamma_0}.$$

Pondermotive force is exerted by the FEL radiation and the surface wave on the beam electrons with the equation of motion as

$$m\frac{\partial\vec{v}}{\partial t} = -e\vec{E} + \vec{F}_p - \frac{1}{n}\nabla(nT_e), \tag{3.3}$$

where $\vec{F}_p = -m(\vec{v}\cdot\nabla)\vec{v} - \frac{e}{c}(\vec{v}\times\vec{B})$ is the pondermotive force. The z-component of the pondermotive force is

$$F_{p_z} = e\nabla\phi_p$$

The pondermotive force produces perturbed oscillatory velocity $v_{2b}^0$ of the electrons in the axial direction with density perturbation as $n_{2b}$, obtained using the equation of motion and continuity respectively.

$$v_{2b}^0 = -\frac{ek_z\phi_p}{m_e\gamma_0^3(\omega - k_z v_b^0)}, \tag{3.4}$$

$$n_{2b} = \frac{k_z^2}{4\pi e}\chi_b\phi_p, \tag{3.5}$$

where $k_z = k_{wz} + k_{1z}$, $\omega^0 = \omega_0^0 + \omega_1^0$ are the wave number and frequency of the space charge wave, respectively.

$\phi_p = \frac{m\gamma_0}{2e}v_{1x}^0 v_{0x}^0$ is the pondermotive potential

and

$\chi_b = -\frac{\omega_{pb}^2}{(\omega - k_z v_b^0)^2\gamma_0^3}$ is the beam susceptibiliiy.

In case of Compton regime, the potential of the beam mode is much less than the pondermotive potential and hence can be neglected ($\phi \ll \phi_p$). The beam density is $n_b^0 =$

$n^0_{0b}+n^0_{1b}+n^0_{bm}$, where $n^0_{bm}$ is the modulated beam density such that $n^0_{bm}=\Delta n^0_{0b}$, $\Delta$ being the modulation index. The phase of the perturbed beam as $e^{-i(\omega^0 t-k_z z)}$ and that of the modulated beam is $e^{-i(\omega^0_0 t-k_{wz}z)}$.

On solving the equation of continuity, we get

$$n_{1b}=\frac{n_{0b}\vec{v}^0_{1b}}{(\omega^0-k_z v^0_{0b})}\left[k_z(1+\Delta)+k_{wz}\Delta\right]. \tag{3.6}$$

The perturbed non-linear current density can be given as

$$\vec{J}^{NL}_1=-en^0_{0b}\vec{v}^0_{1b}-en^0_{1b}\vec{v}^0_{0b}-en^0_{bm}\vec{v}^0_{1b}. \tag{3.7}$$

On substituting the values, we obtain

$$\vec{J}^{NL}_1=\frac{ie^2n^0_{0b}k_z v^0_{0x}\vec{A}_1}{2m_e\omega^0_1\gamma^3_0(\omega-v^0_{0b}k_z)}\left[(1+\Delta)+\frac{v^0_{0b}}{(\omega-v^0_{0b}k_z)}(k_z(1+\Delta)+k_{wz}\Delta)\right]\left[e^{-i\left(\omega^0_1 t-\left(k_{1z}+\frac{\omega^0_1}{v^0_{0b}}z\right)\right)}\right]. \tag{3.8}$$

In using Maxwell's III and IV equations

$$\nabla\times\vec{E}=-\frac{1}{c}\frac{\partial\vec{B}}{\partial t},$$

$$\nabla\times\vec{H}=\frac{4\pi}{c}\vec{J}_1+\frac{1}{c}\frac{\partial\vec{E}_1}{\partial t},$$

$$(\omega^{02}_1-k^2_{1z}c^2)(\omega^0-v^0_{0b}k_z)^2=\frac{4\pi\omega^0_1e^2n^0_{0b}k_z v^0_{0x}v^0_{0b}}{2m_e\omega^0_1\gamma^3_0}\left[k_z(1+\Delta)+k_{wz}\Delta\right].$$

On assuming that $\omega^0=k_z v^0_{0b}+\delta$ and $\omega^0_1=k_{1z}c+\delta$ we obtain

$$\delta=\left[\frac{\pi e^2n^0_{0b}k_z v^0_{0x}v^0_{0b}}{m_e\omega^0_1\gamma^3_0}(k_z(1+\Delta)+k_{wz}\Delta)\right]^{\frac{1}{3}}e^{\frac{2in\pi}{3}}. \tag{3.9}$$

The growth rate is obtained by taking the imaginary part of $\delta$ i.e. $\Gamma=\mathrm{Im}\,\delta$, where $\Gamma$ is the growth rate of the generated wave instability.

Hence, the growth rate is given as

$$\Gamma=\left[\frac{\omega^2_{p_b}v^0_{0x}v^0_{0b}}{c\gamma^3_0}\left((1+\Delta)\frac{\omega^0_1}{c}+k_{wz}\Delta\right)\right]^{\frac{1}{3}}\frac{\sqrt{3}}{2}, \tag{3.10}$$

where $\omega^2_{pb}=\frac{4\pi n^0_{0b}e^2}{m_e}$.

The power of the wave generated can be calculated using

$$P=\omega^0_0\frac{\partial\epsilon_0}{\partial\omega_0}\frac{E^2_0}{8\pi}v_g\pi r^2_b, \tag{3.11}$$

where $v_g \simeq v_{th} = \sqrt{\frac{T_e}{m_e}}$ is the group velocity of the beam, $v_{th}$ is the electron thermal velocity. $T_e$ is the temperature of the plasma, $m_e$ is the mass of the electron. $\pi r_b^2$ is the area of the beam.

The efficiency of the beam is given as

$$\eta = \frac{\Gamma}{\omega_1} \frac{\gamma_0^3}{\sqrt{3}(\gamma_0 - 1)},$$

on substituting the value of growth rate, efficiency is obtained as

$$\eta = \left[ \frac{\omega_{pb}^2 v_{0x}^0 v_{0b}^0}{c} \left( (1+\Delta)\frac{\omega_1^0}{c} + k_{wz}\Delta \right) \right]^{\frac{1}{3}} \frac{\gamma_0^2}{2\omega_1^0(\gamma_0 - 1)}. \tag{3.12}$$

## 4. Results and Discussions

Standard parameters of THz radiation have been used for calculating the required parameters of the radiation which is obtained from the surface plasma wave pumped FEL. In Figure 2 the variation of the growth rate of the unstable wave instability has been plotted against the modulation index using the typical parameters: beam energy $E_b$ = 0.12 MeV, beam current $I_b$ = 1.4 A, beam radius $r_b$ = 2.4 cm, electric field $E_0$ = 100 esu, radiation frequency $\omega_1^0 = 3 \times 10^{12}$ rad/sec, and modulation frequency $\omega' = 2.5 \times 10^{10}$ rad/sec. From Figure 2 we can see that the growth rate increases with the increase in the modulation index $\Delta$ and has reached the largest value when $\Delta \to 1$ and when the frequency and wave number of the generated radiation wave is of the order of the pre-bunched modulated electron beam. For the largest value of $\Delta$ i.e., $\Delta = 1$, the growth rate comes out to be $\Gamma = 2.87 \times 10^9$ (rad/sec). When $\Delta = 0$ i.e., without pre-modulated beam, the growth rate of the THz radiation is $\Gamma = 1.85 \times 10^9$ (rad/sec).

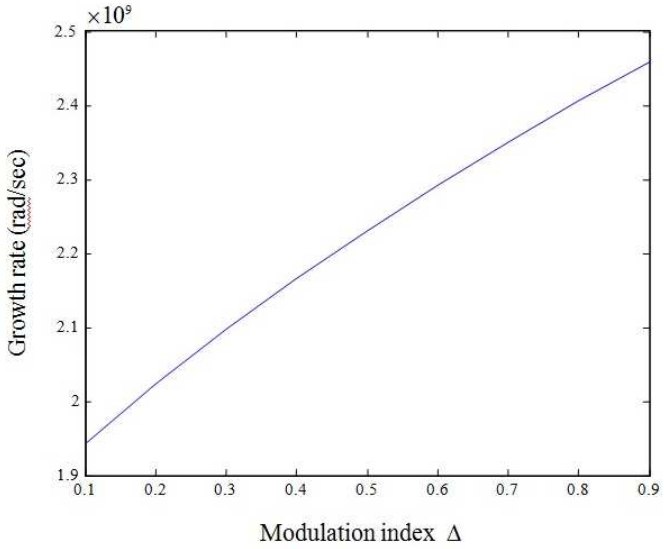


**Figure 2.** The figure shows the variation of growth rate (rad/sec) as a function of the modulation index for $E_b$ = 0.12 Mev, $I_b$ = 1.4 A, $\omega_1^0 = 3 \times 10^{10}$ (rad/sec).

In Figure 3, we have plotted the effect of electric field $E_0$ (esu) on the radiated power $P_0$ (in Watt) of the radiation obtained using electron thermal velocity $v_g = 5.9 \times 10^7$ (cm/sec), $\omega_0^0 \frac{\partial \epsilon_0}{\partial \omega_0} \simeq 1$ and the other parameters are same as taken for the Figure 2. It was observed that the power increases as we increase the electric field and comes out to be the order of kilo watt. Hence by providing the suitable magnetic field, we can obtain an electric field of optimum value and therefore can be able to obtain the radiation of more high power, which is our motive.

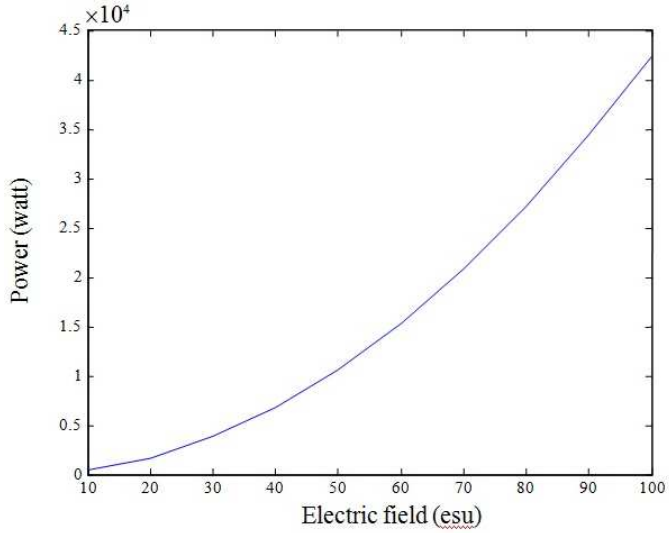


**Figure 3.** The figure shows the variation of the power (erg/sec) with the electric field (esu) with the parameters $v_g = 5.9 \times 10^7$ (cm/sec) and $r_b = 2.4$ cm.

Figure 4 shows that the power $P_0$ (in Watt) of the beam increases as the electron thermal velocity $v_g$ (cm/sec) of electrons increases with $E_0 = 100$ esu. The plot shows that the power increases linearly with the electron thermal velocity.

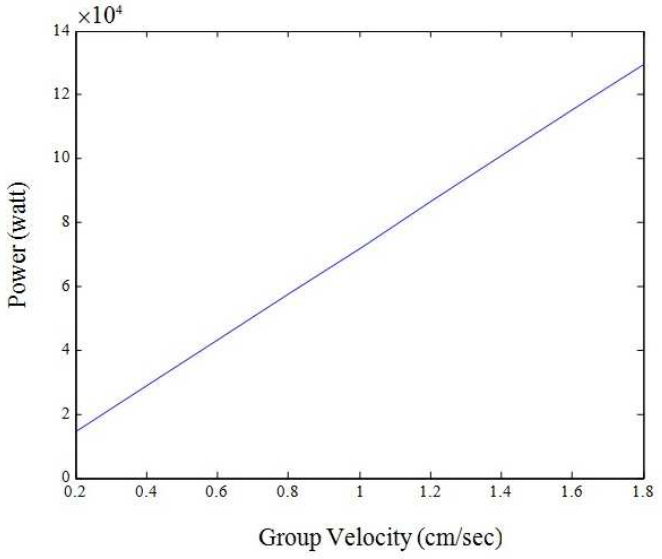


**Figure 4.** The figure shows the variation of the power (erg/sec) with the group velocity (cm/sec) i.e. electron thermal velocity with $E_0 = 100$ esu.

Figure 5 shows the variation of the efficiency of the SPW-pumped FEL instability with respect to the modulation index. From Figure 5 it can be seen that the efficiency increases with the modulation index. The growth rate and efficiency scales as two-third power of the plasma frequency. Hence, it improves with an increase in plasma frequency, thus the plasma density.

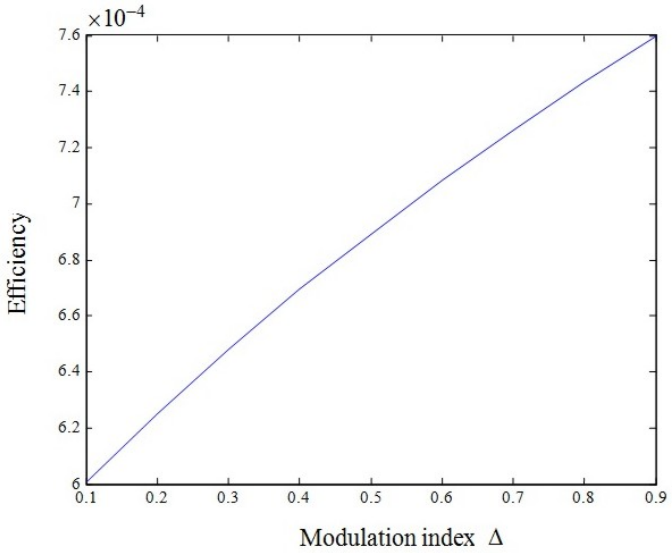


**Figure 5.** The figure shows the effect of modulation index on the efficiency radiation with $\omega' = 2.5 \times 10^{10}$ (rad/sec), $E_b = 0.12$ Mev, $I_b = 1.4$ A.

## 5. Conclusion

It can be concluded that the SPW are driven to instability by pre-bunched relativistic beam, which is density modulated leading to the increase in growth rate, amplitude and efficiency of the radiation wave with the modulation index and attained the largest value when $\Delta$ approached unity. The beam and plasma interaction leads to the growth of the radiation beam and the growth rate increases with the increase in plasma density. Using the SPW as a wiggler, it has been possible to generate high power radiation even at lower beam current. The density modulation has led to an improvement in the radiation generation of FEL instability and the radiation of desired frequency and power can be obtained by varying the frequency and modulation index of the incident relativistic beam. Further plasma can help in reducing the phase velocity of the radiation wave significantly, thus helping in the decrease of beam energy required for generating THz radiation.

### Competing Interests

The authors declare that they have no competing interests.

### Authors' Contributions

All the authors contributed equally and significantly in writing this article. All the authors read and approved the final manuscript.

## References


[1] M. Singh, S. Kumar and R.P. Sharma, *Phys. Plasmas* **18** (2011), 022304-1.

[2] V. B. Pathak, D. Dahiya and V. K. Tripathi, *J. Appl. Phys.* **105** (2009), 013315-1.

[3] T. M. Antonsen, Jr., J. Palastro and H. M. Milchberg, *Phys Plasmas* **14** (2007), 033107-1.

[4] M. Cohen, A. Kugel, D. Chairman, M. Arbel, H. Kleinman, D. Ben-Haim, A. Eichenbaum, M. Draznin, Y. Pinhasi, I. Yakover and A. Grover, *Nucl. Instr. & Meth. in Phys. Res. A* (1995), 358.

[5] C. Kraft, G. Matthieussent, P. Thevenet and S. Bresson, *Phys. Plasmas* **1** (1994), 2163.

[6] V. Beniwal, S. C. Sharma and M. K. Sharma, *Phys. Plasmas* **11** (2004), 5716 .

[7] Z.-Y. Chen, X.-Y. Li and W. Yu, *Phys. Plasmas* **20** (2013), 103115.

[8] M. Kumar and V. K. Tripathi, *Phys. Plasmas* **19** (2012), 073109-1.

[9] J. G. Neumann, R. B. Fiorito, P. G. S'Ohea, H. Loos, B. Sheehy, Y. Shen and Z. Wu, *J. Appl. Phys.* **105** (2009), 053304.

[10] S. C. Sharma, J. Sharma, A. Bhasin and R. Walia, *J. Plasma Physics* **78** (2012), 635.

[11] N. Yugami, T. Higashiguchi, H. Gao, S. Sakai, K. Takahashi, H. Ito, Y. Nishida and T. Katsouleas, *Phys. Rev. Letter* **89** (2002), 065003-1.

[12] D. B. Singh, G. Kumar and V. K. Tripathi, *J. Appl. Phys.* **101** (2007), 043306-1.

[13] C. Kraft, G. Matthiuessent and B. Lembege, *Phys. Plasmas* **1** (1994), 4082.

[14] S. C. Sharma and V. K. Tripathi, *IEEE Trans. Plasma Sci.* **23** (1995), 792.

[15] V. B. Pathak, D. Dahiya and V. K. Tripathi, *J. Appl. Pays.* **105** (2009), 013315-1.

[16] C. S. Liu and V. K. Tripathi, *IEEE Trans. Plasma Sci.* **23** (1995), 459.

[17] R. P. Sharma and R. K. Singh, *Phys. Plasmas* **21** (2014), 073101-1.

[18] W. P. Leemans, J. van Tilborg, J. Faure, C. G. R. Geddes, Cs. Toth, C. B. Schroeder, E. Esarey, G. Fubiani and G. Dugan, *Phys. Plasmas* **11** (2004), 2899.

[19] C. S. Liu and V. K. Tripathi, *Electromagnetic Theory for Telecommunications*, Foundation (Delhi, 2007).

[20] C. S. Liu and V. K. Tripathi, *Interaction of Electromagnetic waves with Electron Beams and Plasmas* (World Scientific Singapore, 1994).

Volume 3, Issue 4 (2015) 619-625 ISSN 2347 - 3258
International Journal of Advance Research and Innovation

# Thermodynamic Performance Comparison Using HFO-1234yf and HFO-1234ze in the High Temperature Cascade Refrigeration Systems and Ecofriendly Refrigerants in Low Temperature Applications

R. S. Mishra
Department of Mechanical Engineering, Delhi Technological University, Delhi, India

**Article Info**

Article history:
Received 25 September 2015
Received in revised form
20 October 2015
Accepted 28 November 2015
Available online 15 December 2015

**Keywords**
HFO-1234ze/HFO-1234yf,
Cascade Refrigeration System,
Ecofriendly Refrigerants,
Alternative Refrigerants

**Abstract**

The present paper relates to a cascade refrigeration system which circulates a HFO refrigerant in the high temperature circuit and HFC-134a in the low temperature (173K) circuit for cryogen applications .The thermodynamic analysis using entropy generation for finding exergy destruction ratio indicating that R1234ze (GWP=6) gives better performance than R-1234yf (GWP=4) in the high temperature circuit. The numerical computation has been carried out for 173 K evaporator temperature for ten ecofriendly refrigerants in the low temperature circuit and HFO-1234yf, HFO-1234ze, R152a and R717 in the high temperature circuit. The effect of condenser temperature from temperature (303K to 333K), cascade evaporator range (253K to 293K) and evaporator temperature range 173K to 223K and temperature overlapping (Approach) rages from zero to 10 on thermodynamic performance have been investigated. It was observed that R1234ze in high temperature circuit and R 134a in lower temperature circuit is a best alternative than R1234yf in high temperature circuit and R 134a in lower temperature circuit.

## 1. Introduction

Low global warming potential refrigerants R1234ze and R1234yf are anticipated to be the refrigerants of choice for high-temperature refrigeration systems and heat pump in the industrial applications. HFO-1234ze is a global warming potential (GWP) rating one 225th and HFO-1234yf is the first in a global warming potential (GWP) rating one 335th that of R-134a [1] Cascade refrigeration systems for Low-Temperature are typically uses a refrigerant such as 1,1,1,2-tetrafluoroethane (R134a) or blends thereof with HFC-125 and HFC-143a (i.e., R404A) and carbon dioxide (C02) in the low temperature loop in the low temperature loop to provide cooling at 173K for crygen applications. HFC-134a and HFO-1234yf & HFO1234ze being the most widely used now a day , have zero ozone depletion potential and thus are not affected by the current regulatory phase out as a result of the Montreal Protocol.

This paper mainly deals with HFO refrigerants used in HTC and HFC-134a include pure hydrocarbons such as butane or propane, in the low temperature refrigerants for maintaining 173"K" for crygen applications. These replacements are found, new uses of such alternative refrigerants are being sought in order to take advantage of their low or zero ozone depletion potential and lower global warming potential.

## 2. Literature Review

The cascade refrigeration system has at least two refrigeration loops, each circulating a ecofriendly refrigerant there comprising: a first expansion device for reducing the pressure and temperature of a HFO refrigerant and evaporator having an inlet and an outlet, wherein the first refrigerant liquid from the first expansion device enters the evaporator through the evaporator inlet and is evaporated in the evaporator to form a HFO refrigerant vapor, thereby producing cooling, and circulates to the outlet;

The first compressor having an inlet and an outlet, wherein the first refrigerant vapor from the evaporator circulates to the inlet of the first compressor and is compressed, thereby increasing the pressure and the temperature of the first refrigerant vapour, and the compressed first refrigerant vapour circulates to the outlet of the first compressor. The cascade heat exchanger system having:(i) a first inlet and a first outlet, wherein the first refrigerant vapour circulates from the first inlet to the first outlet and is condensed in the heat exchanger system to form a first refrigerant liquid, thereby rejecting heat, and (ii) a second inlet and a second outlet, wherein a second refrigerant liquid circulates from the second inlet to the second outlet and absorbs the heat rejected by the first refrigerant and forms a second refrigerant vapour; and second compressor having an inlet and an outlet, wherein the second refrigerant vapour from the cascade heat exchanger system is drawn into the compressor and is compressed, thereby increasing the pressure and temperature of the second refrigerant vapour; The condenser having an inlet and an outlet for circulating the second refrigerant vapour there through and for condensing the second refrigerant vapour from the compressor to form a second refrigerant liquid, wherein the second refrigerant liquid exits the condenser through the condenser outlet; and (g) a second expansion device which reduces the pressure and temperature of the second refrigerant liquid exiting the condenser and entering the second inlet of the cascade heat exchanger system. The cascade heat exchanger system may include a first and a second cascade heat exchanger, and a secondary heat transfer loop which extends between the first and the second cascade heat exchanger. In this system, the second refrigerant liquid indirectly absorbs the heat rejected

**Corresponding Author,**
**E-mail address:** professor_rsmishra@yahoo.co.in
**All rights reserved:** http://www.ijari.org

by the first refrigerant vapour through a heat transfer fluid which circulates between the first cascade heat exchanger and the second cascade heat exchanger through the secondary heat transfer loop. The first cascade heat exchanger has a first inlet and a first outlet, and a second inlet and a second outlet, wherein the first refrigerant vapour circulates from the first inlet to the first outlet and rejects heat and is condensed, and a secondary heat transfer fluid circulates from the second inlet to the second outlet and absorbs the heat rejected from the first refrigerant vapour and circulates to the second cascade heat exchanger. The second cascade heat exchanger has a first inlet and a first outlet, and a second inlet and a second outlet, wherein the heat transfer fluid circulates from the second outlet of the first cascade heat exchanger to the first inlet of the second cascade heat exchanger and to the first outlet of the second cascade heat exchanger and rejects the heat absorbed from the first refrigerant. The second refrigerant liquid circulates from the second inlet to the second outlet of the second cascade heat exchanger and absorbs the heat rejected by the heat transfer fluid and forms a second refrigerant vapour. In accordance there is provided a method of exchanging heat between at least two refrigeration loops, comprising:

(a) absorbing heat from a body to be cooled in a first refrigeration loop and rejecting this heat to a second refrigeration loop; and (b) absorbing the heat from the first refrigeration loop in the second refrigeration loop and rejecting heat to ambient, as discussed in literature[2-3]

## 3. System Description

The object of the present study is to provide cascade refrigeration systems which use HFO-1234yf and HFO-1234ze refrigerant in the high temperature circuit which have unique characteristics to meet the demands of low or zero ozone depletion potential and lower global warming potential as compared to R11, R12 and R22 refrigerants.

In addition to lower global warming potential advantages, using R-1234yf and R1234ze in the high temperature circuit and R134a in the low temperature cascade refrigeration circuit the present investigation may have several advantages than currently used cascade refrigeration systems.

## 4. Results and Discussions

Table-1a and Table-2a showing the effect of ecofriendly refrigerants on first law efficiency (i.e. Overall system COP) and exergetic efficiency of cascade refrigeration system using R1234yf (of GWP 6) in the high temperature circuit and it was found that both thermal efficiencyies (i.e. overall first law efficiency and also second law efficiency) have highest values in case , when R123 is used in the low temperature circuit and R407c is used in the low temperature circuit. Similarly system exergy destruction ratio (EDR) is lowest when R600 hydrocarbon is used in the low temperature circuit. The low temperature circuit first law performance is lowest when R407c is used in the low temperature circuit. However high temperature circuit frist law performance does not affect. The temperature variation of high temperature circuit condenser with thermodynamic performances of cascade refrigeration system is also shown in Table-1(b) and Table-2(b) respectively and it is found that by increasing condenser's temperature in the high temperature circuit, the first law thermodynamic efficiency (overall system COP) second law efficiency (exergetic efficiency) is decreases Similarly system exergy destruction ratio is increases. The temperature overlapping (Difference of temperature between cascade condenser and cascade evaporator) is known as approach is greatly influencing the thermodynamic performances of cascade refrigeration system using R1234ze/R1234yf in the high temperature circuit and R134a in the low temperature circuit as shown in Table-1(c) and Table-2(c) respectively. The best performance of the cascade refrigeration system is achieved without temperature overlapping. As increasing approach, the first and second law efficiency have ben decreasing and system exergy destruction ratio is increasing. The temperature variation of low temperature circuit evaporator with thermodynamic performances of cascade refrigeration system is also shown in Table-1(d) and Table-2(d) respectively and it is found that by increasing evaporator's temperature in the low temperature circuit, the first law thermodynamic efficiency (overall system COP) second law efficiency (exergetic efficiency) is increases Similarly system exergy destruction ratio is decreases. Effect of variation in temperature of cascade evaporator on thermal performance of cascade Refrigeration system using R-1234yf/R1234ze in HighTemperature Circuit and R134a ecofriendly refrigerant in the Low Temperature Circuit is shown in Table-1(e) & Table-2(e) respectively and it was observed that by increasing cascade evaporator temperature, the first law efficiency (overall system COP) increases and reached to a optimum (maximum) value at 268K temperature and then decreases significantly and it strongly affecting circuit first law efficiency as high temperature circuit first law efficiency ($COP_{HTC}$ ) increases while low temperature circuit first law efficiency ($COP_{LTC}$ ) decreases. The performance of cascade refrigeration system using various ecofriendly refrigerants in the high temperature circuit and R134a in the also shown in Table-3 respectively and it was observed that First law efficiency in terms of overall system COP and second law efficiency (i.e. exergetic efficiency) is highest with lowest exergy destruction ratio using R717 which is toxic in nature and performance of R-152a is nearly approaching the same value which is also flammable in nature. Therefore the next alternative is R1234ze a (of GWP=4) and R1234yf (of GWP=6) for high temperature circuit gives better options after 2030 in terms of environmental aspects and it was found that R1234ze gives better thermodynamic performance than using R1234yf in the high temperature circuit.

**Table: 1.a (i).** Effect of ecofriendly refrigerants on thermal performance of cascade Refrigeration system using R-1234yf in High Temperature Circuit and following ecofriendly refrigerants in the Low Temperature Circuit ($Compressor_{Efficiency-1}$=0.80,$T_{eva2}$=173K, $T_{cond}$=333K, $T_{cascade-evaporator}$=253K, $Compressor_{Efficiency-2}$=0.80, Approach=temperature overlapping=10

| Ecofriendly Refrigerants in Lower Temp. | Overall System First law Performance | Overall Exergy Destruction Ratio of | Cascade System Exergetic Efficiency |
|---|---|---|---|

| Circuit | $COP_{Overall}$ | system $EDR_{System}$ | |
|---|---|---|---|
| R-134a | 0.3894 | 2.554 | 0.2814 |
| R-290 | 0.3928 | 2.523 | 0.2838 |
| R-600a | 0.3917 | 2.533 | 0.2830 |
| R-600 | 0.4004 | 2.456 | 0.2893 |
| R-404a | 0.3695 | 2.746 | 0.2670 |
| R-125 | 0.3628 | 2.814 | 0.2622 |
| R-123 | 0.4004 | 2.546 | 0.2894 |
| R-407c | 0.3365 | 3.113 | 0.2431 |
| R-410a | 0.3873 | 2.579 | 0.2799 |

**Table: 1.a. (ii).** Effect of ecofriendly refrigerants on thermal performance of cascade Refrigeration system using R-1234yf in High Temperature Circuit and following ecofriendly refrigerants in the Low Temperature Circuit ($Compressor_{Efficiency-1}$=0.80,$T_{eva2}$=173K, $T_{cond}$=333K, $T_{cascade-evaporator}$=253K, $Compressor_{Efficiency-2}$=0.80, Approach=temperature overlapping=10

| Ecofriendly Refrigerants in Lower Temp. Circuit | High Temperature Circuit First law Performance $COP_{HTC}$ | Low Temperature Circuit First law Performance $COP_{LTC}$ |
|---|---|---|
| R-134a | 1.258 | 1.020 |
| R-290 | 1.258 | 1.025 |
| R-600a | 1.258 | 1.021 |
| R-600 | 1.258 | 1.054 |
| R-404a | 1.258 | 0.9390 |
| R-125 | 1.258 | 0.9152 |
| R-123 | 1.258 | 1.054 |
| R-407c | 1.258 | 0.8244 |
| R-410a | 1.258 | 1.004 |

**Table: 1.b. (i).** Effect of High temperature condenser on thermal performance of cascade Refrigeration system using R-1234yf in High Temperature Circuit and following ecofriendly refrigerants in the Low Temperature Circuit ($Compressor_{Efficiency-1}$=0.80,$T_{eva2}$=173K, $T_{cond}$=333K, $T_{cascade-evaporator}$=253K, $Compressor_{Efficiency-2}$=0.80, Approach=temperature overlapping=10

| Variation of condenser temperature of cascade system in High Temp. Circuit (K) | Overall System First law Performance $COP_{Overall}$ | Overall Exergy Destruction Ratio of system $EDR_{System}$ | Cascade System Exergetic Efficiency |
|---|---|---|---|
| 333 | 0.3893 | 2.555 | 0.2813 |
| 328 | 0.4281 | 2.233 | 0.3093 |
| 323 | 0.4654 | 1.974 | 0.3363 |
| 318 | 0.5017 | 1.758 | 0.3625 |
| 313 | 0.5373 | 1.576 | 0.3382 |

**Table: 1.b(ii).** Effect of High temperature condenser on thermal performance of cascade Refrigeration system using R-1234yf in High Temperature Circuit and following ecofriendly refrigerants in the Low Temperature Circuit ($Compressor_{Efficiency-1}$=0.80,$T_{eva2}$=173K, $T_{cond}$=333K, $T_{cascade-evaporator}$=253K, $Compressor_{Efficiency-2}$=0.80, Approach=temperature overlapping=10

| Variation of condenser temperature of cascade system in High Temp. Circuit (K) | High Temperature Circuit First law Performance $COP_{HTC}$ | Low Temperature Circuit First law Performance $COP_{LTC}$ |
|---|---|---|
| 333 | 1.258 | 1.012 |
| 328 | 1.476 | 1.012 |
| 323 | 1.714 | 1.012 |
| 318 | 1.979 | 1.012 |
| 313 | 2.279 | 1.012 |

**Table: 1c(i).** Effect of Temperature overlapping on thermal performance in cascade temperature-evaporator on Thermal Performance of cascade Refrigeration system using R-1234yf in High Temperature Circuit and R134a ecofriendly refrigerant in the Low Temperature Circuit ($Compressor_{Efficiency-1}$=0.80,$T_{eva2}$=173K, $T_{cond}$=333K, $T_{cascade-evaporator}$=253K, $Compressor_{Efficiency-2}$=0.80, Approach=temperature overlapping=10

| Effect of Approach (Effect of temperature overlapping) | Overall System First law Performance $COP_{Overall}$ | Overall Exergy Destruction Ratio of system $EDR_{System}$ | Cascade System Exergetic Efficiency |
|---|---|---|---|
| 0 | 0.4389 | 2.154 | 0.3171 |
| 2 | 0.4286 | 2.229 | 0.3096 |
| 4 | 0.4184 ` | 2.307 | 0.3023 |
| 6 | 0.4085 | 2.388 | 0.2952 |
| 8 | 0.3988 | 2.470 | 0.2882 |
| 10 | 0.4201 | 2.294 | 0.3036 |

**Table: 1c(ii).** Effect of Temperature overlapping on thermal performance in cascade temperature-evaporator on Thermal Performance of cascade Refrigeration system using R-1234yf in High Temperature Circuit and R134a ecofriendly refrigerant in the Low Temperature Circuit ($Compressor_{Efficiency-1}$=0.80,$T_{eva2}$=173K, $T_{cond}$=333K, $T_{cascade-evaporator}$=253K, $Compressor_{Efficiency-2}$=0.80, Approach=temperature overlapping=10

| Effect of Approach (Effect of temperature overlapping) | High Temperature Circuit First law Performance $COP_{HTC}$ | Low Temperature Circuit First law Performance $COP_{LTC}$ |
|---|---|---|
| 0 | 1.258 | 1.210 |
| 2 | 1.258 | 1.167 |
| 4 | 1.258 | 1.125 |
| 6 | 1.258 | 1.086 |
| 8 | 1.258 | 1.048 |
| 10 | 1.258 | 1.012 |

**Table: 1.d(i).** Effect of low temperature evaporator on thermal performance of cascade Refrigeration system using R-1234yf in High Temperature Circuit and following ecofriendly refrigerants in the Low Temperature Circuit ($Compressor_{Efficiency-1}$=0.80,$T_{eva2}$=173K, $T_{cond}$=333K,

$T_{cascade\text{-}evaporator}$=253K, $Compressor_{Efficiency\text{-}2}$=0.80, Approach=temperature overlapping=10

| Effect of low temperature evaporator (K) | Overall System First law Performance $COP_{Overal}$l | Overall Exergy Destruction Ratio of system $EDR_{System}$ | Cascade System Exergetic Efficiency |
|---|---|---|---|
| 173 | 0.3893 | 2.555 | 0.2813 |
| 178 | 0.4219 | 2.516 | 0.2844 |
| 183 | 0.4562 | 2.488 | 0.2867 |
| 188 | 0.492 | 2.474 | 0.2879 |
| 193 | 0.5292 | 2.472 | 0.2880 |
| 198 | 0.5686 | 2.482 | 0.2872 |
| 203 | 0.6095 | 2.506 | 0.2852 |
| 208 | 0.6522 | 2.544 | 0.2822 |
| 213 | 0.6967 | 2.597 | 0.2780 |
| 218 | 0.7431 | 2.667 | 0.2727 |
| 223 | 0.7915 | 2.756 | 0.2662 |

**Table: 1. d(ii).** Effect of low temperature evaporator on thermal performance of cascade Refrigeration system using R-1234yf in High Temperature Circuit and following ecofriendly refrigerants in the Low Temperature Circuit ($Compressor_{Efficiency\text{-}1}$=0.80,$T_{eva2}$=173K, $T_{cond}$=333K, $T_{cascade\text{-}evaporator}$=253K, $Compressor_{Efficiency\text{-}2}$=0.80, Approach=temperature overlapping=10

| Effect of low temperature evaporator (K) | High Temperature Circuit First law Performance $COP_{HTC}$ | Low Temperature Circuit First law Performance $COP_{LTC}$ |
|---|---|---|
| 173 | 1.258 | 1.012 |
| 178 | 1.258 | 1.14 |
| 183 | 1.258 | 1.285 |
| 188 | 1.258 | 1.45 |
| 193 | 1.258 | 1.641 |
| 198 | 1.258 | 1.862 |
| 203 | 1.258 | 2.122 |
| 208 | 1.258 | 2.431 |
| 213 | 1.258 | 2.803 |
| 218 | 1.258 | 3.259 |
| 223 | 1.258 | 3.832 |

**Table: 1.e(i).** Effect of variation in temperature of cascade evaporator on thermal performance of cascade Refrigeration system using R-1234yf in HighTemperature Circuit and R134a ecofriendly refrigerant in the Low Temperature Circuit ($Compressor_{Efficiency\text{-}1}$=0.80,$T_{eva2}$=173K, $T_{cond}$=333K, $T_{cascade\text{-}evaporator}$=253K, $Compressor_{Efficiency\text{-}2}$=0.80, Approach=temperature overlapping=10

| Effect of cascade evaporator temperature (K) | Overall System First law Performance $COP_{Overal}$l | Overall Exergy Destruction Ratio of system $EDR_{System}$ | Cascade System Exergetic Efficiency |
|---|---|---|---|
| 253 | 0.3894 | 2.554 | 0.2814 |
| 258 | 0.3967 | 2.489 | 0.2866 |
| 263 | 0.4009 | 2.452 | 0.2897 |
| 268 | 0.4020 | 2.443 | 0.2905 |
| 273 | 0.3998 | 2.462 | 0.2889 |
| 278 | 0.3943 | 2.510 | 0.2849 |
| 283 | 0.3855 | 2.590 | 0.2785 |
| 288 | 0.3734 | 2.706 | 0.2698 |
| 293 | 0.3582 | 2.864 | 0.2588 |

**Table: 1. e(ii).** Effect of variation in temperature of cascade evaporator on thermal performance of cascade Refrigeration system using R-1234yf in HighTemperature Circuit and R134a ecofriendly refrigerant in the Low Temperature Circuit ($Compressor_{Efficiency\text{-}1}$=0.80,$T_{eva2}$=173K, $T_{cond}$=333K, $T_{cascade\text{-}evaporator}$=253K, $Compressor_{Efficiency\text{-}2}$=0.80, Approach=temperature overlapping=10

| Effect of cascade evaporator temperature (K) | Effect of cascade evaporator temperature (K) | Overall System First law Performance $COP_{Overal}$l |
|---|---|---|
| 253 | 253 | 0.3894 |
| 258 | 258 | 0.3967 |
| 263 | 263 | 0.4009 |
| 268 | 268 | 0.4020 |
| 273 | 273 | 0.3998 |
| 278 | 278 | 0.3943 |
| 283 | 283 | 0.3855 |
| 288 | 288 | 0.3734 |
| 293 | 293 | 0.3582 |

**Table: 2.a(i).** Effect of ecofriendly refrigerants on thermal performance of cascade Refrigeration system using R-1234ze in High Temperature Circuit and following ecofriendly refrigerants in the Low Temperature Circuit ($Compressor_{Efficiency\text{-}1}$=0.80,$T_{eva2}$=173K, $T_{cond}$=333K, $T_{cascade\text{-}evaporator}$=253K, $Compressor_{Efficiency\text{-}2}$=0.80, Approach=temperature overlapping=10

| Ecofriendly Refrigerants in Lower Temp. Circuit | Overall System First law Performance $COP_{Overal}$l | Overall Exergy Destruction Ratio of system $EDR_{System}$ | Cascade System Exergetic Efficiency |
|---|---|---|---|
| R-134a | 0.4221 | 2.294 | 0.3036 |
| R-290 | 0.4239 | 2.265 | 0.3063 |
| R-600a | 0.4227 | 2.274 | 0.3054 |
| R-600 | 0.4323 | 2.202 | 0.3123 |
| R-404a | 0.3982 | 2.476 | 0.2877 |
| R-125 | 0.3908 | 2.541 | 0.2814 |
| R-123 | 0.4323 | 2.201 | 0.3124 |
| R-407c | 0.3619 | 2.824 | 0.2615 |
| R-410a | 0.4178 | 2.312 | 0.3019 |
| R5.07a | 0.4043 | 2.424 | 0.2921 |

**Table: 2.a(ii).** Effect of ecofriendly refrigerants on thermal performance of cascade Refrigeration system using R-1234ze in High Temperature Circuit and following ecofriendly refrigerants in the Low Temperature Circuit ($Compressor_{Efficiency\text{-}1}$=0.80,$T_{eva2}$=173K, $T_{cond}$=333K, $T_{cascade\text{-}evaporator}$=253K, $Compressor_{Efficiency\text{-}2}$=0.80, Approach=temperature overlapping=10

| Ecofriendly Refrigerants in Lower Temp. Circuit | High Temperature Circuit First law Performance $COP_{HTC}$ | Low Temperature Circuit First law Performance $COP_{LTC}$ |
|---|---|---|
| R-134a | 1.428 | 1.012 |
| R-290 | 1.428 | 1.025 |
| R-600a | 1.428 | 1.021 |
| R-600 | 1.428 | 1.054 |
| R-404a | 1.428 | 0.939 |
| R-125 | 1.428 | 0.9152 |
| R-123 | 1.428 | 1.054 |
| R-407c | 1.428 | 0.8244 |
| R-410a | 1.428 | 1.004 |
| R5.07a | 1.428 | 0.959 |

**Table: 2.b(i).** Effect of High temperature condenser on thermal performance of cascade Refrigeration system using R-1234ze in High Temperature Circuit and following ecofriendly refrigerants in the Low Temperature Circuit ($Compressor_{Efficiency-1}$=0.80,$T_{eva2}$=173K, $T_{cond}$=333K, $T_{cascade-evaporator}$=253K, $Compressor_{Efficiency-2}$=0.80, Approach=temperature overlapping=10

| Variation of condenser temperature of cascade system in High Temp. Circuit (K) | Overall System First law Performance $COP_{Overall}$ | Overall Exergy Destruction Ratio of system $EDR_{System}$ | Cascade System Exergetic Efficiency |
|---|---|---|---|
| 333 | 0.4201 | 2.294 | 0.3036 |
| 328 | 0.4534 | 2.052 | 0.3276 |
| 323 | 0.4863 | 1.846 | 0.3514 |
| 318 | 0.5189 | 1.687 | 0.3749 |
| 313 | 0.5514 | 1.510 | 0.3984 |
| 308 | 0.5841 | 1.369 | 0.4221 |
| 303 | 0.6172 | 1.242 | 0.4460 |

**Table: 2.b(ii).** Effect of High temperature condenser on thermal performance of cascade Refrigeration system using R-1234ze in High Temperature Circuit and following ecofriendly refrigerants in the Low Temperature Circuit ($Compressor_{Efficiency-1}$=0.80,$T_{eva2}$=173K, $T_{cond}$=333K, $T_{cascade-evaporator}$=253K, $Compressor_{Efficiency-2}$=0.80, Approach=temperature overlapping=10

| Variation of condenser temperature of cascade system in High Temp. Circuit (K) | High Temperature Circuit First law Performance $COP_{HTC}$ | Low Temperature Circuit First law Performance $COP_{LTC}$ |
|---|---|---|
| 333 | 1.428 | 1.012 |
| 328 | 1.633 | 1.012 |
| 323 | 1.86 | 1.012 |
| 318 | 2.116 | 1.012 |
| 313 | 2.407 | 1.012 |
| 308 | 2.745 | 1.012 |
| 303 | 3.143 | 1.012 |

**Table: 2c(i).** Effect of Temperature overlapping on thermal performance in cascade temperature-evaporator on Thermal Performance of cascade Refrigeration system using R-1234ze in High Temperature Circuit and R134a ecofriendly refrigerant in the Low Temperature Circuit ($Compressor_{Efficiency-1}$=0.80,$T_{eva2}$=173K, $T_{cond}$=333K, $T_{cascade-evaporator}$=253K, $Compressor_{Efficiency-2}$=0.80, Approach=temperature overlapping=10

| Effect of Approach (Effect of temperature overlapping) | Overall System First law Performance $COP_{Overall}$ | Overall Exergy Destruction Ratio of system $EDR_{System}$ | Cascade System Exergetic Efficiency |
|---|---|---|---|
| 0 | 0.475 | 1.914 | 0.3432 |
| 2 | 0.4636 | 1.985 | 0.3350 |
| 4 | 0.4524 | 2.059 | 0.3269 |
| 6 | 0.4414 | 2.135 | 0.3190 |
| 8 | 0.4307 | 2.214 | 0.3112 |
| 10 | 0.4201 | 2.294 | 0.3036 |

**Table: 2c(ii).** Effect of Temperature overlapping on thermal performance in cascade temperature-evaporator on Thermal Performance of cascade Refrigeration system using R-1234ze in High Temperature Circuit and R134a ecofriendly refrigerant in the Low Temperature Circuit ($Compressor_{Efficiency-1}$=0.80,$T_{eva2}$=173K, $T_{cond}$=333K, $T_{cascade-evaporator}$=253K, $Compressor_{Efficiency-2}$=0.80, Approach=temperature overlapping=10

| Effect of Approach (Effect of temperature overlapping) | High Temperature Circuit First law Performance $COP_{HTC}$ | Low Temperature Circuit First law Performance $COP_{LTC}$ |
|---|---|---|
| 0 | 1.428 | 1.211 |
| 2 | 1.428 | 1.167 |
| 4 | 1.428 | 1.126 |
| 6 | 1.428 | 1.087 |
| 8 | 1.428 | 1.049 |
| 10 | 1.428 | 1.012 |

**Table: 2d(i).** Effect of low temperature evaporator on thermal performance of cascade Refrigeration system using R-1234ze in HighTemperature Circuit and following ecofriendly refrigerants in the Low Temperature Circuit ($Compressor_{Efficiency-1}$=0.80,$T_{eva2}$=173K, $T_{cond}$=333K, $T_{cascade-evaporator}$=253K, $Compressor_{Efficiency-2}$=0.80, Approach=temperature overlapping=10

| Effect of low temperature evaporator (K) | Overall System First law Performance $COP_{Overall}$ | Overall Exergy Destruction Ratio of system $EDR_{System}$ | Cascade System Exergetic Efficiency |
|---|---|---|---|
| 173 | 0.4201 | 2.294 | 0.3036 |
| 178 | 0.4562 | 2.252 | 0.3075 |
| 183 | 0.4941 | 2.22 | 0.3105 |
| 188 | 0.5340 | 2.201 | 0.3124 |
| 193 | 0.5759 | 2.192 | 0.3133 |
| 198 | 0.6198 | 2.194 | 0.3130 |
| 203 | 0.6659 | 2.209 | 0.3117 |
| 208 | 0.7143 | 2.235 | 0.3091 |
| 213 | 0.7650 | 2.275 | 0.3053 |

| | | | |
|---|---|---|---|
| 218 | 0.8182 | 2.330 | 0.3003 |
| 223 | 0.874 | 2.402 | 0.2939 |
| 228 | 0.9324 | 2.493 | 0.2863 |
| 233 | 0.9936 | 2.608 | 0.2772 |
| 238 | 1.058 | 2.75 | 0.2667 |
| 243 | 1.125 | 2.927 | 0.2546 |

**Table: 2d(ii).** Effect of low temperature evaporator on thermal performance of cascade Refrigeration system using R-1234ze in HighTemperature Circuit and following ecofriendly refrigerants in the Low Temperature Circuit ($Compressor_{Efficiency-1}$=0.80,$T_{eva2}$=173K, $T_{cond}$=333K, $T_{cascade-evaporator}$=253K, $Compressor_{Efficiency-2}$=0.80, Approach=temperature overlapping=10

| Effect of low temperature evaporator (K) | High Temperature Circuit First law Performance $COP_{HTC}$ | Low Temperature Circuit First law Performance $COP_{LTC}$ |
|---|---|---|
| 173 | 1.428 | 1.012 |
| 178 | 1.428 | 1.14 |
| 183 | 1.428 | 1.285 |
| 188 | 1.428 | 1.451 |
| 193 | 1.428 | 1.641 |
| 198 | 1.428 | 1.863 |
| 203 | 1.428 | 2.123 |
| 208 | 1.428 | 2.431 |
| 213 | 1.428 | 2.803 |
| 218 | 1.428 | 3.260 |
| 223 | 1.428 | 3.832 |
| 228 | 1.428 | 4.571 |
| 233 | 1.428 | 5.558 |
| 238 | 1.428 | 6.943 |
| 243 | 1.428 | 9.025 |

**Table: 2.e(i).** Effect of low temperature evaporator on thermal performance of cascade Refrigeration system using R-1234ze in HighTemperature Circuit and following ecofriendly refrigerants in the Low Temperature Circuit ($Compressor_{Efficiency-1}$=0.80,$T_{eva2}$=173K, $T_{cond}$=333K, $T_{cascade-evaporator}$=253K, $Compressor_{Efficiency-2}$=0.80, Approach=temperature overlapping=10

| Effect of cascade evaporator temperature (K) | Overall System First law Performance $COP_{Overall}$ | Overall Exergy Destruction Ratio of system $EDR_{System}$ | Cascade System Exergetic Efficiency |
|---|---|---|---|
| 253 | 0.4201 | 2.294 | 0.3036 |
| 258 | 0.4235 | 2.268 | 0.3060 |
| 263 | 0.4240 | 2.264 | 0.3064 |
| 268 | 0.4216 | 2.283 | 0.3046 |
| 273 | 0.4161 | 2.326 | 0.3007 |
| 278 | 0.4076 | 2.395 | 0.2945 |
| 283 | 0.3961 | 2.494 | 0.2862 |
| 288 | 0.3817 | 2.625 | 0.2758 |
| 293 | 0.3645 | 2.797 | 0.2645 |
| 298 | 0.3446 | 3.016 | 0.2490 |
| 303 | 0.3221 | 3.297 | 0.2327 |
| 308 | 0.2971 | 3.658 | 0.2147 |
| 313 | 0.2694 | 4.13 | 0.1949 |
| 318 | 0.2403 | 4.761 | 0.1736 |
| 323 | 0.2086 | 5.634 | 0.1507 |

**Table: 2.e(ii).** Effect of low temperature evaporator on thermal performance of cascade Refrigeration system using R-1234ze in HighTemperature Circuit and following ecofriendly refrigerants in the Low Temperature Circuit ($Compressor_{Efficiency-1}$=0.80,$T_{eva2}$=173K, $T_{cond}$=333K, $T_{cascade-evaporator}$=253K, $Compressor_{Efficiency-2}$=0.80, Approach=temperature overlapping=10

| Effect of cascade evaporator temperature (K) | High Temperature Circuit First law Performance $COP_{HTC}$ | Low Temperature Circuit First law Performance $COP_{LTC}$ |
|---|---|---|
| 253 | 1.428 | 1.012 |
| 258 | 1.621 | 0.9273 |
| 263 | 1.843 | 0.8496 |
| 268 | 2.102 | 0.7781 |
| 273 | 2.407 | 0.7120 |
| 278 | 2.77 | 0.6504 |
| 283 | 3.209 | 0.5928 |
| 288 | 3.747 | 0.5385 |
| 293 | 4.424 | 0.4871 |
| 298 | 5.298 | 0.4381 |
| 303 | 6.467 | 0.3914 |
| 308 | 8.109 | 0.3461 |
| 313 | 10.58 | 0.303 |
| 318 | 14.71 | 0.2609 |
| 323 | 22.97 | 0.2197 |

**Table: 3.** Effect of ecofriendly refrigerants in High temperature circuit on thermal performance of cascade refrigeration system using R-134a in LowTemperature Circuit and following ecofriendly refrigerants in the High Temperature Circuit ($Compressor_{Efficiency-1}$=0.80,$T_{eva2}$=173K, $T_{cond}$=333K, $T_{cascade-evaporator}$=253K, $Compressor_{Efficiency-2}$=0.80, Approach=temperature overlapping=10

| Ecofriendly Refrigerants | Overall System First law Performance $COP_{Overall}$ | Overall Exergy Destruction Ratio of system $EDR_{System}$ | Cascade System Exergetic Efficiency |
|---|---|---|---|
| R-717 | 0.4764 | 1.905 | 0.3442 |
| R-1234yf | 0.3898 | 2.554 | 0.2814 |
| R-152a | 0.4615 | 1.999 | 0.3334 |
| R-1234ze | 0.4201 | 2.294 | 0.3036 |

**Table: 3.** Effect of ecofriendly refrigerants in High temperature circuit on thermal performance of cascade refrigeration system using R-134a in LowTemperature Circuit and following ecofriendly refrigerants in the High Temperature Circuit ($Compressor_{Efficiency-1}$=0.80,$T_{eva2}$=173K, $T_{cond}$=333K, $T_{cascade-evaporator}$=253K, $Compressor_{Efficiency-2}$=0.80, Approach=temperature overlapping=10

| Ecofriendly Refrigerants | High Temperature Circuit First law Performance $COP_{HTC}$ | Low Temperature Circuit First law Performance $COP_{LTC}$ |
|---|---|---|
| R-717 | 1.789 | 1.012 |
| R-1234yf | 1.258 | 1.012 |
| R-152a | 1.686 | 1.012 |
| R-1234ze | 1.428 | 1.012 |

## 5. Conclusions

The following conclusions have been drawn from present investigations;

(i) The use of HFO in the high temperature circuit is promising feature in the cascade refrigeration systems
(ii) The ecofriendly HFO-1234ze gives better first and second law performance than HFO-1234yf in high temperature circuit applications
(iii) The use of HFC-134a gives better performance in the low temperature circuit of cascade refrigeration systems
(iv) R-1234ze in high temperature circuit and R 134a in lower temperature circuit is a best alternative than R1234yf in high temperature circuit and R 134a in lower temperature circuit.
(v) The use of pure hydrocarbons (R-290(propane) , R600 (Butane) and R600a (isobutene) and R152a is limited use due to flammable nature.

## References

[1] Honeywell Novel Low-Global-Warming, Honeywell press, 2008
[2] M. Kanoglu, Exergy analysis of the multistage cascade refrigeration cycle used for natural gas liquefaction, Int J Energy Res, 2002
[3] C. Nikolaidis, D. Probert, Exergy method analysis of a two stage vapour compression refrigeration-plants performance, Applied energy, 60, 1998, 241-256

Int. J. Electron. Commun. (AEÜ) xxx (2015) xxx–xxx

Contents lists available at ScienceDirect

International Journal of Electronics and Communications (AEÜ)

journal homepage: www.elsevier.com/locate/aeue

# Unified framework for human activity recognition: An approach using spatial edge distribution and ℜ-transform

D.K. Vishwakarma*, Rajiv Kapoor, Ashish Dhiman

*Department of Electronics and Communication Engineering, Delhi Technological University, Bawana Road, Delhi 110042, India*

ARTICLE INFO

*Article history:*
Received 23 March 2015
Accepted 17 December 2015

*Keywords:*
Human activity recognition
Spatial edge distribution
ℜ-transform
Fusion of translational and rotational features
Still images

ABSTRACT

In this paper, a unified approach for the recognition of human activity using the spatial edge distribution of gradients and orientation of the human silhouettes in a video sequence is presented. The spatial edge distribution is computed on still image at different levels of resolution of sub-images to extract out the shape of the activity posture. The fuzzy trapezoidal membership function is used to extract the key frames of the activity, and the single still key image is extracted according to the histogram distance. The temporal content of the activity is extracted by the computation of orientation of the silhouettes using ℜ-transform. The ℜ-transform is applied on the binary human silhouettes, and the extraction of human silhouettes from the video sequence is done using texture based segmentation techniques. The high dimensionality of the ℜ-transform features is handled by applying Local linear embedding (LLE) dimension reduction approach. A unified model is constructed by integrating the spatial edge distribution of gradients and temporal content of the activity. The performance of the developed model is demonstrated on publicly available datasets, and the highest classification accuracy achieved on each datasets is compared with the similar state-of-the-art techniques and shows the superior performance.

© 2015 Elsevier GmbH. All rights reserved.

## 1. Introduction

In recent years, human activity recognition has been an active area of research in computer vision due to its potential applications in the field of surveillance, assistive healthcare, sports event analysis, robotics, terrorist activities, content-based video analysis and human-computer interactions [1–3]. However, human activity recognition is both challenging and multifaceted due to viewpoint variations, occlusion, cluttered background, intra-class motion variability and inter-class motion ambiguity. Faced with these challenges several researchers are trying to devise a general, competent and robust method for recognition of human activity.

Over the last few decades, numerous human activity recognition techniques have been proposed, which are mainly focused on the local and global feature based representations. Some of the popular existing approaches for the human activity recognition are as follows; motion flow or optical flow, point trajectories, space-time volume, Bag-of-words model, and spatio-temporal interest points (STIP's) [3–5]. The advantages of these approaches are that they do not require background subtraction and are efficient in handling partial occlusions but all of these techniques have their limitations like optical flow approach is less accurate when the video quality is poor and rough. Similarly, point trajectories based approach requires an efficient tracking of the human motion and if human is moving with variable speed then tracking trajectories may be inefficient. In case of STIPs the distribution of the interest points should be stable around the object. Even the bag of words approach is inadequate to capture the spatial and temporal information and only focus on the global saliency and ignores the structure of the body.

In these days, a trend in the human activity recognition (HAR) has been realized, where multiple features [6–8] are used to improve the recognition accuracy. These methods include global and local information and admit that an individual feature based methods are less effective as compared to the multiple features based methods. In this context more recently, researchers [9,10] supported that multiple features based fusion techniques can provide better performance than the individual features. Wu and Shao [12] presented the combination of local and holistic representation for human action recognition where they effectively worked on the Bag of correlated poses for the local representation and involved MHI/GEI images for the holistic representation. This combined approach is robust to viewpoint, scale and orientation but has plenty of scope for improvement using multiple features. Liu et al.

* Corresponding author. Tel.: +91 1127871044x1308/9971339840.
*E-mail addresses:* dvishwakarma@gmail.com, dkvishwakarma@dce.ac.in (D.K. Vishwakarma), rajivkapoor@dce.ac.in (R. Kapoor), ashish.dhiman1@gmail.com (A. Dhiman).

http://dx.doi.org/10.1016/j.aeue.2015.12.016
1434-8411/© 2015 Elsevier GmbH. All rights reserved.

Please cite this article in press as: Vishwakarma DK, et al. Unified framework for human activity recognition: An approach using spatial edge distribution and ℜ-transform. Int J Electron Commun (AEÜ) (2015), http://dx.doi.org/10.1016/j.aeue.2015.12.016

[13] proposed the adaptive learning methodology where they used the genetic programming for the representation of spatio-temporal features. Simultaneously, they fused the color and motion information for high-level activity recognition. The main drawback was that they required a large number of generations for good results that further lead to heavy computation. Liu et al. [14] give a probabilistic model, which effectively combined the Gaussian process (GP) regression with sparse covariance matrix for realistic action recognition. However, GP is limited to large-scale computer vision tasks because modeling the large dataset with stochastic process remain a challenge. Hu et al. [15] introduced the spatial pose based exemplars to characterize the Human–Object Interaction (HOI) from still images but it did not work accurately for complex images. This approach does not provide the motion information in the short or long duration of time and hence, scarce in representing the human action from a video sequence. Shao et al. [16] presented the content based search algorithm for localization of human action in the video database. Their work mainly focused on the temporal and spatial localization to decrease the search time of the algorithm. Even though it has a limitation with the large online database, it opens the window for a robust and effective content-based searching algorithm with the existing human action recognition approaches.

Recently, the concept of still images [17–23] has emerged as a popular means for detecting a person's activity or behavior. In these approaches the visual appearance of the object is used to describe the information content. Wang et al. [19] introduce the concept of action recognition based on still images. The shape of human action is represented using a Canny edge detector, and similar body poses are clustered using the spectral clustering method. Li and Ma [20] gave "exemplarlet" based feature descriptor that contains enough visual information to identify in still images. Li and Fei-Fei [21] presented an integrated method that is based on the appearance information on still image and occurrence of action scenes. Thurau and Hlavac [24] proposed the method based on pose information of human action, where they determined the region of interest (ROI) images and further calculated the histogram of gradients with non-matrix factorization to represent the feature vectors. Lopes and Santos [22] proposed the transfer learning approach, where contextual information is extracted from the still images, and a similar approach is used by Zheng et al. [23] for the representation of human action by combining the poselet with contextual information. But in general it is observed that still image based human activity recognition is less effective due to missing temporal information. Hence, more holistic solution is that which utilizes the shape as well motion information together.

Motion temporal information at different orientation is extracted by using the $\Re$-transform [25–27] and extensively used for representing human activity. The $\Re$-transform is applied on the silhouettes of the human body and provides the orientation of the silhouettes. Also, the rate of change of orientation of the human body is different for dissimilar activity. Wang et al. [19] use $\Re$-transform to represent the low-level features due to its advantages of low computational complexity, geometrical invariance. Zhang et al. [25] used a simple approach to the representation of the human activity by using the shape information. They used the $\Re$-transform as a shape descriptor and reported that it works better for the activities that are being performed by the rotation of the human body. Similar work based on $\Re$-transform by Khan et al. [26] for representation of abnormal human activities were carried and it was observed that it is a good descriptor for the orientation based human activity. The properties of $\Re$-transform i.e. invariant to translation, scaling [28] and effectively depicts the change in rotation makes robust feature descriptor.

Nevertheless, most of the reviewed work reveals that an individual feature descriptor has advantages of their own as a single still image based feature representation does not require any background subtraction, morphological operation, or tracking trajectories, thus reducing the computation time and complexity of the system. Therefore, it can be said that these images become, occlusion free and robust to noise. But apart from these benefits, it is also observed that a single still image based technique requires effective positioning of the posture, and it alone does not always provide enough information for recognizing all kinds of activities because it does not contain the temporal information in short or long time duration. In earlier works, it has been observed that $\Re$-transform is effectively used to incorporate the spatio-temporal content of the human activity and found more effective for the abnormal activities representation as compared to the normal activities. In general, human activities are performed by the translation and rotation of human body, and the normal activities have more translation than the rotation while abnormal activities have more rotation than translation.

More recently, several researchers [6,7,10,11] have promoted that multiple feature based fusion techniques give better performance than the individual feature based technique. Hence, in this work a unified structure is proposed by considering the facts of action dynamics. The action dynamics of the human body state that an activity cannot be accomplished without translation and rotation characteristics of the human body. Therefore, for effective representation of human action, an effective descriptor may be formed by incorporating these two characteristics, which could be occlusion free, robust to noise, and computationally less complex.

In this paper, multiple features based integrated structure is proposed where the shape of human pose is recorded in single 2D posture and the motion of the human body is recorded in human silhouettes. The translation provides the change in shape, and sequence of orientation provides the nature of the activity. Due to the translation, the appearance of 2D human postures of different activities is different, and the single key pose is chosen, which have highest variations among the postures of the video sequences. The rotation of key binary human silhouette is computed by applying $\Re$-transform. The binary human silhouette is obtained using texture based foreground segmentation, which is a robust and reliable approach to the illumination change and noise [29]. The key contributions of the work are as follows:

- The appearance of 2D human pose is chosen from the video sequences using fuzzy logic based model. The edge of human body pose is extracted using canny edge detector.
- The edge spatial distribution of gradients at various orientation bins is computed at different sublevels of the single 2D posture for the representation shape of activity.
- The spatio-temporal motion content of human activity is extracted by applying the $\Re$-transform on the key poses of the binary human silhouette. The key poses of binary human silhouettes are chosen on the basis of high energy.
- An integrated model is constructed using the 2D shape information and spatio-temporal motion information of the human activity.
- The performance of the integrated model is measured on publicly available standard datasets using K-nearest neighbor (K-NN) and support vector machine (SVM).
- The comparative analysis of the result achieved through the proposed model is done with the earlier state-of-the-art methods, and an additional analysis of the speed of computation and robustness test of the proposed algorithm is done.

The rest of this paper is structured as follows: Section 2 gives the proposed methodology, which includes the overview of proposed model, extraction key pose, fuzzy logic model, abstraction of spatial edge distributions and motion temporal information using $\Re$-transform, and silhouette extraction. Section 3 gives the details

Please cite this article in press as: Vishwakarma DK, et al. Unified framework for human activity recognition: An approach using spatial edge distribution and $\Re$-transform. Int J Electron Commun (AEÜ) (2015), http://dx.doi.org/10.1016/j.aeue.2015.12.016

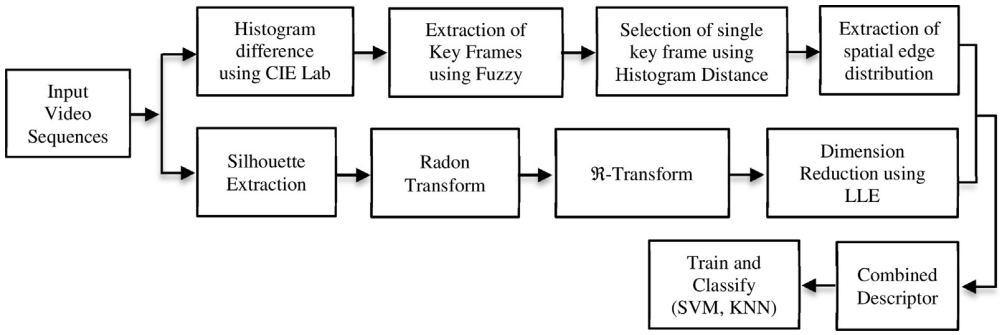


**Fig. 1.** Workflow diagram of human activity recognition.

of experimental works and discussion of results. The conclusion of the work is explained in Section 4.

## 2. Proposed methodology

Based on the earlier frameworks for activity recognition used in [6,7,11,12,30] the framework for the action recognition by integrating the translational-based appearance and rotational based motion information is illustrated, which includes overview of propose model, key pose selection, fuzzy logical model, computation of edge spatial distribution and spatio-temporal motion of the human silhouettes. The detailed explanation about the proposed framework is presented in the subsequent sections.

### 2.1. Overview of the framework

The proposed framework comprises abstraction of spatial edge distribution of 2D postures, extraction of the orientation of silhouettes by using ℜ-transform and integration of spatial edge distribution vector with orientation feature vector. The spatial edge distribution gives shape information of the action, which is computed on the still image, whereas still images are single key frame extracted from video sequence using fuzzy approach.

The workflow diagram of the proposed framework is shown in Fig. 1 and every block is explained in the upcoming sections.

### 2.2. Extraction of key poses

For the accurate representation of body posture, the key poses of the activity in video sequences are extracted, and these key poses are used to represent the human activity in the video. For selecting key poses, a stack of frames is formed by selecting the frames after a certain interval length in the video sequence because the deviation in the action does not vary instantaneously. These stacks of frames are converted into CIELab color space because it closely conforms to human perception of colors and device independent [31] as compared to the rest of color spaces. In this color space model, $L$ stands for the luminance and $a$, $b$ components define the color opponent dimensions. The histogram distances $D$ between the frames are computed for all the three components $L$, $a$ and $b$ as per Eq. (1).

$$D = \left\| \sum_{i=1}^{M} \sum_{j=1}^{N} S_{ij}^{t} - S_{ij}^{t+1} \right\| \tag{1}$$

$S$, $t$ denotes the frames of the stack, and frame number respectively. The size of frame is $M \times N$. The distance that we computed for the subsequent frames is used to make the Fuzzy logic model.

#### 2.2.1. Fuzzy logic model

In some videos, the information content may be large, and hence, it is difficult to extract the key frames using normal distance metric because some of the information regarding the frames have the risk of being lost. Hence, the fuzzy approach is used to find the key frames, which as explained in Algorithm 1.

The fuzzy logic system is based on the probability model, where the knowledge about the system is partial rather than being accurate. The fuzzy set theory, given by Zadeh [32], was an extension of Boolean logic than the Crisp logic, and provides the measure of uncertainty. Crisp logic gives a hard decision whether it belongs to a group or not.

Consider an example of crisp function represented by set $A$. This function assigns a value $\mu_A(x)$ to every $x \in A$ such that:

$$\mu_A(x) = \begin{cases} 1 & \text{if and only if } x \in A \\ 0 & \text{if and only if } x \notin A \end{cases}. \tag{2}$$

Fuzzy logic deals with the membership function that defines the probability of a variable belonging to a particular group. The membership function assigns a variable value between 0 and 1. As the value increases from 0 to 1, the degree of membership value also starts increasing for the variable and the membership function is chosen on the basis of the set interval length. Fuzzy logic makes decisions by using simple and flexible 'IF...THEN' statements, which maps the set input to the set of output.

**Algorithm 1.** Key frames extraction.

**Step 1:** Input the video sequence and select the frames with the difference of certain frames.
**Step 2:** Convert these frames into CIELab color space.
**Step 3:** Compute the histogram distance for '$L$', '$a$', '$b$' components between the frames using Eq. (1).
**Step 4:** Compute the mean, '$\mu_d$' for all consecutive frame differences as: $\mu_d = [count'L' + count'b' + count'a']/3$.
**Step 5:** Create the trapezoidal membership functions dynamically using the computed mean $\mu_d$ as shown in Fig. 2, where {small, medium, large} are the linguistic variables.
**Step 6:** Compute the value of parameters using: $A = (\mu_d - \mu_d * 0.4)$, $B = (\mu_d - \mu_d * 0.3)$, $C = (\mu_d - \mu_d * 0.2)$, $D = (\mu_d + \mu_d * 0.4)$, $E = (\mu_d + \mu_d * 0.5)$, $F = (\mu_d + \mu_d * 0.8)$.
**Step 7:** Define fuzzy rules, i.e. if the distance between segment frame and its neighboring frame is small or large then it is a key frame. The extracted key frames are as shown in Fig. 3.

#### 2.2.2. Selection of single key frame

The extracted key frames are compared internally and ranked according to the histogram distance values. Higher distance values show that the corresponding frame has higher variations as

Please cite this article in press as: Vishwakarma DK, et al. Unified framework for human activity recognition: An approach using spatial edge distribution and ℜ-transform. Int J Electron Commun (AEÜ) (2015), http://dx.doi.org/10.1016/j.aeue.2015.12.016

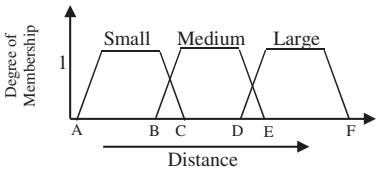


**Fig. 2.** Fuzzy trapezoidal membership function.

compared to the other frames. Histogram difference is normally considered as a global change in a video sequence, and it helps in detecting abrupt changes in the frame. If the extracted key frames are represented as ''$f_1, f_2, \ldots\ldots\ldots\ldots, f_n$'', then the histogram distance between the successive frames is computed and highest distance key frame is the single key frame that is highest pixel variation to others and denoted as a single still image as shown in Fig. 4(b) and 5.

$$\text{Single Key Frame} = arg\max(D_i), \quad i \in n \tag{3}$$

### 2.3. Computation of spatial edge distribution

The computation of spatial edge distribution feature is based upon the visual appearance of human body pose. Human body pose provides a significant amount of information for nonverbal communication and based on appearance, certain patterns of body movements are indicative of specific action. Human posture gives the information about the motion of the human body, and the 2-D representations of images give the spatial distribution of posture and characteristics of action or the attitude of the person. The shape based appearance is represented by dividing the ROI of key pose still image into sub-regions at multilevel, and orientations of the edges are counted on the finer scale and is further expressed in the form vector. Edges are more useful for the shape analysis and the Canny edge detector combines the derivative and smoothing properties efficiently to obtain the edges. To remove the edges which are insignificant, a threshold value is selected based on the pixel variation and only those edges are kept, which are having the pixel value greater than the threshold value. The detailed flow of step used for computation of spatial edge distribution is as explained in Algorithm 2.

**Algorithm 2.** Computation of spatial edge distribution.

**Step 1** – Input video sequence $\mathcal{F}(x, y, t)$; $t$ set of frames.
**Step 2** – Select a single key frame as explained in Section 2.2.
**Step 3** – Select ROI and normalize to the fixed dimension of $50 \times 50$, and denote as: $\mathfrak{B}(x, y, \varphi)$, where $0 \le x, y \le 50$.
**Step 5** – Compute the edges of ROI using canny edge detector and denoted as: $\varepsilon(x, y, \varphi) = \text{Canny}(\mathfrak{B}(x, y, \varphi))$.
**Step 6** – Compute the spatial edge distribution vector at different levels as follows:
a. At level-0, the magnitude $\mathcal{M}(x, y)$ and orientation $\varphi(x, y)$ at any point $(x, y)$ of the entire image $\varepsilon(x, y, \varphi)$ is determined as:
$\mathcal{M}(x, y) = \sqrt{\mathcal{G}_X(x, y)^2 + \mathcal{G}_y(x, y)^2}$ and $\varphi(x, y) = \arctan\left[\frac{\mathcal{G}_y(x,y)}{\mathcal{G}_x(x,y)}\right]$.
Where $\mathcal{G}_x(x, y)$ and $\mathcal{G}_y(x, y)$ are image gradients along the $x$ and $y$ directions. Each sub-region is quantized into the 8-orientation bins, evenly spaced over 0°–360°. The obtained feature vector for entire image is of $8 \times 1$ dimension.
b. At level-1, the entire image $\varepsilon(x, y, \varphi)$ is divided into 4 sub-image regions, and denoted as: $\varepsilon(x, y, \theta) = \{\mathcal{S}_1(x, y, \varphi), \mathcal{S}_2(x, y, \varphi), \mathcal{S}_3(x, y, \varphi), \mathcal{S}_4(x, y, \varphi)\}$. The feature vector is computed as in **step 6-a**, and dimension is of $8 \times [1 + 4]$.
c. At level-2, each sub-image region is further divided into 4 sub-blocks, and feature vector is computed as in **step 6-a.** The obtained feature vector for 16 sub blocks is of $8 \times [1 + 4 + 16]$.
**Step 7** – The final feature vector is formed by combining all the levels and obtained as: $\mathcal{F}_a = [8 \times 1] + [8 \times 1] \times 5 + [1 \times 8] \times 21 = 216$. The result of spatial edge distributions at different levels are as shown in Fig. 6.

Fig. 7 shows that the spatial edge distribution of gradients of different activities postures and these distributions are distinct from each other because the representation of the patterns of the histograms of different activities is different with an increase in the degree. At a lower degree (near zero) the peaks are higher and much more variant in magnitude. Hence, these features are proficient in the representation of human activities. The spatial edge disribution of gradients are computed at the mixed levles of 0, 1, and 2. The compuation of these features are the magnitude of gradients at different orienation bins, which is easy and simple to compute. This representation may be less effective for the recognition of activities like "walking" and "jogging" because of reasonably similar histogram of these activities. Hence, to alleviate these shortcomings the temporal content of the activities are computed and integrated with the global information obtained through the kinematics of geometric orientation distribution points.

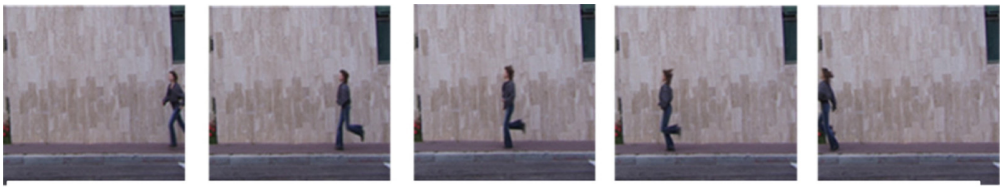

**Fig. 3.** Extracted key frames.

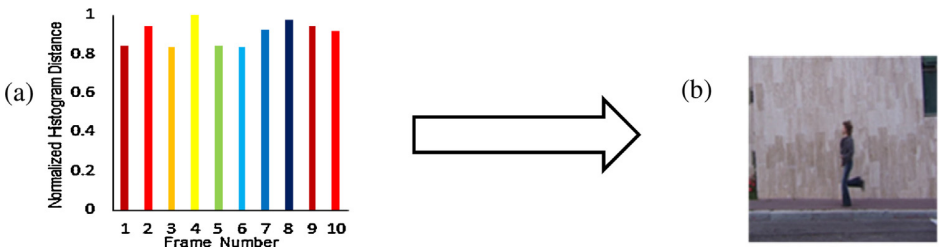


**Fig. 4.** (a) Plot of histogram distance of key frames (b) single frame i.e. third having maximum distance.

Please cite this article in press as: Vishwakarma DK, et al. Unified framework for human activity recognition: An approach using spatial edge distribution and ℜ-transform. Int J Electron Commun (AEÜ) (2015), http://dx.doi.org/10.1016/j.aeue.2015.12.016

**Fig. 5.** Single key frames extracted from different activities of two different video datasets Row 1: Wiezmann, Row 2: KTH.

### 2.4. Computation of orientation features

The orientation features give the directional information of the object, and most of the human activities are perfomed by changing the orientation of the body. The directional information of human activity is computed using the ℜ-transform and further this information is integrated with the translated information, which is computed in the previous section. The ℜ-transform gives the orientation information of an object, and it is used for the abnormal human activity recognition [26]. The ℜ-transform is computed via Radon transform (RT), by applying the RT on the binary silhouettes of the human activity. Radon transform gives the directional features in the range of angle (0–179°) and is defined as the integral of a silhouette image $I(x, y)$ from $-\infty$ to $\infty$, and is denoted as:

$$R_f(\rho, \theta) = \int_{-\infty}^{\infty}\int_{-\infty}^{\infty} I(x, y)\delta(\rho - x\cos\theta - \sin\theta)\partial x\partial y \tag{4}$$

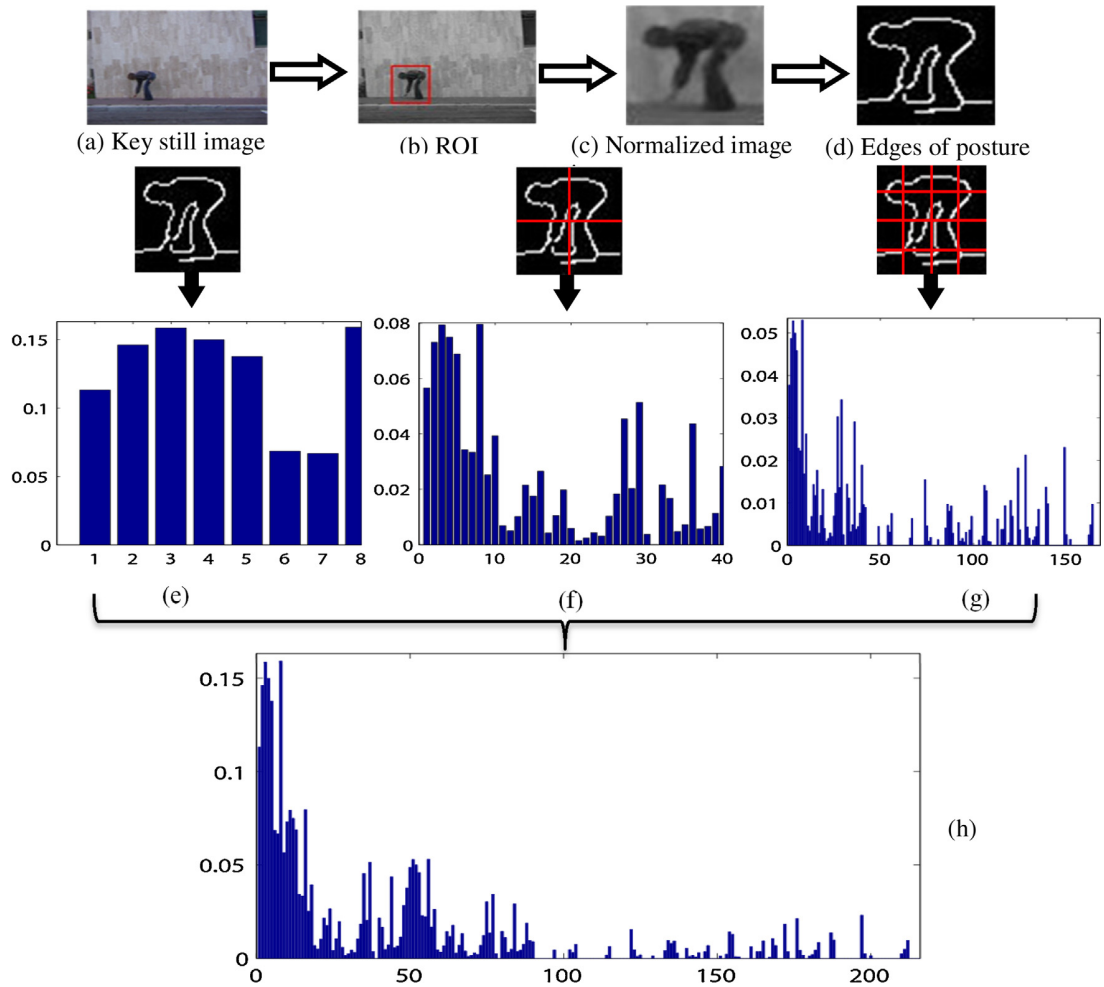


**Fig. 6.** Simulation results: (a)–(d) preprocessing steps, (e)–(h) shows the computation of spatial edge distribution vector at level 0, 1, 2 and final feature vector respectively.

Please cite this article in press as: Vishwakarma DK, et al. Unified framework for human activity recognition: An approach using spatial edge distribution and ℜ-transform. Int J Electron Commun (AEÜ) (2015), http://dx.doi.org/10.1016/j.aeue.2015.12.016

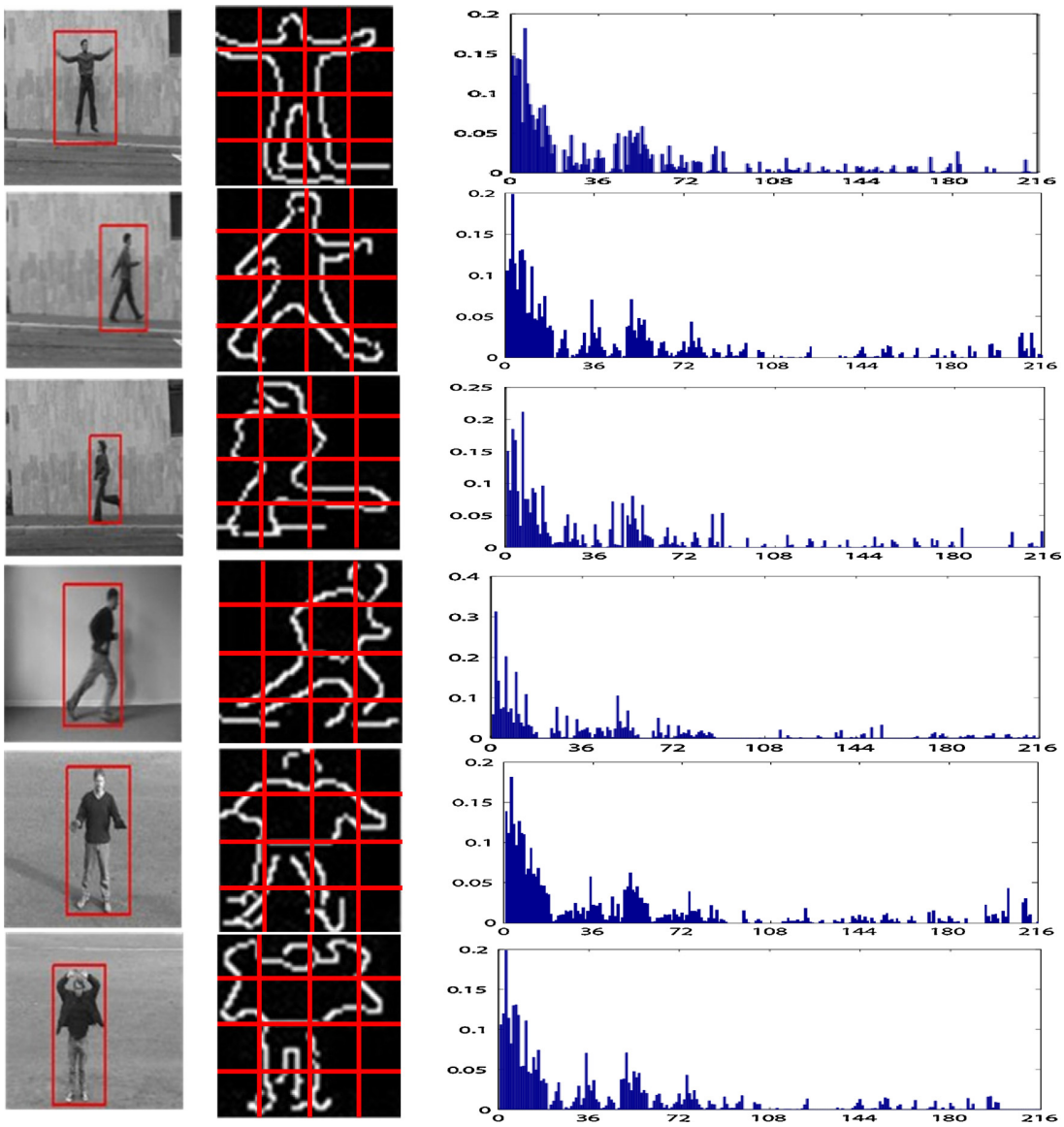

**Fig. 7.** Result of spatial edge distribution vector of different activities: Column 1: ROI of still images, Column 2: edges of postures, Column 3: spatial edge distribution at final level.

where $\delta(.)$ is defined as the Dirac delta function that is zero everywhere except at the origin. The perpendicular distance from the origin to the radon line is defined as:

$$\rho = x\cos\theta + y\sin\theta \quad \text{for}(0 \le \theta \le \pi), (-\infty \le \rho \le \infty) \tag{5}$$

and shown in Fig. 8(b), where '$\theta$' is the angle between the horizontal axis and the projection line.

RT cannot restore all the parameters of the original geometric transformation when translated, rotated, or scaled the image. Tabbone et al. [28] introduce the $\Re$-transform that is defined as integral transform of the squared values of RT and expressed as:

$$\Re(\theta) = \int_{-\infty}^{\infty} R_f^2(\rho,\theta)\partial\rho \tag{6}$$

RT gives the feature representation in 2-D while $\Re$-transform gives the compact representation in 1-D. Normalization of $\Re$-transform will further improve the similarity measure, and thus,

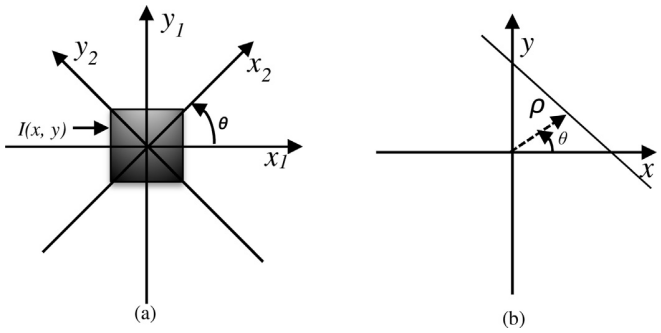


**Fig. 8.** (a) Illustrates the projection of lines over 2-D function $I(x, y)$. (b) The position of the projection line.

Please cite this article in press as: Vishwakarma DK, et al. Unified framework for human activity recognition: An approach using spatial edge distribution and $\Re$-transform. Int J Electron Commun (AEÜ) (2015), http://dx.doi.org/10.1016/j.aeue.2015.12.016

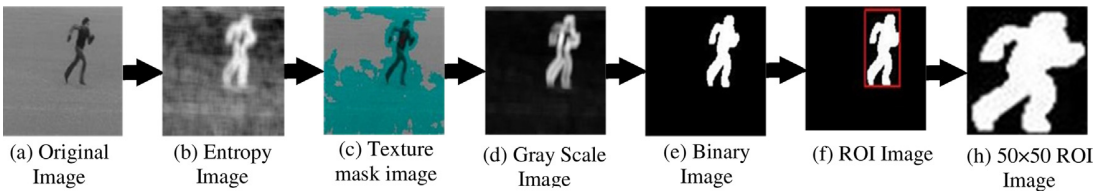


**Fig. 9.** Illustration of finding a normalized ROI binary silhouette image.

representation of features in a very compact manner can be achieved. The normalized form of the ℜ-transform is defined by Khan et al. [26].

$$\Re\text{norm}(\theta) = \frac{\int_{-\infty}^{\infty} \Re(\theta)\mathrm{d}\theta}{\max(\Re(\theta))} \tag{7}$$

The RT is applied on the ROI of binary silhouette images, which are obtained from the key poses of the frames. Binary silhouette images are obtained using texture based segmentation method (Haralick et al. [33]) and texture is one of the important features to identify the objects.

### 2.4.1. Silhouette extraction

The silhouette is the basic unit of human activity, which is formed by extracting the foreground object from the rest of the video sequences. A method for describing different textures as presented in [33] is used for silhouette extraction. Entropy is one of the most important parameters that describe the texture information in an image and can be expressed as:

$$\zeta = \sum_i \sum_j \rho(i,j)\log(\rho(i,j)) \tag{8}$$

where $\rho(i,j) = \frac{M(i,j)}{\sum_{i,j} M(i,j)}$ is the probability density function; where $i$ and $j$ are indices to the co-occurrence matrix $M$. The entropy of the image is used to describe the complexity of the background and a higher value indicates greater complexity in the image background.

The filter matrix is generated for a pixel and its entropy is calculated in a $9 \times 9$ neighborhood mask. Converting this filter matrix in binary form gives an image with white spots in different areas. Applying this mask to the raw image provides a silhouette image which is as shown in Fig. 9.

The segmented image may contain different white blocks, but not all of them are of human silhouettes. By comparing the sizes of these blocks, the image with the largest area is selected, which is a human silhouette.

The key poses of the frames are the most discriminating frames that are extracted using the concept of the size of the silhouettes, which is explained as Algorithm 3.

**Algorithm 3.** Extraction of key poses of the human silhouette.

**Step 1:** Input the Video Sequence.
**Step 2:** Extract the silhouette using texture based segmentation.
**Step 3:** Apply Weiner filter for smoothing.
**Step 4:** Calculate the size of each silhouette images using

$$U_t = \sum_i^M \sum_j^N ||I(i,j,t)||^2.$$

**Step 5:** Find the mean value ($\mu$) as: $\mu = \frac{[U_1, U_2, \ldots U_n]}{n}$, where $U_1, U_2, \ldots U_n$ denotes the size of silhouette images and '$n$' is the *total* number.
**Step 6:** If the size of the silhouette is greater than the mean value, then it is a key frame.
**Step 7:** Otherwise EXIT.

### 2.4.2. Properties of ℜ-transform and Radon transform

The important properties of RT and ℜ-transform described in Table 1 shows that it has the robustness to the scale, translation, and rotation.

These properties are experimentally verified using MATLAB 2012b and are shown in Fig. 10.

In Fig. 10, the rotated image shows more variation in the brighter portion of RT than the other images because there is more deviation in the pixel values corresponding to projection lines. The magnitude of the translated image varies as compared to the scaled image, but the signal representation of ℜ-transform remains the same. Therefore, from Table 1 and Fig. 10 it can be said that ℜ-transform is invariant to translation and scaling in the plane, but orientation in the plane will change due to the phase shift. Hence, ℜ-transform is an efficient method for describing the motion temporal of the actions that have more variation in the orientation such as bending, walking, and running. The representation of ℜ-transform of different activities is as shown in Fig. 11, and it can be visualized that ℜ-transform representation of different activities is different. Hence, it can be said that ℜ-transform is a discriminating feature,

**Table 1**
Comparison of Radon and ℜ-transform properties.

| Properties | Radon transform | ℜ-transform |
|---|---|---|
| Scaling by 'α' | $[(R_f(\alpha\rho,\theta))] = \frac{1}{\alpha^2}(R_f(\alpha\rho,\theta))$ | $\frac{1}{\alpha^3}\int_{-\infty}^{\infty} R_f^2(x,\theta+\theta_0)\partial x = \frac{1}{\alpha^3}\Re(\theta)$ |
| Translation by $(x_o, y_o)$ vector | $R_f(\rho,\theta) = R_f(\rho - x_o\cos\theta - y_o\sin\theta,\theta)$ | $\Re(\theta) = \int_{-\infty}^{\infty} R_f^2((\rho - x_o\cos\theta - y_o\sin\theta),\theta)\partial\rho$ |
| Periodicity | $R_f(\rho,\theta) = R_f(\rho,\theta+2k\pi)$, $k$ is any integer value | $\Re(\theta\pm\pi) = \Re(\theta)$, period is $\pi$ |
| Rotation by '$\theta_o$' | $R_f(\rho,\theta) = R_f(\rho,\theta+\theta_1)$ | $\Re(\theta) = \int_{-\infty}^{\infty} R_f^2(\rho,\theta+\theta_0)\partial\rho$ |

Please cite this article in press as: Vishwakarma DK, et al. Unified framework for human activity recognition: An approach using spatial edge distribution and ℜ-transform. Int J Electron Commun (AEÜ) (2015), http://dx.doi.org/10.1016/j.aeue.2015.12.016

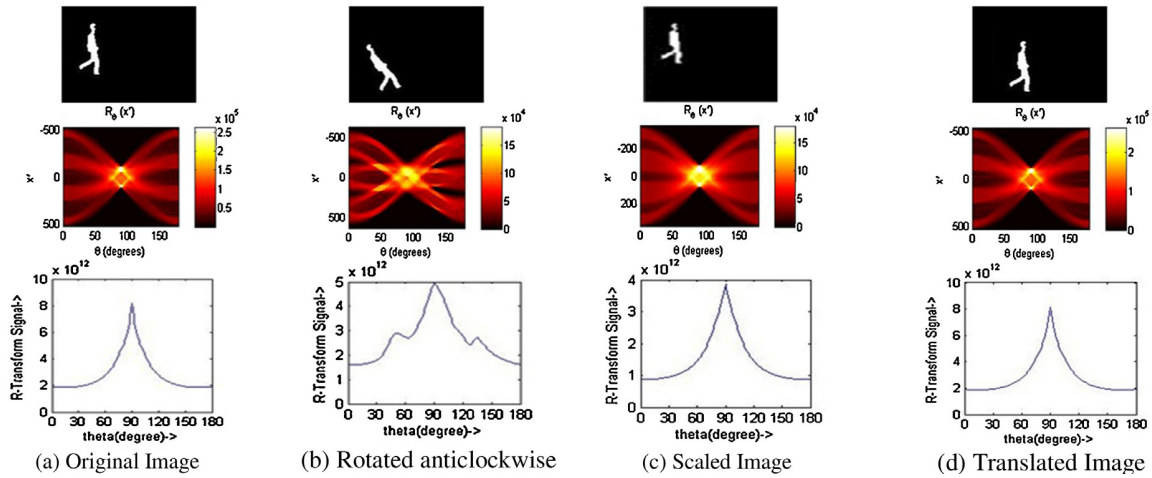


**Fig. 10.** Shows $\Re$-transform is variant to the rotation and invariant to scaling and translation Row 1: silhouette images, Row 2: Radon transform (RT), Row 3: $\Re$-transform signal.

which gives the directional information by calculating the pixel variations at different angles. But in some activity where the change in orientation is quite similar, as in the case of walking and running, it may not be able to discriminate exactly. It can also be said that the $\Re$-transform alone cannot represent all kinds of human actions efficiently. The actions that have similar orientation characteristics like walking and running can be distinguished by the spatial change in the video sequence.

The $\Re$-transform is computed on the binary silhouette of size $50 \times 50$ and after concatenation, it can be represented as a $1 \times 2500$ feature vector. The $\Re$-transform gives the reduced dimension of a silhouette image to $1 \times 180$ and for single action representation the dimension of the feature vector is $7 \times 180$. Further, to represent features in a reduced set, the LLE is applied.

### 2.4.3. Dimension reduction using local linear embedding

LLE is defined as the unsupervised manifold learning based dimension reduction method. Unlike PCA, LDA, KPCA which is based on the maximization of the variance, LLE searches the nearest neighbors around the data point in high-dimensional space. For each nearest neighbor, weights are assigned, which describe whether the data points are linear to neighbors or not. The weights are assumed to be invariant against translational, rotational, and scaling parameters, which possesses the local properties as in the original space. These weights reconstruct the data points into another dimensional space $\simeq\mathcal{D}\simeq$ and furthermore in the $\simeq\mathcal{D}\simeq$ dimensional space, data points are mapped into lower dimension '$d$' ($d \leq \mathcal{D}$). While transforming the features data points from 1-D space to another dimensional space, it maintains

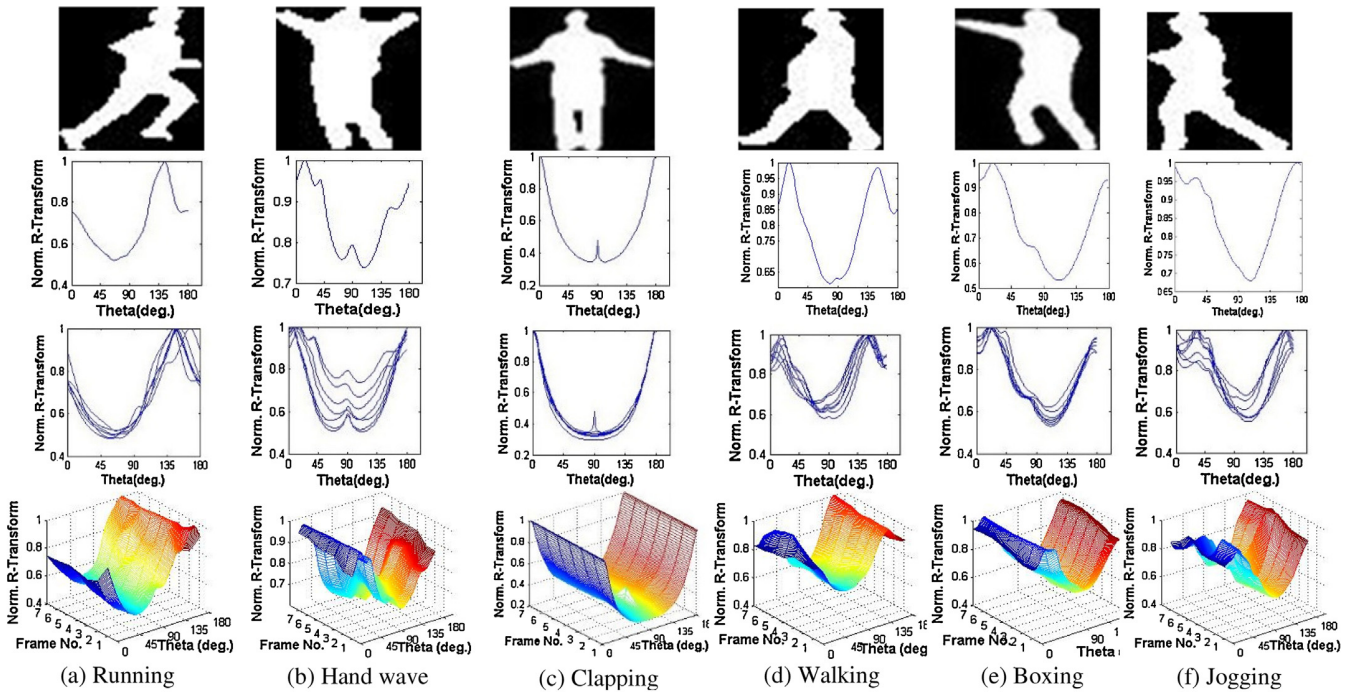


**Fig. 11.** Representation of $\Re$-transform for different activities: Row 1: $50 \times 50$ silhoutte image, Row 2: $\Re$-transform, Row 3: $\Re$-transforms of key frames, Row 4: 3D $\Re$-transform of sequence.

Please cite this article in press as: Vishwakarma DK, et al. Unified framework for human activity recognition: An approach using spatial edge distribution and $\Re$-transform. Int J Electron Commun (AEÜ) (2015), http://dx.doi.org/10.1016/j.aeue.2015.12.016

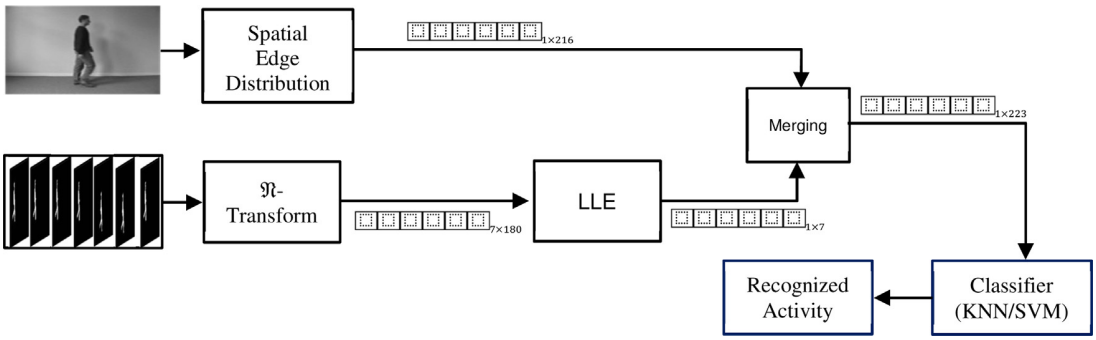


**Fig. 12.** Flow diagram of combing features.

the local characteristics of the features, which is explained as Algorithm 4.

**Algorithm 4.** LLE computation.

**Step 1:** Define training set vector $Z = \{x^{(n)} \in \mathbb{R}^d\}_{n=1}^{\mathcal{N}}$, of $d \times \mathcal{N}$ dimension.
**Step 2:** Construct the weight matrix '$\mathcal{W}$' to record the linear reconstruction coefficients, where the $i$th row $[\mathcal{W}_{ij} = 0]_{1 \le j \le \mathcal{N}}$ contains the initial coefficients of the sample '$i$' from its neighbors.
**Step 3:** The set containing all the neighbors of $x^{(i)}$ is denoted as $\Psi(i)$
$\Psi(i) = |\Psi(i)| =$ neighbors of $x^{(i)}$.
**Step 4:** Define linear coefficients $\mathcal{W}^{(i)}$ for each sample $i$ with the least reconstruction error using $\varepsilon(\mathcal{W}) = argmin_{\mathcal{W}} \left\| x^{(i)} - \sum_j \mathcal{W}_{ij} x_j \right\|^2$.
**Step 5:** Two constraints are set on $\mathcal{W}^{(i)}$
i. $\mathcal{W}_j^{(i)} = 0$, if $j \neq \mathcal{N}(i)$ (Neighborhood constraint). It means that $x^{(i)}$ is only reconstructed from its neighbor.
ii. $\sum_{j=1}^{\mathcal{N}} \mathcal{W}_j^{(i)} = 1$ (For translation invariant).
**Step 6:** Re-embedding in the reduced feature space, $\mathcal{Z} = \{z^{(n)} \in \mathbb{R}^m\}_{n=1}^{\mathcal{N}}$ of $m \times \mathcal{N}$ dimension and to maintain the local structures in $\mathcal{Z}$, it is represented as: $\phi(\mathcal{Z}) = \sum_{i=1}^{\mathcal{N}} \left\| \mathcal{Z}^{(i)} - \sum_{j=1}^{\mathcal{N}} \mathcal{W}_{ij} \mathcal{Z}^{(j)} \right\|^2$.

To get the coefficient in reduced feature set, the function $\phi(\mathcal{Z})$ is minimized. This method is better for representation of a non-linear distribution of data points and also maintains the local structures [34]. LLE is dependent upon the representation of data points in higher dimensional space; if they are different in representation, then LLE cannot ensure their reconstruction in lower dimensional space. In this case, the dimension of ℜ-transform feature set of $7 \times 180$ is reduced to $1 \times 7$ by applying the LLE algorithm.

### 2.5. Final feature vector formation

The final feature vector is formed by integrating the feature set obtained in Sections 2.3 and 2.4 which is shown in Fig. 12. The formed feature vectors are used for training and testing of the video sequence.

The spatial edge distribution feature vectors are computed as explained in the previous section and have a dimension of $1 \times 216$. Further, these feature vectors are combined with ℜ-transform features computed on the binary silhouettes. The ℜ-transform computed feature vector had the dimension of $7 \times 180$. Here, the number of key frames used are 7. The dimension of ℜ-transform feature is reduced using LLE, which gives the reduced discriminative feature vector of $1 \times 7$. Finally, the spatial edge feature vectors and ℜ-transform feature vectors are combined and give the resultant feature vector of $[1 \times 216 + 1 \times 7] = 1 \times 223$ dimension. The resultant feature vector is used to represent the activities of the dataset and these are classified using K-NN and SVM.

#### 2.5.1. K-nearest neighbors

The K-nearest neighbor (K-NN) is a simple machine learning algorithm for classifying objects based on a similarity measure (distance function). It is called the non-parametric method as it does not learn an explicit mapping from the training data. There are various distance functions which are used to measure the similarity, but they depend on the type of features of the data. If the distance is small, then there is more similarity between the two samples. Euclidean distance, Mahalanobis distance and Hamming distance are some of the common distance functions. If the features are real valued then, Euclidean distance is used and if the features are binary valued, then Hamming distance is used. The Euclidean distance between any two points $w = (x_1, x_2, \ldots\ldots\ldots, x_n)$ and $z = (y_1, y_2, \ldots\ldots\ldots, y_n)$ is as given in [35];

$$\text{Distance}(w, z) = \sqrt{\sum_{i=1}^{n=m} (x_i - y_i)^2} \quad (9)$$

K-NN classifier is simple and easy to implement. It gives better results in the case of large training data with the high value of '$K$' and it uses the local information of data which makes it highly adaptable.

#### 2.5.2. Support vector machine

SVM algorithm is based on the supervised learning [36] i.e. it has prior knowledge about the features that are to be used to predict the state of the class labels. It transforms the set of vectors into higher dimensional space where it continuously finds the optimal hyperplane that separates the class labels. The hyperplane is called a decision boundary that distinguishes the two classes and maximizes the separation, margin between itself and those lying nearest to it. The nearest set of points are called support vectors. Support vectors are features of the samples which are closest to the hyperplane of an SVM. Therefore, the determination of the location of most important data is near the hyperplane and which is formed by the set of lines drawn between the class samples. Initially, it is used for classification of two classes, but later on it is extended to multiclass problems. In two class problems, it is one of the most efficient and robust classifier. Hence, by utilizing the advantages of the two classes of SVM, it is extended to multiclass SVM. The frequently used approaches of multiclass SVMs are: (I) one-against-rest (II) one-against-one (III) directed acyclic graph SVM. In this paper, the multiclass SVM, the one-against-rest approach has been used. To perform the classification of the two classes, a nonlinear kernel based SVM can be applied by mapping the input data into the higher dimensional feature space. Consider $N$ training samples of feature set $\mathcal{T}_k$. Whereas:

Please cite this article in press as: Vishwakarma DK, et al. Unified framework for human activity recognition: An approach using spatial edge distribution and ℜ-transform. Int J Electron Commun (AEÜ) (2015), http://dx.doi.org/10.1016/j.aeue.2015.12.016

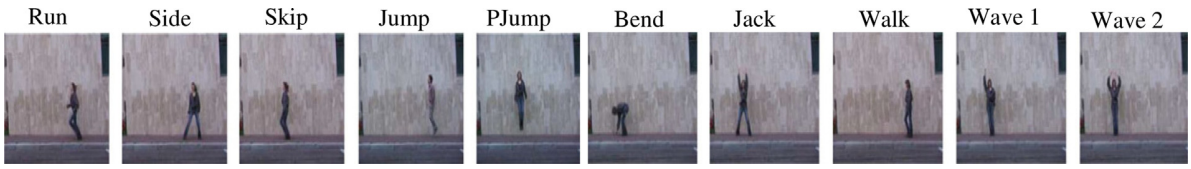


**Fig. 13.** Sample frames of Weizmann human action dataset.

$$\mathcal{T}_k = \{(x_i, y_i) \| x_i \in \mathbb{R}^m, y_i \in (-1, 1)\} \tag{10}$$

where $m$ is the dimensional feature vector signifying the $i$th training sample and $y_i \in (-1, 1)$ is the class label of $x_i$. An optimal hyper plane can be expressed as:

$$\psi(x) = sgnf\left(\sum_i^N \alpha_i y_i \mathcal{K}(x_i, x_j) + \mathfrak{b}\right) \tag{11}$$

where $sgnf(.)$ represents the signum function, and $\mathcal{K}(x_i, x_j)$ is a nonlinear predefined kernel function that satisfies the condition of Mercer's [25]. In this work the radial basis function used is as follows:

$$\mathcal{K}(x_i, x_j) = \exp(-p||x_i - x_j||^2), \quad p > 0 \tag{12}$$

The coefficient $\alpha_i$ and b can be determined using the concept of maximization of hyperplane value and written as:

$$argmax\left[\sum_i^N \alpha_i - \frac{1}{2}\sum_{i,j} \alpha_i \alpha_j y_i y_j \mathcal{K}(x_i, x_j)\right] \tag{13}$$

where $\underbrace{\min}_{\alpha} \sum_i \alpha_i y_i = 0, \quad 0 \le \alpha_i \le C, \quad \forall i \quad \text{and} \quad y_i = \mp 1.$

where $C$ is the penalty parameter that signifies the tradeoff between the maximizing the margin and minimizing the training set error. Although, the SVM is a binary classifier, it can still be extended for $M$-class classification in human activity recognition. One of the widely used multiclass techniques is one-against-rest [37], and the same approach is used in this work.

## 3. Experiment and results

In order to test the performance of proposed fusion method, an experiment is conducted on three publicly available datasets i.e. Weizmann [38], KTH [39] and Ballet movement [40] datasets. The classification accuracy is computed in terms of recognition rate using SVM and K-NN classifier with a testing scheme of leave-one-out manner. In leave-one-out test scheme, one sequence is used as a test video while others are used as training sets. This procedure continues until all the sequences are tested for single activity, and it further proceeds to other activities. The advantage of this method is that whole information of the dataset is used to calculate the precision. The effectiveness of the approach is measured in terms of average recognition rate (ARR), which is defined as:

$$\text{ARR} = \frac{\text{TP} + \text{TN}}{\text{TP} + \text{TN} + \text{FP} + \text{FN}} \times 100 \quad \text{(In percentage)} \tag{14}$$

where TP, TN, FP, and FN are the true positive, true negative, false positive, and false negative. The highest average recognition rate achieved on each dataset is compared with the similar state-of-the-art techniques.

***Weizmann dataset:*** This dataset is introduced by Gorelick et al. [38]. This dataset contains 90 videos with a frame rate of 15 fps and each frame having a size of $144 \times 180$. In a video sequence, nine people are performing ten different actions, categorized as walk, run, jump-jack, bend, jumping forward on one leg, jumping on two legs in the forward direction, jumping in place, sideways jump, one hand wave, two hand wave is shown in Fig. 13.

***KTH dataset:*** This dataset is introduced by Schuldt et al. [39] and it is a more challenging dataset as compared to the Weizmann dataset. The dataset consists of six basic activities, namely; 'hand-clapping' 'hand-waving', 'jogging', 'jumping', 'running', and 'walking'. Each activity has 100 videos for four different scenarios in different lighting conditions, indoor and outdoor conditions. All these video sequences are recorded in a uniform background with a static camera of frame rate 25 fps and further down-sampled to the spatial resolution of $160 \times 120$ pixels. Sample images of the dataset are shown as in Fig. 14.

***Ballet dataset:*** Ballet dataset [40] is the one of the most challenging dataset, which is consist of eight ballet movements. The sample postures of this dataset are as shown in Fig. 15.

The name of various activity postures areas: "Hopping (HP)," "Jump (JP)," "Left-to-Right Hand Opening (LRHO)," "Leg Swinging (LS)," "Right-to-Left Hand Opening (RLHO)," "Standing with Hand Opening (SHO)," "Stand Still (SS)" and "Turning (TR)". The key challenges of the dataset are the considerable amount of intra-class dissimilarities in terms of spatial and temporal scale, speed, and clothing.

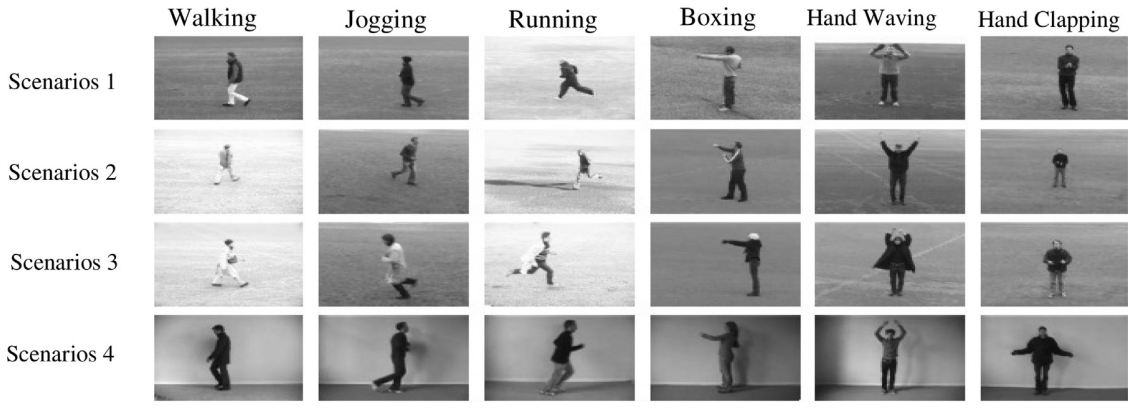


**Fig. 14.** Sample frames of KTH dataset.

Please cite this article in press as: Vishwakarma DK, et al. Unified framework for human activity recognition: An approach using spatial edge distribution and ℜ-transform. Int J Electron Commun (AEÜ) (2015), http://dx.doi.org/10.1016/j.aeue.2015.12.016

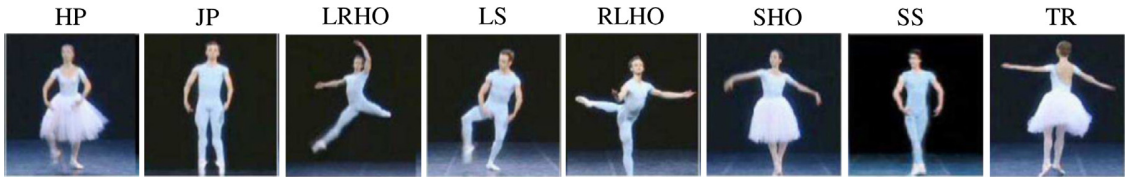


**Fig. 15.** Images of the Ballet data set depicting eight movement of actions.

**Table 2**
The classification result on Weizmann dataset.

| Activities | Bend | Jack | Jump | Pjump | Run | Side | Skip | Walk | Wave 1 | Wave 2 | ARR (%) |
|---|---|---|---|---|---|---|---|---|---|---|---|
| KNN (%) | 100 | 100 | 100 | 100 | 89 | 89 | 89 | 100 | 89 | 100 | 95.6 |
| SVM (%) | 100 | 100 | 100 | 100 | 100 | 100 | 100 | 100 | 100 | 100 | 100 |

**Table 3**
The classification result on KTH dataset.

| Activities | Boxing | Hand waving | Hand clapping | Jogging | Running | Walking | ARR (%) |
|---|---|---|---|---|---|---|---|
| KNN (%) | 100 | 92 | 92 | 92 | 78 | 100 | 92.3 |
| SVM (%) | 100 | 100 | 92 | 92 | 89 | 100 | 95.5 |

**Table 4**
The classification result on Ballet dataset.

| Activities | HP | JP | LRHO | LS | RLHO | SHO | SS | TR | ARR (%) |
|---|---|---|---|---|---|---|---|---|---|
| KNN (%) | 83 | 82 | 100 | 91 | 85 | 100 | 86 | 87 | 89.25 |
| SVM (%) | 88 | 87 | 100 | 100 | 100 | 93 | 92 | 94 | 94.25 |

### 3.1. Performance evaluations

Tables 2–4 show the performance of proposed methodology on Weizmann, KTH and Ballet movement datasets. From these tables, it can be clearly perceived that our proposed method gives a comparable result with the state-of-the-art methods.

From Tables 2–4 the highest recognition accuracy achieved on each dataset is through the SVM in comparison with K-NN. The ARR achieved on Weizmann dataset is 100% due to the less variation in intra-class activity, and the clean background. Due to clean background, the accurate extraction of the silhouette is accomplished which favors to achieve high accuracy. The KTH dataset is more challenging as compared to Weizmann dataset due to variations in lighting conditions, camera angle and human size within the sequence. Therefore, the silhouette extraction is quite difficult as compared to the previous data set. Hence, we achieved less ARA (95.50%) as compared to Weizmann dataset.

The Ballet movement data set is highly complex data set in terms of intra-class dissimilarities like execution, speed, clothing, etc. The ARA achieved on this data set is 94.25% that is less than the Weizmann and KTH dataset due to the complex actions. The maximum error is caused due to high similarity between the hopping and the jumping action. In some actions, it was observed that there is occlusion in the extracted silhouette frames, which poses difficulties in the computations of orientation features from the $\Re$-transform but the multiple fusion of the orientation and spatial distribution gives significant improvement in the recognition accuracy. The spatial edge distribution of gradients vector greatly improves the accuracy of the ballet dataset as it gives distinguishable features, which are more evident as compared to the $\Re$-transform characteristics. For $\Re$-transform, the human silhouette is extracted but as given that the dataset is complex as in some cases, hands and body parts get occluded which creates the confusion in recognizing the action. But with fusion techniques it involves all the parameters and efficiently improves the recognition in this dataset.

The performance of the proposed approach is also assessed in terms of processing speed. The algorithm is implemented using MATLAB 2012a on a computer, which has a specification of corei5, 1.60 GHz Intel processor with 2 GB RAM. For a single video in each dataset i.e. Weizmann, KTH and Ballet, the feature extraction time is 34 s, 45 s and 43 s respectively. For testing a video sequence, the classification time for each dataset i.e. Weizmann, KTH and Ballet are 0.0012 s, 0.0018 s and 0.0015 s respectively. The computation time can be further reduced if all algorithms are implemented in C++/Open CV on high configuration machine.

### 3.2. Comparison of results

The highest recognition rate achieved on these datasets are compared with similar state-of-the-art techniques, which is as presented in Tables 5 and 6.

Table 6 shows the comparison of our result with the similar state-of-the-art methods, which use the Ballet data set. In this experiment the similar setup is used as Fathi and Mori [40], Wang and Mori [45], Ming et al. [46], Iosifidis et al. [47], and Vishwakarma and Kapoor [44] thus this comparison is fair. From Table 6, it can be seen that the ARR achieved through proposed approach is highest among the compared earlier techniques. Hence, it can be said that the proposed approach gives better recognition result.

**Table 5**
Comparison of ARR on KTH and Weizmann datasets.

| Methods | Weizmann (%) | KTH (%) |
|---|---|---|
| Dollar et al. [41] | 85.20 | 81.17 |
| Niebles et al. [42] | 90.00 | 83.33 |
| Ikizler et al. [43] | 100.00 | 89.40 |
| Bregonzio et al. [7] | 96.66 | 94.33 |
| Dou and Li [11] | 94.20 | 92.70 |
| Vishwakarma and Kapoor [44] | 97.7 | 92.4 |
| Proposed method | 100.00 | 95.50 |

Please cite this article in press as: Vishwakarma DK, et al. Unified framework for human activity recognition: An approach using spatial edge distribution and $\Re$-transform. Int J Electron Commun (AEÜ) (2015), http://dx.doi.org/10.1016/j.aeue.2015.12.016

**Table 6**
Comparison of ARR on Ballet movement dataset.

| Methods | Fathi and Mori [40] | Wang and Mori [45] | Ming et al. [46] | Iosifidis et al. [47] | Vishwakarma and Kapoor [44] | Proposed method |
|---|---|---|---|---|---|---|
| ARR (%) | 51 | 91.3 | 90.8 | 91.1 | 92.75 | **94.25** |

**Table 7**
Independent test result.

| Input sequences (Weizmann-testing) | Predicted sequences (KTH-training) (%) | | | |
|---|---|---|---|---|
| | Running | Walking | Jogging | Waving |
| Running | 94 | 2 | 4 | 0 |
| Walking | 0 | 98 | 2 | 0 |
| Waving | 0 | 0 | 0 | 100 |

### 3.3. Independent test analysis

In order to evaluate the robustness of the algorithm under the independent test sample of a video sequence, a training and testing experiment is performed using support vector machine as a classifier. In this process, two different environmental settings of the video sequences (KTH and Weizmann) of the similar kind of activities are chosen for training and testing. The running, walking and 2-hand waving activities of Weizmann dataset is similar to the running, walking, jogging, and waving activities of KTH dataset. These four activities of the KTH dataset are labeled to train the classifier because KTH dataset is having the adequate number of video samples compared to Weizmann dataset, which is considered to be a good training environment. The three activities of the Weizmann dataset are used for testing and the result of testing is as shown in Table 7.

From the test result shown in Table 6, it is observed that the proposed algorithm is robust due to significant prediction rate. There are cases, where prediction rate is less due to inter-similarity of actions, but results are optimum and satisfactory considering the variations of datasets.

## 4. Conclusion and future work

In this paper, two important characteristics of human activity i.e. appearance and orientation are used to recognize the human activity. For representation of appearance and rotation the still images based edge spatial distribution and human silhouette based $\Re$-transform are used. A single still image is extracted from a video sequence using histogram distances between the key poses of the frames, and further spatial edge distribution is determined. The spatial distributions of edge gradients are computed at different levels of various orientation bins. For the computation spatial distribution feature, as the number of levels for the computation of spatial edge distribution increases, the dimension of feature vector increases but the recognition accuracy does not increase significantly.

The $\Re$-transform gives the orientation feature of human activity, which is computed on the silhouettes of the activities and silhouettes are extracted using texture based segmentation method. The orientation provides the knowledge about the flow of action relating to time and the global change in the object. As the increase in the number of silhouette frames, the recognition accuracy is incremental but the computation time increases significantly, which may lead to the high complexity of the system.

A final feature descriptor is formed by incorporating the appearance and orientation features of the activity. The final descriptor offers numerous distinctive feature vectors, which escort us to robust and noise free action modeling. This approach is an example of the integration of global rotation characteristics with localized structural information, and it is believed that this integration methodology can be further explored on the varied datasets making an improvement and combining the wide variety of existing human action techniques.

In future, this work can be extended to the more complex as well as varied data sets, which may be close to the real life unconstraint environment.

## References

[1] Turaga P, Chellappa R, Subrahmanian VS, Udrea O. Machine recognition of human activities: a survey. IEEE Trans Circuits Syst Video Technol 2008;18(11):1473–88.
[2] Holte M, Moeslund T, Nikolaidis N, Pitas I. 3D human action recognition for multi-view cameras systems. In: 3DIMPVT; 2011.
[3] Agrawal J, Rayoo M. Human activity analysis: a review. ACM Comput Surv 2011:16–43.
[4] Lim HC, Vats E, Chan CS. Fuzzy human motion analysis: a review. Pattern Recognit 2015;48(5):1773–96.
[5] Ziaeefard M, Bergevin R. Semantic human activity recognition: a literature review. Pattern Recognit 2015;48(8):2329–45.
[6] Shao L, Gao R, Liu Y, Zhang H. Transform based spatio-temporal descriptors for human action recognition. Neurocomputing 2011;74(6):962–73.
[7] Bregonzio M, Xiang T, Gong S. Fusing appearance and distribution information of interst points for action recognition. Pattern Recognit 2012;45(3):1220–34.
[8] Shao L, Ji L, Liu Y, Zhang J. Human action segmentation and recognition via motion and shape analysis. Pattern Recognit Lett 2012;33:438–45.
[9] Zhang Y, Lu H, Zhang L, Ruan X. Combining motion and appearance cues for anomaly detection. Pattern Recognit 2016;51(March):443–52.
[10] Zhao D, Shao L, Zhen X, Liu Y. Combining appearence and structural features for human action recogntion. Neurocomputing 2013;113(3):88–96.
[11] Dou J, Li J. Robust human action recognition based on spatio-temporal descriptors and motion temopral templates. Optik 2014;125(7):1891–6.
[12] Wu D, Shao L. Silhouette analysis-based action recognition via exploiting human poses. IEEE Trans Circuits Syst Video Technol 2013;23(2):236–43.
[13] Liu L, Shao L, Li X, Lu K. Learning spatio-temporal representations for action recognition: a genetic programming approach. IEEE Trans Cybern 2016;46(1):158–70.
[14] Liu L, Shao L, Zheng F, Li X. Realistic action recognition via sparsely-constructed Gaussian processes. Pattern Recognit 2014;47(12):3819–27.
[15] Hu J-F, Zheng W-S, Lai J, Gong S, Xiang T. Recognising human-object interaction via exemplar based modelling. In: IEEE International Conference on Computer Vision (ICCV). 2013.
[16] Shao L, Jones S, Xuelong L. Efficient search and localization of human actions in video databases. IEEE Trans Circuits Syst Video Technol 2014;24(3):504–12.
[17] Guo G, Lai A. A survey on still image based human action recogntion. Pattern Recognit 2014;47:3343–61.
[18] Bosch A, Zisserman A, Munoz X. Representing shape with a spatial pyramid kernel. In: ACM International conference on Image and Video Retrieval. 2012.
[19] Wang Y, Jiang H, Drew M, Li Z, Mori G. Unsupervised discovery of action classes. In: IEEE Conference on Computer Vision and Pattern Recognition. 2006.
[20] Li P, Ma J. What happening in a still picture? IEEE Asian Conference on Pattern Recognition. 2011.
[21] Li JL, Fei-Fei L. What, where and who? Classifying events by scene and object recognition. In: IEEE Conference on Computer Vision. 2007.
[22] Lopes A, Santos E, Valle E, Almeida J, Araujo A. Transfer learning for human action recognition. In: International Conference on Graphics Patterns and Images. 2011.
[23] Zheng Y, Zhang Y, Li X, Liu B. Action recognition in still images using a combination of human pose and context information. In: 19th International Conference on Image Processing (ICIP). 2012.
[24] Thurau C, Hlavac V. Pose primitive based human action recognition in videos or still images. In: IEEE Conference on Computer Vision and Pattern Recognition. 2008.
[25] Zhang H, Liu Z, Zhao H. Recognizing human activities by key frame in video sequence. J Softw 2010;5(8):818–25.
[26] Khan Z, Sohn W. Abnormal human activity recogntion system based on R-transform and Kernel Discriminant Technique for Eldely Home Care. IEEE Trans Consum Electron 2011;57(4):1843–50.
[27] Jalal A, Uddin M, Kim T. Depth video based human activity recognition system using translation and scaling invariant features for life logging at smart home. IEEE Trans Consum Electron 2012;58(3):863–71.
[28] Tabbone S, Wendling L, Salmon JP. A new shape descriptors defined on the Randon transform. Comput Vis Image Underst 2006;102(1):42–51.

Please cite this article in press as: Vishwakarma DK, et al. Unified framework for human activity recognition: An approach using spatial edge distribution and $\Re$-transform. Int J Electron Commun (AEÜ) (2015), http://dx.doi.org/10.1016/j.aeue.2015.12.016

[29] Li L, Leung MKH. Integrating intensity and texture differences for robust change detection. IEEE Trans Image Process 2002;11(2):105–12.
[30] Vishwakarma DK, Kapoor R. Integrated approach for human action recognition using edge spatial distribution, direction pixel, and R-transform. Adv Robot 2015;29(23):1551–61.
[31] Zeng P, Chen Z. Perceptual quality measure using JND model of the human visual system. In: in EEE International Conference on Electric Information and Control Engineering. 2011.
[32] Zadeh LA. Fuzzy sets. Inf Control 1965;8(3):338–53.
[33] Haralick R, Shanmugam K, Dinstein I. Textural features for image classification. IEEE Trans Syst Man Cybern 1973;6:610–21.
[34] Roweis ST, Saul LK. Nonlinear dimensionality reduction by locally linear embedding. Science 2000;260:2323–6.
[35] Cover TM, Hart PE. Nearest neighbor pattern classification. IEEE Trans Inf Theory 1967;13(1):21–7.
[36] Vapnik VN. An overview of statistical learning theory. IEEE Trans Neural Netw 1999;10(5):989–99.
[37] Qian H, Mao Y, Xiang W, Wang Z. Recognition of human activities using SVM multi-class classifier. Pattern Recognit 2010;31(2):100–11.
[38] Gorelick L, Blank M, Shechtman E, Irani M, Basri R. Actions as space-time shapes. IEEE Trans Pattern Anal Mach Intell 2007;29(12):2247–53.
[39] Schuldt C, Laptev I, Caputo B. Recognizing human actions: a local SVM approach. In: Proceedings of the International conference on Pattern Recognition. 2004.
[40] Fathi A, Mori G. Action recognition by learning mid-level motion features. In: Proceedings of IEEE conference on Computer Vision and Pattern Recognition. 2008.
[41] Dollar P, Rabaud V, Cottrell G, Belongie S. Behavior recognition via sparse spatio-temporal features. In: 2nd Joint IEEE International Workshop on Visual Surveillance and Performance Evaluation of Tracking and Surveillance. 2005.
[42] Niebles JC, Wang H, Fei-Fei L. Unsupervised learning of human action categories using spatial-temporal words. Int J Comput Vis 2008;79(3):299–318.
[43] Ikizler N, Duygulu P. Histogram of oriented rectangles: a new pose descriptor for human action recognition. Image Vis Comput 2009;27(10):1515–26.
[44] Vishwakarma DK, Kapoor R. Hybrid classifier based human activity recognition using the silhouette and cells. Expert Syst Appl 2015;42(20):6957–65.
[45] Wang Y, Mori G. Human action recognition by semi-latent topic models. IEEE Trans Pattern Anal Mach Intell 2009;31(10):1762–4.
[46] Ming XL, Xia HJ, Zheng TL. Human action recognition based on chaotic invariants. J South Central Univ 2013;20:3171–9.
[47] Iosifidis A, Tefas A, Pitas I. Discriminant bag of words based representation for human action recognition. Pattern Recognit Lett 2014;49:185–92.

Please cite this article in press as: Vishwakarma DK, et al. Unified framework for human activity recognition: An approach using spatial edge distribution and ℜ-transform. Int J Electron Commun (AEÜ) (2015), http://dx.doi.org/10.1016/j.aeue.2015.12.016

Volume 3, Issue 4 (2015) 647-652 ISSN 2347 - 3258
International Journal of Advance Research and Innovation

# Vapour Compression Refrigeration Technology for Sustainable Development

R.S. Mishra
Department of Mechanical Engineering , Delhi Technological University, Delhi, India

**Article Info**

Article history:
Received 2 October 2015
Received in revised form
20 October 2015
Accepted 28 November 2015
Available online 15 December 2015

**Keywords**

Sustainable Technologies,
Green Technologies,
Energy and Exergy Analysis,
Sustainable Development,
Eco Friendly refrigerants,
First and second law Analysis

**Abstract**

This paper mainly focus on CFCs and their alternatives to their use. The main critical issue in the field of green technologies is to develop the relationship between ODP and GWP and suggest new and alternative refrigerants which do not damage ozone layer and not to increase global warming. The first and second law thermodynamic analysis of vapor refrigeration system of 1.5 ton capacity for five eco-friendly refrigerants such as (R-1234yf, R-1234ze, propane (R-290), isobutene (R-600a), butane (R-600)) have been carried out in terms of performance parameters such as COP, Exegetic efficiency, ratio of exergy destruction in components such as condenser, compressor, throttle valve and evaporator. These performance parameters have been evaluated by varying condenser temperatures in the range from 300K to 327K and evaporator temperatures in the range from 274 K to 279K. It was observed that R-290 and R-600 (butane) and R-600a (isobutene) of zero ODP and zero GWP is best alternatives if its flammable problem will mitigate and R-1234ze (of zero ODP), are the next option of R-22 refrigerant.

## 1. Introduction

An eminent philosopher has defined Science as "TAPASAYA" and Technology as "Bhog" where as science is pure selfless and open to all search for truth where as technology is the exploitation of scientific knowledge for selfish purposes and profit motive and hence it tends to be secretive in this competititive world of today with a throat cutting environment. Sustainable Development is a process in which development can be sustained for generations. It also focuses attention on inter generational fairness in the exploitation of development opportunities while social development is a function of technological advancement, and also the technological advancement, in turn is a function of scientific know how for a streamlined development of the society. Technology is one of the crucial determinants of sustainable development. Technological import through collaborations has been one of the most important sources of technological inputs for Indian conditions. The use of technologies originating in rich countries often ten to create many social, ecological and resource problems in poor countries. The exploitation of the vast natural resources through progressive development of science, engineering and technology that has brought about the vast changes in the civilization and society from the stone age to the present high technology era. In facts, the mad race for industrialization and economic development has resulted in over exploitation of natural resources, leading to a situation where the two worlds of mankind- the biosphere, lithosphere and hydrosphere of his inheritance and the techno sphere of his creation, are out of balance with each other, indeed on a collision path. To facilitate optimal utilization of finite natural resources for ensuring a sustainable benefit steam for better quality of life on the one hand and to simultaneously keep in mind the conservation of natural resources on the other hand, it is essential that the technology conservation process must be made as efficient as possible. Therefore sustainable economic development depends on the careful choice of technologies and judicious management of resources for productive activities to satisfy the changing human needs without degrading the environment or depleting the natural resources base.

**Corresponding Author,**
**E-mail address:** professor_rsmishra@yahoo.co.in
**All rights reserved:** http://www.ijari.org

## 2. Application of Ecofriendly Refrigerats in the Vapour compression Refrigeration Systems

The efforts under the Montreal protocol to protest the OZONE layer, the alternative refrigerants have been proposed as a substitutes for ozone depleting substances. HFCs ( Hydrofluoro carbons) PFCs (Perfluro carbons ) have zero ODP potential but they are producer of green house gases and are subjected to limitation and reduction commitments under UNFCC(United Nations Framework Convention on Climate change). With the entry into force of Kyoto protocol on 16th February 2005 developed countries have already planning and implementing rational measures intended to contribute towards meeting green house gas reduction targets during the first commitment period of Kyoto protocol (2008-2012). The countries have also started together with developing countries to size up projects that qualify under Kyoto clean development mechanism. As what lies behyond 20-12 all Governments will work together over next few years to decide on future intergovernmental action on the climate change. In this light, it is vital that there should be continuous work on the replacement options for ozone depleting substances in way that serve the aim of the Montreal protocol and UNFCC alike. In the developing countries the conversion of CFCs to alternate is still a major issue. In this paper the first law and second law analysis of various eco friendly refrigerants have been carried out which will help in deciding about the path to be followed to satisfy Montreal and Kyoto protocol. On the basis of theoretical analysis, an extensive experiment

have been conducted in the Advanced centre for studies and research in green energy technologies of Delhi college of Engineeing, and It was observed thatR1234yf and R-1234ze refrigerant is the best alternatives for replacing R134a after 2030 due to its low ODP and GWP.

## 3. Thermodynamic Analysis of Vapour Compression Refrigeration systems

Thermodynamic processes in refrigeration system releases large amount of heat to the environment. Further, heat transfer between the system and the surrounding environment takes place at a finite temperature difference, which is a major source of irreversibility for the cycle and also responsible for the system performance degradation. The losses in the cycle need to be evaluated considering respective individual thermodynamic processes by applying first and second laws. Energy analysis (First Law) is still the most commonly used method in the analysis of thermal systems which only concern with the conservation of energy, and gives no information on how, where, and how much the system performance is degraded. On the other hand, second law is used to describe the quality of energy of materials. The first law optimization results in maximizing the coefficient of performance (COP) thus providing maximum heat removal from minimum power input; while the second law optimization is used for maximizing the exergy efficiency and minimizing entropy generation within the system, hence providing maximum cooling for the smallest distraction of available energy (exergy).

The exergy method, known as the second law analysis calculates the exergy loss caused by irreversibility which is an important thermodynamic property that measures the useful work that can be produced by a substance or the amount of work needed to complete a process. Thus exergy analysis is powerful tool in the design, optimization, and performance evaluation of energy systems. The principles and methodologies of exergy analysis are well established [1-4]. An exergy analysis is usually aimed to determine the maximum performance of the system and identify the sites of exergy destruction. Exergy analysis of a complex system can be performed by analyzing the components of the system separately. Identifying the main sites of exergy destruction shows the direction for potential improvements. An important objective of exergy analysis for system that consume work such as refrigeration, liquefaction of gases, and distillation of water is to find the minimum work required for a certain desired result [5].

There are several studies on the exergy analysis of refrigeration system [6, 7]. Bejan [7] showed that the exergetic efficiency decreases as the refrigeration temperature decreases. He offered two simple models to explain this trend. In his model, thermodynamic imperfections are explained largely by the heat transfer irreversibility. The behaviour of two stage compound-cycle with flash intercooling, using refrigerant R22 has been investigated by Nikolaidis and Probert [8] using exergy method. A computational model based on the exergy analysis is presented by Yumrutas et. al [9] for the investigation of the effects of the evaporating and condensing temperatures on the pressure losses, exergy losses, second law of efficiency, and the COP of a vapour compression cycle.

In the present research work, exergy analysis is performed on the operating data of vapour compression refrigeration cycle of an industrial ice plant. The expressions for the exergy losses (lost works) for the individual processes of the cycle as well as the coefficient of performance (COP) and second law efficiency for the entire cycle has been obtained. Effect of variation of condensing and evaporating temperatures on exergy losses, second law efficiency and COP has been investigated. The concept of structure coefficient (coefficient of structure bond) is used to explain the relation between irreversibilities of system & its component. The main components of an refrigeration are compressor, expansion valve, condenser and evaporator (brine chiller connected with ice box). Ice tank is made of mild steel plates and having heavy insulation of granulated corks around 300 mm in thickness. The tank is filled with recirculated brine in which cans filled with water are immersed. The tank is provided with piping for blowing air into ice cans to create agitation. In the present analysis, single stage vapour compression system has been used for ice production. Reverse osmosis water is being used in the system for production of ice cubes.The corresponding temperature versus entropy diagram for this system. At the starting point , the circulating refrigerant enters the compressor as a saturated vapour. From firstpoint to secondpoint , the refrigerant vapour is isentropically compressed and exits the compressor as a superheated vapour. From second point to point third', the superheated vapour travels through part of the condenser which removes the superheat by cooling the vapour.Between third point ' and fourth point , the vapour travels through the remainder of the condenser and is condensed into a saturated liquid. The condensation process occurs essentially at constant pressure. Between fourthpoints and fifth point, the saturated liquid refrigerant passes through the expansion valve and undergoes an abrupt decrease of pressure. This process results in the adiabatic flash evaporation and causes auto-refrigeration of a portion of the liquid refrigerant (typically, less than half of the liquid flashes). The adiabatic flash evaporation process is isenthalpic (i.e., occurs at constant enthalpy) in nature. Between fifth points and first point , the cold and partially vaporized refrigerant travels through the coil or tubes in the evaporator where it is totally vaporized by the warm water (from the space being refrigerated) that circulates across the coil or tubes in the evaporator. The evaporator operates at essentially constant pressure. The resulting saturated refrigerant vapor returns to the compressor inlet at the first point to complete the thermodynamic cycle

## 4. Eco Friendly Referants used in vapour compression refrigeration systems

The performance of Vapour compression refrigeration systems of 1.5 tons refrigerating capacity are given using following ecofriendly refrigerants.

**R-410a:** is a azeotropic mixture of HFC-32 and HFC-125 in the proportions 50%, 50% by weight with 2% tolerance allowed for each of the components. It has very low temperature glide around 0.1K and its vapor pressure is roughly 50% higher than that of HCFC22.

**R-32/124a:** R-32 is a near azeotropic mixture of HFC-32 (Difluromethane) and R-124a in the proportions of 30% and 70% by weight.

**R-134a:** is a member of the family of HFC refrigerants. The HFC refrigerants are similar composition to CFCs and HCFCs and they have become the primary focus of the refrigeration and air conditioning industries as a long term substitute for traditional refrigerants. HFCs are not miscible with traditional mineral oil so alternative synthetic lubricants are recommended synthetic polyester either alkyl benzene or polyalkylen glycol

**R-407c:** is a mixed zoetrope refrigerant consisting of three HFC components such as R-32, R-125 and R-134a in the proportions 23%, 25% and 52% by a weight +_ 2% tolerances allowed for each of the components. R-407c has properties very similar to R-22 which was replaced in air conditioning applications in terms of both its operating pressures and its performance in dry expansion air conditioning systems.

**Propane (R-290)** can be used as substitute for R-11, R12 and R22 because of zero ODP and GWP. The pressure levels and refrigerating capacity are similar to R-22 and R-502 along with its temperature behavior is as favorable as with R-22 & R-502. There is no material problems in compressor of hermetic and semi hermetic types in air conditioning units and heat pumps. The first law and second law performances in terms of variation of condenser and evaporator temperatures with COP, Exergy Destruction Ratio(EDR), exegetic efficiency, exergy destruction in each components of vapor compression refrigeration system of 1.5 tons capacity using R-290 refrigerant for 298K of ambient temperature.

**Propylene (R-1270)** can be used as substitute because of good refrigerant by higher volumetric refrigeration capacity and low boiling temperature however higher pressure level and discharge gas temperature have to be taken into consideration which restricting the possible application range. R-1270 is also easily inflammable and due to chemical double linkage it is relatively reaction friendly and there is a danger of polymerization at higher pressure and temperature levels. The component dimensions have to be altered when using R-1270 refrigerant due to higher volumetric refrigeration capacity along with lower compressor displacement. Because of higher vapor density , the mass flow rate is almost the same as for R-290 and liquid density is nearly identical for the liquid volume in circulation.

## 5. Modelling of vapour compression refrigeration system using ecofriendly refrigerants

The major disadvantage of hydrocarbon refrigerants is their inflammability therefore system must be designed by consideration of flame proof regulations however with open compressors additional safety devices may be required. For practically mass flow rate of refrigerant may be low as 55% to 60% approximately as compared to R-22 and internal heat exchanger between the suction and liquid line is improved the refrigeration capacity along with COP. Due to good solubility with mineral oils, it may be necessary to use an oil it lower mixing characteristics or increasing viscosity for higher suction pressure, the use of internal heat exchanger is advantageous because it leads to higher oil temperatures to lower solubility improves its viscosity. Due to favorable temperature behavior of R-290, the single stage compressor is used down to approximately 233K evaporator temperature respectively and can also be considered as a direct substitute for R-502. For the thermodynamic analysis of the industrial ice plant working on vapour compression system, the principles of mass conservation, first and second laws of thermodynamics are applied to each component of the system. Each component can be treated as control volume with inlet and outlet streams, heat transfer and work interactions. For the system, the mass conservation is governed by following equation:

$$\sum m_i - \sum m_o = 0 \quad (1)$$

Where m is the mass flow rate and suffix i and o represents inlet and outlet of the component.

The first law of thermodynamics yields the energy balance of each component of the system as follows:

$$\sum (mh)_i - \sum (mh)_o + [\sum Q_i - \sum Q_o] + W = 0 \quad (2)$$

The overall energy balance of the system requires that the sum of the evaporator, condenser and compressor must be zero. The vapour compression system is assumed to be in steady state condition and further if the pump work for brine solution circulation and the environmental heat losses are neglected, the energy balance for the entire system can be written as

$$Q_0 = Q_c + W \quad (3)$$

The energy balance equations of various components of a vapour compression system are given below:

Mass flow rate of circulated refrigerant can be calculated as

$$m_R = Q_c / (h_1 - h_4) \quad (4)$$

For the compressor (by convention, the work done by compressor is presumed to be negative);

$$W_c = - m_R (h_2 - h_1)/\eta_m\eta_e \quad (5)$$

Where $\eta_m$ and $\eta_e$ are mechanical and electric motor efficiencies respectively.

Heat transfer rate in the condenser (zone B) is given by

$$Q_0 = m_R (h_3 - h_2) \quad (6)$$

Coefficient of performance of refrigeration is

$$COP = Q_c/W \quad (7)$$

For state point 4 dryness fraction and specific entropy can be represented as:

$$x_4 = (h_3 - h_f) / (h_1 - h_f) \quad (8)$$

Where $h_f$ is the enthalpy of saturated liquid refrigerant at evaporator pressure.

Specific entropy is:

$$s_4 = s_f + x_4 (s_1 - s_f) \quad (9)$$

Where $s_f$ is the entropy of saturated liquid refrigerant at evaporator pressure. Second law analysis is a relatively new concept, which has been used for understanding the irreversible nature of real thermal processes and defining the maximum available energy. The second law analysis is based on the concept of exergy, which can be defined as a measure of work potential or quality of different forms of available energy relative to the environmental conditions. In other words, exergy can be defined as the maximum theoretical work derivable by the interaction for an energy resource with the environment.

Exergy analysis is applied to a system describes loses both in the components of the system and for the system as a whole. With the help of exergy analysis the magnitude of

these losses or irreversibility's and their order of importance can be understood respectively. With the use of irreversibility, which is a measure of process imperfection, the optimum operating conditions can be easily determined. It is possible to say that exergy analysis throw an insight to indicate the possibilities of thermodynamic improvement for the process under consideration. The formulation for exergy analysis is described below:

The difference of the flow availability of a stream and that of the same stream at its restricted dead state is called flow exergy (ε) and by ignoring chemical exergy terms, flow exergy (ε) is given by

$$\varepsilon = (h - T_0 s) + V^2/2 + gZ - (h_0 - T_0 s_0) \quad (10)$$

Ignoring the potential and kinematic energy terms, Eq. (10) becomes

$$\varepsilon = (h - T_0 s) - (h_0 - T_0 s_0) \quad (11)$$

The exergy balance equation is given by

$$E_w = \sum E_Q + \sum(m\varepsilon)_i - \sum(m\varepsilon)_o + T_0 S_{gen} \quad (12)$$

In equation (12) the term $T_0 S_{gen}$ is defined as the irreversibility (I) and can be written as:

$$I = T_0 S_{gen} \quad (13)$$

The above exergy analysis formulation has been performed on each component of the vapour compression system shown in Figure 3, and corresponding irreversibility of each component is calculated. Using this formulation described below:

By carrying out an exergy-rate balance for the compressor, the irreversibility rate (zone A):

$$I_A = W + E_1 - E_2 \quad (14)$$

The exergy-rate balance for the evaporator (zone D):

$$I_D = E_4 - E_1 - E_Q^D \quad (15)$$

where, for the evaporator

$$E_Q^D = Q_C (T_0 - T_c)/T_c \quad (16)$$

The exergy rate balance for the condenser, (zone B) is given by

$$I_B = E_2 - E_3 \quad (17)$$

The exergy-rate balance in the throttling valve, (zone C) is given by

$$I_C = E_3 - E_4 \quad (18)$$

Efficiency defect ($\delta_k$) of $k^{th}$ component of the system may be expressed as fractions of input which are lost through irreversibility

$$\delta_k = I_k/W \quad (19)$$

Where $I_k$ is the irreversibility rate of the $k^{th}$ component of the system under consideration.

The total irreversiblitities of the system components is expressed as

$$I_t = I_A + I_B + I_C + I_D \quad (20)$$

The relative irreversibility of the $k^{th}$ component of plant is $= I_k/I_t$ (21)

Structural coefficients are used in the study of the system structure, optimization of plant components and product pricing in multi-product plants. The change of local irreversibility rates and exergy fluxes in relation to the overall plant's irreversibility rate is effectively expressed by the coefficient of structural bonds (CSB) which is defined by

$$\sigma_{k,i} = [\partial I_t / \partial x_i]/[\partial I_k / \partial x_i] \quad (22)$$

Where $x_i$ is the $i^{th}$ parameter of the system which produces the changes in $k^{th}$ component.

The effect of a change in $x_i$ on the system would be to alter the rate of exergy input while leaving the output constant. This acceptance confirms to the usual practice of specifying a plant in terms of its output rather than its input. From the exergy balance of the system

$$E_{IN} = E_{OUT} + I_t \quad (23)$$

But $E_{OUT}$ = constant, thus

$$\Delta E_{IN} = \Delta I_t \quad (24)$$

As seen from equation (24) changes in the irreversibility of the system are equivalent to changes in the exergy input. In general, the ratio of the rates of exergy output to exergy input is less than unity. This ratio denotes the degree of thermodynamic perfection of the process and is called the rational efficiency($\eta_R$).

$$\eta_R = E_{OUT}/E_{IN} \quad (25)$$

Plant rational efficiency $\eta_{R,\,plant} = 1 - \sum\delta_k$ (26)

## 6. Results & Discussions

The computation modeling of vapor compression refrigeration systems was carried out with the help of engineering equation solver of Hon'ble Dr. S.A. Klein (2002) for first and second law analysis in terms of energetic analysis i.e. COP (First law analysis) and exegetic analysis in terms of exergetic efficiency, exergy destruction ratio (EDR) and percentage exergetic destruction in each components (second law analysis). In this analysis we assumed negligible pressure losses and heat losses. The comparative performance of 4.75 KW window air conditioner is evaluated for condenser temperature varying between 300K to 327K with increment of 3 and evaporator temperature is varying from 274K to 278 K with increment of 1. The energy and exergy change in vapour compression refrigeration cycle have been calculated for various eco friendly refrigerants such as R-1234yf, R-1234ze, R404a, R-290 (propane), R600 (butane), R-600a (isobutene) for environmental temperature of 298K. The variation of fist law efficiency in terms of cop and second law eficiency in terms of exergetic are shown in Table-1to Table 2 respectively. As condenser temperature increses the first law efficiency decreases while second law efficiency decreases. Similarly with increasing evaporator temperature, the first law efficiency increases while second law efficiency decreases. The effect of various eco friendly refrigerants for condenser temperature of 321 (K) and Evaporator temperature of 277 K is also shownin table 3. Respectively.

**Table: 2a.** First Law Performance Of Vapour Compression Refrigeration System With Evaporator Temperatures Using Ecofriendly Refrigerants (Tcond=321 K Tamb=300 K )

| Evaporator Temp (K) | COP R1234yf | COP R1234ze | COP R600a | COP R290 | COP R600 |
|---|---|---|---|---|---|
| 274 | 2.27 | 5.214 | 2.514 | 2.424 | 2.623 |
| 275 | 2.345 | 5.466 | 2.592 | 2.498 | 2.703 |
| 276 | 2.423 | 5.738 | 2.675 | 2.576 | 2.787 |
| 277 | 2.505 | 6.034 | 2.76 | 2.658 | 2.874 |
| 278 | 2.591 | 6.358 | 2.851 | 2.743 | 2.966 |
| 279 | 2.681 | 6.712 | 2.946 | 2.833 | 3.061 |

**Table: 2b:** Second law Performance of Vapour Compression Refrigeration System With Evaporator Temperatures Using Ecofriendly Refrigerants (Tcond=321 K Tamb=300 K,)

| Eva. Temp(K) | Second LawEff_R1234yf | Second LawEff | Second LawEff_R600a | SecondLawEff_R290 | Second LawEff_R600 |
|---|---|---|---|---|---|
| 274 | 0.8507 | 0.8791 | 0.8555 | 0.8538 | 0.8574 |
| 275 | 0.6926 | 0.7505 | 0.7023 | 0.6988 | 0.7061 |
| 276 | 0.5247 | 0.6132 | 0.5392 | 0.5340 | 0.5447 |
| 277 | 0.2356 | 0.4661 | 0.3647 | 0.3573 | 0.3720 |
| 278 | 0.1535 | 0.3077 | 0.1772 | 0.1678 | 0.1864 |
| 279 | 0.0 | 0.1364 | 0.0 | 0.0 | 0.1420 |

**Table: 2a.** Firstlaw Performance of Vapour Compression Refrigeration System with Condenser Temperatures Using Ecofriendly Refrigerants (TEVA=277 K, Tamb=300 K)

| Condeser temperature (K) | COP R1234yf | COP R1234ze | COP R600a | COP R290 | COP R600 |
|---|---|---|---|---|---|
| 300 | 5.818 | 6.034 | 6.036 | 5.914 | 6.141 |
| 303 | 5.034 | 5.249 | 5.252 | 5.140 | 5.355 |
| 306 | 4.4080 | 4.624 | 4.629 | 4.521 | 4.737 |
| 309 | 3.894 | 4.113 | 4.12 | 4.0160 | 4.23 |
| 312 | 3.465 | 3.686 | 3.696 | 3.594 | 3.806 |
| 315 | 3.099 | 3.325 | 3.337 | 3.236 | 3.446 |
| 318 | 2.782 | 3.013 | 3.029 | 2.927 | 3.141 |
| 321 | 2.505 | 2.742 | 2.761 | 2.658 | 2.874 |
| 324 | 2.259 | 2.503 | 2.526 | 2.42 | 2.640 |
| 327 | 2.038 | 2.29 | 2.317 | 2.207 | 2.431 |

**Table: 2b.** Second Law Performance of Vapour Compression Refrigeration System with Condenser Temperatures Using Ecofriendly Refrigerants (TEVA=277 K Tamb=300 K)

| Condeser temperature(K) | SECONDLAWETA_R1234yf | SECONDLAWETA_R1234ze | SECONDLAWETA_R600a | SECONDLAWETA_R290 | SECONDLAWETA_R600 |
|---|---|---|---|---|---|
| 300 | 0.4629 | 0.4661 | 0.4661 | 0.4643 | 0.4676 |
| 303 | 0.4491 | 0.4533 | 0.4534 | 0.4512 | 0.4553 |
| 306 | 0.4345 | 0.44 | 0.4401 | 0.4375 | 0.4427 |
| 309 | 0.4191 | 0.4261 | 0.4263 | 0.4231 | 0.4296 |
| 312 | 0.4027 | 0.4116 | 0.412 | 0.4080 | 0.4160 |
| 315 | 0.3851 | 0.3963 | 0.3970 | 0.3921 | 0.4020 |
| 318 | 0.3661 | 0.3803 | 0.3812 | 0.3753 | 0.3873 |
| 321 | 0.3456 | 0.3633 | 0.3647 | 0.3573 | 0.3720 |
| 324 | 0.3231 | 0.3453 | 0.3472 | 0.3382 | 0.2504 |
| 327 | 0.2983 | 0.3261 | 0.3288 | 0.3177 | 0.3393 |

**Table: 1a:** Performance of Vapour Compression Refrigeration Systems Using Ecofriendly Refrigerants

| Refrigerants | $Q_{EVA}$ | $W_{COMP}$ | $Q_{CON}$ | COP ACTUAL | COP CARNOT | EFFICIENCY$_{SECOND}$ |
|---|---|---|---|---|---|---|
| R717 | 1047 | 398.7 | 1445 | 2.625 | 5.383 | 0.4876 |
| R407c | 134.04 | 65.97 | 200 | 2.031 | 5.383 | 0.3774 |
| R404a | 90.03 | 45.01 | 139 | 2.089 | 5.383 | 0.3830 |
| R123 | 128.6 | 48.12 | 176.7 | 2.672 | 5.383 | 0.4965 |
| R152a | 220.8 | 84.77 | 305.5 | 2.60 | 5.383 | 0.4838 |

**Table: 1b:** Performance Of Vapour Compression Refrigeration Systems Using Ecofriendly Refrigerants

| Refrigerant | $Q_{EVA}$ | $W_{COMP}$ | $Q_{CON}$ | $COP_{ACTUAL}$ | $COP_{CARNOT}$ | $EFF_{SECOND}$ |
|---|---|---|---|---|---|---|
| R-1234yf | 93.12 | 42.06 | 135.2 | 52.214 | 5.383 | 0.4113 |
| R1234ze | 117.8 | 47.93 | 165.8 | 2.459 | 5.383 | 0.4567 |
| R134a | 130.2 | 53.1 | 183.2 | 2.451 | 5.383 | 0.45540 |
| R410a | 148.6 | 63.83 | 212.4 | 2.329 | 5.383 | 0.4326 |
| R600 | 259.7 | 100.9 | 360.6 | 2.574 | 5.383 | 0.4782 |
| R-290 | 244.3 | 101.3 | 345.6 | 2.412 | 5.383 | 0.4481 |
| R600a | 224.1 | 91.56 | 315.7 | 2.448 | 5.383 | 0.4547 |

## 7. Conclusions and Recommendation

The analysis of the single stage vapour compression refrigeration system performance by the exergy method demonstrates how effective this method is for analyzing behavior. Employing the concepts of efficiency defect and exergetic efficiency has enabled the proportions of input lost through irreversibility's, in various refrigeration systems sub systems, to be evaluated easily. Using the technique of the coefficient of structural bond has demonstrated that a change in any component variable in a system component significantly influences the other component in the system as a whole, and a reduction of irreversibility's rate in a plant component give a greater reduction in the irreversibly rate of system as whole. The greater the value of condeser temperature, the greater the irreversibly. Because $T_{cond}$ and $T_{evap}$ affect the system exergetic efficiency, they need to be optimized each particularly heat transfer area chosen for the two heat exchanger in therefrigerating system.

## References

[1] M. J. Moran, Availability Analysis: A guide to efficient energy use (Prentice Hall & engle wood Cliffs, NJ) 1982

[2] J. Szargut, D R Morris, F R Steward, Energy analysis of thermal, chemical, and metallurgical processes

(Hemisphere publishing corporation, Springler-Verlag, NJ) 1988.
[3] T. J. Kotas, The exergy method of thermal plant analysis, 2nd edn, (Krieger publishing company, USA) 1995.
[4] A. Bejan, G. Tsatsaronis, M. Moran, Thermal Design and Optimization (John Wiley & Sons, INC.) 1996.
[5] M Kanoglu, Exergy analysis of the multistage cascade refrigeration cycle used for natural gas liquefaction, Int J Energy Res., 2002
[6] A. Bejan, Theory of heat transfer irreversible refrigeration plants, Int J Heat mass transfer, 32(9), 1989, 1631-39.
[7] G. Wall, Optimization of refrigeration machinery, Int J Ref, 14, 1999, 336-340.
[8] C. Nikolaidis, D. Probert, Exergy method analysis of a two stage vapour-compression refrigeration-plants performance, Applied energy, 60, 1998, 241-256
[9] R Yumrutas, M. Kunduz, M. Kanoglu, Exergy analysis of vapour compression refrigeration systems, Exergy, an Int J, 2, 2002, 266-272